

RECENT ADVANCES in POWER SYSTEMS, ENERGY, ENVIRONMENT

**Proceedings of the 2014 International Conference on Power Systems,
Energy, Environment (PSEE 2014)**

**Interlaken, Switzerland
February 22-24, 2014**

RECENT ADVANCES in POWER SYSTEMS, ENERGY, ENVIRONMENT

**Proceedings of the 2014 International Conference on Power Systems,
Energy, Environment (PSEE 2014)**

**Interlaken, Switzerland
February 22-24, 2014**

Copyright © 2014, by the editors

All the copyright of the present book belongs to the editors. All rights reserved. No part of this publication may be reproduced, stored in a retrieval system, or transmitted in any form or by any means, electronic, mechanical, photocopying, recording, or otherwise, without the prior written permission of the editors.

All papers of the present volume were peer reviewed by no less than two independent reviewers. Acceptance was granted when both reviewers' recommendations were positive.

Energy, Environmental and Structural Engineering Series - 22

ISSN: 2227-4359

ISBN: 978-1-61804-221-7

RECENT ADVANCES in POWER SYSTEMS, ENERGY, ENVIRONMENT

**Proceedings of the 2014 International Conference on Power Systems,
Energy, Environment (PSEE 2014)**

**Interlaken, Switzerland
February 22-24, 2014**

Organizing Committee

General Chairs (EDITORS)

- Professor Aida Bulucea,
University of Craiova,
Craiova, Romania
- Professor Eduardo Mario Dias
Electrical Energy and Automation
Engineering Department /
Escola Politecnica da Universidade de Sao Paulo
Brazil

Senior Program Chair

- Lecturer Dr. George Tsekouras
Hellenic Naval Academy, Greece

Program Chairs

- Professor Germano Lambert-Torres,
Itajuba, MG,
Brazil
- Professor Claudio Talarico,
Gonzaga University, Spokane,
WA, USA
- Professor Zhuo Li,
Beijing University Of Technology,
Beijing, China

Tutorials Chair

- Professor Pradip Majumdar
Department of Mechanical Engineering
Northern Illinois University
DeKalb, Illinois, USA

Special Session Chair

- Professor Shuliang Li,
The University of Westminster,
London, UK

Workshops Chair

- Prof. Frangiskos V. Topalis,
National Technical University of Athens,
Greece

Local Organizing Chair

- Professor Jan Awrejcewicz,
Technical University of Lodz,
Lodz, Poland

Publication Chair

- Professor Vincenzo Niola
Departement of Mechanical Engineering for Energetics
University of Naples "Federico II"
Naples, Italy

Publicity Committee

- Professor Fotios Rigas,
School of Chemical Engineering,
National Technical University of Athens,
Greece
- Professor Myriam Lazard
Institut Supérieur d'Ingenierie de la Conception
Saint Die, France

International Liaisons

- Prof. Jiri Klima,
Technical faculty of CZU in Prague,
Czech Republic
- Prof. P. Pardalos, Department of
Industrial and Systems Engineering,
University of Florida, USA
- Professor S. Sohrab,
Northwestern University, IL,
USA

Steering Committee

- Professor Aida Bulucea, University of Craiova, Romania
- Professor Zoran Bojkovic, Univ. of Belgrade, Serbia
- Professor Claudio Talarico, Gonzaga University, Spokane, USA
- Professor Imre Rudas, Obuda University, Budapest, Hungary

Program Committee

Prof. Germano Lambert-Torres, Itajuba, MG, Brazil
Prof. Jiri Klima, Technical faculty of CZU in Prague, Czech Republic
Prof. Goricanec Darko, University of Maribor, Maribor, Slovenia
Prof. Ze Santos, Rua A, 119. Conj. Jardim Costa do Sol, Brazil
Prof. Ehab Bayoumi, Chalmers University of Technology, Goteborg, Sweden
Prof. Luis Tavares Rua, Cmte Guyubricht, 119. Conj. Jardim Costa do Sol. Atalaia, Brazil
Prof. Igor Kuzle, Faculty of electrical engineering and computing, Zagreb, Croatia
Prof. Nikolay Djagarov, Technical University of Varna, Bulgaria
Prof. Darko Goricanec, University of Maribor, Maribor, Slovenia
Prof. Maria do Rosario Alves Calado, University of Beira Interior, Portugal
Prof. Gheorghe-Daniel Andreescu, "Politehnica" University of Timisoara, Romania
Prof. Patricia Jota, Av. Amazonas 7675, BH, MG, Brazil
Prof. Frangiskos V. Topalis, National Technical University of Athens, Greece
Prof. Bharat Doshi, John Hopkins University, Maryland, USA
Prof. Gang Yao, University of Illinois at Urbana - Champaign, USA
Prof. Lu Peng, Louisiana State University, Baton Rouge, LA, USA
Prof. Pavel Loskot, Swansea University, UK
Prof. N. Afgan, UNESCO Chair Holder, Instituto Superior Tecnico, Lisbon, Portugal
Prof. F. Akgun, Gebze Kocaeli, Turkey
Prof. Y. Baudoin, Royal Military Academy, Brussels, Belgium
Prof. M. Dasenakis, Dept. of Chemistry, University of Athens, Greece.
Prof. G. E. Froudakis, University of Crete, Herakleion, Greece
Prof. R.S.R. Gorla, Cleveland State University, Cleveland, Ohio, USA
Prof. M. Heiermann, Dr., Department of Technology Assessment and Substance Flow, Potsdam, Germany
Prof. C. Helmis, University of Athens, Athens, Greece
Prof. I. Kazachkov, National Technical University of Ukraine (NTUU KPI), Kyiv, Ukraine
Prof. A. M.A. Kazim, UAE University, United Arab Emirates
Prof. G. Kiriakidis, University of Crete, Herakleion, Greece
Prof. D. Kotzias, Institute for Health and Consumer Protection, European Commission-Joint Research Centre, Italy
Prof. A. Kurbatskiy, Novosibirsk State University, Department of Physics, Russia
Prof. S. Linderoth, Head of Research on Fuel Cells and Materials Chemistry at Riso National Laboratory. Denmark
Prof. P. Lunghi, Dipartimento di Ingegneria Industriale, University degli Studi di Perugia, Italy
Prof. C. Makris, A, Department of Computer Engineering and Informatics., University of Patras, Greece
Prof. J. Van Mierlo, Department of Electrotechnical Engineering and Energy Technology (ETEC) Vrije Universiteit Brussel, Belgium
Prof. S. Ozdogan, Marmara University, Goztepe Campus, Kuyubasi, Kadikoy, Istanbul, Turkey
Prof. P. Pardalos, Department of Industrial and Systems Engineering, University of Florida, USA
Prof. I. Poullos, Dept. of Chemistry, Aristotle University of Thessaloniki, Greece.
Prof. F. Rigas, School of Chemical Engineering, National Technical University of Athens, Greece.
Prof. S. Sohrab, Northwestern University, IL, USA
Prof. A. Stamou, National Technical University of Athens, Greece
Prof. A. I. Zouboulis, Dept. of Chemistry, Aristotle University of Thessaloniki, Greece.
Prof. Z. A. Vale, ISEP - Instituto Superior de Engenharia do Porto Rua António Bernardino de Almeida, Portugal

Additional Reviewers

Matthias Buyle	Artesis Hogeschool Antwerpen, Belgium
Lesley Farmer	California State University Long Beach, CA, USA
Deolinda Rasteiro	Coimbra Institute of Engineering, Portugal
Sorinel Oprisan	College of Charleston, CA, USA
Santoso Wibowo	CQ University, Australia
Yamagishi Hiromitsu	Ehime University, Japan
Kei Eguchi	Fukuoka Institute of Technology, Japan
Shinji Osada	Gifu University School of Medicine, Japan
Tetsuya Yoshida	Hokkaido University, Japan
Xiang Bai	Huazhong University of Science and Technology, China
Philippe Dondon	Institut polytechnique de Bordeaux, France
José Carlos Metrôlho	Instituto Politecnico de Castelo Branco, Portugal
João Bastos	Instituto Superior de Engenharia do Porto, Portugal
Takuya Yamano	Kanagawa University, Japan
Hessam Ghasemnejad	Kingston University London, UK
Konstantin Volkov	Kingston University London, UK
Eleazar Jimenez Serrano	Kyushu University, Japan
Jon Burley	Michigan State University, MI, USA
Manoj K. Jha	Morgan State University in Baltimore, USA
Frederic Kuznik	National Institute of Applied Sciences, Lyon, France
Stavros Ponis	National Technical University of Athens, Greece
Ole Christian Boe	Norwegian Military Academy, Norway
Imre Rudas	Obuda University, Budapest, Hungary
Masaji Tanaka	Okayama University of Science, Japan
Francesco Rotondo	Polytechnic of Bari University, Italy
George Barreto	Pontificia Universidad Javeriana, Colombia
Dmitrijs Serdjuks	Riga Technical University, Latvia
Andrey Dmitriev	Russian Academy of Sciences, Russia
Tetsuya Shimamura	Saitama University, Japan
Francesco Zirilli	Sapienza Universita di Roma, Italy
Minhui Yan	Shanghai Maritime University, China
Valeri Mladenov	Technical University of Sofia, Bulgaria
Jose Flores	The University of South Dakota, SD, USA
James Vance	The University of Virginia's College at Wise, VA, USA
Genqi Xu	Tianjin University, China
Zhong-Jie Han	Tianjin University, China
Kazuhiko Natori	Toho University, Japan
Moran Wang	Tsinghua University, China
M. Javed Khan	Tuskegee University, AL, USA
Bazil Taha Ahmed	Universidad Autonoma de Madrid, Spain
Alejandro Fuentes-Penna	Universidad Autónoma del Estado de Hidalgo, Mexico
Miguel Carriegos	Universidad de Leon, Spain
Angel F. Tenorio	Universidad Pablo de Olavide, Spain
Abelha Antonio	Universidade do Minho, Portugal

Table of Contents

Plenary Lecture 1: Discrete Lyapunov Controllers for an Actuator in Camless Engines <i>Paolo Mercorelli</i>	13
Plenary Lecture 2: EMG-Analysis for Intelligent Robotic based Rehabilitation <i>Thomas Schrader</i>	14
Plenary Lecture 3: Atmospheric Boundary Layer Effects on Aerodynamics of NREL Phase VI Windturbine in Parked Condition <i>Mohammad Moshfeghi</i>	15
Plenary Lecture 4: Laminar and Turbulent Simulations of Several TVD Schemes in Two-Dimensions <i>Edisson S. G. Maciel</i>	16
Plenary Lecture 5: The Flocking Based and GPU Accelerated Internet Traffic Classification <i>Zhiguang Xu</i>	18
Plenary Lecture 6: The State of Civil Political Culture among Youth: Goals and Results of Education <i>Irina Dolinina</i>	19
Modelling and Cost Estimation of Stirling Engine for CHP Applications <i>Ana C. Ferreira, Ricardo F. Oliveira, Manuel L. Nunes, Luís B. Martins, Senhorinha F. Teixeira</i>	21
Energy-Economical Efficiency of Building Heating and Cooling by Heat Pump Systems <i>Ioan Sarbu, Daniel Dan, Calin Sebarchievici</i>	30
Problems of Fast Frequency Variation Control in Interconnected Power Systems <i>V. Chuvychin, A. Sauhats, R. Petrichenko, G. Bochkarjova</i>	38
A Robust Stabilizer H₂-PSS Applied to Power System (Application under GUI/MATLAB) <i>Ghouraf Djamel Eddine, Nacéri Abdellatif</i>	44
The Stochastic Approach for Determination of Transmission Line Wire Cross Section <i>Lubov Petrichenko, Antans Sauhats, Svetlana Guseva, Svetlana Berjozkina, Viktoria Neimane</i>	50
Multi-Objective Optimization using NDSPSO with Cost, Emission and Loss Objectives <i>S. Sivanagaraju, Ch. V. Suresh, K. Srikumar, A. V. Naresh Babu</i>	57
Study of the Voltage Stability of Distribution Network Connected Induction Machines <i>Trinh Trong Chuong, Truong Viet Anh</i>	63
Genetic-based Neuro-Fuzzy Design of FACTS Controller in Power System <i>Sattar Jaber Al-Isawi</i>	69

The Efficiency of the Active Power Filters in High Power DC Drive Systems	74
<i>B. Miedzinski, A. Kozlowski, J. Wosik, M. Kalus</i>	
A Comparative Analysis of UPQC-P, UPQC-Q and UPQC-VAmin - A Simulation Study	80
<i>Yash Pal, A. Swarup</i>	
A MULTISCALE-based Model for Composite Materials with Embedded PZT Filaments	86
<i>Tarek M. Hatem, Mohamed Abdel-Meguid</i>	
An Approach for Optimal Placement, Rating and Investment Cost Recovery of a TCSC in Double Auction Power Market	91
<i>Prashant Kumar Tiwari, Yog Raj Sood</i>	
Influence of Environmental Parameters on Spatial Distribution of Pollen Grains in Columbia Basin	98
<i>Peter Šiška, Štefan Poláček</i>	
Android Application Front-end for an Energy Brokerage Agent	105
<i>Christos Petsos, Kostas Kalogirou, Evangelos Bekiaris</i>	
Distribution System Analysis with Time Varying Winter Load and Growth	111
<i>V. V. S. N. Murty, Ashwani Kumar</i>	
Assessment of Restructured Indian Power Sector: Availability, Demand and Shortage	118
<i>Yog Raj Sood, Rajnish Shrivastava, Naveen Kumar Sharma</i>	
A Robust AVR-PSS Synthesis using Genetic Algorithms (Application under GUI/MATLAB)	123
<i>Ghouraf Djamel Eddine, Kabi Wahiba, Naceri Abdellatif, Horch Abdessamed</i>	
Energy Efficiency Potential Assessment and Ranking for Schools in Teresina City	130
<i>E. K. Yamakawa, A. R. Aoki, L. C. Siebert, J. F. Silva Filho, J. B. Lopes, W. G. R. Lopes</i>	
Power Management System in Electro-Solar Vehicle	134
<i>Hemza Saidi, Abdelhamid Mudoun</i>	
Optimal DFIG Location and Impact of Load Model in Pool Electricity Market	149
<i>Ashwani Kumar, Manish Kumar, K. S. Sandhu</i>	
MODELING of Dislocation Evolution in Multi-Junction based Photovoltaic Devices	157
<i>Tarek M. Hatem, Mohamed T. Elewa</i>	
On an Accurate Estimation of HV Insulators Contamination: Combined Image Statistical Features and Neural Networks Approach	160
<i>Luqman Maraaba, Hussain Al-Duwaish, Zakariya Al-Hamouz</i>	

Intelligent Control of DFIG based Variable Speed Wind Turbine System using Artificial Neural Network	166
<i>Sathans, Jitender Rohilla</i>	
Daylighting Rules of Thumb and a Comparison of Different Floor Depth under Overcast and Intermediate Sky Without Sun	173
<i>M. F. M. A. Sadin, N. L. N. Ibrahim, K. Sopian, E. Salleh</i>	
Ecological Refrigerants used in Refrigeration, Airconditioning and Heat Pump Systems	178
<i>Ioan Sarbu, Emilian Stefan Valea</i>	
Ordinal Optimization Approach to Power System Objectives in the Presence of SVC and TCSC	185
<i>K. Srikumar, Ch. V. Suresh, S. Sivanagaraju, V. Ganesh</i>	
Removal of Anionic Dyes from Aqueous Solutions using Local Activated Kaolins as Adsorbers	191
<i>F. Z. El Berrichi, S. Zen</i>	
Plasma-Assisted Ignition and Combustion of Pulverized Coal at Thermal Power Plants of Kazakhstan	197
<i>V. E. Messerle, A. B. Ustimenko, O. A. Lavrichshev</i>	
A Novel STATCOM Wide Area Feedback Controller for Improving Stability in Multimachine System	204
<i>Aman Ganesh, Ratna Dahiya, G. K. Singh</i>	
Sliding Mode Control of Chopper Connecting Wind Turbine with Grid based on Synchronous Generator	211
<i>Ahmed Tahour, Abdel Ghani Aissaoui, Mohamed Abid, Najib Essounbouli, Frederic Nollet</i>	
The Fundamental Problems of Transmission of Data and Voice by Using PLC via High Voltage Lines	216
<i>Javad Abdi, Azam FamilKhalili</i>	
Economic Analysis of Wind Turbine Using New Cost Model	220
<i>Sahil Bajaj, Kanwarjit Singh Sandhu</i>	
Comparative Germination Studies in Mature Seeds of Haloxylon Salicornicum	224
<i>L. Almulla</i>	
Applying GIS to Assessment of Ecosystems in the Landscape Level Case Study from the Czech Republic	227
<i>Vilém Pechanec, Ivo Machar, Aleš Vávra, Helena Kiliánová</i>	
Controlled Output of Wind Turbine during Wind Variations	232
<i>Navjot Singh Sandhu, Shelly Vadhera, Kanwarjit Singh Sandhu</i>	

Comparison for Performance and Exhaust Emissions of Steam Injected and Thermal Barrier Layer (TBL) Coated Piston Spark Ignition Engine	236
<i>Adnan Parlak, Idris Cesur, Vezir Ayhan, Barış Boru, Görkem Kökkülünk</i>	
Authors Index	240

Plenary Lecture 1

Discrete Lyapunov Controllers for an Actuator in Camless Engines



Professor Paolo Mercorelli
Leuphana University of Lueneburg
Germany
E-mail: mercorelli@uni.leuphana.de

Abstract: This paper deals with a hybrid actuator composed by a piezo and a hydraulic part controlled using two cascade Lyapunov controllers for camless engine motor applications. The idea is to use the advantages of both, the high precision of the piezo and the force of the hydraulic part. In fact, piezoelectric actuators (PEAs) are commonly used for precision positionings, despite PEAs present nonlinearities, such as hysteresis, saturations, and creep. In the control problem such nonlinearities must be taken into account. In this paper the Preisach dynamic model with the above mentioned nonlinearities is considered together with cascade controllers which are Lyapunov based. The sampled control laws are derived using the well known Backward Euler method. An analysis of the Backward and Forward Euler method is also presented. In particular, the hysteresis effect is considered and a model with a switching function is used also for the controller design. Simulations with real data are shown.

Brief Biography of the Speaker: Paolo Mercorelli received the (Laurea) M.S. degree in Electronic Engineering from the University of Florence, Florence, Italy, in 1992, and the Ph.D. degree in Systems Engineering from the University of Bologna, Bologna, Italy, in 1998. In 1997, he was a Visiting Researcher for one year in the Department of Mechanical and Environmental Engineering, University of California, Santa Barbara, USA. From 1998 to 2001, he was a Postdoctoral Researcher with Asea Brown Boveri, Heidelberg, Germany. From 2002 to 2005, he was a Senior Researcher with the Institute of Automation and Informatics, Wernigerode, Germany, where he was the Leader of the Control Group. From 2005 to 2011, he was an Associate Professor of Process Informatics with Ostfalia University of Applied Sciences, Wolfsburg, Germany. In 2010 he received the call from the German University in Cairo (Egypt) for a Full Professorship (Chair) in Mechatronics which he declined. In 2011 he was a Visiting Professor at Villanova University, Philadelphia, USA. Since 2012 he has been a Full Professor (Chair) of Control and Drive Systems at the Institute of Product and Process Innovation, Leuphana University of Lueneburg, Lueneburg, Germany.

Research interests: His current research interests include mechatronics, automatic control, signal processing, wavelets; sensorless control; Kalman filter, camless control, knock control, lambda control, robotics.

The full paper of this lecture can be found on page 19 of the Proceedings of the 2014 International Conference on Circuits, Systems and Control, as well as in the CD-ROM proceedings.

Plenary Lecture 2

EMG-Analysis for Intelligent Robotic based Rehabilitation

Professor Thomas Schrader

University of Applied Sciences Brandenburg
Germany

E-mail: thomas.schrader@computer.org

Abstract: The establishment of wireless sensor network (WSN) technology in physiotherapy and rehabilitation is a clue for improvement of the therapeutic process, quality assessment and development of supporting technologies such as robotics. Especially for complex therapeutic interventions such as sensorimotor training, a continuous monitoring during the therapy as well as for all sessions would be quite useful. For the usage of robotic support in rehabilitation various input information about the status of patient and his/her activity status of various muscles have to be detected and evaluated. The critical point for robotic intervention is the response time. Under physiotherapeutic and rehabilitation conditions, the robotic device should be able to react differently and in various patterns. A complex analysis procedure of input signals such as EMG is essential to ensure an effective response of the robot. However sensor nodes in a wireless (body) area network have limited resources for calculating and storage processes. A stepwise procedure with distributed analysis tasks is proposed. Electromyogram (EMG) measurements of eight muscles were collected and evaluated in an experimental setting of a sensorimotor training using different types of balance boards. Fast and easy methods for detection of activity and rest states based on time domain analysis using low pass IIR filter und dynamic threshold adaption. These procedures can be done on the sensor nodes themselves or special calculation nodes in the network. More advanced methods in frequency domain or analysis of dynamical system behavior request much more system power in calculation as well as storage. These tasks could be done on the level of mobile devices such as mobile phones or tablet computer. A broad range of resources can be provided by cloud/internet. Such level based organization of analysis and system control can be compared with biological systems such as human nervous system.

Plenary Lecture 3

Atmospheric Boundary Layer Effects on Aerodynamics of NREL Phase VI Windturbine in Parked Condition



Professor Mohammad Moshfeghi
Sogang University, South Korea
E-mail: mmoshfeghi@sogang.ac.kr

Abstract: In a natural condition, the wind is affected by the groundcover and the type of terrains which impose vertical velocity profile to the wind. This wind profile, which is also called atmospheric boundary layer (ABL), dramatically influences the aerodynamic behaviors and loadings of horizontal axis wind turbines. However, for the sake of simplicity, many numerical simulations only deal with the uniform wind speed. To consider the effects of the ABL, numerical simulations of the two-bladed NREL Phase VI wind turbines aerodynamic at the parked condition are conducted under both uniform and ABL. The Deaves-Harris (DH) model is applied to the ABL. The wind turbine blades are kept at the six o'clock position and are considered at two different pitch angles. The aerodynamic forces and moments of the uniform the DH model are compared. The results show that the pitch angle at which the HAWT is parked plays an important role on the blade loading. Also it is observed that for the fully separated conditions, the Down-blade and the blade in the uniform wind are under approximately similar aerodynamic loadings, while the Up-blade encounters more aerodynamic loads, which is even noticeable value for this small wind turbine. This in turn means that for an appropriate and exact design, effects of ABL should be considered with more care.

Brief Biography of the Speaker: Dr. Mohammad Moshfeghi works in Multi-phenomena CFD Engineering Research Center (ERC) Sogang University, Seoul, South Korea. He is also Lecturer in Qazvin Azad University. He has a registered patent: "Split-Blade For Horizontal Axis Wind Turbines" (Inventors: Mohammad Moshfeghi, Nahmkeon Hur).

Plenary Lecture 4

Laminar and Turbulent Simulations of Several TVD Schemes in Two-Dimensions



Professor Edison S. G. Maciel

Federal University of Great Dourados, Brazil

E-mail: edisavio@edissonsavio.eng.br

Abstract: This work, first part of this study, describes five numerical tools to perform perfect gas simulations of the laminar and turbulent viscous flow in two-dimensions. The Van Leer, Harten, Frink, Parikh and Pirzadeh, Liou and Steffen Jr. and Radespiel and Kroll schemes, in their first- and second-order versions, are implemented to accomplish the numerical simulations. The Navier-Stokes equations, on a finite volume context and employing structured spatial discretization, are applied to solve the supersonic flow along a ramp in two-dimensions. Three turbulence models are applied to close the system, namely: Cebeci and Smith, Baldwin and Lomax and Spalart and Allmaras. On the one hand, the second-order version of the Van Leer, Frink, Parikh and Pirzadeh, Liou and Steffen Jr., and Radespiel and Kroll schemes is obtained from a “MUSCL” extrapolation procedure, whereas on the other hand, the second order version of the Harten scheme is obtained from the modified flux function approach. The convergence process is accelerated to the steady state condition through a spatially variable time step procedure, which has proved effective gains in terms of computational acceleration (see Maciel). The results have shown that, with the exception of the Harten scheme, all other schemes have yielded the best result in terms of the prediction of the shock angle at the ramp. Moreover, the wall pressure distribution is also better predicted by the Van Leer scheme. This work treats the laminar first- and second-order and the Cebeci and Smith second- order results obtained by the five schemes.

Brief Biography of the Speaker: Professor Edison Sávio de Góes Maciel was born in Recife, Pernambuco, Brazil in 1969, February, 25. He studied in Pernambuco until obtains his Master degree in Thermal Engineering, in 1996, August. With the desire of study aerospace and aeronautical problems using numerical methods as tools, he obtains his Doctor degree in Aeronautical Engineering, in 2002, December, in ITA and his Post-Doctor degree in Aerospace Engineering, in 2009, July, also in ITA. He is currently Professor at UFGD (Federal University of Great Dourados) – Mato Grosso do Sul – Brasil. He is author in 47 papers in international journals, 2 books, 67 papers in international conference proceedings. His research interestes includes a) Applications of the Euler equations to solve inviscid perfect gas 2D and 3D flows (Structured and unstructured discretizations) b) Applications of the Navier-Stokes equations to solve viscous perfect gas 2D and 3D flows (Structured and unstructured discretizations) c) Applications of the Euler and Navier-Stokes to solve magneto gas dynamics flows 2D and 3D; (Structured and unstructured discretizations) d) Applications of algebraic, one-equation, and two-equations turbulence models to predict turbulent effects in viscous 2D flows (Structured and unstructured discretizations), e) Study of artificial dissipation models to centered schemes

in 2D and 3D spaces (Structured and unstructures discretizations) f)Applications of the Euler and Navier-Stokes equations to solve reentry flows in the Earth atmosphere and entry flows in Mars atmosphere in 2D and 3D (Structured and unstructured discretizations).

The full paper of this lecture can be found on page 79 of the Proceedings of the 2014 International Conference on Mechanics, Fluid Mechanics, Heat and Mass Transfer, as well as in the CD-ROM proceedings.

Plenary Lecture 5

The Flocking Based and GPU Accelerated Internet Traffic Classification



Professor Zhiguang Xu
Valdosta State University
USA
E-mail: zxu@valdosta.edu

Abstract: Mainstream attentions have been brought to the issue of Internet traffic classification due to its political, economic, and legal impacts on appropriate use, pricing, and management of the Internet. Nowadays, both the research and operational communities prefer to classify network traffic through approaches that are based on the statistics of traffic flow features due to their high accuracy and improved robustness. However, these approaches are faced with two main challenges: identify key flow features that capture fundamental characteristics of different types of traffic in an unsupervised way; and complete the task of traffic classification with acceptable time and space costs. In this paper, we address these challenges using a biologically inspired computational model that imitates the flocking behavior of social animals (e.g. birds) and implement it in the form of parallel programs on the Graphics Processing Unit (GPU) based platform of CUDA from NVIDIA™. The experimental results demonstrate that our flocking model accelerated by GPU can not only effectively select and prioritize key flow features to classify both well-known and unseen network traffic into different categories, but also get the job done significantly faster than its traditional CPU-based counterparts due to the high magnitude of parallelism that it exhibits.

Brief Biography of the Speaker: Prof. Zhiguang Xu received his Ph.D. in Computer Science from University of Central Florida, FL, USA in 2001. He is currently Professor of Computer Science in the Department of Math and Computer Science at Valdosta State University, GA, USA. His research and teaching interests include Computer Networking, Artificial Intelligence, Parallel and Distributed Computing, and Computer Science Education. Professor Xu is author or co-author of more than 25 published papers in refereed journals or conference proceedings. He has been awarded many grants from both academic and industrial entities. He is actively serving as committee member, reviewer, or lecturer of many national and international conferences and organizations.

The full paper of this lecture can be found on page 88 of the Proceedings of the 2014 International Conference on Mathematical Methods, Mathematical Models and Simulation in Science and Engineering, as well as in the CD-ROM proceedings.

Plenary Lecture 6

The State of Civil Political Culture among Youth: Goals and Results of Education



Professor Irina Dolinina

Perm National Research University, Russia

E-mail: irina_edu@mail.ru

Abstract: Political culture is viewed as a phenomenon of social reality. Attitudes toward it (its meaning or significance) are historically conditioned. This research studies enduring presuppositions about (dispositions toward) society and the state, and how these are reflected in conscious stereotypes and cognitive structures among young people within the sociocultural mechanisms that form and modify the basic characteristics of political culture.

Brief Biography of the Speaker: Prof. Irina Dolinina was born in 1960, in Perm, Russia. She is Team Leader in the Research Project «Formation of the political culture of the students», and Professor of Philosophy and Law of the Faculty of Humanities, Perm National Research Technical University since 2012. She has received a lot of honors and awards (2012 - Diploma of the All-Russian Roswitha fund national education and the Education Committee of the State Duma of the Federal Assembly of the Russian Federation. 2013 - Diploma of the All-Russian Roswitha fund national education and the Education Committee of the State Duma of the Federal Assembly of the Russian Federation. Diploma-Russian contest "Best Science Book in the humanitarian sphere - 2013). Prof. Dolinina has various professional organizations and activities.

(Expert on the legislative activities of the Council of Federation of Russia. Board member of the Interregional Association "For civic education." Director of the Research Centre of the political culture).

The full paper of this lecture can be found on page 57 of the Proceedings of the 2014 International Conference on Educational Technologies and Education, as well as in the CD-ROM proceedings.

Modelling and Cost Estimation of Stirling Engine for CHP Applications

Ana C. Ferreira, Ricardo F. Oliveira, Manuel L. Nunes, Luís B. Martins, and Senhorinha F. Teixeira

Abstract—Thermodynamic analysis of the Stirling engine's performance has been conducted, using specially designed computing codes along with the thermal balance study of the technology. The performance of the unit has been evaluated considering different operational conditions, which include the electrical and thermal production, working fluid mean pressure or mass, components geometrical sizing. The thermal-economic evaluation represents an effective tool to optimize a power plant with this type of technology. This study presents a mathematical model that includes a set of equations able to describe and simulate the physical system, as well as a set of equations that define the cost of each plant component. This paper presents a numerical study faithfully simulating the real conditions of a micro-CHP unit based on an alpha type Stirling Engine. The simulations were performed through a MatLab® code that assesses the thermodynamic efficiency, including heat transfer limitations and pumping losses throughout the system. Results showed the Stirling engine performance depends on geometrical and physical parameters which optimization is required in order to obtain the best performance. It is verified that cost estimation based on sizing and quality parameters has a good correlation with the capital investment costs of commercial models.

Keywords—CHP Applications, High-efficient energy conversion, Stirling engines, Cost estimation.

I. INTRODUCTION

CURRENTLY, there is a strong pressure for the development of energy systems able to deliver a less pollutant and more efficient energy conversion process. The growing worldwide demand for those energy conversion

systems has led to a renewed attention in the use of cogeneration technologies. The concept of micro-Combined Heat and Power (μ -CHP) or micro cogeneration has been a known for long time. Cogeneration systems have the ability to produce both useful thermal energy and electricity from a single source of fuel. Concerning to this framework, great interest has been shown in low power systems able to deliver an energy output of 1-10 kW_e [1], [2]. These power plants are specially designed to cover fairly higher heat loads, which appears to be a good opportunity to meet the global energy needs of households [3].

Stirling Engines (SE) technology is based on an external combustion or other external heat-source, thus allowing the use of different primary energy sources including fossil fuels (oil derived or natural gas) and renewable energies (solar or biomass). In these engines, the working gas (e.g. helium, hydrogen, nitrogen or air) operates on a closed regenerative thermodynamic cycle, with cyclic compression and expansion of the working gas at different temperature levels [4]. Despite the fact that this technology is not widely used, there is a proved interest on Stirling engines because of their high-global efficiency, good performance at partial load, fuel flexibility and low gas and noise emission levels [5]. Stirling engines have the potential of achieving higher efficiencies because they closely approach the Carnot cycle. Presently, these engines are able to get an electrical efficiency of about 30% and a total efficiency of 85-98% (based on Low Heating Value, LHV) operating in cogeneration mode [6]. Commonly, the potential heat sources for SE operation are fossil fuels and solar energy. Nevertheless, more recently, several recent practical applications uses biomass or the waste heat as fuel [7]. Also, the nature of external combustion means that there is no transient combustion or mechanical valves; therefore with careful technical design, a low-noise and low-vibration system can be achieved. The SE is also characterized by longer operational lifetimes when compared with internal combustion engines.

Nevertheless, there are some limitations for SE technologies. Some components of the engine should be manufactured with special alloys because of the high temperature and pressure operational conditions endured by the system. This increases the production costs requiring, therefore, high investment costs. Plus, the choice of the "ideal" gas can bring some difficulties associated with its

The first author would like to express her acknowledgments for the support given by the Portuguese Foundation for Science and Technology (FCT) through the PhD grant SFRH/BD/62287/2009. This work was financed by National Funds-Portuguese Foundation for Science and Technology, under Strategic Project and PEst-OE/EME/UI0252/2011 and also the PEst-C/EME/UI4077/2011.

A. C. Ferreira is with CGIT R&D center, Department of Production and Systems, University of Minho, Guimarães, 4800-058 Portugal (corresponding author to provide e-mail: acferreira@dps.uminho.pt).

R. F. Oliveira is with the CT2M R&D center, Department of Mechanical Engineering, University of Minho, Guimarães, 4800-058 Portugal (e-mail: ricardo.falcao.oliveira@gmail.com).

M. L. Nunes is with CGIT R&D center, Department of Production and Systems, University of Minho, Guimarães, 4800-058 Portugal (e-mail: lnunes@dps.uminho.pt).

L. B. Martins is with the CT2M R&D center, Department of Mechanical Engineering, University of Minho, Guimarães, 4800-058 Portugal (e-mail: lmartins@dem.uminho.pt).

S. F. Teixeira is with CGIT R&D center, Department of Production and Systems, University of Minho, Guimarães, 4800-058 Portugal (e-mail: st@dps.uminho.pt).

ability to diffuse through materials, which works at high operation pressures.

Despite these limitative aspects of SE, this technology fulfils a number of requirements for thermal applications. Table I presents the actual energy requirements and the attractive features of the SE technology.

TABLE I. POWER PLANT NEEDS AND ATTRACTIVE FEATURES OF SE

Technological Needs	SE Characteristics
Reducing conventional fuels use	Flexible fuel sources
Increasing fossil fuel costs	Low fuel consumption
Use of alternative fuels	Low noise and vibrational levels
Reduction of gas emissions	Clean combustion
Waste heat recovery	High thermal efficiency

The Stirling engine performance depends on geometrical and physical features of the engine and on the working fluid properties, such as regenerator effectiveness, engine swept and dead volumes or the temperature of heat sources. Several studies have been reported in the literature concerning to the study of SE optimization for small and micro-scale applications. Puech and Tishkova [8] performed a thermodynamic analysis of a Stirling engine conducting an investigation about the influence of regenerator dead volume. The results showed that the dead volume amplifies the imperfect regeneration effect. Boucher et al. [9] related a theoretical study of the dynamic behaviour of a dual free-piston Stirling engine coupled with an asynchronous linear alternator. The objective was the evaluation of the thermo-mechanical conditions for a stable operation of the engine. Formosa and Despesse [10] developed an analytical thermodynamic model to study a free-piston Stirling engine architecture. The model integrated the analysis of the regenerator efficiency and conduction losses, the pressure drops and the heat exchangers effectiveness. The model was validated using the whole range of the experimental data available from the General Motor GPU-3 Stirling engine prototype. The influence of the technological and operating parameters on Stirling engine performance was investigated. The results from the simplified model and the data from the experiment showed a reasonable correlation. Rogdakis et al. [1] studied a Solo Stirling Engine V161 cogeneration module via a thermodynamic analysis. Calculations were conducted using different operational conditions concerning the heat load of the engine and the produced electrical power. The authors achieved good results in terms of electrical and thermal efficiencies as well as a positive primary energy saving.

Asnaghi et al. [11] also performed a numerical simulation and thermodynamic analysis of SOLO 161 Solar Stirling engine. He and his co-authors considered several imperfect working conditions, pistons' dead volumes, and work losses in the simulation process. According to their studies, regenerator effectiveness, heater and cooler temperatures, working gas, phase difference, average engine pressure, and dead volumes are parameters that affect Stirling engine

performance, which was estimated for different input considerations. Also, the results indicated that the increase in the heater and cooler temperature difference and the decrease in the dead volumes will lead to an increase in thermal efficiency. Kongtragool and Wongwises [12] investigated the effect of regenerator effectiveness and dead volume on the engine network; heat input and efficiency by using a theoretical investigation on the thermodynamic analysis of a Stirling engine.

Besides the thermodynamic efficiency evaluation, it is of utmost importance to integrate technical variables and the costs in order to simultaneously optimize the physical and the economic output.

Thermal-economics combines thermodynamic analysis and economic principles, in each of power plant components, in order to evaluate the costs of energy production. These analysis can be useful to disclose the most cost-effective components and thus in improvement of the overall system design [13]. This type of evaluation requires the definition of a thermodynamic and economic model of the system [14]. In literature, different studies can be found concerning the thermal-economic optimization of power plants for CHP applications, that apply different methodologies and approaches [13], [15]–[19].

The main objective of this study is to analyse an alpha Stirling engine (non-ideal analysis), by trying to disclose the best operational parameters for a SE engine for cogeneration applications. The paper presents a mathematical model able to describe the physical system, using a software-code developed in the MatLab® environment. The physical model was based on the work of Urieli and Berchowitz [20] while the cost equations were developed based on a methodology also applied in gas turbines optimization [14]. Cost equations depend on physical parameters that also affect the thermodynamic performance of the engine and the solution will be the combination of parameter values that will lead to the best economic output. The system costs are estimated for the best physical model result.

II. SYSTEM DESCRIPTION

This study is focused on the optimization of a CHP system based on a Stirling engine as prime mover, able to produce 1-5 kW of electricity and a larger heat load considering a heat-to-power ratio of about 3.5 to 5.0. This case study pretends to analyse a system able to fulfil the energy requirements of a residential dwelling. Accordingly to the literature [3], for individual dwellings, most decentralized energy systems are characterized by a thermal power output in the range of 2-35 kW_{th}.

The chosen alpha-Stirling configuration consists of two mechanically linked pistons located in separate cylinders that define the compression and expansion spaces. The working gas flows between these two spaces by alternate crossing of, a low temperature heat exchanger (cooler), a regenerator and a high temperature heat exchanger (heater), connected in series.

Thus, the engine is considered as a set of five connected components, consisting of the compression space (c), cooler (k), regenerator (r), heater (h) and the expansion space (e). Each engine component represents an entity endowed with its respective volume (V), temperature (T), absolute pressure (p) and mass (m). Fig. 1 shows a general representation of a SE with thermal interfaces.

Heat is transferred from the external heat source to the working gas in the heater, cyclically stored and recovered in the regenerator, and rejected by the working gas in the cooler. Thus, Stirling engine works between two temperatures T_h and T_c (hot and cold sink, respectively). These temperatures correspond to the values of 725 K and 353 K, respectively. The value for the hot temperature was assumed considering that the energy source is concentrated solar radiation. The cold sink of the engine is refrigerated by a mass flow of water which removes heat from the cooler to produce hot water. It was assumed that the mass flow of water is heated from 288 K to 343 K.

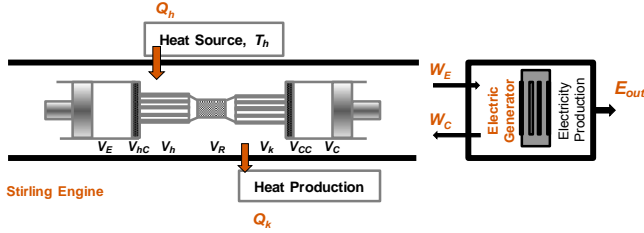


Fig. 1 Representation of a general Stirling Engine.

Several input parameters are required for the analysis. The mass of the operating gas is determined by the Schmidt analysis [21], which requires some design parameters: mean operating pressure (p_{mean}), cylinder swept volumes, clearance volumes, hot and cold temperatures.

Three working fluids have been previously studied [22]: air, helium and hydrogen. Hydrogen and helium were selected here to perform the numerical simulations due to their best results in terms of engine efficiency [23]. On one hand, the working gas should have a high thermal conductivity, for improved efficacy of the heat exchangers, and a low density and specific heat capacity so that a given amount of heat leads to a larger increase in pressure or volume. The combined property is the thermal diffusivity (thermal conductivity divided by density and heat capacity) and helium is the best option. On the other hand, a lower dynamic viscosity and density reduces the pumping losses, improving engine specific power and efficiency. Hydrogen scores better here, primarily because the engine can run at higher speeds [22].

III. MATHEMATICAL MODEL

A. Physical Model

The mathematical model in the present works integrates two analyses to reach the numerical solution of the thermodynamic cycle. Firstly, it invokes an Ideal Adiabatic simulation and, sequentially, a Non-ideal simulation that

evaluate the heat transfer and pressure loss effects in the Stirling engine [22].

In the adiabatic analysis, the model is treated as a "quasi steady-flow" system. A set of ordinary differential equations is iteratively solved, considering an initial-value problem in which the initial values of all the variables are known and the equations are integrated from that initial state over a complete engine cycle. The final state of the cycle is then used as a new initial-value for a new cycle and several iterations are made until cycle convergence is obtained. The resulting equations are linked by applying the mass and energy equations across the entire system. Enthalpy is transported by means of mass flow and temperature at each component. In the Ideal Adiabatic analysis, the energy equation can be written as in (1)

$$dQ + C_p T_{in} dm_{in} - C_p T_{out} dm_{out} = dW + C_v d(mT) \quad (1)$$

where the derivative operator is denoted by d , thus for example dm refers to the mass derivative $dm/d\theta$, where θ is crank the cycle angle.

After running the Ideal adiabatic analysis, the numerical process follows with a Non-Ideal simulation which includes the effects of non-perfect regeneration and the pumping losses. The term "pumping loss" refers to the work required to press on the working gas through the heat exchangers and regenerator, thus reducing the net power output of the engine. The non-ideal effects of the regeneration are mainly due to the convective thermal resistance between the gas and the regenerator surface, and can be modelled by using the Number of Transfer Units (NTU) method, with NTU defined in terms of a Stanton number (St), as in (2):

$$NTU = St \cdot \left(\frac{A_w}{A} \right) \cdot \frac{1}{2} \quad (2)$$

where A_w refers to the wall/gas, or "wetted" area of the heat exchanger surface and A is the free flow area through the matrix. The St can be defined as in (3):

$$St = \frac{h}{\rho u c_p} \quad (3)$$

where h is the convective heat transfer coefficient, ρ is the gas density, u is the velocity and c_p is the specific heat capacity of the gas. The factor 2 in Eq. (2) is due to the fact that St is usually defined for heat transfer from a gas stream to a wall, whereas in the cyclic process of the regenerator, heat is also transferred from the matrix to the gas flow. In the "loading" process, the hot working gas is pre-cooled, while flowing through the regenerator from the heater to the cooler, transferring heat to the regenerator matrix. Then, in the reverse process, the heat that was previously stored in the matrix is "discharged" and pre-heats the cold gas that flows into the heater and expansion space. The regenerator effectiveness for Stirling engines can be defined as the ratio between the real amount of heat transferred from the matrix to the working fluid and the maximum possible amount of pre-heating used in the ideal adiabatic model. The regenerator effectiveness can be obtained by (4).

$$\varepsilon_r = \frac{NTU}{1 + NTU} \quad (4)$$

The effectiveness of the heater and cooler can also be evaluated by NTU method, considering constraint wall temperatures. The heat exchanger effectiveness for both exchangers are defined as in (5).

$$\varepsilon = 1 - e^{-NTU} \quad (5)$$

The mean effective temperatures in the heater (T_h) and the cooler (T_k) are, respectively, lower and higher than the corresponding heat exchanger wall temperatures, heater ($T_{h,w}$) and cooler ($T_{k,w}$). This implies that the engine is operating between lower temperature limits than originally specified which effectively reduces the thermodynamic engine efficiency (see Fig. 2).

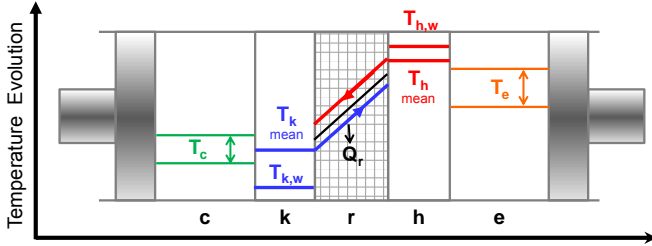


Fig. 2 Evolution of heater, cooler and regenerator effective temperatures for non-ideal analysis.

So, the total heat transfer can be calculated as in (6):

$$Q = h \cdot A_w (T_w - T) \quad (6)$$

where T_w is the wall temperature, and T the mean effective gas temperature (heater or cooler). As the temperatures are determined iteratively, Q_h and Q_k can be evaluated and the regenerator heat transfer reduction, $Q_{r,loss}$, is quantified in terms of the regenerator effectiveness. Thus, the reduction of heat transfer in the regenerator can be quantified as in (7).

$$Q_{r,loss} = (1 - \varepsilon_r) \cdot Q_{r,ideal} \quad (7)$$

The less heat transfer in the regenerator leads to increases in the heats of the hot and cold sources so that, the heat for both heat exchangers is determined in (8) and (9), respectively.

$$Q_k = Q_{k,ideal} + Q_{r,loss} \quad (8)$$

$$Q_h = Q_{h,ideal} + Q_{r,loss} \quad (9)$$

Fluid friction associated with the flow through the heat exchangers, results in a pressure drop, reducing the output power of the engine. The pressure drop (ΔP) is taken over the three heat exchangers and then, the value of the corresponding work can be achieved by integration over the complete cycle. The total engine work per cycle, W is given by (10):

$$W = \oint P(dV_e + dV_c) - \oint \sum \Delta P dV_e \quad (10)$$

where V_e and V_c are, respectively, the expansion and compression volumes. The first term in the equation represents the ideal adiabatic work done per cycle and the

second one represents the pressure drop per cycle, ΔW , converted to work loss, as in (11):

$$\Delta W = \int_0^{2\pi} \left(\sum_{i=1}^3 \Delta P_i \frac{dV_e}{d\theta} \right) \cdot d\theta \quad (11)$$

where θ is the crank angle. The pressure drop is evaluated by (12).

$$\Delta P = \frac{-2C_f \text{Re} \mu u V}{d^2 A} \quad (12)$$

where C_f is the friction coefficient, Re is the Reynolds number, μ and u are the gas viscosity and velocity, d is the hydraulic diameter of the small parallel passages and V the void volume. The friction coefficient is the non-dimensional wall shear-stress, calculated according to (13):

$$C_f = \frac{\tau}{0.5 \rho u^2} \quad (13)$$

where τ , is the wall shear stress, ρ is the working fluid density and u is velocity. The choice of working gas is typically made, considering the gas that allows the best efficiencies.

B. Cost Estimation of the Thermal Components

The mathematical expressions that define the cost of each component were based on the methodology developed by Marechal et al. [24]. The costing methodology consists on a derivation of an expression for each component by integrating thermodynamic and cost coefficients adjusted for this kind of technology and also taking into account real market data. Each cost equation was defined considering some of the physical variables that integrate the thermodynamic model. These variables can be divided in size and quality variables. In terms of methodology, the equations were defined considering that the cost of each component of the system, being defined a purchase cost equation representative of each component. Thus, the cost equation was defined according to: $C = C_{ref} F_m F_c$.

The term C_{ref} is the reference cost coefficient which corresponds to a cost per unit of (one or more than one) physical parameter. The term F_m is the sizing factor which scales the system component from a reference case, as presented in (14):

$$F_m = F_{ref} \cdot \left(\frac{F_i}{F_{ref}} \right)^b \quad (14)$$

where F_{ref} and F_i are the reference and the physical variable value and b the sizing exponent. Due to the high temperatures at which certain system components operates, an additional term can be included into the cost component equation. The temperature factor, F_T , can be defined as in (15).

$$F_T = \frac{1 + e^{C_i \cdot (T_i - T_{ref})}}{2} \quad (15)$$

This temperature factor was included into the purchase cost equation of the heater and the regenerator. The temperature factor is defined considering a constant, C_i , the reference and the effective temperature, T_i and T_{ref} , respectively.

As a result, the cost estimation can be performed in order to evaluate the overall cost of the system considering the cost share of each component. The purchase cost equations for heater, regenerator and cooler are presented by: (16), (17) and (18), respectively.

$$C_h = C_{11,h} \cdot A_{ref,wh} \cdot \left(\frac{A_{wh}}{A_{ref,wh}} \right)^{0.5} \cdot \left[\frac{1 + e^{C_{12,h} \cdot (T_h - 725)}}{2} \right] \quad (16)$$

$$C_r = C_{21,r} \cdot A_{ref,wr} \cdot \left(\frac{A_{wr}}{A_{ref,wr}} \right)^{0.6} \cdot \left[\frac{1 + e^{C_{22,r} \cdot (T_{reg} - 600)}}{2} \right] \quad (17)$$

$$C_k = C_{31,k} \cdot A_{ref,wk} \cdot \left(\frac{A_{wk}}{A_{ref,wk}} \right)^{0.4} \quad (18)$$

For the heater, regenerator and cooler, the equations relate the cost of the exchanger with its effective heat transfer area. In the specific case of the heater and regenerator, an additional correction term must be added in order to include the temperature effect in their cost. The design of these two special heat exchangers is affected by working fluid temperatures, pressures and the type of heat source. For instance, the flow at heater's outer surface is characterized by a high temperature, low-pressure steady conditions, while, in the internal surface, the fluid flows at high temperature and high pressure, subjected to turbulence. These constraints make these thermal components more expensive because of the materials used in their manufacture. Several correlations must be done before assuming the cost coefficients or the sizing exponents. The cost of each component is estimated considering a reference case from the available market. Reference values for the heat transfer area and cost coefficients are assumed by estimating their share in the total capital cost. Fig. 4 presents the regenerator cost estimation considering three different sizing exponents. The regenerator can be considered the heart of the Stirling engine; thus, adequate materials have to be used in its manufacturing because this special heat exchanger is responsible for the critical temperature changes in the working fluid. The heat transfer was calculated assuming that the regenerator has a fine wired matrix in order to improve the heat transfer process by exposing the maximum surface area of the matrix. Therefore, parameters such as the matrix porosity and the wire diameter are important to optimize in the design of the regenerator.

A cost equation representative of the engine body must be also included. Thus, the engine bulk cost equation can be defined as in (19).

$$C_{eng} = C_{41,eng} \left[V_{ref,eng} \left(\frac{V_{eng}}{V_{ref,eng}} \right)^{0.2} \cdot P_{ref,eng} \left(\frac{P_{eng}}{P_{ref,eng}} \right)^{0.2} \right] \quad (19)$$

The power of Stirling engines is affected by changing the operational parameters such as the pressure, phase angle, volume and speed.

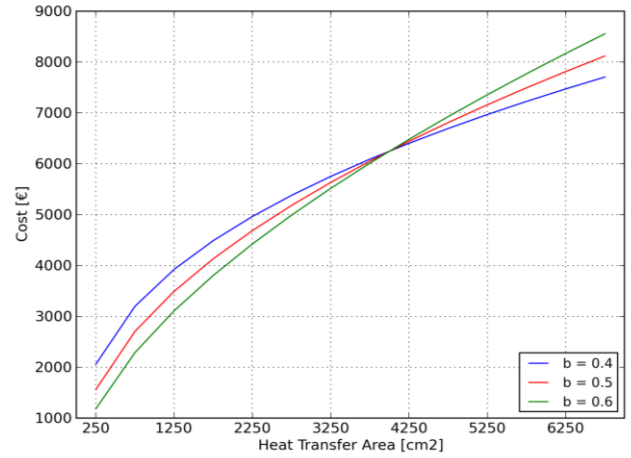


Fig. 4 Regenerator cost estimation.

Because of the complexity of system modelling, the engine bulk cost equation was estimated considering the volume and the mean pressure as the main relevant physical parameters in cost definition. Engine bulk cost includes the mean operational pressure of the system because of the proportionality between the mean pressure and the power output. Higher pressures also mean higher material costs and the need for better sealing solutions. Fig. 5 presents the engine bulk cost estimation as a function of the volume and mean operational pressure.

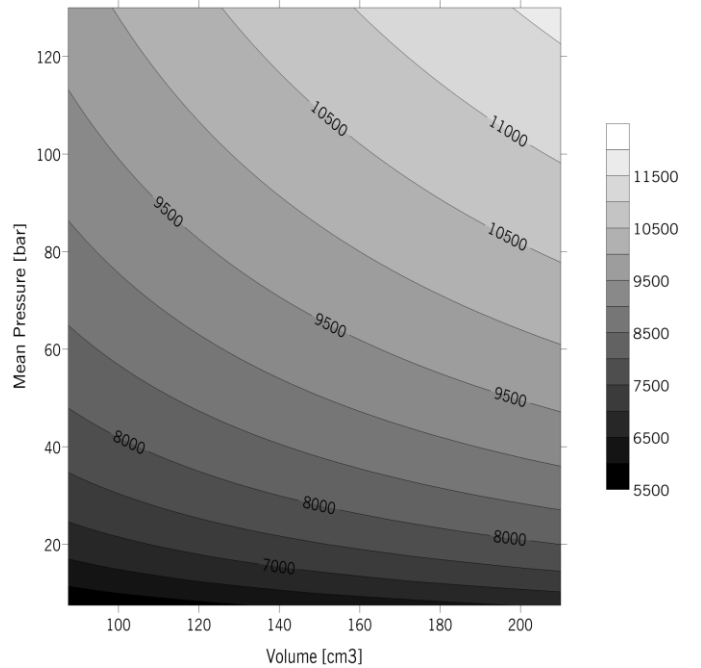


Fig. 5 Engine bulk cost estimation.

There is a significant variation on costs for different sizing parameters. Its choice must take into account the application and the power output of the thermal engine. Similar approaches were performed for the remaining components.

IV. RESULTS AND DISCUSSION

A. Physical Model

The simulations were carried out by running a non-ideal analysis which accounts for the pumping losses and the effects of non-perfect regeneration. Engine's geometric characteristics for the cooler, regenerator and heater, as well as the cylinders volumes and other operating input parameters were defined as in table II. Simulations were carried out considering the heater and the cooler as smooth pipes and the regenerator a wired matrix. The geometric input parameters for the heat exchangers were already presented in [22].

TABLE II. INPUT PARAMETERS FOR SIMULATIONS

Parameter,	value
Cooler volume V_k ,	106 cm ³
Heater volume V_h ,	84.8 cm ³
Regenerator Volume V_r ,	69.8 cm ³
Cylinders Swept volumes,	130 cm ³
Cylinders Clearance volumes,	25 cm ³
Phase angle,	90°
Engine speed,	1500 rpm
Tested working gases,	He, H ₂
Tested mean pressure,	30 bar

Fig. 6 shows the pressure versus compression space volume diagram (P-V_c), the pressure versus expansion space volume diagram (P-V_e) and the pressure versus total space volume (P-V). This simulation was carried out considering the Helium as the working fluid.

The pressure rises during the compression phase followed by the gas pre-heating phase, where it gets to its maximum value. The minimum pressure occurs in the reverse process, when the working gas is pre-cooled and the volume is at maximum, after the gas has been expanded. The regenerator pre-heating and pre-cooling phases are not exactly isochoric due to the sinusoidal volume variations of the two pistons.

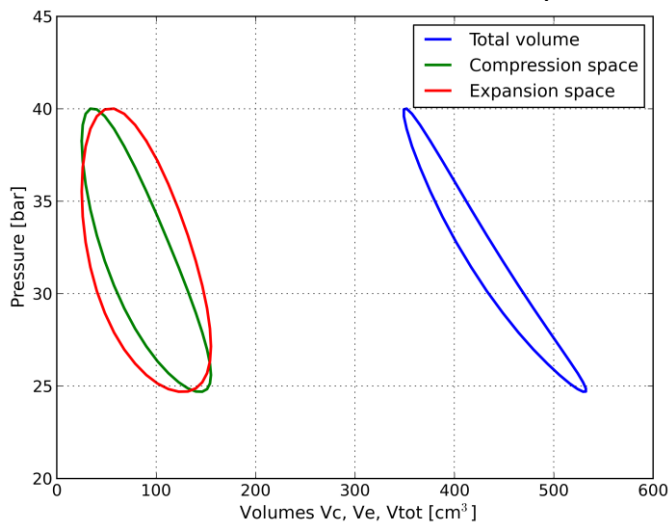
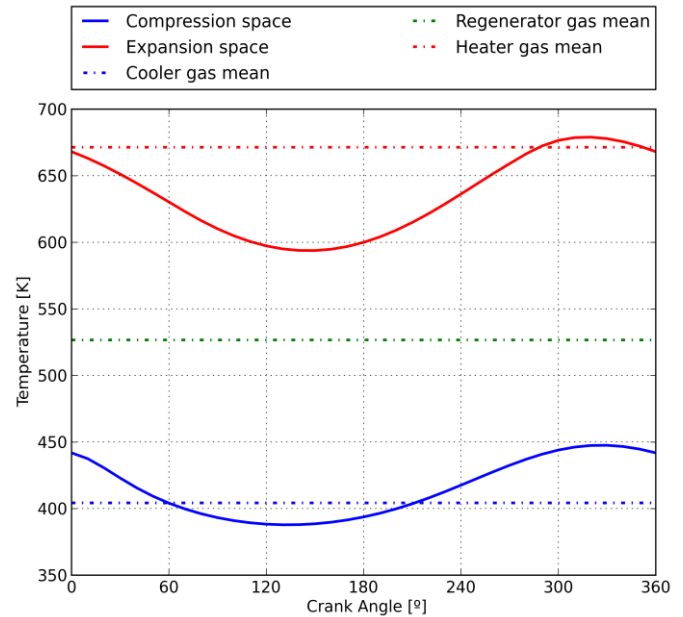
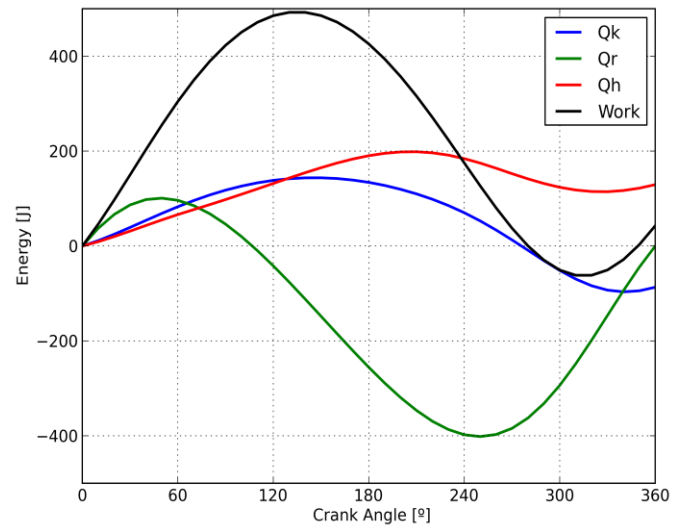

 Fig. 6 Pressure versus space volume diagrams for $p_{mean} = 30$ bar.

Figure 7 presents the temperature variation in the heat exchangers, expansion and compression spaces. The working gas temperature in the compression and expansion spaces fluctuate along the cycle, while a mean effective temperatures for the working gas within heater and cooler is calculated.

Results show that mean effective temperatures in heater and cooler are, respectively, lower and higher than the heat exchanger wall temperatures (671.4 K and 404.2 K, correspondingly). It is also found that temperature at the expansion space could exceed the hot gas temperature and that the temperature at compression space could be less than the cold fluid mean temperature, which could be explained by compression and expansion processes in the adjacent cylinders.


 Fig. 7 Temperature variation in the heat exchangers, expansion and compression spaces, for $p_{mean} = 30$ bar.

The transferred thermal energy and the total work output over an ideal adiabatic cycle are shown in Fig. 8.


 Fig. 8 Energy variation diagram for a $p_{mean} = 30$ bar.

The maximum heat transferred to and from the regenerator matrix is higher than the energy transferred to heater or to the cooler. This reveals the importance of this SE component, since a loss in the heats transferred by the regenerator in the pre-heating and pre-cooling processes leads to an increase in the hot and cold source and thus to a significant decrease in engine efficiency. The maximum total work reached over a complete cycle is 492.4 J for a mean pressure of 30 bar. Work is proportional to the mean pressure, which rise leads to an increase of total work.

Table III presents the results corresponding to a simulation performed at 1500 rpm and 30 bar, comparing helium and hydrogen performance.

TABLE III. NON-IDEAL SIMULATIONS FOR HYDROGEN AND HELIUM

Engine Speed (1500 rpm)	He	H ₂
Hot source heat, Q _h (J)	164.8	176.3
Cold source heat, Q _k (J)	118.1	124.4
Regenerator reduction, Q _{loss} (J)	30.26	45.36
Work (J)	46.96	52.08
Power (kW)	1.17	1.30
Efficiency (%)	28.5	29.6

Despite small, hydrogen presents a better output in terms of engine thermal efficiency, 29.6% against 28.5% for the helium. Also, power output is greater for the engine working with the hydrogen. Nevertheless, the energy reduction at the regenerator reaches higher values.

The working gas suffer friction when flowing through the heat exchangers. This effect results into pressure drop, which is higher for higher operational mean pressures and engine speed. In previous studies, it was proved that hydrogen is the working gas with lowest pressure drop. Also, the pressure drop is higher in the case of the regenerator, when compared with the heater and the cooler [22], [25].

Heat exchangers effectiveness is an important parameter for the evaluation of efficiency. Fig. 9 presents the heat exchanger effectiveness results considering helium and hydrogen at two different pressure values: 5 and 30 bar.

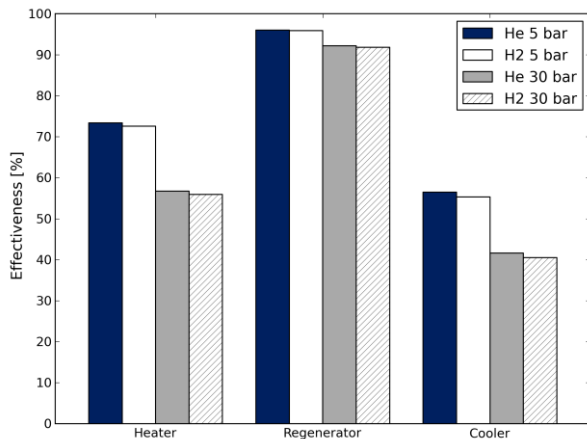


Fig. 9 Effectiveness of the heat exchangers considering helium and hydrogen as working fluids at different values of mean pressure.

The regenerator is the heat exchanger with higher effectiveness above 90% for all the tested cases, as in Fig. 9. Results also show that the heat exchangers effectiveness is slightly higher for helium when compared with hydrogen. Purely in heat transfer terms, helium is slightly better than hydrogen. Comparing the results for 5 and 30 bar, it is shown that the heat exchangers effectiveness decreases for higher values of mean pressure.

B. Cost Estimation

Considering the input conditions and using the calculated values from the physical model, the cost of the SE was estimated. Table IV presents the cost estimation for each system component as well as the total capital cost.

TABLE IV. COST ESTIMATION

System Component	Cost (€)
Heater	6 089.5
Regenerator	4 916.5
Cooler	2 509.8
Engine bulk	7 884.4
Total capital cost of Stirling engine	21 400.0

According to the results, the total cost of the equipment is 21 400€. This value is relatively close to the capital investment cost of a Solo Stirling 161 (25 000€). Considering the cost of each system component, the heater, the regenerator, the cooler and the engine represent, respectively, 28.5%, 23.0%, 11.7% and 36.8% of the total cost. Thus, the heater and the engine bulk are the most costly components.

The cost equations presented in this work allow the combined variation of size and performance aspects. Therefore, varying the operational and the geometric characteristics of the Stirling engine and optimizing the costs of the system, seems to be the best commitment in optimizing these thermal plants. For instance, there is an optimal value for the internal diameter of the heater pipes for which the engine efficiency is maximum (see Fig. 10).

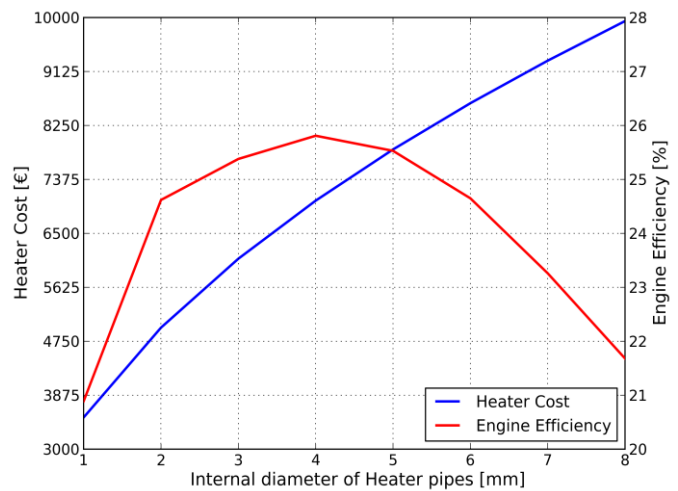


Fig. 10 Stirling engine efficiency and heater cost as a function of the internal diameter of the heater pipes.

According to the results, the Stirling engine efficiency is maximum (i.e. 25.8%) when the internal diameter of the pipes is 4 mm. For this geometrical input, the heater cost corresponds to 7 031.6 €.

V. CONCLUSION

In this work, the mathematical modelling of a Stirling engine is presented in order to study its performance. For this purpose, numerical simulations for non-ideal engine working conditions were performed, including the heat transfer limitations and pumping losses throughout the Stirling thermodynamic cycle. The paper also discloses a methodology to estimate the costs of the system. The system total cost was decomposed in four cost equations, representative of the heater, cooler, regenerator and engine bulk, respectively.

Results show that heat-transfer limitations strongly affect engine efficiency, particularly in the regenerator case. The pumping losses increase with gas mean pressure and engine rotational speed. The heat exchangers effectiveness is slightly higher for helium when compared with hydrogen.

Considering the defined input parameters, the total capital costs are close to real commercial models for similar applications. Plus, the engine bulk and the heater are the most expensive components.

Stirling engines have been identified as a promising technology for the conversion of primary energy into useful power due to their high efficiency levels, low pollutant emissions, low noise levels and mostly due to their flexibility in terms of fuel sources. The possible use of a renewable energy source is very important from the point of primary energy savings and reduction of carbon emissions.

The main purpose behind this study is the definition of a thermal-economic model applied to a cogeneration system for a residential application. The system to be modeled is based on Stirling engine technology combined with a solar collector as a renewable energy source. After defining the cost equations for the system components, they should be integrated in the thermal-economic optimization model in order to achieve the best technical and economic output of the system under analysis.

REFERENCES

- [1] E. D. Rogdakis, G. D. Antonakos, and I. P. Koronaki, "Thermodynamic analysis and experimental investigation of a Solo V161 Stirling cogeneration unit," *Energy*, vol. 45, no. 1, pp. 503–511, Sep. 2012.
- [2] G. Angrisani, C. Roselli, and M. Sasso, "Distributed microtrigeneration systems," *Prog. Energy Combust. Sci.*, vol. 38, no. 4, pp. 502–521, Aug. 2012.
- [3] C. Konrad, E. Obé, and H. Frey, "Distributed generation potential in the German residential sector," *Cogeneration & On-Site Power Reviews*, pp. 59–65, 2009.
- [4] C. Roselli, M. Sasso, S. Sibilio, and P. Tzscheuschler, "Experimental analysis of microcogenerators based on different prime movers," *Energy Build.*, vol. 43, no. 4, pp. 796–804, Apr. 2011.
- [5] Y. Timoumi, I. Tlili, and S. Ben Nasrallah, "Design and performance optimization of GPU-3 Stirling engines," *Energy*, vol. 33, no. 7, pp. 1100–1114, Jul. 2008.
- [6] A. C. M. Ferreira, M. L. Nunes, L. A. S. B. Martins, and Teixeira, "A Review of Stirling Engine Technologies applied to micro-Cogeneration Systems," in *ECOS 2012 - 25th International Conference on Efficiency, Cost, Optimization, Simulation and Environmental Impact of Energy Systems*, 2012, pp. 1–11.
- [7] E. Bilgen, "Exergetic and engineering analyses of gas turbine based cogeneration systems," *Energy*, vol. 25, no. 12, pp. 1215–1229, Dec. 2000.
- [8] P. Puech and V. Tishkova, "Thermodynamic analysis of a Stirling engine including regenerator dead volume," *Renew. Energy*, vol. 36, no. 2, pp. 872–878, Feb. 2011.
- [9] J. Boucher, F. Lanzetta, and P. Nika, "Optimization of a dual free piston Stirling engine," *Appl. Therm. Eng.*, vol. 27, no. 4, pp. 802–811, Mar. 2007.
- [10] F. Formosa and G. Despesse, "Analytical model for Stirling cycle machine design," *Energy Convers. Manag.*, vol. 51, no. 10, pp. 1855–1863, Oct. 2010.
- [11] A. Asnaghi, S. M. Ladjevardi, P. Saleh Izadkhast, and a. H. Kashani, "Thermodynamics Performance Analysis of Solar Stirling Engines," *ISRN Renew. Energy*, vol. 2012, pp. 1–14, 2012.
- [12] B. Kongtragool and S. Wongwises, "Thermodynamic analysis of a Stirling engine including dead volumes of hot space, cold space and regenerator," *Renew. Energy*, vol. 31, no. 3, pp. 345–359, Mar. 2006.
- [13] A. Lazzaretto and a. Toffolo, "Energy, economy and environment as objectives in multi-criterion optimization of thermal systems design," *Energy*, vol. 29, no. 8, pp. 1139–1157, Jun. 2004.
- [14] A. C. M. Ferreira, M. L. Nunes, S. F. C. F. Teixeira, C. P. Leão, Â. M. Silva, J. C. F. Teixeira, and L. A. S. B. Martins, "An economic perspective on the optimisation of a small-scale cogeneration system for the Portuguese scenario," *Energy*, vol. 45, no. 1, pp. 436–444, Sep. 2012.
- [15] M. R. Von Spakovsky, "Application of Engineering Functional Analysis to the Analysis and Optimization of the CGAM Problem," *Energy*, vol. I, no. 3, pp. 343–364, 1993.
- [16] M. Valdés, M. D. Durán, and A. Rovira, "Thermoeconomic optimization of combined cycle gas turbine power plants using genetic algorithms," *Appl. Therm. Eng.*, vol. 23, no. 17, pp. 2169–2182, Dec. 2003.
- [17] M. A. Rodríguez-Toral, W. Morton, and D. R. Mitchell, "Using new packages for modelling, equation oriented simulation and optimization of a cogeneration plant," *Comput. Chem. Eng.*, vol. 24, pp. 2667–2685, 2000.
- [18] F. Gulli, "Small distributed generation versus centralised supply: a social cost–benefit analysis in the residential and service sectors," *Energy Policy*, vol. 34, no. 7, pp. 804–832, May 2006.
- [19] D. A. Manolas, C. A. Frangopoulos, T. P. Gialamas, and D. T. Tsalhalis, "Operation Optimization of an Industrial Cogeneration System by a Genetic Algorithm," *Energy Convers. Manag.*, vol. 38, no. 15, pp. 1625–1636, 1997.
- [20] I. Urieli and D. M. Berchowitz, "Stirling Engine Simple Analysis," *Ohio University*, 2010. [Online]. Available: <http://www.ohio.edu/mechanical/stirling/me422.html>. [Accessed: 10-Feb-2010].

- [21] SCHMIDT, "SCHMIDT ANALYSIS FOR STIRLING ENGINES." 1972.
- [22] A. C. Ferreira, C. Ferreira, S. F. Teixeira, M. L. Nunes, J. C. F. Teixeira, and L. B. Martins, "Thermal- Economic Modeling of a Micro-CHP Unit based on a Stirling Engine," in *Proceedings of the ASME 2013 International Mechanical Engineering Congress & Exposition IMECE2013*, 2013, pp. 1–9.
- [23] D. G. Thombare and S. K. Verma, "Technological development in the Stirling cycle engines," *Renew. Sustain. Energy Rev.*, vol. 12, no. 1, pp. 1–38, Jan. 2008.
- [24] F. Marechal, F. Palazzi, J. Godat, and D. Favrat, "Thermo-Economic Modelling and Optimisation of Fuel Cell Systems," *Fuel Cells*, vol. 5, no. 1, pp. 5–24, Feb. 2005.
- [25] A. C. Ferreira, S. F. C. F. Teixeira, J. C. Teixeira, M. L. Nunes, and L. B. Martins, "Modeling a Stirling Engine for Cogeneration Applications," in *Proceedings of the ASME 2012 International Mechanical Engineering Congress & Exposition IMECE2012*, 2012, pp. 1–9.

Energy-economical efficiency of building heating and cooling by heat pump systems

Ioan Sarbu, Daniel Dan and Calin Sebarchievici

Abstract—In the actual economic and energy juncture, the reduction of thermal energy consumption in buildings became a major, necessary and opportune problem, general significance. The heat pumps are alternative heating systems more energy efficiency and unless pollutant if we make a comparison with classic plants (liquid or gas fuel thermal boiler). This paper presents the energy and economical efficiency criteria which show the opportunity to implement a heat pump in a heating-cooling system. It is developed a computational model of annual energy consumption for an air-to-water heat pump based on the degree-day method and the bin method implemented in a computer program. Also, from a case study is performed a comparative economical analysis of heating solutions for a building and are presented the energy and economic advantages of building heating solution with a water-to-water heat pump.

Keywords—Heating-cooling, Heat pumps, Performance indices, Annual energy consumption, Energy-economical analysis.

I. INTRODUCTION

BUILDINGS are an important part of European culture and heritage, and they play an important role in the energy policy of Europe. Studies have shown that saving energy is the most cost effective method to reduce green house gas emissions (GHG). It has also pointed out that buildings represent the biggest and most cost effective potential for energy savings. The reduction of 26% energy use is set as a goal for buildings by the year 2020 which corresponds to 11% of the reduction of total energy use in European Union (EU) countries.

The buildings sector is the largest user of energy and CO₂ emitter in the EU, and is responsible for more than 40% of the EU's total final energy use and CO₂ emissions. At present heat use is responsible for almost 80% of the energy demand in houses and utility buildings for space heating and hot water generation, whereas the energy demand for cooling is growing year after year. There are more than 150 millions dwellings in Europe. Around 30% are built before 1940, around 45% between 1950 and 1980 and only 25% after 1980. Retrofitting is a means of rectifying existing building deficiencies by

improving the standard and the thermal insulation of buildings and/or the replacement of old space conditioning systems by energy-efficient and environmen-tally sound heating and cooling systems [1]-[3].

In order to realize the ambitious goals for the reduction of fossil primary energy consumption and the related CO₂ emissions to reach the targets of the Kyoto-protocol besides improved energy efficiency the use of renewable energy in the existing building stock have to be addressed in the near future [4], [5].

On 17 December 2008, the European Parliament adopted the Renewable Energy Directive. It is establishes a common framework for the promotion of energy from renewable sources. For the first time, this Directive recognizes aero-thermal, geothermal and hydrothermal energy as renewable energy source. This directive opens up a major opportunity for further use of heat pumps for heating and cooling of new and existing buildings.

Heat pumps enabling the use of ambient heat at a useful temperature level need electricity or other auxiliary energy to function. Therefore, the energy used to drive heat pumps should be deducted from the total usable heat. Aero-thermal, geothermal and hydrothermal heat energy captured by heat pumps shall be taken into account for the purposes provided that the final energy output significantly exceeds the primary energy input.

The amount of ambient energy captured by heat pumps to be considered renewable energy E_{res} , shall be calculated in accordance with the following formula [6]:

$$E_{res} = E_U \left(1 - \frac{1}{SPF} \right) \quad (1)$$

where: E_U is the estimated total usable thermal energy delivered by heat pumps; SPF – the estimated average seasonal performance factor for these heat pumps.

Only heat pumps for which $SPF > 1.15/\eta$ shall be taken into account, where η is the ratio between the finally produced electric energy and the primary energy consumption for electricity production. For EU-countries average $\eta=0.4$. Meaning that minimum value of seasonal coefficient of performance should be $SPF = COP_{seasonal} > 2.875$.

Heat pump enables the use of ecological heat (solar energy accumulated in the soil, water and air) for an economic and ecological heating. For practical use of these energy sources we have to respect the following criteria: sufficient availability, higher accumulation capacity, higher temperature, sufficient regeneration, economical capture, reduced waiting

Ioan Sarbu is currently a Professor at the Civil Engineering and Building Services Department, Polytechnic University Timisoara, 300006 ROMANIA, e-mail address: ioan.sarbu@ct.upt.ro

Daniel Dan is currently a Professor at the Civil Engineering and Building Services Department, Polytechnic University Timisoara, 300006 ROMANIA, e-mail address: daniel.dan@ct.upt.ro

Calin Sebarchievici is currently a Assistant Professor at the Civil Engineering and Building Services Department, Polytechnic University Timisoara, 300006 ROMANIA, e-mail address: calin.sebarchievici@ct.upt.ro

time. In the development of modern constructions with improved thermal insulation and reduced heat demand use heat pumps are a good alternative [7]-[9].

This paper presents the energy and economical efficiency criteria which show the opportunity to implement a heat pump in a heating/cooling system. It is developed a computational model of annual energy consumption for an air-to-water heat pump based on the degree-day method and the bin method and it is performed a comparative economical analysis of different heating solutions for a building.

II. ENERGY-ECONOMICAL INDICATORS FOR HEAT PUMPS

The performances of the heat pump and the system building – heating/cooling installation are determined based on economical and energy indicators of these systems. The opportunity to implement a heat pump in a heating/cooling system results on both energy criteria and the economic [10].

- *Economical indicators.* Usually the heat pump (HP) realizes a fuel economy ΔC (operating expenses) comparatively of the classical system with thermal station (TS), which is dependent on the type of heat pump. On the other hand, heat pumps involve an additional investment I_{HP} from the classical system I_{TS} , which produces the same amount of heat.

Thus, it can be determined *the recovery time* TR , in years, to increase investment, $\Delta I = I_{HP} - I_{TS}$, taking into account the operation economy realized through low fuel consumption $\Delta C = C_{TS} - C_{HP}$:

$$TR = \frac{\Delta I}{\Delta C} \leq TR_n \quad (2)$$

where TR_n is normal recovery time.

It is estimated that for TR_n a number 8–10 years is acceptable, but this limit varies depending on the country's energy policy and environmental requirements.

Another economical indicator is total updated cost (TUC):

$$TUC = I_0 + \sum_{j=1}^{\tau} \frac{C}{(1 + \beta_0)^j} \quad (3)$$

in which: I_0 is the initial investment cost, in the operation beginning date of the system; C – annual operating cost of the system; β_0 – the average rate of the inflation; τ – number of years for which is made update (20 years).

Could be rather easy demonstrated the equality:

$$\sum_{j=1}^{\tau} \frac{1}{(1 + \beta_0)^j} = \frac{(1 + \beta_0)^{\tau} - 1}{\beta_0 (1 + \beta_0)^{\tau}} \quad (4)$$

and is defined update rate

$$r_a = \frac{(1 + \beta_0)^{\tau} - 1}{\beta_0 (1 + \beta_0)^{\tau}} \quad (5)$$

Taking into account (4) and (5) equation (3) gets the form:

$$TUC = I_0 + r_a C \quad (6)$$

- *Energetically indicators.* The operation of a heat pump is characterized by *the coefficient of performance* (COP) or *thermal efficiency* (ε_{HP}), defined as the ratio between useful effect produced (useful thermal energy E_U) and energy consumed to obtain it (drive energy E_D):

$$COP = \varepsilon_{HP} = \frac{E_U}{E_D} \quad (7)$$

If both usable energy and consumed energy are summed during a season (year) is obtained by equation (7) seasonal (annual) coefficient of performance ($COP_{seasonal}$), which is often expressed as SPF.

In the heating operate mode is defined COP by equation:

$$COP = \varepsilon_{HP} = \frac{Q_{HP}}{P_e} \quad (8)$$

in which: Q_{HP} is the thermal power of heat pump, in W; P_e – the drive power of heat pump, in W.

If the reversible heat pump operate in cooling mode is defined *energy efficiency ratio* EER, in Btu/(h·W) by equation:

$$EER = \frac{Q_0}{P_e} \quad (9)$$

in which: Q_0 is the cooling thermal power, in British thermal unit per hour (Btu/h); P_e – drive power of heat pump, in W.

The coefficient of performance of heat pump in cooling state is obtained by equation:

$$COP = \frac{EER}{3.413} \quad (10)$$

in which 3.413 is the transformation factor from Watt to Btu/h.

From the energy balance of the heat pump:

$$E_U = E_S + E_D \quad (11)$$

can highlight the link between the efficiency of a plant working as a heat pump (ε_{HP}) and as refrigeration plant (ε_{RP}):

$$\varepsilon_{HP} = \frac{E_S + E_D}{E_D} = 1 + \frac{E_S}{E_D} = 1 + \varepsilon_{RP} \quad (12)$$

The most effective systems are those which use simultaneously the produced heat and the adjacent refrigeration effect, in which case the total efficiency is:

$$\varepsilon_{HP+RP} = \frac{E_U + E_S}{E_D} = \frac{E_S + E_D + E_S}{E_D} = \varepsilon_{HP} + \varepsilon_{RP} \quad (13)$$

If you take into account the Π_j energy losses that are accompanying both the accumulation and release heat from the real processes, the efficiency becomes real $\varepsilon_{HP,r}$ and its expression is [10]:

$$\varepsilon_{HP,r} = \frac{T_c}{T_c - T_o} (1 - \sum \Pi_j) \quad (14)$$

where T_c and T_o are the condensation and vaporization absolute temperatures of refrigerants.

In Figure 1 is represented the real efficiency variation of heat pumps according to the source temperature t_s and temperature t_u at the consumer.

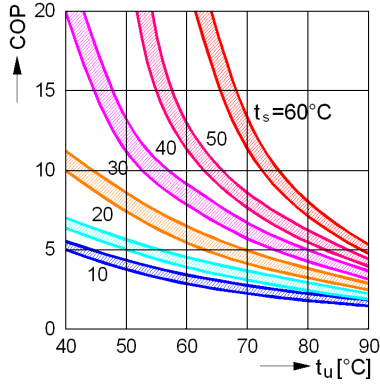


Fig. 1 Variation of heat pumps efficiency

To determine the real efficiency of the heat pump with electro-compressor can be used the equation [11]:

$$\varepsilon_{HP,r} = \frac{T_u + \Delta t_c}{T_u + \Delta t_c - (T_s - \Delta t_o)} \eta_r \eta_i \eta_m \eta_{em} + \eta_m \eta_{em} (1 - \eta_i) \quad (15)$$

where:

$$\eta_r = 1.666 - 0.004(T_s - \Delta t_o) - 0.00625(T_u + \Delta t_c) \quad (16)$$

$$\eta_i = \left(0.425 + \frac{0.493 Q_{HP}}{1.16 Q_{HP} + 0.06} \right) \left(3.23 - 1.835 \frac{T_u + \Delta t_c}{T_s - \Delta t_o} \right) \quad (17)$$

$$\eta_m = 0.85 + \frac{0.158 Q_{HP}}{1.16 Q_{HP} + 0.1513 \frac{T_u + \Delta t_c}{(T_u + \Delta t_c) - (T_s - \Delta t_o)}} \quad (18)$$

$$\eta_{em} = 0.85 + \frac{0.139 Q_{HP}}{1.335 Q_{HP} + 0.0904 \frac{T_u + \Delta t_c}{(T_u + \Delta t_c) - (T_s - \Delta t_o)}} \quad (19)$$

in which: T_u , T_s are the hot and cold source absolute temperatures; Δt_c , Δt_o – temperature differences between the condensation temperature and hot source temperature, respectively, between the cold source temperature and vaporization temperature; η_r – efficiency of the real cycle toward a reference Carnot cycle; η_i , η_m – internal and mechanical efficiency of the compressor; η_{em} – electromotor efficiency; Q_{HP} – heat pump thermal power.

In case of a heat pump with electro-compressor is introduced the global efficiency η_g as a product between the electric energy production efficiency η_p , its transportation efficiency η_t and the electromotor efficiency η_{em} :

$$\eta_g = \eta_p \eta_t \eta_{em} \quad (20)$$

Taking into account that the heat pump has an over-unit theoretical efficiency, for the evaluation in which way is valued the consumed primary energy is using the synthetic indicator η_s , representing the product [12]:

$$\eta_s = \eta_g \varepsilon_{HP} \quad (21)$$

which has to satisfy the condition $\eta_s > 1$ for justify the use of heat pump

Also, only if the real efficiency $\varepsilon_{HP,r} > 2.78$ the use of the heat pumps can be considered.

Another energy indicator for heat pumps is the specific consumption of electricity w_{HP} , in kW/GJ:

$$w_{HP} = \frac{10^3}{3.6 \varepsilon_{HP,r}} \quad (22)$$

In Figure 2 is illustrated the electricity consumption for heat pumps depending on the heat source temperature t_s and the consumer temperature t_u .

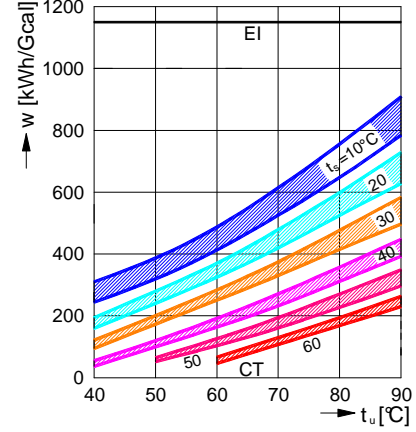


Fig. 2 Specific electricity consumption for the heat production

The sizing factor ($SF = \alpha_{HP} = Q_{HP}/Q_{max}$) of the heat pump is defined as ratio of the heat pump capacity Q_{HP} to the maximum heating demand Q_{max} and can be optimized in terms of energy and economic, depending on the source temperature and the used adjustment schedule.

The energy indicators of heat pumps are determined as average values, taking into account the annual heat consumption variation.

In Figure 3 is represented variation of the average annual electric energy specific consumption, in function of α_{HP} and different graphics adjustments.

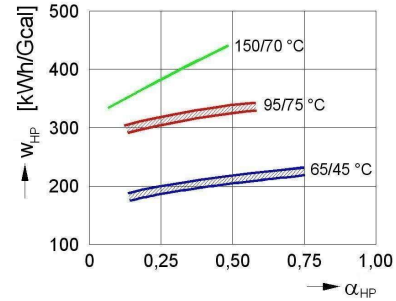


Fig. 3 Variation of the average annual electricity specific consumption

The annual fuel economy variation ΔB , obtained by using heat pump, expressed as percentage of total annual fuel consumption in a referential classic system is presented in Figure 4.

For absorption heat pump system, driven by thermal energy, it is agreed at European level to consider $\eta = 1.0$ and therefore $SPF \geq 1.15$.

In order to properly compare the performances of various heat pumps types, have to uniform the action energy. In this sense, is reported the useful heat delivered annually $Q_{u,year}$ at annual equivalent fuel consumption $B_{fe,year}$, necessary for

driving power production, achieving the degree of fuel use ϕ_{year} , in kW/kg [13]:

$$\phi_{year} = \frac{Q_{u, year}}{B_{fe, year}} \quad (23)$$

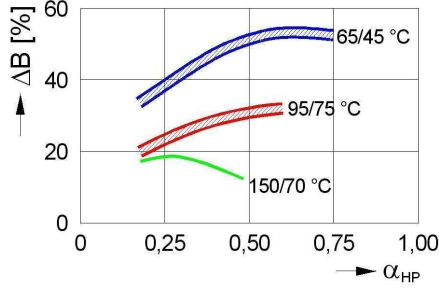


Fig. 4 Variation of annual fuel economy

Table 1. Energy analysis of heat generation

No	Plant type	Degree of fuel use ϕ_{year} [kW/kg]	Primary energy E_p [%]	Fuel economy ΔC [%]
0	1	2	3	4
1	Gas boiler	0.800	125.00	0
2	Heat pump with electro-compressor	1.083	92.34	-32.66
3	Heat pump with electro-compressor and thermal boiler	0.969	103.20	-21.80
4	Heat pump with thermal motor compressor	1.416	70.62	-54.38
5	Absorption heat pump	1.219	82.03	-42.97
6	Ejection heat pump	0.970	103.09	-21.91

III. COMPUTATION OF ENERGY CONSUMPTION FOR AN AIR-TO-WATER HEAT PUMP

Annual energy consumption of heating/cooling system for a building contributes to minimizing the life cost of the building. This consumption is obtained by time integration of instantaneous consumption during the cold season, warm season respectively. Instantaneous consumption depends on the efficiency of the HVAC system.

For computation of the annual energy consumption of a heating/cooling system can be used the degree-day method or bin method [14].

- *Degree-day method.* The degree-day method and its generalizations can provide a simple estimate of annual loads, which can be accurate if the indoor temperature and internal gains are relatively constant and if the heating or cooling systems operate for a complete season.

The balance point temperature t_{ech} of a building is defined as that value of the outdoor temperature t_e at which, for the specified value of the interior temperature t_i , the total heat loss is equal to the heat gain Q_{ap} from sun, occupants, lights, and so fort:

$$Q_{ap} = U(t_i - t_{ech}) \quad (24)$$

in which U is the heat transfer coefficient of the building, in W/K.

Heating is needed only when t_e drops below t_{ech} . The rate of energy consumption of the heating system is:

The fuel economy depends by heat pump type, according to Table 1.

Reduction of GHG emissions, key to limiting global warming is associated with the replacement of classical solutions for heating/cooling with heat pumps, especially ground-source heat pumps (GSHP). But must be taken into account also items related to electricity production, mainly used to drive them.

Nowadays it is not recommended to replace a heating gas boiler with electrically operated heat pump if electricity is produced using coal or based on old technologies, because resulting carbon dioxide emissions may increase with 1–2 tons/year.

$$Q_{inc} = \frac{U}{\eta} [t_{ech} - t_e(\tau)]_{t_e < t_{ech}} \quad (25)$$

in which: η is the efficiency of the heating system; τ – time.

If η , t_{ech} , and U are constant, the annual heating consumption can be written as an integral:

$$E_{inc} = \frac{U}{\eta} \int [t_{ech} - t_e(\tau)]_+ dt \quad (26)$$

where the plus sign (+) above the bracket indicates that only positive values are counted.

This integral of the temperature difference conveniently summarizes the effect of outdoor temperature on a building. In practice, it is approximated by summing averages over short time intervals (daily) and the result N_{inc} , in (K·days) is called degree-days:

$$N_{inc} = (1 \text{ day}) \sum_{days} (t_{ech} - t_e) \quad (27)$$

Here the summation is to extend over the entire year or over the heating season. The balance point temperature t_{ech} is also known as the base of the degree-days. In terms of degree-days, the annual heating consumption is:

$$E_{inc} = \frac{U}{\eta} N_{inc} \quad (28)$$

Cooling degree-days can be calculated using an equation analogous to equation (27) for heating degree-days as:

$$N_{rac} = (1 \text{ day}) \sum_{\text{days}} (t_e - t_{ech}) \quad (29)$$

Since the balance point temperature varies widely from one building to another because of widely differing personal preferences for thermostat settings and setbacks and because of different building characteristics is used the variable-base model. The basic idea is to assume a typical probability distribution of temperature data, characterized by its average \bar{t}_{ej} and by its standard deviation σ . Erbs *et al.* [15] developed a model that needs as input only the average \bar{t}_{ej} for each month of the year. The standard deviations σ_j , in °C, for each month are then estimated from the correlation:

$$\sigma_j = 1,45 - 0,029\bar{t}_{ej} + 0,0664\sigma_{an} \quad (30)$$

where:

$$\sigma_{an} = \sqrt{\frac{1}{12} \sum_{j=1}^{12} (\bar{t}_{ej} - \bar{t}_{e,an})^2} \quad (31)$$

in which: σ_{an} is the standard deviation of the monthly temperature about the annual average $\bar{t}_{e,an}$.

The monthly heating degree-days $N_{inc,j}$ for any location are well approximated by [14]:

$$N_{inc,j} = \sigma_j n^{1.5} \left[\frac{\theta_j}{2} + \frac{\ln(e^{-a\theta_j} + e^{a\theta_j})}{2a} \right] \quad (32)$$

where:

$$\theta_j = \frac{t_{ech} - \bar{t}_{ej}}{\sigma_j \sqrt{n}} \quad (33)$$

in which: θ_j is a normalized temperature variable; n – number of days in the month; $a = 1.698$.

The annual heating degree-days can be estimated with relation:

$$N_{inc} = \sum_{j=1}^{12} N_{inc,j} \quad (34)$$

The computer program GRAZIL has been elaborated based on variable-base model, in EES for PC microsystems.

- *Bin method.* For many applications, the degree-day method should not be used, even with the variable-base method, because the heat loss coefficient, the efficiency of the HVAC system, or the balance point temperature many not be sufficiently constant. Heat pump efficiency, for example, varies strongly with outdoor temperature t_e ; efficiency of HVAC equipment may be affected indirectly by t_e when efficiency varies with load (common for boilers and chillers). Furthermore, in most commercial buildings, occupancy has a pronounced pattern, which affects heat gain, indoor temperature, and ventilation rate.

In such cases, steady-state calculation can yield good results for annual energy consumption if different temperature intervals and time periods are evaluated separately. This approach is known as the *bin method* because consumption is

calculated for several values of the outdoor temperature t_e and multiplied by the number of hours N_{bin} in the temperature interval (bin) centered on that temperature:

$$Q_{bin} = N_{bin} \frac{U}{1000\eta} (t_{ech} - t_e)_+ \quad (35)$$

in which: Q_{bin} is the energy consumption, in kW, for each temperature interval; N_{bin} – number of yearly hours in the temperature interval (bin) centered around outdoor temperature; U – heat transfer coefficient of building, in W/K; t_{ech} – balance point temperature, in °C; t_e – outdoor temperature, in °C; η – efficiency of the HVAC system.

The superscript plus sign indicates that only positive values are counted; no heating is needed when t_e is above t_{ech} ($t_e > t_{ech}$). Equation (35) is evaluated for each bin, and the total energy requirement E_{bin} , in kWh, is the sum of the Q_{bin} over all bins.

This method is defined in European Standard EN 15316-4.2 [16].

Knowing the thermal power Q_{HP} and power drive P_e of the heat pump for each bin temperature interval, can determinate the following:

– Heat loss (heat demand) of the building Q_{nec} , in kW:

$$Q_{nec} = \frac{U}{1000} (t_{ech} - t_e) \quad (36)$$

– Heat pump efficiency, ε_{HP} :

$$\varepsilon_{HP} = \frac{Q_{HP}}{P_e} \quad (37)$$

– Heat pump operation coefficient, f :

$$f = \min\left(1, \frac{Q_{nec}}{Q_{HP}}\right) \quad (38)$$

– Thermal energy provided by heat pump E_{HP} , in kWh:

$$E_{HP} = f Q_{HP} N_{bin} \quad (39)$$

– Electric energy to drive heat pump E_D , in kWh:

$$E_D = f P_e N_{bin} \quad (40)$$

Energy requirement E_{bin} , in kWh, is obtained by summing the values Q_{bin} given by (35).

– Energy delivered by auxiliary source E_{aux} , in kWh:

$$E_{aux} = E_{bin} - E_{HP} \quad (41)$$

– Total energy consumed by the heat pump and auxiliary source E_t , in kWh:

$$E_t = E_D + E_{aux} \quad (42)$$

The computer program METBIN has been elaborated based on this computational model, in EXCEL for PC compatible microsystems.

- *Numerical application.* For a building heated by a heat pump are known: heat transfer coefficient $U = 850$ W/K and balance temperature $t_{ech} = 17.8$ °C, and is determined energy consumption during heating period using METBIN program. The results are summarized in Table 2. In Figure 5 is shown the variation of heat loss and thermal power of the heat pump depending on the outdoor temperature.

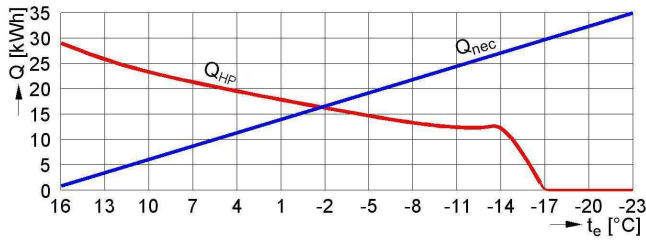


Fig. 5 Variation of heat requirement and HP thermal power with outdoor temperature

IV. COMPARATIVE ECONOMIC ANALYSIS OF SOME HEATING SOLUTIONS FOR A BUILDING

• *Assumptions for calculation.* A study is performed for the heating of a living building in rural areas with a water-water heat pump, using as heat source the underground water comparative to other sources of primary energy.

The building with useful surface of 240 m² (basement-floor, ground-floor, floor, and bridge) is heated from 1993 with radiators from thermal station with gas-oil.

Table 2. Results provided of computer program METBIN

Temp. (bin) t_e [°C]	$t_{ech}-t_e$ [°C]	Hours N_{bin} [h]	Q_{nec} [kW]	Q_{HP} [kW]	P_e [kW]	ϵ_{HP}	Coef. f	E_{HP} [kWh]	E_D [kWh]	E_{bin} kWh]	E_{aux} kWh]	E_t [kWh]	
0	1	2	3	4	5	6	7	8	9	10	11	12	
16	1.8	904	1.53	28.9	7.11	4.06	0.05	1383.12	340.3	1383.1	0	340.3	
13	4.8	766	4.08	26.8	6.87	3.90	0.15	3125.28	801.1	3125.3	0	801.1	
10	7.8	647	6.63	24.1	6.58	3.66	0.28	4289.61	1171.2	4289.6	0	1171.2	
7	10.8	601	9.18	21.6	6.31	3.42	0.43	5517.18	1611.7	5517.2	0	1611.7	
4	13.8	650	11.73	18.2	5.80	3.14	0.64	7624.50	2429.8	7624.5	0	2429.8	
1	16.8	691	14.28	16.1	5.47	2.95	0.89	9867.48	3349.4	9867.5	0	3349.4	
-2	19.8	644	16.83	14.6	5.23	2.79	1.00	9402.45	3368.1	10838.5	1430.1	4804.2	
-5	22.8	497	19.38	13.3	5.01	2.65	1.00	6610.15	2490.0	9631.9	3021.8	5511.7	
-8	25.8	312	21.93	12.1	4.76	2.59	1.00	3775.25	1485.1	6842.2	3067.0	4552.1	
-11	28.8	162	24.48	11.6	4.66	2.49	1.00	1879.25	754.6	3965.8	2086.6	2841.5	
-14	31.8	77	27.03	10.2	4.37	2.33	1.00	785.45	336.5	2081.3	1295.9	1632.4	
-17	34.8	34	29.58	0	0	0	0	0	0	1005.7	1005.7	1005.7	
-20	37.8	15	32.13	0	0	0	0	0	0	482.0	482.0	482.0	
-23	40.8	5	34.68	0	0	0	0	0	0	173.4	173.4	173.4	
T O T A L									54259.47	18138.2	66827.9	12568.4	30706.0

Indoor air temperatures were considered in accordance with the wishes of the client: +20 °C for the stairway and annex spaces; +22 °C for day rooms and bedrooms; 24 °C for baths. Construction materials which distinguish heated spaces are: 50 cm brick for exterior walls, concrete 10 cm and 15 cm layer of expanded polystyrene insulation for the bridging, double glazing in oak. Exterior walls will be isolated from the outside with expanded polystyrene (10 cm).

Calculation of heat demand Q_{nec} was performed for the existing building envelope (exterior walls without insulation) and after thermal rehabilitation of it (exterior walls insulated with 10 cm expanded polystyrene), for more outdoor air temperatures (Table 3) in order to choose efficient heat source.

Table 3. Heat demand for heating

t_e [°C]	Q_{nec} [kW]	
	Actual envelope	Rehabilitated envelope
+5	18.9	13.6
0	20.2	15.5
-5	21.6	17.4
-10	23.0	18.3
-15	24.3	19.1
-20	25.6	21.1

For the preparation of domestic hot water is necessary to consider a heat $Q_{dhw} = 3$ kW (3 persons, 3 bathrooms and a kitchen).

• *Proposed solution.* Building heating is realized as follows:

- heating of living spaces (living rooms, bedrooms, and stairway) with the floor convector-radiator;
- bathroom heating with radiators (towel- port);
- hot water temperature to radiators and convector-radiator: 50/40 °C;
- for supply of radiators and convector-radiators are used distributor/collector systems;
- distribution network for radiators and convector-radiators, pexal made, is placed at ceiling, basement-floor, ground-floor and floor.

The heat demand of building will be provided by a heat pump type Thermia Eko 180 and a boiler with the capacity of 300 liters. Mechanical compression heat pump (scroll compressor) operates with ecological refrigerant R404A. The heat source is the groundwater aquifers with minimum temperature of 10 °C.

In the operating conditions with $t_o = 8$ °C and $t_c = 50$ °C the thermal power of heat pump is $Q_{HP} = 21$ kW. It finds that this thermal power assure part of the building heat demand, only for outdoor temperatures higher than -5 °C, in the actual

situation, and almost entirely (even for the outdoor temperature of $-20\text{ }^{\circ}\text{C}$), in conditions of thermal rehabilitated envelope (exterior walls isolated additional). To assure the rest of heat demand (heating and preparation of domestic hot water) heat pump is equipped with 3 electrical resistances by 3 kW, which operate automatically, depending on the set indoor temperature. For flow rate control in the hot water distribution network from the heating circuit, there are provided the following measures:

- a first adjustment of the flows rate that are supplied the terminal units (radiators or convector-radiators), achieved by progressive reduction of the pipe diameters;
- base adjustment, achieved through the regulating valves of flow for each column;

– final adjustment at the terminal units, developed by the thermostat valves set at the comfort temperature in each room.

• *Economical analysis.* Comparing the solution described for building heating with other possible variants of primary energy sources (LPG, gas-oil and natural gas) results a superior investment for heat pump, but also an economy in operating costs, which enable the recovery of additional investment.

In Tables 4 and 5 are presented the necessary investments and operating costs over a period of 10 years for the considered variants.

Table 4. Investment costs I , in €, for heat pump (HP) and different thermal boilers.

Solution components	HP	Thermal boiler with fuel:		
		LPG	Gas-oil	Natural gas
0	1	2	3	4
Heat pump/Boiler	7700	3000	3000	3000
Underground water capture	4900	–	–	–
Heat exchanger	1300	–	–	–
Circulation pumps	1200	–	–	–
Fuel tank	–	3500	3500	–
Gas connection	–	–	–	4000
Total	15100	6500	6500	7000

Table 5. Operating costs C , in €, for heat pump (HP) and different thermal boilers.

Solution characteristics	HP	Thermal boiler with fuel:		
		LPG	Gas-oil	Natural gas
0	1	2	3	4
Thermal power, [kW]	21+9	24	24	24
Fuel calorific power, [kW/l]	–	6.30	10.0	9.44
TS Efficiency / HP- COP	2.33	0.90	0.85	0.90
Hour consumption (fuel, [l/h]; [m ³ /h] / electric energy, [kW])	9.00	4.23	3.02	2.84
Annual operating, [h/year]	1870 ^{*)}	1700	1700	1700
Fuel price, [€/l]; [€/m ³] / Electricity price, [€/kWh]	0.087	0.500	0.900	0.300
Annual consumption, [l/year; m ³ /year; kWh/year]	16830	7191	5134	4828
Annual energy cost, [€/year]	1464	3595.5	4620.5	1448.5
Estimated energy price increase in 10 years	1.30	1.40	1.40	2.00
Operating costs (10 years), C [€]	1903.2	5033.7	6468.7	2897.0

^{*)} Annual operation of electrical resistances is considered 10% of the normal operation period, so at the 1700 hours/year is adding 170 hours/year.

Results the recovery time of additional investment for heat pump, compared with thermal boilers:

– toward boiler to LPG:

$$TR = \frac{I_{HP} - I_{TS,LPG}}{C_{TS,LPG} - C_{HP}} = \frac{15100 - 6500}{5033.7 - 1903.2} = 2.74 \text{ years}$$

– toward gas-oil boiler:

$$TR = \frac{I_{HP} - I_{TS,gas-oil}}{C_{TS,gas-oil} - C_{HP}} = \frac{15100 - 6500}{6468.7 - 1903.2} = 1.88 \text{ years}$$

– toward natural gas boiler:

$$TR = \frac{I_{HP} - I_{TS,natural\ gas}}{C_{TS,natural\ gas} - C_{HP}} = \frac{15100 - 7000}{2897.0 - 1903.2} = 8.15 \text{ years}$$

It is noted that compared to any of the heating solutions to boilers, heating with water-to-water heat pump has a recovery period of investment TR smaller than normal recovery period TR_n , of 8–10 years.

V. CONCLUSIONS

Correct adaptation of the heat source and the heating system for operating regime of heat pumps, leads to safe and economic operation of the heating system using heat pumps.

Heat pump provides the necessary technical conditions for efficient use of solar heat for heating and production of domestic hot water.

Heating installations with heat pumps produces minimum energy consumption in operation and are certainly a solution for energy optimization of buildings.

The heat pump mode requires some additional investments. If the capacity of the heat pump is selected larger than the condensing capacity in the pure refrigeration mode, also the additional capacity costs have to be covered by the savings in energy costs.

A combined cooling and heating system with a heat pump is always more effective than a traditional system if its requirements are taken into the consideration in the design process. For renovation, the applicability is more limited and always depending on the case.

The main barrier for the use of heat pumps for retrofitting is the high distribution temperature of conventional heating systems in existing residential buildings with design temperatures up to 70–90 °C which is too high for the present heat pump generation with maximum, economically acceptable heat distribution temperature of around 55 °C. Besides the application of existing heat pumps in already improved standard buildings with reduced heat demand, the development and market introduction of new high temperature heat pumps is a mayor task for the replacement of conventional heating systems with heat pumps in existing buildings.

REFERENCES

- [1] I. Sarbu, F. Kalmar, M. Cinca, *Thermal Building Equipments – Energetically Optimization and Modernization*, Polytechnic Publishing House, Timisoara, 2007.

- [2] R.D. Ellison, The effects of reduced indoor temperature and night setback on energy consumption of residential heat pumps, *ASHRAE Transactions*, vol. 84, no. 2, pp. 352-363.
- [3] I. Sarbu, C. Sebarchievici, Heat pumps – Efficient heating and cooling solution for buildings, *WSEAS Transaction oh Heat and Mass Transfer*, vol. 5, no. 2, pp. 31-40, 2010.
- [4] G.V. Bendea, M.F. Prada, C. Bendea, C. Secui, Ground coupled heat pump systems – a key for a sustainable development of heating and cooling buildings, In: *Recent Advances in Environmental Science, Proceedings of the 9th Int. Conference on Energy, Environment, Ecosystems and Sustainable Development*, Lemesos, Cyprus, March 21-23, 2013, pp. 133-138.
- [5] <http://www.heatpumpcentre.org>. *Heat pumps can cut global CO₂ emissions by nearly 8%*. Heat Pump Program, Heat Pump Centre, 2008.
- [6] O. Seppänen, European parliament adopted the directive on the use of renewable energy sources, *Rehva Journal*, vol. 46, no. 1, Brussels, pp. 12-14, 2009.
- [7] L. Garberi, S. Mehes, System models of different types of heat pumps, *Proceedings of the 2th IASME/WSEAS Int. Conference on Energy & Environment*, Portoroz, Slovenia, May 15-17, 2007, pp. 104-110.
- [8] M. Lubliner, J. Andrews, D. Baylon, Heating with residential heat pumps, *ASHRAE Journal*, vol. 47, no. 10, Atlanta, pp. 36-43, 2005
- [9] L. Verstaen, Variable refrigerant flow heat pump technology offers superior heating performance under cold ambient conditions, *Rehva Journal*, vol. 46, no. 2, Brussels, pp.40-43, 2009.
- [10] I. Sarbu, C. Sebarchievici, *Heat pumps*, Polytechnic Publishing House, Timisoara, 2010 (in Romanian).
- [11] V. Radcenco, *Heat pump systems*, Technical Publishing House, Bucharest, 1985 (in Romanian).
- [12] I. Sarbu, C. Sebarchievici, General review of ground-source heat pump systems for heating and cooling of buildings, *Energy and Buildings*, doi: 10.1016/j.enbuild.2013.11.068, 2013 (in press).
- [13] C. Sebarchievici, *Optimization of thermal systems from buildings to reduce energy consumption and CO₂ emissions using ground-coupled heat pump*, PhD thesis, Polytechnic University Timisoara, Romania, 2013.
- [14] ASHRAE, *Fundamentals Handbook*, American Society of Heating, Refrigerating and Air-Conditioning Engineers, Atlanta, 2009.
- [15] D.G. Erbs, S.A. Klein, W.A. Beckman, Estimation of degree-days and ambient temperature bin data from monthly-average temperatures, *ASHRAE Journal*, vol. 25, no. 6, pp. 60, 1983.
- [16] J. Zirngib, Standardization activities for heat pumps, *Rehva Journal*, vol. 46, no. 3, Brussels, 2009.

Problems of fast frequency variation control in interconnected power systems

V. Chuvychin, A. Sauhats, R. Petrichenko, G. Bochkarjova

Abstract—This paper describes problem of fast frequency variation control in large interconnected power system. Interconnection of the large power system with different philosophy of frequency control can cause ineffective and sometimes nonselective behavior of frequency automation. Paper presets results of analysis of frequency control using spinning reserve. Optimal distribution of the primary reserve can be based on cooperative game theory method. Severe system disturbances can result in fast frequency drop, which makes fast governor and boiler response impossible. If the governor action cannot activate spinning reserve quickly enough to restore the system to its normal operating frequency, underfrequency load shedding (UFLS) serves as a last-resort tool to prevent the system from collapse. Application of smart metering and communication can improve efficiency of emergency automation during underfrequency condition. A new load shedding method is suggested. Simulation of frequency behavior was conducted for existing load shedding system and a new one.

Keywords—Interconnected power systems, smart metering system, cooperative game theory, load shedding.

I. INTRODUCTION

DURING the last years many international projects were devoted to the problem of interconnection of the large transmission networks in Europe [1], [2]. There are many problems that complicate such interconnection:

- 1) Initial period of interconnected operation of power systems usually is characterized by relatively weak intersystem ties. There will be problem of control the intersystem ties.
- 2) Different philosophy of frequency and active power control can cause oscillations of power transmitted through the intersystem tie line.
- 3) Methods of frequency control for normal and emergency operational conditions in different systems are different.

This work has been supported by the European Social Fund within the project «Support for the implementation of doctoral studies at Riga Technical University».

V.Chuvychin is with the Faculty of Power and Electrical Engineering, Riga Technical University, Riga, LV-1010 Latvia (e-mail: chuvychin@eef.rtu.lv).

A. Sauhats is with the Faculty of Power and Electrical Engineering, Riga Technical University, Riga, LV-1010 Latvia (e-mail: sauhatas@eef.rtu.lv).

R. Petrichenko is with the Faculty of Power and Electrical Engineering, Riga Technical University, Riga, LV-1010 Latvia (e-mail: romans.petrichenko@rtu.lv).

G. Bochkarjova is with the Faculty of Power and Electrical Engineering, Riga Technical University, Riga, LV-1010 Latvia (e-mail: galina@eef.rtu.lv).

Compatibility problem of operation during normal and emergency conditions of interconnected power systems is aroused.

During emergency situation in the power system caused by generating power deficiency frequency decline takes place. Dynamics of frequency behavior can have very different character. It depends on the value of disturbance, response of emergency automation, governor system and reasons of emergency situation. If governor action cannot activate spinning reserve fast enough to restore the system to its normal operating frequency, frequency actuated automatic load shedding serves as a last-resort tool to prevent the system from the collapse [3], [4]. Interconnection of large power systems with different underfrequency automation and systems' parameters can cause ineffective behavior of frequency in the interconnection.

For small frequency deviation primary and secondary frequency control form a resource to improve efficiency of power system. Many papers are dedicated to the quality improvement of frequency control. The introduction of market conditions in the task of the power system operation changes formulation and solving of energy cost minimization problem in the transient conditions.

For fast and deep frequency decline load shedding automation systems will be applied to restore a normal frequency. Smart metering and communication systems should be used for creation of new solution.

Paper describes possible approach to use smart technology for control fast frequency variation in the interconnected power system.

II. POSSIBLE APPROACH FOR FREQUENCY CONTROL USING SPINNING RESERVE

This chapter illustrates example of frequency control using spinning reserve operation. For integrated power system distribution of spinning reserves is important problem. The operation of several power companies (players), which simplified scheme is presented in Fig.1, is observed. Let us suppose that each company contains several power plants, which are operating in market conditions. At the same time the cooperation between power plants is possible and the support of generated and consumed energy balance at the nominal frequency and costs minimization are the general targets of this cooperation.

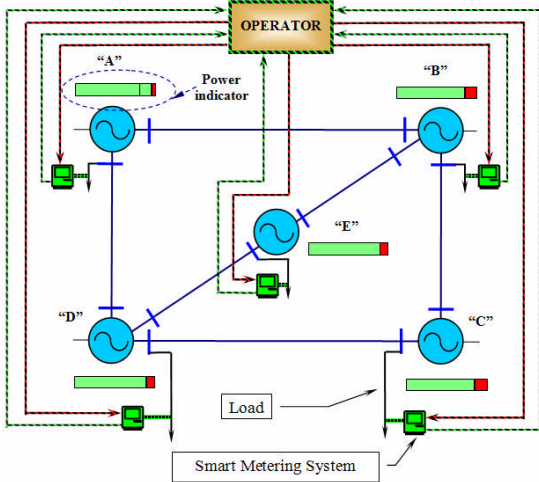


Fig.1 simplified diagram of interconnected power plants involved in primary frequency control

Each power plant is equipped with smart metering system information from which is supplied to the central processing block "Operator".

Let us consider two possible approaches for spinning reserve distribution:

- 1 - Five plants operate independently, supporting specified part (reserve) of the planned power (classical approach);
- 2 – All five plants strive to most profitable operation and costs minimization.

Let's suppose, that five power plants are operating – A, B, C, D, E (Fig.1). The power capacities of each plant are - P_1, P_2, P_3, P_4, P_5 . Production cost values - C_1, C_2, C_3, C_4, C_5 (EUR/MWh). Each plant provides a reserve - p_1, p_2, p_3, p_4, p_5 , with production costs c_1, c_2, c_3, c_4, c_5 (EUR/MWh).

The resulting costs RC_j for each Δt_j (where $j = 1, \dots, N$) are

$$RC_j = \sum_{i=1}^5 (P_i \cdot C_i + p_i \cdot c_i) \cdot \Delta t, \quad (1)$$

Assume, that generators must provide a planned power P_Σ of interconnected power system, as well as possible random deviations of power p_Σ for all i of $C_i < C_i + I$ and $c_i < c_i + I$. Suppose that density of power deviations $f_{ij}(p_{ij})$ is known for each time interval Δt .

The goal is to provide balance of powers:

$$\sum_{i=1}^5 (P_i + p_i) = P_\Sigma + p_\Sigma, \quad (2)$$

with minimal RC_j in the interval Δt .

Selecting generators' powers P_i and reserves p_i it is necessary to take into account many technical limitations, which depend on: thermal and electrical loads of consumers, operational condition of thermal and electrical network, water levels in reservoir of hydro power plants.

To provide these limitations the fulfillment of conditions (3) is required:

$$\{P_{ij}, p_{ij}\} \ni A, \quad (3)$$

where A is the domain of the allowed states of the power system. The task for selection of spinning reserve can be formulated as:

$$\{P_{ij}^*, p_{ij}^*\} = \operatorname{argmin} \sum_{j=1}^N \sum_{i=1}^n (P_{ij} \cdot C_{ij} + E_{ij}(c_R)) \cdot \Delta t_j, \quad (4)$$

with (2) and (3) conditions fulfillment in equation (4) $E_{ij}(RC_{ij})$ is mathematical expectation of the spinning reserve expenses i -th power plant at j -th time interval of Δt .

$$E_{ij}(RC_{ij}) = \int_0^{P_{ijmax}} P_{ij} \cdot c_{ij} \cdot f_{ij}(P_{ij}) dP_{ij}, \quad (5)$$

P_{ij}^* and p_{ij}^* - optimal capacity of considered plants (providing the minimum cost).

Redistribution of network primary power reserve must be done by information and control center "operator". Taking into account complexity of processes, "operator" has to be realized by IT technologies. Let's describe steps of information and control center's algorithm:

- a) algorithm ranks all players (power districts) by value of profitability, from the least to the most profitable (as example see Table 1, 2nd column);
- b) algorithm solves all possible combinations of the primary reserve allocation among the players and calculates the most profitable variant. During analysis of variants the initial data for creation coalition of players can be received.
- c) algorithm calculates the sharing of benefit among the players;
- d) "operator" generates control signals to change the settings of the primary reserve control equipment for each players.

III. BENEFIT SHARING APPROACH

The mentioned above algorithm's point c) is most interesting, because benefit sharing is one of the main power market issues. In the case of the coalition formed by two players, profit sharing is equally distributed between the players (50%/50%).

However, in the case of three, four or five players' coalition, the problem of equitable profit sharing appears. So, if the optimal variant is a coalition of more than two players, profit sharing is done by using the Shapley vector [5].

Let's suppose that the i -th player gets benefit equal to the average value of this player contributions to all coalitions [5]:

$$\phi_i(v) = \sum_{S \subset N} \frac{(|S|-1)!(n-|S|)!}{n!} (v(S) - v(S \setminus \{i\})) \quad (9)$$

The number $v(S) - v(S \setminus \{i\})$ is the contribution of i player when he is joining the coalition $S \setminus \{i\}$, but the weight factor

$$\frac{(|S|-1)!(n-|S|)!}{n!},$$

can be interpreted as the probability of the coalition $S \setminus \{i\}$ forming.

Shapley's value of cooperative game is a vector [5]:

$$\phi(v) = (\phi_1(v), \dots, \phi_n(v))^T \quad (10)$$

IV. CASE STUDY

Let's consider operation of proposed automation using a specific example. Suppose that initial capacities of power plants are known, as well as prices, reserves, etc. Frequency control reserve is stated by system operator equal to 4% of maximal generated power P_{Max} . The initial parameters required for calculations are shown in the Table 1.

The power system operates in normal condition, when the generated and consumed active powers are equal (initial situation): $P_{Generated} = P_{Load} = 6.2$ (p. u.).

Table 1 Parameters of Players Before Optimization

Player	C Cost Price (p. u.)	P _{Max} (p. u.)	P _{Min} (p. u.)	P _{Res} (%)	P _{Pot. Res.} (%)	P _{Generation} (%)
"A"	0.9	1.500	1.410	4.00	0.67	94.66
"B"	0.8	1.400	1.334	4.00	0.43	95.57
"C"	0.7	1.300	1.238	4.00	0.15	95.38
"D"	0.6	1.200	1.132	4.00	1.67	96.00
"E"	0.5	1.100	1.046	4.00	0.36	95.45
Σ		6.5		4.00		95.38
Initial situation						

$C_{cost\ price}$ – production cost value of produced power (p. u.).

Let's assume that the selling price of electricity is equal to 1.1 (p. u.). Algorithm calculates profitability of all possible combinations of players. In our case, using the basic parameters listed in Table 1 and using equations (9) and (10), the algorithm calculates (Fig.2 situation 1) that the best variant would be a coalition of all players ("A+B+C+D+E") with a total additional profit equal to 0.0076 (p. u.).

As a result of proposed optimization, the primary reserve control function is redistributed from more effective power station to a less one (with a higher production cost). The total value of the primary reserve isn't changed.

The maximum additional profit arises in case when the primary reserve was not activated in specific time interval. Using equations (9) and (10), it is possible to calculate the sharing of profit among the players. The results of the sharing are presented in Table. 2

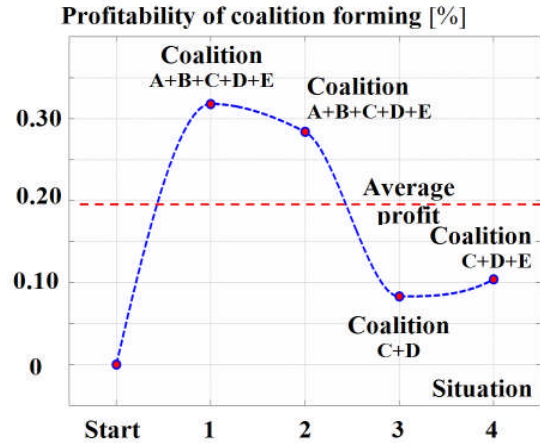


Fig.2 players' profitability in different situations

Table 2 Players' Profitability in Different Situations and Results of Profit's sharing

Number of situation	1	2	3	4
Additional profit of coalition (p. u.)	0.0076	0.0068	0.0020	0.0025
Benefit of player (%)				
"A"	35.74	31.37	0.00	0.00
"B"	10.61	12.60	0.00	0.00
"C"	5.26	18.63	50.00	46.66
"D"	18.86	23.28	50.00	36.66
"E"	29.52	14.12	0.00	16.66

A. Example of Possible Annual Profit Calculation

The visual demonstration of advantage to use suggested method is practical calculation of additional profit using denominated quantities of power system parameters.

When average value of additional profit is equal (see Fig.2) to 0.2% for power system with average capacity equal to 1000 MW and average price of energy is 50EUR/MWh. Additional profit is 876000 EUR.

Such additional benefit will cover the cost of creation the appropriate control system.

V. APPLICATION OF SMART LOAD SHEDDING SYSTEM

Severe system disturbances can result in fast frequency drop, which makes fast governor and boiler response impossible. If the governor action cannot activate spinning reserve quickly enough to restore the system to its normal operating frequency, underfrequency load shedding (UFLS) serves as a last-resort tool to prevent the system from collapse.

In most power systems up-to-date automatic load shedding systems practically foresee disconnection of the load at underfrequency without time delay or with small delay [6]-[8]. The numbers of load shedding steps and the value of load to be shed vary for different power systems. Some power systems use rate-of-change of frequency as additional factor to shed a load [9]. Fig. 3 presents an example of a frequency variation during operation of the frequency actuated load shedding system. The point $f < f_{nom}$ corresponds to the moment of active power deficiency appearance in the power system. From this moment the frequency drop starts. When the power system frequency reaches the level of a first load shedding setting f_{set1} , the first part of the load is disconnected. The next part of the

load will be disconnected when frequency reaches second load shedding setting f_{set2} .

With each next load shedding step rate-of-change of frequency decline is cut down and after a certain moment the increase of frequency takes place. Such logics of the load shedding operation apply to most of the power system utilities [9].

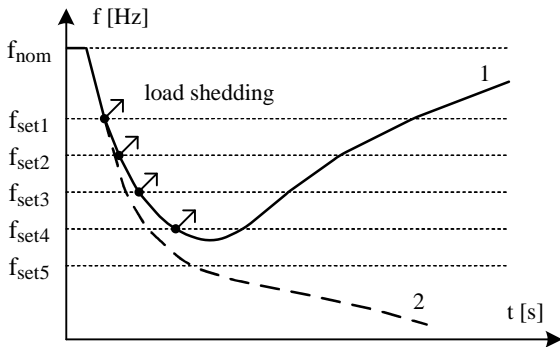


Fig.3 power system frequency variations during the UFLS operation

UFLS schemes can be categorized into three groups [3]:

1. the traditional UFLS schemes;
2. the semi-adaptive UFLS schemes;
3. the adaptive UFLS schemes.

Existing UFLS automation has drawbacks, which limit the adaptability of emergency situation control to a change of underfrequency situation in a power system. UFLS tripping frequency settings are selected for some specific emergency situation, which is considered as more probable for a specific power system. It is not possible to foresee all situations that can occur in the power system. UFLS operation will be secure effective only for the pre-calculated emergency cases. Problems related to the value of a load to be shed are very topical. Redundantly tripped load can create overfrequency situations, which sometimes is more dangerous than underfrequency. Mentioned situation is presented in Fig.4.

The overfrequency situation after UFLS operation happens because the total disconnected load of the steps of UFLS is two times as large as the deficiency of active power in the network [9].

A. Analysis of Frequency Behavior for Different Algorithms of UFLS

Authors investigated frequency behavior during sever disturbances in united ENTSO-E power system and IPS/UPS power system of Russia. Appropriate model was developed with the real settings of load shedding automation. Different variants of frequency behavior were investigated [9].

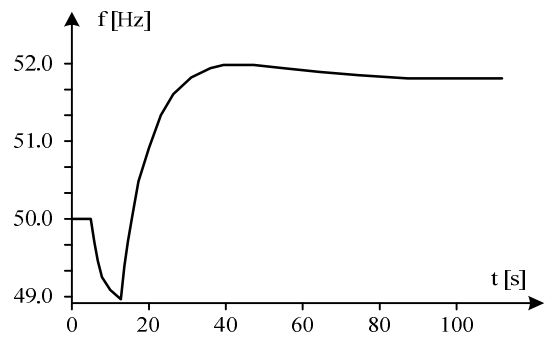


Fig.4 frequency behavior for 10.8% of active power deficiency

As an example frequency behavior at a load deficiency of 20% and an iterative deficiency of the active power of 6.7% is shown in Fig.5. During cascaded event the stabilization of frequency can occur at a dangerously low level without being noticed by UFLS. It can happen if the active power disconnected by UFLS is not sufficient to return frequency back to permissible range. In the considered case the frequency stays at 48.9 Hz. The reason for that is different load shedding philosophy of two interconnected power systems.

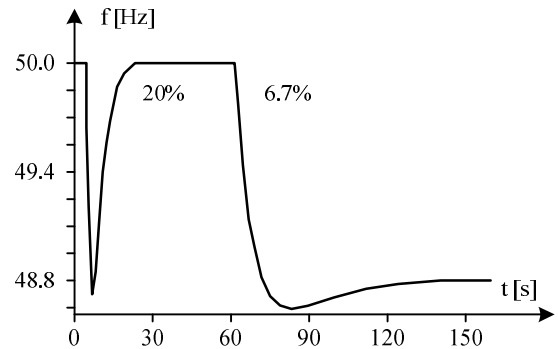


Fig.5 frequency behavior for 26.7% of active power deficiency

B. Application of Smart Technology Approach to the Load Shedding System

Let us return to example of Fig.1 and explain behavior of load shedding automation.

Each district is equipped with an interactive power measuring device (a smart meter) [10]-[14].

The information center “Operator” receives full information about the current condition of the consumption of active power in each power district, about the location and value of the power deficiency that has arisen. In that way, an interactive information system between the districts’ load and emergency automation is set up.

Using described metering system the automation operating process (let us call it smart underfrequency load shedding system — SUFLS) can be presented by few calculation cycles:

1. Determination of the value of the deficiency. Transformed rotor swing equation can be used for calculation of this deficiency [6], [7]:

$$\Delta P = T_J \cdot \frac{df}{dt} + \frac{\Delta f}{k_{gov}} + \Delta f \cdot k_{load} , \quad (11)$$

where T_J – rotor's inertia constant; k_{gov} – governor speed droop; k_{Load} – load-damping constant; f – frequency.

2. Memorization of the value of deficiency and its location;
3. Calculation of the number of substations to compensate the deficiency;
4. Calculation the optimum variant for load disconnection.

To compare the results of the operation of UFLS and SUFLS automation, a mathematical model has been constructed by using Matlab/Simulink software. Fig.6 illustrates frequency behavior in the case of emergency situation for existing UFLS and smart SUFLS automation.

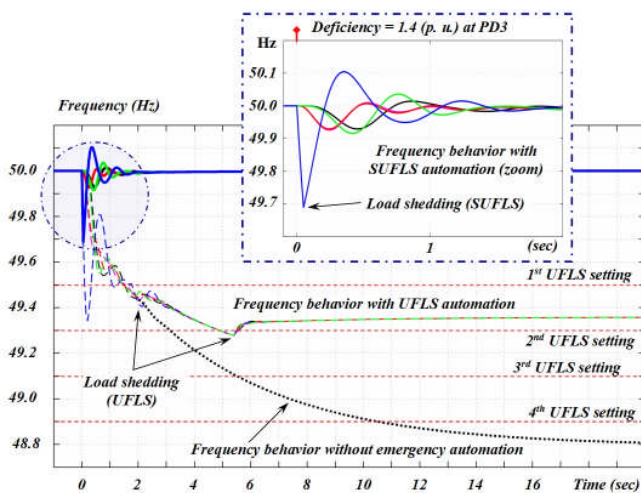


Fig.6 frequency behavior in the case of emergency situation

The more effective operation of SUFLS automation is obvious. The more effective approach is to activate load shedding automation in districts, where power deficiency takes place.

VI. CONCLUSION

Smart metering systems can be used for both – small frequency variations and deep frequency decline operation.

Optimal distribution of the primary reserve can be based on cooperative game theory method.

Proposed algorithm, which takes into account technical limitations and economic aspects of the primary frequency control participants, has to be used.

Results of practical calculation of additional profit prove feasibility of application of game theory method for optimal distribution of frequency control reserves.

The mathematical model of the power system with proposed calculation algorithm can be performed using computer program Matlab Simulink.

Integration of large power systems with different philosophy of underfrequency load shedding systems can cause ineffective

and sometimes not selective frequency control.

A new load shedding method is suggested. Simulation of frequency behavior was conducted for existing load shedding system and a new one.

ACKNOWLEDGMENT



This work has been supported by the European Social Fund within the project «Support for the implementation of doctoral studies at Riga Technical University».

REFERENCES

- [1] Seventh Framework Programme, Energy.7.2, Collaborative Project - Large-scale integrated project PEGASE: Pan European Grid Advanced Simulation and state Estimation, Grant agreement no.: 211407.
- [2] Collaborative Project ICOEUR: Intelligent Coordination of Operation and Emergency Control of EU and Russian Power Grids, Grant Agreement no.: 227122.
- [3] U. Rudez, R. Mihalic, "Analysis of Underfrequency Load Shedding Using a Frequency Gradient", IEEE Trans. Power Syst., vol. 26, no. 2, pp 565 – 575, Apr., 2011.
- [4] V. Chuvychin, N. Gurov, S. Venkata, R. Brown, "An adaptive approach to load shedding and spinning reserve control during underfrequency conditions", IEEE Trans. Power Syst., vol. 11, no. 4, pp. 1805 – 1810, Nov. 1996.
- [5] Lloyd S. Shapley. *A value for n-person games. In contribution to the Theory of Games*, Volume II, by H.W. Kuhn and A.W.Tucker, editors. Annals of Mathematical Studies v.28, pp. 307 -317. Princeton University Press.
- [6] V. Chuvychin, N. Gurov, S. Kiene, "Application of New Emergency Control Principle in Power Systems", Proceedings of IEEE PowerTech2009 Conference, Romania, Bucharest, 29 June – 2 July , 2009 – pp 1-6.
- [7] L. Sterninson, Transient processes in power systems during operation of frequency and power, Moscow: Energy, 1975 (in Russian).
- [8] A. Barzam, System's automation, Energoatomizdat, 1986 (in Russian).
- [9] A. Sauhats, V. Chuvychin, V. Strelkovs, R. Petrichenko, E. Antonov, "Underfrequency Load Shedding in Large Interconnection", PowerTech2013 conference, Grenoble, France, 16-20 June 2013.
- [10] M. Larson, C. Rehtanz, "Predictive frequency stability control based on wide-area phasor measurements", in Proc. 2002 IEEE Power Eng. Soc. Summer Meeting, Chicago, IL, Jul. 2002, vol. 1, pp. 233-238.
- [11] H. Seyedi, M. Sanaye-Pasand, "New centralized adaptive load-shedding algorithms to mitigate power system blackouts", IET Gener. Transm. Distrib., vol. 3, no. 1, pp. 99-114, Jan. 2009.
- [12] F. Pilo, G. Pisano, G. G. Soma, „Advanced DMS to Manage Active Distribution Networks”, IEEE Bucharest Power Tech Conference, Bucharest, Romania, 29 June – 2 July , 2009.
- [13] H. Lemmen, "SMART Transmission System" presentation, IEEE Smart Grid World Forum, Brussels, Belgium, 2-3 december, 2010.
- [14] O. Samuelsson, M. Hemmingsson, A. H. Nielsen, K. O. H. Pedersen, J. Rasmussen, "Monitoring of power system events at transmission and distribution level", IEEE Trans. Power Syst., vol. 21, no. 2, pp. 1007-1008, May, 2006.

Vladimir Chuvychin (M'1979, SM'1990) was born in Russia on January 17, 1941. He received diploma engineer degree in 1965, Candidate of Technical Science degree (Ph.D) in 1975 and Dr.habil.sc. degree in 1997 from Riga Technical University, Riga, Latvia.

Since 1965 he is with Riga Technical University, Faculty of Electrical and Power Engineering where is currently Professor. He was a visiting Fulbright Scholar at the University of Texas, Arlington, in 1990 and at the University of Washington, Seattle in 1994. His research interests include

protective relaying and power system automation and control. He holds many patents in this area.

Antans Sauhats received Dipl. Eng., Cand.Techn.Sc., and Dr.hab.sc.eng. degrees from Riga Technical University (former Riga Polytechnic Institute) in 1970, 1976, and 1991 respectively. Since 1991 he is Professor at Electric Power Systems. Since 1996 he is the Director of the Power Engineering Institute of Riga Technical University. Area of research activity: power system automation and optimisation, protective relaying, development of methods and means for control of normal and emergency conditions in electric power systems, HV Transmission lines fault location.

He has more than 200 scientific publications.

Principal investigator of the Latvian Scientific Council grants; Principal investigator, projects with Latvia, Lithuania, Estonia, Russia power systems and utilities. Developed and implemented disturbance recording systems, fault location system, protective relaying, out of step condition system for 110-330 kV transmission lines and power plants. Developed hardware and software widely used power systems in Latvia, Lithuania, Estonia, and Russia. Total number of implementation more than 500 protective relaying and automation terminals.

Corresponding Member, Latvian Academy of Sciences, 2003. Awarded with Year Prize of the Latvian Academy of Sciences and Public Joint Stock Company "Latvenergo" for life contribution in energetics and engineering, 2003.

Roman Petrichenko received B.Sc. degree in electrical engineering from the Riga Technical University (RTU) in 2006 and 2008, from 2010 he is PhD student at RTU, Latvia. His research interests include power system automation and optimisation, smart grid technologies. He is author of more than 15 papers. He is IEEE student member.

Galina Bochkarjova received Electrical engineer degree from the RTU in 1970. At present she is Research Engineer at Faculty of Power and Electrical Engineering. Area of research activity: protective relaying, power system automation, development of methods and means for control of emergency conditions in electric power systems, HV Transmission lines fault location. She has 37 scientific publications.

A robust stabilizer H_2 -PSS applied to power system (Application under GUI/MATLAB)

GHOURAF Djamel Eddine¹, NACERI Abdellatif¹

Abstract— This article presents a comparative study between two control strategies, a classical regulator PID, and a robust controller H_2 based on LQG control applied on automatic excitation control of powerful synchronous generators, to improve transient stability and its robustness of a single machine- infinite bus system (SMIB). The computer simulation results have proved the efficiency and robustness of the robust H_2 approach, in comparison with using classical regulator PID, showing stable system responses almost insensitive to large parameter variations. This robust control possesses the capability to improve its performance over time by interaction with its environment. The results proved also that good performance and more robustness in face of uncertainties (test of robustness) with the linear robust H_2 controller (optimal LQG controller with Kalman Filter) in comparison with using the classical regulator PID. Our present study was performed using a GUI realized under MATLAB in our work.

Keywords— powerful synchronous generators and Excitations, AVR and PSS, LQG control, Kalman filter, stability and robustness.

I. INTRODUCTION

Power system stability continues to be the subject of great interest for utility engineers and consumers alike and remains one of the most challenging problems facing the power community. Power system oscillations are damped by the introduction of a supplementary signal to the excitation system of a power system. This is done through a regulator called power system stabilizer. Classical PSS rely on mathematical models that evolve quasi-continuously as load conditions vary.

Conventional PSS based on simple design principles such as PI control and eigenvalue assignment techniques have been widely used in power systems [1, 2]. Such PSS ensure optimal performance only at their nominal operating point and do not guarantee good performance over the entire operating range of the power system. This is due to external disturbances such as changes in loading conditions and fluctuations in the mechanical power. In practical power systems networks, a priori information on these external disturbances is always in the form of certain frequency band in which their energy is concentrated.

Remarkable efforts have been devoted to design appropriate PSS with improved performance and robustness. These have led to a variety of design methods using optimal and output feedback methods [3, 5]. The shortcoming of these models-

based control strategies is that uncertainties cannot be considered explicitly in the design stage.

The stabilizer of this new generation for the system AVR – PSS, aimed-at improving power system stability, was developed using the robust controller H_2 based on LQG. This has been advantage of maintaining constant terminal voltage and frequency irrespective of conditions variations in the system study. The H_2 control design problem is described and formulated in standard form with emphasis on the selection of the weighting function that reflects robustness and performances goals [6]. The proposed system has the advantages of robustness against model uncertainty and external disturbances (electrical and mechanical), fast response and the ability to reject noise.

Simulation results shown the evaluation of the proposed linear control methods based on this advanced frequency techniques applied in the automatic excitation regulator of powerful synchronous generators: the robust H_2 linear stabilizer and conventional PID control schemes against system variation in the SMIB power system, with a test of robustness against parametric uncertainties of the synchronous machines (electric and mechanic), and make a comparative study between these two control techniques for AVR – PSS systems.

II. DYNAMIC POWER SYSTEM MODEL:

A. Power System description

In this paper the dynamic model of an IEEE - standard of power system, namely, a single machine connected to an infinite bus system (SMIB) was considered [4]. It consists of a single synchronous generator (turbo-Alternator) connected through a parallel transmission line to a very large network approximated by an infinite bus as shown in figure 1

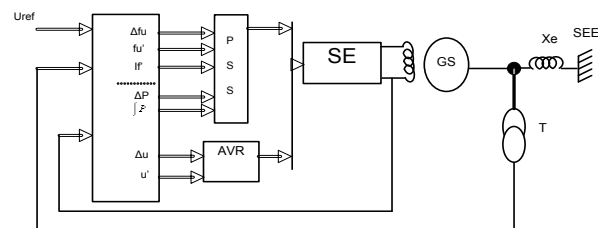


Fig. 1. Standard system IEEE type SMIB with excitation control of powerful synchronous generators

B. The permeances networks modeling (Park-Garivov) of powerful synchronous generators

In this paper we based on the permeances networks modeling of powerful synchronous generators for eliminating simplifying hypotheses and testing the control algorithm. The PSG model is defined by equations and Figure 2 and 3 below [4]:

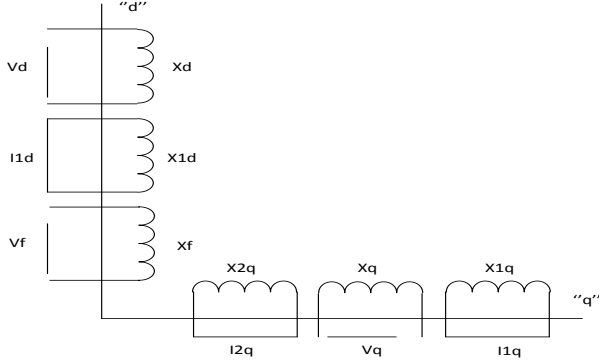


Fig. 2. PARK Transformation of the synchronous machine

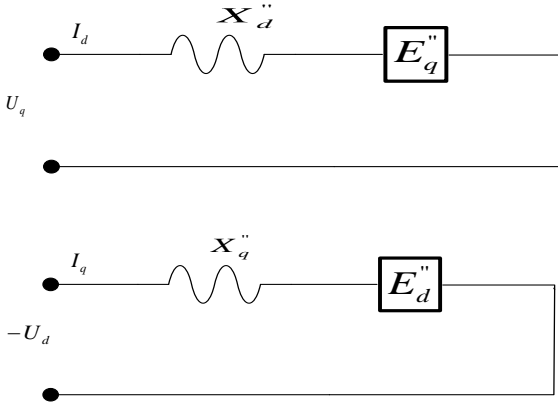


Fig. 3. Equivalent diagrams simplifies of the synchronous machine with damping circuits (PARK-GARIOV model)

1- Currants equations:

$$\begin{aligned} I_q &= (U_q - E_q'') / X_d'' & I_{1q} &= (\Phi_{1q} - \Phi_{aq}) / X_{sr1q} \\ I_d &= -(U_d - E_d'') / X_q'' & I_{2q} &= (\Phi_{2q} - \Phi_{aq}) / X_{sr2q} \\ I_{1d} &= (\Phi_{1d} - \Phi_{ad}) / X_{srd} & I_f &= (\Phi_f - \Phi_{ad}) / X_{sr} \end{aligned} \quad (1)$$

$$E_q'' = \frac{1/X_{sf} \cdot \frac{X_f}{X_{ad}} E_q' + 1/X_{sfd} \cdot \frac{X_{fd}}{X_{ad}} E_{fd}'}{\frac{1}{X_{ad}} + \frac{1}{X_{sf}} + \frac{1}{X_{sfd}}} \quad E_d'' = \frac{1/X_{sfq} \cdot \frac{X_{fq}}{X_{aq}} E_{fd}'}{\frac{1}{X_{ad}} + \frac{1}{X_{sfq}}} \quad (2)$$

2- Flow equations:

$$\begin{aligned} \Phi_{ad} &= E_q'' + (X_d'' - X_s) I_d, \quad \Phi_{aq} = E_d'' + (X_q'' - X_s) I_q \\ \Phi_{1q} &= \omega_s \int_0^{\Phi_{1q}} (-R_{1q} I_{1q}) dt & \Phi_{2q} &= \omega_s \int_0^{\Phi_{2q}} (-R_{2q} I_{2q}) dt \\ \Phi_f &= \omega_s \int_0^{\Phi_f} (-R_f I_f + U_{f0}) dt & \Phi_{1d} &= \omega_s \int_0^{\Phi_{1d}} (-R_{1d} I_{1d}) dt \end{aligned} \quad (3)$$

3- Mechanical equations

$$d\delta = (\omega - \omega_s) dt, \quad s = \frac{\omega - \omega_s}{\omega_s} \quad (4)$$

$$M_T + M_j + M_e = 0 \quad \text{avec } M_j: \text{moment d'inertie} \quad \left(M_j = -j \frac{d\omega}{dt} \right)$$

$$T_j \frac{d}{dt} s + (\Phi_{ad} I_q - \Phi_{aq} I_d) = M_T \quad \text{ou} \quad T_j \frac{d}{dt} s = M_T - M_e \quad (5)$$

$$j \frac{d\omega}{dt} + \frac{P_e}{\omega_s} = M_T$$

C. Models of regulators AVR and PSS:

The AVR (Automatic Voltage Regulator), is a controller of the PSG voltage that acts to control this voltage, thought the exciter. Furthermore, the PSS was developed to absorb the generator output voltage oscillations [1].

In our study the synchronous machine is equipped by a voltage regulator model "IEEE" type - 5 [7, 8], as is shown in Figure 4.

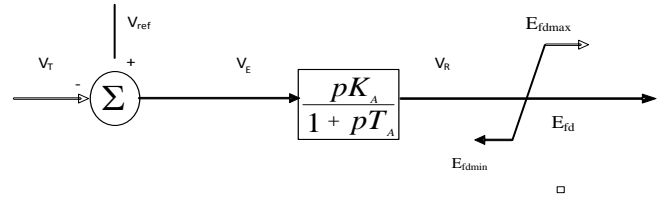


Fig. 4. A simplified "IEEE type-5" AVR

$$V_R = \frac{K_A V_E - V_R}{T_A}, \quad V_E = V_{ref} - V_F \quad (6)$$

About the PSS, considerable's efforts were expended for the developpement of the system. The main function of a PSS is to modulate the SG excitation to [1, 2, 4].

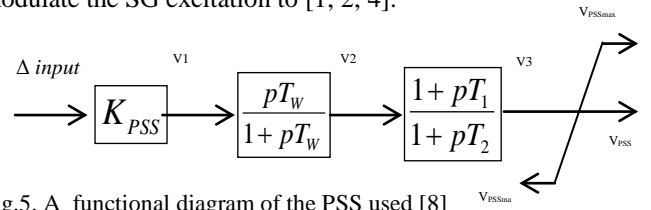


Fig.5. A functional diagram of the PSS used [8]

In this paper the PSS signal used, is given by: [9]

$$\begin{aligned} \dot{V}_1 &= \frac{V_2 - V_1}{T_1} + \frac{T_2}{T_1} \dot{V}_2; \\ \dot{V}_2 &= \frac{V_3 - V_2}{T_2} + \frac{T_3}{T_2} \dot{V}_2; \\ \dot{V}_3 &= \frac{V_3}{T_w} \dot{V}_1; \quad \dot{V}_1 = K_{PSS} \cdot \Delta input \end{aligned} \quad \Delta input = \begin{cases} \Delta P, \int P \\ \text{or} \\ \Delta \omega = \omega_{mch} - \omega_0 \\ \text{and} \\ \Delta I_f = I_f - I_{f0} \\ \text{and} \\ \Delta U_f = U_f - U_{f0} \end{cases} \quad (7)$$

D. Simplified model of system studied SMIB

We consider the system of Figure 6. The synchronous machine is connected by a transmission line to infinite bus type SMIB. With Re: a resistance of the transmission line and Le: an inductance of the transmission line [4].

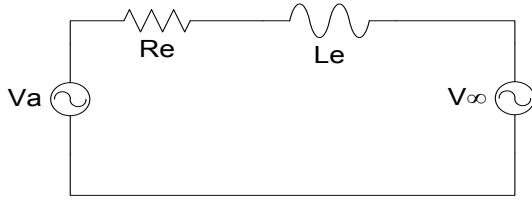


Fig. 6. Synchronous machine connected to an infinite bus network

We define the following equation of SMIB system

$$V_{\infty abc} = P V_{abc} = \sqrt{2} V_{\infty} \begin{bmatrix} 0 \\ -\sin(\delta - \alpha) \\ \cos(\delta - \alpha) \end{bmatrix} + L_e I'_{odq} + X_e \begin{bmatrix} 0 \\ -i_q \\ i_d \end{bmatrix} \quad (8)$$

III. THE ROBUST H_2 -PSS DESIGN BASED ON LQG CONTROL AND KALMAN FILTER

The control system design method by means of modern FSM algorithms is supposed to have some linear test regulator. It is possible to collect various optimal adjustment of such a regulator in different operating conditions into some database. Linear – Quadratic – Gaussian (LQG) control technique is equivalent to the robust H_2 regulator by minimizing the quadratic norm of the integral of quality [13]. In this work, the robust quadratic H_2 controller (corrector LQG) was used as a test system, which enables to trade off regulation performance and control effort and to take into account process and measurement noise [11,5]. LQG design requires a state-space model of the plant:

$$\begin{cases} \frac{dx}{dt} = Ax + Bu \\ y = Cx + Du \end{cases} \quad (9)$$

Where x , u , y is the vectors of state variables, control inputs and measurements, respectively.

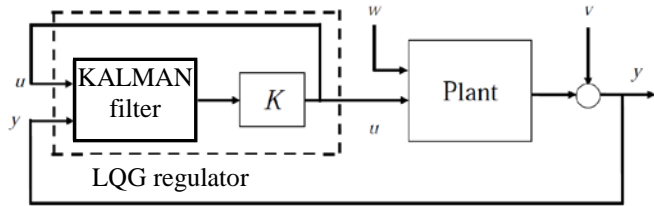


Fig.7. Optimal LQG regulated system with Kalman filter.

The goal is to regulate the output y around zero. The plant is driven by the process noise w and the controls u , and the regulator relies on the noisy measurements $y_v = y + v$ to generate these controls. The plant state and measurement equations are of the form:

$$\begin{cases} \dot{x}(t) = A(t)x(t) + B(t)u(t) + v(t) \\ y_v(t) = C(t)x(t) + w(t) \end{cases} \quad (10)$$

Both w and v are modeled as white noise.

In LQG control, the regulation performance is measured by a quadratic performance criterion of the form:

$$J(u) = \int_0^{\infty} (x^T Q x + u^T R u + 2x^T N u) dt \quad (11)$$

The weighting matrices Q , N and R are user specified and define the trade-off between regulation performance and control effort.

The LQ-optimal state feedback $u = -kx$ is not implemental without full state measurement. However, a state estimate \hat{x} can be derived such that $u = -k\hat{x}$ remains optimal for the output-feedback problem.

This state estimate is generated by the Kalman filter:

$$\frac{d\hat{x}}{dt} = A\hat{x} + Bu + L(y_v - C\hat{x} - Du) \quad (12)$$

Thus, the LQG regulator consists of an optimal state-feedback gain and a Kalman state estimator (filter), shown in figure 7

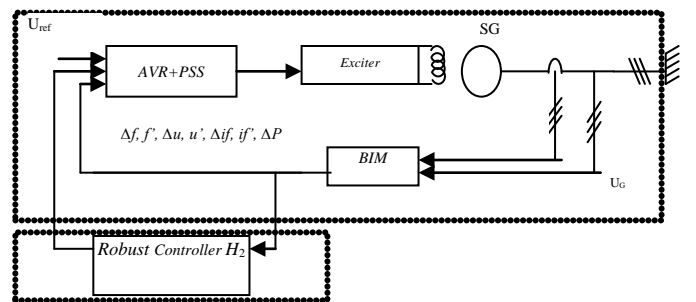
On the basis of investigation carried out, the main points of fuzzy PSS automated design method were formulated [6]. The nonlinear model of power system can be represented by the set of different linearized models (9). For such models, the linear compensator in the form of $u = -Kx$ can be calculated by means of LQG - method. The family of test regulators is transformed into united fuzzy knowledge base with the help of hybrid learning procedure (based variable structure sliding mode). In order to solve the main problem of the rule base design, which called “the curse of dimensionality”, and decrease the rule base size the scatter partition method [13] was used. In this case, every rule from the knowledge base is associated with some optimal gain set. The advantage of this method is the practically unlimited expansion of rule base. It can be probably needed for some new operating conditions, which are not provided during learning process. Finally, the robust H_2 stabilizer was obtained by minimizing the quadratic norm $\|M\|_2^2$ of the integral of quality $J(u)$ in (3), where

$$Z(s) = M(s)x_0 \quad \text{and} \quad Z = [x^T Q^{1/2} u^T R^{1/2}]^T, s = j\omega. \quad [6]. \quad (13)$$

A. Structure of the power System with Robust Controllers H_2

The basic structure of the control system a powerful synchronous generator with the robust controller shown in Figure 8 [3]

As command object we have synchronous generator with regulator AVR-FA (PID with conventional PSS), an excitation system (exciter) and an information block and measures (BIM) of output parameters to regulated


 Fig 8. structure of the power system with robust controllers H_2

IV. THE SIMULATION RESULT UNDER GUI/ MATLAB

A. Creation of a calculating code under MATLAB / SIMULINK

The "SMIB" system used in our study includes:

- A powerful synchronous generator (PSG) ;
- Tow voltage regulators: AVR and AVR-PSS connected to;
- A Power Infinite network line

We used for our simulation in this paper, the SMIB mathematical model based on permeances networks model culled Park-Gariov, and shown in Figure 9 [10]

B. A Created GUI/MATLAB

To analyzed and visualized the different dynamic behaviors we have creating and developing a "GUI" (Graphical User Interfaces) under MATLAB .This GUI allows as to:

- Perform control system from PSS controller;
- View the system regulation results and simulation;
- Calculate the system dynamic parameters ;
- Test the system stability and robustness;
- Study the different operating regime (under-excited, rated and over excited regime).

The different operations are performed from GUI realized under MATLAB and shown in Figure 10.

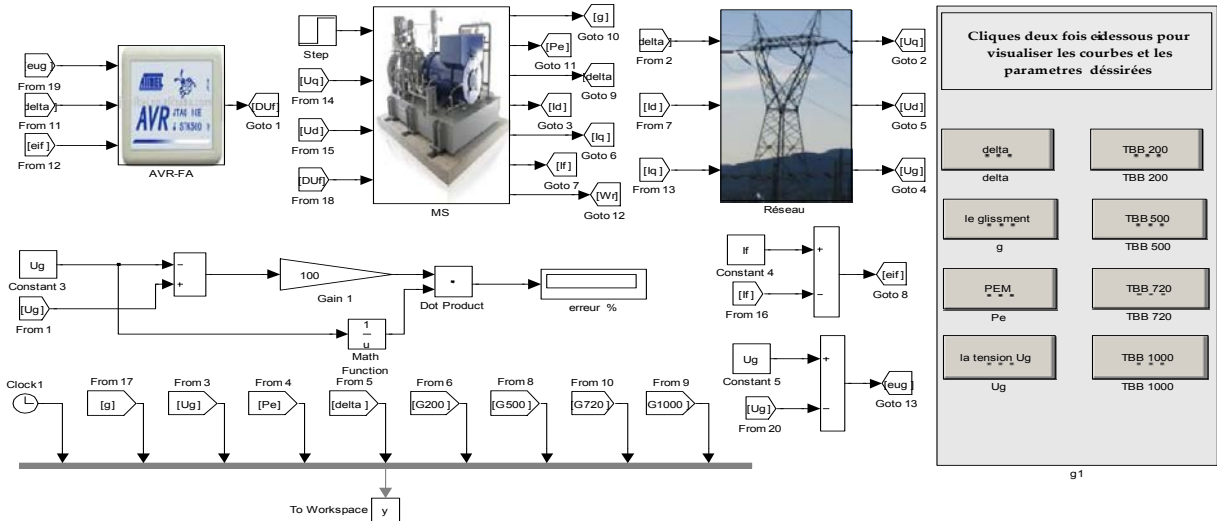


Fig 9. Structure of the synchronous generator (PARK-GARIOV model) with the excitation controller under [10].

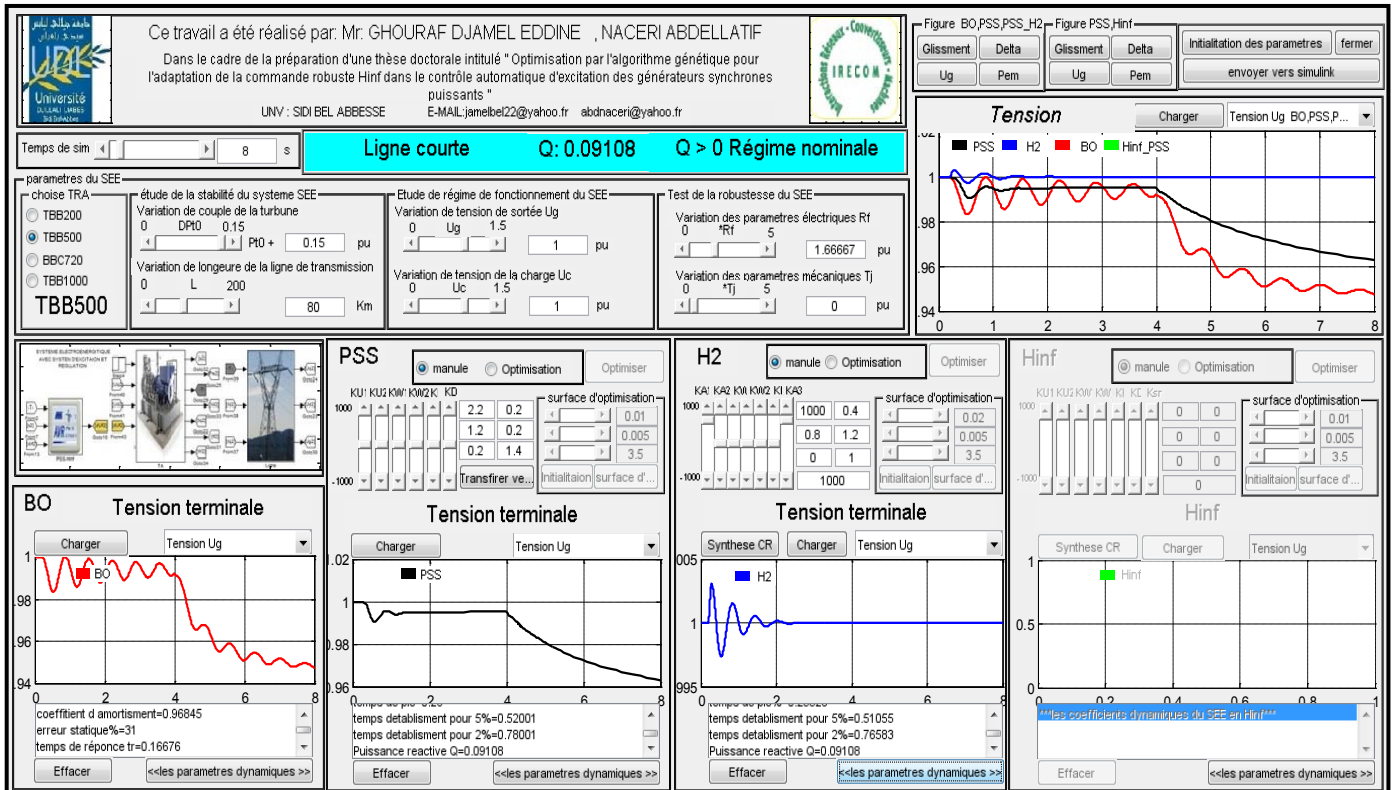


Fig.10.The realised GUI / MATLAB

C. Simulation result and discussion

• Stability study

We performed an perturbations by abrupt variation of turbine torque ΔT_m of 15% at $t = 0.2s$,

The following results (Table 1 and Figure 11, 12) were obtained by studying the “SMIB” static and dynamic performances in the following cases:

1. SMIB in open loop (without regulation) (OL)
2. Closed Loop System with the conventional stabilizer PSS-FA and robust control H_2 -PSS [10].

We simulated three operating: the under-excited, the rated and the over-excited.

Our study is interested in the powerful synchronous Generators of type: TBB-200, TBB-500 BBC-720, TBB-1000 (parameters in Appendix) [10].

Table 1 presents the BBC -720 static and dynamic performances results in (OL) and (CL) with PSS and H_2 -PSS, for an average line ($X_e = 0.3 pu$), and an active power $P=0.85 pu$, for more details about the calculating parameters see GUI-MATLAB in the Appendix created.

Where: α : Damping coefficient ε %: the static error, $d\%$: the maximum overshoot, t_s : the setting time

TABLE 1 THE “SMIB” STATIC AND DYNAMIC PERFORMANCES

Q	Damping coefficient α				The static error			
	OL	AVR	PSS	H_2 -PSS	OL	AVR	PSS	H_2 -PSS
-0.1372	Unstable	-0.709	-1.761	-2.673	Unstable	2.640	1.620	negligible
-0.4571	Unstable	-0.708	-1.731	-2.593	Unstable	2.673	1.629	negligible
0.1896	-0.0813	-0.791	-1.855	-2.766	5.038	2.269	1.487	negligible
0.3908	-0.1271	-0.634	-1.759	-2.695	5.202	1.807	1.235	negligible
0.5078	-0.1451	-0.403	-1.470	-2.116	3.777	0.933	0.687	negligible
0.6356	-0.1588	-0.396	-1.442	-2.099	3.597	0.900	0.656	negligible
The setting time for 5%					The maximum overshoot %			
Q	OL	AVR	PSS	H_2 -PSS	OL	AVR	PSS	H_2 -PSS
-0.1372	Unstable	4,231	1,704	rapid	9,572	9,053	7,892	3,682
-0.4571	Unstable	4,237	1,713	rapid	9,487	9,036	7,847	3,482
0.1896	-	3,793	1,617	rapid	10,959	9,447	8,314	3,915
0.3908	-	4,732	1,706	rapid	10,564	8,778	7,883	3,737
0.5078	14,320	7,444	2,041	rapid	9,402	6,851	6,588	2,290
0.6356	14,423	7,576	2,080	rapide	9,335	6,732	6,463	6,012

In the Figures 11,12 and 13 show an example of simulation result with respectively: 's' variable speed, 'delta' The internal angle, 'Pe' the electromagnetic power system, 'Ug' the stator terminal voltage; for powerful synchronous generators BBC -720 with $P = 0.85$, $X_e = 0.3$, $Q1 = -0.1372 (pu)$

• Robustness tests

In a first step we performed an variations electrical parametric (increase 100% of R). then, we performed an variations mechanical parametric (lower bound 50% of inertia J)

The simulation time is evaluated at 8 seconds.

We present in Figure 10 (For electrical uncertainties) and Figure 11 (For mechanical uncertainties)

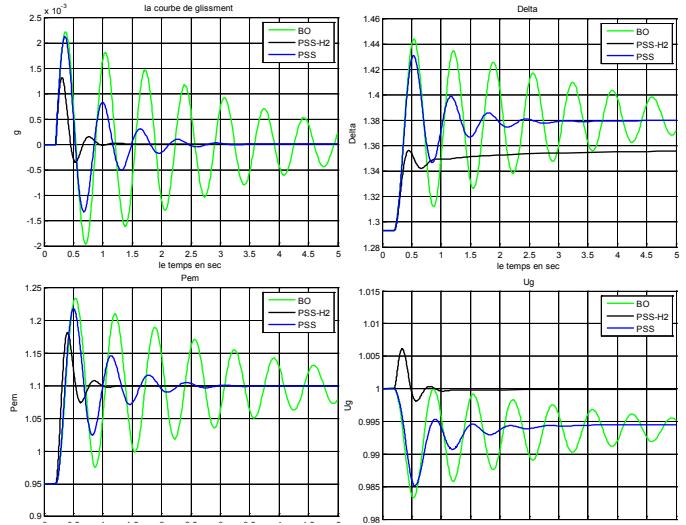


Fig .11. Functioning system in the under-excited used of BBC 720 connected to a average line with PSS , H_2 -PSS and OL (Stability study)

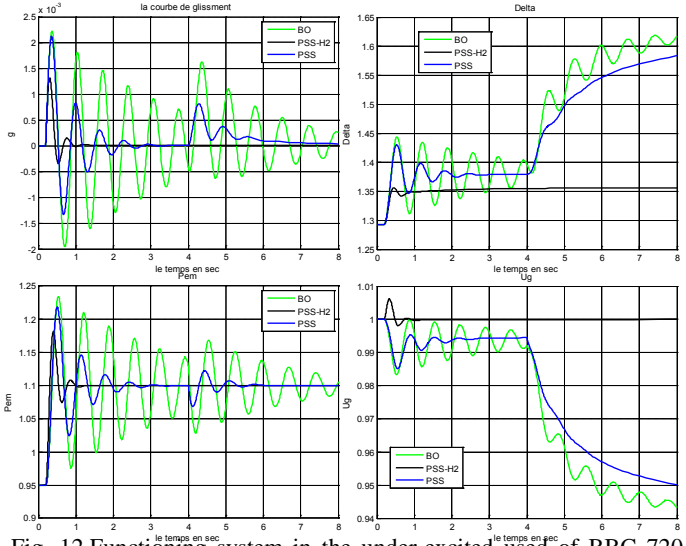


Fig .12. Functioning system in the under-excited used of BBC 720 connected to a average line with PSS , H_2 -PSS and OL (Robustness tests)

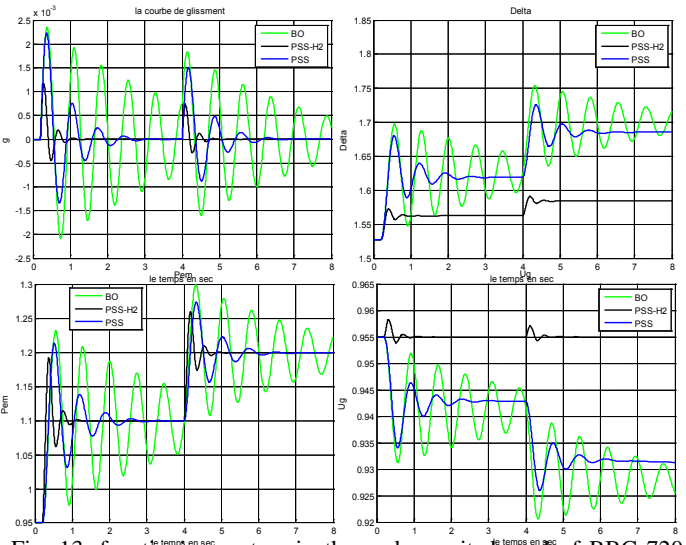


Fig .13. functioning system in the under-excited used of BBC 720 connected to a average line with PSS , H_2 -PSS and OL (Robustness tests)

From the simulation results, it can be observed that the use of H₂-PSS improves considerably the dynamic performances (static errors negligible so better precision, and very short setting time so very fast system, and we found that after few oscillations, the system returns to its equilibrium state even in critical situations (specially the under-excited regime) and granted the stability and the robustness of the studied system.

V. CONCLUSION

This paper proposes an advanced control method based on advanced frequency techniques: robust H₂ approach's (an optimal LQG controller with Kalman Filter), applied on the system AVR - PSS of powerful synchronous generators, to improve transient stability and its robustness of a single machine- infinite bus system (SMIB). This concept allows accurately and reliably carrying out transient stability study of power system and its controllers for voltage and speeding stability analyses. It considerably increases the power transfer level via the improvement of the transient stability limit.

The computer simulation results (with test of robustness against electric and mechanic machine parameters uncertainty), have proved a high efficiency and more robustness with the Robust H₂- PSS, in comparison using a conventional stabilizer (with a strong action) realized on PID schemes, showing stable system responses almost insensitive under different modes of the station. This robust H₂ generator voltage controller has the capability to improve its performance over time by interaction with its environment.

REFERENCES

[1] LA. GROUZDEV, A.A. STARODEBSEV, S.M. OUSTINOV "Conditions d'application des meilleurs amortissements des processus transitoires dans les systèmes énergétiques avec optimisation numérique des paramètres du régulateur AVR-FA" Energie -1990-N°II-pp.21-25 (traduit du russe).

[2] DEMELLO F.P., FLANNETT L.N. and UNDRILL J.M., « Practical approach to supplementary stabilizing from accelerating power », IEEE Trans., vol. PAS-97, pp. 1515-1522, 1978.

[3] DEMELLO F.P. and CONCORDIA C., « Concepts of synchronous machine stability as affected by excitation control », IEEE Trans. on PAS, vol. PAS-88, pp. 316–329, 1969.

[4] S. V. SMOLOVIK "Méthodes de modélisation mathématique des processus transitoires des générateurs synchrones plus usuels et non traditionnels dans les systèmes électro -énergétiques" Thèse doctorat d'état, Institut polytechnique de Leningrad, 1988 (traduit du Russe).

[5] G. STEIN and M. ATHANS "The LQG/LTR procedure for multivariable feedback control design" , IEEE Transaction on Automatic Control, vol. 32, No 2, 1987.

[6] NACERI A., "Study and Application of the advanced methods of the robust H₂ and H_∞ control theory in the AVR-PSS systems of Synchronous machines", PhD Thesis, SPBSPU, Saint Petersburg, Russia, 2002 (In Russian).

[7] P. KUNDUR, "Definition and Classification of power System Stability", Draft 2, 14 January,2002

[8] P.M. ANDERSON, A. A. FOUAD "Power System control and Stability", IEE Press, 1991.

[9] HONG Y.Y. and WU W.C.,« A new approach using optimization for tuning parameters of power system stabilizers », IEEE Transactions on Energy Conversion, vol. 14, n°. 3, pp. 780–786, Sept. 1999.

[10]GHOURAF D.E., "Study and Application of the advanced frequency control techniques in the voltage automatic regulator of Synchronous machines", Magister Thesis, UDL-SBA, 2010 (In French).

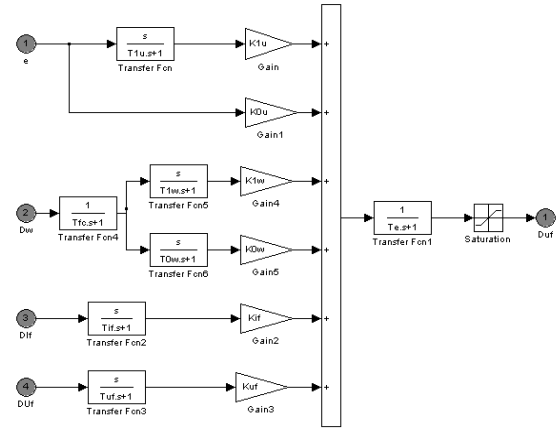
[11]KWAKERNAAK H., SIVAN R. Linear Optimal Control Systems, Wiley-Interscience, 1972.

[12]G. STEIN and M. ATHANS "The LQG/LTR procedure for multivariable feedback control design" , IEEE Transaction on Automatic Control, vol. 32, No 2, 1987.

[13] YURGANOV A.A., SHANBUR I.J. 'Fuzzy regulator of excitationwith strong action, proceeding of SPbSTU scientific conference"Fundamental Investigation in Technical Universities", Saint- Petersburg, 1998. (In Russian)Kwakernaak H., Sivan R. Linear Optimal Control Systems, Wiley-Interscience, 1972.

APPENDIX

1. The PSS-AVR model



2. Parameters of the used Turbo –Alternators

Parameters	TBB-200	TBB-500	BBC-720	TBB1000	Units of measure
power nominal	200	500	720	1000	MW
Factor of power nominal	0.85	0.85	0.85	0.9	p.u.
X_d	2.56	1.869	2.67	2.35	p.u.
X_q	2.56	1.5	2.535	2.24	p.u.
X_s	0.222	0.194	0.22	0.32	p.u.
X_f	2.458	1.79	2.587	2.173	p.u.
X_{sf}	0.12	0.115	0.137	0.143	p.u.
X_{sfd}	0.0996	0.063	0.1114	0.148	p.u.
X_{sf1q}	0.131	0.0407	0.944	0.263	p.u.
X_{sf2q}	0.9415	0.0407	0.104	0.104	p.u.
R_a	0.0055	0.0055	0.0055	0.005	p.u.
R_f	0.000844	0.000844	0.00176	0.00132	p.u.
R_{1d}	0.0481	0.0481	0.003688	0.002	p.u.
R_{1q}	0.061	0.061	0.00277	0.023	p.u.
R_{2q}	0.115	0.115	0.00277	0.023	p.u.

GHOURAF. D.E A Phd student at the Djilali EL Yabess University of Sidi Bel Abbes Department of Electrical Engineering, member of IRECOM laboratory, BP 98, SBA, Algeria
 E-MAIL:jamelbel22@yahoo.fr
 GHOURAF. Djamel Eddine: born 16/01/1985 in Algeria.

The stochastic approach for determination of transmission line wire cross section

Lubov Petrichenko, Antans Sauhats, Svetlana Guseva, Svetlana Berjozkina, Viktoria Neimane

Abstract—In this paper two approaches to choosing the optimum cross-section for an overhead line in the market conditions are considered: the deterministic approach and the stochastic one. This paper presents a new approach for implementing stochastic optimization procedure and comparing the results obtained by the two methodologies. The paper proposes a stochastic method of minimizing the annual costs for the construction of the line based on a statistical representation of the electric power prices, ambient temperature and electrical current loads in the electrical networks. The use of the Monte-Carlo method and the mentioned statistical data allow the synthesis of a user-friendly algorithm to solve this problem. As examples of stochastic approach 110 kV and 330 kV line were chosen. The solution tasks are done in MATLAB and “SAPR LEP 2011” softwares.

Keywords— Costs minimization, network development, stochastic approach, transmission lines.

I. INTRODUCTION

PLANNING of the development of transmission networks pursues a number of conflicting, in common case, objectives, which include the following minimization tasks: power losses, capital investments, operation and maintenance costs and costs of energy not supplied due to interruptions in the network [1]. The complexity of the set task is caused by multiple objectives, the large number of variables, and random or uncertain character of initial information as well as dynamic nature of the problem.

In recent years, power industries have faced considerable changes including deregulation, open markets, appearance of local generation and renewable generation sources. These factors significantly change the planning task and the solution

conditions and inspire a search for a new, more adequate method. Therefore, it is necessary to carry out more adequate technical and economic calculations in order to determine the compromise solution between the construction and exploitation costs [2].

One of the main elements of a rational construction of electric networks is the correct choice of conductor cross-sections at the new overhead power line design stage or in the network reconstruction situation. Therefore the choice of the optimum cross-section of conductors at design stage of networks determines the further costs in the operation of networks.

All the existing methodologies for selection the optimum conductor cross-section can be divided into the following two categories: the deterministic approach and the stochastic approach.

Significant changes in the conditions of power systems operation are leading to the necessity to consider significant fluctuations in the electricity prices. As a result there is a need for modification and verification of suitability of traditional deterministic approach. To test the validity of deterministic approach the stochastic method, which is outlined below, has been developed. However, convenience of employ, simplicity of obtaining additional information can pose the task of its development and use as a basic tool for the choice of the parameters of the wires.

This paper initially is devoted to a stochastic formulation of the problem. The complexity of the problem and two ways to simplify it are shown. The first way is based on the refusal to account dispersion of random variables [3], [4]. The second applies a user-friendly model for modeling of random processes.

II. SUBSTANCE OF STOCHASTIC APPROACH

The anticipated optimization problem is based on minimization of annual costs, which can be described as:

$$C = \varphi(I, \beta, T_{amb}, II) \quad (1)$$

where I, β, T_{amb} are respectively line power, energy price and the ambient temperature;

II includes the set of other parameters influencing annual

L. Petrichenko is with the Faculty of Power and Electrical Engineering, Riga Technical University, Riga, LV-1010 Latvia (e-mail: lubova.petrichenko@rtu.lv).

A. Sauhats is with the Faculty of Power and Electrical Engineering, Riga Technical University, Riga, LV-1010 Latvia (e-mail: sauhatas@eef.rtu.lv).

S. Guseva is with the Faculty of Power and Electrical Engineering, Riga Technical University, Riga, LV-1010 Latvia (e-mail: guseva@eef.rtu.lv).

S. Berjozkina is with the Faculty of Power and Electrical Engineering, Riga Technical University, Riga, LV-1010 Latvia (e-mail: svetlana.berjozkina@gmail.com).

V. Neimane is with Power Technology department at Vattenfall Research&Development (VRD) (e-mail: viktorija.neimane@vattenfall.com).

costs (such as maintenances cost, investments, interest rate).

Analyzing (1) one can claim that power and temperature are random time dependent parameters [3], which are correlated to each other. Correspondingly also C is a random time function, since it includes random time dependent parameters.

Multidimensional random process $C(t)$ can be simplified by discretisation [3] of the function to a number of time periods:

$$t_1, t_2 \dots t_n < T_{PL}, \quad (2)$$

where T_{PL} is the length of planning period.

Probability distribution function can be assigned for each time period. These distribution functions can be described as [5]:

$$\left\{ \begin{array}{l} \Phi_{(1)}(C_1, t_1) \equiv P\{C(t_1) < C_1\}, \\ \Phi_{(2)}(C_1, t_1; C_2, t_2) \equiv \\ \equiv P\{C(t_1) < C_1; C(t_2) < C_2\}, \\ \dots \end{array} \right. \quad (3)$$

Probability distribution function is as following:

$$\left\{ \begin{array}{l} p_{(1)}(C_{G,1}, t_1) \equiv P\{C_G(t_1) = C_{G,1}\}, \\ p_{(2)}(C_{G,1}, t_1; C_{G,2}, t_2) \equiv P\{C_G(t_1) = \\ = C_{G,1}; C_G(t_2) = C_{G,2}\}, \\ \dots \\ \varphi_{(1)}(C_{G,1}, t_1) = \frac{\partial \Phi_{(1)}}{\partial C_{G,1}}, \\ \varphi_{(2)}(C_{G,1}, t_1; C_{G,2}, t_2) = \frac{\partial^2 \Phi_{(2)}}{\partial C_{G,1} \partial C_{G,2}} \end{array} \right. \quad (4)$$

Having the probability distribution functions the average costs can be calculated as:

$$\begin{aligned} M\{f[C(t_1), \dots, C(t_n)]\} = \\ = \int_{-\infty}^{\infty} \dots \int_{-\infty}^{\infty} f(C_1, \dots, C_n) d\Phi_{(n)}(C_1, t_1, \dots, C_n, t_n) \end{aligned} \quad (5)$$

Analyzing the equation (5) one can easily state that stochastic approach has lead us to formulation of extremely complicated target function, especially for minimization problems solution. Indeed, use of a stochastic approach requires large-scale statistical data and performance of labour-intensive calculations. Existence of this fact has formed the main barrier for stochastic approach implementation. Therefore, due to the rapid development of technologies, especially in the data communication and computing areas, this

drawback of stochastic approach becomes insignificant.

III. SUBSTANCE OF DETERMINISTIC APPROACH

To explain the deterministic approach, we have to go back to (1) and assume that this equation does not include random parameters. In this case the total annual line exploitation costs depending on cross-section and line maximal current can be defined as follows [6, 7]:

$$\begin{aligned} C_1 &= (i + p_{\Sigma}) \cdot K_{L1} + 3 \cdot I_{maks}^2 \cdot R_1 \cdot (\tau \cdot \beta' + \beta'') \cdot 10^{-3} \\ C_2 &= (i + p_{\Sigma}) \cdot K_{L2} + 3 \cdot I_{maks}^2 \cdot R_2 \cdot (\tau \cdot \beta' + \beta'') \cdot 10^{-3} \\ &\dots \\ C_i &= (i + p_{\Sigma}) \cdot K_{Li} + 3 \cdot I_{maks}^2 \cdot R_i \cdot (\tau \cdot \beta' + \beta'') \cdot 10^{-3} \end{aligned} \quad (6)$$

where i is the market interest rate, r.u.;

p_{Σ} are the total deductions on amortization, running repair and maintenance from the capital investments in the line construction, r.u.;

K_L is capital investments of overhead line, €km.

τ is the annual utilization period per year, $\tau = f(T_{max})$, h;

T_{max} is the utilization time of maximum load per year, h;

β' is the specific price of electric power losses, €/kWh;

β'' is the specific price of capacity at the maximum time of power system load, €/kW.

R is active resistance of the wire line, Ω/km.

To simplify the choice of the line cross-section one can calculate and outline nomograms by using equation (6). The method of nomograms is also called the method of economical intervals [6]-[9]. This graphical representation has a shape of intersecting parabolic lines. The intersections of these lines indicate the values of the line current $I_{12} \dots I_{(i-1),i}$ at which the transition from one cross-section to another is economically viable. The segment between two marginal current values corresponds to certain cross-section optimal for this segment. The new set of parameters p_{Σ} , β' , β'' in (6) results in a new set of intersecting parabolic lines. The thick bottom line points at calculated minimal costs and the corresponding optimal cross-sections for each segment.

The choice of cross sections can be made knowing the maximal current and the parameters in equation (6). The examples of economic intervals for 110kV and 330 kV overhead lines are presented in Fig.1, Fig.2. Capital investments are calculated by special program "SAPR LEP 2011" and are described in VII part of the paper.

In Fig.1 it is seen that transfer from cross section 1xAS-185mm² to 1xAS-240mm² is economically profitable at line current value 100A. In Fig.2 transfer from cross section 1xAS-400mm² to 1xAS-500mm² is profitable at 350A, but from 2xAS-300mm² to 2xAS-400mm² – 600A. If curves that don't have any crossing with other ones, then corresponding cross sections are economically unprofitable and are not used for line construction.

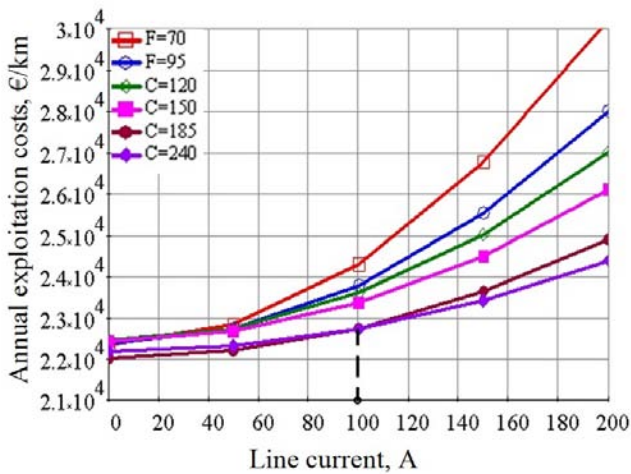


Fig.1. Current economic intervals for 110 kV overhead lines with AS wire

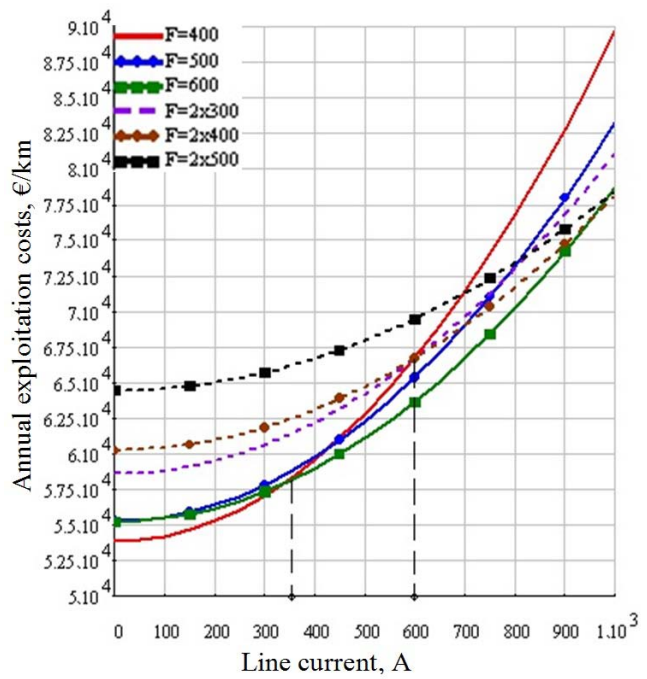


Fig.2. Current economic intervals for 330 kV overhead lines with decomposed AS wires and single AS wire in phase.

IV. DETERMINISTIC APPROACH'S SHORTCOMINGS

The deterministic approach is simpler; however, it uses a number of assumptions, the validity of which at the new (market) conditions is questionable. By using the deterministic approach, it is difficult to reflect non-linear behavior of the system.

The main drawback of the deterministic method is assumptions leading to disregarding of random parameters in equation (1). In addition, according to the equation (6) the relation between costs and the load current is a nonlinear function. It can be stated that the dispersions of the load current, electricity prices, line resistances (considering temperature dependence) are considerable and influence the final calculation result. Variability of the load current in (6) is

taken into account by choosing annual utilization period per year τ , price variation is not taken into account at all.

Thus, there is a need to investigate suitability of deterministic approach or necessity to replace it with a more accurate stochastic approach.

V. SYNTHESIS OF ALGORITHM BASED ON STOCHASTIC APPROACH

Let us return to the stochastic problem formulation described by equation (5). In order to estimate annual costs according to (5) the complicated multidimensional integral should be calculated. It should be added that for the considered task the dimension of the integral can be huge, since the planning period for the transmission lines is normally 25-40 years at the same time the electricity prices can vary considerably on hourly bases. This means that the number of discrete time periods leading to the dimension of the integral can become hundreds of thousands.

Moreover, in specified task it is necessary to operate with a minimum of three correlated processes. In this case autocorrelation and correlation functions [2], [10] should be taken into account. It can be confirmed, that in order to avoid labor intensive calculating it is necessary to limit the number of sampling time moment, because each moment should be described by the distribution function. For this purpose it is possible to use detachment of year into few specific days (winter, spring and autumn, summer, work or holidays) [1]. The distribution functions of the parameters for each of such days can be approximated for example by Pearson charts [2]. However, this kind of analysis still demands a lot of efforts. This paper presents the new approach to solve the problem.

The algorithm for estimation of cost of power losses described below is based on the following assumptions:

- 1) Cost of power losses is the random time dependent function;
- 2) Considerable amount of data from the past is available (databases formed by supervisory control and data acquisition (SCADA) system);
- 3) The records from the past can be projected into the future processes;
- 4) Projection of the records from the „past” ($T_{amb}^P(t)$, $\beta^P(t)$, $I^P(t)$) into the „future” processes ($T_{amb}^F(t)$, $\beta^F(t)$, $I^F(t)$) can be performed by using one of the load forecasting parametric or artificial intelligence based methods [11].

In this paper there is a use of the following two algorithms (see Fig. 3):

- using the linear algebraic expressions that describe changes in the characteristics of the random process in time (for example average value and standard deviation of line power changes in the future).
- by summing up the records of past processes with anticipated changes. In this case, to the load of past years can be attached the planned new energy objects load.

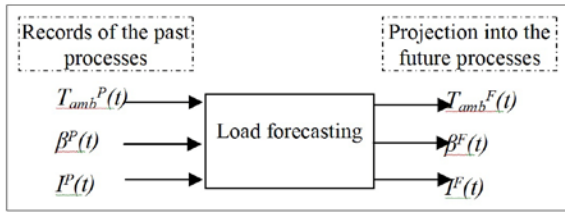


Fig. 3. Load forecasting scheme structure

5) The random process of variations in cost of power losses is ergodic [5]: (the term is used to describe a dynamical system which, broadly speaking, has the same behavior averaged over time as averaged over the space of all the system's states). In this case:

$$M\{C(t)\} \approx \int_{T_i}^{T_i+8760} \varphi(P(t), \beta(t), T_{amb}(t), II) dt \quad (7)$$

where T_i-T_i+8760 is duration year long period.

Adopting (7) instead of (5) allows calculating the average value of annual costs based on multidimensional random process with $I(t)$, $B(t)$, $T_{amb}(t)$.

In this approach due to the implementation of new smart grid technologies realization of (7) became very simple and allows to perform multidimensional registration of parameters (power, air temperature, prices, etc.) and to create an electronic database (library).

The key points of each method for determining annual costs are presented in Fig. 4.

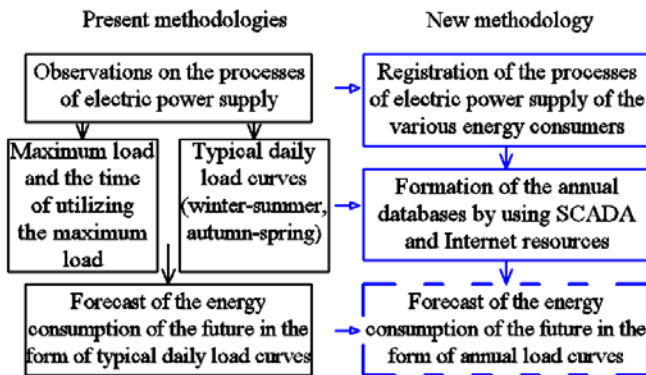


Fig.4. The key points of each method for determining the annual costs

VI. DESCRIPTION OF STOCHASTIC APPROACH'S ALGORITHM

The new approach is based on following stochastic processes realization records application:

- Price change records of market.
- Ambient temperature records.
- Line load records.

The process of price and load changes during the time is expressed as non-stationary process that is why the historical records should be corrected.

The load records for the new line simply do not exist. There are two ways how to solve this problem:

- 1) select the line, which is analogue to the new one (by consumer type and number)
- 2) use the individual consumer load records and calculate the total line load by the summing up all the consumer loads.

Ambient temperature change process can be considered as stationary (if not taking into account climate changes). This means that the temperature records can be used without correction.

The structure the proposed algorithm is given in Fig. 5.

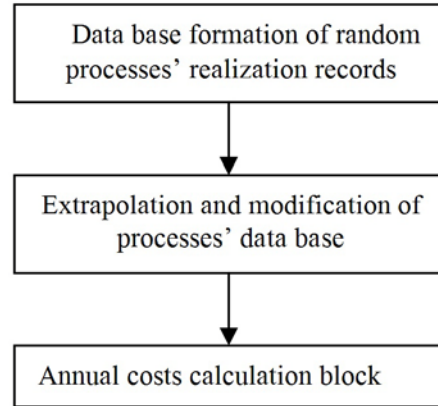


Fig.5. Simplified algorithm for calculation of annual line exploitation costs

Annual costs are calculated using the extrapolated and modified data.

Let's determine two problems, which appear using this algorithm:

- 1) Calculation of line annual costs demands a huge amount of input data and extensive calculations.
- 2) Extensive calculations.

The first problem can be solved, using Internet opportunities and public available data bases, besides the load data which is formed and recorded by power utility companies. But extensive calculations can be simplified using Monte-Carlo method.

The method of Monte-Carlo [10], [12] for average costs (7) calculation is very applicable. The new approach is realized in a software and enables quickly and easily to solve the set task. In our case, the solution task is done in MATLAB.

VII. CASE STUDY

In general, the capital investments of transmission line construction are calculated by using simplified formulas, but nowadays due to the constantly changing conditions of the design – the transition from typical model design solutions to an individual approach as well as economic factors and modern energy market conditions directly affect the changes in prices, thus creating significant differences in costs. In consequence, it is necessary to evaluate capital investments in more precise formulation of the posed problem, taking into account the particular transmission line route, its length; the

climatic conditions; the choice of the type of mass support, conductor, insulator; the regional perspective of the development of electricity supply; land alienation, etc. [1]

In this paper both 110 kV and 330 kV overhead lines (OHL) were considered for revealing the economic efficiency of power line designing based on the minimization concept of the total annual exploitation cost. The length of each line was conditionally assumed as 100 km.

A number of the competitive variants concerning the selected conductor cross-sections as well as mass tower heights were selected based on the OHL design practice and experience. The comparison was based on two specific cases:

1. There is a 110 kV OHL, which must provide current 160 A. Due to the specific requirements of the load development in a particular region, the tower height to a lower conductor is assumed as 20 m;
2. There is a 330 kV OHL, which must provide current 750 A. Because of the same reason as for the 110 kV circuit, the tower height to a lower conductor – 22 m.

The following cross-sections of aluminium steel (AS) conductor were selected:

- ✓ For 110 kV: AS-120/19, AS-150/19, AS-185/29, AS-240/32.
- ✓ For 330 kV: 2xAS-300/39, AS-400/22, AS-500/27, AS-600/72.

To achieve the posed objective of this paper taking into account a great amount of the necessary informative data about line parameters: the line length, line support types, insulator types, line mounting costs and many others, the modern integrated software designed for automated design of transmission line can be implemented, which will significantly speed up the process of choosing the optimum transmission line design variants and provide the more adequate and cost-effective solution.

Nevertheless, the more adequate estimation of capital investments requires a sufficiently complete possession of the whole database of conductors, towers and line fittings. In view of the above, this paper considers the refined approach, which consists of three steps and the process of an evaluation of the total annual exploitation cost is the following:

1. There is an assessment of the capital investments for the OHL by using a comprehensive software solution, which takes into account previously defined competitive variants of the transmission line design, including selection of the conductor type (in this paper the steel aluminium (AS) conductor was chosen), the cross-sections of this conductor, the number of conductor per phase and the number of circuit in line (to provide the necessary capacity of a particular line); mass tower type and its heights; the insulator type as well as a line route.
2. Using the data on power losses in OHL, depending on the previously adjusted and selected cross-sections of the AS conductor, recalculation of total annual exploitation costs taking into account the cost of power

losses was done; Selection of the best variant of transmission line design with the minimum total annual exploitation costs, which corresponds to appropriate cross-section of AS conductor.

3. As far as consider the first step, here the competitive variants were selected by using a special program “SAPR LEP 2011”, which allows choosing the most suitable cross-sections of AS conductor, the tower type and its’ height to lower conductor according to climate conditions along the OHL route placement and provides the determination of the total number of towers [13].

Price of losses, line current and ambient temperature for the period of time determined on the basis of sustainable statistical data [14], [15].

Fig. 6 presents the obtained results of the calculations of the total capital investments for both particular 110 kV and 330 kV OHL cases from a minimization point of view.

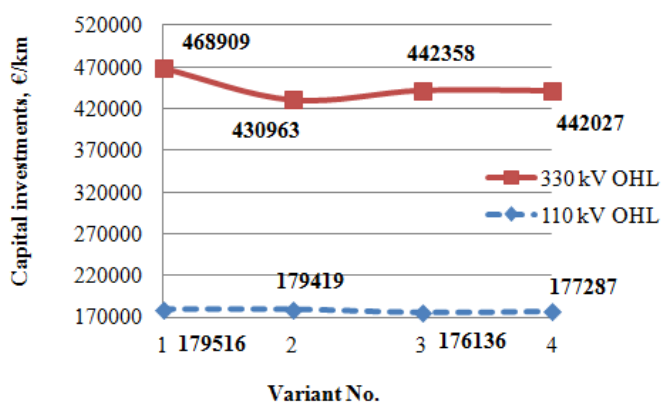


Fig.6 The diagram of total capital investments for designing OHL

Fig. 6 reveals the following:

- 1) Variant No. 1 – for 110 kV OHL: the load is 160 A, 1xAS-120/19 conductor; for 330 kV OHL: the load is 750 A, 2xAS-300/39 conductor;
- 2) Variant No. 2 – for 110 kV OHL: the load is 160 A, 1xAS-150/19 conductor; for 330 kV OHL: the load is 750 A, 1xAS-400/22 conductor;
- 3) Variant No. 3 – for 110 kV OHL: the load is 160 A, 1xAS-185/19 conductor; for 330 kV OHL: the load is 750 A, 1xAS-500/27 conductor;
- 4) Variant No. 4 – for 110 kV OHL: the load is 160 A, 1xAS-240/32 conductor; for 330 kV OHL: the load is 750 A, 1xAS-600/72 conductor.

The analysis shows the following:

- A. The amount of capital investments for 110 kV OHL is approximately 2.5 times smaller as compared with the 330 kV OHL;
- B. If there is a 110 kV OHL, the line with 1xAS-150/19 conductor has the lowest capital investments (the tower height to a lower conductor is 20 m) – 176136 €/km;
- C. If there is a 330 kV OHL, the line with 1xAS-400/22 conductor has the lowest capital investments (the tower height to a lower conductor is 22 m) – 430963 €/km.

As a result, the total capital investments must be calculated taking into account whole initial data concerning the main designing components of the OHL, which relates to the determination of the optimum solution already at the stage of feasibility study and the obtained results of capital investment, will greatly impact the final result of the calculations of the annual total cost.

The second step presents the obtained results of the possible competitive variants after the first step realization, which in this case takes into account power losses. The total deductions on amortization, running repair and maintenance are assumed as 7.6 %, and market interest rate – 5 %.

Taking into account all factors and values of parameters, overhead line cross- section under open market conditions is estimated by two methods: economic intervals method and Monte Carlo method.

The method of Monte Carlo is applied as following: for each cross-section annual average cost is calculated by using the past records data base and certain number of trials (N=1000). From all obtained average costs the minimal cost and the corresponding optimal cross-section is chosen. Fig. 7 and Fig. 8 illustrate the results of calculations by the Monte Carlo method.

Accordingly to Fig. 1 and Fig. 2, optimal cross-sections were chosen by economic intervals method. Two variants are offered: single AS wire and decomposed AS wire.

Finally, the variants with minimum total annual exploitation costs of OHL design and appropriate the optimum cross-section of AS conductor based on the two specific cases, which were formulated previously, can be founded (see Table I and Table II).

TABLE I. RESULTS COMPARISON OF METHODS (110 kV)

	MC method	Economic intervals method
Maximum line current, A	160	160
Annual exploitation costs, €/km	2.3082e+004	2.358 e+004
Corresponding cross-section, mm ²	240	240

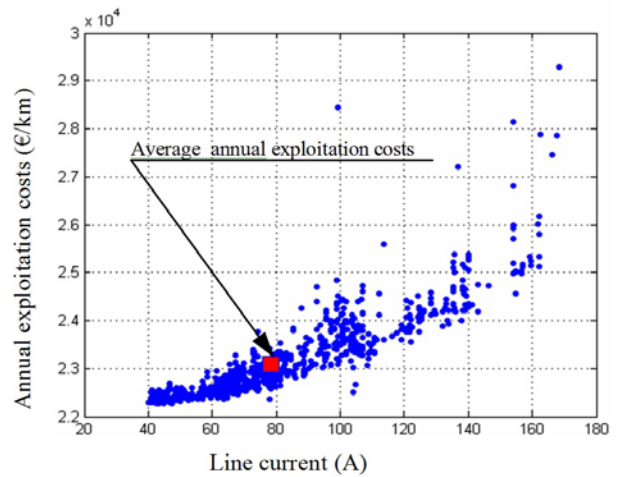


Fig.7. Calculated annual exploitation costs' of 1xAS-240 depending on line current (Monte Carlo method, 110 kV).

Let us consider the second case, when there is a 330 kV OHL, which shows the other obtained results of the annual costs.

TABLE II. RESULTS COMPARISON OF METHODS (330 kV)

	MC method	Economic intervals method
Maximum line current, A	750	750
Annual exploitation costs, €/km	6.2323e+004	6.837e+004/ 7.029e+004
Corresponding cross-section, mm ²	1xAS-600	1xAS-600/ 2xAS-400

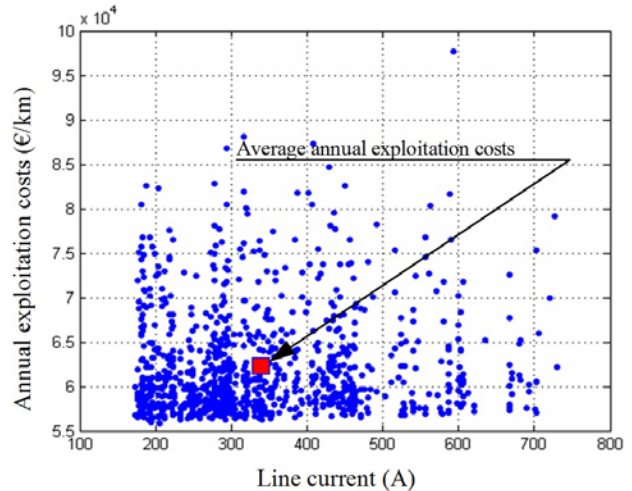


Fig.8. Calculated total annual exploitation costs' of 1xAS-600 depending on line current (Monte Carlo method, 330 kV).

As a result, the following can be concluded:

- If there is a first case (110 kV OHL), then preferable AS conductor cross-section is 1xAS-240/32.
- If there is a second case (330 kV OHL), here AS conductor cross-section by using the Monte Carlo method is 1xAS-600/72, but by using economic

interval method there are two possible variants: 1xAS-600/72 or 2xAS-400/22.

- If there is first case (110kV, 160 A), then it can be concluded that there is insignificant difference in values of the total annual exploitation costs for Monte Carlo method – 23082 €/km, for economic interval method – 23580 €/km (2,11%).
- If there is second case (330kV, 750 A), then it can be concluded that there is quite closed values of the total annual exploitation costs. For first variant the difference is 8%, but for second variant it is 11%.

After all estimations it can be resulted that chosen optimal cross-sections by two approaches differ. Given calculations prove that two methods are suitable for optimal cross section choice. However, stochastic approach is more accurate and reliable one.

VIII. CONCLUSION

1) New tendencies and conditions in organization of electric power supply (deregulation, open market and appearance of local generation) increase level of uncertainty in planning tasks and inspire the search for new accurate methods, based on stochastic positions and Monte-Carlo method application.

2) The developed algorithm takes into consideration the stochastic nature of energy prices, ambient temperature and load lines.

3) The proposed algorithm allows finding the minimum overhead line annual cost and the choice of wires optimal cross-section.

REFERENCES

- [1] F. Kiessling, P. Nefzger, J.F. Nolasco, U. Kaintzyk, "Overhead Power Lines Planning, Design, Construction", Springer-Verlag Berlin Heidelberg New York: 2003, 759 p.
- [2] V. Neimane, On development planning of electricity distribution networks. Doctoral dissertation, Stocholm: 2001.
- [3] V.Zhelnikov, Random distributions of numbers//cryptography from papyrus till computer, Moscow: ABF, 1996, 335p. (in Russian)
- [4] E.D.Knut, Random numbers// The art of computer programming, 3-rd ed., Moscow: Wiljams, 2000, 832p. (in Russian)
- [5] G.Korn, T.Korn, Mathematical handbook for scientists and engineers, 4-th enlarged and revised ed., Moscow: 1978, 832p. (in Russian)
- [6] V.A.Venikov, L.A.Zhukov, A.A.Glazunov, Power systems//Power networks: Handbook for power engin.univ., 2-nd ed., Moscow: High school, 1998, 510p. (in Russian)
- [7] V.M.Block, Power networks and systems, Moscow: High school, 1986. (in Russian)
- [8] S.Guseva, L.Petrichenko, "Approach of Optimum Cross-Section Choice for Cable Lines in Market Prices Conditions", Power Engineering 2012, Slovakia, High Tatras - Tatranske Matliare, 15-17 May, 2012, pp. 87-88.
- [9] S.Guseva, L.Petrichenko, "Optimum cross-sections' of 20-110-330 kV overhead lines choice under market conditions", Latvian Journal of Physics and technical sciences, Riga, Latvia, 2012, pp.13-22.
- [10] T.Gomez, J. Rivier, „Distribution and Power Quality Regulation under Electricity Competition. A Comparative Study”, Proc. Ninth International Conference on Harmonics and Quality of Power, 2000, Vol.2, pp.462-468
- [11] L. Ghods, M. Kalantar, "Different methods of long-term electric load demand forecasting; a comprehensive review", Iranian Journal of

Electrical & Electronic Engineering, Vol. 7, No. 4, Dec. 2011, pp. 249-259

- [12] I.M.Sobol, Monte Carlo method, Moscow: 1985. (in Russian)
- [13] The special program "SAPR LEP 2011" description. Modern dsign System. [Online]. Available:
- [14] <http://www.nordpoolspot.com/>
- [15] <http://www.meteoprog.lv>

Ļubov Petrīchenko received B.Sc. degree in electrical engineering from the Riga Technical University (RTU) in 2006 and 2008, from 2010 she is PhD student at RTU, Latvia. Her research interests include power supply systems and its development, transmission and distribution lines.

She is author of more than 15 papers.

She is engineer of Design Institute "A/S Rupnicprojekts".

Antans Sauhats received Dipl. Eng., Cand.Techn.Sc., and Dr.hab.sc.eng. degrees from Riga Technical University (former Riga Polytechnic Institute) in 1970, 1976, and 1991 respectively. Since 1991 he is Professor at Electric Power Systems. Since 1996 he is the Director of the Power Engineering Institute of Riga Technical University. Area of research activity: power system automation and optimisation, protective relaying, development of methods and means for control of normal and emergency conditions in electric power systems, HV Transmission lines fault location. He has more than 200 scientific publications.

Principal investigator of the Latvian Scientific Council grants; Principal investigator, projects with Latvia, Lithuania, Estonia, Russia power systems and utilities. Developed and implemented disturbance recording systems, fault location system, protective relaying, out of step condition system for 110-330 kV transmission lines and power plants. Developed hardware and software widely used power systems in Latvia, Lithuania, Estonia, and Russia. Total number of implementation more than 500 protective relaying and automation terminals.

Corresponding Member, Latvian Academy of Sciences, 2003

Awarded with Year Prize of the Latvian Academy of Sciences and Public Joint Stock Company "Latvenergo" for life contribution in energetics and engineering, 2003.

Svetlana Guseva received Dipl. Eng. from Riga Polytechnic Institute (RPI) in 1964, Cand. Techn. Sc. degree from Byelorussian Polytechnic Institute (BPI) in 1987 and Dr. Sc. Ing. degree in 1992 from Riga Technical University (RTU). She has been working in RTU (earlier RPI) from 1965, from 2003 she is Associated professor of RTU. Her research includes Power System Mathematical Simulation and Optimization.

Svetlana Berjokzina received B.Sc., M.Sc. in Power Engineering from Riga Technical University, Riga, Latvia in 2008 and 2010 respectively. Now she continues studying as PhD student in RTU and since 2010 works as senior electrical engineer at joint stock company „Siltumelektroprojekts” of Latvia. Her research interests include power supply, transmission lines state evaluation, analysis of power systems as well as their mathematical modeling.

She is author of more than 30 papers.

IEEE student member.

Victoria Neimane Viktoria Neimane received MSc from the RTU in 1995 and PhD from the Royal Institute of Technology in Stockholm, Sweden in 2001. She joined Vattenfall Research&Development (VRD) as a Senior Research Engineer at 2002. Presently she is a Manager of Power Technology department at VRD.

She is author of more than 15 papers.

Multi-Objective Optimization using NDSPSO with Cost, Emission and Loss Objectives

S.Sivanagaraju*, Ch.V.Suresh, K.Srikumar, A.V. Naresh Babu

Abstract— This paper presents a new multi-objective optimization approach based on non-dominated sorting to solve complex problem subject to the heavy equality and inequality constraints in power system. The proposed approach employs application of non-dominated sorting mechanism based on crowding distance calculation to produce a well distributed Pareto-optimal set of non-dominated solutions. Moreover, fuzzy set theory is employed to extract the best compromise solution over the trade-off curve. Several optimization runs of the proposed approach are carried out on the standard IEEE-30 bus test system. The results demonstrate the capabilities of the proposed approach to generate true and well-distributed Pareto-optimal non-dominated solutions of the multi-objective problem in one single run. Finally, some of the system objectives are improved by sacrificing other objectives. The transmission losses, emission and generation fuel cost objectives are optimized simultaneously using the proposed algorithm.

Keywords— Nondominated Sorting, Particle swarm optimization, Generation Cost, Emission, Losses.

I. INTRODUCTION

THE Optimal Power Flow (OPF) is a popularly used method in electrical power system for effective controlled operation and proper planning towards meeting the load growth subjected to meeting various objectives. The chief necessity of the optimization of the power flow is to estimate the proper combination of the controllable parameters like voltage and real power generation at generator buses, tap setting of the transformers in transmission lines, value of compensating capacitors towards minimization of the specific objective functions. A problem with more number of controllable parameters makes the system non-linear and discontinues. So, traditional solution methodologies failed to give an optimized global solution.

The conventional dynamic technique is applied to OPF problem and benders decomposition for effective scheduling in a power system to meet the required demand at minimum production cost [1, 2]. At power stations, various strategies like installation of electrostatic precipitators and gas scrubbers, replacement of fuel-burners, efficient cleaners and shifting towards low emission fuels are the alternatives for low

emission dispatch. These options can be made for long-run planning. In [3], a strategy to minimize emission was proposed.

In power system, minimizing of transmission real power losses can be considered as one of the objective functions for the effective reactive power dispatch [4].

The literature concentrated on the application of evolutionary optimization techniques to OPF problems like, linear and non-linear programming [5-7], Newton's method [8], Quadratic Programming [9], Fast Successive Linear Programming algorithm [10], etc. At present, these evolutionary algorithms are promoted to overcome the drawbacks of the traditional optimization techniques, as their inherent capability of processing towards the best result and extensive exploration in search space [11].

The algorithms like Multi-Objective Stochastic Search Techniques (MOSST) [12], Multi-Objective Evolutionary Algorithm (MOEA) [13], Strength Pareto Evolutionary Algorithm (SPEA) [14], Niche Pareto Genetic Algorithms (NPGA) [15] and Nondominated sorting in Genetic Algorithms (NSGA) [16], etc., can be used to solve multi objective optimization problem.

PSO is a stochastic algorithm that can be applied to non-linear optimization problems. PSO has been developed from the simulation of simplified social systems such as bird flocking and fish schooling by Kennedy and Eberhart [17].

The main contribution of this paper is “the application of Nondominated Sorting methodology with Particle Swarm Optimization (NDSPSO)” to organize objectives on a given system subjected to satisfy multiple objectives and to find globally compromised solution using fuzzy decision-making tool.

The proposed methodology is applied to IEEE-30 bus test system. Some of the results of the proposed method were compared with the results of the existing method [5].

II. PROBLEM STATEMENT

Many of the optimization problems discussed in the literature is restricted to either of the certain objectives like Generation Cost, Emission, and Losses etc. But in practice it is necessary to optimize many of the above objectives simultaneously, subjected to equality, inequality, practical and operating constraints. Hence, it is clear that the effectiveness and efficiency of multi-objective algorithm gives best compromised solution subjected to constraints on a system.

S.Sivanagaraju, Ch.V.Suresh, K.Srikumar is with the Electrical & electronics Engineering Department, Jawaharlal Nehru Technological University Kakinada, Kakinada, Andhra Pradesh, India, 533 003. (*venkatasuresh3@gmail.com, 09989254335).

A.V.Naresh babu is with department of Electrical and Electronics Engineering, DVR & Dr.HS MIC College of Technology, Kanchikacherla, Andhra Pradesh, India, 533 003.

A multi-objective optimization technique NDSPSO is applied to optimize system objectives such as Generation Cost, Emission, and Losses simultaneously subjected to the system constraints.

Aggregating all objectives and constraints, the problem can be formulated mathematically as a constrained nonlinear multi-objective optimization problem as follows:

$$\text{Minimize } [F(x), E(x), Loss] \quad -- (1)$$

Subject to

$$g_i(x) = 0; \quad \forall i = 1, 2, 3, \dots, J \quad - (2)$$

$$h_k(x) \leq 0; \quad \forall k = 1, 2, 3, \dots, K \quad - (3)$$

where 'g' and 'h' are the equality and inequality constraints respectively and x is a control vector of variables corresponding to solution. J and K are number of objective functions.

The organization of the paper is given as: Constrained Problem formulation, multi-objective optimization approach with algorithm and corresponding numerical results are given in sections III, IV, and V respectively.

III. PROBLEM FORMATION

Multi-objective optimization can have two or more objective functions to be optimized at same time. As a result, there is no unique solution to multi-objective optimization problems, but the aim is to find all possible compromised solutions available in search space (called Pareto front set).

A. Generation Fuel Cost

The fuel cost function which satisfies particular operating constraints and practical loading concern can be represented approximately by a simple quadratic function, under the assumption that the incremental cost curves of the generating units are monotonically increasing piecewise linear functions. The fuel cost function of any generator can be mathematically expressed as

$$F(P_{G_i}) = \sum_{i=1}^{N_G} a_i P_{G_i}^2 + b_i P_{G_i} + c_i \text{ \$/h} \quad -- (4)$$

where N_G is the number of generators, a_i , b_i and c_i are the cost coefficients and P_{G_i} is the real power output of i^{th} generator.

B. Emission

While minimizing fuel cost of generating units, may produce high levels of SO_2 and NO_2 emissions [18].

The total ton/h atmospheric pollutants such as Sulphur oxides SO_x and Nitrogen oxides NO_x emitted by $E(P_{G_i})$ [5] is

$$E(P_{G_i}) = \sum_{i=1}^{N_G} (\alpha_i + \beta_i P_{G_i} + \gamma_i P_{G_i}^2 + \xi_i \exp(\lambda_i P_{G_i})) \text{ ton/h} \quad -- (5)$$

where $\alpha_i, \beta_i, \gamma_i, \xi_i$ and λ_i are emission coefficients of the i^{th} generator.

C. Power System Active Power Losses

In power system to enhance power delivery performance, one of the important issues to be considered is active power loss.

$$\text{Losses } (L) = \sum_{i=1}^{N_{line}} g_i [V_i^2 + V_j^2 - 2V_i V_j \cos(\delta_i - \delta_j)] \text{ MW} \quad -- (6)$$

where N_{line} is total number of transmission lines, g_i is the conductance of i^{th} line which connects buses i and j . V_i, V_j and δ_i, δ_j are voltage magnitude and angle of i^{th} and j^{th} buses.

D. Constraints

Equality constraint

This constraint is typically load flow equations.

- Power balance constraint

$$\sum P_G = \sum P_{Load} + \sum P_{Losses}$$

E. Inequality constraints

These constraints represent system operating limits.

- Active and reactive power generation constraint

$$P_{G_i}^{min} \leq P_{G_i} \leq P_{G_i}^{max}; \quad \forall i \in N_G$$

$$Q_{G_i}^{min} \leq Q_{G_i} \leq Q_{G_i}^{max}; \quad \forall i \in N_G$$

where P_{G_i} and Q_{G_i} are the active and reactive power generations of i^{th} generator, $P_{G_i}^{min}$, $P_{G_i}^{max}$ and $Q_{G_i}^{min}$, $Q_{G_i}^{max}$ are the corresponding minimum and maximum active and reactive power generation limits of the i^{th} generator.

- Security constraint

$$S_{l_i} \leq S_{l_i}^{max}; \quad i = 1, 2, 3, \dots, n_l$$

where S_{l_i} is the line MVA flow and $S_{l_i}^{max}$ is the maximum MVA flow limit of the i^{th} line, n_l is the total number of lines.

- Transformers tap position constraint

$$T_i^{min} < T_i < T_i^{max}; \quad i = 1, 2, 3, \dots, n_t$$

where T_i^{min} and T_i^{max} are the minimum and maximum tap positions of the i^{th} transformer, respectively, n_t is the total number of tap positions.

- Bus voltage magnitude constraint

$$V_{i,min} \leq V_i \leq V_{i,max}$$

where V_i is the i^{th} bus voltage magnitude, $V_{i,min}$ and $V_{i,max}$ are the minimum and maximum voltage magnitude values of the i^{th} bus, respectively.

- Switchable VAr sources constraint

$$Q_{C_i}^{min} < Q_{C_i} < Q_{C_i}^{max}; \quad i = 1, 2, \dots, n_c$$

where $Q_{C_i}^{min}$ and $Q_{C_i}^{max}$ are the minimum and maximum values of the reactive power compensated by the i^{th} capacitor and n_c is the number of compensators respectively.

A penalty function [19] is added to the objective function, if any of the controllable parameters violates any of the constraints. The methodology of the penalty handling is considered as in [20]. The penalized objective function can be written as the sum of unpenalized objective function ($f(x)$) plus penalty.

$$F(x) = f(x) + \lambda_p (P_{G_1} - P_{G_1}^{limit})^2 + \lambda_v \left(\sum_{i=1}^{NL} (V_{L_i} - V_{L_i}^{limit})^2 \right) + \lambda_q \left(\sum_{i=1}^{NG} (Q_{G_i} - Q_{G_i}^{limit})^2 \right) + \lambda_s \left(\sum_{i=1}^{nl} (S_{L_i} - S_{L_i}^{limit})^2 \right)$$

where $\lambda_p, \lambda_v, \lambda_q$ and λ_s are penalty factors. 'NL' is the number of buses, x^{limit} is the limit value of the dependent variable 'x' given as

$$x^{limit} = \begin{cases} x^{max}, & x > x^{max} \\ x^{min}, & x < x^{min} \end{cases}$$

IV. MULTI-OBJECTIVE SOLUTION APPROACH

Multi-objective optimization means optimizing multiple objectives of a system simultaneously and systematically. Generally, these objective functions are peculiar and often challenging and inconsistent. Multi-objective optimization with such challenging objectives produces set of optimal solutions, instead of a single optimal solution. The reason for this type of optimality is that, choosing better choice to all objective functions as per the requirement consist many issues. These optimal solutions are known as Pareto front sets.

A general multi-objective optimization problem consists of a number of objectives to be optimized (either minimization and/or maximization) simultaneously and is associated with a number of equality and inequality constraints given in Eq (1), Eq(2) and Eq(3) subject to control vector U consisting of generator bus voltage magnitudes, active power generations, transformer tap settings, and reactive shunt compensators.

$$U = [V_{G1}, \dots, V_{GN_g}, P_{G1}, \dots, P_{GN_g}, T_1, \dots, T_{nt}, Q_{c1}, \dots, Q_{cnc}] \quad -- (7)$$

where N_g, n_t, n_c are the number of generators, number of regulating transformers, and number of shunt compensators, respectively.

For a multi-objective optimization problem, let any two solutions S_1 and S_2 can have one of two possibilities: one prevails the other or none prevails the other. If S_1 leads the solution S_2 , S_1 is called the nondominated solution. The solutions that are nondominated within the search space are expressed as Pareto front and composed as Pareto optimal set.

A. Non Dominated Sorting

Deb [21] proposed a nondominated sorting method to solve multi-objective optimization problems. There is a requirement to find multiple Pareto front sets in a single run. The fundamental reason behind this multi-objective problem formulation is that it is not probable to have a single solution which optimizes all objectives [22].

In order to find the superiority of each solution in a population of size 'N' with respect to other solutions corresponds to other populations, sorting and comparison operations are performed. This needs $C(mN)$ comparisons for each solution, where m is the number of objectives. At first the nondominated front set is found by using comparison operation on all individuals. In order to find the next front, the comparison procedure for the remaining individuals needs to be repeated.

Again new population is generated along with the current population, comparison and sorting procedures are applied to

obtain best N individuals from the total individuals where N is the population size. The sorting is based on the crowding distance between the Pareto front sets.

B. Detailed description

1) Population initialization

The population for the control parameters is initialized between the ranges.

2) Nondominated sort

The generated population is ordered based on individual domination with the other individuals. The algorithm is described in [21] is used for sorting Pareto front solutions.

3) Crowding distance

Crowding distance is calculated for the individuals after nondominated sorting procedure is completed. Finally main front sets are selected based on crowding distance of the individuals in the front set.

The fundamental idea behind the calculation of crowding distance is to find the Euclidian distance between each individual in a Pareto front, based on their 'm' objectives in the m dimensional solution space. The individuals in the boundary are always selected since they have infinite distance assignment.

C. Particle Swarm Optimization [28]

Particle swarm optimization conducts its search using a population of particles. Each particle in PSO changes its position according to new velocity and the previous positions in the problem space.

Because of the advantages of the PSO, like simple concept and implementation mechanism, handling of control parameters, finding procedure of the global best solution is chosen to implement the defined solution methodology.

In PSO, the particle velocity and the position in $(k+1)^{th}$ iteration is updated using Eq's (13) and (14)

$$V_j^{k+1} = \omega \cdot V_j^k + C_1 \cdot rand1(\cdot) \cdot (P_{best,j} - X_j^k) + C_2 \cdot rand2(\cdot) \cdot (G_{best} - X_j^k) \quad -- (8)$$

$$X_j^{k+1} = X_j^k + V_j^{k+1} \quad -- (9)$$

$$\forall j = 1, 2, 3, \dots, n$$

where k is the iteration count, C_1 and C_2 are acceleration coefficients, $rand1$ and $rand2$ are uniformly distributed random numbers in [0 1]. $P_{best,j}$ is the best position found by the particle j so far, G_{best} is the position among all particles. Here, the second part is a cognitive part and has its own thinking and memory. The third term is the social parameter on which the particle changes its velocity. ' ω ' is the inertia weight and can be calculated as follows

$$\omega^{k+1} = \omega_{max} - \frac{\omega_{max} - \omega_{min}}{k_{max}} \cdot k \quad -- (10)$$

Equations (13) and (14) have three tuning parameters ω , C_1 and C_2 that greatly influence the PSO algorithm performance. The value of ' ω ' was proposed linearly with time from a value of 1.4–0.5 [23]. As such global search starts with a large weight value and then decreases with time to favor local search over global search [24]. In this paper, the methodology to find values for the tuning parameters and the procedure of updating dynamic inertia weight is implemented

[5]. Because this provides a balance between global and local explorations, thus it needs less number of iterations to get an optimal solution.

D. Best compromise solution

Upon having the multiple nondominated Pareto front sets, fuzzy decision maker is used to select the best compromised solution. The m^{th} objective function ' F_m ' is represented by a membership function μ_m defined as in [25]

$$\mu_m = \begin{cases} 1 & ; \text{for } F_m \leq F_m^{min} \\ \frac{F_m^{max} - F_m}{F_m^{max} - F_m^{min}} & ; \text{for } F_m^{min} < F_m < F_m^{max} \\ 0 & ; \text{for } F_m \geq F_m^{max} \end{cases}$$

for minimization of objectives where F_m^{min} and F_m^{max} are the minimum and maximum value of the m^{th} objective function among all non-dominated solutions, respectively.

For each solution in nondominated front set ' k ', the normalized membership function μ^k is calculated as

$$\mu^k = \max \left\{ \frac{\sum_{i=1}^{N_{obj}} \omega_k \cdot \mu_i^k}{\sum_{k=1}^M \sum_{i=1}^{N_{obj}} \omega_k \cdot \mu_i^k} \right\} \quad --(11)$$

where ' M ' is the number of non-dominated solutions. The best compromised solution is the one corresponds to the value of ' μ^k '.

E. The computational flow

The main objective is to find the multi-objective optimized loadability estimation on a system by satisfying the constraints. In NR load flow, the ' Q_{gen} ' limits at generator buses are verified and the same bus has been converted into the load bus if any of the minimum/maximum values is violated. The chaotic formula for the inertia weight and the self adaptive method for computing the learning factors beside the proposed algorithm work well for multi-objective optimization problems. So, proper weight should be given to the objectives to get an optimized performance on a system. As a matter of fact, after acquiring the Pareto front solutions, the decision maker needs to choose one best solution according to the requirement. In this study, W_1 , W_2 and W_3 are the weights of corresponding objective functions, respectively, and also $\sum_{i=1}^{N_{obj}} W_i = 1$.

F. Setting of the proposed approach

The methodology used in this study was developed and tested on 2.19 GHz PC with 2GB RAM using MATLAB platform. On all optimization runs, the PSO population size and the maximum number of iterations were considered as 100 and 100 respectively.

V. NUMERICAL RESULTS

In this study, the standard IEEE 30-bus, 6-unit test system is considered to investigate the effectiveness of the proposed approach. The system data is taken from [26, 27].

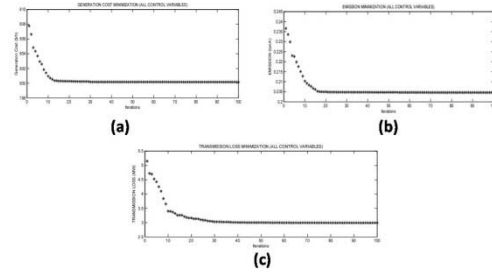
The entire analysis is divided into cases I, II, and III which corresponds to single, two and three objectives optimization problem respectively. The detailed analysis of each case is presented in the following sections. Some of the results of the proposed method are compared with the existing method [5] and are given in Appendix A.

i. Case – I (Single objective)

The result of control variable variation corresponding to the multiple objectives is given in Table 1. It is observed that the minimization of cost function results in increase of the emission by a factor of 0.7904 and losses by 1.9874 (all factors are with respect to their minimized values). Table 1 reveals that the minimization of emission function results in increase of the cost by a factor of 0.1801 and losses by 0.0709. Minimization of losses in the system increases the cost by a factor of 0.2089 and emission by 0.0119. The corresponding convergence patterns are shown in Fig 2.

Table 1. Control variables related to multiple objectives

	Cost, \$/h	Emission, ton/h	Loss, MW
Pg ₁ , MW	177.22929	64.00868	51.39099
Pg ₂ , MW	48.550303	67.59438	80.00
Pg ₃ , MW	21.462934	50.00	50.00
Pg ₄ , MW	21.211045	35.00	35.00
Pg ₅ , MW	11.881975	30.00	30.00
Pg ₆ , MW	12.000032	40.00	40.00
Vg ₁ , pu	1.1	1.092719	1.1
Vg ₂ , pu	1.0370108	1.082577	1.041686
Vg ₃ , pu	1.0646606	1.057189	1.083148
Vg ₄ , pu	1.0544999	1.068489	1.087906
Vg ₅ , pu	0.9634969	0.944209	1.099556
Vg ₆ , pu	1.1	1.093477	1.1
Tap ₆₋₉ , pu	0.9514214	1.015055	1.017291
Tap ₆₋₁₀ , pu	0.9910521	0.9562	0.968865
Tap ₄₋₁₂ , pu	0.9919611	0.994948	0.983142
Tap ₂₇₋₂₈ , pu	0.9679805	0.966505	0.970435
QC ₁₀	15.974439	17.78494	21.07306
QC ₂₄	10.460198	17.53809	11.67689
Cost	800.17747	944.3457	967.4024
Emission	0.3664768	0.204683	0.207122
Loss	8.9355744	3.203066	2.99099



(a) Cost minimization, (b) Emission minimization, (c) Loss minimization,

Figure 2. Convergence pattern of the objective functions

ii. Case – II (Two objectives)

In this case, the proposed methodology handles two objectives together as multi-objective optimization problem. There are three possible combinations with three objective functions. For each combination there are nine sets, which are selected based on the distribution of weights between objectives. Due to space limitation, the results of the best compromised over Pareto optimal solutions for Cost-Emission combination is given in Table 2. The corresponding variation of active power generations, voltages, tap positions and Q_C values with respect to sets is shown in Fig 3.

Table 2. Multi-objective optimized result for different sets (weight factors)

W1	W2	COST	EMISSION
0.9	0.1	805.9989	0.311993
0.8	0.2	805.9989	0.311993

0.7	0.3	814.6776	0.279295
0.6	0.4	820.8772	0.265939
0.5	0.5	830.0619	0.251936
0.4	0.6	844.5205	0.23754
0.3	0.7	862.3286	0.225341
0.2	0.8	880.9416	0.217372
0.1	0.9	907.6102	0.211557

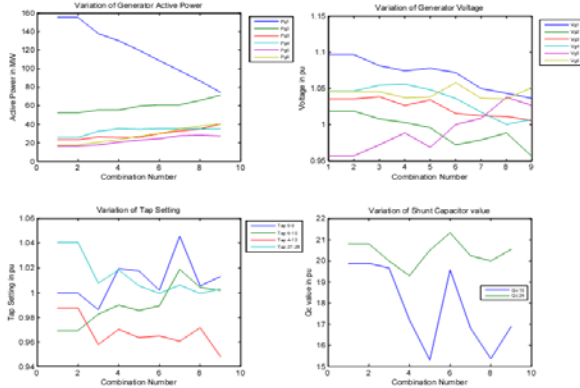


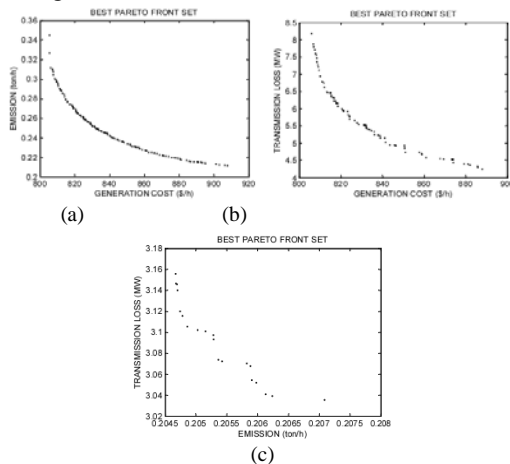
Figure 3. Variation of P_G , V_G , Tap, and Q_C for different Cost-Emission sets

For the remaining combinations, selective analysis is given Table 3.

Table 3. Multi-objective result for different weight factors (Two objectives)

W1	W2	W3	Cost (\$/h)	Emission (ton/h)	Loss (MW)
0.8	0.2	0	805.9989	0.3119	-
0.5	0.5	0	830.0619	0.2519	-
0.2	0.8	0	880.9416	0.2174	-
0.8	0	0.2	809.8782	-	6.9513
0.5	0	0.5	824.0478	-	5.6957
0.2	0	0.8	860.8800	-	4.5731
0	0.8	0.2	-	0.2047	3.1200
0	0.5	0.5	-	0.2054	3.0738
0	0.2	0.8	-	0.2062	3.0391

Table 3 reveals that the importance of the objective function gives the suitable minimized value. Highest generation cost (880.9416 \$/h) is possible with the emission (0.2174 ton/h). Two dimensional plots for the following combinations are shown in Fig 4.



(a) Cost – Emission (b) Cost – Loss (c) Emission – Loss

Figure 4. Two dimensional best Pareto-optimal fronts

iii. Case – III (Three objectives)

Here in this case all the three objectives are considered to form multi-objective optimization problem. With three objectives the possible number of sets is 34 based on weights

distribution, here some sample sets are considered and are tabulated in Table 4, which shows the effectiveness of the algorithm.

Table 4. Multi-objective result for different weight factors (Three objectives)

W1	W2	W3	Cost (\$/h)	Emission (ton/h)	Loss (MW)
0.8	0.1	0.1	807.0440	0.305555	7.733541
0.1	0.8	0.1	914.1322	0.211742	4.766982
0.1	0.1	0.8	883.9452	0.223555	4.571413
0.4	0.4	0.2	857.5084	0.230174	5.067601
0.4	0.2	0.4	857.5084	0.230174	5.067601
0.2	0.4	0.4	882.7626	0.221819	4.629423
0.3	0.3	0.4	869.4727	0.22509	4.856591

From the Table 4 it is clear that, the maximum cost (914.1322) is possible with the emission (0.2117) and loss (4.7669). The generated Pareto fronts confines to entire trade-off regions; this is because of the effectiveness of the proposed methodology.

The three dimensional Pareto fronts for three objective functions is shown in Fig 5.

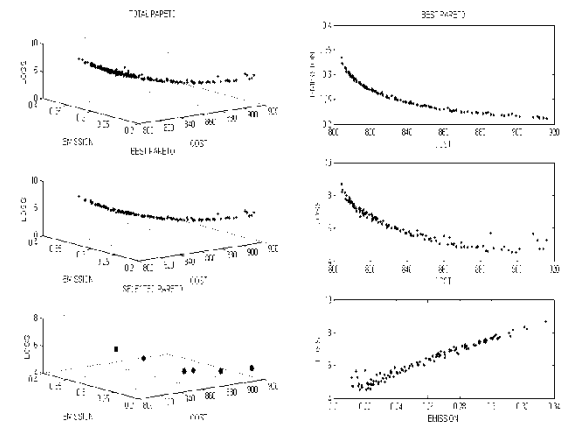


Figure 5. Three dimensional Pareto fronts for Cost-Emission-Loss

VI. CONCLUSION

The stated hypothesis has been proved and validated with proposed NDS PSO algorithm. The handling of the multiple objectives needs a lot of expertise and estimating simultaneous control actions towards the objective optimization has been validated with the proposed method. The objectives generation cost, emission and loss are optimized subjected to equality, inequality and physical constraints. The proposed evolutionary algorithm named “NDS PSO” shows its capability to handle different objectives based on its nature (i.e minimizing certain objectives). The fuzzy decision making tool to select best Pareto front from the generated Pareto optimal solutions proves its effectiveness in selection of globally best solution. The developed code takes around 60-80 seconds for the combinations. Since the proposed methodology uses the calculation of acceleration coefficients and inertia weight based on the nature of the solution and it can be applied to any type of the objectives

APPENDIX

The results validation of proposed method is compared with the existing method [5] and is tabulated in Table.A1.

From Table.A1, it is observed that, the proposed methodology yields better results.

Table A1. Comparison between Multi-objective results for IPSO & NDSPSO

Weights			Existing IPSO [5]			Proposed NDSPSO		
W1	W2	W3	Cost (\$/h)	Emission (ton/h)	Loss (MW)	Cost (\$/h)	Emission (ton/h)	Loss (MW)
0.8	0.2	0	823.134	0.2751	-	805.998	0.312	-
0.5	0.5	0	841.052	0.2585	-	830.061	0.252	-
0.2	0.8	0	860.421	0.2383	-	880.941	0.217	-
0.8	0	0.2	839.843	-	8.976	809.878	-	6.951
0.5	0	0.5	850.916	-	7.893	824.047	-	5.696
0.2	0	0.8	869.731	-	6.775	860.880	-	4.573
0	0.8	0.2	-	0.2061	5.213	-	0.205	3.120
0	0.5	0.5	-	0.2063	5.179	-	0.205	3.074
0	0.2	0.8	-	0.2066	5.162	-	0.206	3.039

REFERENCES

[1] Costa. A.L, Simoes Costa. A., 2007, "Energy and ancillary service dispatch through dynamic optimal power flow," *Electrical Power Systems Research*, Vol.77, No.8, pp. 1047-1055.

[2] Martinez-Crespo. J, Usaola. J, Fernandez. J.L, 2007, "Optimal security constrained power scheduling by Benders decomposition," *Electrical Power Systems Research*, Vol.77 No. 7, pp. 739-753.

[3] A.A. El-Keib, H.Ding, C.C.Carroll, et al., 1991, "Current Challenges for the Electric Power Industry," U.S. Dept of Energy., Workshop of Real Time Control and Operation of Electric Power Systems, Denver, Colorado.

[4] Bansilal, Thukaram. D, Parthasarathy., 1996, "Optimal reactive power dispatch algorithm for voltage stability improvement," *Electric Power Energy Systems*, Vol. 18, No.7, pp. 461-468.

[5] T.Niknam, M.R.Narimani, J.Aghaei, R.Azizpanah-Abarghoee., 2012, "Improved particle swarm optimization for multi-objective optimal power flow considering the cost, loss, emission and voltage stability index," *IET Generation, Transmission & Distribution.*, Vol. 6, No. 6, pp. 515-527.

[6] Momoh, JA., El-Hawary, ME., Adapa R., 1999, "A review of selected optimal power literature to 1993. Part I: non-linear and quadratic programming approaches," *IEEE Transactions on Power Systems.*, Vol. 14, No. 1, pp. 96-104.

[7] Momoh, JA., El-Hawary, ME., Adapa R., 1999, "A review of selected optimal power literature to 1993. Part II:Newton, linear programming and interior point methods," *IEEE Transactions on Power Systems.*, Vol. 14, No. 1, pp. 105-111.

[8] H.Ambriz-Perez., E.Acha., C.R.Fuerte-Esquivel., De La Torre A., 1998, "Incorporation of a UPFC model in an optimal power flow using Newton's method," *IEEE Proceedings on Generation Transmission Distribution.*, Vol. 145, No. 3, pp. 336-344.

[9] C.R.Fuerte-Esquivel., E.Acha., H.Ambriz-Perez, 2000, "A Comprehensive Newton-Raphson UPFC Model for the Quadratic Power Flow Solution of Practical Power Networks," *IEEE Transactions on Power Systems.*, Vol. 15, No. 1, pp. 102-109.

[10] Khaled Z., Sayah S., 2008, "Optimal power flow with environmental constraints using a fast successive linear programming algorithm, applications to the Algerian power system," *Energy Conversion and Management.*, Vol. 49, No. 11, pp. 3363-3366.

[11] Taher Niknam., Mohammad rasoul Narimani., Masoud Jabbari., Ahmad Reza Malekpour, 2011, "A modified shuffle frog leaping algorithm for multi-objective optimal power flow," *Journal of Energy.*, Vol. 36, pp. 6420-6432.

[12] Coello CAC., 1999, "A comprehensive survey of evolutionary-based multi-objective optimization techniques," *Knowledge Information System.*, Vol. 1, No. 3, pp.269-308.

[13] Toffolo A, Lazzaretto A., 2002, "Evolutionary algorithms for multi-objective energetic and economic optimization in thermal system design," *Energy.*, Vol. 27, No. 6, pp. 549-567.

[14] Abido MA., 2003, "Environmental /economic power dispatch using multi-objective evolutionary algorithms," *IEEE Transactions on Power Systems.*, Vol. 18, No. 4, pp.1529-1537.

[15] Andrew K.,Haiyang Z., 2010, "Optimization of wind turbine energy and power factor with an evolutionary computation algorithm," *Energy.*, Vol. 35, No. 3, pp. 1324-1332.

[16] N Srinivas and Kalyanmoy Deb., 1994, "Multiobjective Optimization Using Nondominated Sorting in Genetic Algorithms," *Evolutionary Computation.*, Vol. 2, No. 3, pp. 221-248.

[17] Kennedy J, Eberhart R., 1995, "Particle Swarm Optimization," *IEEE International conference on Neural Networks*, Vol. 4., pp. 1942-1948.

[18] El-Keib. A. A, Ma. H, Hart. J. L., 1994, "Economic Dispatch in view of the clean AIR ACT of 1990," *IEEE Transactions on Power Systems*, Vol. 9, No. 2., pp. 972-978.

[19] Lai. LL, Ma JT, et al., 1997, "Improved genetic algorithms for optimal power flow under both normal and contingent operation states," *Electric Power Energy Systems.*, Vol. 19, No. 5., pp. 287-292.

[20] Alsac O, Scott B., 1974, "Optimal power flow with steady state security," *IEEE Transactions on Power Apparatus Systems.*, Vol. 93, No. 3.

[21] Kalyanmoy Deb, Samir Agarwal, Amrit Pratap, and T Meyarivan., "A Fast Elitist Non-Dominated Sorting Genetic Algorithm for Multi-Objective Optimization:NSGA-II," *Kanpur Genetic Algorithms Laboratory, IIT Kanpur*, <http://www.iitk.ac.in/kangal>.

[22] Srinivas. N, Deb. K., 1995, "Multi-Objective function optimization using non-dominated sorting genetic algorithms," *Evolutionary Computation*, Vol.2, No. 3, pp. 221-248.

[23] Shi.Y, Eberhart.R., 1998, "A modified particle swarm optimizer," *Proceedings of the IEEE international conference on evolutionary computation.*, Piscataway, NJ: IEEE Press., pp. 69-73.

[24] Eberhart. R, Shi. Y., 1998, "Computation between genetic algorithms and particle swarm optimization," *Proceedings of the 7th annual conference on evolutionary programming.*, Berlin: Springer, pp. 611-618.

[25] J.S. Dhillon, S.C. Parti, D.P. Kothari, 1993, "Stochastic economic emission load dispatch," *Electric Power Syst. Res.*, Vol. 26., pp. 179-186.

[26] O.Alsac, B.Stott., 1973, "Optimal Load Flow with steady state security," *IEEE PES summer meeting & EHV/UHV conference.*, July, pp. 745-751.

[27] M.A.Abido., 2002, "Optimal power flow using Tabu Search Algorithm," *Electric Power Components and Systems*, Vol. 30., pp. 469-483.

[28] M.A.Abido., 2002, "Optimal power flow using particle swarm optimization," *Electric Power and Energy Systems*, Vol. 24., pp. 563-571.

Study of the voltage stability of distribution network connected induction machines

⁽¹⁾Trinh Trong Chuong; ⁽²⁾Truong Viet Anh

⁽¹⁾Hanoi University of Industry; ⁽²⁾ University of Technical Education HoChiMinh City

Abstract — Now there are a lot of distributed generation using induction machine are connected to distribution grid. This machines is usually not found interest by reactive power (even reactive power consumption), so they generally affect the entire grid voltage stability, and can cause instability in itself it is no longer balanced by the torque to work. This paper presents a method to study the relationship between the active power and voltage at the Point of common coupling (PCC) connected wind power plant to identify the voltage stability limit. It is a foundation to build a permitted working operation region in complying with the voltage stability limit at the PCC connected wind power.

Keywords—Voltage stability; DFIG, PV curve, Thevenin; PCC.

I. INTRODUCTION

In distribution grids without distributed generation using induction machine (IM) usually occurs voltage instability when increasing load power or changing operating conditions. The main factor causing voltage instability is responding inability of demand reactive power in the distribution grid. The parameters related to voltage collapse are the active power and reactive power of the grid. When distributed generation (DG) is connected to the grid this problem becomes more complex because DG have many potential factors causing voltage instability. If the DG is the synchronous generator, it may be unstable sync. If DG is induction, then it does not supply the reactive power, so DG can affect overall stability to the entire grid voltage, and can cause instability in itself by no longer balance work torque [1]. This is the case of wind power connection with induction machine in the distribution grids. Therefore, the study of voltage stability in the distribution grids having DG relation to understand the structure causing voltage instability, and reliability analysis work stability (sufficient reserve stability coefficients) of DG themselves. This paper studies the factors ensures stable voltage for induction machine of the wind turbines working in distribution grids. First of all, the article will be modeling distribution grids having induction machine, then build voltage stability analysis tool in node connection induction machine.

II. MODEL OF INDUCTION MACHINE IN WIND TURBINES

2.1. Model of induction machine squirrel cage type in wind turbines (IM)

Equivalent Diagram of machine when the rotor turns is shown in figure 1, the relationship between the slided coefficient torque is shown in Figure 2 [2].

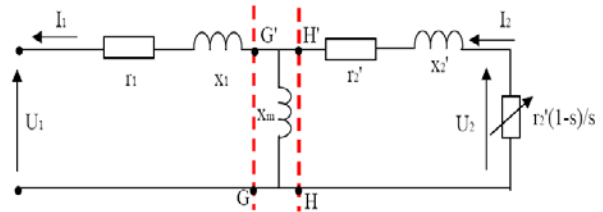


Figure 1. The equivalent circuit of IM

In the equivalent circuit, the load is replaced by a resistive $r_2'(1-s)/s$. Dissipation energy in the resistor equivalent of electrical energy converts into mechanical energy on drive shaft when it turns. In the induction machine, due to large magnetizing current, magnetizing reactance x_m is unchanged (ignoring resistance r_m), the loss of motor includes iron losses. In Fig. 1: U_1 and I_1 are the voltage and current of the stator; U_2 and I_2 are the current voltage and rotor circuit; r_1 and x_1 are the resistance and reactance of the stator winding; r_2' and x_2' are resistance and reactance of the rotor circuit. From the equivalent circuit in Fig.1 [2]:

$$R(s) = \frac{x_m^2 \cdot (r_2' / s)}{(r_2' / s)^2 + (x_m + x_2')^2}; \quad (1)$$

$$X(s) = \frac{x_m^2 \cdot x_2' + x_m \cdot x_2'^2 + x_m \cdot (r_2' / s)^2}{(r_2' / s)^2 + (x_m + x_2')^2}$$

Combined with the impedance of stator, it will calculate the power of generator [2]:

$$P_e(U, s) = \frac{-[r_1 + R(s)]U^2}{[r_1 + R(s)]^2 + [x_1 + X(s)]^2} \quad (2)$$

$$Q_e(U, s) = \frac{-[x_1 + X(s)]U^2}{[r_1 + R(s)]^2 + [x_1 + X(s)]^2} \quad (3)$$

The equation above shows that: the capacity of the power depends mainly on two parameters: the sliding coefficient and connecting voltage node. Further torque characteristics of the generator in this case is the same with induction motor's. Specifically, in Fig.2 if the power is reversed (positive with generation capacity) and calculating the coefficient of sliding, it will have the characteristics completely the same with the characteristics of motor, the formulas do not change:

$$s = [(\omega - \omega_0) / \omega_0] \quad (4)$$

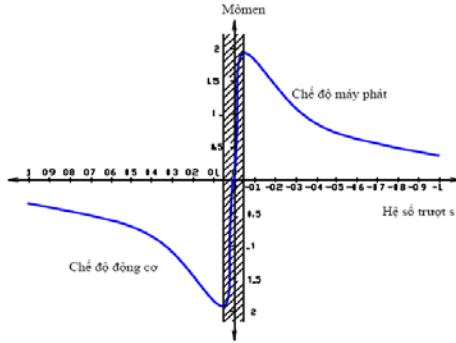


Figure 2. The relationship of torque and sliding coefficient in IM squirrel cage type

2.2. Model of induction machine dual power type in wind turbine (DFIM) [5]

DFIM able to supply power from the rotor to the grid (through power converters) and stator (Figure 3). This converter allows DFIM work in all four quadrants of the complex plane, it means that DFIM can have ability to supply reactive power Q to the grid. Reactive power which is exchanged between network and DFIM can be controlled independently of the real power. In DFIM, the magnitude of the torque shows of the magnitude of emitted power and power to take on - Figure 4.

Total active power to the grid of DFIM is power of the rotor ($P_r = -sP_s$) and stator's (P_s) of the generator:

$$P_{DFIM} = P_s + P_r = (1-s).P_s \tag{5}$$

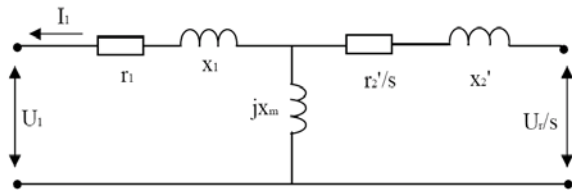


Figure 3. The circuit equivalent of induction machine dual power DFIM

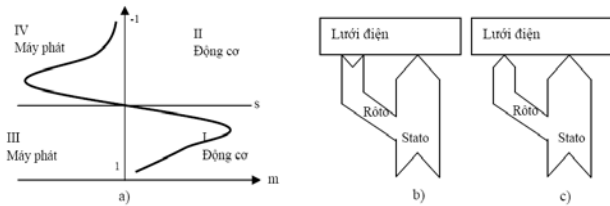


Figure 4. Speed torque characteristics and distribution of electric power DFIM

Distribution of power between the stator and rotor windings of DFIM depend on sliding coefficient. Power through the rotor circuit opposite and approximately equal to the product of the stator coil power and sliding coefficient. Depending on operating conditions, the power in rotor circuit can follow in both directions: from the grid through power

converters to the rotor, $P_r < 0$, under the synchronous mode (Figure 4b) and from the rotor circuit through the inverter to power grids, $P_r > 0$, upper the synchronous mode (Fig. 4c). In both cases, stator circuit still supplies power to the grid, $P_s > 0$. Total reactive power that the generator supplies to the grid, will be the sum of the stator reactive power and reactive power grid side converter. This generator type has very large magnetizing reactance, so it can be considered equivalent diagram in Figure 3 the same with Figure 5. In this figure, the stator voltage generator is complex-valued voltage $U_1 \angle 0$ and the generator rotor is $U_r/s \angle \delta$.

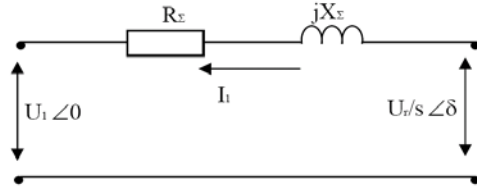


Figure 5. Simplified diagram of power DFIM

From the diagram, it is easily to calculate the stator output power is: $P_s = \text{Re}[U_1.I_1^*]$.

Specifically:

$$P_s = - \frac{\left[X_\Sigma(s) \cdot \frac{U_r}{s} \cdot \sin \delta - R_\Sigma(s) \left(U_1 - \frac{U_r}{s} \cdot \cos \delta \right) \right]}{R_\Sigma^2(s) + X_\Sigma^2(s)} U_1 \tag{6}$$

Ignoring resistors of generator,(6) becomes:

$$P_s = - \left(U_1 \frac{U_r}{s} \cdot \sin \delta \right) / X_\Sigma(s) \tag{7}$$

As δ change will draw the relationship curve (P_s, s). Thus, when modeled by (7), DFIM be viewed as a hybrid generator between synchronization and asynchronous. Nowadays, with modern control technology, the generators are usually adjusted to always generate power to the grid through the stator circuit or operating in constant power factor [4].

III. LIMITATION OF VOLTAGE STABILITY IN CONNECTION BUS HAVING DG

There are 2 scenes to identify voltage stability limit in distribution grid with induction machine:

- Firstly: Due to load capacity growth, while the amount of reactive power load exceeds the limit of the grid;

- Secondly: When they are closed on the grid, then there will be the high risk of voltage instabilities due to strong influence of reactive power;

This content refers to the latter scene. From the static model of induction machine as shown in Figure 6. After solving the problem power flow, active and reactive power of DG was completely determined [1], [3], DG voltage stability depends only on the parameters of the connection node voltage. So, it

can change the form of diagrams 6a to the simple diagram (Figure 6b). As shown in Figure 6b, the equation for power node T is represented as equation (8) [1].

$$\frac{-AU_T^2}{B} \angle \beta - \alpha + \frac{U_{HT} \cdot U_T}{B} \angle (\beta - \delta) = P_T + jQ_T \quad (8)$$

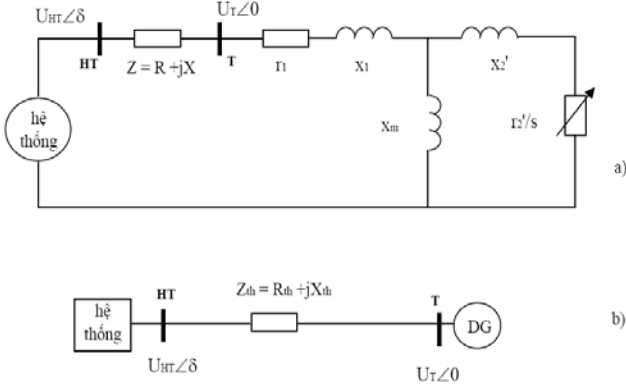


Figure 6. Diagram LDPP power connection KDB (a) and the equivalent model (b)

Because the power factor of T node has slower angle phase than the system node, so the diagram 6b can be represented as shown in Figure 7a.

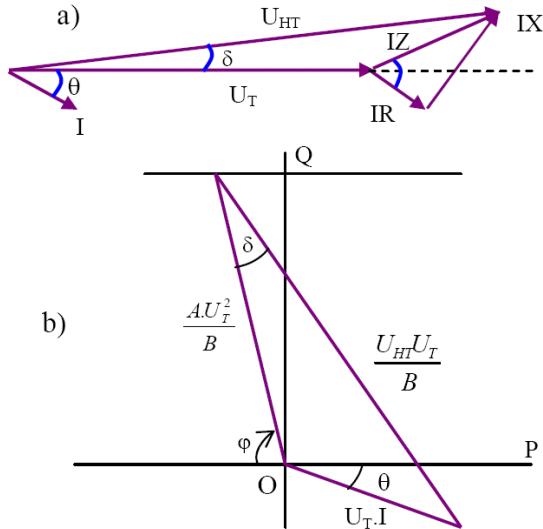


Figure 7. Chart phase voltage

Here A, B are equivalent constants of the network. Multiplying the value of 7a fig with U_T/B ; and rotating chart 7a angle $-\theta$ around the base and attaching to the complex plane; getting results is shown in Figure 7b chart. Drawing a straight line KC' so that $OC'K$ angle = OKC angle = ζ . KC' and KO straight line made with an angle δ' . The intersections and phase angle are shown in figure 8.

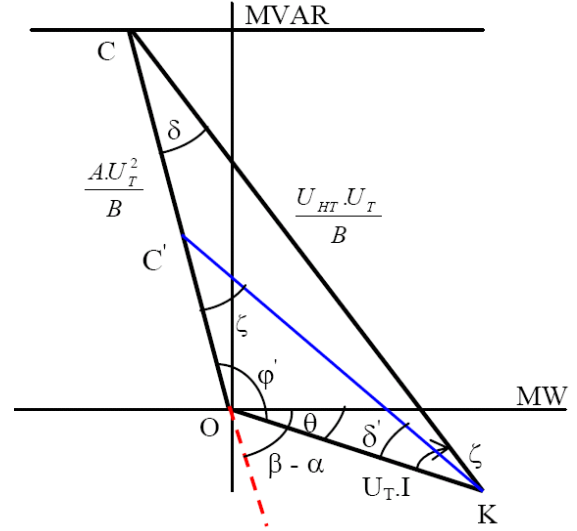


Figure 8. Vector diagram on the PQ complex power plane

Having: $\varphi' = 180^\circ - (\beta - \alpha) + \theta$ và $\delta' = \delta - \alpha$

From the fig. 8:

$$OC = \frac{AU_T^2}{B}; \quad OK = S_T; \quad CK = \frac{U_T U_{HT}}{B} \quad (9)$$

Application of the OCK triangular relation:

$$\frac{OK}{\sin \delta'} = \frac{CK}{\sin \varphi'} = \frac{OC}{\sin \zeta} \quad (10)$$

From (10) calculated:

$$S_T = \frac{AU_T^2 \cdot \sin \delta'}{B \cdot \sin \zeta} = \frac{U_T U_{HT} \cdot \sin \delta'}{B \cdot \sin \varphi'} \quad (11)$$

$$\text{So: } U_T = \frac{U_{HT} \cdot \sin \zeta}{A \cdot \sin \varphi'} \quad (12)$$

To replace U_T in (12) to (11):

$$S_T = \frac{U_{HT}^2 \cdot \sin \zeta \cdot \sin \delta'}{AB \cdot \sin^2 \varphi'} \quad (13)$$

S_T value is reached limit: $\frac{dS_T}{d\delta} = \frac{dS_T}{d\delta'} = 0$ or:

$$\frac{dS_T}{d\delta} = \frac{U_{HT}^2}{AB} \cdot \frac{\sin(\beta - \theta + \alpha - 2\delta)}{\sin^2(\beta - \theta - \alpha)} = 0 \quad (14)$$

So: $\delta_{th} = 1/2(\beta + \alpha - \theta)$ và $\delta_{th}' = \delta_{th} - \alpha$. To replace this value to (13):

$$S_{T-th} = \frac{U_N^2 \sin^2 [(1/2)(\beta - \theta - \alpha)]}{AB \cdot \sin^2(\beta - \theta - \alpha)} \quad (15)$$

To replace $\varphi' = [180^\circ - (\beta - \alpha) + \theta]$ to (15):

method to build PV curve in Section 4.1 to draw the stable curve.

4.1. Analysis of Voltage Stability at nodes connected WP with IM generator

In the first mode, DG generates active power and receives reactive power, the power factor angle is defined as: $\theta = \arctan(Q/P) = -0,67^0$ (lated phase) [4]. The results showed that in the basic operating modes, when Ninh Phuoc wind power generates active power and receives reactive power. P_{gh} power at connected node reaches 20.72 MW. U_{gh} voltage is 0.68 pu (Table 1).

Table 1. Limited numbers of connected node as operating naturally mode of IM

θ , degrees	φ , degrees	S_{Tgh} , MVA	P_{Tgh} , MW	Q_{Tgh} , MVAR	δ_{gh} , degrees	U_{Tgh} , pu
0,67	117,3	20,72	20,71	0,24	31,3	0,68

To improve the power and voltage limits, we can propose a number of measures such as putting capacitors, reconfiguring area having wind turbines, or using on load tap changer (OLTC) for power transformers. Here, the 5 MVAR compensation capacity is placed in connected node, and adjusting the voltage distribution head of the winding OLTC added 1.5%.

the aggregate results of the proposed methods mentioned above are showed in Figure 12. It is easy to show that The placing compensate capacitors and using OLTC help the operating voltage well, however, they make loss voltage largely due to operation voltage near U_{gh} . Using reconfiguration grid has better results, Power P_{gh} increased to 25.5 MW, (23.2% increasing). This result also shows that reconfiguration the grid not only reduced loss power [3], but also significantly improves stability voltage when the grid having induction machine.

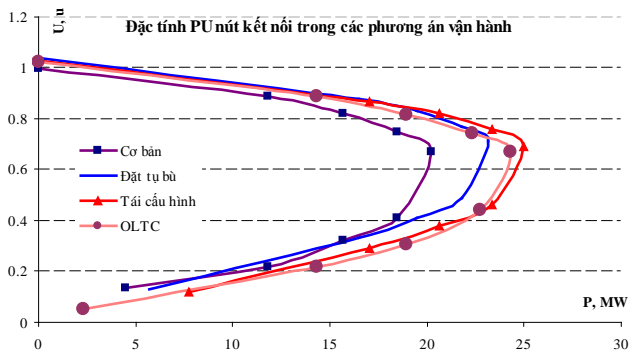


Figure 12. Results of computation schemes at WP Ninh Thuan connected node

4.2. Analysis of Voltage Stability at nodes connected WP with DFIM generator

With the given parameters [4], after finding the initial conditions, we apply the formula 5: $P_{DFIM} = P_{stato} + sP_{stato} = 2,0005MW$. It follows that: $Q = \text{Im}[U_1 I_1] = 0,33MVAR$ và $\theta = 9,3^0$. The results of the calculations limited values in Table 2

Table 2. Limited numbers of connected node of DFIM

θ , degrees	φ , degrees	S_{Tgh} , MVA	P_{Tgh} , MW	Q_{Tgh} , MVAR	δ_{gh} , degrees	U_{Tgh} , pu
9,3	107,4	22,85	22,55	3,69	36,3	0,69

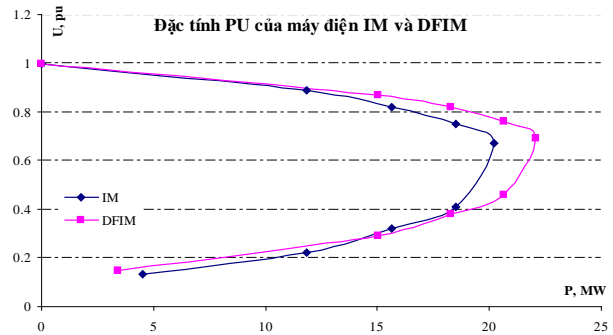


Figure 13. PV curve between IM and DFIM

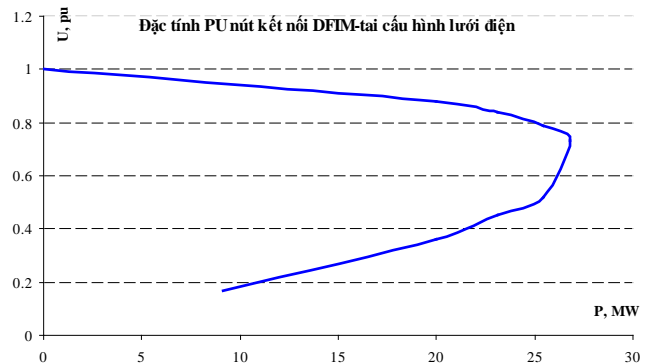


Figure 14. PV curve after reconfiguration

Comparing with the use of IM in table 2 and Figure 13 shows that the same value of output power, the use DFIM gets better voltage quality. In addition, limited power at connected node increased by 9% compared to the use of IM. The limited power reached 22.55 MW and limited voltage is 0.69 pu. Method of reconfiguration the WP region grid got good results in PV characteristic format in figure 14.

Voltage at connected DFIM node down to 0.88 pu. Resolving the power flow again, because the power of WP will decline by WP's power depends on (U, s). Found result $P_{stato} = 1,178$ MW, inferred $P_{DFIM} = P_{stato} + P_{roto} = 1,337$ MW and $Q = -0,18$ MVAR. Then calculated $\theta = \arctan(Q/P) = - 7,7$ (lated phase). And then $\varphi' = [180^0 - (\beta - \alpha) + \theta] = 109,3^0$. Calculation results are shown in Figures 15.

When the voltage of connecting node will be reduced, it causes sliding coefficient increasing, the voltage at this node

decreases and the amount of reactive power, which receives from the grid is greater, the process lead to faster voltage instability proceeds, P_{gh} power declined dramatically.

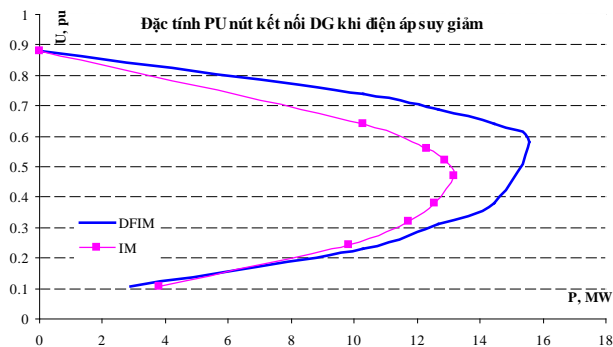


Figure 15. PU characters at connected DFIM and IM node when the voltage decline

V. CONCLUSIONS

This paper analyzed and built the tool to evaluate stable voltage connecting induction machine node in distribution network. This tool allows us to identify voltage stability limit according to the characteristics of DG is very effective. The results showed that:

- The distribution network connected wind turbine (induction machine type) have many potential factors affecting the voltage quality, including the risk of voltage instability. Therefore, considering the voltage stability limits when operating the distribution network connected induction machine is an imperative content. The connecting node with this machine type should be considered first priority because of the most loss of voltage [1, 3]. The limits on the voltage and power should be most interested to propose measures for improvement.

- DFIM generators produce capable of reactive power, so most distribution network with DFIM may not need compensate equipments installation. The distribution network with DFIM give voltage quality better than IM.

- PV character of DFIM has the stability area extension than the use of IM. When connecting node voltage decline, the ability to stabilize the voltage of DFIM better than IM.

- Through the expression (16) to (19) also showed that, in order to improve stability, the ratio X/R and short-circuit

power of the system have important significance. Due to the impedance system calculated by short-circuited S_N Power, so the larger value of S_N the stability limit has been improved, while also reducing the probability of shutdown generator due to voltage drops in neighboring area with nodes connected wind generators.

- With induction wind turbines, the survey stable voltage features at node is sufficient to characterize this source, because wind speed is only a factor affecting the sliding coefficient of induction machine.

REFERENCES

- [1] Prabha Kundur (1994); *Power System Stability and Control*. New York: McGraw- Hill.
- [2] P. Aree (2006); *Load Flow Solution with Induction Motor*; Songklanakarin J. Sci. Technol., 28(1): 157-168.
- [3] RISØ (2006); *Feasibility Assessment and Capacity Building for Wind Energy Development in ASEAN*; November 2006.
- [4] Trinh Trong Chuong (2008); *Voltage Stability Investigation of Grid Connected Wind Farm*; PROCEEDINGS OF WORLD ACADEMY OF SCIENCE, ENGINEERING AND TECHNOLOGY VOLUME 32 AUGUST 2008 ISSN 2070-3740.
- [5] J. G. Slootweg (2003); *Wind Power: Modelling and Impact on Power System Dynamics*; PhD thesis - Universiteit Delft.

Trinh Trong Chuong was born in Haiduong, Vietnam. He received the PhD degrees in electrical power systems at the Hanoi University of Science and Technology, Vietnam, in 2012. He research interests include: Distributed Generation, power quality, voltage stability

Truong Viet Anh was born in HCM city, Vietnam. He received the PhD degrees in electrical power systems at the HCM city University of Technology, Vietnam, in 2005. He research interests include: Reconfiguration, power quality, FACTS.

Genetic-based neuro-fuzzy Design of FACTS Controller in Power System

Associate Prof. Dr. Sattar Jaber Al-Isawi

The Collage of Industrial Technology /Dept. of Electromechanical Eng., Misrata, LIBYA

sattarjaber@yahoo.com

Abstract: This paper introduces a critical assessment for the effectiveness of thyristor controlled reactor (TCR) and voltage source inverter (VSI) based FACTS devices on multi-machine power system oscillation damping. The oscillation problem is analyzed from the point of view of damping and synchronizing torque components. An eigenanalysis is adopted to study different controllers, their location, and use of various control signals for the effective damping of these oscillations. To improve system damping over a wide range of operating conditions, it is desirable to adapt the parameters of each damping controller in the system. In order to do this, on-line measurements of local system signals at converter are chosen as input signals to an adaptive neuro-fuzzy inference system (ANFIS). The outputs of each neuro-fuzzy controller are the desired parameters of system damping controllers.

Keywords: Power Electronics, static exciters, TCSC, UPFC, Power system, Genetic, neuro-fuzzy.

I. INTRODUCTION

A problem of current interest in power system industry is the mitigation of low frequency oscillations. These oscillations are related to the dynamics of interarea power transfer and often exhibit poor damping. Although power system stabilizers (PSSs) provide supplementary feedback stabilizing signals, they play no roles in power flow control or voltage support. FACTS devices can be used to control the power flow and enhance system stability. A well-designed FACTS controller can not only increase the transmission capability but also improve the power system stability. A series of approaches have been made in developing damping control strategy for FACTS devices. In [1] a conventional lead-lag controller for UPFC to improve the oscillation damping of a single-machine infinite bus system is proposed. On the basis of the linearized model, the damping function of the UPFC is investigated.

A robust fixed-structured power system damping controllers using genetic algorithm is presented in [2]. The GA searches for an optimum solution over the controllers' parameter space over wide spectrum of operating conditions. But this approach does not insure good damping at each individual operating point. The approach is used to design SVC and TCSC damping controllers.

A linear optimal controller is proposed [3] to enhance the system dynamics and to coordinate three SVCs depending on two control levels, the local control to insure optimum performer's at the local level and the global control to make the coordination by decoupling the state

equation for each area. Also a state observer is suggested to obtain the unmeasured states.

The problem of coordination is also handled in [4], a coordinated controller is designed to control a TCSC and a TCPAR. The controller is designed according to the linear quadratic problem, the gain matrix is modified to allow the controller to depend on output feedback. Also, the system states are reduced since the controller is concerned with the range of frequencies of the inter-area modes. But, conversion from optimal into output feedback controller deviates the controller performance and results in a sub-optimal approach.

In [5], a coordinated design of PSS and SVC for single machine-infinite bus system is proposed. The coordinated design problem of robust excitation and SVC based controllers over a wide range of loading conditions and system configurations are formulated as an optimization problem with an eigenvalue-based objective function. The real-coded genetic algorithm is employed to search for optimal controller parameters. However, FACTS devices are always installed in multi-machine systems.

In this paper, the design problem is transformed into an optimization problem, where the continuous-parameter genetic algorithm is employed to search for the optimal settings of all system damping controllers for each individual operating point. Then, the controllers' parameters in the system are tuned according to each operating point by an individual hybrid neuro-fuzzy controller. The procedure is implemented in a multi-machine power system with two thyristor controlled series capacitors (TCSCs).

II. NETWORK EQUATIONS

In order to establish the relationship between the internal quantities of different machines in the power system, a common reference frame (D, Q) which rotates at synchronous frequency of the steady state network currents is considered. This selection is based on those derived in [6]. This selection has many advantages, the important one is that the angle δ between the d-q frame of each machine and the selected D-Q frame is itself the rotor angle that is between the system slack bus and the q-axis of the generators. Each individual machine can be referred to the general reference frame as:

$$\begin{bmatrix} v_{Di} \\ v_{Qi} \end{bmatrix} = \begin{bmatrix} \cos\delta_i & \sin\delta_i \\ -\sin\delta_i & \cos\delta_i \end{bmatrix} \begin{bmatrix} v_{di} \\ v_{qi} \end{bmatrix} \quad (1)$$

Where V_{Di} and V_{Qi} are the voltages w.r.t. common frame while V_{di} and V_{qi} are the voltages w.r.t. the internal machine axis. The nodal admittance matrix can describe the network:

$$I_N = Y_{bus} V_n \quad (2)$$

Equation 2 can be written as:

$$\begin{bmatrix} I_{D1} \\ I_{Q1} \\ \vdots \\ I_{Dn} \\ I_{Qn} \end{bmatrix} = \begin{bmatrix} G_{11} & B_{11} & \cdots & G_{1n} & B_{1n} \\ -B_{11} & G_{11} & \cdots & -B_{1n} & G_{1n} \\ \vdots & \vdots & \ddots & \vdots & \vdots \\ G_{n1} & B_{n1} & \cdots & G_{nn} & B_{nn} \\ -B_{n1} & G_{n1} & \cdots & -B_{nn} & G_{nn} \end{bmatrix} \begin{bmatrix} V_{D1} \\ V_{Q1} \\ \vdots \\ V_{Dn} \\ V_{Qn} \end{bmatrix} \quad (3)$$

Where G_{ii} and B_{ii} are the real and imaginary parts of Y_{ii} respectively. Perturbing equation (3) gives:

$$\Delta I_{D,Q} = G_o \Delta V_{D,Q} + V_{D,Q,o} \Delta G \quad (4)$$

Equation (4) indicates the way the FACTS devices models can be connected to the system.

To obtain the initial conditions of the system, load flow study should be carried out to the system. Load flow of a power system with TCSC using Newton Raphson method is discussed in [7-9]. Let the TCSC be connected in the network between bus m and bus k as shown in Figure 1. The equivalent admittance matrix is:

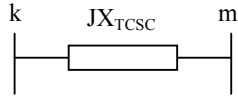


Fig. 1. The equivalent bus circuit.

$$\Delta Y_{bus} = \begin{bmatrix} -JB_{TCSC} & JB_{TCSC} \\ JB_{TCSC} & -JB_{TCSC} \end{bmatrix} \quad (5)$$

The primary function of the TCSC considered here is to control the active power flow through the line m-k. Varying the impedance of the TCSC through the appropriate firing angle controls this power. In this case the dimension of the Jacobian matrix of the system will be increased by one to calculate $\Delta\alpha$ of the TCSC from the equation of ΔP_{mk} .

The way by which the TCSC model is connected to the power system power is through the matrix ΔG so that:

$$\begin{bmatrix} \Delta I_{Dm} \\ \Delta I_{Qm} \\ \Delta I_{Dk} \\ \Delta I_{Qk} \end{bmatrix} = G_o \Delta V_{D,Q} + \begin{bmatrix} V_{Qm,0} - V_{Qk,0} \\ V_{Dk,0} - V_{Dm,0} \\ V_{Qk,0} - V_{Qm,0} \\ V_{Dm,0} - V_{Dk,0} \end{bmatrix} \Delta B_{TCSC} \quad (6)$$

where

$$\Delta B_{TCSC} = B_{TCSC}^2 \frac{\partial X_{TCSC}}{\partial \alpha} \Delta \alpha \quad (7)$$

ΔB_{TCSC} is considered as the control input to the system. The relation between the TCSC fundamental reactance and the thyristors firing angle is given in [7].

III. FACTS DEVICES DAMPING CONTROLLERS

A. Linearized Power System Model

In steady state stability studies, since it's difficult to linearize and write the multi-machine power system equations directly in the form

$$\begin{aligned} \dot{x} &= Ax + Bu \\ y &= Cx + Du \end{aligned} \quad (8)$$

The equations can be written in the following form:

$$P \begin{bmatrix} \dot{x} \\ z \end{bmatrix} = Q[x] + R[u] \quad (9)$$

Where P, Q, and R are real constant matrices with appropriate dimensions. The entries of these matrices are function of all the system parameters and depend on the operating conditions. The matrices P and Q can be partitioned as

$$P = \begin{bmatrix} I & A_1 \\ 0 & A_2 \end{bmatrix} \quad \& \quad Q = \begin{bmatrix} Q_1 \\ Q_2 \end{bmatrix} \quad (10)$$

The P matrix is of dimension (n x n) where n is the total number of state and algebraic variables. [I] is a unit matrix, [0] is a null matrix.

B. Partial Pole-Placement Damping Controller

Pole-placement technique is used to locate the critical mechanical modes of the power system in a satisfactory location in the complex plain by using PSS [10]. The feedback control signal considered to the PSS is the generator speed which is one of the system states. Here, the same method will be used but it will be extended to feedback local algebraic variables (available at the FACTS devices location) to the FACTS devices damping controllers.

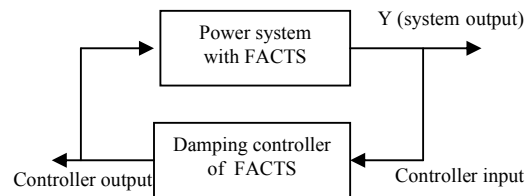


Fig. 2. Block diagram of a power system with damping

For comparison study, a conventional P-I damping controller is considered for both the TCSC and the UPFC. The parameters of the controller are calculated by examining Figure 2. The transfer function of the controller is equal to the inverse transfer function of the system.

$$H_{damp}(\lambda) = [C(\lambda I - A)^{-1}B + D]^{-1} = \frac{\tau_w \lambda}{1 + \tau_w \lambda} (k_p + \frac{k_I}{\lambda}) \quad (11)$$

The gains k_p and k_I of the damping controller can be determined by substituting a pair of the pre-scribed mechanical mode eigenvalues $\lambda_{1,2}$ into equation 10, so we have a pair of algebraic equations with two unknown k_p, k_I .

C. Location and Input Signal to The Controller

There are many criterion in the literature used to determine the location and the feedback signal for the damping controllers. The residue index is used by [11] for the same purpose. The residue index together with the participation matrix [12] are used to determine the best location and feedback signal to the damping controller.

IV. SOFT COMPUTING

It is now realized that complex real-world problems require intelligent systems that combine knowledge, techniques and methodologies from various sources. These intelligent systems are supposed to possess humanlike expertise within a specific domain, adapt themselves and learn to do better in changing environments, and explain how they make decisions or take actions. It is frequently advantageous to use several computing techniques synergistically rather than exclusively, resulting in construction of complementary hybrid intelligent systems. The quintessence of designing intelligent systems of this kind is neuro-fuzzy computing: neural networks that recognize patterns and adapt themselves to cope with changing environments; fuzzy inference systems that incorporate human knowledge and perform inference and decision making. The integration of these two complementary approaches, together with certain derivative-free optimization techniques, results in a novel discipline called neuro-fuzzy and soft computing [13]. Jang and Sun [14] introduced the adaptive Neuro-Fuzzy inference system. This system makes use of a hybrid learning rule to optimize the fuzzy system parameters of a first order Sugeno system.

A. ANFIS Hybrid Training Rule

The ANFIS architecture consists of two training parameter set

- 1-The antecedent membership function parameters
- 2-The polynomial parameters [p, q, r]

In [14], The ANFIS training paradigm uses gradient descent algorithm to optimize the antecedent parameters and a least square algorithm to solve for the consequent parameters. Because it uses two very different algorithms to reduce the error, the training rule is called hybrid.

V. CONTINUOUS CODE D GENETEC ALGORITHM

Heuristically informed search techniques are employed in many artificial intelligence (AI) applications. When a search space is too large for an exhaustive search and it is difficult to identify knowledge that can be applied to reduce the search space, we have no choice but to use other, more efficient search techniques to find optimum solutions. The genetic algorithm (GA) is a candidate technique for this purpose

Genetic algorithms are derivative-free stochastic optimization method based on the concepts of natural selection and evolutionary processes. There were first and investigated by John Holland in 1975[14].When the space parameters are continuous, it is more logically to represent them by floating-point numbers, in this case continuous parameter genetic algorithm has the advantage of requiring less storage than the binary genetic algorithm.

GAs usually keep a set of points as a population, which is then evolved repeatedly toward a better overall fitness value. In each generation, the GA constructs a new population using genetic operators such as crossover and mutation.

VI. SYSTEM UNDER STUDY

The studied system is the IEEE 9-bus, 3-machine system, shown in Figure 3. The system consists of three generating stations; one of them is hydro while the others are steam stations. To address the problem of dynamic stability, each unit is equipped with static exciters, system data are found in [6].

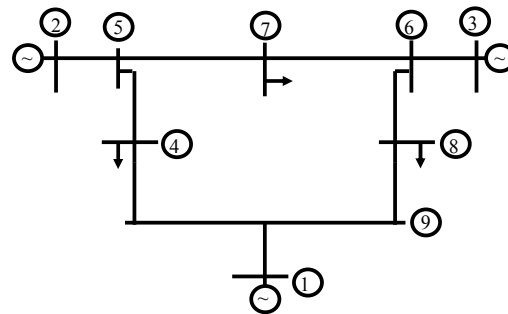


Fig .3. System under Study.

Participation matrix [14] is used to classify system modes. Table I shows the mechanical and the interaction modes of the system after classification.

TABLE I. SYSTEM MODES AFTER CLASSIFICATION

Mechanical Modes	$\Delta\omega_1, \Delta\delta_1$	$0.12 \pm 1.06i$
	$\Delta\omega_2, \Delta\delta_2$	$-0.59 \pm 7.9i$
	$\Delta\omega_3, \Delta\delta_3$	$-0.71 \pm 10.6i$
Interaction Modes		$-1.23 \pm 0.77i$
		-3.74
		$-0.73 \pm 0.85i$
		-1.25

Table II shows the elements of the participation matrix corresponding to the mechanical modes. The three generators are equipped with static exciters, the effect of these exciters is to add negative damping torque component on generators shafts. This is the main cause of the unstable mode in the system.

TABLE II.
APART OF THE PARTICIPATION MATRIX
CORRESPONDING TO THE MECHANICAL MODES

Mech. States	$\lambda_{1,2} =$ $-0.71 \pm 10.6i$	$\lambda_{3,4} =$ $-0.59 \pm 7.9i$	$\lambda_{5,6} =$ $0.12 \pm 1.06i$
$\Delta\omega_1, \Delta\delta_1$	0.0056	0.1394	0.3240
$\Delta\omega_2, \Delta\delta_2$	0.0841	0.3349	0.0895
$\Delta\omega_3, \Delta\delta_3$	0.4180	0.0502	0.0548

VII. THE POWER SYSTEM WITH TCSCS

The effective location of TCSCs will be examined by checking the following locations:

- 1-In series with line 4-5 that connects generators #1 and #2.
- 2-In series with line 8-6 that connects generators #1 and #3
- 3-In series with line 6-7 that connects generators # 2 and # 3.

The three lines are the longest lines in the system and each line is compensated to the same level. Table III shows the residue index for the selected locations and with the line current and the line power as the feedback signal. The residue index coincides with the participation matrix elements in that, regarding system damping, lines 4-5 and 8-6 are the favorable lines to be installed with the TCSCs. The residue index of the line power is greater than that of the line current.

TABLE III.
THE RESIDUE INDEX FOR THE LINE CURRENT AND
POWER FEEDBACK SIGNALS FOR TCSC IN
DIFFERENT LOCATIONS

Location	Line current	Line power
Line 4-5	0.0594	0.7248
Line 8-6	0.0248	0.6091
Line 6-7	0.0003	0.0007

A TCSC with $X_c = 0.05$ pu and $X_l = 0.01$ pu is installed between bus's 4 and 5 (these values insure about 30 % line compensation when the thyristors are off). Line 8-6 will be compensated by 65% using another TCSC. System modes without damping controller are given in Table IV. The series capacitors slightly enhance the damping ratio of the critical mode and has no effect on the oscillation frequency or on the field-excitation modes.

The first TCSC in line 4-5 will now be installed with damping controller to locate this unstable mode to a stable location. System modes with the first damping controller are given in Table V. The calculated gains for the controller are $k_{p1} = -0.0759$ and $k_{i1} = -0.1163$.

TABLE IV.
SYSTEM MODES WITHOUT THE DAMPING
CONTROLLERS

Mechanical Modes	$\Delta\omega_1, \Delta\delta_1$	$0.08 \pm 0.93i$
	$\Delta\omega_2, \Delta\delta_2$	$-0.59 \pm 7.9i$
	$\Delta\omega_3, \Delta\delta_3$	$-0.73 \pm 10.57i$
Interaction Modes		$-1.18 \pm 0.80i$
		-3.83
		$-0.73 \pm 0.85i$
		-1.22

TABLE V.
SYSTEM MODES WITH THE FIRST DAMPING
CONTROLLER

Mechanical Modes	$\Delta\omega_1, \Delta\delta_1$	$-0.15 \pm 0.90i$
	$\Delta\omega_2, \Delta\delta_2$	$-0.54 \pm 8.18i$
	$\Delta\omega_3, \Delta\delta_3$	$-0.73 \pm 10.57i$
Interaction Modes		$-1.11 \pm 0.74i$
		-3.71
		$-0.74 \pm 0.85i$
		-1.20
TCSC Modes		-12.11, -0.06

The second TCSC (with line 8-6) damping controller will be designed to enhance the damping in the second mechanical mode. This mode will be shifted from $-0.54 \pm 8.18i$ to $-0.73 \pm 8.5i$. The required controller gains are $k_{p2} = 0.6604$ and $k_{i2} = -0.6349$. System modes with the second TCSC damping controller are given in Table VI.

GA will be used to search in the parameter space of the two controllers to maximize the damping ratio of system modes.

TABLE VI.
SYSTEM MODES WITH THE TWO DAMPING
CONTROLLER

Mechanical Modes	$\Delta\omega_1, \Delta\delta_1$	$-0.21 \pm 1.17i$
	$\Delta\omega_2, \Delta\delta_2$	$-0.73 \pm 8.50i$
	$\Delta\omega_3, \Delta\delta_3$	$-0.99 \pm 11.22i$
Interaction Modes		$-0.83 \pm 0.82i$
		-2.71
		$-0.72 \pm 0.41i$
		-1.38
TCSCs Modes		-12.26, -0.03 $-5.14 \pm 3.46i$

IX. APPLICATION OF ANFIS TO ADAPT TCSCS
SUPPLEMENTARY DAMPING CONTROLLERS GAINS

The fixed-gain controllers as determined in previous section have been designed based on the nominal operating conditions of the system. In reality, the operating conditions change with time and, as a result, the dynamic performance of the system will change. Thus, to maintain good dynamic response at all possible operating conditions, the controllers' gains need to be adapted based on system operating conditions. ANFIS will be used in this work to adapt the controllers' gains of both the TCSCs damping controllers in real time. Before ANFIS can be used, it is necessary to determine a proper set of training patterns. Each training pattern comprises a set of input data and

corresponding output data. For each TCSC damping controller, an ANFIS will be designed to adapt its gains. The input for each ANFIS will be the line active power and line current. For a pair of P_{ser} and I in each line, we can proceed to determine a set of PI controllers' gains using GA, and the results are employed as the ANFIS outputs.

Table VII shows a part of the training patterns obtained by GA for each ANFIS. For each operating point, the obtained controllers' parameters are quite different.

TABLE VII.
PART OF THE TRAINING PATTERNS FOR THE FIRST ANFIS

Case #	P_{45}	I_{45}	K_{P45}	K_{I45}
1	-0.8063	0.8692	-0.1238	0.4451
2	-0.8933	0.9492	0.4656	2.3275
3	-1.1077	1.1870	-0.0906	-0.0723
4	-1.3173	1.4339	-0.0625	1.6305

IX. SYSTEM PERFORMANCE WITH ANFIS DAMPING CONTROLLERS

The performance of the proposed ANFIS damping controllers has been investigated. The response of the system with fixed-gain genetic-based damping controllers designed at normal operating conditions and with the adaptive ANFIS damping controllers is compared.

A 0.05 p.u step increase in the mechanical power reference input of generator # 1 is applied at $t = 0.0$ and not removed. System response for this disturbance is shown in Figure 4.

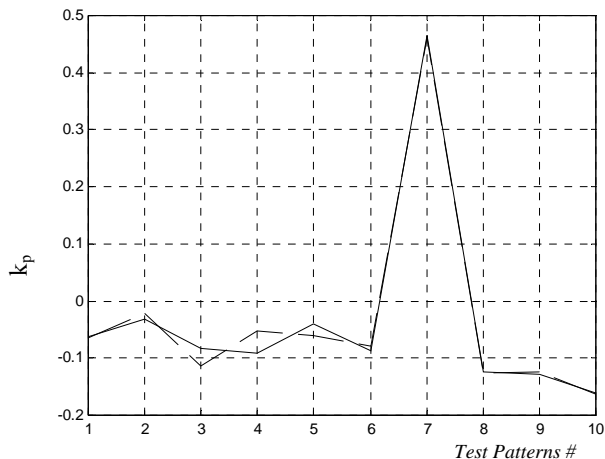


Fig. 4. Actual and predicted k_p from the first ANFIS
 ——— Actual k_p , - - - - - Predicted k_p

X. CONCLUSION

1- This paper illustrates the superiority of the FACTS devices damping controllers based upon ANFIS and GA over the fixed parameter controllers. The proposed controllers stabilize the system for different operating conditions. A novel hybrid technique based on ANFIS is proposed to adapt system damping controllers' gains to improve the damping characteristics of system over a wide range of operating conditions. The proposed ANFISs were trained based on real-time measurements of local signals available at pendulum's angle and position. Damping controllers' gains can be determined by the ANFISs, which

makes the proposed stabilizer relatively simple and suitable for practical on-line implementation.

REFERENCES

- [1] H. F. Wang, "Damping Function of Unified Power Flow Controller", IEE Proc., Gen. Trans. Distrib., Vol. 146, No. 1, Jan. 1999, pp. 81-87.
- [2] G. N. Taranto, D. M. Falcao, "Robust Decentralized Control Design Using Genetic Algorithm in power System Damping Control", IEE Proc., Gener. Transm. Distrib., Vol. 145, No. 1, Jan. 1998, pp. 1-6.
- [3] G. Li, T. T. Lie, G. B. Shrestha, "Design and application of coordinated Multiple FACTS Controllers", IEE Proc., Gener. Transm. Distrib., Vol. 147, No. 2, March 2000, pp. 112-120.
- [4] J. J. Sanchez, "Coordinated Control of Two FACTS Devices for Damping Interarea Oscillations", IEEE Transaction on Power System, Vol. 13, No. 3, May 1998, pp. 428-434.
- [5] M.A. Abido, Y.L. Abdel-Magid, "Coordinated design of a PSS and an SVC-based controller to enhance power system stability", Journal of Electrical Power and Energy Systems (25), 2003, pp. 695-704.
- [6] P. M. Anderson and A. A. Fouad, Power System Control and Stability, Iowa State University Press, Iowa, 1977.
- [7] C.R. Fuerte, E. Acha and H. Amprez-Pérez, "A Thyristor Controlled Series Compensation Model for the Power Flow Solution of Practical Power Networks", IEEE Trans. on Power System, Vol. 15, No. 1, Feb. 2000, pp. 58-64.
- [8] S. Y. Ge and T S Chung, "Optimal power flow incorporating Power Flow Control Needs in Flexible AC Transmission Systems", IEEE Transaction on Power System, Vol. 14, No. 2, May 1999, pp. 738-744.
- [9] Douglas J. Gotham and G. T. Heydt, "Power Flow Control and Power Flow Studies for Systems with FACTS Devices", IEEE Transaction on Power System, Vol. 13, No. 1, Feb. 1998, pp. 60-65.
- [10] S. M. Al-Alawi, K. A. Ellithy and Z. S. El-Razaz, "Tuning of Damping Controllers for SVC Over a Wide Range of Load Models Using Artificial Neural Networks", CIGRE, Cairo, Egypt, Sept. 1997, pp. 1-8.
- [11] H. F. Wang, "Selection of Robust Installing Locations and Feedback Signals of FACTS-Based Stabilizers in Multi-Machine Power Systems", IEEE Transaction on Power System, Vol. 14, No. 2, May 1999, pp. 569-574.
- [12] H. F. Wang, "Selection of Robust Installing Locations and Feedback Signals of FACTS-Based Stabilizers in Multi-Machine Power Systems", IEEE Transaction on Power System, Vol. 14, No. 2, May 1999, pp. 569-574.
- [13] J. Wesley Hines, MATLAB Supplement to Fuzzy and Neural Approaches in Engineering, John Wiley & Sons, 1997.
- [14] Randy L. Haupt and Sue Ellen Haupt, Practical Genetic Algorithms, John Wiley & Sons, 1998.

The efficiency of the active power filters in high power DC drive systems

Miedzinski B., Kozlowski A., Wosik J., Kalus M.

Abstract— Reasons for the current and voltage waveform distortion in high power DC loads are discussed. The ways to reduce the negative impact of such customers on supplying network are presented illustrating them with the results of simulations. Explained the idea of reactive power compensation and limitation of impact of the large power load on supplying network when energize heavy DC drive systems. Simulation results were verified by tests on physical model and respective conclusions are formulated.

Keywords— DC motor, reactive power compensation, high harmonics filter, theory of current physical components (CPC).

I. INTRODUCTION

In industry the electric drives of a high power are commonly used. In cases where precise regulation of rotational speed is required the DC motors are often used. They provide good control characteristics and much better energy properties (e.g. smaller active power loss comparing to this in regulatory resistors of ring AC motors). Example of such application are hoisting machinery drives in the mining industry. Supply systems of these engines require DC voltage source. To the end of the 60s of last century the Leonard drive system was dominant. It was composed of three electric machines:

- Synchronous motor for driving DC generator,
- DC generator,
- DC motor as the key element of the system.

sometimes was installed a DC exciter on a common shaft.

Since the late 60s of the last century this system began to modify replacing 2-machines of DC source (DC generator plus AC synchronous motor) by static rectifier. Currently are employed mostly semiconductor, thyristor circuits. However, they reveal negative impact on the supply network resulting in:

- increased reactive power consumption drawn by static converters (rectifiers) from supplying network. It is

particularly onerous at the ignition delay angle of the thyristor up to 90^0 producing so-called reactive power stroke,

- power factor deterioration ($\cos \varphi$, $\tan \varphi$) at the connection to the plant what is a commonly used criterion under calculation of the fee charged for electrical energy delivered from the producer,

- the occurrence of the so-called commutation kinks in the supply voltage waveform as a result of cyclical arising in time, (depending on number of pulses) two phase short-circuits in rectifier system,

- deformation of the sine wave of supply voltage at the connection point to the plant,

- generation of electromagnetic disturbances that negatively affect operation of any other devices powered from the same network (control and automation equipment, power protection etc.)

II. WAY TO REDUCE THE NEGATIVE IMPACT OF CONVERTERS ON POWER SUPPLY

Reduction of voltage waveform distortion, from the sinusoidal, and minimizing the content of higher harmonics in current (and voltage) can be obtained by installing passive filters of high current harmonics and by feeding power converters by the phase-shifted voltage values. Depending on the inverter structure in the current drawn from the network occur characteristic harmonics "h" related to number of pulses:

$$h = nk \pm 1, \quad (1)$$

where: n-number of pulses,

$$k = 0, 1, 2, 3, \dots$$

For example for 6-pulse rectifier the harmonics are:

$$h = 5, 7, 11, 13, 17, 19, \dots$$

whereas, for 12-pulse they are respectively:

$$h = 11, 13, 23, 25, 35, 37, \dots$$

According to the Fourier series representation of periodic distorted waveform with increasing harmonic number its amplitude decreases. It is worth to know that inaccurate activation of the converter components may cause incidence of other harmonic numbers than resulting from eqn. (1). In practice the number of pulses of the converter is commonly increased through the use of transformers with different vector

Miedzinski Bogdan Institute of Innovative Technologies EMAG. Katowice, Poland (e-mail: bogdan.miedzinski@emag.pl)

Kozlowski Artur Institute of Innovative Technologies EMAG. Katowice, Poland (e-mail: artur.kozlowski@emag.pl)

Wosik Julian Institute of Innovative Technologies EMAG. Katowice, Poland (e-mail: julian.wosik@emag.pl)

Kalus Marian Institute of Innovative Technologies EMAG. Katowice, Poland (e-mail: marian.kalus@emag.pl)

groups that provide the output voltages shifted in phase. An example of such a supply system is shown in Fig.1.

Current and voltage waveforms and their harmonics spectra for this case are illustrated in Fig. 2.

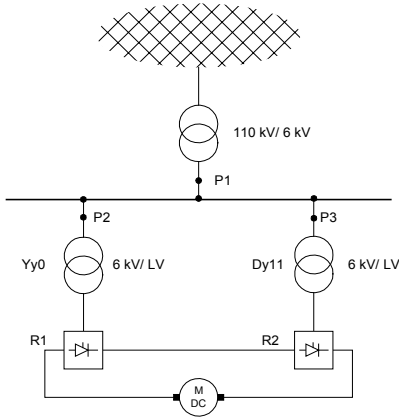


Fig. 1 Simplified scheme of the DC drive power supply

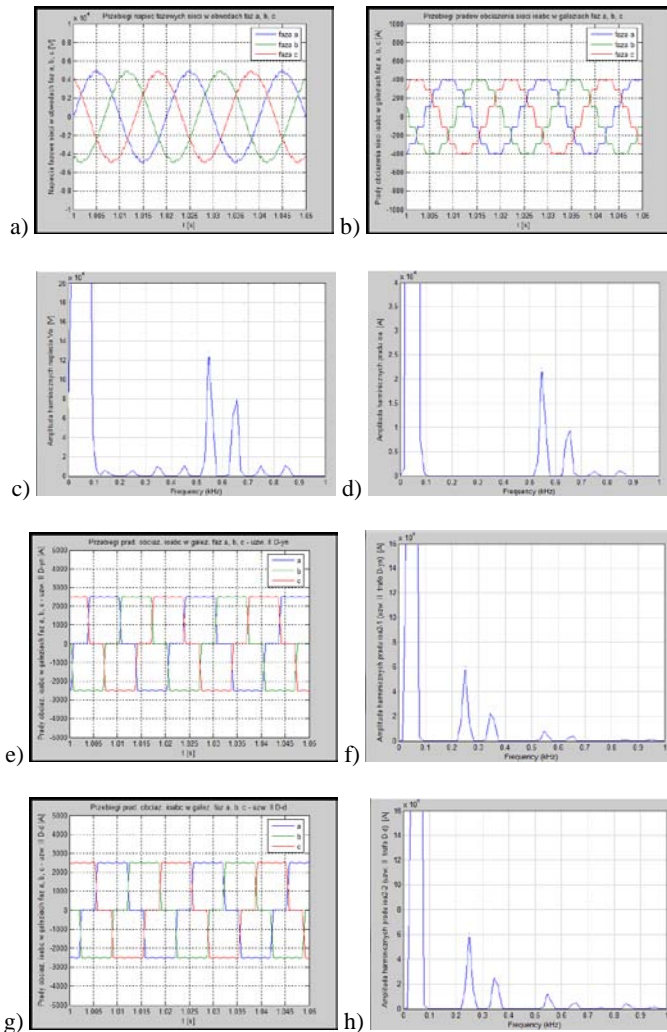


Fig. 2 (a-h).Current and voltage waveforms and harmonics spectra for DC drive system as in Fig.1. a,b,c,d –at measurement point P1; e,f,g,h – at measurement point P2

Application of passive filters of current harmonics results from the fact that non-linear loading (solid-state converters) represents a source of current producing high harmonics that flow into the supply network. So through bypassing of any non-linear load by passive LC filter with resonance frequency specified by eqn.(2):

$$f_{rez} = \frac{1}{2\pi\sqrt{LC}} \quad (2)$$

one can limit the amount of current value entering the network. The characteristics of such a filter is presented in Fig. 3

As one can see for frequency less than resonance value the filter presents capacitive load whereas, for higher-inductive

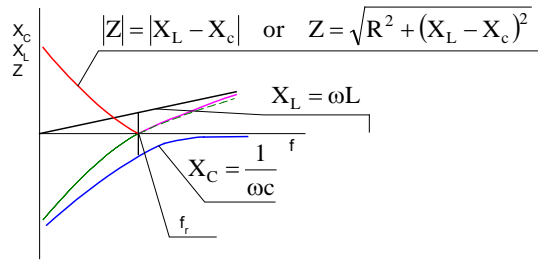


Fig. 3 Passive filter characteristics of the f_{rez} resonant frequency

respectively. It can therefore ,compensate inductive current flow for harmonics of number $h < h_{rez}$. Its filtration efficiency is dependent on accuracy of tuning. However, there are some factors limiting this efficiency like:-

- changes in configuration of the supply network,
- change in short-circuit power of the system during the day,
- changing of filter parameters with time due to aging (in particular, the capacity change).

Current harmonics distributed between the filter and the supply network is illustrated in Fig. 4

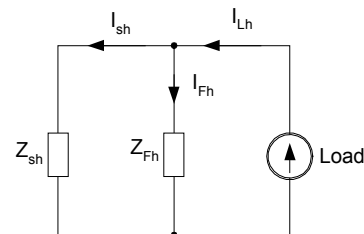


Fig.4 Current harmonics distribution depending on the parameters of the filter and supply network.

Value of current through the network and filter for given higher harmonics due to non-linear load can be estimated from eqn.(3)

$$I_{Sh} = I_{Lh} \frac{z_{Fh}}{z_{Sh} + z_{Fh}} \quad I_{Fh} = I_{Lh} \frac{z_{Sh}}{z_{Sh} + z_{Fh}} \quad (3)$$

In the case of fine –tuning of the filter to the resonance frequency occurs:

$$z_{Fh} = 0 \text{ and } I_{Fh} = I_{Lh}$$

Such a situation is, however, onerous in practice since the filter/filters are provided with high harmonics of the network current due to deformed voltage waveform at the power. It may then lead to an overloading of the filter and related thermal destruction of its elements (reactors, capacitors).

Therefore, preventive measure used in practice is to tune the filter to the frequency slightly lower than the given harmonic for example, by about 5% thus, to $f = 0.95 \text{ frez.}$. Then, non-zero value of the impedance of the filter ($z_{Fh} \neq 0$) effectively reduces the value of the current flowing into it from the network. A side effect, however is the deterioration of filtration efficiency and outflow to the network of respective amount of current high harmonics generated by non-linear load (converter). Current and voltage waveforms and their harmonics spectra when apply perfectly tuned filter for required harmonic are presented in Fig. 6 as an example.

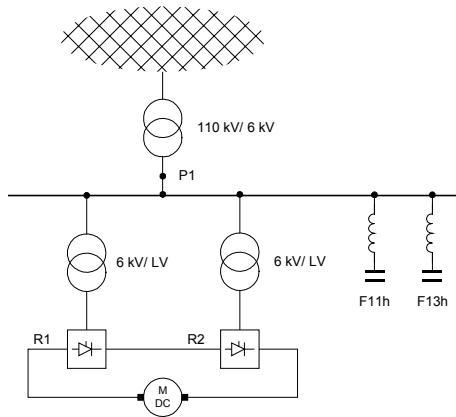


Fig.5 Compensation system of reactive power and high harmonics of current (11th and 13th) by means of passive LC filters

Because, current of the non-linear load is characterized by a

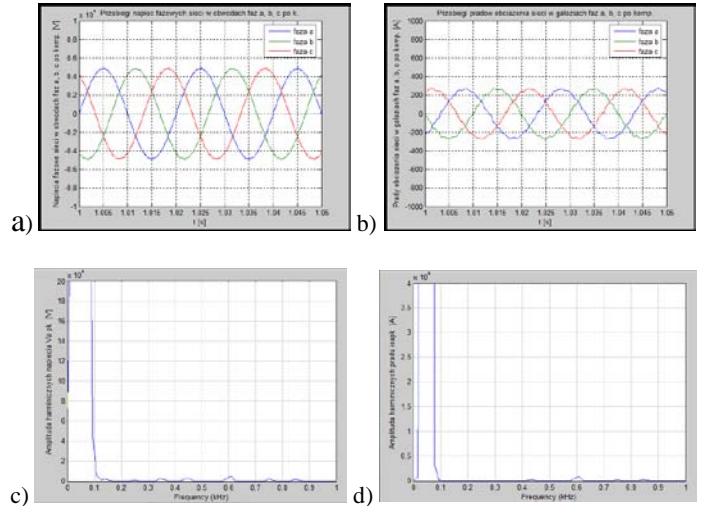


Fig.6 Current and voltage waveform in network with non-linear load when apply passive filters (at measurement point P1)

broad spectrum of harmonics, hence their compensation would require the use of multiple filters or combined filters of a complex structure. In this case for the filter construction consideration the generic algorithm can be employed successfully. In practice however, it is limited to the installation of a few filters of a selected harmonics (usually 2-3) of the highest numbers (amplitude) only to reduce the level of both current and voltage high harmonics. Reactive power compensation by means of sectional static capacity banks or by quasi on-line way using thyristor switches to adjust the capacity do not allow for perfect compensation of the reactive power flows in power system with non-linear loads.

Static capacitor banks can be tuned to the needs of the system with a resolution of the power of the smallest degree of compensation step. Speed of this way of compensation is also limited by speed of control unit as well as thyristor switches of particular sections (switching frequency must be limited because of durability requirements). The capacity bank can be overloaded by current harmonics of much higher frequency as well. However, the highest risk of damage occurs during the series resonance. In spite of application of this type of compensation the current waveform in power supply is far from sinusoidal what can be compared from Fig. 7

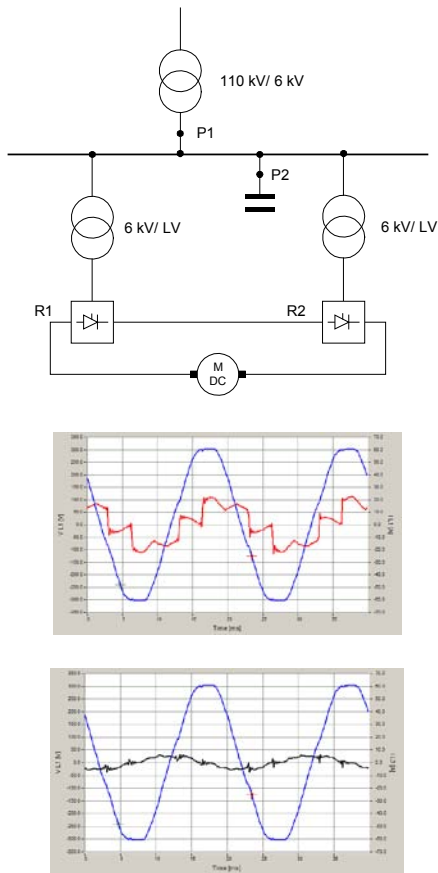


Fig.7 Compensation system of reactive power non-linear load by capacitor bank; a- waveform of voltage and current at measurement point P1 phase L1; b- waveform of capacitor bank current at measurement point P2 phase L1

The use of very fast thyristor switches for each capacity section or to control inductive current value through the reactance component of the LC system can improve the power balance for the required period of time in a statistical sense. However, the shape of the current flowing through the reactance element is still highly distorted. Hence, this compensation system is also non-linear and represents an additional source of harmonics (current and voltage). For this reason, it is also unfavorable for cooperating another loads. In the recent period there is developed a completely new approach to the problem of reactive power compensation in circuits with non-linear loads resulting in distorted waveforms of both current and voltage. This new approach has resulted in the development of a new power theory enabling implementation in practice of so-called active compensation

III. MODERN METHODS OF REACTIVE POWER COMPENSATION

The problem of reactive power compensation in circuit with non-linear loads and therefore, with distorted from sinusoidal waveforms of voltage and current were of interest to scientists and engineers from the end of the nineteenth century, i.e. almost from the beginning of AC application. For many decades, however, failed to create a coherent theoretical basis for such compensation, which would allow for construction of practical compensation systems of high efficiency. In 1971 appeared a concept of the so-called active filters that allow for high harmonics compensation using keying by means of semiconductor devices (SCRs). The problem remained to create a theoretical basis for determining the current reference (desired quantity) for the compensator and the supply network as well. The principal difficult was the incidence of various reasons for current flows(voltage deformation, load non-linearity) as well as imbalance of the voltage source and asymmetry of the load. In 1983-84 created two independent theories of power in circuits with deformed voltage and current waveforms so-called theory of instantaneous power (IPT) [1], [2], [3] and the theory of the physical component of the current (CPC) [3], [4]. The first one is based on an analysis of current and voltage signals in the time domain and the other on the analysis of the signals in the frequency domain. IPT output theory is based on the transformation of phase voltages and currents in the single phase circuit into the stationary rectangular system "p,q" in the α and β axes. However, this theory did not allow to compensate the harmonics caused by distorted supply voltage. Further works on its development led to the transformation from "p,q" system to rectangular coordinate system rotating with angular speed equal to this of phase voltage and current vectors and to its respective adaptation to the various multi-phase circuits without and with the neutral conductor [2]. There is also no physical interpretation of the phenomena of electric energy possible.

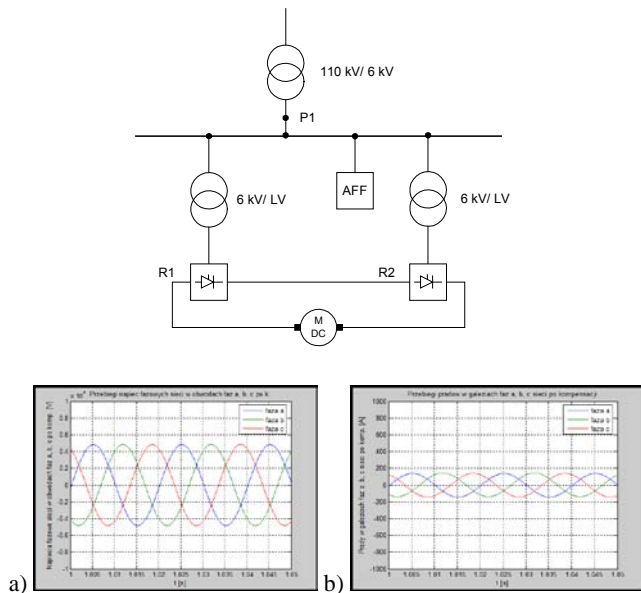


Fig.8 Compensation system of reactive power based on active power filter; scheme, waveform of voltage and current at measurement point P1

The CPC theory does not have these disadvantages.[4] Developed on its basis a control algorithm for active filter allows for compensation:

- current higher harmonics,
- reactive power of phase shift,
- currents due to source imbalance,
- so-called scatter current (new physical quantity).

Developed active filter control algorithm (APF) based on the CPC theory has been verified in simulation studies and laboratory tests on physical model.

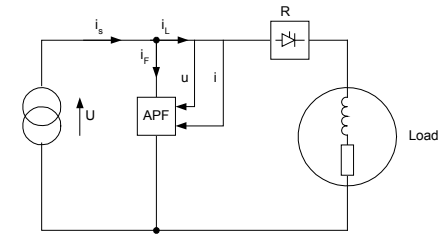


Fig. 10 Model of system used for the simulation study (control algorithm APF was developed based on the CPC theory [3])

IV. THE RESULTS OF THE SIMULATION OF REACTIVE POWER COMPENSATION USING THE ACTIVE POWER FILTER

The simulation tests of the effectiveness of compensation in circuit with non-sinusoidal currents and voltages and in unbalanced circuits were conducted on a simulation model developed in the software package Matlab/Simulink. Model adopted for the simulation studies is shown in Fig. 8

The results of voltage and current waveforms and their harmonics spectra after use of the active power filter are presented in Fig. 8. [5], [6]

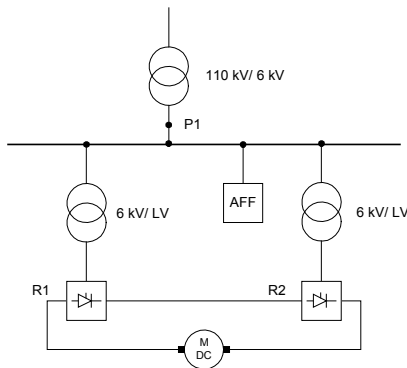


Fig. 9 Model of system used for the simulation study (control algorithm APF was developed based on the CPC theory [3])

V. THE RESULTS OF THE EFFECTIVENESS OF REACTIVE POWER COMPENSATION FOR THE PHYSICAL MODEL

To conduct laboratory tests a network model composed of power source with non-linear load RL (6th pulse controlled rectifier) has been developed and assembled. Active power filter of 10kVA, operated in open control system, was connected as in Fig.10. The resulting voltage and current waveforms and their harmonics spectra for characteristic point of the system are presented in Fig.11

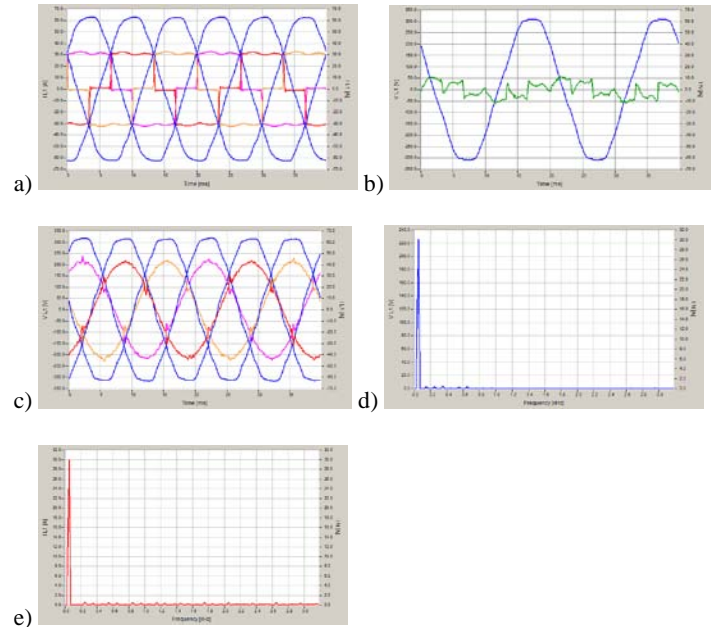


Fig. 11 (a-e) Voltage and current waveforms in system with non-linear-load and with active power filter,

VI. CONCLUSIONS

-Application of passive filters neither allow for effective compensation of high current harmonics nor for compensation of reactive power flows in circuits with non-sinusoidal voltage and current waveforms.

-Compensation based on stationary capacity banks employment is not suitable for circuits with non-linear voltage and current waveforms due to high risk of ferro/resonance.

-Installing of lag compensators with thyristor switches however, allows you to improve the balance of power and increase power factor value $\cos \varphi$ ($\tan \varphi$) but introduces to the system distorted currents.-Reactive power compensation by means of active power filter (APF) based on the control algorithm developed on the basis of theory of physical current components allow for successful compensation of reactive power flow of phase shift and in addition to:

- elimination of current harmonics in the supply network,
- load symmetrization (in case of unbalanced load),

-elimination of the scatter current occurring for deformed source voltage and when the load impedance is frequency dependent.

REFERENCES

- [1] H. Akagi, Y. Kanazawa, A. Nabae” „Generalized theory of the instantaneous reactive power in three phase circuits”; Proceedings of the Int. Power Electr. Conf (JIEE IPEC), pp 1375-1386, Tokyo/Japan 1983
- [2] A. Ferrero, G. Superti-Furga: “A new approach to the definition of power components in three-phase systems under nonsinusoidal conditions”. IEEE Trans. Instrum. Meas., Vol40, pp. 568-577, June 1991
- [3] L.S. Czarnecki: “Dynamic, power quality oriented approach to theory and compensation of asymmetrical system under nonsinusoidal conditions”, Europ. Trans. Electr. Power, 5, pp.347-358, ETEP199
- [4] L.S. Czarnecki: “Power in Electrical Circuits under nonsinusoidal conditions Waveform Currents and Voltages”, (in polish), Oficyna Wydawnicza Politechniki Warszawskiej, Warszawa 2005
- [5] J. Wosik, M.Kalus, A.Kozlowski, B.Miedzinski, M.Habrych: „The Efficiency of Reactive Power Compensation of High Power Nonlinear Loads” Elektronika I Elektrotechnika, vol.19, No7, pp.29-32,2013
- [6] J.Wosik, M.Kalus, A.Kozlowski, B.Miedzinski” “Improvement of the Electric Energy Quality by use of active Power Filters” Proceedings of ICREPQ'13, Bilbao, March 2013.

B.Miedzinski (Prof.)– bogdan.miedzinski@emag.pl – Institute of Innovative Technologies EMAG, Katowice Poland. Area of his activity are: contact materials, power theory, research of signals by using Rogowsky coil, switches.

A.Kozlowski (PhD)– artur.kozlowski@emag.pl - Institute of Innovative Technologies EMAG, Katowice Poland. Area of his activity are: contact materials, switches, power quality, power electronics, flameproof power supply devices. Head of R&D Department.

J.Wosik (PhD)– julian.wosik@emag.pl - Institute of Innovative Technologies EMAG, Katowice Poland. Area of his activity are: dispatching systems, theory of power, power quality, construction flameproof devices, compensation systems of reactive power and active power filters.

M.Kalus (PhD) – marian.kalus@emag.pl - Institute of Innovative Technologies EMAG, Katowice Poland. Area of his activity are: drive AC and DC systems and simulation research, converters power.

A Comparative Analysis of UPQC-P, UPQC-Q and UPQC- VA_{min} - a simulation study

Yash Pal and A. Swarup

Abstract—Different approaches have been reported for the mitigation of voltage sag on a single-phase distribution system using Unified Power Quality Conditioner (UPQC). These are popularly known as UPQC-P, UPQC-Q, and UPQC- VA_{min} . In this paper a comparative analysis of these approaches is carried out based on the required magnitude of injected voltage, reactive and active power shared by the series and shunt Active Power Filter (APF) for the mitigation of voltage sag using a single-phase UPQC. This study may be useful to choose a best approach for the mitigation of voltage sag depending on the rating of shunt and series APF. Performances of different approaches of UPQC for voltage sag mitigation are validated through simulations using MATLAB software with its Simulink and Sim Power System (SPS) toolboxes

Keywords—UPQC-P, UPQC-Q, UPQC- VA_{min} , voltage sag

I. INTRODUCTION

BECAUSE of increasing use of nonlinear loads, the modern power distribution system is becoming highly vulnerable to different Power Quality (PQ) problems [1-3] and voltage sag/swell is one of the most important PQ problems. For the mitigation of current as well as voltage based distortions simultaneously, the Unified Power Quality Conditioner (UPQC) is one of the most attractive custom power devices [4-5]. The block diagram of UPQC is shown in Fig.1. Two back to back connected voltage source inverters (VSI) to a common DC link is used to realize a UPQC. One of the VSI connected in shunt is called shunt active power filter (APF), while series connected VSI is called series APF. Other custom power devices such as dynamic voltage restorer (DVR) [6-7] and distribution STATCOM (DSTATCOM) [8] are also reported for the effective mitigation of voltage sag/swell, while the UPQC has a better sag/swell compensation capability [5]. Different approaches have been reported for the mitigation of voltage sag using a UPQC[9-17] Four significant approaches reported in the literature for the mitigation of voltage sag on a distribution system are: 1) UPQC-P [9]; 2) UPQC-Q [10-13]; 3) UPQC- VA_{min} [14-15] and 4) UPQC-S [16-17]. Out of these approaches, the UPQC-S control approach is complex one ,

Yash Pal is with Department of Electrical Engineering, National Institute of Technology, Kurukshetra, Haryana, India-136119(corresponding author to provide phone: 01744-133400; fax: 01744-233380; e-mail: yash_pal1971@yahoo.com).

A. Swarup is with Department of Electrical Engineering, National Institute of Technology, Kurukshetra, Haryana, India-136119 (e-mail: aswarup@nitkkr.ac.in).

hence not considered here for the comparative analysis purpose.

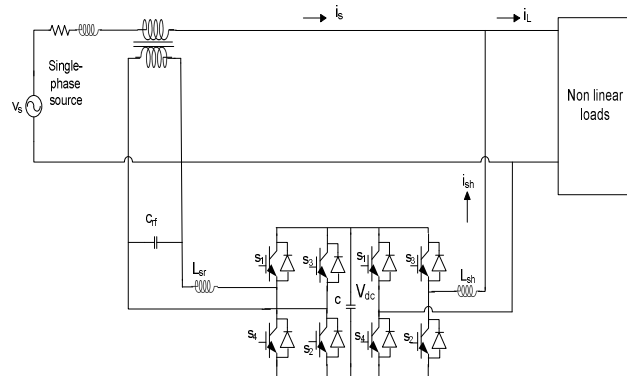


Fig.1. Block diagram of single-phase UPQC

In UPQC-P approach, series APF injects a voltage in-phase with the source voltage, while in case of UPQC-Q, a quadrature voltage is injected through series APF to mitigate the voltage sag. In case of UPQC- VA_{min} voltage is injected at a certain angle by the series APF to keep an overall VA rating of the UPQC minimum. Among these approaches a UPQC-P requires a minimum magnitude of required voltage injection, while UPQC-Q requires a maximum voltage injection for the mitigation of same voltage sag. In all these three approaches, series APF injects voltage for the mitigation of voltage based distortions, while the shunt APF mitigates the current based distortions and maintain the DC link voltage and the overall power balance in the distribution system.

In this paper, comparative analyses of these approaches are made for mitigation of voltage sag on a single-phase distribution system. This comparative analysis is based on the different parameters such as active and reactive power shared by series APF (P_{ser} , Q_{ser}), as active and reactive power shared by shunt APF (P_{sh} , Q_{sh}), source current (I_s), Injected voltage by series APF (V_{sr}), angle between source and load voltage(δ) etc. The feasibility and effectiveness of these approaches are validated through simulations using MATLAB software with its Simulink and SimPower System (SPS) toolboxes.

II. FUNDAMENTAL OF DIFFERENT APPROACHES

A. UPQC-P

The phase representation of UPQC-P is shown in Fig.2. In this approach the series APF injects a voltage in-phase with the source voltage, while the shunt APF compensates for the required reactive power of the load.

$$I_{loss(n)}^* = I_{loss(n-1)}^* + K_{pd} \{V_{de(n)} - V_{de(n-1)}\} + K_{id} V_{de(n)} \quad (6)$$

where $V_{de(n)} = V_{dcr} - V_{dca(n)}$ denotes an error in V_{dc} calculated over reference value of V_{dcr} and average value of V_{dc} . K_{pd} and K_{id} are proportional and integral gains of the DC bus voltage PI controller.

The term i_{sp}^* represents imaginary component of original system and thus can be neglected. It can be observed from eqn. (5) that the generated reference source current is independent of the supply voltage, hence the single-phase d-q theory can be used even under distorted supply voltage without any modification. In this proposed control strategy, the control is made over the fundamental supply current and fundamental supply voltage instead of fast changing APFs current and voltage, thereby reducing the effect of computational delay. In this proposed control algorithm for the shunt APF of single-phase UPQC, the sensed source current (i_s) and reference source currents (i_s^*) are compared in a hysteresis current controller to generate the switching signals for switches of shunt APF.

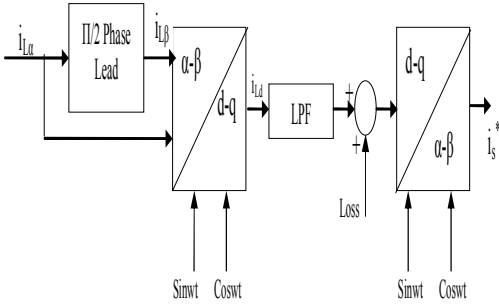


Fig.5 Control of Shunt APF using 1-P d-q Theory

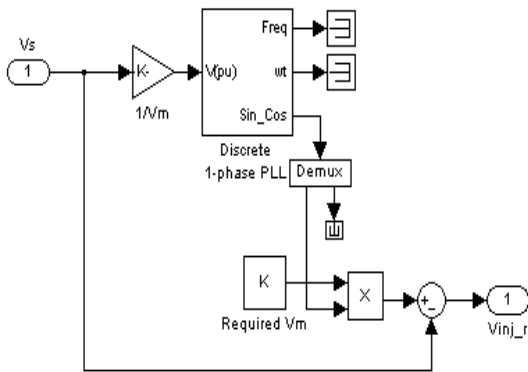


Fig.6 Reference signal generation of series APF using UPQC-P

IV. CONTROL SCHEME OF SERIES APF

A. For UPQC-P

The MATLAB based model for reference signal generation for series APF is shown in Fig. 6. The sensed source voltage is given to single-phase phase locked loop (PLL) to generate $\text{Sin}\omega t$ and it is multiplied with a desired maximum voltage at across the load. The reference voltage for series APF is obtained by subtracting the sensed voltage as shown in Fig. 6.

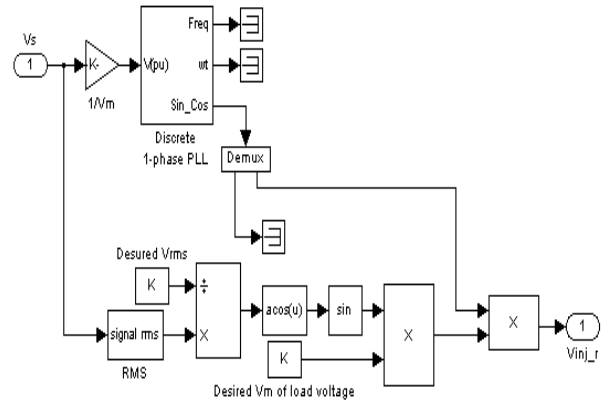


Fig.7 Reference signal generation of series APF using UPQC-Q

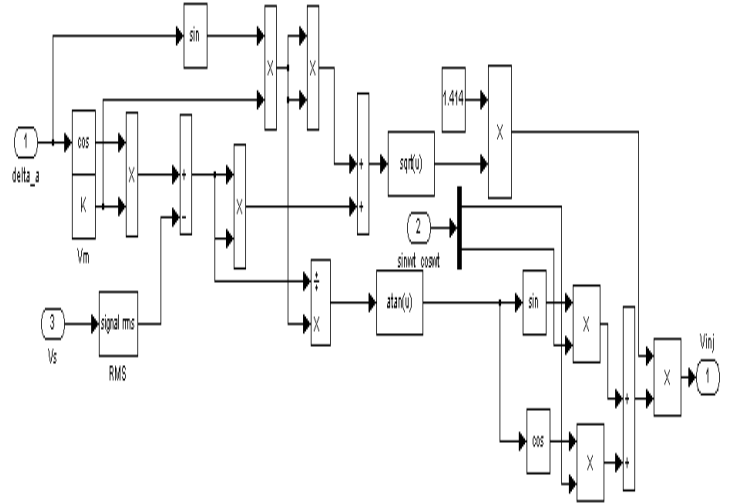


Fig.8 Reference signal generation of series APF using UPQC-VA_{min}

B. For UPQC-Q

A MATLAB based model for reference signal estimation for series APF using UPQC-Q approach is shown in Fig. 7 The sensed source voltage is sensed and its fundamental *rms* value is computed using a discrete *rms* value block from the MATLAB/SPS library. The computed *rms* value is divided by a desired *rms* value of the load voltage to calculate $\text{Cos } \delta$. Taking an inverse of $\text{Cos } \delta$, the power angle δ is extracted. Taking a Sin value of angle δ , it is multiplied by V_m of desired load voltage to get magnitude of required voltage injection by series APF. This magnitude is then multiplied by a 90° phase leading signal from PLL ($\text{Cos}\omega t$) to obtain required reference voltage signal of series APF using UPQC-Q approach.

C. For UPQC-VA_{min}

A MATLAB based model for reference signal generation of series APF using UPQC-VA_{min} approach is shown in Fig. 8. For an optimized angle δ , magnitude and angle of required injected voltage of series APF is calculated for the minimum value of overall KVA rating of UPQC as given in eqn.(7).

$$KVA_{Total} = \sqrt{P_{sr}^2 + Q_{sr}^2} + \sqrt{P_{sh}^2 + Q_{sh}^2} \quad (7)$$

By substituting system parameters values (given in Appendix) in eqn. (8), overall rating of the UPQC is calculated as:

$$KVA_{Total} = 4973.75\sqrt{1.64 - 1.6\cos\delta} + 3198.8\sqrt{3.53 - 2.48(\cos\delta)} \quad (8)$$

In this present work, an optimization is done using general algebraic modeling system (GAMS) software for a fixed load. An online optimization may be carried out for variable load conditions.

V. SIMULATION RESULTS

The performance of UPQC-P, UPQC-Q and UPQC-VA_{min} approaches are evaluated using simulation in MATLAB/SIM SPS for voltage sag mitigation and reactive power compensation in a single-phase distribution system. The supply voltage is considered as 230 V at 50 Hz. At time t=0.6 s, a sag of 20% is introduced in the system, which lasts up to t=0.8s. After t=0.8 s, the system is settled again at steady state condition. To evaluate the performance for reactive power compensation, a load with a maximum load power demand of 4kW+j4kVAR, having power factor 0.707 is connected between the phase and the neutral terminal.

A. Performance of UPQC-P Approach

Fig. 9 shows the performance of UPQC-P approach for power-factor correction and voltage sag mitigation, while Fig.10 shows the active and reactive power flow during the UPQC-P approach for the mitigation of voltage sag.

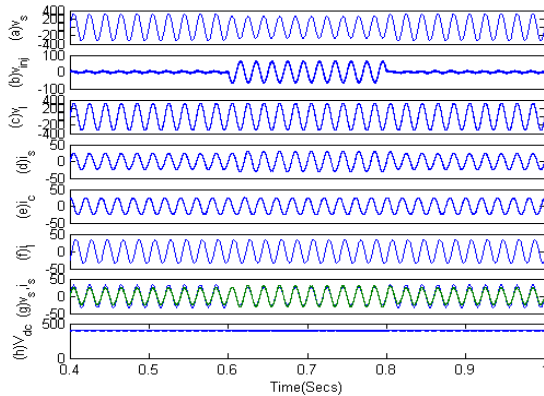


Fig.9 Performance of UPQC-P approach

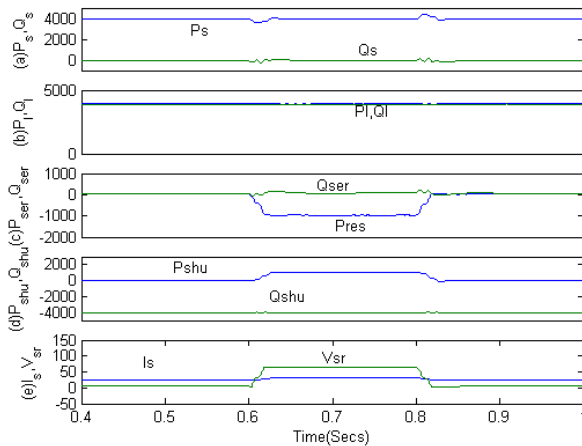


Fig.10 Active and Reactive power flow during UPQC-P approach

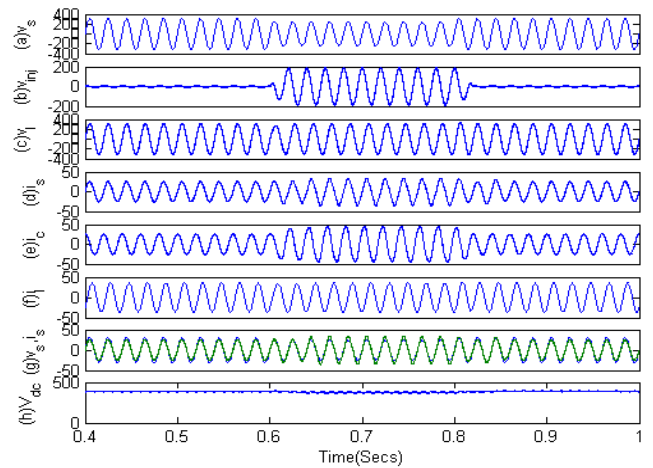


Fig.11 Performance of UPQC-Q approach

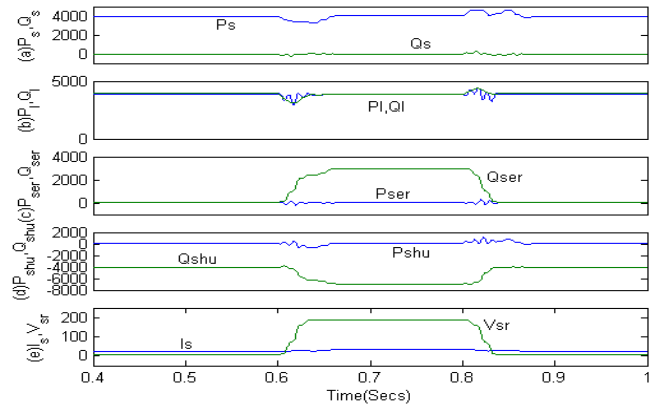


Fig.12 Active and Reactive power flow during UPQC-Q approach

B. Performance of UPQC-Q Approach

The performance of UPQC-Q approach for power-factor correction and voltage sag mitigation is shown in Fig. 11 and Fig.12 shows the active and reactive powers flow during the UPQC-Q approach for the mitigation of voltage sag.

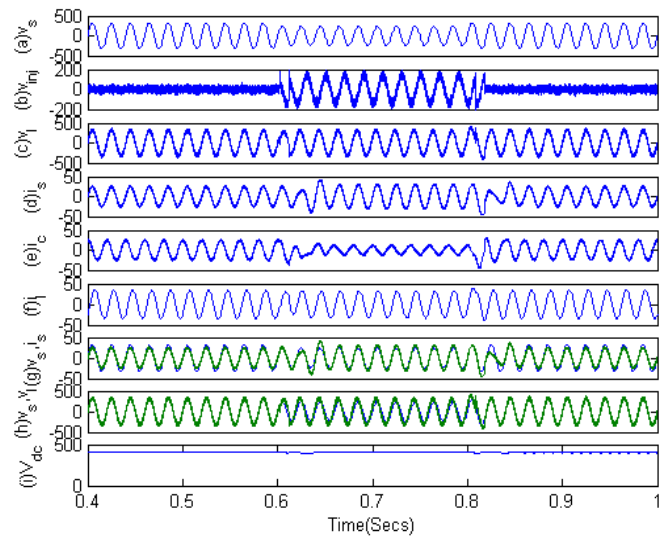


Fig.13 Performance of UPQC-VA_{min} approach

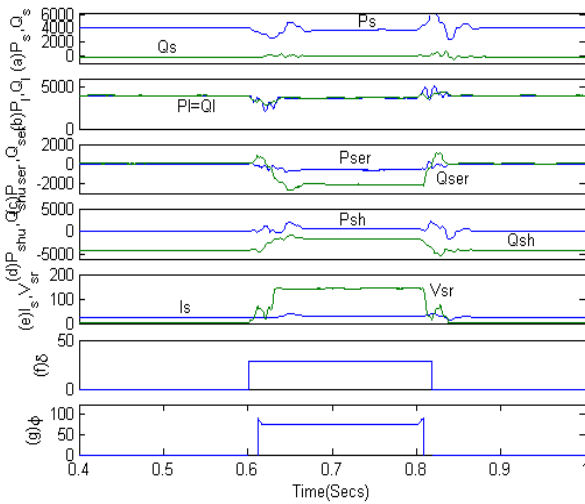


Fig.14 Active and Reactive power flow during UPQC-VA_{min} approach

C. Performance of UPQC-VA_{min} Approach

Fig. 13 shows the performance of UPQC-VA_{min} approach for power-factor correction and voltage sag mitigation and Fig. 14 shows active and reactive powers flow during the UPQC-VA_{min} approach for the mitigation of voltage sag. In this paper, to find out the optimum angle δ , a standard optimization algorithm using non-linear programming solver in GAMS software is applied. The minimum value of total KVA rating of UPQC given in eqn. (8) is found 3.7 kVA at an angle of 27.80° .

VI. COMPARATIVE ANALYSIS OF DIFFERENT APPROACHES

A comparative study of various approaches of voltage sag mitigation in terms of active and reactive powers shared by shunt and series APFs and other parameters such as source current, injecting voltage, angle δ and angle Φ_{sr} are given in Table-I. During voltage sag mitigation using UPQC-P approach, series APF injects voltage using an active power. This active power is drawn from source through shunt APF. In case of UPQC-Q approach, voltage sag is mitigated using reactive power only. During voltage sag, the reactive power shared by shunt APF is increased heavily. The injecting voltage is maximum in case of UPQC-Q as compared to other approaches. In case of UPQC-VA_{min}, series APF shares both active and reactive powers, while the load reactive power demand is shared by both shunt and series APFs..

VII. CONCLUSIONS

Different approach namely UPQC-P, UPQC-Q and UPQC-V_{min} have been validated through simulations for mitigation of voltage sag in a single-phase distribution system. It has been observed that the required injecting voltage is minimum in case of UPQC-P, while it is maximum in case of UPQC-Q. The overall rating of UPQC is minimum in case of UPQC-VA_{min}. The series APF shares active power for mitigation of voltage sag in case of UPQC-P, and UPQC-VA_{min}. During steady state, the series APF does not share any power

(active/reactive), while shunt APF only shares reactive power for UPQC-P, UPQC-Q and UPQC-VA_{min} approaches. Hence, this paper is considered as a helpful guide for the design engineers, consultants and customers for improving power quality.

APPENDIX

The system parameters used are as follows:
 Supply voltage and frequency: 230V (r.m.s), $f=50$ Hz.
 Load: 4 kW, 4 kVar.
 Ripple Filter: $R=7 \Omega$, $C=5\mu F$.
 DC bus capacitance: $C_{dc}=5000\mu F$.
 DC bus voltage of UPQC: $V_{dc}=400V$.
 Series Transformer: 2.5 KVA, 1:1 ratio.
 Interfacing Inductors: $R_{sh}=0.1\Omega$, $R_{se}=0.01 \Omega$, $L_{sh}=L_{se}=5$ mH.
 Proportional and Integral gains: $k_p=2$, $k_i=2$.

TABLE I
 COMPARISON OF DIFFERENT APPROACHES OF VOLTAGE SAG MITIGATION

DIFFERENT APPROACHES	UPQC-P		UPQC-Q		UPQC-VAMIN	
	STEADY STATE	DURING SAG	STEADY STATE	DURING SAG	STEADY STATE	DURING SAG
Ps(W)	4000	4000	4000	4000	4000	4000
Qs(VAR)	0	0	0	0	0	0
PL(W)	4000	4000	4000	4000	4000	3700
QL(VAR)	4000	4000	4000	4000	4000	3700
PSER(W)	0	-1000	0	0	0	-500
QSER(VAR)	0	0	0	3000	0	-2000
PSH(W)	0	1000	0	0	0	0
QSH(KVAR)	-4000	-4000	-4000	-7000	-4000	-2000
IS(A)	24	30	25.5	32.5	25	30
VSR(V)	5	64	5	186	0	140
Δ (DEGREE)	0°	0°	1°	36.88°	0°	27.80°
Φ_{SR} (DEGREE)	0°	0°	0°	90°	0°	74°

REFERENCES

- [1] M. H. J. Bollen, *Understanding Power Quality Problems: Voltage Sags and Interruptions*, IEEE Press Power Eng. NJ: IEEE, 2000.
- [2] Arindam Ghosh, Gerard Ledwich, *Power Quality Enhancement Using Custom Power Devices*, Kulwer International Series in Engineering and Computer Science, 2002.
- [3] E. W. Gunther, H. Mehta, "A survey of distribution system power quality," IEEE Trans. Power Del.10 (January (1))(1995)322-329.

- [4] H. Fujita, H. Akagi, The unified power quality conditioner: the integration of series and shunt active filters, *IEEE Trans. on Power Electronics*.13 (2) (1998)315-322.
- [5] A. Ghosh, A. K. Jindal, A. Joshi, "A unified power quality conditioner for voltage regulation of critical load bus, in *IEEE Power Eng. Society General Meeting*, June 2004, vol.1, pp.471-476.
- [6] D. M. Vilathgamuwa, A.A. Perera, S.S. Choi, Voltage sag compensation with energy optimized dynamic voltage restorer," *IEEE Trans. Power Delivery*, 18(July) (2003)928-936.
- [7] C.-S. Lam, M.-C. Wong, Y.-D Han, Voltage Swell and Overvoltage Compensation with Unidirectional Power Flow Controlled Dynamic Voltage Restorer, *IEEE Trans. Power Del.*,(2003)1-9.
- [8] A. Elnady, M. M. A. Salama, Unified approach for mitigating voltage sag and voltage flicker using the DSTATCOM, *IEEE Trans. Power Delivery*,20(April)(2005)992-1000.
- [9] M. Basu, S. P. Das, G. K. Dubey, Comparative evaluation of two models of UPQC for suitable interface to enhance power quality, *Journal of Electric Power System Research*,77(May(7))(2007) 821-830.
- [10] M. Basu, S.P. Das, G.K. Dubey, Investigation on the performance of UPQC-Q for voltage sag mitigation and power quality improvement at a critical load point, *IET Gen.Trans.Dist.*, (2)(2008)414-423.
- [11] M. Basu, S. P. Das, G. K. Dubey, Investigation on the performance of UPQC-Q for voltage sag, *IET Gen. Trans. Dist.*, 2(2008)414-423.
- [12] W. C. Lee, D. M. Lee, T. K. Lee, New control scheme for a unified power quality conditioner-q with minimum active power injection, *IEEE Trans. on power Del.*,25(2010)1068-1076.
- [13] V. Khadkikar A. Chandra, A novel control approach for unified power quality conditioner Q without active power injection for voltage sag compensation," in *IEEEICIT'06*, 779-784.
- [14] Y. Y. Kolhatkar, S. P. Das, "Experimental Investigation of a Single-Phase UPQC With Minimum VA Loading, *IEEE Tran. Power Delivery*, 22(2007) 373- 380.
- [15] Y. Y. Kolhatkar, S. P. Das, Simulation and Experimental Investigation of an Optimum UPQC with Minimum VA Loading, in *IEEE PEDS'05*, 1(2005) 526 -531.
- [16] V. Khadkikar, A. Chandra, A New Control Philosophy for a Unified Power Quality Conditioner (UPQC) to Coordinate Load-Reactive Power Demand Between Shunt and Series Inverters, *IEEE Trans. Power Delivery*,23(2008) 2522-2534.
- [17] V. Khadkikar, A. Chandra, UPQC-S: A Novel Concept of Simultaneous Voltage Sag/Swell and Load Reactive Power Compensations Utilizing Series Inverter of UPQC, *IEEE Trans. Power Electronics*, 26 (September(9))2414-2425.
- [18] J. Liu, J. Yang, Z. Wang, A new approach for single-phase harmonic current detecting and its application in a hybrid active power filter, in *Procd. Annu. Conf.IEEE.IECON'99*, 2(1999)849-854.
- [19] M. T. Haque, Single-Phase p-q Theory, in *Procd. IEEE PESC*, 4 (2002)1815-1820.
- [20] R. Zhang, M. Carddnal, P. Szczesny, M. Dame, A grid simulator with control of single-phase power converter in D-Q rotating frame, in *Procd. IEEE PESC*, 3 (2002)1431-1436

Yash Pal graduated from MMMEC, Gorakhpur in 1994 and obtained his M.Tech and PhD from NIT, Kurukshetra, Haryana in 1996 and 2013, respectively. Presently he is working as a Professor in the Department of Electrical Engineering, NIT, Kurukshetra, Haryana, India. His fields of interest are Active Power Filters, Custom Power Devices, UPQC and renewable energy sources.

A.Swarup currently working as Professor in the Department of Electrical Engineering at N.I.T, Kurukshetra, India. He received his Ph.D. from IIT Delhi. He is a Senior Member of the Institute of Electrical and Electronics Engineers (IEEE). His research interests include Robotics and Artificial Intelligence, System identification, Computer Networking and Control Systems.

A MULTISCALE-based model for Composite Materials with embedded PZT filaments

Tarek M. Hatem and Mohamed Abdel-Meguid

Abstract—The complexity of engineering structures dictates a paradigm shift from traditional inspection and damage detection techniques to more reliable and efficient approach. Smart materials such as piezoelectric materials are being studied as onboard sensors to detect damage progression inside composite structures. Nevertheless, predictive models of such complex structures coupled to piezoelectric materials been absent, especially related to damage detection and prediction. In the current study, a multiscale approach is suggested to predict the behavior of piezoelectric fiber-based composites. Micromechanical model based on transformation field analysis is described to quantify the overall material properties of electrically active composite structure. Capitalizing on the extracted properties, single-phase analysis of a homogeneous structure is conducted using Carrera Unified formulation; a refined plate theory extended to include electric behavior of active materials. Results obtained here are validated against experimental results. Furthermore, the impact of damage on local and global fields is evaluated on macro-level through simulated voids inside a beam-like structure

Keywords— Piezoelectric, Composites, Damage identification

I. INTRODUCTION

Early failure in engineering structure became a concern with the increased employment of composite structures and the complexity of its applications. Conventional inspection techniques are no longer reliable to assess the integrity of these complex structures, especially composite-based structures. The use of composites has been substantially enhancing the mechanical properties of engineering structures; however, their nature still increases the susceptibility of the structure to incipient failure. Accordingly, continuous real-time health monitoring systems are being considered to replace conventional inspection techniques, mainly, to actively identify damage progression inside these complex structures. Several studies identified the role of adaptive smart materials in structural health monitoring applications; embedded smart materials that are responsive toward external stimuli can be actively utilized as sensors or actuators inside structures [1]. Electrically active materials, that couple mechanical and electrical properties such as piezoelectric material, became a top candidate in damage identification applications. Initial

investigations focused on the applicability of piezoelectric wafers embedded within the composite laminates [2]-[5]. However, with recent advancements in manufacturing technology, the focus shifted towards the behavior of polymer-based composites with embedded electrically active Lead Zirconate Titanate fibers (PZT) [6]-[8].

Numerical modeling of piezoelectric fiber-based composites (PFC) is mainly focused on interpretations of overall behavior of composite-structures subjected to electric or mechanical actuation. Analytical quantification of effective properties in active composites was subject to rigorous scrutiny. However, only few studies described the impact of damage on the coupled behavior of PFCs been published. The spectrum of solutions suggested for composites with active constituents are based on expanded problems for inactive composite material, which include electro-mechanical coupled effect. Earlier models computed effective electro-mechanical properties of a composite material based on the Eshelby proposed solution for an infinite matrix with ellipsoidal inclusion [9]-[12]. A different methodology involves asymptotic expansion homogenization techniques to extrapolate the electro-mechanical behavior of electrically active composite materials. Imposing mechanical and non-mechanical boundary conditions, a unit cell model can be used to characterize an idealized periodic geometry through the governing equations of local fields [13]. Bahei-El-Din further expanded on this approach to compute the overall electro-mechanical response of electrically active woven composites using transformation field analysis while accounting for damage progression in composite lamina [14].

On the other hand, Carrera [15]-[16] developed a computational method to conduct beam analysis on piezoelectric ceramics for actuating and sensing purposes using advanced plates and shells theories. Expanding beam theories to incorporate the electrical response associated with piezoelectricity, Carrera Unified Formulation [CUF] enhances the result's precision through higher order thickness expansions.

II. PROCEDURE

The suggested computational approach discussed in this paper follow a multiscale approach to model the electric and mechanical behavior of electrical-active-fiber embedded in a polymeric-matrix. The two stage approach consist of numerical quantification of overall electro-elastic coefficients using Transformation Field Analysis (TFA) scheme and static

Tarek M. Hatem, was with North Carolina State University, Raleigh, NC 27695 USA. He is now with Mechanical Engineering Department, British University in Egypt, El Sherouk, CA 11837 Egypt. (phone: 202-2689-0000; fax: 202-263-00010; e-mail: tarek.hatem@bue.edu.eg)

Mohamed Abdel-Meguid is with the British University in Egypt (e-mail: mohamed_ezz_nasr@hotmail.com).

structural analysis using Carrera Unified Formulation (CUF) to model the impact of damage on electrical response of PFCs. Electrically induced strains in active medium is treated as transformation strains and resultant local fields and overall composite response is quantified through the TFA originally described by Dovark, G. J.[17]; TFA computes the local fields using microgeometry dependent concentrations factors. Microproperties of composite are used to assemble the stiffness matrices in the governing equations using CUF and variable fields are solved using in-house developed finite element software.

A. Constitutive Equations

Piezoelectric response can be defined through two reversible effects; first, the production of an electric field as a direct response to an applied stress; and second, a converse effect represented by mechanical deformation as a response to an applied electric potential. The linearly formulated constitutive equations binding the response of piezoelectric material are standardized by [18]. The constitutive equations for piezoelectric material are derived from the thermodynamical principles correlating the electric field (E), strain (S), stress (T) and electrical displacement (D) [16]-[19].

$$S = s^E T + d E \quad (1)$$

$$D = d^T T + \varepsilon E \quad (2)$$

s^E is the [6x6] compliance vector for piezoelectric material, d is the [6x3] piezoelectric coupling co-efficient vector, ε is the [3x3] permittivity vector. The two equations can be symmetrically combined in matrix notation.

$$\begin{pmatrix} S \\ D \end{pmatrix} = \begin{bmatrix} s & d \\ d^T & \varepsilon \end{bmatrix} \begin{pmatrix} T \\ E \end{pmatrix} \quad (3)$$

Rearranging the constitutive equations for stress function

$$T = C^E S - e E \quad (4)$$

Where, C^E is the [6x6] stiffness matrix

$$e = C^E d \quad (5)$$

For transversely isotropic piezoelectric material, the coefficients can be expressed in matrix notation as the following:

$$s^E = \begin{bmatrix} s_{11} & s_{12} & s_{13} & 0 & 0 & 0 \\ s_{21} & s_{22} & s_{23} & 0 & 0 & 0 \\ s_{31} & s_{32} & s_{33} & 0 & 0 & 0 \\ 0 & 0 & 0 & s_{44} & 0 & 0 \\ 0 & 0 & 0 & 0 & s_{55} & 0 \\ 0 & 0 & 0 & 0 & 0 & s_{66} \end{bmatrix}$$

$$d = \begin{bmatrix} 0 & 0 & 0 & 0 & d_{15} & 0 \\ 0 & 0 & 0 & d_{15} & 0 & 0 \\ d_{21} & d_{21} & d_{23} & 0 & 0 & 0 \end{bmatrix}$$

$$\varepsilon = \begin{bmatrix} \varepsilon_{11} & 0 & 0 \\ 0 & \varepsilon_{11} & 0 \\ 0 & 0 & \varepsilon_{33} \end{bmatrix} \quad (6)$$

Piezoelectric fiber-based composites consist of transversely isotropic ceramic piezoelectric fibers aligned in an isotropic polymer based matrix. The resultant composite material will be transversely isotropic material represented by 11 mutually

exclusive coefficients representing the electro-mechanical response of the homogenized composite.

B. Transformation Field Analysis (TFA)

The micromechanical analysis is conducted using the TFA scheme [17] to quantify the overall effective electro-mechanical properties of active PFC composites. Transformation field analysis represents overall response of the material through separating elastic and inelastic fields. All non-mechanical fields due to thermal or electrical actuation are considered as inelastic and treated as transformation fields, which remain in material after removing mechanical loads. The accuracy of the two-phase representation is affected by large variations in the transformation field, thus further subdivision for constituents is conducted through a *Representative Volume Element* (RVE). The RVE demonstrated in Fig. 1 represents a single cell repeated throughout the material, which under an idealized assumption can provide periodic arrangement. The unit cell used in this transformation field analysis is *Periodic Hexagonal Array* (PHA) [20]

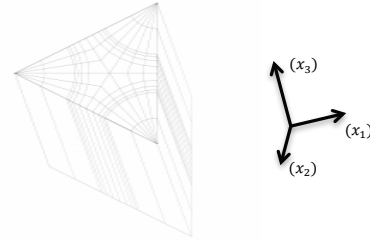


Figure 1 PHA Representative volume element

Eigen stresses [λ] and strains [μ] are used to describe transformation fields for the representative volume element. Accordingly the constitutive equations for each element in an RVE can be written to incorporate induced transformation fields due to uniform stress [T_i] or strain [S_i].

$$S_i = s_i^E T_i + \mu_i \quad (7)$$

$$T_i = C_i^E S_i + \lambda_i \quad (8)$$

Where i represent number of elements inside the RVE [1,2...Q]. Comparing equations with constitutive equations for PFC, the transformation fields can be attributed to an applied electric field in electrically active piezoelectric fiber-based composites.

$$\mu_i = d_i E_i \quad (9)$$

$$\lambda_i = -e_i E_i \quad (10)$$

For the RVE entity, the strains and stress caused by uniform stress or strain are super-positioned across the entire volume.

$$S_i = A_i S + \sum_{j=1}^{\Omega} D_{ij} \mu_j \quad (11)$$

$$T_i = B_i T + \sum_{j=1}^{\Omega} F_{ij} \lambda_j \quad (12)$$

Where, Ω is the number of elements carrying transformation fields inside the RVE, A_i and B_i are concentration factors used to describe the volume strain and stress in terms of overall counterparts. D_{ij} and F_{ij} are constant influence functions depends mainly on the elastic moduli of each element. These matrices are numerically attained through finite element analysis of the RVE under unit load and respective boundary

conditions.

C. Carrera Unified Formulation

With overall properties extracted from the transformation field analysis, the extended plate theory can be used to describe the behavior of idealized composite layer. The governing equations for piezoelectric material using Physical Vapor Deposition (PVD) can be described with two variables, displacement and electric potential [16].

$$K_{uu}u + K_{u\phi}\phi = p_u - M_{uu}\ddot{u} \quad (13)$$

$$K_{\phi u}u + K_{\phi\phi}\phi = 0 \quad (14)$$

Where u, ϕ stand for the displacement vector and electric potential respectively. Whereas the matrices K are functions of the electrical and mechanical properties of the material, for multiple layers the matrices are assembled accordingly. M_{uu}, \ddot{u} stand for the inertia matrix and the second derivative of the displacement respectively, and p_u signifies the mechanical load exerted.

The variables can be presented by using the unified formation as function of $u(x, y, z)$ and expansion functions in the z direction.

$$u(x, y, \phi) = \begin{bmatrix} u_x \\ u_y \\ \phi \end{bmatrix} \quad (15)$$

$$u(x, y, z, \phi) = \sum_{\tau=1}^Q F(z) u(x, y, \phi) \quad \tau = 1, 2, \dots, Q \quad (16)$$

The expansion functions are used to achieve higher order approximation across the thickness direction, τ signifies the order of the expansion in the z direction ranging from 1 to Q , however, in the formulation the equation can be expanded up to the fourth order. Legendre polynomials are used to express the expansion functions; their value depends on the element shape and natural coordinates.

The computation of the variables is done through a finite element model. Shape functions are used to define the relation between the nodal values and the element variable. Accordingly the equation is written as following;

$$u(x, y, z, \phi) = N_i \sum_{\tau=1}^Q F(z) q_i(x, y, \phi) \quad (17)$$

In the above equation the q describe the nodal value of the variable vector. Using the above relation the governing equation can be rearranged:

$$K_{uu}^{ijkl\tau s} u^k + K_{u\phi}^{ijkl\tau s} \phi^k = p_u - M_{uu} \ddot{u} \quad (18)$$

$$K_{\phi u}^{ijkl\tau s} u^k + K_{\phi\phi}^{ijkl\tau s} \phi^k = 0 \quad (19)$$

The subscripts i, j, τ, s are the indices used in the assembly of the stiffness matrix, where i, j and τ, s are related to the shape functions and expansion functions respectively. Subscript k indicates layer wise analysis for laminated plate structures.

III. RESULTS

A. Pristine structure

The multiscale model applied in the current study is evaluated against experimental data obtained from a manufacturer of PFCs {Advanced Ceramics Inc}. The single ply, unidirectional composite consists of PZT-5A fibers and

epoxy matrix with 0.45 fiber content. In the RVE the analysis proceeds with applying directional electric field in fiber direction and accordingly the overall composite mechanical deformation is computed at different voltages as shown in Fig. 2. Furthermore, the composite mechanical and electrical properties are extracted for macro-scale analysis using CUF.

Table 1 Material Properties of PZT-5A as extracted from [22]-[14]

Material	E_L (GPa)	ν_L	d_{33} ($\frac{m}{V} \times 10^{-12}$)	d_{31}	d_{15}	ϵ_{33} ($\frac{C}{V.m} \times 10^{-9}$)
PZT 5-A	69	0.34	374	171	584	15000
Epoxy	3.35	0.35	-	-	-	-

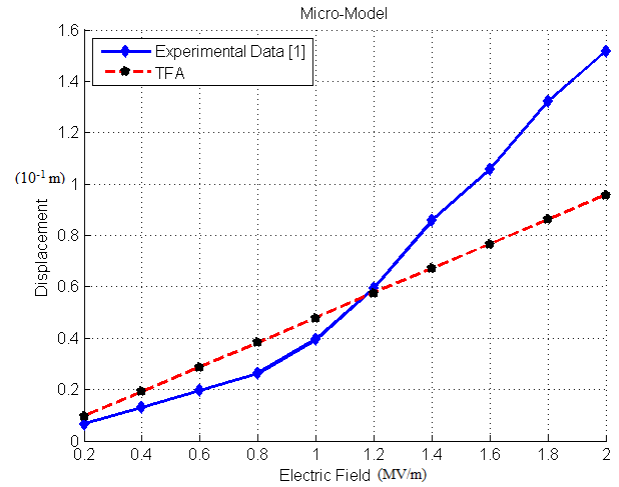


Figure 2 Experimental data compared with TFA results for mechanical deformation under applied electrical load¹

Structural analysis using CUF is conducted on the same composite material to verify the modeling approach. The displacement is computed at different applied voltages and compared with experimental results. The mesh geometry and mesh convergence analysis for the finite element model, whereas the dimensions of the composite are shown in Fig. 4. The CUF electrically extended the constitutive equations for the same linearized pattern.

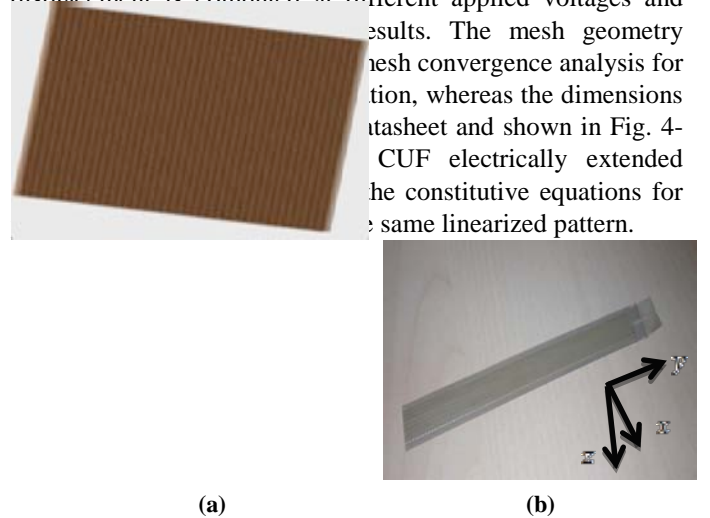


Figure 3 PFC composite: (a) Finite element mesh, (b) PFC composite provided by Advanced Ceramics Incorporated

¹ Experimental data are obtained from Advanced Ceramics Inc. data sheet for PFC-14 specimen

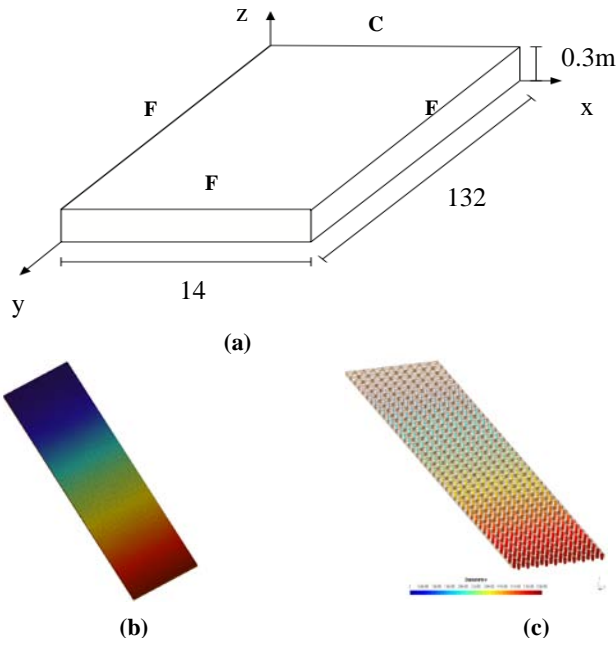


Figure 4 CUF solution for electrical actuation model (a) Geometry, dimensions and boundary conditions of the numerical model [C indicates clamped side while F is free], (b) Voltage distribution along length grounded at blue and applied at red, (c) Displacement distributions induced by electro-mechanical coupling displayed in fig. [5]

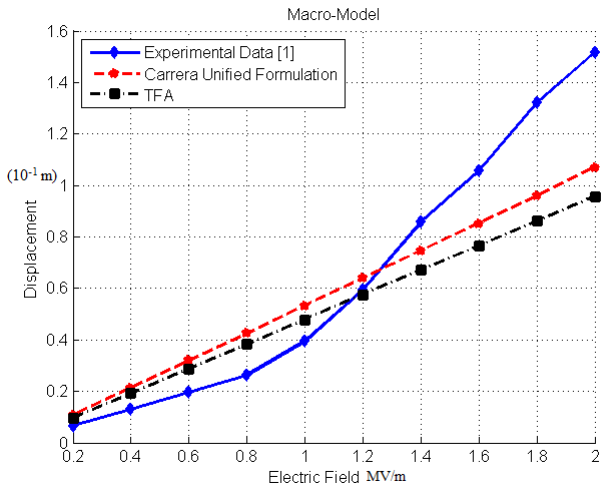


Figure 5 Displacement against Electrical Field solved using Carrera Unified Formulation and compared to the experimental and TFA results

B. Damaged Structure

Damage is introduced throughout the structure by introducing an elongated (in the y-direction) and through (through thickness – z direction) void inside the model in different locations across the composite structure. For constant applied uniaxial load in y-direction Fig. 6 represents the adjusted voltage distribution due to void interference. The induced void inside the model caused a global voltage increase from pristine condition across the two electrodes ends. The impact of void location is studied through analyses of local voltage fluctuations. For different void locations the

local voltage variation is plotted in Fig. 7, the result indicates varying voltage variations.

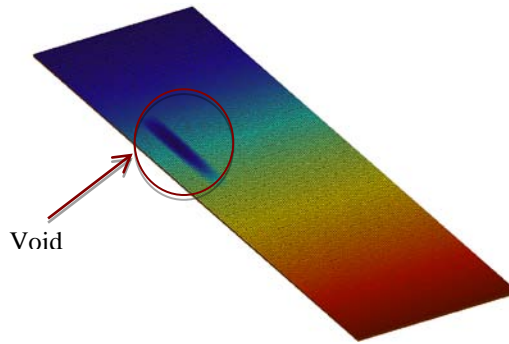


Figure 6 Voltage distribution in a damaged model with introduced void

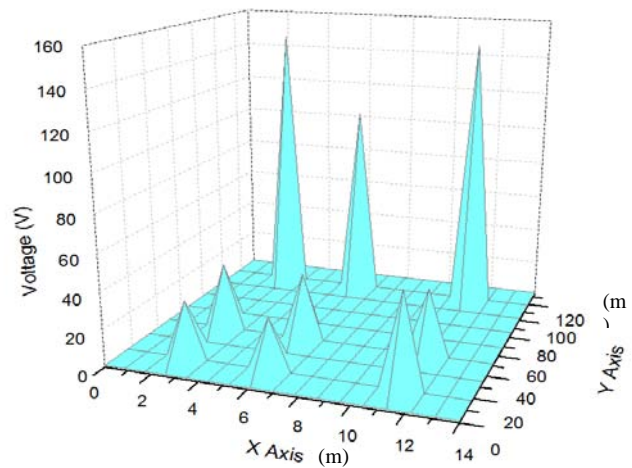


Figure 7 Voltage variation in proximity of void for varying damaged locations along the length of the model

IV. DISCUSSION

As shown in Fig. 2, the TFA results present purely linear behavior based on the constitutive equations for piezoelectric material, whereas the experimental behavior demonstrate a nonlinear behavior. The voltage is applied along the fiber direction $[x_3]$ and the displacement is measured in the same direction for alternating voltages. Both the TFA model and experimental results match well on the initial linear part of the curve with low voltage applied, yet at very high voltages the experimental data starts to diverge from linear behavior. The nonlinear behavior is attributed to multiple factors, mainly heat and polarization shifting at high voltages. The coupling coefficients dictate the mechanical deformation of the composite under pure electric loading in the direction of the fibers. In analogy, the mechanical deformation of the composite under pure mechanical loading is dictated by the composite stiffness matrix.

In the macro-scale boundary conditions such as mechanical constraints significantly affect the structural response, thus the values computed through CUF diverge slightly from the TFA as shown in In Fig. 5. Similar to TFA during the initial part of the curve the Finite Element model match well with

experimental results accordingly this model presents an adequate approximation of the structural behavior and can be extended to evaluate the behavior of the structure in damaged conditions.

The voltage increase in the damaged model is expected due to the stiffness drop of the entire structure. The amplitude of the voltage fluctuates depending on the location of the void along the length. The global change in voltage signifies clear indication of damage occurrence in the structure. Localization through local voltage drops in the vicinity of the void is evaluated. Fig. 7 demonstrates the voltage variation in the proximity of the void; with the void being located at different locations relative to the x, y coordinates. The local voltage difference descends the further the location of the applied load from the damaged area. However, the sensitivity also diminishes; indicating the significance of the distance between void location and applied load in damage localization.

V. CONCLUSION

In the current study a multiscale approach been utilized to extract the behavior of composite structures with electrically active fibers. The model demonstrated proper approximation of the experimental results. Both models, the microscale (TFA) model and macro-scale (CUF-FEM) model, been successfully utilized through a hierarchal approach; accuracy is increased substantially with fiber-fiber interaction scheme of the TFA in microscale and the structural response in macro-scale. Extracting the electro-mechanical properties of the composite material from the micromechanical model allows a significant reduction in the computational cost at the macro-scale and therefore enables the modeling of more complex geometry and structures utilizing the proposed multiscale approach.

Furthermore, damage had been introduced and evaluated in a macro-scale finite element analysis through introducing voids at different locations of the model. Damage identification and localization is done through analyzing the impact of the damage. Global voltage variation along the entire model provides clear indication of damage occurrence, whereas localized fluctuation of voltage near the vicinity of the damage due to different void's location demonstrated a dependence on the distance from the applied load and boundary condition. With sufficient database of results the work presented in this paper can be further expanded to include damage characterization through proper implementation of Genetic Algorithms (GA) and Neural Networks (NN) [23].

REFERENCES

[1] I. Chopra, "Review of State of Art of Smart Structures and Integrated Systems". AIAA, 2002, 40, 2145-2187.
 [2] E. Crawley and J. de Luis, "Use of Piezoelectric actuators as elements of intelligent structures". AIAA, 1987, 25, 1373-1385.
 [3] V. Giurgiutiu and A. N. Zagrai. "Embedded Self Sensing Piezoelectric Active Sensors for On-line Structural identification. Vibration and Acoustics", 2002, 124, 116-125.

[4] A. Zagrai, and V. Giurgiuti, "Electro-Mechanical Impedance Method for Crack Detection in Thin Plates. Intelligent Materials systems and Structures", 2001, 12, 709-718.
 [5] V. Giurgiutiu, and C. Rogers, "Recent Advancements in the Electro-Mechanical (E/M) Impedance Method for Structural Health Monitoring and NDE". Annual International Symposium on Smart Structures and Materials, 1998, 3329-3353.
 [6] W. A. Smith and B. A. Auld, "Modeling 1-3 Composite Piezoelectrics: Thickness-Mode Oscillations. Ultrasonics, Ferroelectrics, and Frequency Control", 1991, 38, 40-47.
 [7] A. A. Bent, N. W. Hagood, Rodgers, J. P. "Anisotropic Actuation with Piezoelectric Fiber Composites. Intelligent Material Systems and Structures", 1995, 6, 338-349.
 [8] R. B. Williams, G. Park, D. J. Inman, and W. K. Wilkie, "An overview of Composite Actuators with Piezoceramics". Conference on Structural Dynamics, Westin Los Angeles Airport Hotel, Los Angeles, CA, February 4th -7th, 2002. 421-427.
 [9] J. D. Eshelby, "The determination of the elastic field of an ellipsoidal inclusion", and related problems. Proceedings of Royal Society of London, 1957, A241, 376-396.
 [10] M. L. Dunn and M. Taya, "Micromechanics Predictions of the Effective Electroelastic Moduli of Piezoelectric Composites". International Journal of Solids and Structures, 1993, 443, 161-175.
 [11] T. Mori and K. Tanaka "Average stress in matrix and average elastic energy of materials with misfitting inclusions". Acta Metallurgica, 1973, 21, 571-574.
 [12] Li Jiang Yu and M. L. Dunn, "Micromechanics of Magneto-electroelastic Composite Materials: Average Fields and Effective Behavior". Intelligent Material Systems and Structures, 1998, 9, 404-416.
 [13] H. Berger *et al.*, "An analytical and numerical approach for calculating effective material coefficients of piezoelectric fiber composites". International Journal of Solids and Structures, 2005, Vol. 42, 5692-5714.
 [14] Y. A. Bahei-El-Din, "Modelling electromechanical coupling in woven composites exhibiting damage". Proceedings of IMechE 223, Part G: J Aerospace Engineering, 2009, 485-495.
 [15] E. Carrera, "Theories and Finite Elements for Multilayered Plates and Shells: A Unified compact formulation with numerical assessment and benchmarking". Archives of Computational Methods in Engineering, 2003, 10, 215-296.
 [16] E. Carrera, "Plates and Shells for Smart Structures: Classical and Advanced Theories for Modelling and Analysis". Torino : Wiley, 2008.
 [17] G. J. Dvorak, "Transformation field analysis of inelastic composite materials". Proceeding of Royal Society of London, 1992, A437, 311-327.
 [18] IEEE, Std 176. Institute of Electrical and Electronics Engineers Standard on Piezoelectricity : ANSI/IEEE, 1987.
 [19] T. Ikeda, "Fundamentals of Piezoelectricity" : Oxford University Press, 1996.
 [20] J. L. Teply, "Periodic Hexagonal Array Models for Plasticity Analysis of Composite Materials". Ph. D. Dissertation: University of Utah, 1984.
 [21] Advanced Ceramics Incorporated. Piezoelectric Fiber Composites.
 [22] D. Berlincourt, H. H. A. Krueger, and C. Near. "Technical Publications 226: Important Properties of Morgan Electro Ceramics Piezoelectric Ceramics (PZT-4, PZT-5A, PZT-5H, PZT-8)". Morgan Electro Ceramics, 2013.
 [23] T. M. Hatem, M. N. Abulfoutouh, H. M. Negm. "Application of Genetic Algorithms and Neural Networks to Health Monitoring of Composite Structures". Proceedings of the whileond European Workshop on Structural Health Monitoring, Munich, Germany, July 7-9, 2004, 616-632; Boller, C., Staszewski, W. J.; DEStech Publications Inc, 2004.

An Approach for Optimal Placement, Rating and Investment Cost Recovery of a TCSC in Double Auction Power Market

Prashant Kumar Tiwari, and Yog Raj Sood

Abstract—This paper presents an investment cost recovery based reliable optimization approach to optimal placement of thyristor controlled series compensator (TCSC) in competitive power market. The double auction bidding model has been used in which generation companies (gencos) as well as distribution companies (discos) both are allowed to offer and bid their prices to independent system operator (ISO). The amount to be paid by each disco and amount to be received by each genco has been determined by actual bidding price approach. The objective is to maximize the social welfare with minimization of device investment cost by suitable location and rating of single TCSC in the system. The effectiveness of proposed approach for location of TCSC has been tested on 39-bus New England and 246-bus Indian practical NRP (Northern Regional Power Grid) systems.

Keywords— Competitive power market, double auction bidding, optimal placement, TCSC.

I. INTRODUCTION

NOW these days greater demands have been placed on the transmission network, and these demands will continue to increase because of the increasing number of nonutility generators and heightened competition among utilities themselves. The increased demand on transmission, absence of long-term planning and the need to provide open access to generating companies and customers, all together have created tendencies towards less security and reduced quality of supply. Flexible AC transmission systems (FACTS) are considered to be one technology that can benefit the emerging power system in terms of enhancing the system stability, providing better voltage control and increased loading capability of existing transmission systems with possibility to load lines much closer to their thermal limits [1], [2].

Since a decade, there has been growing interest in allocation of FACTS devices for achieving different objectives for transmission network. Gerbex *et al.* [3] have used a genetic algorithm to seek the optimal location of FACTS devices in a power system. Optimizations have been performed on the location of the device as well as their values. However, in [3] the number of devices to be installed is decided arbitrarily not by optimization. The impact of TCSC on congestion and spot

pricing is presented in [4]. The paper demonstrated that the TCSC could reduce congestion as well as the losses. References [5] and [6] have proposed optimal allocation methods for TCSC to eliminate the line overloads, where sensitivity index is introduced for ranking the optimal placement. Priority list method for TCSC allocation for congestion management has been proposed in [7]. However the works presented in [3]-[7] have not taken into account the cost of installation and maintenance of FACTS devices.

Reference [8] proposes an approach for optimal location of FACTS devices and evaluating its impact on annual total cost, device investment cost and benefit due to device installation. Song *et al.* [9] suggested the proper location of each device to enhance the steady state security. In [10], application of different FACTS devices has been presented to control the power flow in the power system. Recently some other optimization techniques based on various artificial intelligence techniques like evolutionary programming (EP) [11], particle swarm optimization (PSO) [12], hybrid particle swarm optimization (HPSO) [13] etc. have also been developed for the analysis of deregulated power sector. However, these techniques take much more time to simulate the problem and sometimes do not converge to a single optimal value and provide approximate solutions.

Review of works from the literature reveals that the limited attempts have been made to suggest a simple, efficient and reliable approach for optimal location, rating, cost of FACTS controllers, social welfare and investment cost recovery of FACTS devices simultaneously in the deregulated power sector.

This paper presents a simple and reliable optimization approach for optimal placement of TCSC in the competitive power sector. The proposed approach is based on investment recovery of FACTS devices with step by step variation in control parameters of the device. MATLAB programming codes for the proposed technique have been developed and incorporated for the simulation purpose. In this paper, the MATPOWER [14] m-files are modified with adding the proposed optimization codes to solve the problem.

II. MATHEMATICAL FORMULATION

In the considered power market model, bulk loads as well as retailers are required to bid their maximum demand and price function. All generators are also required to bid their generation cost function along with their maximum generation.

Prashant Kumar Tiwari is with the Department of Electrical Engineering, National Institute of Technology Silchar, Assam, 788010, India (e-mail: prashant081.in@gmail.com).

Yog Raj Sood is with the Department of Electrical Engineering, National Institute of Technology Hamirpur, Hamirpur 177005, India (e-mail: yrsood@gmail.com).

A. TCSC Modeling

The TCSC can serve as the capacitive or inductive compensation respectively by directly modifying the reactance of the transmission line. In this paper, the model of the TCSC has been developed to be suitable for steady-state. It has modeled as variable reactance connected in series with transmission line. The model of transmission line with a TCSC connected between bus i and bus j is shown in Fig. 1.

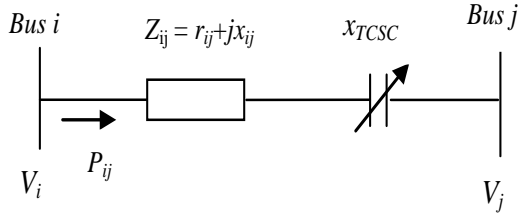


Fig. 1. Model of transmission line with TCSC.

The rated value of TCSC is a function of the reactance of transmission line where TCSC has been installed:

$$x_{line} = x_{ij} + x_{TCSC} \quad (1)$$

where $x_{TCSC} = k_{TCSC} \cdot x_{line}$

' x_{line} ' is the overall line reactance between bus i and j with TCSC installation. ' x_{TCSC} ' is the reactance of TCSC and ' k_{TCSC} ' is a coefficient which represents the compensation level of TCSC ($-0.7 \leq k_{TCSC} \leq 0.2$). The working range of reactance of TCSC has been fixed between $-0.7x_{line}$ and $0.2x_{line}$ [3], [15]. Normally up to 70% of line reactance is chosen for compensation because 100% compensation will raise a problem of series resonance in the system [16].

B. Investment Cost

According to Wibowo *et al.* [8], Saravanan *et al.* [12] and Siemens AG database [17], the investment cost of TCSC is given by:

$$C_{TCSC} = 0.0015 \cdot S_{TCSC}^2 - 0.7130 \cdot S_{TCSC} + 153.75 \quad \$/kVar \quad (2)$$

where ' C_{TCSC} ' is the cost of TCSC in $\$/kVar$ and ' S_{TCSC} ' is the operating point of TCSC in $MVar$. Overall investment cost ' IC_{TCSC} ' (in $\$$) is calculated as follows:

$$IC_{TCSC} = (C_{TCSC} \times S_{TCSC} \times 1000) \quad \$ \quad (3)$$

The following expression has been used to convert the investment cost of TCSC into annual term [8]:

$$AIC_{TCSC} = IC_{TCSC} \frac{ir(1+ir)^{LT}}{(1+ir)^{LT} - 1} \quad \$/year \quad (4)$$

where ' AIC_{TCSC} ' is the annual TCSC investment cost, ' ir ' is the interest rate and ' LT ' is the life time of device. In this work, it is assumed that the interest rate $ir = 0.05$, $LT = 5$ years.

In order to calculate the hourly cost of TCSC (in $\$/h$), the following formula is used:

$$HIC_{TCSC} = \left[\frac{AIC_{TCSC}}{8760} \right] \quad \$/h \quad (5)$$

here, ' HIC_{TCSC} ' is the cost of TCSC in $\$/h$.

C. Objective Function and Constraints

Consider a system having total ' nb ' number of buses, ' ng ' number of generators and ' nd ' number of loads. Let the generation cost curve offer to the pool by generator at bus i be denoted by $C_i(Pg_i^p)$ and the worth function (which is also called benefit curve [18]) for load that is price dependent be $B_j(Pd_j^p)$. It represents the price the load is willing to pay to purchase an amount of power Pd_j^p .

Mathematically, the objective function is to maximize the social welfare and minimize the investment cost of TCSC. So the objective function is given as:

$$F_{obj} = \max \left\{ \sum_{j=1}^{nd} B_j(Pd_j^p) - \sum_{i=1}^{ng} C_i(Pg_i^p) - HIC_{TCSC} \right\} \quad \$/h \quad (6)$$

subject to the following transmission network constraints and FACTS device constraints:

- Power balance equations (equality constraints)

$$P_i(V_i) - Pg_i^p + Pd_i^p = \theta, \quad \text{for any bus } i \quad (7)$$

$$Q_i(V_i) - Qg_i^p + Qd_i^p = \theta, \quad \text{for any bus } i \quad (8)$$

- The inequality constraints

$$\left. \begin{aligned} Pg_i^{\min} \leq Pg_i \leq Pg_i^{\max}, Qg_i^{\min} \leq Qg_i \leq Qg_i^{\max}, \\ V_i^{\min} \leq V_i \leq V_i^{\max}, MVA_{fij} \leq MVA_{fij}^{\max}, \\ -0.7x_{ij} \leq x_{TCSC} \leq 0.2x_{ij} \end{aligned} \right\}; i \text{ and } j \forall nb \quad (9)$$

where, Pg_i^{\min} , Pg_i^{\max} are real power generation limits at bus i ; V_i is voltage magnitude at bus i ; Qg_i^{\min} , Qg_i^{\max} are reactive power generation limits at bus i ; MVA_{fij}^{\max} is maximum apparent power flow limit of transmission line connecting bus i and bus j ; x_{TCSC} , x_{ij} are reactance added to the line by placing TCSC and reactance of the line connecting bus i and bus j .

During optimization process each disco will considered to be paid an amount to ISO for purchase the power and each genco to be received an amount from the ISO to sale the power to disco. The amount to be paid by each disco and amount to be received by each genco has been determined by actual bidding price approach [19]. The social welfare has been then determined based on total payments and receipts.

III. PROPOSED OPTIMIZATION ALGORITHM

The optimization problem of (6) - (9) is a complex large scale nonlinear programming problem that cannot be easily solved by conventional approaches. This paper presents an approach in which optimization has been done by placing TCSC and varying all control parameters step by step manner between the specified ranges and getting optimal solutions. The only OPF part of proposed technique has been constituted by modifying the m-files of MATPOWER [14]. In the proposed approach, this OPF has been run several times for each and every possible location and sizing of TCSC and best location will be decided at which objective function gets maximum value.

The proposed approach is capable of handling generating units having any type of cost characteristics such as quadratic, piecewise linear, piecewise quadratic etc.

A. Flow Chart of Proposed Approach

The flow chart of the proposed approach has been given in Fig. 2. In this figure, 'N' is number of TCSC; ' k_{TCSC} ' is compensation level of TCSC; ' Δk_{TCSC} ' is increment in k_{TCSC} ; k_{TCSC}^{max} is maximum value of k_{TCSC} (0.2); k_{TCSC}^{min} is minimum value of k_{TCSC} (-0.7); F_{obj} is value of objective function; $F_{without}$ is value of objective function without TCSC in the network and F_{with} is value of objective function with TCSC in the network; 'I' is a counter which shows a step increment by 1 for every Δk_{TCSC} increase in TCSC compensation level. As the value of 'I' increase, the size of column matrix F_{with} also increase.

B. Investment Cost Recovery

Investment cost of TCSC has been calculated by the equations (2) - (5). The objective function has two parts: one is social welfare and another part is investment cost of TCSC. The social welfare is combination of the equations for maximization of consumer benefit and minimization of generation cost. There is considerable increase in social welfare with installation of TCSC by proposed approach. This increase in social welfare is more than installation cost of TCSC. Hence there is complete recovery of installation cost of the TCSC.

IV. APPLICATION OF PROPOSED ALGORITHM

The proposed approach for optimal location of TCSC has been tested and analyzed on 39-bus New England system [14] and 246-bus Indian practical NRPG system [20] with quadratic as well as linear cost functions.

The proposed approach based on deterministic model, in which OPF has been run several times for each and every possible locations and sizing of the TCSC and best location has been determined by the maximum optimal value of objective function. Since, the proposed approach is evaluating the objective function for all possible locations, so there is no chance to ignore the global optimal point. Due to this reason, it may reliable than other approaches and provides unique global optimal results.

For both the considered systems, the generator offer cost functions and demand bidding cost functions have been taken as quadratic as well as linear as follows:

For quadratic cost function:

$$C_i(Pg_i^p) = a_i(Pg_i^p)^2 + b_iPg_i^p \tag{10}$$

$$B_j(Pd_j^p) = a_j(Pd_j^p)^2 + b_jPd_j^p \tag{11}$$

For linear cost functions the value of coefficients a_i and a_j have been taken as zero. These linear functions are shown as follows:

$$C_i(Pg_i^p) = b_iPg_i^p \tag{12}$$

$$B_j(Pd_j^p) = b_jPd_j^p \tag{13}$$

The minimum value of all generators i.e. $(Pg^p)^{min}$ and minimum value of all variable demands i.e. $(Pd^p)^{min}$ has been taken as zero.

A. TCSC Placement in 39-bus New England System

First, the proposed optimization technique has been applied to 39-bus New England system. The generation offer coefficients of all generators and demand bidding coefficients of all demands for this system is given in Table V and Table VI in the Appendix.

The social welfare has been determined for with and without TCSC cases for this practical system. From Table I it is observed that social welfare increased by 33.611 \$/h after locating TCSC in line number 40 (line segment 25-26). The investment cost of TCSC is 4.9093 \$/h which has been recovered by enhanced social welfare. Table I also shows the investment cost recovery of TCSC. The additional social welfare after recovery is 28.7017 \$/h which is still more than the investment cost of TCSC.

TABLE I
INVESTMENT RECOVERY BY ADDITIONAL SOCIAL WELFARE BY PROPOSED APPROACH (39-BUS SYSTEM)

S.N.	Items	Value (\$/h)
1.	Social Welfare Without TCSC; (A)	18034.429
2.	Social Welfare With TCSC Allocation; (B)	18068.040
3.	Additional Social Welfare Without Investment Recovery of TCSC; (C) = (B - A)	33.611
4.	Investment Cost of TCSC; (D)	4.9093
5.	Additional Social Welfare After Investment Recovery of TCSC; (E) = (C - D)	28.7017

TABLE II
OPTIMAL PARAMETERS OF PLACED TCSC (39-BUS SYSTEM)

S.N.	TCSC Parameters	Optimal Value/Mode
1.	Optimal Location	Line Number - 40
2.	Compensation Level (k_{TCSC}) in p.u.	-0.64
3.	Operating Mode	Capacitive
4.	Reactance of TCSC (x_{TCSC}) in p.u.	-0.0207
5.	Cost of TCSC (\$/h)	4.9093

The optimal parameters of allocated TCSC are shown in Table II. As per this table, the compensation level of TCSC is -0.64 p.u. which provides capacitive series compensation for the system. The reactance of selected TCSC should be -0.0207 p.u. in order to gets better compensation.

B. TCSC Placement in 246-bus Indian NRPG System

The proposed technique has been also applied to another practical system i.e. 246-bus Indian NRPG system. The generation offer coefficients of all generators and demand bidding coefficients of all demands for this Indian system are given in Table VII and Table VIII in the Appendix.

TABLE III
INVESTMENT RECOVERY BY ADDITIONAL SOCIAL WELFARE BY PROPOSED APPROACH (NRPG SYSTEM)

S.N.	Items	Value (\$/h)
1.	Social Welfare Without TCSC; (A)	653439.191
2.	Social Welfare With TCSC Allocation; (B)	654287.672
3.	Additional Social Welfare Without Investment Recovery of TCSC; (C) = (B - A)	848.481
4.	Investment Cost of TCSC; (D)	36.8074
5.	Additional Social Welfare After Investment Recovery of TCSC; (E) = (C - D)	811.6736

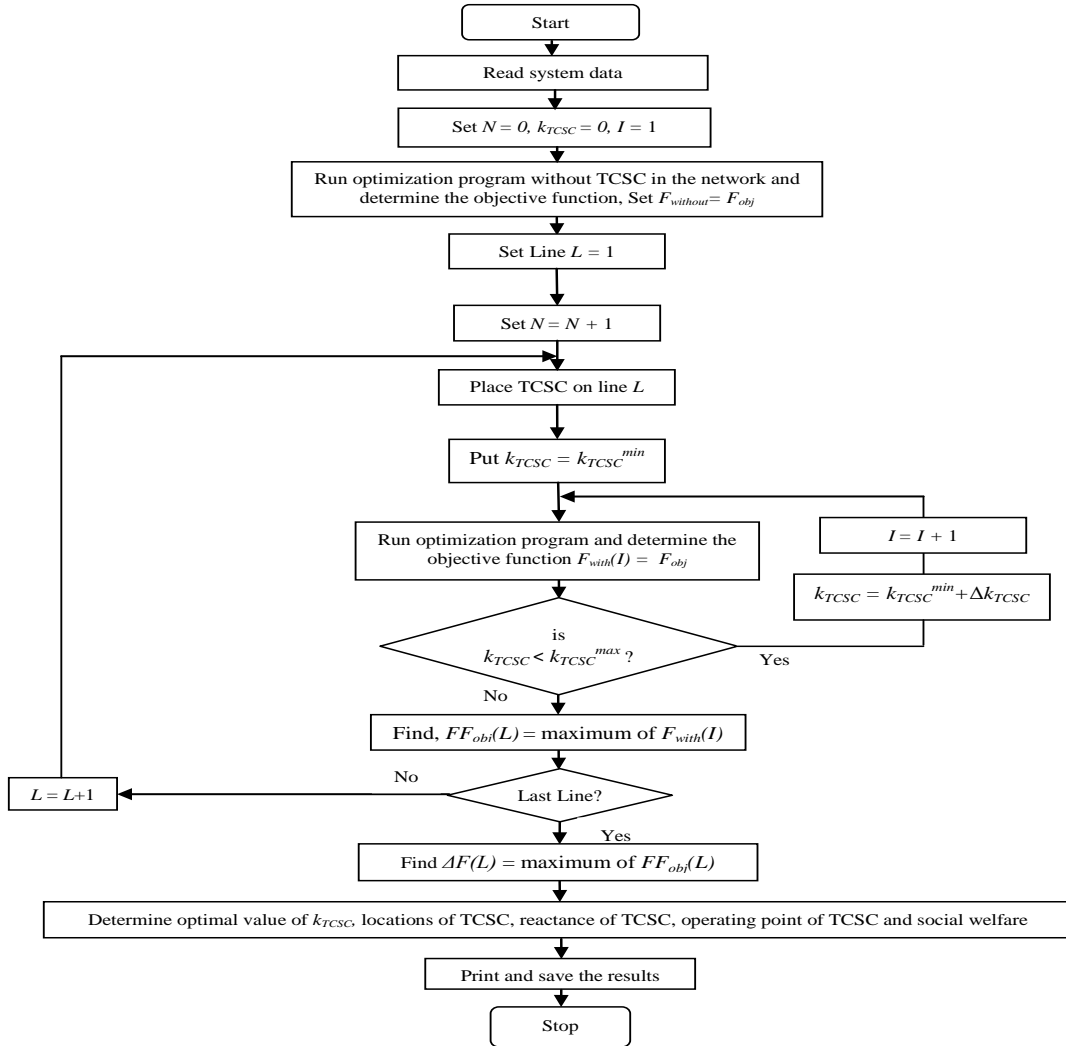


Fig. 2. Flowchart of proposed approach.

 TABLE IV
 OPTIMAL PARAMETERS OF PLACED TCSC (NRPG SYSTEM)

S.N.	TCSC Parameters	Optimal Value/Mode
1	Optimal Location	Line Number - 12
2	Compensation Level (k_{TCSC}) in p.u.	-0.7
3	Operating Mode	Capacitive
4	Reactance of TCSC (x_{TCSC}) in p.u.	-0.0087
5	Operating Point (S_{TCSC}) in MVar	17.5725
6	Cost of TCSC (\$/h)	36.8074

Table III presents the improvement in social welfare when TCSC is optimally placed at line number 12 (line segment 73-74). As per this table, the proposed method provides large additional social welfare i.e. 848.4810 \$/h by optimal placement of TCSC that also recovers the investment cost of TCSC. This table also shows that investment cost of TCSC is 36.8074 \$/h and additional social welfare with recovery of TCSC cost is 811.6736 \$/h. This additional welfare (after recovery) is significant and provides the motivation to ISO for installing TCSC in the network for enhanced market trading capability by relieving the congestion.

The optimal location, compensation level, operating mode, reactance and cost of desired TCSC have been determined by proposed optimization approach and presented in Table IV.

V. OBSERVATIONS

The following observations have been made by the simulation with the proposed technique:

- 1) By proposed approach, there is considerable increase in social welfare with installation of TCSC. The increase in social welfare is so much that it even recovers the installation cost of TCSC. In other words, the installation cost of TCSC has been recovered from enhanced social welfare. Therefore no additional revenue is required for the FACTS device in this optimal approach.
- 2) The proposed technique not only provides the unique optimal location of TCSC but also determines the optimal parameters of TCSC with enhanced social welfare.
- 3) The proposed technique can be used for placement of TCSC in any small as well as large power systems.

VI. CONCLUSION

This paper presents a simple and reliable optimization technique for simultaneously determining the optimal location

and parameters of TCSC in the competitive power market. Social welfare has been determined for with and without TCSC in the networks. The test results demonstrate the effectiveness of the proposed approach in terms of maximizing the social welfare with minimizing the TCSC investment cost and recovery of the TCSC investment cost.

The optimal operating costs in market environments depend on bids submitted by generating companies and on consumer benefit functions. Both may vary considerably in a daily/hourly basis. In this paper, submitted offers and bids have been considered only for the single interval (1 hour). It can also be extended for the multiple intervals (24 hours).

APPENDIX

TABLE V
OFFER COEFFICIENTS AND LIMITS FOR GENERATORS (39-BUS SYSTEM)

Bus No.	Offer Price Coefficients		Generation Limit $(P_g^p)^{max}$
	a_i	b_i	
30	0.01249	45	1040
31	0.04213	40	646
32	0	40	725
33	0.00807	35	652
34	0.01124	55	508
35	0.02667	20	687
36	0.06452	25	580
37	0.03448	55	564
38	0	20	865
39	0.08547	55	1100

TABLE VI
BIDDING COEFFICIENTS AND LIMITS FOR DEMANDS (39-BUS SYSTEM)

Bus No.	Bid Price Coefficients		Demand Limit $(P_d^p)^{max}$
	a_i	b_i	
3	0	41	644
4	-0.00889	49	1000
7	-0.00533	55	467.6
8	0	41	1044
9	-0.00533	55	13
15	-0.02794	44	640
16	-0.01865	41	658
20	-0.00533	61	1360
21	-0.00889	49	548
23	-0.00741	70	495
24	0	41	617.2
25	-0.00741	70	448
27	0	49	562
28	-0.00659	49	412
29	-0.00889	55	567

TABLE VII
OFFER COEFFICIENTS AND LIMITS FOR GENERATORS (NRPG SYSTEM)

Bus No.	Offer Price Coefficients		Generation Limit $(P_g^p)^{max}$	Bus No.	Offer Price Coefficients		Generation Limit $(P_g^p)^{max}$	Bus No.	Offer Price Coefficients		Generation Limit $(P_g^p)^{max}$	Bus No.	Offer Price Coefficients		Generation Limit $(P_g^p)^{max}$
	a_i	b_i													
1	0.01249	45	690	12	0.04167	20	600	23	0	35	750	34	0.03559	20	840
2	0.04213	40	120	13	0	40	1260	24	0.00807	40	450	35	0.02222	25	431
3	0	40	840	14	0.00807	40	440	25	0.04386	20	690	36	0.04114	20	695
4	0.00807	35	480	15	0.03559	20	440	26	0	35	640	37	0.033	55	419
5	0.01124	55	324	16	0	45	1360	27	0.05216	20	220	38	0	30	2649
6	0.02667	20	324	17	0.11905	20	390	28	0	20	450	39	0.03333	20	1050
7	0.06452	25	785	18	0.04608	20	1000	29	0.00833	25	440	40	0.01667	25	2000
8	0.03448	55	660	19	0.09709	25	350	30	0.02105	20	150	41	0.04114	25	2000
9	0	20	180	20	0.02688	25	550	31	0	45	500	42	0.01818	20	390
10	0.08547	55	330	21	0.04629	20	1075	32	0.02358	20	1630				
11	0.00518	45	396	22	0.00807	40	750	33	0.03676	25	850				

TABLE VIII

BIDDING COEFFICIENTS AND LIMITS FOR DEMANDS (NRPG SYSTEM)

Bus No.	Bid Price Coefficients		Demand Limit (Pd^P) ^{max}	Bus No.	Bid Price Coefficients		Demand Limit (Pd^P) ^{max}	Bus No.	Bid Price Coefficients		Demand Limit (Pd^P) ^{max}	Bus No.	Bid Price Coefficients		Demand Limit (Pd^P) ^{max}
	a_j	b_j													
43	-0.00533	100	43	99	0	35	65	142	-0.00889	80	72	186	-0.02794	125	43
44	-0.00889	80	56	100	-0.00889	80	124	143	-0.02794	125	136	187	-0.00659	90	220
45	-0.00741	65	63	101	0	35	65	144	0	35	166	188	0	35	153
46	0	20	71	105	-0.00533	100	71	145	-0.00533	100	201	189	-0.00533	100	29
47	-0.00659	90	145	106	-0.00659	90	46	146	-0.02794	125	92	190	0	20	408
48	0	35	96	108	-0.01865	85	124	148	0	35	91	191	-0.00741	65	124
49	-0.00741	65	36	109	-0.00889	80	141	149	-0.00741	65	128	192	0	45	86
52	0	20	49	110	-0.01865	85	58	150	0	45	120	193	-0.00533	100	153
55	-0.00533	100	44	111	0	20	64	151	-0.00533	100	68	194	-0.02794	125	269
57	-0.00533	100	143	112	-0.00533	100	121	152	0	38	97	195	0	45	198
60	0	35	111	113	-0.01865	85	110	153	0	45	75	197	-0.00741	65	181
64	-0.00889	80	50	114	-0.02794	125	69	156	-0.00659	90	270	198	-0.02794	125	186
65	-0.00741	65	13	115	-0.00889	80	60	157	0	45	84	199	0	35	329
66	0	35	149	116	0	35	112	158	-0.00533	100	175	200	-0.00533	100	49
67	-0.00889	80	428	117	-0.00659	90	131	159	-0.02794	125	80	201	-0.00533	100	212
76	-0.00533	100	73	118	-0.00533	100	183	160	0	45	254	202	-0.00889	80	238
77	0	35	181	119	-0.02794	125	53	161	-0.00741	65	97	203	-0.02794	125	139
78	-0.02794	125	30	120	-0.00889	80	60	162	-0.02794	125	210	204	0	20	89
79	-0.00533	100	140	121	-0.00889	80	232	163	0	35	124	205	-0.00741	65	365
82	-0.00889	80	281	123	-0.01865	85	166	164	-0.00533	100	89	206	-0.00533	100	39
83	-0.02794	125	300	124	-0.00533	100	36	165	-0.00533	100	51	207	-0.00659	90	128
84	-0.02794	125	467	125	0	38	71	166	0	35	139	208	0	35	115
85	0	35	264	127	-0.00741	65	48	168	0	20	230	218	-0.00533	100	160
87	-0.00533	100	141	128	-0.00741	65	35	169	-0.00741	65	119	220	-0.00889	80	95
88	-0.00533	100	410	130	0	45	35	170	-0.01865	85	134	223	-0.00741	65	78
89	-0.02794	125	39	132	0	38	256	171	-0.02794	125	138	224	0	20	36
90	-0.00533	100	254	133	-0.00533	100	221	172	-0.00889	80	95	225	-0.00659	90	70
91	-0.02794	125	178	134	-0.00889	80	75	173	-0.01865	85	49	227	0	35	75
92	0	35	65	135	0	38	89	174	-0.00659	90	170	228	-0.00741	65	92
93	-0.00889	80	142	136	-0.00659	90	324	176	-0.02794	125	138	235	0	20	8
94	-0.02794	125	54	137	0	20	333	177	-0.00533	100	60	242	-0.00533	100	28
95	0	20	65	138	-0.00533	100	71	181	-0.00533	100	72	245	-0.00533	100	201
96	-0.00741	65	166	139	0	20	124	182	-0.02794	125	115				
97	-0.00533	100	171	140	-0.00741	65	48	184	0	20	26				
98	-0.00659	90	114	141	0	35	86	185	-0.00889	80	80				

REFERENCES

[1] N. G. Hingorani and L. Gyugyi, *Understanding FACTS-Concepts and technology of FACTS systems*. New York: IEEE Press, 2000.

[2] N. G. Hingorani, "Flexible AC transmission," *IEEE Spectr.*, vol. 30, no. 4, pp. 40-45, Apr. 1993.

[3] Stephane Gerbex, Rachid Cherkaoui, and Alain J. Germond, "Optimal location of multi-type FACTS devices in a power system by means of genetic algorithms," *IEEE Trans. Power Syst.*, vol. 16, no. 3, pp. 537-544, Aug. 2001.

[4] Naresh Acharya, and Nadarajah Mithulananthan, "Influence of TCSC on congestion and spot price in electricity market with bilateral contract," *Elect. Power Syst. Res.*, vol. 77, pp. 1010-1018, 2007.

[5] S. N. Singh, and A. K. David, "Optimal location of FACTS devices for congestion management," *Elect. Power Syst. Res.*, vol. 58, no. 2, pp. 71-79, 2001.

[6] Y. Lu, and A. Abur, "Static security enhancement via optimal utilization of thyristor- controlled series capacitor," *IEEE Trans. Power Syst.*, vol. 17, no. 2, pp. 324-329, May 2002.

[7] N. Acharya, and N. Mithulananthan, "Locating series FACTS devices for congestion management in deregulated electricity market," *Elect. Power Syst. Res.*, vol. 77, no. 3-4, pp. 352-360, 2007.

[8] Rony Seto Wibowo, Naoto Yorino, Mehdi Eghbal, Yoshifumi Zoka, and Yutaka Sasaki, "FACTS devices allocation with control coordination considering congestion relief and voltage stability," *IEEE Trans. Power Syst.*, vol. 26, issue 1, pp. 2302-2310, 2011.

[9] Sung-Hwan Song, Jung-Uk Lim, and Seung-II Moon, "Installation and operation of FACTS devices for enhancing steady state security," *Elect. Power Syst. Res.*, vol. 70, no. 1, pp. 7-15, June 2004.

[10] Narayana Prasad Padhy, and M.A. Abdel moamen, "Power flow control and solutions with multiple and multi-type FACTS devices," *Electr. Power Syst. Res.*, vol. 74, no. 3, pp. 341-351, 2005.

[11] Yog Raj Sood, "Evolutionary programming based optimal power flow and its validation for deregulated power system analysis," *Int. J. Electr. Power & Energy Syst.*, vol. 29, pp. 65-75, 2007.

[12] M. Saravanan, S.M.R. Slochanal, P.Venkatesh, and J.P.S. Abraham, "Application of particle swarm optimization technique for optimal location of FACTS devices considering cost of installation and system loadability," *Elect. Power Syst. Res.*, vol. 77, pp. 276-283, 2007.

[13] T.A.A. Victoire, and A.E. Jeyakumr, "Unit commitment by tabu-search-based hybrid optimization technique," *IEE Proc.-Gener. Transm. Distrib.*, vol. 152, no. 4, pp. 563-574, July 2005.

[14] R. D. Zimmerman, C. E. Murillo-Sanchez, and D. Gan. MATPOWER: a matlab power system simulation package 2006 [Online]. Available: <http://pserc.cornell.edu/matpower>.

[15] T.T. Lie, and W. Deng, "Optimal flexible AC transmission systems (FACTS) devices allocation," *Int. J. Electr. Power & Energy Syst.*, vol. 19, issue 2, pp. 125-134, 1997.

[16] S. Meikandasivam, R.K. Nema, and S.K. Jain, "Selection of TCSC parameters: Capacitor and inductor," *2010 India International Conference on Power Electronics (IICPE)*, pp. 1-5, 2011.

[17] K. Habur, and D. O'Leary, "FACTS for cost effective and reliable transmission of electrical energy," [Online]. Available at: http://www.worldbank.org/html/fpd/em/transmission/facts_siemens.pdf.

[18] L. L. Lai, *Power system restructuring and deregulation*, New York: John Wiley and Sons Ltd., 2001.

- [19] Yog Raj Sood, N. P. Padhy, and H. O. Gupta, "Deregulated model and locational marginal pricing," *Elect. Power Syst. Res.*, vol. 77, pp. 574-582, 2007.
- [20] Northern Regional Load Dispatch Centre Website. [Online]. Available at: <http://www.nrlc.org>.



Prashant Kumar Tiwari received his B.Tech in Electrical Engineering with "Honours" from U.P.T.U. Lucknow, India and M. Tech from National Institute of Technology (NIT) Hamirpur (HP)-India. Presently he is pursuing Ph.D in the Department of Electrical Engineering, N. I. T. Hamirpur (H.P.), India. His research interests are in the area of FACTS, power sector deregulation, and renewable energy sources.



Yog Raj Sood received his B.E. in Electrical Engineering with "Honours" and M.E. in Power System from Punjab Engineering College Chandigarh (U.T.), in 1984 and 1987 respectively. He has obtained his Ph.D. from Indian Institute of Technology (IIT), Roorkee (India), in 2003. Presently he is working as Professor in the Department of Electrical Engineering, N. I. T. Hamirpur (H.P.), India. He has been honored with many awards, prizes, appreciation letters/certificates for his excellent research, academic and administrative responsibilities. He has published a number of research papers in reputed international journals including IEEE Transaction, Elsevier etc. His research interests are in the area of power sector deregulation, FACTS, power system optimization, high voltage engineering, and renewable energy sources.

Influence of environmental parameters on spatial distribution of pollen grains in Columbia Basin

Peter Šiška and Štefan Poláčik

Abstract – The natural environment is a complex open system consisting of geologic, atmospheric, hydrologic and biologic elements that are interconnected through energy and genetic information exchange; in addition, numerous internal and external relations within and between each subsystems are interwoven into the fabric of space. In order to understand and model the complexity of pollen dispersion and accumulation in Columbia Basin one hundred thirteen environmental parameters were included into factorial analysis, geostatistical interpolation was applied to one hundred twenty nine point locations and conclusions were drawn from statistical analysis. The results revealed existence of five most influential factors in the studied area. The regional typology was based on factor scores and resulted into delineation of generic regions in the study area.

Keywords – Environment, factor analysis, geostatistics, pollen grains.

I. INTRODUCTION

AIRBORNE pollen is a regionalized variable that indicates spatial auto correlation [1], [2]. Therefore in this paper, geostatistical methods (ordinary kriging estimators) were used to predict the pollen grain values in unsampled locations. The test area selected for this project was the Columbia Basin in the Pacific Northwest region of the United States. The reason for selecting this particular region was due to its bio-climatic characteristics that exhibit an arid region surrounded by mountainous complexes. A sample of 129 geo-referenced irregular point locations represents the geographic data in the Columbia Basin [3].

The spatial distribution of pollen grains on the ground is a result of complex natural forces that include factors related to climate, the biosphere, and geomorphology. In order to explain the patterns of pollen accumulation and distribution in the Columbia Basin, numerous parameters had to be taken into consideration, and appropriate methods used to capture these complex relationships.

The North American pollen database [3] contains data for over 5,000 locations. From this group, pollen quantities from forty-four plant species were selected. In addition, sixty-nine bio-climatic variables and elevation values were also provided for every sample location. From forty-four plant pollen types, a group of eight: *Pinus*, *Artemisia*, *Poaceae*, *Cheno-Ams* (a combination of *Chenopodiaceae/Amaranthus*), *Aster*, *Alnus*, *Ambrosia*, and *Picea* had sufficient quantities of distribution of pollen grains to satisfy the necessary normal distribution patterns; therefore, they were included for further analysis.

The rest of the pollen types from various plants produced insignificant amounts of pollen in the study area, so we grouped them into one residual pollen category: *Abies* and *Larix* represented the largest amount of residual pollen (27.3%). The sixty-nine bioclimatic variables were divided into two groups based on the criteria of data complexity. The first group included thirty-six variables in three subcategories: monthly temperature, monthly precipitation and monthly sunshine (thirty-six parameters altogether). The second group consisted of thirty-three more complex parameters including temperatures during growing days (0°C , 5°C), the Priestly-Taylor (alpha) parameter, and annual actual as well as potential evapotranspirations. (The full list of variables is found in the Appendix). Each category was scrutinized using factor analysis, and eleven bioclimatic variables were selected for the final complex factor analysis based on a variety of variable loadings.

These bioclimatic variables are as follows: the mean temperature in July (tjul), mean precipitation in February (pfeb), mean precipitation in July (pjul), minimum annual temperature (tmin), chill factor. In addition, there are the number of days when the pseudo-daily temperature was below 5°C , actual evapotranspiration (aaetp), total snow-water equivalent from the bucket model (totsnopt), January versus annual precipitation ratio (pjanpan), and July versus annual precipitation ratio (pjulpan). Finally, the mean sunshine value for March, April and May (smam), and the mean sunshine value for December, January and February (sdjf) are included. Elevation was also added to the set of eleven relevant bioclimatic variables and eight pollen variables totaling the final set of variables to twenty-one.

Mathematically, each variable X_i can be defined as a linear combination of a smaller number of hypothetical factors F_m i.e.

$$X_i = a_{i1}F_1 + a_{i2}F_2 + a_{i3}F_3 + \dots + a_{im}F_m + e_i \quad (1)$$

for $i = 1, 2, 3, \dots, k$ where “k” is the number of variables (21), m is the number of factors and e_i is the residual error variable. Note the correlations between X_i with F_i is 0. The correlation between factors (F_i) is also zero. The a_i s are the factors’ constants or loadings. The variance of X_i can be expressed as

$$\text{Var}(X_i) = \text{Var}(a_{i1}F_1 + a_{i2}F_2 + a_{i3}F_3 + \dots + a_{im}F_m + e_i) = \text{Var}(a_{i1}F_1) + \text{Var}(a_{i2}F_2) + \text{Var}(a_{i3}F_3) + \dots + \text{Var}(a_{im}F_m) + \text{Var}(e_i) \quad (2)$$

Because we use standardized variables then:

$$\text{Var}(X_i) = a_{i1}^2 + a_{i2}^2 + a_{i3}^2 + \dots + a_{im}^2 + \text{Var}(e_i) = 1 \quad (3)$$

As mentioned above, the constants a_{ij} are called factor weights or factor loadings and they take on values between -1 to 1. They can be interpreted as correlation coefficients between observed variables and factors similarly to linear

function. The matrix of factor loadings is called the factor matrix. The sum of squared factor loadings $a_{i1} + a_{i2} + a_{im}$ represents a part of X_i variance explained by all factors F_j . This sum is called the communality of the variable X_i . In another words, the communality is that part of the variable variance which is explained by all factors. The maximum value of communality is 1. The values near one indicate that the variance is well explained by the factor analysis method. The expression $Var(e_i)$ is the portion of the variance of a variable X_i that is not explained by factors and is called “uniqueness.” Hence the sum of uniqueness and communality equals one. In addition, we included only those factors into the final complex factor analysis with a standard deviation greater than one. The purpose of factor analysis is to extract a small number of factors that describe complex relationships. However, the natural processes and laws are extremely complex. An advantage is that by using the process of factor analysis, we can reduce the number of variables into a few factors (unobserved or latent variables). The “observed” variables are modeled as a linear combination of potential factors, plus the error terms. It is a technique used to estimate the common variance among original variables. In this project, we used varimax rotation (orthogonal rotation) that minimizes the number of variables into factors that indicate high loadings (relationships between variables X_i and all common factors F_i). The transformation of rotated factors F_i' from original factors F_i is given by linear combinations of new coefficients and original factors F_i :

$$F_i' = g_{i1}F_1 + g_{i2}F_2 + \dots + g_{im}F_m + e_i' \quad (4)$$

for $i = 1, 2, 3 \dots m$.

Factor scores (F_i') are determined for every point sample location, i.e. for 129 locations in the studied area. Those locations represent another spatial characteristic that help us to divide the study area into unique major regions that are specific to bioclimatic variation and pollen characteristics. The varimax rotation does not further reduce the number of original factors but rather changes the number of loadings. The small loading values are maximalized. Note: the transformed factor matrix F_i' contains a small number of loadings allowing an optimal interpretation of factors and computation of the factor score.

II. GEOSTATISTICAL METHODS AND POLLEN DATA

The pollen counts are regionalized variables; their spatial distribution in the upper soil layer is a function of distance from source areas. The first attempt to study spatial distributions of pollen distribution patterns using geostatistical methods was in [1]; kriging interpolation was used to study pine, oak, juniper and *Cheno-Am* pollen in Big Bend National Park. Later, the composite pollen was also mapped in the same area using three spatial algorithms; the corregionalization model achieved the smallest error variance [2]. The usage of geostatistical methods is justified due to the fact that the local pollen sources in close proximity exhibit similar properties, and the similarity between samples decreases with increasing distance. Interpolation methods such as ordinary kriging predict the values in an unsampled location with the smallest

mean square error of prediction [4]. Kriging is the best linear unbiased estimate in the form of:

$$\hat{z}(x_0) = \sum_{i=1}^n \lambda_{0i} z(x_i) \text{ where } \sum_{i=1}^n \lambda_{0i} = 1. \quad (5)$$

where $z(x_i)$, $i=1, 2, 3 \dots n$, are known pollen (sample) values and λ_{0i} are the kriging weights for location x_0 . Because kriging is an unbiased estimator, the sum of weights is equal to one. This is true for all the predictions of pollen values at locations x_0 . Practically, there are two correlation matrices [3] that drive the entire process of kriging. The first correlation matrix contains correlations (covariance values) between known (sample) data, the second vector matrix contains correlations (covariance values) between a point being estimated and surrounding sample data. This is possible due to a measure of spatial continuity called a variogram or semivariogram:

$$\gamma(h) = \frac{1}{2N(h)} \sum_{i=1}^{N(h)} [z(x_i) - z(x_i + h)]^2 \quad (6)$$

where $[z(x_i) - z(x_i + h)]$ is a spatial increment (h) of the attribute z (pollen grains count or percentages). Using this relationship, the correlation (variogram value) between the unknown sample and known data can be computed based on the distance between the point being estimated and the sample value. The relationship between the gamma value and covariance is then determined from: $\gamma(h) = Cov(0) - Cov(h)$. The kriging weights area are computed from the following matrices, as mentioned above:

$$\begin{bmatrix} Cov_{11} & Cov_{12} & Cov_{1n} & -1 \\ Cov_{21} & Cov_{22} & Cov_{2n} & -1 \\ Cov_{m1} & Cov_{m2} & Cov_{mn} & -1 \\ 1 & 1 & 1 & 0 \end{bmatrix} * \begin{bmatrix} \lambda_1 \\ \lambda_2 \\ \lambda_n \\ \mu \end{bmatrix} = \begin{bmatrix} Cov_{10} \\ Cov_{20} \\ Cov_{n0} \\ 1 \end{bmatrix} \quad (7)$$

The μ is the Lagrange parameter that is necessary for solving the system of linear equations. After the kriging weights are determined, they are substituted into the ordinary kriging estimator. Hence, the prediction of values in an unsampled location only require a knowledge of the variogram model and the distance between the sample as well as any location in the studied area.

III. DETERMINING FACTORS

The mapping of pollen distribution patterns permits the visualization of the pollen continuous surfaces across any region in North America. These maps reveal the existence of pollen patterns on the ground that would otherwise be invisible to the naked eye. Once the pollen distribution patterns are known, we can expect similar quantities of pollen to enter the human breathing system or ecosystems as well as being trapped on clothing, shoes, or on any used material objects. Additional examples where pollen is found are motor vehicles (air filters), cell phones, or laptop computers. Examples of pollen distribution patterns that were created using kriging are portrayed in figures 1 and 3. The comparison of spatial distributions of pine and *Cheno-Ams* pollen reveals the existence of opposite spatial patterns. The pine pollen distribution tends to be eccentric while the cheno-ams pollen

is concentric. The reason for the existence of both patterns lies, to a large extent but not entirely, to the distribution pattern of the plant source material.

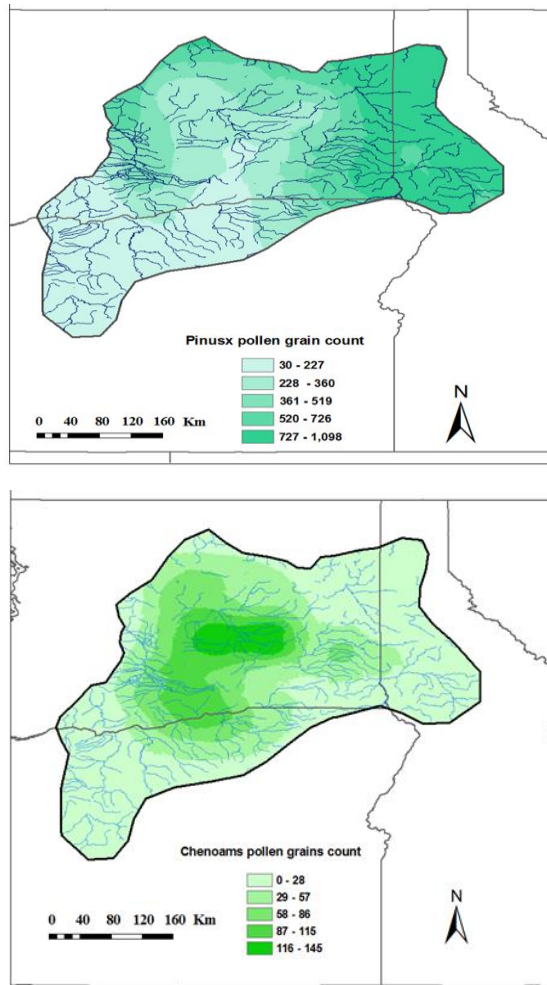


Fig. 1 Spatial distribution of pine pollen (top) and *Cheno-Ams* (bottom).

Therefore, the mapping of landuse and landcover using satellite imagery is also an essential part of this process. Figure 2, indicates that evergreen forests grow on the rim of the Columbia Basin while shrubs and grasses tend to occupy the interior part of the basin, even though they are not exactly in the central part. Therefore, one of the goals is to establish a more nearly accurate relationship between dispersed pollen on the ground and the plant sources. This would allow for the prediction of pollen distributional patterns without having to collect and analyze control samples of pollen data collected from ground locations. It is also worth noticing that minimum amounts of pine pollen are located in the western part of the Columbia Basin despite there still being a significant strip of pine source plants. In addition, the large accumulation of *Cheno-Ams* pollen in the central section does not directly follow the distribution of plant source material, but rather follows the surface geomorphology that was created by local hydrological features during the late Pleistocene. An interesting result is seen when we compare the next two maps (Fig. 3). The pollen distribution of *Alnus glutinosa* (broadleaf

alder) and *Poaceae* (grass pollen) repeats the same pattern as seen in Figure 1. Similarly to the previous distribution, the “forest” pollen type forms an eccentric pattern while grass pollen (on the right) appears in a concentric pattern. The large amounts of *Alnus* pollen in the western area does not directly correspond to the plant source distribution as seen in the case of pine pollen.

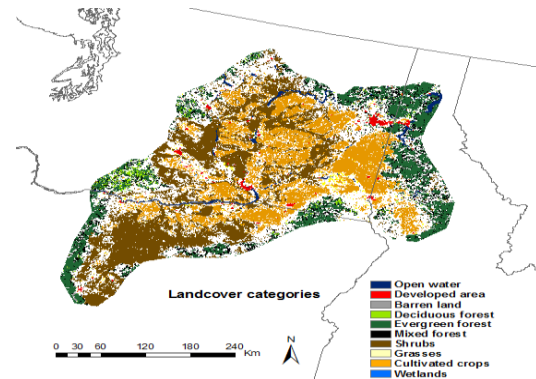


Fig. 2 distribution of pollen sources

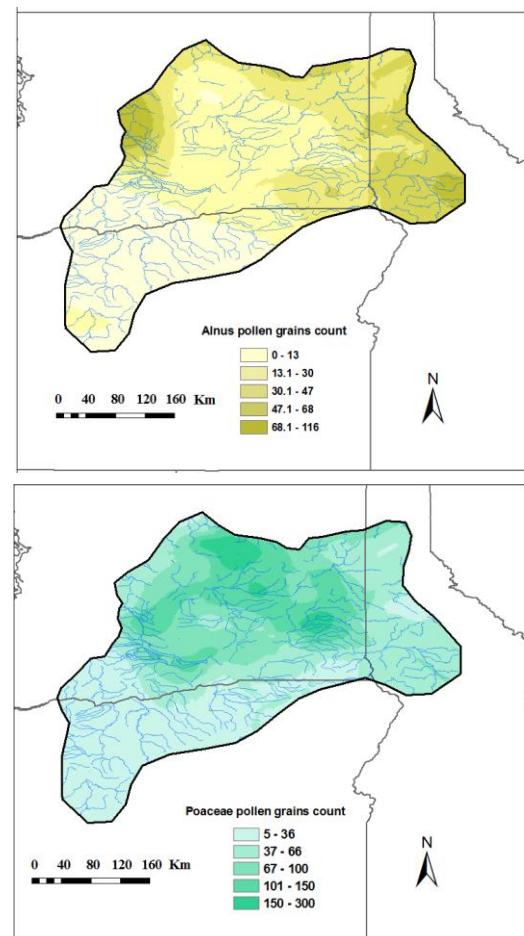


Fig. 3 distribution of *Alnus* pollen (top) and grass (bottom)

The matching pollen spatial distribution patterns with source plants is a complex process, and additional information is needed to develop a better understanding of factors that control the distribution of pollen on the ground. The factor

Variable		F1	F2	F3	F4	F5	Communality h^2
VAR8	pjanpann		0.353	-0.338	-0.678		0.816
VAR5	chill	0.437		-0.502	0.633		0.905
VAR9	pjulpann				0.884		0.836
VAR10	smam		0.937				0.904
VAR11	sdjf	0.350	0.823				0.916
VAR4	tmin	-0.341	-0.692	0.308	-0.454		0.896
VAR1	tjul	-0.507	-0.435	0.489	-0.460		0.911
VAR3	pjul	0.739	0.394		0.460		0.951
VAR6	aaetpt	0.812	0.407				0.840
VAR7	totsnopt	0.844		-0.322			0.901
VAR2	pfeb	0.889					0.889
VAR12	ELEVATION	0.452	0.376	-0.439	0.625		0.931
VAR13	PINUSX	0.796					0.659
VAR21	OSTPEL+	0.500		-0.383			0.410
VAR14	ARTEMISIA	-0.581	-0.465				0.658
VAR16	CHENOAMX	-0.418	-0.410	0.489			0.621
VAR15	POACEAE		-0.347	0.649			0.609
VAR17	ASTERX			0.694			0.553
VAR19	AMBROSIA			0.746			0.701
VAR18	ALNUSX	0.310				-0.589	0.550
VAR20	PICEAX					0.801	0.719
Variance		5.323	3.563	3.230	2.877	1.184	16.177

Table 1. Factor loadings and variables

analysis (FA) took into account bioclimatic features, pollen, and elevation data for each of the 129 geographic locations in Columbia Basin. From the analysis of forty-four pollen data, sixty- nine bioclimatic variables, and elevation, a group of twenty-one variables was selected using the principal component analysis. The final analyses of twenty-one variables were reduced into five major factors deemed the most influential for the current distribution of pollen in Columbia Basin. These variables created five main factors that

represent the most influential underlying forces controlling spatial distribution of pollen. Overall, these five factors were able to describe 77% of the variation in the data. Table 1 shows the results of factor analysis after varimax rotation. The shaded cells indicate the highest significance of variables in a factor (factor loadings). Communality (the proportion of the variation in a particular variable explained by all five factors) indicate that bioclimatic variables fit better to the model. The average communality value for bioclimatic variables is 0.88 while the corresponding parameter for pollen variables is

significantly lower at 0.61. Hence, there is more spatial continuity in bioclimatic variables than in pollen variables. The results from the factor analysis indicate that the first factor is the most influential and explains 25.35% of the variance in these data. This factor strongly ties together bioclimatic variables that are associated with a cooler environment, such as precipitation in February, total snow cover, pine pollen amounts, elevation, actual evapotranspiration in one group (positive loadings values) along with average temperatures in July, *Cheno-Ams* pollen, *Artemisia* pollen (negative loadings) – characteristics of a warmer environment. Therefore the underlying factor that ties all variables together and controls the pollen distribution is geomorphology; the basin consists of a cooler, moist rim area and a warmer, drier interior.

The second factor is clearly represented by the length of sunlight that appears to be a dominating factor controlling the environment and pollen distribution. The variable, the mean length of sunshine in the months of March, April, May and the mean length of sunshine for December, January and February indicate the highest factor loadings values. As can be seen from the data in Table 1, the second factor explains almost 17 % of the variations in the data.

The third factor combines grass pollen, *Cheno-Ams*, *Ambrosia*, and *Aster* pollen which survive in drier climates with a total snow cover, chill factor, and precipitation in January. Therefore, the third factor underlines the significance of *Ambrosia* and *Aster* pollen production and moisture. Its power of explanation is on the same level as the previous one. All three factors explain more than half of the variation in the data (almost 60%). Hence, the last two factors have a much smaller meaning.

The fourth factor combines the elevation with climatic variables; it emphasizes the role of precipitation in the summer especially in July. The high negative value of precipitation in January confirms that summer precipitation is the main factor causing distribution of pollen in the Columbia Basin. The significance of elevation is also notable; it makes sense to combine elevation parameter with precipitation in July. During this period orographic uplift of air mass from Pacific Ocean cause increase in precipitation.

The fifth factor points out the significance of local conditions. It is not associated with production of *Picea* pollen and to some extent also pollen from *Alnus*. There is no correlation with other pollen or climatic variables. Therefore, this factor represents mountainous influence exacerbated with pollen production from *Picea*.

IV. REGIONALIZATION

The next step in this research is determine types of regions that are quasi homogeneous with respect to environmental conditions. It consists of the computation of factors scores and the grouping of 129 geographic locations into regions that exhibit similar characteristics based on factor scores. Table 2 contains the average factor scores. Factor scores were computed for each variable and then grouped based on similarity. Factor scores are the linear combination of factor weights (loadings) and variables. After obtaining the factor score, geographic regionalization was developed based on

cluster analysis and Ward's Method [5] and [6]. This process creates the categorization of geographic locations (129) into optimal number of regions that indicate similar properties, and it maximizes the differences between regional types. As Table 2 indicates, the first regional type is represented by high average factor scores, especially factors 1, 2 and 3 (FS1, FS2, FS3) play significant roles.

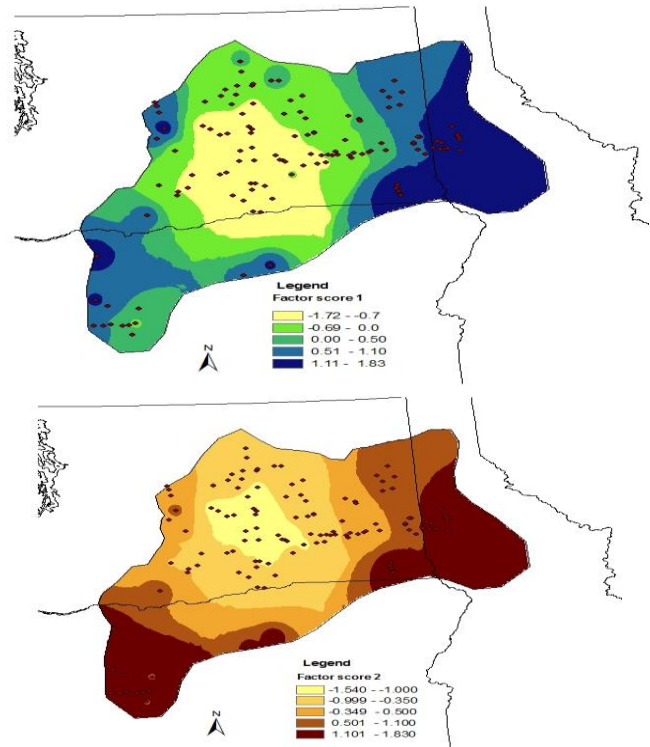


Fig. 4 region type 1 (top) and region type 2 (bottom)

Because factor 4, has no pollen variables, it is excluded from the regionalization process. Region type 1 comprises 38 geographic location in the Columbia Basin; the most influential is FS2 whose factor scores range from 0.78 to 1.83 (mean value 1.289). As mentioned previously, it consists of variables that measure the length of incoming solar radiation during the months of March, April, and May as well as December, January, and February. Factor scores FS3 indicate the same mean values; however, the values have a negative sign. This factor is mostly represented by variables such as chill, elevation, and pollen grains from rare plant sources or the least productive plants in the region. The mean factor score (FS1) is above 1.0; it is computed by averaging the individual factor scores of bioclimatic variables such as the precipitation in July (pjul), total snow cover (totsnopt), precipitation in February (pfeb), actual evapotranspiration (aetpt), pine pollen and elevation. The synthesis of all these scores, variables, and factors leads to the conclusion that this first type of region indicates mountainous characteristics. When we compare the spatial distribution of the first and the

second factor scores, we observe similarities, i.e. the negative factor scores exist in the central part of the basin, and their values increase symmetrically towards the basin rim. However, spatial pattern in both cases is diametrically different. The factor scores in region 2 are predominantly generated by grass pollen, *Artemisia*, *Cheno-Ams* - all herbs and shrubs that can survive in dry conditions. This significant role also indicates July temperatures and the minimum annual temperature. The average factor scores of this regional type are lower.

Reg. type	Average factor scores				%
	FS1	FS2	FS3	FS5	
5	0.690	0.451	-0.439	-1.861	9.30
1	1.104	1.289	-1.284	-0.236	29.46
3	0.045	-0.179	0.153	0.267	19.38
2	-0.890	-0.837	0.869	-0.302	21.71
4	-1.041	-1.015	0.995	1.257	20.16

Tab. 2 regional types and factor scores

Region type 3 comprises 25 geographic sample locations which represents 19.38% of the total (129). As can be seen from Table 2, all factor scores are significantly lower in comparison to the previous region types. Therefore, this region indicates less dependency on external conditions such as bioclimatic variables or geomorphology. Figure 5 exhibits the spatial distribution of factor scores in region types 4 and 5. Both regions are very different in their structural content.

Region type 4 shows low values of factors 1 and 2 with a high (1.257) of factor five. Overall, all factors play significant roles in this region while in region type 5, there are extreme differences in factor scores; FS5 indicates the most extreme value from all factor scores (-1.861). The most influential variable is *Picea* pollen, and this region is cooler and wetter. The second dominant is *Alnus* pollen; the parameter has a negative sign, which confirms the existence of cooler and wetter condition. This regional type comprises 12 geographic location (9.3%). The spatial distribution of factor scores between both regions is significantly different. Region 4 preserves a typical concentric pattern while region type 5 indicates a more irregular pattern.

I. CONCLUSION

The spatial patterns of pollen distribution and accumulation on the ground depict the environmental processes that control airborne pollen transport and deposition. In addition, this research contributes to developing numerous applications for studying biodiversity, the occurrence of allergies, and forensics. Geostatistical methods are suitable for predicting

pollen in unsampled locations. The amount of pollen grains from each individual plant must be predicted in every place with high accuracy; it results in obtaining distribution patterns.

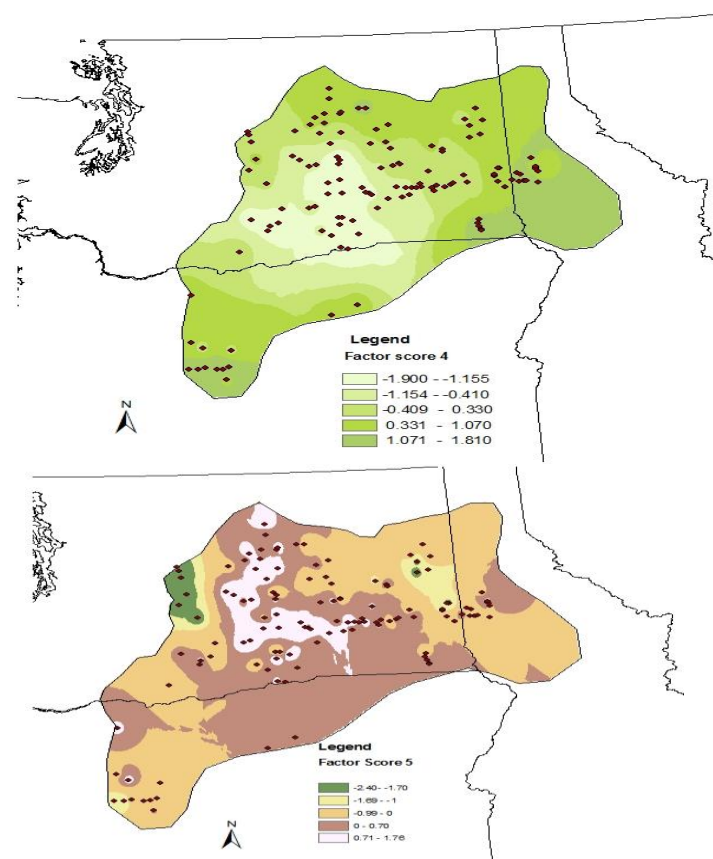


Fig. 5 region type 4 (top) and 5 (bottom)

The spatial patterns of pollen distribution and accumulation on the ground depict the environmental processes that control airborne pollen transport and deposition. In addition, this research contributes to developing numerous application models for studying biodiversity, the occurrence of allergies, and forensics. The amount of pollen grains from each individual plant must be predicted in every place with high accuracy.

Factor analysis is a complex method that contributed to this research in the understanding of the natural environment as well as the factors that control the distribution of pollen in the Columbia Basin, an area representing a diverse geomorphic region with a dry climate. Perhaps the most important step in the future would be to develop an effective model that correlates the spatial distribution of pollen quantities to its source plants so that no sampling in the terrain would be necessary. Delineating the study area into four complex regions is another significant contribution of this project. To our knowledge, there is no current study in scientific literature that has developed geographic regions using complex environmental criteria that brings together bioclimatic and geomorphic environmental characteristics with pollen distribution patterns. The existence of four factor scores demonstrates the significant variability in the Columbia Basin and its complexity in terms of relationship between quantities of pollen grains and environment of the studied area

APPENDIX

Complete list of variables

PINUSX (Pinus - Pine /nigra, sylvestris);
 ARTEMISIA (Artemisia - Sagebrush, Wormwood);
 POACEAE (Poaceae - Grass /angustifolia, annua, pratensis);
 CHENOAMX (Chenopodiaceae/Amaranthaceae - Goosefoot/Pigweed Families);
 ASTERX (Asteraceae - Daisy tribe);
 ALNUSX (Alnus - Alder);
 AMBROSIA (Ambrosia - Ragweed);
 PICEAX (Picea – Spruce);
 RESID (represents the rest of the pollen data that contain smaller counts of pollen grains. The most important pollen is ABIES (Abies – Fir) representing 27.31% of pollen grains in this category, LARIXPSEU (Larix/Pseudotsuga - Larch/Douglas Fir) 16,44%, CYPERACE (Cyperaceae – Sedge) 15,89%, CUPRESSA (Cupressaceae - Cedar Family) 14,95%, TSUGAX (Tsuga - Hemlock unifferentiated) 7,64%, BETULA (Betula – Birch) 4,40%, PINDIPL0 (Pinus diploxylon - Hard Pines, 4,21%.
 The twenty nine plant sources of pollen indicating smaller amount of grains (less than 80) were excluded from further analysis.
 The data were transformed to conform normal distribution requirement.

3.2. Climate and bioclimate variable.

The thirty six variables were tested using factor analysis:

t [jan]...[dec] - mean monthly temperature in °C in month [January]...[December];

p [jan]...[dec] mean monthly precipitation in mm;

s [jan]...[dec] mean monthly percent possible sunshine (no clouds);

The factor analysis indicated that tjul, pfeb, pjul were relevant.

The second set of variables was represented by thirty three more complex variables:

tave - average annual temperature;

tmax - maximum temperature;

tmin – minimum temperature;

gdd0 - growing-degree days, 0 °C base;

gdd5 - growing-degree days, 5 °C base;

chill - chilling requirement (number of days when pseudo-daily temperature was below 5°C);

mtco - mean temperature of the coldest month of the year (not the absolute minimum temperature);

mtwa - mean temperature of the warmest month of the year (not the absolute maximum temperature);

mipt - Priestley-Taylor (alpha) parameter (AE/PE);

aaetpt - actual evapotranspiration (AE);

apetpt - potential evapotranspiration (PE);

miptev - alpha calculated for the evergreen pft assimilation period (days when the pseudo-daily temperature > -4 °C);

aaetptev - AE calculated for the evergreen pft assimilation period;

apetptev - PE calculated for the evergreen pft assimilation period;

miptdc - Annual Priestley-Taylor moisture index (alpha) for deciduous assimilation period (when pseudo-daily

temperatures are greater than 5°C and are calculated using Cramer & Prentice approach);

aaetptdc - Annual actual evapotranspiration for deciduous assimilation period (when pseudo-daily temperatures are greater than 5 °C and calculated using Cramer & Prentice approach);

apetptdc - Annual potential evapotranspiration for deciduous assimilation period (when pseudo-daily temperatures are greater than 5 °C and calculated using Cramer & Prentice approach);

totsnopt - total snow-water equivalent from bucket model (computed);

annp - total annual precipitation;

pjanpann – ratio January/Annual precipitation ratio;

pjulpann - July/Annual precipitation ratio;

tmam - Mean temperature for March, April, May;

tjja - Mean temperature for June, July, August;

tson - Mean temperature for September, October, November;

tdjf - Mean temperature for December, January, February;

pmam - Mean precipitation for March, April, May;

pjja - Mean precipitation for June, July, August;

pson - Mean precipitation for September, October, November;

pdjf - Mean precipitation for December, January, February;

smam - Mean sunshine for March, April, May;

sjja - Mean sunshine for June, July, August;

sson - Mean sunshine for September, October, November;

sdjf - Mean sunshine for December, January, February.

REFERENCES

- [1] P. P. Siska, V.M. Bryant, and J. J. Jones, The Spatial Analysis of Modern Pollen Rain in Big Bend National Park. *Palynology*, vol. 25, pp. 199-216, Feb. 2001.
- [2] P.P. Siska, I. K. Hung, and V. M. Bryant, The Mapping of Composite Pollen From Point Data and Cartographic Generalization. *Papers of the Applied Geography Conferences*, vol. 35, Oct. 2012, pp. 191-200.
- [3] Whitmore, J., Gajewski, K., Sawada, M., Williams, J. W., Shuman, B., Bartlein, P. J., Minckley, T., Viau, A. E., Webb III, T., Shafer, S., Anderson, P., Brukaker, L. (2007). Modern pollen data from North American and Greenland for multi-scale paleoenvironmental applications. *Quaternary Science Reviews*, vol. 24, pp. 1828-1848, Jul. 2007.
- [4] P. Goovaerts, *Geostatistics for Natural Resources Evaluation*. Oxford University Press, 1998, ch, 7.
- [5] R. A. Johnson, and D.W. Wichern, *Applied Multivariate Statistical Analysis*. Kindle Direct Publishing, 2001, ch, 10.
- [6] J. H. Ward, Hierarchical grouping to optimize and objective function. *Journal The American Statistical Association*, vol. 58, pp. 236 – 244, Mar. 1963.

Android Application Front-end for an Energy Brokerage Agent

Christos Petsos, Kostas Kalogirou, and Evangelos Bekiaris

Abstract—This paper outlines the development process of an energy management model, the Brokerage Agent Front-End application (BAF) for Android smart phone devices. This application is addressed to end users who consume and produce energy from any type of source such as photovoltaic panels and wind turbines. The application is a front-end illustration of data from smart meters that enables the user to achieve a more efficient energy management. Moreover, this paper analyses the technical issues that were considered in order to reuse the code created for the Brokerage Agent Front-End web application [12] and the additional implementation activities needed for the native Android application.

Keywords— Android native application, energy management system, solar energy, interactive charts.

I. INTRODUCTION

THE initial approach was to investigate whether the code from the BAF web application [12] could be used also for the Android version. Although Android technology fully supports RESTful web services and Google protocol buffers, additional classes had to be written in order to be fully functional. Then, the user interface requirements had to be considered during the design process. The limited screen size of the Android smart phone mandated the rendering of graphical charts in a landscape format rather than portrait. The following paragraphs analyze the research that took place in order to investigate the technical requirements, presenting the functionalities provided by the BAF Android native application to the standard prosumer user (is defined from words producer and consumer).

II. TECHNICAL REQUIREMENTS

The paradigm of smartphone applications, like that of the BAF for Android, poses a number of additional challenges to

This work was realized during the European research FP7 funded project NOBEL and the submission of this paper is supported by the Hellenic Institute of Transport of Centre for Research and Technology Hellas (H.I.T./C.E.R.T.H.)

K. Kalogirou, software engineer with MSc at Digital Signal Processing, H.I.T./C.E.R.T.H., Thessaloniki, 57001, Macedonia, Greece, phone: 0030-2310498461; e-mail: kalogir@certh.gr.

C. Petsos, MSc Software Engineering, H.I.T./C.E.R.T.H., Thessaloniki, 57001, Macedonia, Greece, phone: 0030-2310498431; e-mail: cpetsos@certh.gr.

E. Bekiaris, Dr. Mechanical Engineer, Research Director in H.I.T./C.E.R.T.H., Thessaloniki, 57001, Macedonia, Greece, phone: 0030-211069551; e-mail: abek@certh.gr.

the ones of the initial web-based application. The first thing that had to be evaluated was whether the web-based application was fully functional in the smartphones' browsers. The Android application had to be able to serialize/deserialize Google Protocol Buffer (GPB) messages and send/receive them through a secure RESTful communication channel. Additionally, time-based energy data should support the end-user's timezone as selected in the Android device. The Android devices used for evaluation were HTC Sensation Z710e, Samsung Galaxy S3 and Sony Ericsson XPERIA X10 mini E10i.

A. JSF 2.0 application compatibility

After the research that took place during the design of the BAF web-based application, the JSF 2.0 implementation selected was the open-source Mojarra 2.0.3 provided by Oracle [2]. In addition, the PrimeFaces 3.0.M1 for JSF was used as component suite library [3] for the composite UI elements. The application server used to deploy the web application was Apache Tomcat 6.0. Finally, the chart component used to visualize the smart meter's historical data was Flot 0.7 [1] which is an HTML 5 component controlled with JavaScript through JQuery.

The optimum scenario would be that the web application could run as it is on the smartphones' web browsers. Unfortunately, this was not succeeded. During the evaluation on HTC Sensation Z710e and Samsung Galaxy S3 certain HTML rendering errors occurred along with the inability to select time slot in the Marketplace's chart. Android applications introduce new semantics in human-machine interaction [6] and those were not taken under consideration during the implementation of the web based application. For instance, in the web-based application selecting a time period in the chart's graph was simply a "mouse-down, drag, mouse-up" sequence. However, in smartphones' web browsers this procedure corresponds to the panning of the browser window, so an essential piece of functionality was not available in the smartphones. In the case of Sony Ericsson XPERIA X10 mini E10i the situation was even worse since the browser was complaining with parsing errors and could not launch the application at all.

Following the feedback acquired from the evaluation of the web-based application in these devices, it has been decided that a native Android application should be implemented for the smartphone version of the BAF application.

B. Reuse of existing code

Having to re-implement the whole application for the Android platform was initially a large frustration. However, a rather pleasant surprise came up very early in the design phase of the Android application. It seems that the use of JSF, and inherently the Java platform, bridged a large percentage of the gap between the web-based and the native Android application, since Android development means Java development. The design of the initial web-based application was as follows: the JSF front-end was communicating with the JSF back-end using the specific JSF semantics and the JSF back-end was consuming a secure RESTful web service that provided user authentication and energy data using a Java client, specifically the Jersey open source JAX-RS (JSR 311) reference implementation [7]. GPB messages were transmitted over this communication channel. So, for the Android version of the application, the only thing that needed to be replaced was the JSF front/back-end with that of the native Android application front-end, including Intents, Layouts, Dialogs and graphical components. The whole design stack and the reusable elements are presented in the following figure.

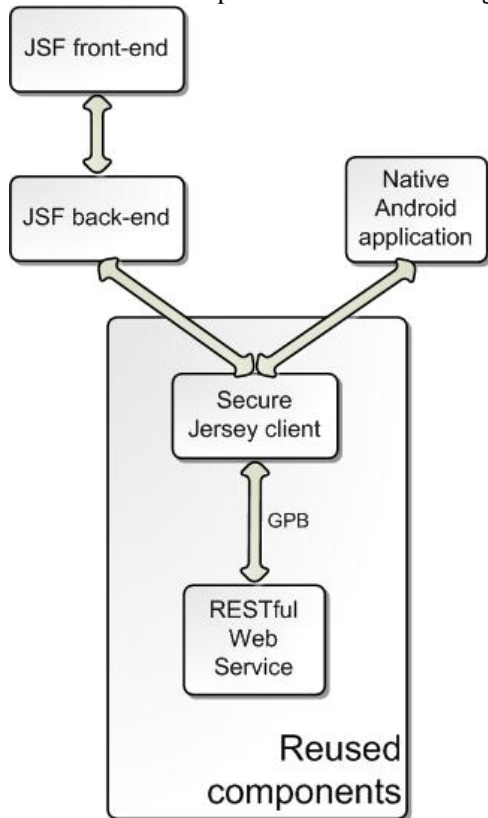


Fig. 1 BAF application design stack and reused components

C. Reusable components integration

Re-using the parts of code that used the Jersey client to consume the RESTful web services was a big advantage in the design and implementation of the Android BAF application. However even following this path obstacles were faced. During the first tests with the Jersey client, a number of

“NullPointerException” errors occurred during run-time. Jersey client was designed for desktop and server applications, so an official Android port did not yet exist. Jersey has to read a file located at “META-INF/services/” location in order to operate correctly. However, the Android platform compiles all application files to Dalvik Virtual Machine specific bytecode and there is no way to reference internal application files by location. Implementing a Jersey client version for Android was out of scope for the NOBEL European funded research project [5]. Hopefully, a less time-consuming solution could be employed by providing a custom ServiceIteratorProvider instance to the client’s ServiceFinder [8].

Serialization and deserialization of GPB messages operated with no additional effort for the Android application. Additionally, timezone support mechanisms incorporated in the web-based application were also used intact by feeding them the timezone that the user has selected in the Android platform.

III. USER INTERFACE REQUIREMENTS

Apart from the technical challenges that are introduced when porting a web-based application to a smartphone platform, another important point arises; that of user interface design and interaction paradigm shift.

A. Smartphone device use case

The first notable difference when comparing an application targeting desktop machines and one that is designed for smartphones is that of the screen size difference. Small screens on smartphones enforce a total redesign of the Human Machine Interaction (HMI) protocol. This was very easily observed when evaluating the web-based application on the HTC Sensation Z710e device and Samsung S3. Both smartphones have a rather large screen for a handheld device, 4.3 inches. Even in that size, interacting with the web application using the touch screen was rather cumbersome. Text size was too small and interaction cues, such as buttons and drop-down menus, were difficult to be clicked. When the user zoomed in order to easily read text and press buttons, he/she had to constantly pan to all directions to follow the application flow. It looks like a web application designed for desktop screens, without any provision for small-screen devices, is impossible to be used in a smartphone. Considering that, it can be argued that the only components that could be reused in the Android application were the ones that were actually reused. The JSF front-end should have been redesigned for small-screen devices and the back-end should have to be altered.

Another important thing in Android applications is that of the orientation support. Most smartphones’ screen aspect ratio demands for different components layout in portrait and landscape view. Orientation support has been implemented in the BAF Android application by using the built-in mechanisms provided by the Android SDK.

Limitations in screen’s real estate enforce a new way of thinking the user input too. Navigation and action cues are

replaced by means of haptic input [9, 10]. Since there is not much screen to place many buttons, links, sliders etc, user input is captured in gestures and special screen touches. In the BAF application for Android a back gesture has been implemented for navigating to the previous screen, apart from using the home button. In addition, long clicks, dragging and sliding have been used for interacting with the graph charts. These means of user input may puzzle someone used to traditional desktop applications at first. In a small period though they become intuitive and in some cases more user-friendly than the traditional ones.

B. Android Charting tool

The specifications of the BAF application contain the ability to draw several types of graphs in order to present information to the user about energy values, orders etc. These requirements are not less than those of the web-application. The charting tools evaluated were the following:

- 1) Google Chart Tools
- 2) AchartEngine
- 3) ChartDroid
- 4) AndroidPlot
- 5) aiCharts
- 6) GraphView
- 7) RChart
- 8) TeeChart

None of the evaluated tools supported interactive charts. An essential element that needed to be supported was that of selecting time periods in the Marketplace. Such a feature was not available in any of the tools. Finally, considering the BAF application requirements and based on a cost/value basis, the RChart library for Android [11] has been selected. This library supported most of the functionality that the BAF application needs for displaying charts. It had some infrastructure available for selecting time-periods but did not support panning and zooming. Hopefully, the source code of this tool was open, so it has been extended rather easily in order to support pan/zoom and selecting time periods.

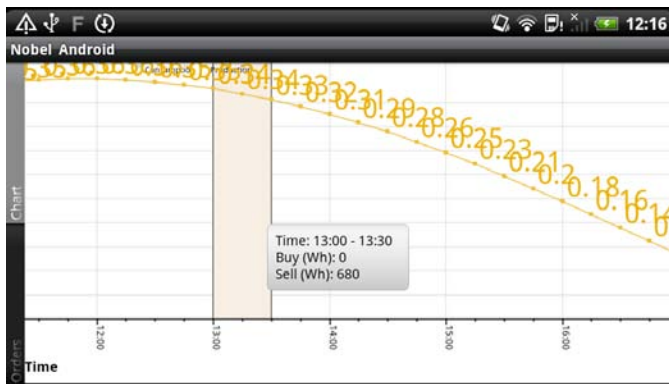


Fig. 1 pan/zoom and selected time period

IV. SUPPORTED FUNCTIONALITY

The current version of the BAF application for Android supports the following pieces of functionality:

- 1) Monitoring of historical and statistical data about consumption/production.
- 2) Prediction of future consumption/production of a single smart meter.
- 3) User profile and device profile management.
- 4) Marketplace where the user can sell or buy excess of energy.
- 5) User authentication/authorization.
- 6) Internationalization.
- 7) User input validation.

Initially, the user is presented with the login screen.

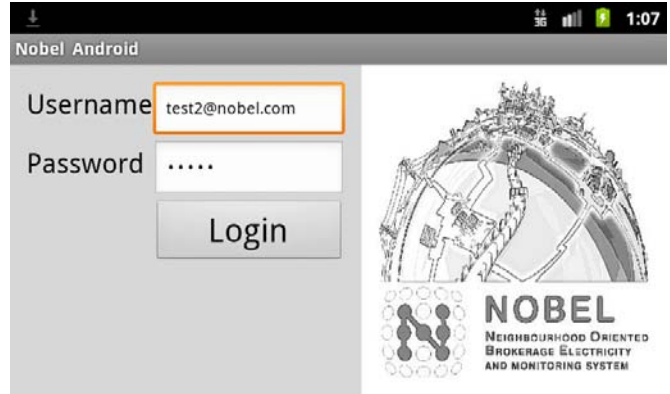


Fig. 2 login screen

Upon successful login the main application menu is loaded.



Fig. 3 main menu

Here the user can select the various operations provided by the BAF application. Clicking the “Monitoring” button leads to the screen where user selects device and time period to monitor.



Fig. 4 monitoring options

Selecting “Monitor” presents the chart graph with the energy production and consumption data fetched over the RESTful Web Service.

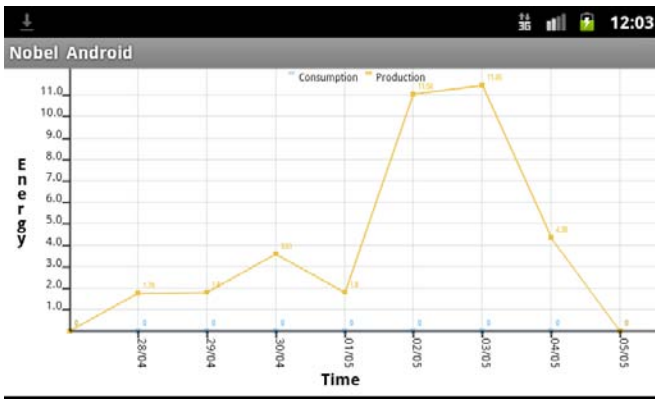


Fig. 5 Monitoring data for last week

Monitoring is allowed only for past dates since it fetches historical data from real devices. On the other hand, the prediction service is only allowed for future dates since it provides an estimation of the energy consumption and production for a specific date in the future.

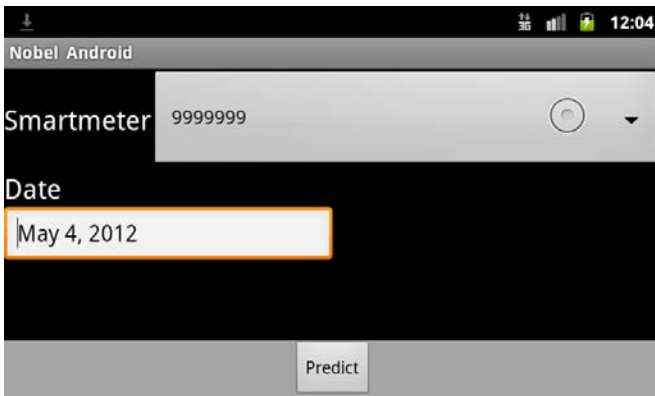


Fig. 6 prediction options

After specifying device and date, clicking “Predict” fetches prediction data and draws the prediction graph for the selected date.

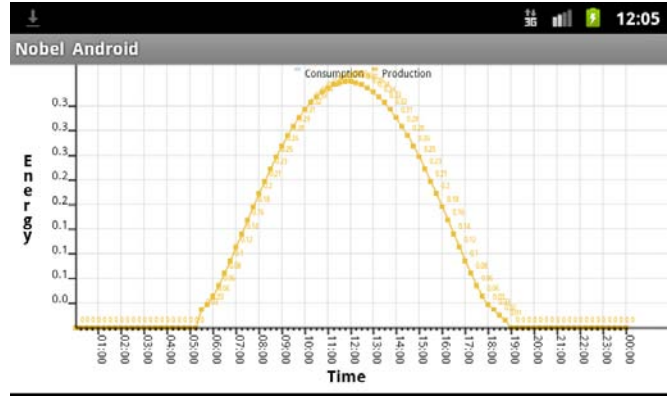


Fig. 7 prediction graph

In the Marketplace scenario the application flow starts exactly as the Prediction service; user fetches prediction data for a future date. However, it continues providing two additional steps of interaction. The user can select a time period and view the amount of energy that he/she can buy/sell. For instance, in the following figure the user has selected time from 12:00 to 14:00 and can observe that he/she has an excess of 2744 Wh of energy which he/she can sell.

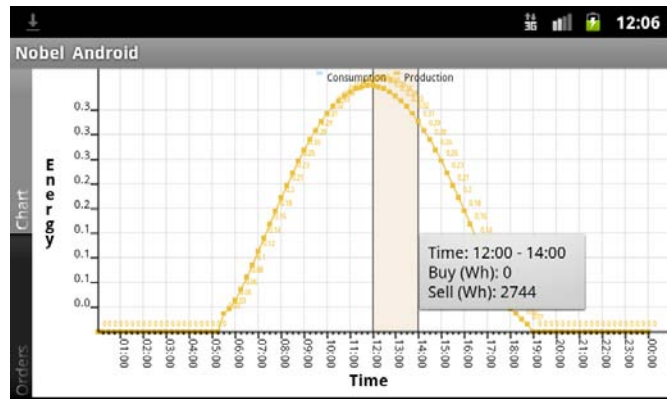


Fig. 8 marketplace time period selection

By clicking the “Buy/Sell” button the user is presented with a set of options that he/she can set in order to complete his/her order.

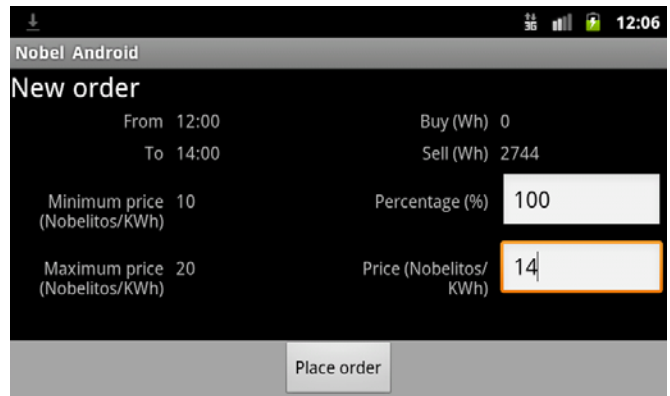


Fig. 9 marketplace order options

Specifically, the user can select the percentage of energy that he/she wishes to buy/sell and the price to which he/she will place the bid in the marketplace. By clicking “Place Order” the user is prompted to confirm his/her order prior to communicating with the RESTful web service.

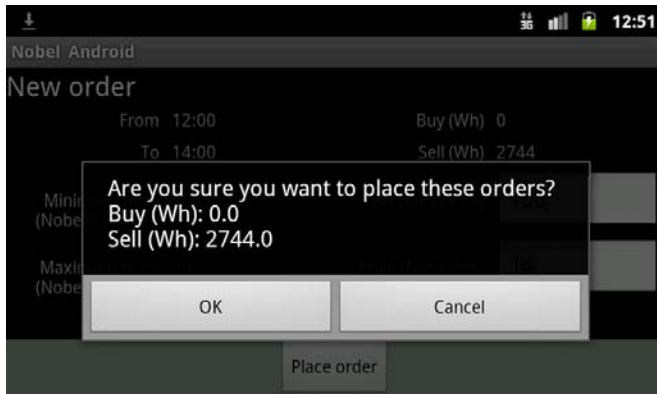


Fig. 10 order confirmation

In the “Management” screen the user is able to view his/her user and device profile.



Fig. 11 customer profile

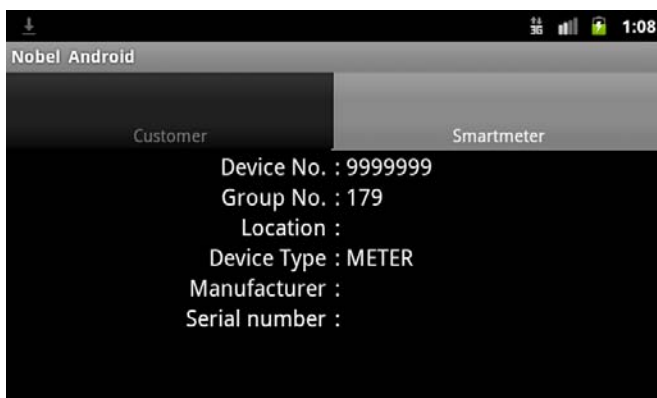


Fig. 12 smart meter profile

Another feature that has been implemented is the support of multiple languages. The following languages are supported:

- 1) English
- 2) Spanish
- 3) Spanish (Valencian)

- 4) Greek
- 5) German
- 6) Swedish

Below, the login screen of the application in the Spanish language is illustrated.



Fig 13 login screen in Spanish language

Finally, the built-in mechanisms of the Android platform were used for validating user input.

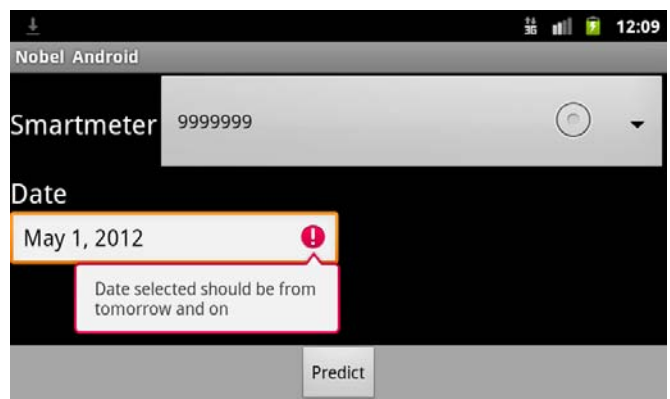


Fig. 14 user input validation

V. FUTURE WORK

An important issue that arose during the design and implementation of the BAF application for Android platform was how a web-application design can target to smartphone devices. The combination of JSF design for desktop application and native Android application may be challenging under the umbrella of Java, however a better solution would be to implement a smartphone-ready web application by simply redesigning the JSF front-end only.

Currently, a certain feature is missing from the Android application, compared to the web-based version; that of displaying the user’s orders in a tabular view. Presenting information in tables is inappropriate for smartphone screens. Certain questions that come up are: how can one present such dense information in a small screen? How are multiple charts combined in such screens?

VI. CONCLUSION

This paper shows an energy management application on the Android OS platform. The user can take advantage of such application for power quality monitor in order to reduce cost and emissions. Furthermore, a robust energy management system on both software (application) and hardware (smart meter) layers may provide additional valuable and consistent historical data for future investments and savings in specific worldwide geographic areas.

APPENDIX

The work described in this paper is also available on Android Tablets 4.1.x. The Android tablet version was evaluated on Samsung Galaxy Tab 2 10'' device [14].

ACKNOWLEDGMENT

The Brokerage Agent Front native Android application was developed and funded by the NOBEL FP7 (Grant agreement no FP7- 247926 - ICT-2009-4) European research project [5]. The technical research, design and implementation of the applications have taken place within the NOBEL project's lifecycle. NOBEL is featured together with some selected projects as best practices in a European Commission booklet [15].

REFERENCES

- [1] Flot Homepage - <http://code.google.com/p/flot/>
- [2] Oracle Mojarra JSF Homepage - <http://jaserverfaces.java.net/>
- [3] Primefaces Homepage - <http://www.primefaces.org/>
- [4] E.Bekiaris, C.Petsos, and K.Kalogirou, "Energy management application: brokerage agent front end application", ICPEs 2012, April 2012, Hong Kong
- [5] <http://www.ict-nobel.eu/> , NOBEL EU project FP7 – 247926-ICT-2009-4, 2009
- [6] M.Song, H.Song and X.Fu , "Methodology of user interfaces design based on Android", Multimedia Technology (ICMT), 2011 International Conference, 26-28 July 2011
- [7] Jersey Homepage - <http://jersey.java.net/>
- [8] Jersey Community Forum - <http://jersey.576304.n2.nabble.com/java-lang-NullPointerException-on-Android-td4212447.html>
- [9] Y.Li, "Beyond Pinch and Flick: Enriching Mobile Gesture Interaction," Computer, vol. 42, no. 12, pp. 87-89, Dec. 2009
- [10] K.Wolf, C.Dicke, and R.Grasset, "Touching the void: gestures for auditory interfaces", In Proceedings of the fifth international conference on Tangible, embedded, and embodied interaction (TEI '11). ACM, New York, NY, USA, 305-308, 2010
- [11] RChart for Android Homepage - <http://www.java4less.com/charts/chart.php?info=android>
- [12] Nobel web application - <https://www.nobel-baf.eu/testChartOffline>
- [13] Nobel Android application - <https://play.google.com/store/apps/details?id=com.certh.nobel.android&hl=en>
- [14] Nobel Android Tablet application- <http://www.hit-projects.gr/TabletAndroidNobelOffline.apk>
- [15] European Union, "ICT for Societal Challenges: Digital Agenda for EU (DAE)", http://ec.europa.eu/information_society/newsroom/cf/dae/document.cfm?doc_id=1944 , p. 27, 2013

Distribution System Analysis with Time Varying Winter Load and Growth

V. V. S. N. Murty and Ashwani Kumar member IEEE

Abstract— In this paper, impact type A and type B unbalances of is investigated for unbalanced radial distribution system. The results are determined for voltage profile, total power losses, cost of energy loss and voltage stability index (VSI). The main contribution of the paper is: identifying the closeness of critical bus from the voltage collapse point of view in ubrds, (ii) the most sensitive bus in terms of voltage stability is determined under these unbalanced scenarios, (iii) investigation of the the impact of time varying load with realistic load model, (iv) the impact of load growth with realistic load model as ZIP load model. The analysis is carried out on 25 bus ubrds.

Keywords: Unbalanced radial distribution systems, voltage stability index, load model, and load growth.

I. INTRODUCTION

With the competitive electricity market structure which has been adopted world- wide, the issues of security and stability has become of serious concerns for secure operation of the system. High penetration of emerging new and renewable energy sources in both distribution and transmission systems pose a great challenge in terms of voltage stability of a system. Issues of voltage stability problems have been reported worldwide [1]. A fast and accurate voltage stability index (VSI) is needed to help monitoring the system condition. Currently, most electrical power systems operate very close to their stability limits and it is crucial to keep both efficiency and security at appropriate levels [2]. An accurate knowledge of how far the current system's operating point is from the voltage instability limit is crucial to system operators. It needs to be assessed with sudden change in system loading [3]. The methods reported by many authors referred in [4-12] and [13-16] have been adopted for the voltage stability analysis of radial balanced and unbalanced distribution systems. Haque [4] proposed a fast method to determine the voltage stability limit of power system. Analytical approach to voltage collapse proximity determination, stability indices are proposed for radial networks [5-10]. A new static voltage stability index of a RDS was developed by Hamada *et al.*, to faithfully evaluate the severity of the loading situation, thereby predicting for voltage instability at definite load value [11]. Authors proposed a new VSI for all the buses for radial distribution networks using the catastrophe theory [12]. Investigation of different load models on voltage stability of unbalanced radial distribution system is presented by Gunalan, *et al.* in [13]. Xiao Ping Zhang, *et al.* proposed a CPFlow approach for voltage stability analysis of unbalanced three-phase power systems in [14]. Authors

proposed voltage stability analysis for unbalanced radial distribution systems in [15-16].

To study the system in a more realistic way, the different load models along with load curve variations must be considered. The time varying load models impact needs to be addressed for voltage stability analysis in unbalanced distribution network. Radial distribution networks comprise of loads like industrial, commercial, residential and lightning loads are generally weak in nature because of high resistance to reactance ratio. Each of these loads is at its maximum at different times of the day and this may cause feeder overloading which may result in voltage collapse. A little attention on the voltage stability analysis of unbalanced radial distribution network under time invariant load conditions has been given.

In this paper, the analyses has been carried out taking dependence of voltage stability on the load unbalance and load growth scenario. The system performance has been evaluated for 24 hours seasonal (winter) load curve variation. The main contribution of the paper is: (i) Analysis of unbalanced radial distribution network with load growth and seasonal load variations, (ii) Impact of type A and type B unbalances in ubrds with load growth and seasonal load variations, (iii) impact of unbalances, ZIP load model, load variation, and load growth on voltage stability index, (iv) total power losses, voltage profiles and VSI, and cost of energy loss are determined. The results have been obtained for unbalanced distribution network of 25 buses [20].

II. ANALYSIS OF UNBALANCED DISTRIBUTION SYSTEM UNDER TYPE A AND B UNBALANCE [18]

Unbalance Type A: Initially the overall network load is balanced for the three phases. Subsequently, a percentage of the c-phase load is increased, while the same value is decreased in phase b. In this way, the total network load remains constant under type A unbalance scenario. The new three-phase loads in type A unbalance operation become as follows:

$$\begin{aligned} SL_a &= SL_a \\ SL_b &= SL_b * (1 - lub) \\ SL_c &= SL_c * (1 + lub) \end{aligned}$$

Unbalance Type B: A percentage of the load of phase b is decreased, while the decrease taken is twice this value in phase c. This kind of unbalance reduces the total network load under type B unbalanced scenario. The new three-phase loads in type B unbalance operation become as follows:

$$\begin{aligned}
 SL_a &= SL_a \\
 SL_b &= SL_b * (1 - lub) \\
 SL_c &= SL_c * (1 - 2 * lub)
 \end{aligned}$$

Where,

lub is the load unbalance factor which determines unbalance in the loads at all nodes in the study system, *lub* = 0.0 represents the balanced system base case study. In this paper work *lub* is taken as 20%. The objective of this section is to study the system behavior under type A and type B unbalance. In the type A unbalance system load in a-phase remains same, but in c-phase it is increasing and in b-phase it decreasing. Due to increased load demand, voltage magnitudes will decrease and total power losses also increase in phase c. Due to decreased load demand, voltage magnitudes will increase and total power losses also decrease in phase b. In the type B unbalance the decrement in c-phase load is twice that of decrement in phase-b. Due to decreased load demand, voltage magnitudes will increase and total power losses also decrease in phase b and c. However the decrement in total power losses and improvement in voltage is more in phase c than phase b. The main objective of this section is to study the effect of the system unbalance on system performance at different unbalance scenarios.

	Case 0	Case 1	Case 2
unbalance	0%	20% of type A	20% of type B

III. VOLTAGE STABILITY INDEX (VSI)

The voltage stability index is a parameter that identifies the nodes which are near to voltage collapse. The node with small voltage stability indices are called weak nodes and these should be reinforced with the support of reactive power. The best location for reactive power compensation to improve voltage stability margins is the weakest bus in the network. Therefore, the best locations to install compensation devices for voltage stability enhancement are the buses with the minimum voltage stability index. Unbalanced operation of distribution networks significantly decreases the voltage stability margins. This analysis will help researchers to identify the weakest bus for voltage stability enhancement under unbalance scenarios.

In this paper, voltage stability margin is calculated for time variant realistic ZIP load model. Type A and type B load unbalances are considered while calculating VSI. Also the impact of load growth on voltage stability indices is determined. Voltage stability index [11] is determined for each bus using Eq. (1) and the bus with minimum VSI is determined. VSI of each bus is a number between 0 and 1.

$$\begin{aligned}
 SI(re(i)) &= V(se(i))^4 - 4(P(i)x(i) - Q(I)r(i))^2 - \\
 &4(V(se(i))^2(P(i)r(i) + Q(i)x(i))) \quad (1) \\
 &\text{for } i = 1, 2, \dots \text{Number of buses}
 \end{aligned}$$

Where,

P = is the sum of the real power loads of all the nodes beyond each node , plus the real power load at each node itself, plus the sum of real power losses of all branches beyond each node.

Q = is the sum of the reactive power loads of all the nodes beyond each node , plus the reactive power load at each node

itself, plus the sum of reactive power losses of all branches beyond each node.

Cost of Energy Loss (CL): The cost of energy losses [19] has been calculated based on the mathematical model represented as: The annual cost of energy loss is given by

$$CL = (\text{Total Real power Loss}) * (E_c * 8760) \$ \quad (2)$$

E_c : Energy rate (\$/kWh)

Where, *E_c* = 0.06 \$/kWh

Model of Load Growth and ZIP load:

$$Load_i = Load \times (1 + \text{rate})^m \quad (3)$$

rate=annual load growth rate, m= plan period up to which feeder can take the load. In this paper work, rate=0.07 and m=5.

Time varying load [20] as a combination of residential, industrial and commercial has been considered. Seasonal (winter) variation of load has also been considered taking suitable exponential components in the ZIP load model. Let *α*, *β* and *γ* the percentages of residential, commercial and industrial load at each load node respectively

$$P = P_o \left[\alpha \left(\frac{V}{V_o} \right)^{n_{pr}} + \beta \left(\frac{V}{V_o} \right)^{n_{pc}} + \gamma \left(\frac{V}{V_o} \right)^{n_{pi}} \right] \quad (4)$$

$$Q = Q_o \left[\alpha \left(\frac{V}{V_o} \right)^{n_{qr}} + \beta \left(\frac{V}{V_o} \right)^{n_{qc}} + \gamma \left(\frac{V}{V_o} \right)^{n_{qi}} \right] \quad (5)$$

IV. RESULTS AND DISCUSSIONS

The results have been obtained for Type A and type B unbalances and load growth has also been considered to study the impact on voltage profile, VSI, losses, and cost of energy loss for 25 bus ubrds system. Peak demand occurred at 18th hour and minimum peak occurred at 7th hour in a day as shown in Fig. 25. A detailed voltage dependent load model has been considered for this, and the three categories of loads considered are: residential, industrial and commercial. The percentage of these loads is also considered as varying with respect to time. The plots of voltage profiles and VSI profiles for two types of unbalance scenarios considering load growth, with 24 hours seasonal (winter) load variation is presented. The voltage and VSI profiles are depicted for all three phases. Voltage profiles for all three phases without load growth for 24 hours load variation are presented in Figs. 1-3, Figs. 7-9 and Figs. 13-15 for case 0 (no unbalance), case 1 (type A unbalance) and case 2 (type B unbalance) respectively. Voltage stability index (VSI) profiles for all three phases without load growth for 24 hours load variation are presented in Figs. 4-6, Figs. 10-12 and Figs. 16-19 for case 0 (no unbalance), case 1 (type A unbalance) and case 2 (type B unbalance) respectively.

It is observed from the figures of voltage profiles that phase A voltage is higher in case 1 (type A unbalance), phase B and phase C voltage is higher in case 2 (type B unbalance). It is observed from the figures of voltage stability index profiles that phase A VSI is higher in case 1 (type A unbalance), phase B and phase C VSI is higher in case 2 (type B unbalance).

With the load growth, the real and reactive powers drawn from the substation increases since total load increases and thereby the losses and cost of energy losses will increase. Minimum bus voltage and minimum VSI with load growth is low than without load growth.

The minimum voltage profile obtained with and without load growth is also shown in Fig. 19 and Fig. 21 respectively. The minimum VSI profile obtained with and without load growth is also shown in Fig. 20 and Fig. 22 respectively. It is observed that the minimum voltage and minimum VSI in phase B and C improved in case 2 (type B unbalance). It is observed that minimum voltage occurs at bus 12th and VSI is minimum at bus 16th. So, 16th bus is the most critical bus in point of voltage stability. The total real power loss variation and cost of energy loss for 24 hours load variation is shown in Figs. 23-24.

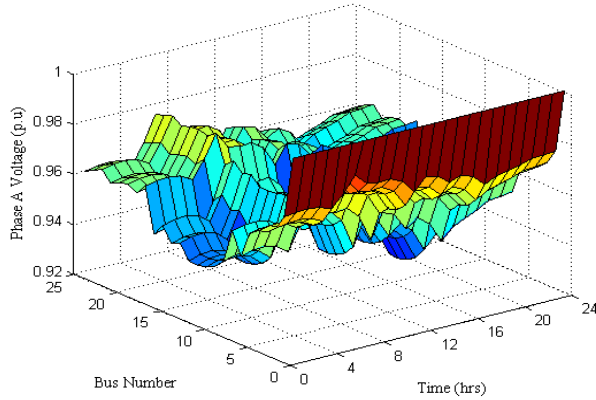


Figure 1. Voltage profile of phase A in case 0

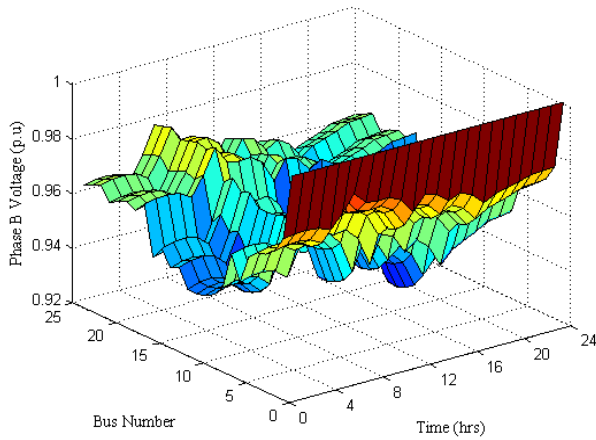


Figure 2. Voltage profile of phase B in case 0

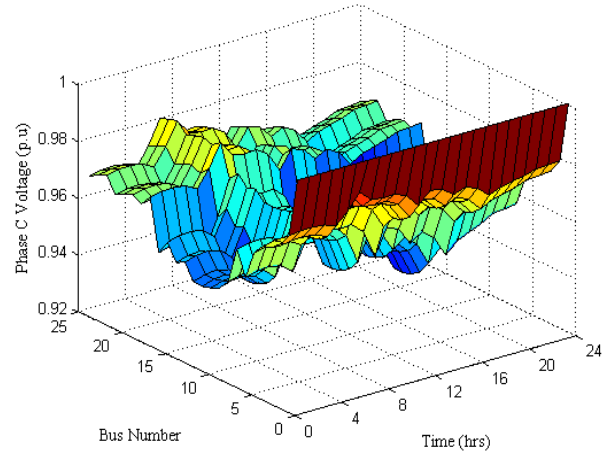


Figure 3. Voltage profile of phase C in case 0

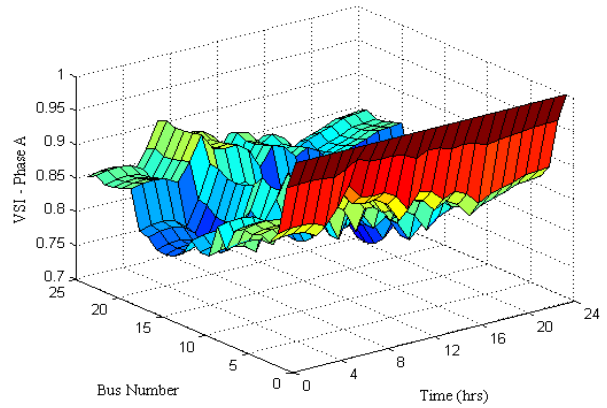


Figure 4. VSI profile of phase A in case 0

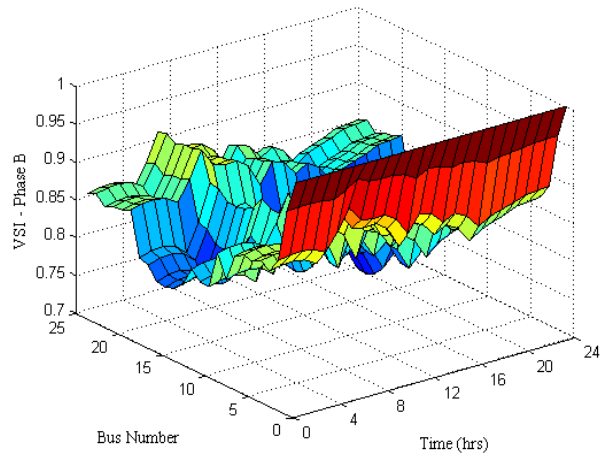


Figure 5. VSI profile of phase B in case 0

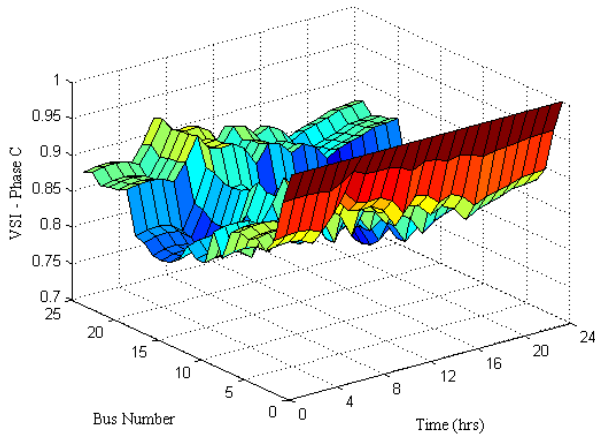


Figure 6. VSI profile of phase C in case 0

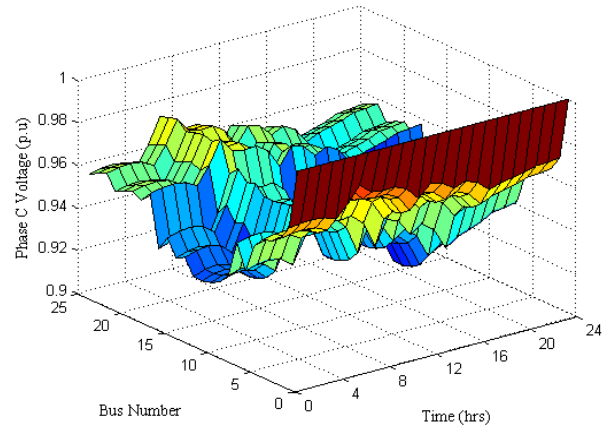


Figure 9. Voltage profile of phase C in case 1

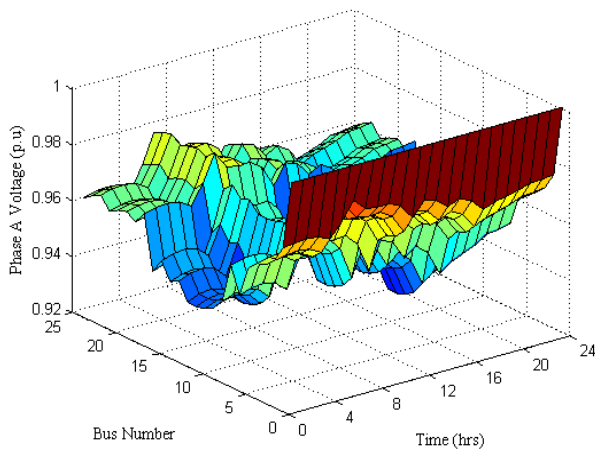


Figure 7. Voltage profile of phase A in case 1

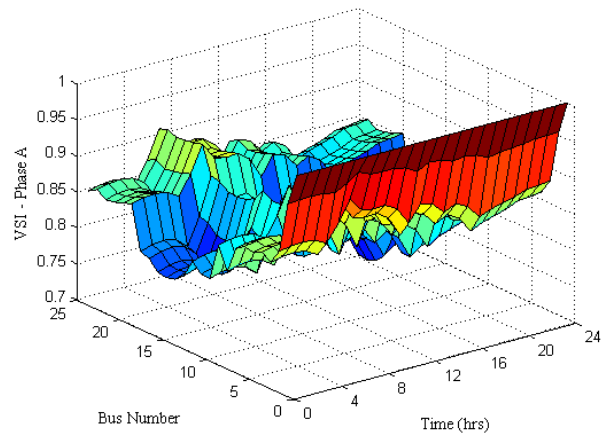


Figure 10. VSI profile of phase A in case 1

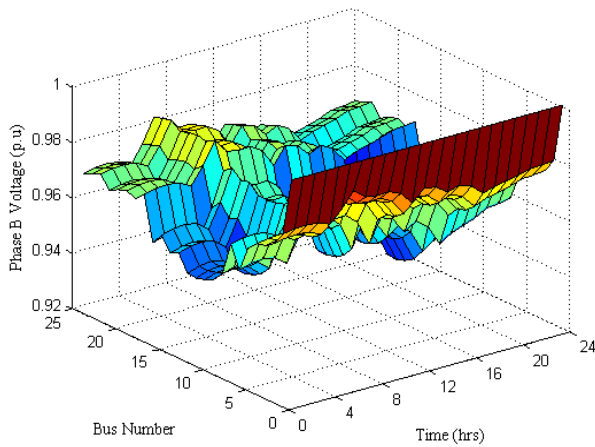


Figure 8. Voltage profile of phase B in case 1

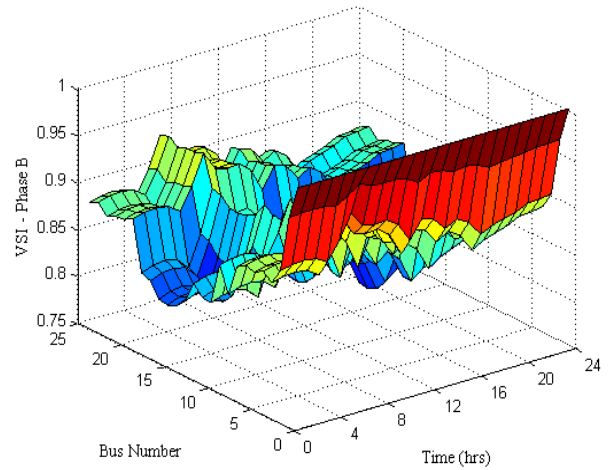


Figure 11. VSI profile of phase B in case 1

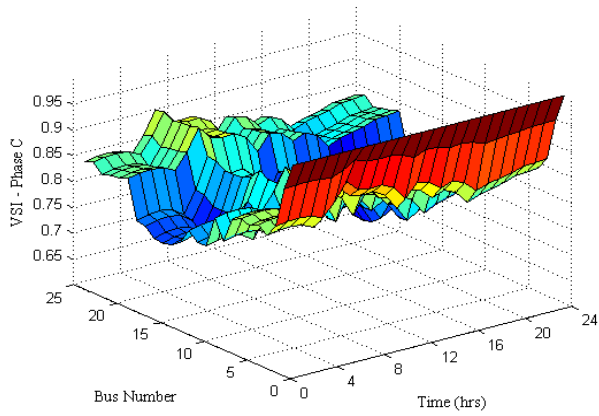


Figure 12. VSI profile of phase C in case 1

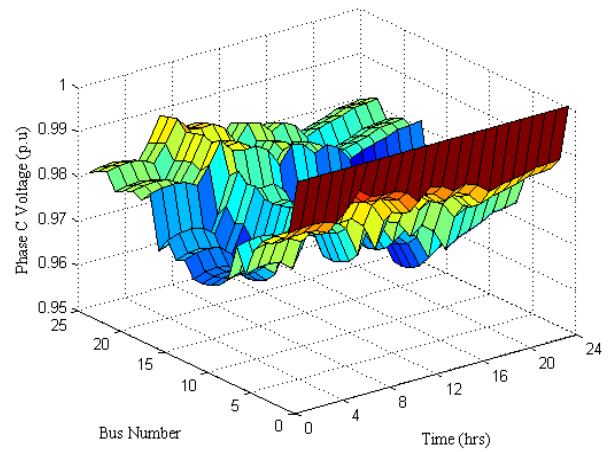


Figure 15. Voltage profile of phase C in case 2

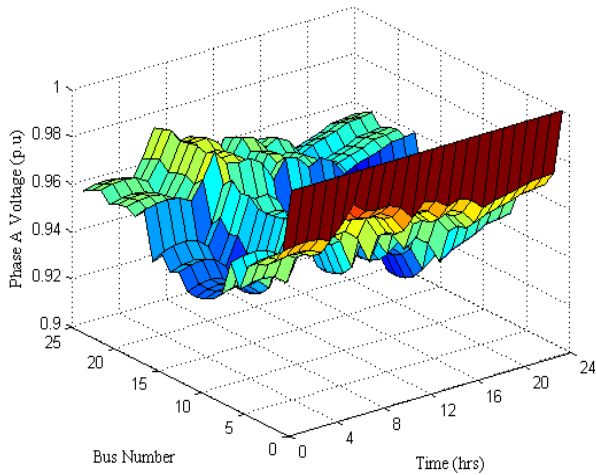


Figure 13. Voltage profile of phase A in case 2

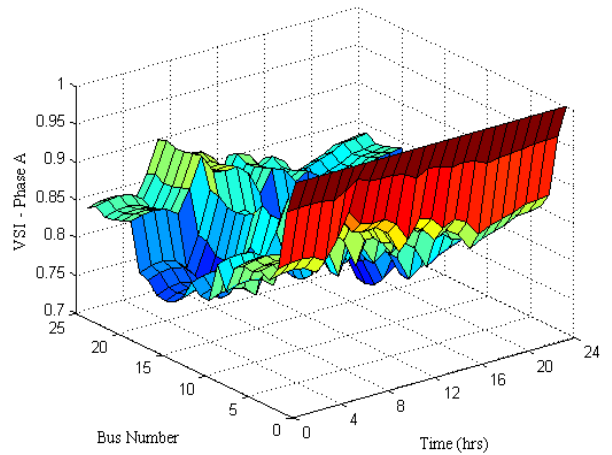


Figure 16. VSI profile of phase A in case 2

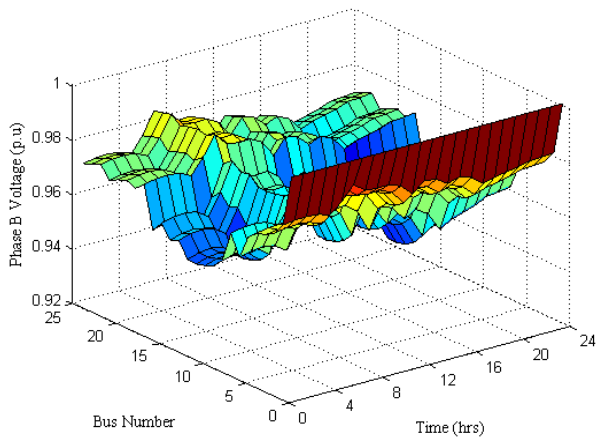


Figure 14. Voltage profile of phase B in case 2

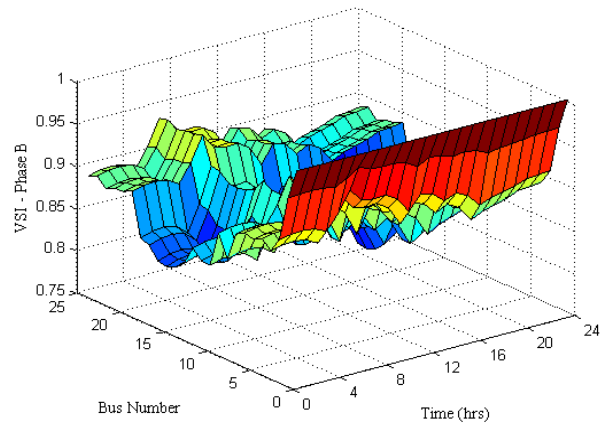


Figure 17. VSI profile of phase B in case 2

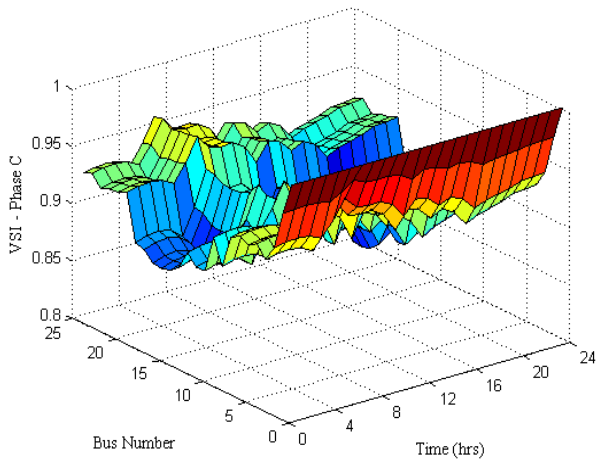


Figure 18. VSI profile of phase C in case 2

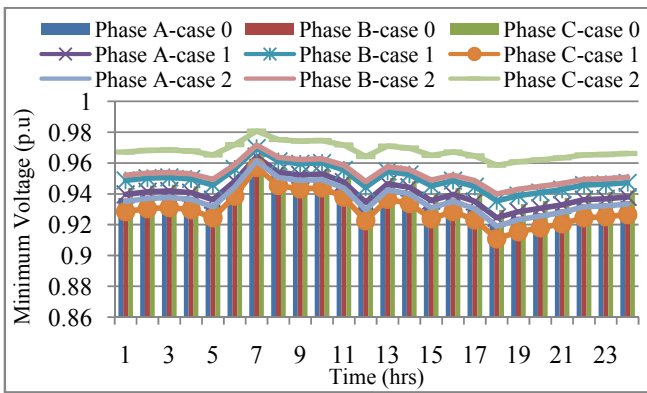


Figure 19. Minimum voltage profile without load growth

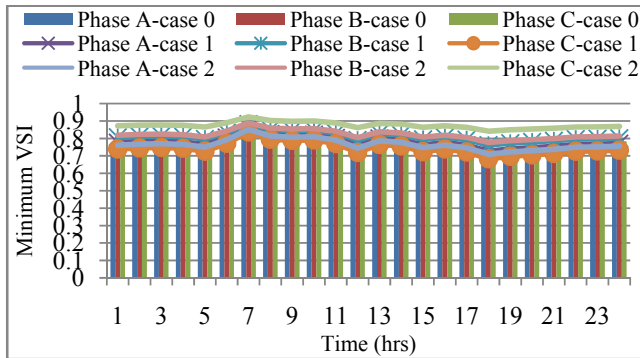


Figure 20. Minimum VSI without load growth

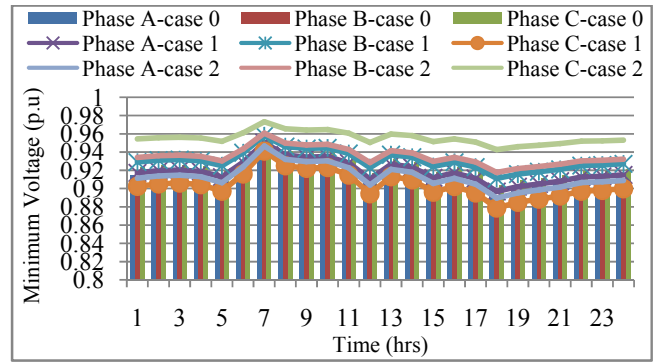


Figure 21. Minimum voltage profile with load growth

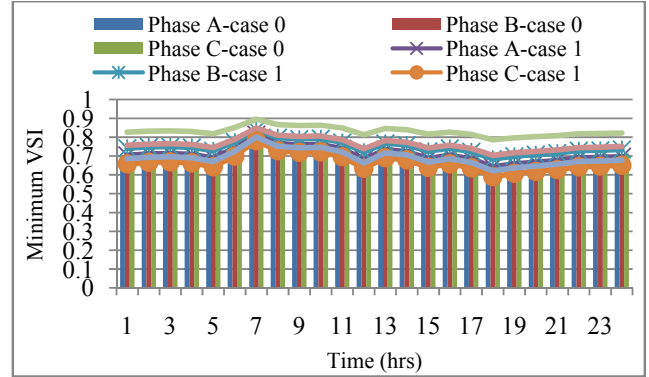


Figure 22. Minimum VSI with load growth

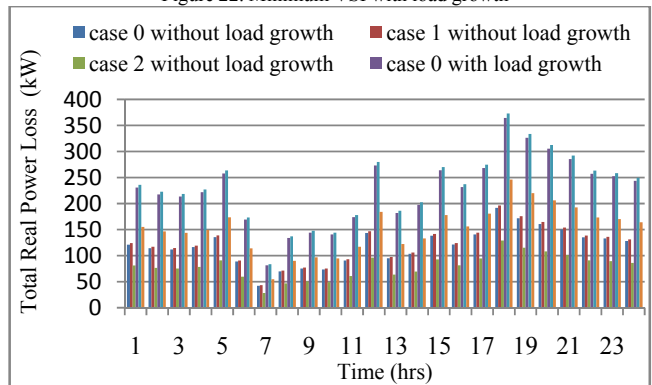


Figure 23. Total real power loss profile with and without load growth

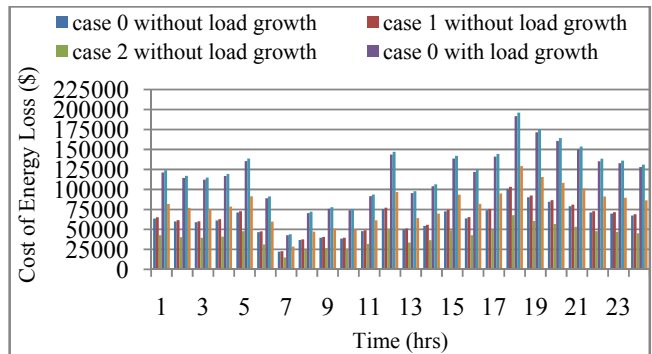


Figure 24. Cost of energy loss with and without load growth.

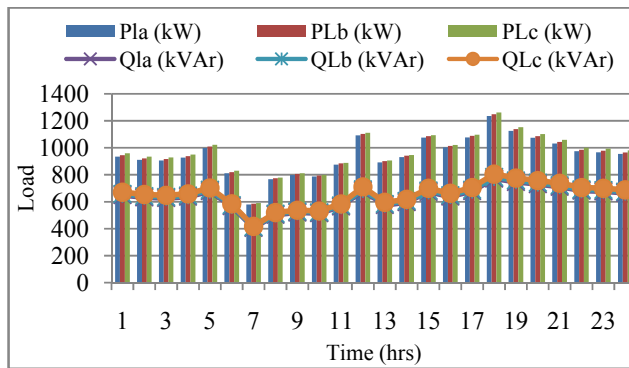


Figure 25. Load curve for 25 bus ubrds with winter load in case 0

V. CONCLUSION

It is observed from analysis that unbalanced distribution network with type B unbalance have better voltage profile, lower total power losses and cost of energy losses. If we consider the load growth, the real and reactive powers received from the substation increases since total load increases, losses also increase. Minimum bus voltage with load growth is low than without load growth for all load models. However minimum bus voltage is better, lower total power losses and cost of energy losses in type B unbalance. Voltage stability index is found better for type B unbalanced scenario. The results show that the unbalance factor is greatly affecting the voltage stability index of the study system. This study will help for the better operation of distribution systems taking the impact of types of load unbalance, load growth and voltage stability index. VSI will provide planning better locations for reactive power sources and better management of reactive power deployment.

ACKNOWLEDGMENT

This part of the work has been carried out under the project SR/S3/EECE/0035/2012 sponsored by SERB, Department of Science and Technology, DST, GOI, New Delhi. The author acknowledges SERB, DST, GOI, New Delhi for the grant of the project.

REFERENCES

- [1] Sadek, M.Z.E.L., "Prevention of repetitive blackouts in the Egyptian power system". Second Middle East Int. Conf. MEPCON 92, Assiut University, Egypt, January, pp. 14–19, 1992.
- [2] S. Sakthivel, D. Mary, and M. Deivarajamani, "Reactive power planning for voltage stability limit improvement with FACTS devices in most critical contingency condition", *Eur. J. Sci. Res.*, 2011, vol. 66, no. 3, pp. 408–420.
- [3] L. A. Ll. Zarate, and C. A. Castro, "Fast computation of security margins to voltage collapse based on sensitivity analysis", *IEE Proc., Gener. Transm. Distrib.*, 2006, vol. 153, no. 1, pp. 35–43.
- [4] M. H. Haque, "A fast method for determining the voltage stability limit of a power system", *Electric Power Syst. Res.*, 1995, vol. 32, pp. 35–43.
- [5] F. Gubina, and B. Strmcnik, "A simple approach to voltage stability assessment in radial networks", *IEEE Trans. Power Delivery.*, 1997, vol. 12, no. 3, pp. 1121–1128.
- [6] M. Moghavvemi, and M. O. Faruque M, "Technique for assessment of voltage stability in ill-conditioned radial distribution network", *IEEE Power Eng. Review*, 2001, pp. 58–60.

- [7] M. Chakravorty, and D. Das, "Voltage stability analysis of radial distribution networks", *Electric Power and Energy System*, 2001, vol.23, pp.129-135.
- [8] A. Augugliaro, L. Dusonchet, and S. Mangione, "Voltage collapse proximity indicators for radial distribution networks", *Proc. Ninth Int. Conf. Electric Power Quality and Utilization, Barcelona*, 2007, pp. 9–11.
- [9] A. Chaturvedi, K. Prasad, and R. Ranjan, "A new voltage stability index for radial distribution network", *International Journal of Power and Energy Systems*, 2006, vol. 26, no. 1, pp.83-88.
- [10] U. Eminoglu, and M. H. Hocaoglu, "A Voltage Stability Index for Radial Distribution Networks", *IEEE, UPEC 2007*, pp. 408-413.
- [11] M. M. Hamada, A. A. Wahab, and G. A. Hemdan, "Simple and efficient method for steady-state voltage stability assessment of radial distribution systems", *Electric Power Syst. Res.*, 2010, vol. 80, pp. 152-160.
- [12] G.A. Mahmoud, "Voltage stability analysis of radial distribution networks using catastrophe theory", *IET Gener. Transm. Distrib.*, 2012, vol. 6, Iss. 7, pp. 612–618.
- [13] S. Gunalan, A. K. Ramasamy, and R. Verayah, "Impact of Static Load on Voltage Stability of an Unbalanced Distribution System", *IEEE International Conference on Power and Energy (PEcon 2010)*, Nov 29-Dec 2, Malaysia, 288-293.
- [14] X. P. Zhang, P. Ju, and E. Handschin, "Continuation Three-Phase Power Flow: A Tool for Voltage Stability Analysis of Unbalanced Three-Phase Power Systems", *IEEE Transactions on Power Systems*, August 2005, vol. 20, no. 3, pp. 1320-1329.
- [15] G. Carpinelli, D. Lauria, and P. Varilone, "Voltage stability analysis in unbalanced power systems by optimal power flow", *IEE Proc.-Gener. Transm. Distrib.*, May 2006, vol. 153, no. 3, pp. 261-268.
- [16] M. Abdel-Akher, "Voltage stability analysis of unbalanced distribution systems using backward/forward sweep load-flow analysis method with secant predictor", *IET Gener. Transm. Distrib.*, 2013, vol. 7, iss. 3, pp. 309–317.
- [17] L. F. Ochoa, R. M. Ciric, A. P. Feltrin, and G. P. Harrison, "Evaluation of distribution system losses due to load unbalance", *15th PSCC, Liege*, 22-26, August 2005, Session 10, Page 1-4.
- [18] D. Das, "Reactive power compensation for radial distribution network using genetic algorithm," *Electric Power Systems Research*, 2002, vol. 24, pp. 573-581.
- [19] k. Qian, C. Zhou, M. allan, and Y. yuan, "Effect of load models on assessment of energy losses in distribution generation planning," *Electric Power System Research*, 2011, vol. 2, pp. 1243-1250.
- [20] V. Ganesh, S. Sivanagaraju, and T. Ramana, "Feeder Reconfiguration for Loss Reduction in Unbalanced Distribution System Using Genetic Algorithm", *World Academy of Science, Engineering and Technology* 28, 2009, pp. 745-753.

Assessment of restructured Indian power sector: Availability, demand and shortage

Yog Raj Sood, Rajnish Shrivastava, and Naveen Kumar Sharma

Abstract— The Indian power sector has undergone significant changes since 1990 by opening gateway for the independent power producers. Power planning will play an important role in the successful power reform. It is essential for India economy growth. Only a financially and commercially sound power sector can attract new investments. India ranks fifth in the world in total energy consumption and needs to accelerate the development of the sector to meet its growth aspirations. The electricity market is undergoing a tremendous transformation not only in India but throughout the world as it move towards a more competitive environment. Five different ministries have structurally handled the Indian energy sector and power is a concurrent subject of both the central government and the states. India had also cross 28 GW milestone installed grid connected renewable energy capacity. For renewable development in India, the renewable energy program has been in existence for more than three decades, but a market for renewable energy technologies still need to be exists. The country is aiming to achieve up to 20% of additional installed capacity to be set up till 2020 to come from RES. In this paper, efforts have been made to summarize the availability, demand, shortage, and current assessment of restructured Indian power sector & strategies of renewable energy options in Indian competitive electricity market.

Keywords— Deregulation, renewable energy, restructuring, power market.

I. INTRODUCTION

THE challenge of supplying the nation with reliable, high quality electrical energy at a reasonable cost is at the heart of a nation's economy. The power sector is a primary mover and an effective engine of economic growth. India is a fast growing developing economy and has progressed despite the challenges on the socio-political front. The country has been experiencing 8.5 % GDP growth rate over the last few years and to sustain this pace of growth, contribution by power sector is substantially important [1]. The power sector in India has been regulated and owned for many years by various government agencies and organizations. The role and the participation of private industry in the Indian power sector has been limited and confined to specific areas of small jurisdiction and consumer base. Power sector is one of the key sectors contributing significantly to the growth of country's economy. Power sector needs a more useful role to be played

Yog Raj Sood, Rajnish Shrivastava, and Naveen Kumar Sharma are with the National Institute of Technology Hamirpur (H.P.), Hamirpur-177005, India. (Phone No: +91 1972 254522; fax: +91 1972 223834; e-mail: yrsood@gmail.com, naveen31.sharma@gmail.com).

in defining, formulating and implementing the research projects with close involvement of all utilities such that the benefit reaches the ultimate consumer. During the past two decade's power sector over worldwide has experienced a rapid change in generation, transmission, and distribution system [11]. India is in the processing on restructuring in power sector. Power planning will play an important role in the successful power reform. Presently Indian power industries are moving rapidly towards restructuring from fully regulated conventional set up. In the modern restructured power industry, the role played by generation, transmission and distribution in power sector are independent [2]. Main benefits obtained from restructuring of power system are, cheaper electricity, efficient capacity expansion planning, cost minimization, more choice and better service.

In the deregulated power system, the challenge of congestion management for the transmission system operator is to create a set of rules that ensure sufficient control over producers and consumers (generators and loads) to maintain an acceptable level of power system security and reliability in both the short term (real-time operations) and the long term (transmission and generation construction) while maximizing market efficiency [3]. The rules must be robust, because there will be many aggressive entities seeking to exploit congestion to create market power and increased profits for themselves at the expense of market efficiency so that rules should also be fair, transparent and clear to all participants in power market [4].

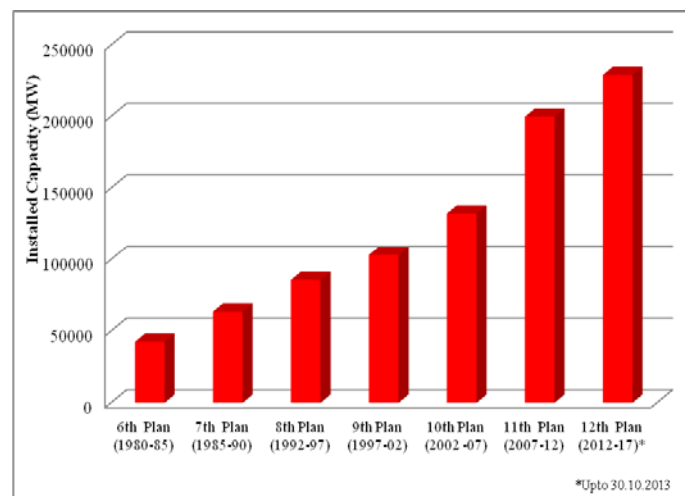


Fig.1 Plan wise groth of Indian power sector

II. INDIAN POWER STRUCTURE

The Indian power sector is presently going through a process of reform and restructuring as is the trend in many other parts of the world. Under reform, independent regulatory commissions are set up to the center as well as state wise and vertically integrated utilities are being unbundled into corporate entities. India's power sector is highly dependent on coal, which has 58% of installed power capacity. At present India is fifth largest country in the world in electricity generation, having aggregate capacity of 229 GWs out of which 68% is from thermal, 18% from hydro, 2% from nuclear and the rest about 12% is from renewable energy sources as shown in Figure 2. Although Over the years, Indian power sector has experienced a six-time increased in its installed capacity a jump from 1362 MW in 1947 to over 2,29,252 MW by September 2013 but still there is a huge gap in generation and demand in India hence need to be establish more generation plants preferably to be come from renewable sources by governmental as well as various private participation [6].

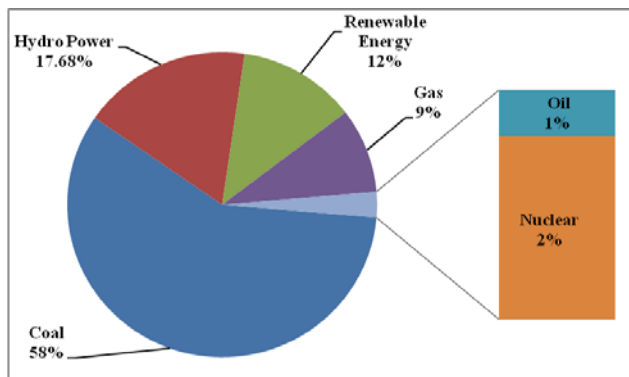


Fig. 2 Indian power Installed capacity

The functions of centre electricity authority (CEA) are to advise the Ministry of Power (MoP) on national power policy, national power planning and regulatory matters on the national level where as state electricity regulatory commissions (SERCs), does the same function at state level [7-8].

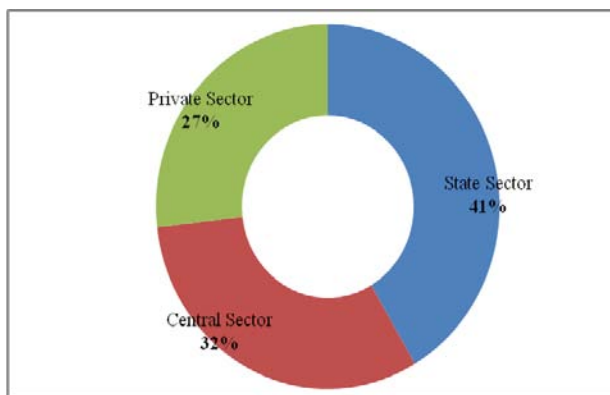


Fig.3 Sector wise Installed capacity

Indian power sector is organized into five Regional Electricity Boards such as northern regional electricity board (NREB), southern regional electricity board (SREB), western

regional electricity board (WREB), eastern regional electricity board (EREB) and north eastern regional electricity board (NEREB) as depicted [3, 7]. In India, power installs capacity sector wise as shown in Figure 3. As shown in Figure 4, percentage of each region regional wise total installed capacity in India.

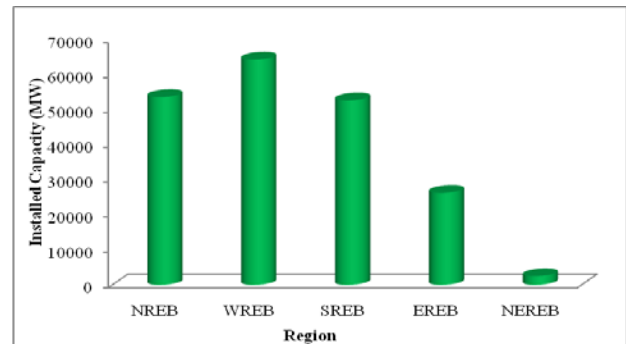


Fig. 4 Percentage of region wise installed capacity

III. DEMAND AND SUPPLY POWER SCENARIO IN INDIA

India has the fifth-largest generation capacity in the world with a total installed capacity of 229252 MW as of September 2013 and by the 12th Plan (2012–2017), capacity addition close to 100,000 MW is anticipated, around 50% of which is expected to come from the private sector. Most of the electricity is consumed in the northern part of India [10]. The states Punjab, Rajasthan, and Uttar Pradesh, and the capital Delhi are together responsible for one fifth of India's final electricity demand. Coal power generation in India is still based entirely on subcritical technology. There is a huge gap in generation and demand in India hence need to be establish more generation plants preferably to be come from renewable sources by governmental as well as various private participation. The Indian power sector is predominantly based on fossil fuels, with about three-fifths of the country's power generation capacity being dependent on vast indigenous reserves of coal.

India has a vast supply of renewable energy resources, and it has one of the largest programs in the world for deploying renewable energy based products and systems. The contribution of green energy as RES to the total power generation is estimated to be 4.7%, 5.5% and 6.4% during 2010-11, 2011-12 and 2012-13 respectively. India, total grid-connected renewable power generation capacity of 28,184MW has been achieved till end of September 2013. A capacity addition of 11,246 MW has been achieved from RES during the last 3 financial years. The total expenditure of Rs.1106.79 crore was incurred by MNRE for development and promotion of renewable energy sources, which is about 80% of the Gross Budgetary Support and over 96% of the Revised Estimates for the year 2012-13. Against the target of 4125 MW grid connected capacity and 126 MW off-grid applications, the achievements have been 3163 MW and 147 MW respectively during 2012-13 [9]. The current policy mechanisms, especially investment or generation- based price-driven and capacity-driven mechanisms, ranging from investment incentives for the development of renewable energy projects, feed-in tariffs,

production tax incentives, tradable green certificates, and their effects upon the prospects of encouraging as well as expanding the development of renewable energy in Indian restructured power sector.

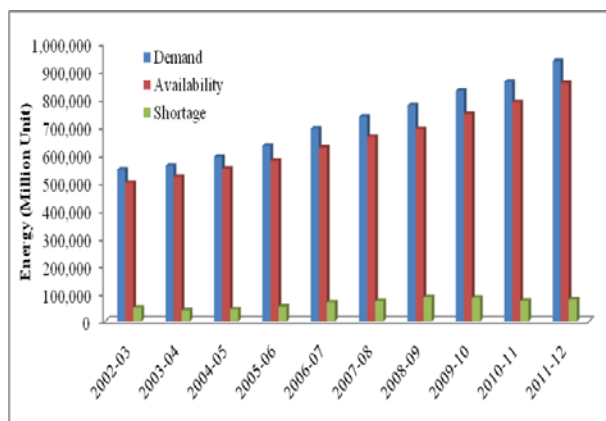


Fig. 5 Status of energy availability, demand and shortage

Status of power energy availability, demand and shortage has given in Figure 5. With the establishment of various inter-regional links, inter-regional power exchange has grown manifold. Growth of inter-regional power exchange has helped in meeting more demand in energy deficit regions besides achieving overall economy. Projections for future electricity demand are very uncertain, because of the expected continuation of India's dynamic development. GDP development, industry structure, population growth and income levels are important drivers for energy and electricity demand as well as their impact on CO₂ emissions. Although reforms in the energy sector are underway, the pace of reform is different in the sub sectors viz, power, coal, oil, gas and renewables. The demand for power is increasing at a rapid pace although the generation of power has not increased at the same proportion. The gap between demand and supply of power is quite significant. The shortage of power generation capacity is estimated to be around 2500MW (Figure 6).

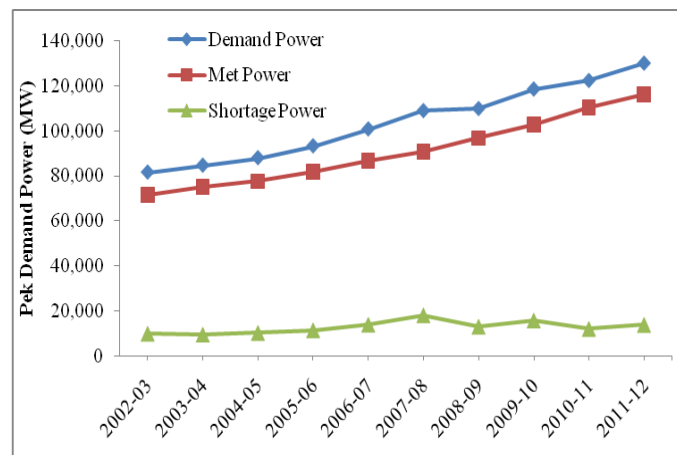


Fig.6 Peak demand, met and shortage power status in India

India currently has a power deficit of 9%, expected to continue its steady increase over the next few years [10]. At present, the country was divided into two grids-one is the

Southern Grid and the other comprises of Eastern, Western Northern, and North-Eastern region grid. The one grid system will resolve the power woes of power deficit states by improving intra-regional transmission of power with inclusion renewable also. The 12th Five-Year Plan (2012-17) is even more ambitious, calling for the addition of over 100,000 MW of power. Planners are confident of realizing this target given that the policy reforms of the Electricity Act would have had time to play out; leading to greater private sector participation is concerned [13].

India has set a very ambitious goal to increase the RE production. By 2017 15% of added electricity capacity should be renewable. Besides direct RES targets, India have also set targets concerning access to electricity. By "13th five year plan 2017-22"; planning commission (GOI) targeted the future development of total RES in India, which is shown in Table 1 [7]. The Committee has placed emphasis on higher use of renewables in all forms of services. It is expected that the contribution from renewables in power generation alone can be of the extent of 60,000MW in the year 2031-2032 [7, 9].

Table I
DEVELOPMENT OF GRID-CONNECTED RENEWABLE POWER IN INDIA (IN MW)

Five-year Plan	In Process	Targets
	Addition proposed target in 12 th Plan	By the End of the 13 th Plan
Years	Through 2017	Through 2022
Wind	15,000	40,000
Small Hydro	2,100	6,500
Biomass	2,700	7,500
Solar	10,000	20,000
Total	29,800	74,000

IV. REFORM OF THE INDIAN POWER MARKET

Restructuring has changed the traditional mission and mandates of utilities in complex ways, and had large impacts on environmental, social, and political conditions for any particular country. At the same time, new regulatory approaches are being found for reducing environmental impacts in restructured power sectors. Electricity reform has been motivated by: technological developments, particularly the improved efficiency of gas turbines; the need for increased investment, especially in developing countries such like India; high electricity prices and a shift away from the view that electricity supply is a natural monopoly [17]. Keeping in view the pros and cons of different restructuring processes in various countries, it is recognized easily that India is not yet ready for electricity restructuring. In a restructured electricity industry, generators will include utilities, federal power authorities, qualifying facilities, merchant power plants, and on-site industrial plants. India also has followed the global change in power sector by establishment of the Regulatory Commissions in 1998 under the Electricity Regulatory Commissions Act 1998 (Central Law) to promote competition, efficiency and economy in the activities of the electricity industry and applied restructuring to Orissa state electricity board firstly and after that to many other states. Central Electricity Regulatory Commission (CERC) has a key role in rationalizing tariff of generating companies owned or

controlled by the Central Government in consultation with State Electricity Regulatory Commission (SERC). Orissa, by enacting a Reforms Legislation and creating an independent tariff regulatory body in 1996, has pioneered the power reform activities in the country. Today, States such as Haryana and Andhra Pradesh have brought in reforms Acts and have established the State Electricity Regulatory Commissions. Several other States such as Arunachal Pradesh, Madhya Pradesh, Delhi, West Bengal, Tamil Nadu, Gujarat, Uttar Pradesh and Punjab have constituted/notified the constitution of the SERC [3, 8]. Increased competition in bulk power and retail electricity markets is likely to lower electricity prices, but will also result in greater price volatility as the industry moves away from administratively determined, cost-based rates and encourages market-driven prices. Price volatility introduces new risks for generators, consumers, and marketers. Electricity futures and other derivatives can help each of these market participants manage, or hedge, price risks in a competitive electricity market [17].

The incorporation of transmission into this competitive framework has proven more complicated and is the subject of an ongoing debate among utilities, consumers and suppliers. For obvious reasons, it is neither feasible nor economical to build independent transmission systems for each generation load pair. This means that virtually the whole power system must be replanted from scratch, which opens up interesting opportunities to truly transform the power sector. Restructuring of the all-electric power industry has refocused attention on renewable energy and the policies that affect it in competitive electricity markets. Public policies favoring renewable energy are nothing new.

Policies including tax and financial incentives and guaranteed purchase power contracts, among others have supported the development of renewable energy in the past also. Such policies have sought to develop a sustainable energy future, reduce dependence on fissile fuel, and reduce the environmental impacts of fossil-fueled electricity generation. The issues of tariffs for transmission access and services are coming when the power industries changes from regulated to competitive environment. The structure of the transmission tariff will determine the allocation of transmission costs to the users of the transmission system, and ultimately, to the respective consumers. The structure of the transmission tariff can impact the prices of transmission for different generation technologies and energy sources, which could affect the economics of these technologies. The transmission tariff is so designed to recover both the marginal and fixed costs of the transmission system. The marginal cost of transmission for completing any given power transfer, including losses, ancillary services (i.e., capacity reserves) and any congestion cost, is typically a small fraction of the embedded cost is included in transmission tariffs. Although renewable energy sources are comparatively more expensive than conventional fuels, but they can be used in distributed generation and local distribution networks to counterbalance the transmission & distribution losses incurred by states depend on government support for development [11-15].

Over the last two decades, the old idea that electric power generation, transmission and distribution represent a natural monopoly best handled centrally, has given way to a general consensus among policy-makers, regulators, industry analysts and economists that the generation and retailing elements of the power supply industry would be more efficiently delivered by firms operating in freely competitive energy markets [19]. Developing countries like India is also moving step by step towards deregulation. In deregulation environment generation, transmission and distribution are independent activities and also there is a competition among generators for customers. The necessary requirement for deregulation is restructuring of electricity supply industry whose basic features are as follows:

- To introduce competition into a hitherto monopolistic industry. In order to achieve this, to separate (vertical unbundling) the functions of power generation, transmission, distribution and electricity supply to consumers.
- To create several competing electricity generations companies (horizontal unbundling).
- To recognize that the power transmission system is a natural monopoly and, accordingly, to make special regulatory provisions in this respect.
- To allow consumers, to exercise choice between suppliers (generation companies) while still using the existing transmission facilities

Main benefits from the deregulation are, cheaper electricity, efficient capacity expansion planning, more choice and better service. The deregulation of power sector provides a fair competition among producers as well as more choice and better service for consumers of electricity. So, in order to support fair competition among producers of electricity, one important aspect is to treat the transmission of electrical energy as a separate business [1, 19]. The deregulation process primarily focuses on enhancing system efficiency, improving service standards and developing competitive market. The market environment typically consists of a pool and privately negotiated bilateral and multilateral contracts. The pricing of transmission service plays also a critical role in the success of deregulation of a power system. The methodologies for determination of transmission pricing can be on the basis of marginal cost or embedded cost or a composite cost, i.e. the combination of marginal and embedded cost [20].

Electricity act 2003 give the authority to SERC for preferential tariff for renewable energy development. SERC shall be guided in specifying the terms and conditions for determination of tariff as per Section 61 of EA-2003 [13-15]. There will be Government owned Transmission Utility at the Central as well as State level, having the responsibility of ensuring that the transmission network is developed in a planned and co-ordinate manner to meet the requirements of the sector. The load dispatch function can be integrated with or separated from the Transmission Utility and in either case it will remain under Government control. SERC shall specify extent of open access in successive phases, determine the wheeling charges, decide the surcharge in addition to the wheeling charges to meet current level of cross-subsidy (e.g. the industrial consumer cross-subsidizes the domestic ones)

and also specify the manner in which such surcharge and cross-subsidies is progressively reduced and eliminated. Such surcharge shall not be levied in case of electricity being carried from captive power plant to the destination of own use.

V. CONCLUSIONS

Indian electricity demand is expected to increase considerably during the next decade at the same time environmental pollution is also increasing with the development of conventional energy source. In this article presents the detailed power scenario and trends of current Indian power sector with availability, demand and shortage power status. India is in the processing on restructuring in power sector. Coal is likely to remain the dominant fuel for electricity generation, but natural gas and hydropower are projected to increase in importance. Renewable and nuclear power must play a crucial role for reform power sector as well as carbon free electricity generation in India. Renewable energy sources especially solar energy is the only option with a large technical potential, and must be included in the decarbonization strategy for Indian power sector with reduced demand growth. Renewable energy development is of great importance from the point of view of long term energy supply security, decentralization of energy supply particularly for the benefit of the rural population, environmental benefits and sustainability in power sector also. So power planning will play an important role in the successful power reform. The electricity market is undergoing a tremendous transformation not only in India but throughout the world as it moves towards a more competitive environment.

REFERENCES

- [1] Y.R. Sood, N.P. Padhy, H.O. Gupta, "Wheeling of power under deregulated environment of power system—a bibliographical survey", *IEEE Transact. Power Syst.* Vol. 17, Issue 3, 2002, pp. 870–878.
- [2] Y. R. Sood, N. P. Padhy, and H. O. Gupta, "Deregulated Model and Locational Marginal Pricing," *Electric Power System Research*, vol. 77, issue 5-6, pp. 574-582, 2010.
- [3] R.Singh, Y.R. Sood, N.P. Padhy, "Development of renewable energy sources for Indian power sector moving towards competitive electricity market", *PES- 2009*, *IEEE, Power & Energy Society General Meeting*, 2009, pp 1 – 6.
- [4] A. Singh, "Power sector reform in India: current issues and prospectus" *Energy Policy*, vol. 34, pp. 2480-2490, (2006).
- [5] R. Bhakar, N.P.Padhy, H. O. Gupta, "State of art of the regulatory process in India" *IEEE Power and Energy Society General Meeting - Conversion and Delivery of Electrical Energy in the 21st Century*, 2008 pp.1 – 8.
- [6] Ministry of Power. Available: <http://www.powermin.nic.in> [online].
- [7] N.K. Sharma, P.K Tiwari, Y.R. Sood, "Environmental Friendly Solar Energy in Restructured Indian Power Sector", *IET Second International Conference on Sustainable Energy and Intelligent System (SEISCON 2011)*, Tamil Nadu, India, 2011, pp. 104-109.
- [8] Government of India. National Electricity Policy 2005. Available: <http://www.powermin.nic.in> [online].
- [9] Ministry of New and Renewable Energy source (MNRE), <http://www.mnre.gov.in/achievements.htm>.
- [10] Government of India. Annual Report 2011-12. New Delhi: Ministry of New and Renewable Energy, Government of India; 2013 [online].
- [11] S.C. Bhattacharyya, "An overview of problems and prospects for the Indian power sector", *Energy*, vol. 19, Issue 7, 1999, pp. 795–803.
- [12] Lai Loi Lai, "Power System Restructuring and Deregulation, (book), Publisher: John Wiley and Sons, Ltd., New York, 2001.

- [13] Government of India, "The Electricity Act, 2003," The Gazette of India, Extraordinary, New Delhi, (2003).
- [14] Government of India, "Tariff policy" 6th January, 2006 [Online]. Available <http://www.powermin.nic.in>
- [15] Government of India "National Electricity policy and plan" [Online]. Available: www.powermin.nic.in
- [16] Electricity, Electricity Feed Laws, Feed-in Tariffs, and Advanced Renewable Tariffs, [Online]. Available: <http://www.wind-works.org>
- [17] Singh R, Sood YR. Current status and analysis of renewable promotional policies in Indian restructured power sector- A review. *Renewable and Sustainable Energy Reviews* 2011; 15: 657-664.
- [18] Ministry of New and Renewable Energy source (MNERS) "Policy support for grid interactive renewable power" [Online]. Available: <http://mnes.nic.in>
- [19] N. P. Padhy, and Y. R. Sood, "Advancement in Power System Engineering Education and Research with Power Industry Moving towards Deregulation", *IEEE Power Engineering Society General Meeting*, vol. 1, pp. 71-76, 2004.
- [20] Y. R. Sood, N.P. Padhy, H.O. Gupta, *Deregulated Model and Locational Marginal Pricing*, *Electric Power Systems Research*, vol. 77, pp. 574-582, 2007.

Yog Raj Sood (SM'10) received his B.E. degree in Electrical Engineering with "Honours" and M.E. in Power System from Punjab Engineering College Chandigarh (U.T.), in 1984 and 1987 respectively. He has been awarded Ph.D. degree from Indian Institute of Technology (IIT), Roorkee (India), in 2003. He joined Regional Engineering College (presently NIT) Kurukshetra in 1986. He has been working as Professor in the Electrical Engineering Department of National Institute of Technology, Hamirpur (H.P.), India since January 2006. He has been honoured with many awards, prizes, appreciation letters/certificates for his excellent research, academic and administrative responsibilities. He has published a number of research papers in reputed international journals. He delivered key note addresses in various international conferences. His research interests are in the area of power sector restructuring and deregulation, renewable energy sources, power system optimization, FACTS, high voltage engineering, and condition monitoring of transformers.

Naveen Kumar Sharma (M'11) was born in Kanpur (Uttar Pradesh), India. He obtained his B.Tech in Electrical & Electronics Engineering in 2008 from Utter Pradesh Technical University Lucknow (U.P.). He received his M. Tech degree in Power System from National Institute of Technology Hamirpur (H.P.)-India, in 2010. Presently he is pursuing Ph.D in the Department of Electrical Engineering, National Institute of Technology Hamirpur (H.P.) - India. His research interests are in the area of Power System, Renewable energy sources, power sector restructuring and deregulation, power transformer diagnosis.

A robust AVR-PSS synthesis using genetic algorithms (application under GUI/MATLAB)

GHOURAF Djamel Eddine

Department of Electrical Engineering University of SBA
IRECOM Laboratory
BP 98 22000 Algeria
E-mail: jamelbel22@yahoo.fr

KABI Wahiba

Department of Electrical Engineering University of SBA
IRECOM Laboratory
BP 98 22000 Algeria
E-mail: gh.mohamed22@gmail.com

NACERI Abdellatif

Department of Electrical Engineering University of SBA
IRECOM Laboratory
BP 98 22000 Algeria
E-mail : abdnaceri@gmail.com

HORCH Abdessamed

Department of Electrical Engineering University of SBA
IRECOM Laboratory
BP 98 22000 Algeria

Abstract— This paper presents the use of genetic algorithms (GA) to synthesize the optimal parameters of Power System Stabilizer (PSS), this later is used as auxiliary of turbo generator excitation system in order to damp electro mechanicals oscillations of the rotor (inductor), and consequently, improve the Electro Energetic System (EES). In this study, we started with the linearization of a system around the operating point, then, we analyzed its stability in slight movement, after that, we have optimized the PSS parameters using the Genetic Algorithms (G.A). The obtained results have proved that (G.A) are a powerful tools for optimizing the PSS parameters, and more robustness for the studied PS. Our present study was performed using a GUI realized under MATLAB in our work.

Keywords— AVR-PSS, Electric power system, genetic algorithm, GUI-MATLAB, powerful synchronous generators, stability and robustness.

I. INTRODUCTION

The electric power system (EPS) stability is viewed as the most necessary condition to regular operating electrical network control systems are required to ensure this stability by identifying the main factors that influence on this one. The Classical controllers AVR and PSS [1,2] (PI or PID) have a leading role in increasing static and dynamic stability degree, and damping electro mechanicals oscillations generated by the rotor (the inductor). However, a robustness test (a disturbance injected on the EPS) showed that PID-AVR and PSS are hardly robust, so, in order to improve their efficiency (robustness), we used the (G.A) for the optimization and the adjusting of PSS parameters [3,4].

The genetic algorithms is a global research technical and an optimization procedure based on natural inspired operators such as crossing, and selection [5,6]. Unlike other optimization methods, the (G.A) operate under several encodings parameters (binary, ternary, real...), to be optimized and not the parameters themselves. In addition, to better guide the

AVR-PSS optimal parameters search, the (G.A) use a performed index to approach this solution [6].

II. DYNAMIC POWER SYSTEM MODEL:

In this paper the dynamic model of an IEEE - standard of power system, namely, a single machine connected to an infinite bus system (SMIB) was considered [4]. It consists of a single synchronous generator (turbo-Alternator) connected through a parallel transmission line to a very large network approximated by an infinite bus as shown in figure 1.

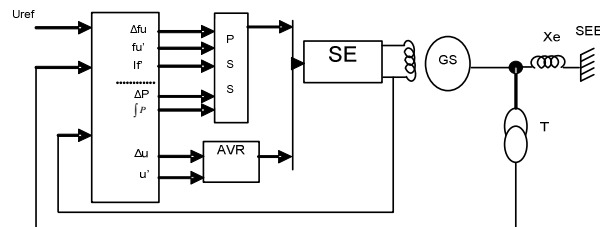


Fig. 1. Standard system IEEE type SMIB with excitation control of powerful synchronous generators

The AVR (Automatic Voltage Regulator), is a controller of the SG voltage that acts to control this voltage, through the exciter. Furthermore, the PSS was developed to absorb the generator output voltage oscillations [5].

In our study the synchronous machine is equipped by a voltage regulator model "IEEE" type - 5 [7, 8], as is shown in Figure 2.

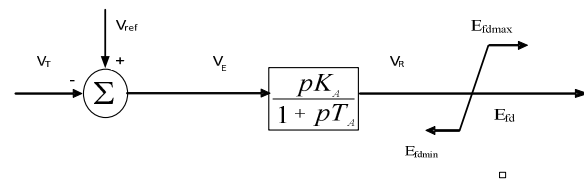


Fig. 2. A simplified "IEEE type-5" AVR

$$V_R = \frac{K_A V_E - V_R}{T_A}, \quad V_E = V_{ref} - V_F \quad (1)$$

About the PSS, considerable's efforts were expended for the developpement of the system. The main function of a PSS is to modulate the SG excitation to [1, 2, 4].

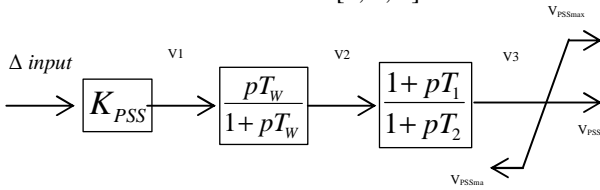


Fig. 3. A functional diagram of the PSS used [8]

In this paper the PSS signal used, is given by:[14]

$$\begin{aligned} \dot{V}_1 &= \frac{V_2 - V_1}{T_1} + \frac{T_2}{T_1} \dot{V}_2; \\ \dot{V}_2 &= \frac{V_3 - V_2}{T_2} + \frac{T_3}{T_2} \dot{V}_3; \\ \dot{V}_3 &= \frac{V_3}{T_w} \dot{V}_1; \quad V_1 = K_{PSS} \Delta input \end{aligned} \quad \Delta input = \begin{cases} \Delta P, \int p \\ \text{or} \\ \Delta \omega = \omega_{mach} - \omega_0 \\ \text{and} \\ \Delta I_f = I_f - I_{f0} \\ \text{and} \\ \Delta U_f = U_f - U_{f0} \end{cases} \quad (2)$$

III. THE GENETICS ALGORITHMS THEORY

A. Introduction

Overall, a Genetic Algorithm handles the potential solutions of a given problem, to achieve the optimum solution, or a solution considered as satisfactory .the algorithm is organized into several steps and works iteratively. The figure 4 shows the most simple genetic algorithm introduced by Holland [6].

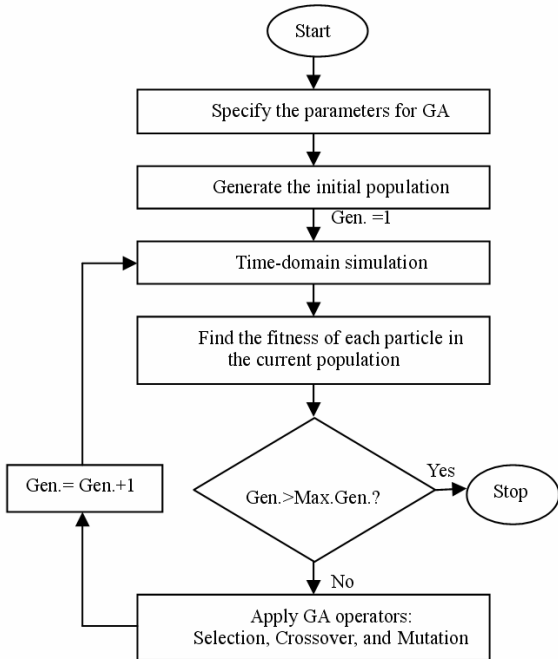


Fig. 4. The genetic algorithm organization

B. The genetic algorithm steps description

In what follows, we will describe in more detail the various steps of a simple genetic algorithm Figure 4

1) Coding and initialization [9]

The first step is the problem parameters coding in order to constitute the chromosomes. The most used type of coding is the binary one, but other coding can be also used for example: ternary, integer, real...the passage from the actual representation to the coded one is done through encoding and decoding functions.

2) Evaluation

It's to measure the performance of each individual in the population; this is done using a function directly related to the objective function which is called "fitness function". This is positive real function that reflects the strength of the individual. An individual with a high fitness value is a good solution to the problem, whereas individual with low fitness value represents a worse solution.

3) Selection

Selection in genetic algorithms plays the same role as natural selection. It follows the survivals Darwinian principle of those most adapted, it decide what are the individuals that survive and which ones disappear ,this selection is according to their fitness functions. a Population called intermediate is then formed by selected individuals.

There are several methods of selection. We mention two of the best known:

- Lottery roulette Méthod ;
- Tournament Method.

4) Crossover

Crossing enables a pair of individuals among those selected, to share their genetic information e. d. their genes. Its principle is simple: two individuals are randomly taken, and they are called "parents", then we draw a random "P" number in the interval [0, 1], after that it will be compared to some crossing probability "Pc".

- If P > Pc, there will be no crossing, and the parents are copied into a new generation.
- If else; P ≤ Pc, crossing occurs and the chromosomes parents are crossed to produce tow children replacing their parents in the next generation.

There are different crossing types, the most known are:

- The multipoint crossover
- The uniforme crossover

5) Mutation

The mutation operator enables to explore new points in the search space and ensures the possibility to leave local optima; mutation applies to each individual gene with a mutation probability (Pm) following the same crossing principle.

- If $P > P_m$, there will be no mutation will and the gene remains as it is.
- If $P \leq P_m$ mutation occurs, and the gene will be replaced with another gene randomly drawn among the possible values. In the case of a binary coding, it is simply to replace a "0" by a "1" and vice versa.

6) *Terminaison criteria*

As in any iterative algorithm, we must define a stopping criteria, this can be formulated in various ways, among which we can mention:

- Stop the algorithm when the result reached a satisfactory solution;
- Stop if there is no improvement for some number of generations;
- Stop if a certain number of generations is exceeded.

Example:

We consider the simple case of function with one variable "x" belonging to the natural numbers set:

Maximise $F_{obj} = 15x - x$
 Subject to $0 < x \leq 15$

The used parameters:

- A 8 bits binary encoding ;
- The search interval [0,15] ;
- A Lottery roulette Method;
- A simple crossing (to one point),with crossing probability $P_c=0.7$;
- A mutation probability $P_m=0.1$.

To run and view the various steps of genetic algorithm, we created and developed a "GUI" (Graphical User Interfaces) in MATLAB software, this latter allows:

- To calculate and display the AG operations (Coding and initialization, Evaluation, Selection, Crossing and mutation);
- To display graphically the problem solution, as is shown in figure 5.

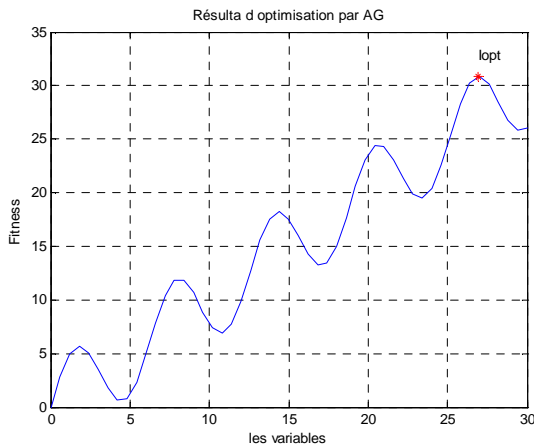


Fig. 5. Optimization result by AG

The problem solution:

$x=26.9412. F(x)=30.8288$

The various operations are developed by the realized "GUI" (shown in figure 6).

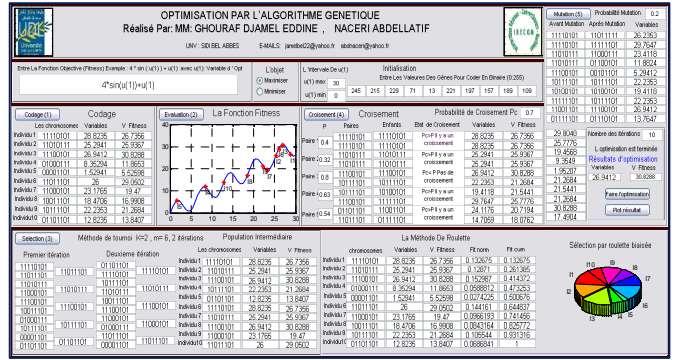


Fig. 6. The genetic algorithm operating developed under GUI / MATLAB

IV. APPLICATION OF THE ALGORITHM GENETIC TO OPTIMEZED AVR-PSS

A) *The Linear System Stability -analytical study*

Recall that the damping factor ζ of method represented by its complex eigenvalue " λ " is given by:

$$\zeta = \frac{-\sigma}{\sqrt{\sigma^2 + \omega^2}} \tag{3}$$

With $\lambda = \sigma \pm j\omega$ (4)

A damping factor ζ leads to a significant well-damped dynamic response, all eigenvalues must be located in the left area of the complex plane defined by two half-lines. For a critical value of the damping factor ζ_{cr} : we impose a relative stability margin [10].

The real part of the eigenvalue σ determines the rapid decay / growth exponential dynamic response of the component system. Thus, σ very negative results in a fast dynamic response. To do this, all the eigenvalues must be located in the left area of the complex plane defined by a vertical through a critical value of the portion real (σ_{cr} : we defined as the absolute stability margin when setting the parameters of PSS, it is desirable that these two criteria are taken into account for proper regulation. The combination between these two criteria leads to an area called D; stability area [11], show in figure 7. Moving eigenvalues in this area ensures robust performance for a large number of points operated [12].

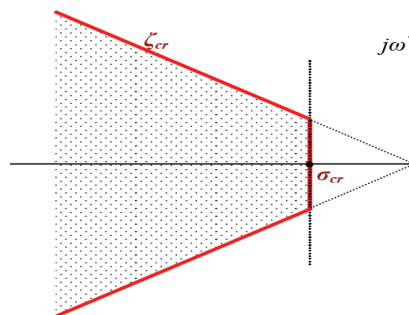


Fig. 7. D. Stability area

B) objective function

The purpose of the PSS use is to ensure satisfactory oscillations damping, and ensure the overall system stability to different operation points. To meet this goal, we using a function composed of two multi-objective functions [13]. This function must maximize the stability margin by increasing damping factors while minimizing the system real eigenvalues . Therefore, all eigenvalues are in the D stability area, the multi-objective function calculating steps are:

- 1-formulate the linear system in an open –loop (without PSS);
- 2-locate the PSS and its parameters initialized by the G.A through an initial population;
- 3- Calculate the closed loop system eigenvalues and take only the dominant modes: $\lambda = \sigma \pm j\omega$
- 4- Find the system eigenvalues real parts (σ) and damping factor ζ ;
- 5- Determine the (ζ) minimum value and the ($-\sigma$) maximum value, which can be formulated respectively as: (minimum (ζ)) and (maximum - (σ));
- 6- Gather both objective functions in a multi-objective function F as follows:
 $F_{obj} = -\max(\sigma) + \min(\zeta)$
- 7- Return this Multi-objective function value the to the AG program to restart a new generation.

Figure 8 shows the proposed in this paper the GA for the AVR-PSS parameters optimization.

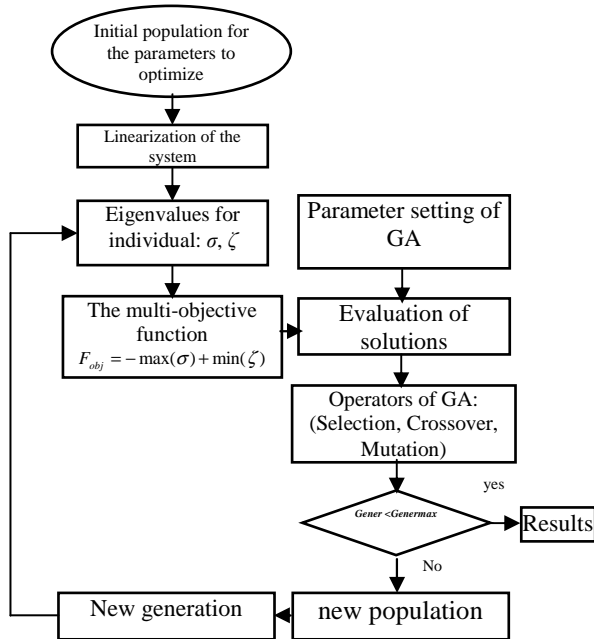


Fig. 8. The multi-objective function and AG program Flowchart for the PSS

Table 1 give a simulation result optimized PSS parameters with different SG

The optimized parameters for PSS are: K_{PSS} , T_w , T_1 , and T_2
 With

- $5 \leq K_{PSS} \leq 150$
- $0.01 \leq T_w \leq 0.05$
- $0.01 \leq T_1 \leq 0.06$
- $0.01 \leq T_2 \leq 0.065$
- Number of Individuals = 120
- Maximum Generation = 100
- A crossing probability $P_c = 0.7$
- A mutation probability $P_m = 0.01$

TABLE I. THE PSS OPTIMIZED PARAMETERS

parameters	TBB-200	TBB-500	BBC-720	TBB-1000
T_w	0.0321	0.029	0.0445	0.0234
T_1	0.054	0.0322	0.0356	0.0214
T_2	0.074	0.011	0.034	0.0142
K_{PSS}	51.43	15.45	100.548	15.506

V. THE SIMULATION RESULT UNDER GUI/ MATLAB

A) Creation of a calculating code under MATLAB / SIMULINK

The “SMIB” system used in our study includes:

- A synchronous generator (SG) ;
- Tow voltage regulators: AVR and AVR-PSS connected to;
- A Power Infinite network line

We used for our simulation in this paper, the SMIB mathematical model based on permeances networks model cullud Park-Gariov [14], and shown in Figure 9 [14].

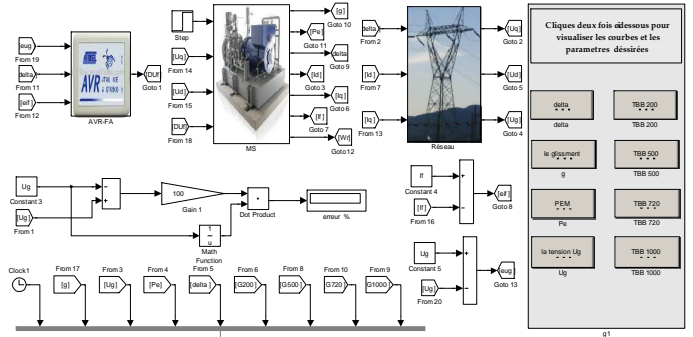


Fig. 9. Structure of the synchronous generator (PARK-GARIOV model) with the excitation controller under [14].

B) A Created GUI/MATLAB Optimization using GA

To analyzed and visualized the different dynamic behaviors we have creating and developing a “GUI” (Graphical User Interfaces) under MATLAB .This GUI allows as to:

- Perform control system from PSS controller;
- To optimized the controller parameters by Genetic Algorithm;
- View the system regulation results and simulation;

- Calculate the system dynamic parameters ;
- Test the system stability and robustness;
- Study the different operating regime (under-excited, rated and over excited regime).

The different operations are performed from GUI realized under MATLAB and shown in Figure 10.

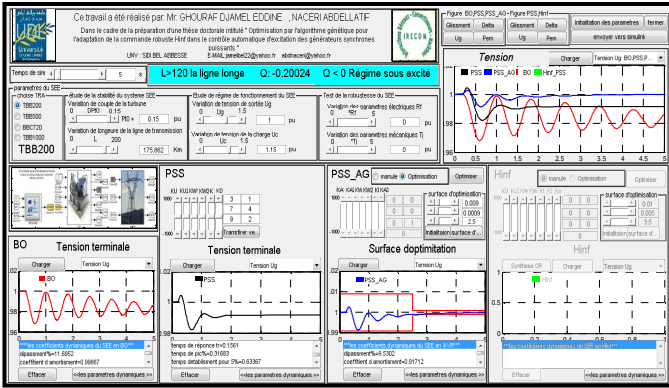


Fig. 10. The realised GUI / MATLAB

C) Simulation result and discussion

The following results (Table 2 and Figure 11, 12) were obtained by studying the “SMIB” static and dynamic performances in the following cases:

1. SMIB in open loop (without regulation) (OL)
2. Closed Loop System with the regulator AVR and conventional stabilizer PSS-FA [14].
- 3 - Optimization of Regulators PSS-AVR using genetic algorithm (PSS-OPT) parameters.

We simulated three operating: the under-excited, the rated and the over-excited.

Our study is interested in the Powerful Synchronous Generators of type: TBB-200, TBB-500 BBC-720, TBB-1000 (parameters in Appendix 2) [14].

Table 2 shows the dominant modes eigenvalues , for more details about the calculating parameters see GUI-MATLAB in the Appendix 3 created.

Table 3 presents the TBB -200 static and dynamic performances results in (OL) and (CL) with PSS and PSS-optimized, for an average line ($X_e = 0.3$ pu), and an active power $P=0.85$ p.u.

Where: α : Damping coefficient ε %: the static error, $d\%$: the maximum overshoot, t_s : the setting time

TABLE II. THE EIGENVALUES OFF THIS SYSTEM

eigenvalues			
Q	λ OL	λ PSS	λ PSS-OPT
-0.1372	instable	-1.6201 ± 4.3629i	-2.3283 ± 3.3747i
-0.4571	instable	-1.6503 ± 4.3582i	-2.3463 ± 3.9866i
0.1896	-0.0813 ± 7.2567i	-1.6865 ± 5.2802i	-2.3906 ± 2.9698i
0.3908	-0.1271 ± 7.9143i	-1.5379 ± 5.9476i	-2.3906 ± 2.9698i
0.5078	-0.1451 ± 8.2203i	-0.9432 ± 5.0531i	-1.9582 ± 3.2602i
0.6356	-0.1588 ± 8.5134i	-0.9283 ± 5.3747i	-1.9803 ± 3.5921i

TABLE III. THE “SMIB “STATIC AND DYNAMIC PERFORMANCES

Damping coefficient α					the static error			
Q	OL	AVR	PSS	PSS-OPT	OL	AVR	PSS	PSS-GA
-0.1372	Unstable	-0.709	-1.6201	-2.3283	instable	-2.640	-1.620	-1.234
-0.4571	Unstable	-0.708	-1.6503	-2.3463	instable	-2.673	-1.629	-1.241
0.1896	-0.0813	-0.791	-1.6865	-2.3906	-5.038	-2.269	-1.487	-1.267
0.3908	-0.1271	-0.634	-1.5379	-2.3906	-5.202	-1.807	-1.235	-1.129
0.5078	-0.1451	-0.403	-0.9432	-1.9582	-3.777	-0.933	-0.687	-0.604
0.6356	-0.1588	-0.396	-0.9283	-1.9803	-3.597	-0.900	-0.656	-0.567
the setting time for 5%					the maximum overshoot %			
Q	OL	AVR	PSS	PSS-OPT	OL	AVR	PSS	PSS-GA
-0.1372	Unstable	4,231	1,704	1,349	9,572	9,053	7,892	7,237
-0.4571	Unstable	4,237	1,713	1,323	9,487	9,036	7,847	7,219
0.1896	-	3,793	1,617	1,408	10,959	9,447	8,314	7,928
0.3908	-	4,732	1,706	1,630	10,564	8,778	7,883	7,659
0.5078	14,320	7,444	2,041	1,877	9,402	6,851	6,588	6,269
0.6356	14,423	7,576	2,080	1,801	9,335	6,732	6,463	6,012

In the Figures 11 and 12 show an example of simulation result with respectively 'Ug' the stator terminal voltage; 'Pe' the electromagnetic power system, 's' variable speed, 'delta' The internal angle TBB200 of Turbo-generator with $P = 0.85$, $X_e = 0.5$, $Q1 = -0.1372$ (pu)

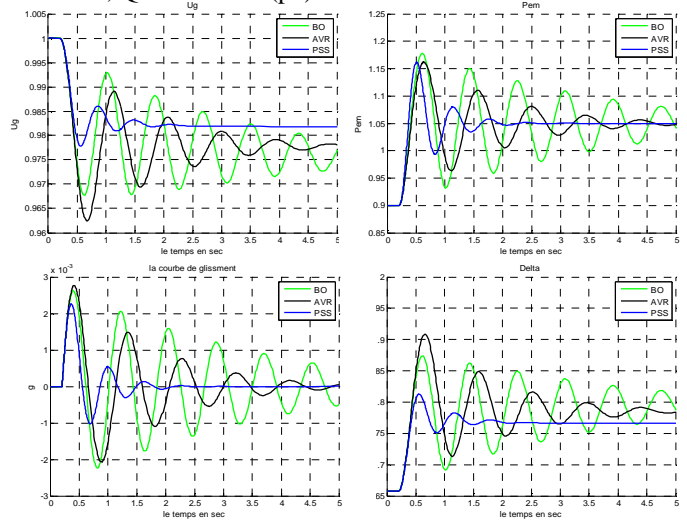


Fig. 11. functioning system in the under-excited of TBB 200 connected to a long line with AVR ,OL and PSS

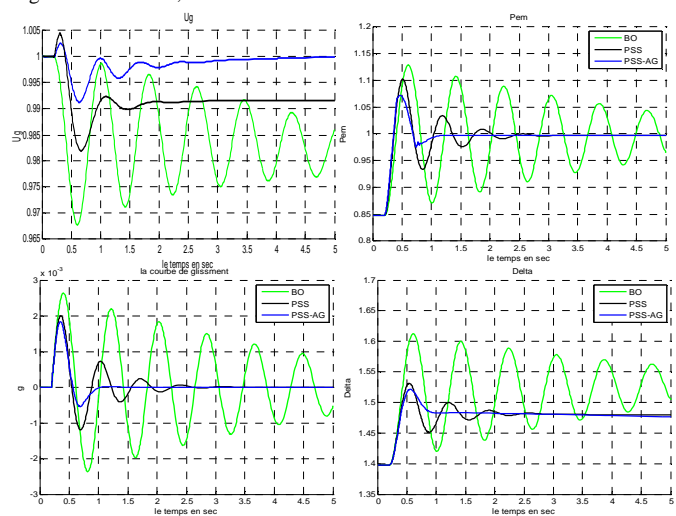


Fig. 12. functioning system in the under-excited used of TBB 200 connected to a long line with PSS , PSS- AG and OL

From the simulation results, it can be observed that the use of PSS optimized by AG improves considerably the dynamic performances (static errors negligible so better precision, and very short setting time so very fast system., and we found that after few oscillations, the system returns to its equilibrium state even in critical situations (specially the under-excited regime) and granted the stability and the robustness of the studied system.

VI. CONCLUSION

In this article, we have optimized the PSS parameters by genetic algorithms; these optimized PSS are used for powerful synchronous generators exciter voltage control in order to improve static and dynamic performances of power system.

This technique (GA) allows us to obtain a considerable improvement in dynamic performances and robustness stability of the SMIB studied.

All results are obtained by using our created GUI/MATLAB.

REFERENCES

[1] LA. GROUZDEV, A.A. STARODEBSEV, S.M. OUSTINOV "Conditions d'application des meilleurs amortissements des processus transitoires dans les systèmes énergétiques avec optimisation numérique des paramètres du régulateur AVR-FA" Energie -1990-N°11-pp.21-25 (traduit du russe).

[2] DeMello F.P., Flannett L.N. and Undrill J.M., « Practical approach to supplementary stabilizing from accelerating power », *IEEE Trans.*, vol. PAS-97, pp. 1515-1522, 1978.

[3] Demello F.P. and Concordia C., « Concepts of synchronous machine stability as affected by excitation control », *IEEE Trans. on PAS*, vol. PAS-88, pp. 316–329, 1969.

[4] S. V. SMOLOVIK "Méthodes de modélisation mathématique des processus transitoires des générateurs synchrones plus usuels et non traditionnels dans les systèmes électro -énergétiques"Thèse doctorat d'état, Institut polytechnique de Leningrad, 1988 (traduit du Russe).

[5] P. KUNDUR, "Definition and Classification of power System Stability", Draft 2, 14 January,2002

[6] J.H. Holland, Adaptation in Natural and Artificial Systems, University of Michigan Press, 1975.

[7] P.M. ANDERSON, A. A. FOUAD "Power System control and Stability", IEE Press, 1991.

[8] Hong Y.Y. and Wu W.C., « A new approach using optimization for tuning parameters of power system stabilizers », *IEEE Transactions on Energy Conversion*, vol. 14, n°. 3, pp. 780–786, Sept. 1999.

[9] R. Asgharian "Asymptomatic approach to performance weights sélection in design of robust H ∞ PSS using genetic algorithms", *IEEE trans. on EC*, vol 11, No 21, September 1996, pp.111-11

[10] Allenbach J.M., Systèmes Asservis, Volume 1, Asservissements linéaires classiques, Ecole d'Ingénieurs de Genève, 2005.

[11] Yee S.K. and Milanović J.V., « Comparison of the optimisation and linear sequential method for tuning of multiple PSSs ». *IEEE Power Engineering Society, General Meeting Denver*, CO, June, 2004.

[12] Singh R., A Novel Approach for Tuning of Power System Stabilizer Using Genetic Algorithm, Ph.D. Thesis, Faculty of Engineering, Indian Institute of Science, Bangalore, July 2004.

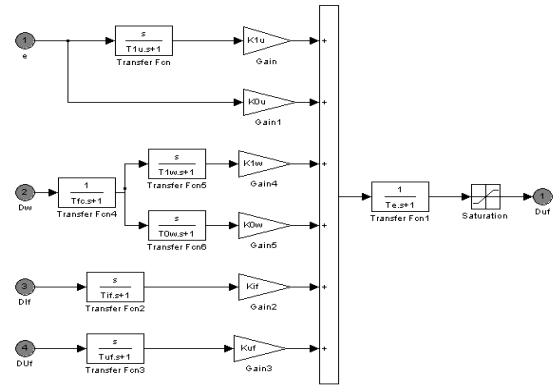
[13] Hasan ALKHATIB "ETUDE DE LA STABILITE AUX PETITES PERTURBATIONS DANS LES GRANDS RESEAUX ELECTRIQUES : OPTIMISATION DE LA REGULATION PAR UNE METHODE METAHEURISTIQUE" Thèse doctorat d'état, UNIVERSITE PAUL CEZANNE D' AIX-MARSEILLE, 2008 .

[14] GHOURAF.D.E"Exploitation des techniques fréquentielles avancées dans le contrôle automatique d'excitation des machines synchrones"

mémoire Magister ETT, op. convertisseur électromécanique, Dept. ETT, université SBA, 2009-20110 (Encadré par . Mr. NACERI).

APPENDIX

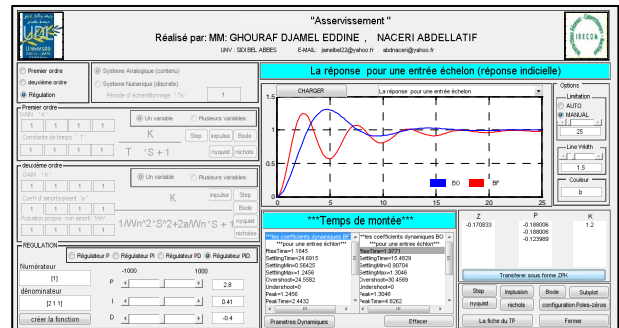
1. The PSS-AVR model



2. Parameters of the used Turbo –Alternators

Parameters	TBB-200	TBB-500	BBC-720	TBB1000	Units of measure
power nominal	200	500	720	1000	MW
Factor of power nominal	0.85	0.85	0.85	0.9	p.u.
X_d	2.56	1.869	2.67	2.35	p.u.
X_q	2.56	1.5	2.535	2.24	p.u.
X_s	0.222	0.194	0.22	0.32	p.u.
X_f	2.458	1.79	2.587	2.173	p.u.
X_{sf}	0.12	.115	0.137	0.143	p.u.
X_{sfd}	0.0996	0.063	0.1114	0.148	p.u.
X_{sf1q}	0.131	0.0407	0.944	0.263	p.u.
X_{sf2q}	0.9415	0.0407	0.104	0.104	p.u.
R_a	0.0055	0.0055	0.0055	0.005	p.u.
R_f	0.000844	0.000844	0.00176	0.00132	p.u.
R_{1d}	0.0481	0.0481	0.003688	0.002	p.u.
R_{1q}	0.061	0.061	0.00277	0.023	p.u.
R_{2q}	0.115	0.115	0.00277	0.023	p.u.

3. Dynamics parameters calculated through GUI-MATLAB



4. Power System model:

Currants equations:

$$I_d = \frac{U_q - E_q''}{X_d'} I_d = -\frac{(U_d - E_d'')}{X_q'} I_f = \frac{(\Phi_f - \Phi_{ad})}{X_{sr}}$$

$$I_{1d} = \frac{(\Phi_{1d} - \Phi_{ad})}{X_{sr1d}} I_{1q} = \frac{(\Phi_{1q} - \Phi_{aq})}{X_{sr1q}} I_{2q} = \frac{(\Phi_{2q} - \Phi_{aq})}{X_{sr2q}}$$

$$E_q'' = \frac{1/X_{sf}' \cdot \frac{X_f}{X_{ad}} E_q' + 1/X_{sfd}' \cdot \frac{X_{fd}}{X_{ad}} E_{fj}'}{\frac{1}{X_{ad}} + \frac{1}{X_{sf}'} + \frac{1}{X_{sfd}'}} E_d'' = \frac{1/X_{sfq}' \cdot \frac{X_{fq}}{X_{aq}} E_{fd}'}{\frac{1}{X_{ad}} + \frac{1}{X_{sfq}'}}$$

Flow equations:

$$\Phi_{ad} = E_q'' + (X_d' - X_s) I_d ; \Phi_{aq} = E_d'' + (X_q'' - X_s) I_q$$

$$\Phi_{1q} = \omega_s \int_0^{\Phi_{1q}} (-R_{1q} I_{1q}) dt \quad \Phi_{2q} = \omega_s \int_0^{\Phi_{2q}} (-R_{2q} I_{2q}) dt$$

$$\Phi_f = \omega_s \int_0^{\Phi_f} (-R_f I_f + U_{f0}) dt \quad \Phi_{1d} = \omega_s \int_0^{\Phi_{1d}} (-R_{1d} I_{1d}) dt$$

Mechanical equations

$$d\delta = (\omega - \omega_s) dt , \quad s = \frac{\omega - \omega_s}{\omega_s}$$

$$M_T + M_j + M_e = 0 \quad \text{With} \left(M_j = -j \frac{d\omega}{dt} \right)$$

$$T_j \frac{d}{dt} s + (\Phi_{ad} \cdot I_q - \Phi_{aq} \cdot I_d) = M_T \quad \text{ou} \quad T_j \frac{d}{dt} s = M_T - M_e$$

Energy efficiency potential assessment and ranking for schools in Teresina City

YAMAKAWA E.K., AOKI, A.R., SIEBERT L.C., SILVA FILHO, J.F., LOPES, J.B., and LOPES, W.G.R.

Abstract— In this article it is described the field research for twenty one schools in Teresina City in Piauí State in the Northeastern Brazil, the modelling of the school's energy efficiency potential (EEP) assessment system using a Multi Criteria Decision Aid (MCDA) method and the model test through the ranking of the visited schools according to the collected data.

Keywords— Energy efficiency potential, multi criteria decision aid, schools, performance assessment.

I. INTRODUCTION

THIS documents describes the field research for twenty one schools in Teresina City in Piauí State in the Northeastern Brazil, the modelling of the school's energy efficiency potential (EEP) assessment system using a Multi Criteria Decision Aid (MCDA) [3] method and the model test through the ranking of the visited schools according to the collected data. This study will be used to implement an energy efficiency management system for schools and it will allow Eletrobras Piauí State Energy Distribution (EDPI) to know the energy efficiency of the schools placed at Teresina City and check the evolution of energy efficiency at these schools after the implementation of energy efficiency programs to change inefficient equipment and devices for some more efficient ones and after educational actions with the students, teachers and school employees.

Teresina city has high average temperatures mainly from September to December, as it is shown at the Figure 1.

So, it is necessary to have air conditioning throughout the school facilities, specially classrooms and administrative rooms, libraries, laboratories and other spaces where students, teachers and employees have to stay to perform the educational activities. It is also necessary to have refrigeration equipment for food and beverages for conservation and chillers for water.

This work is supported by Eletrobras Piauí State Energy Distribution (EDPI) within the Brazilian Electricity Regulatory Agency (ANEEL) Research and Development Program. This R&D project started in September 2012 and it will finish in September 2014

E. K. Yamakawa is with Technology Institute for Development – Lactec, Curitiba, PR Brazil phone: +55 41 33616268, fax: +55 41 33616007; e-mail: eduardo@lactec.org.br

L.C. Siebert is with Technology Institute for Development – Lactec; e-mail: luciano.siebert@lactec.org.br

A.R.Aoki is with is with Technology Institute for Development – Lactec and with Federal University of Parana (UFPR); e-mail: aoki@lactec.org.br

J.R. Silva Filho is with Eletrobras Piauí State Energy Distribution (EDPI) and Piauí State Federal Institute (IFPI); e-mail: Joselito@cepisa.com.br

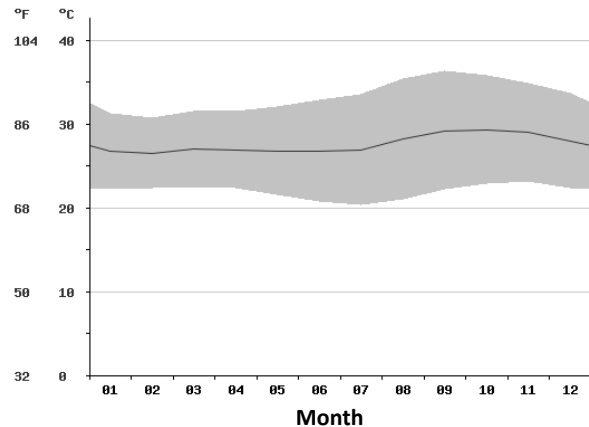


Figure 1: Average temperature at Teresina. Source: [1]

According to [2] energy efficiency is very important in school buildings as it is associated with comfort and air quality conditions in their interior, and energy costs of these buildings are associated with their main operational costs. Moreover, school buildings differ from other types of buildings because they are the places where children are educated and have the opportunity to learn how to become environmentally-aware citizens.

It is shown in [4] that educational buildings such as kindergartens, schools and universities display many similar design, operation and maintenance features in most countries. The two most noteworthy similarities amongst these building types are the high energy consumption and the necessity for retrofitting many buildings within this sector.

A study presented in [5] explains that schools are the most suitable type of building for the application of energy efficiency and good indoor air quality measures. This is justified by the fact that such measures can promote sustainability to the future citizens, and even more, ensure a comfortable and healthy environment for educational purposes.

Some important conclusions are shown in [6] that health and productivity of pupils and teachers is strongly affected by the indoor environmental quality of their school, poor indoor air quality has been reported in published literature, even so for recently constructed school buildings. The same applies for the energy consumption, with large amounts of energy being wasted because no energy saving measures are applied for the operation of schools.

Piauí State, where Teresina City is placed, has the third worse human development index (HDI) and the second highest illiteracy rate in Brazil. So, all the initiatives that can be implemented in schools are very important for the regional development and population life quality.

II. METHOD

First it was elaborated an interview instrument regarding parameters related to energy efficiency such as facilities conditions, opening times, lighting, air conditioning types, high temperature complains, thermal insulation, number of students, teachers and staff, energy consumption as well a description of other important loads. After that, it was randomly selected a sample of twenty one public and private schools, geographically distributed uniformly in Teresina City for the exploratory research. Then, it was performed interviews with school principals using the interview instrument and visited schools facilities to assess the main electrical loads. These data were used to create the energy efficiency indicators, which were used to model the EEP assessment system using MCDA. The methodology process is shown at Figure 2.

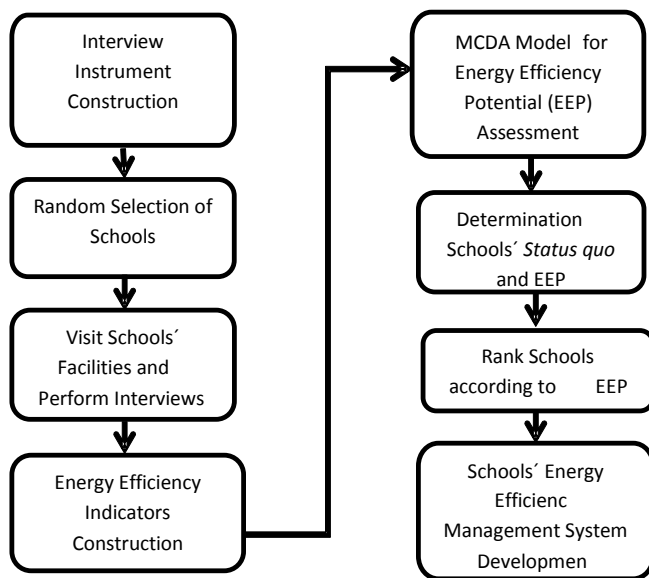


Figure 2: Method process

The indicators used to evaluate the school's EEP are shown below as well as the relation with EEP:

- a. Built area: for this indicator the higher the school's constructed area, the higher the EEP because potentially there will have more loads installed at the facilities;
- b. School age: for this indicator the older the school, the higher EEP because potentially the technology of the installed loads have low efficiency such incandescent lamps, window air conditioning, old refrigerators and freezers, and electrical installation are old with degraded cables, panels and protection devices generating energy losses. The thermal insulation of the classrooms of the old buildings are potentially worse,

where many times the classrooms have no ceiling and windows insulation. The lack of insulation is possible to be observed on Figure 3 and Figure 4.



Figure 3: Walls with holes in a classroom (no thermal insulation)



Figure 4: air conditioning equipment installed in a classroom with open windows

- c. Available area for planting trees: this indicator is not directly related to the energy efficiency but with environmental preservation, that is one of the objectives of energy efficiency, so the larger the area for planting trees, the highest the EEP;
- d. Number of students/number of classrooms: for this indicator the more students per classroom the highest the EEP because if there are more students per classrooms;
- e. Class hours a day, class months a year, class days a week, for these three indicators the objective is to verify the school operation daily, weekly and monthly and the most the school operate, the highest the EEP;
- f. Air conditioning kind and age: for this indicator the new and split air conditioning has the lowest EEP while the old and windows air conditioning has the highest EEP;
- g. Proportion of the school attended by air conditioning: for this indicator the highest the proportion of the school attended by air conditioning the highest the EEP because there are more installed air conditioning equipment and consequently more loads to be regarded and if necessary substituted on a energy efficiency program;

- h. Food and beverage refrigeration existence and age: for this indicator it was evaluated the quantity and the existence of the refrigerators, freezers and water chillers at the visited schools. The highest amount of these kind of loads and the oldest, the highest the EEP.
- i. High temperature complaints by the students, teachers and school employees: this indicator is used to represent the adequacy of the air conditioning equipment and facilities thermal insulation. The levels of temperature complaints were “no complaints”, “a few complaints”, “many complaints” and “chronic complaints”. The highest the complaints level, the highest the EEP.
- j. Illumination kind indoor and outdoor: for this indicator it was verified the kind of lamps like incandescent, tubular fluorescent, compact fluorescent, mercury vapor, sodium vapor, metal halide, and LEDs. The lowest energy efficient the lamps are the highest the EEP.

The indicators were grouped in fundamental point of view (FPV) named Infrastructure, Operations, Air conditioning and Illumination and the related indicators are shown at Figure 5.

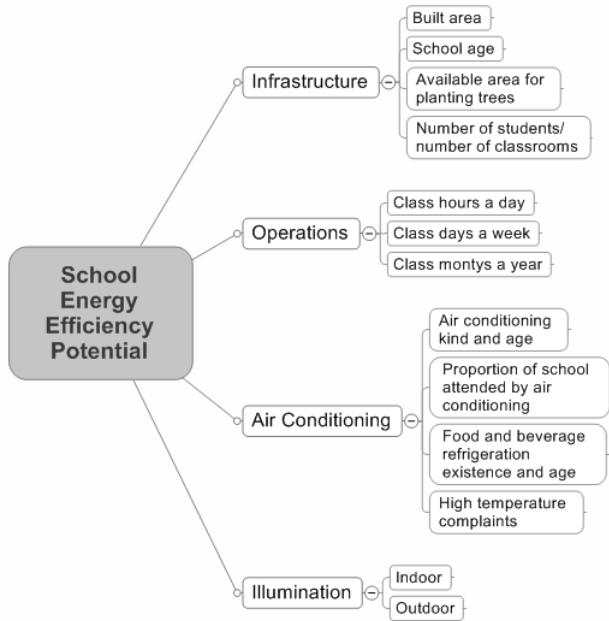


Figure 5: Fundamental point of views and indicators

After the determination of the FPVs it was calculated the weights for indicators and fundamental point of views using the vision of the process decision maker, that in the case of this project is the project manager from Eletrobras Piaui State Energy Distribution (EDPI) and the software Macbeth demo version and the results are shown at Figure 6.

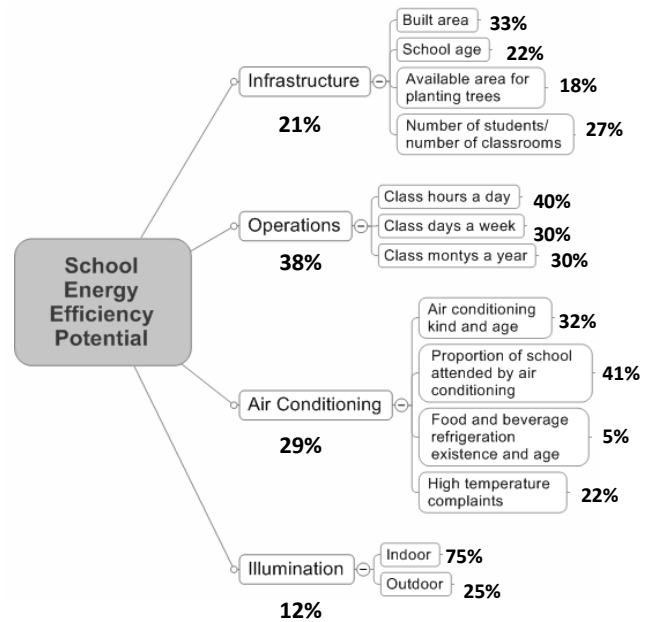


Figure 6: Fundamental point of views and indicators with correspondent weights

The indicators’ scale was transformed from ordinal scale, where the values were related to the indicator itself but had no relation with the other indicators to a cardinal scale, where the indicators had an equivalent scale for all indicators using the Macbeth demo version software, to make it possible to integrate all the indicators in an overall score.

The overall score for each school is given by the equation 1:

$$V(a) = \sum_{j=1}^m w_j \cdot (V_{FPV_j} \cdot (a)) \quad (1)$$

Where:

$V(a)$ is the overall score in terms of energy efficiency potential;

w_j is the weight for the indicators and FPVs

(a) is the impact of (a) in the FPV j

$V_{FPV_j} \cdot (a)$ is the partial value of (a) in the j^{th} FPV

III. RESULTS AND DISCUSSION

After the model creation for EEP using MCDA it was possible to draw the *status quo* of each school using the interviews results and to rank the schools according to the EEP. An example of the status quo for a school is shown at Figure 7.

School 1

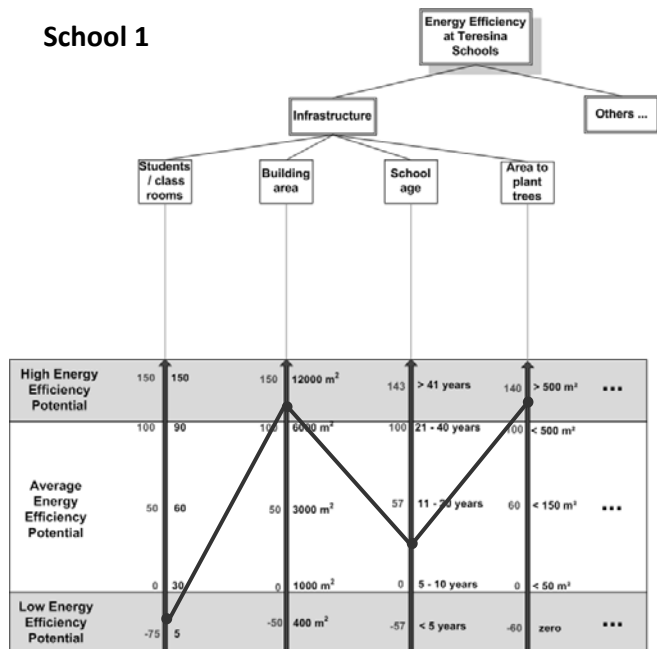


Figure 7: EEP status quo example for a school

After the determination of the *status quo* for the visited schools, it was calculated the EEP score for these schools and rank them according to this score. The ranking of the visited schools is shown at Table 1.

It was possible to observe that the schools with highest EEP have more air conditioning and illumination loads, operated not only during the day but also at night and have activities for the local communities on weekends.

Table 1: EEP ranking for schools

Ranking	School	Score
1	School 1	104,4
2	School 2	99,0
3	School 3	98,1
4	School 4	97,7
5	School 5	92,0
6	School 6	89,3
7	School 7	87,1
8	School 8	82,4
9	School 9	76,9
10	School 10	64,9
11	School 11	63,6
12	School 12	63,0
13	School 13	61,6
14	School 14	58,1
15	School 15	47,8
16	School 16	46,1
17	School 17	40,5
18	School 18	37,5
19	School 19	35,9
20	School 20	33,3
21	School 21	29,2

The complaint about high temperatures was happening in many schools, what is a big problem because it harms the students and teachers performance. It also means that the or

the air conditioning equipment are not effective of there are problems regarding the thermal insulation.

IV. CONCLUSIONS

Data collected in the interviews and site surveys allowed the researchers to know the school operations and main loads, that were very important for the construction of energy efficiency indicators. The energy efficiency management system that is under development in this R&D project will help Eletrobras Piauí State Energy Distribution (EDPI) to direct programs and educational actions to the schools that have the highest potential for energy efficiency, improving not only the energy efficiency of the schools but also the conditions of the classrooms and other school's facilities for the students and teachers.

ACKNOWLEDGMENT

The authors acknowledge Eletrobras Piauí State Energy Distribution (EDPI) and Brazilian Energy Regulatory Agency (ANEEL) for the financial support.

REFERENCES

- [1] Home page of Climate-Data.org available at <http://pt.climate-data.org/location/3935/>. Accessed in December, 10th, 2013.
- [2] A. Dimoudi, P. Kostarela. Energy monitoring and conservation potential in school buildings in the C' climatic zone of Greece. *Renewable Energy* [S.L.], v. 34, n. 1, p. 289-296, 2009..
- [3] C.A. Bana e Costa, L. Ensslin, E.C.Corrêa, J. Vasnick. Decision Support Systems in action: Integrated application in a multicriteria decision aid process. *European Journal of Operational Research* [S.I.], v. 113, n. 2, p. 315-335, 3// 1999.
- [4] H. Erhorn, T. Mroz, O. Morck, F. Schmidt, L. Schoff, K.E.Thomsen. The Energy Concept Adviser—A tool to improve energy efficiency in educational buildings. *Energy and Buildings* [S.I.], v. 40, n. 4, p. 419-428, 2008.
- [5] T.G. Theodosiou, K.T. Ordoumpozanis. Energy, comfort and indoor air quality in nursery and elementary school buildings in the cold climatic zone of Greece. *Energy and Buildings* [S.I.], v. 40, n. 12, p. 2207-2214, 2008.
- [6] E.G. Dascalaki, V.G. Sermepetzoglou. Energy performance and indoor environmental quality in Hellenic schools. *Energy and Buildings* [S.I.], v. 43, n. 2-3, p. 718-727, 2011.

E. K. Yamakawa (M'2012) received his B.S. and M.S. degree in electrical engineering from the Federal University of Parana and currently is pursuing the doctoral degree in industrial engineering at Federal University of Santa Catarina. He is currently a Researcher at Technology Institute for Development (LACTEC) at Power Systems Division. He has more than 10 years of industrial experience in product development for telecommunication equipment and home appliances.

A. R. Aoki (M'2012) received his doctor (2003) and master degree (1999) at the Federal School of Engineering in Itaubá, Brazil. He is a senior researcher at the Institute of Technology for Development (LACTEC), professor at the Federal University of Paraná in Curitiba, Brazil and a committee member of Cigré C6 and IEEE Power & Energy Society. His main research interests are application of intelligent systems for smart grids.

L. C. Siebert is a control systems engineer working as a researcher at the Institute of Technology for Development (LACTEC). He is also a Master student with the Federal University of Paraná in Curitiba, Brazil. His research interests include demand-side management, self-sealing systems, distributed generation and robotics.

J. F. Silva Filho is an electrical engineer at Eletrobras Piauí State Energy Distribution (EDPI) and currently he is the head of Energy Efficiency and R&D department and lecturer at Federal Institute of Piauí State. Also he is currently pursuing the master degree in environment development.

Power Management System in Electro-Solar Vehicle

Hemza SAIDI¹, Abdelhamid MUDOUN²

^{1,2}Electrical Engineering Department, Mohamed Boudiaf University of Science and Technology, Oran, Algeria, e-mail: hamzaing2008@yahoo.fr, ah_midoun@hotmail.com

ABSTRACT

Electric vehicles are ultimately a real answer to current problems related to environmental pollution and noise in cities. In line with current public issues, the electric vehicle is quiet. In addition, it is considered as environmentally friendly since it does not emit CO₂. This paper tries to answer the question 'does solar energy able to compensate fossil energy in the means of land transport? ', and highlight a new approach to improve energy management in a solar car. The global objectives of the energy management system are to guarantee the general power balance, and to get the maximal amount of braking energy. Electric vehicle is a complex assembly that includes various parts like mechanical, electrical, control, pneumatic, electrochemical and management etc... A fully autonomous vehicle in real dimensions was built to implement the new strategy and management control using Matlab/Simulink and electronics compounds.

A prototype electric vehicle was built having reached speed of 100km/h and an autonomy range of 60km with a minimum number of PV module and on-board batteries

Keywords-Solar Car, battery management systems, electric vehicle, hybrid power systems, MPPT, traction power supplies.

1. INTRODUCTION

Algeria is among the first countries producing oil and gas. And that doesn't prevent the government to implement a policy for the development of Renewable Energies (RE) and adopt gradually mix energy. The objective is to attain 40% of its electricity production from renewable energy source, by 2030, according to its international commitments, to protect the planet.

In this context, efforts to improve air quality in heavily populated urban communities- by reducing vehicular emissions - have rekindled interest in the development of electric vehicle technology. To our knowledge until now no electric vehicle is used in Algeria. Fabricate a solar vehicle presents a tremendous engineering challenge requiring the design and the integration of various aspects

of the vehicle as the electric engine, suspensions, the body, the drive train, the fuel system, the electrical systems, and the climate control-chain. All these aspects are time-consuming and costly. The access to energy, the environmental and climate problems, and the need to solve the mobility problems in the cities are all fields in which electric, hybrid and fuel cells vehicles offer a large attractive prototype and necessary solutions.

This paper addresses the design considerations involved in the electric vehicle conversion which includes: removal of internal combustion engine and related parts, choice of electric vehicle components, installation of electric vehicle components, integration of electric vehicle accessory system and design of battery chargers with specific applications to electric vehicles. As the battery is the most important part in an electric vehicle therefore the energy density and the power density are the first battery's parameters to be considered. The power density of proton exchange membrane fuel cells (PEMFC) is significantly higher and it is able to work at ambient temperature. Most of the car companies develop big efforts to integrate the PEM fuel cells in a small part of the car body.

Many solutions regarding friendly alternate vehicles are raised, and the questions regarding practical development of these vehicles owing to their high initial technology development cost. The specialty of these vehicles is they are zero emission vehicles. (Jaegul Lee et al) propose dynamic state, empirical model of energy and power as the state variables derived from electrical behaviour of a lead acid battery system [5].

The empirical model describes the relationship between the total, usable and loss of power and energy under dynamic load conditions. Juan W. Dixon, Micah Ortúzar and Eduardo Wiechmann did work on regenerative braking for an electric vehicle using ultra capacitors [6/7]. (Vidyadhar Gulhane, et al), conclude that the main problems are the poor battery performance, under developed control circuit and inadequate capacity of electric motor to match with the road situation [7].

For the lead-acid batteries used in this work, the energy density is too low to meet the energy requirements when vehicles accelerate, decelerate and brake frequently.

Section II of this paper presents the design environment of the vehicle. **Section III** is devoted to the design of the system. **Sections IV** and **V** present the control and energy management strategy used in the Electro-solar vehicle. Finally, **Section VI** presents a set of simulation results and comments.

Note: During manufacturing, we were constrained to change many parts in the study according to the available means, and that leads to limit the performance. We have to indicate the lack of tools which are necessary to the achievement of our project we need.

2. DESIGN ENVIRONMENT

The urban drive cycle was used as input to represent the road load. Signals of power were passed through the modules. In a mechanical module, the power was the production of torque and rotation speed fig 1. In the electrical module, the power was the production of voltage and current. The reverse simulation showed if the power was transmitted through vehicle module, traction motor module, energy management and control module and battery module. The forward simulation showed if the power was transmitted through the opposite direction.

The road slope torque T is defined by:

$$T_w = \frac{P}{2 \cdot c_w \cdot A \cdot v^2} \tag{1}$$

$$T_R = k_R \cdot m \cdot g \cdot \cos \alpha \tag{2}$$

$$T_A = k_m \cdot m \cdot a \tag{3}$$

$$T_G = m \cdot g \cdot \sin \alpha \tag{4}$$

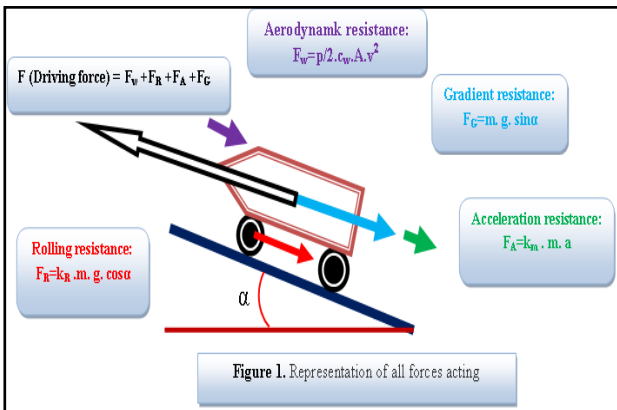
$$T = T_w + T_R + T_A + T_G \tag{5}$$

Where; T_w is aerodynamic torque, T_R : rolling torque, T_A acceleration torque and T_G gradient torque.

Torque evaluation Evaluation of the power flow occurring into a vehicle is in strong relation with his mass and a total couple will be expressed as:

$$C_t = T_A + T_{permanent} \tag{6}$$

Where; m is a vehicle mass, C_t total torque, T_A

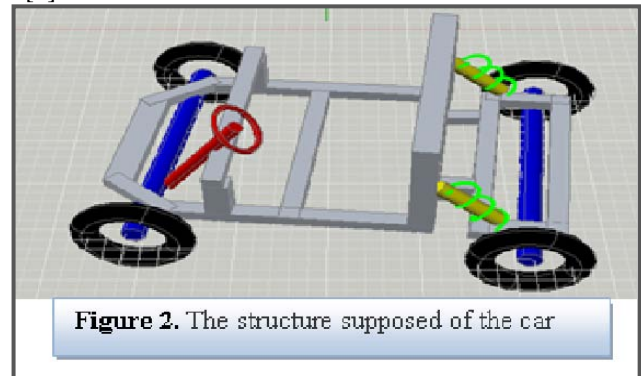


acceleration torque, $T_{permanent}$ permanent torque.

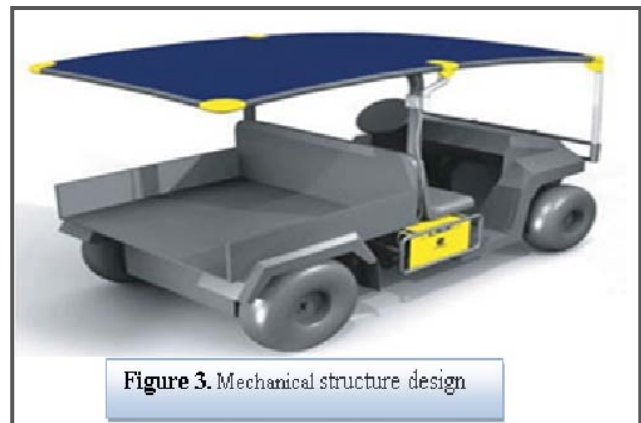
3. SYSTEM DESIGN

The structure of an electro-solar vehicle is a strong evaluating manner because of the more or less rapid but steady evolution of the components technology and performance. As electric vehicles, the different parts are an emerging industry, it is necessary to set time constraints and objectives to be achieved at the level of performance cars, like to improve the acceleration performance of the vehicle. There have been remarkable developments in the area of solar cells and in the development of ultra light weight solar charging battery powered cars. The photovoltaic array could provide a large current in a short time, delivering extra energy to meet the energy requirement when it is needed. In addition, the electronics itself is an important constraint in terms of the shape of the car.

AutoCAD software is used to design the vehicle shape in order to choose the best frame vehicle shape and determining the weak points of the vehicle fig 2, fig 3[8]



The front consists of a suspension system coupled with the vehicle steering system. The suspensions will be considered "double wishbone": they will consist in two triangles, each of them is bound by two hinges one to the frame and the other ball to knuckle. These suspensions are similar to McPherson, often fitted to luxury vehicles or competition one, as they allow an infinite number of



settings positions. The study has been divided into four parts:

- First, the double wishbone system have been designed and studied taking into account the expected load for four people,

then the tendering system management will be discussed, after the complete system will be designed to meet final desired vehicle in terms of safety, functioning, robustness and cost, improvement will be forwarded to the end. The windshield should be made out of a substance with safety in brain.

4. MECHANICAL STRUCTURE DESIGN

This part allowed us to design our vehicle according to standards and technical regulations for Solar Electro Vehicles and the alternative energy imposed by FIA [9] and the equipment available in the market fig4, 5,6,7,8.



Figure 4. The structure of the car industry



Figure5. The first car manufacturer



Figure6. The second car manufacturer



Figure7. Structure of the third car manufacturer



Figure 8. The third car manufacturer

5. ELECTRICAL DESIGN AND CONTROL

In this section all the vehicle elements involved in the energy management will be studied. Management strategies and algorithms will allow us to achieve out a control board, where it will make all the simulations needed for each party. And that, in order to have a reference for comparing the results obtained before and after test operations.

5.1 Solar Cells

The electronic part of this project consist to the objective of the electronic part is the contribution to the optimization of the powering of propulsive parts of the car from batteries powered by photovoltaic panels. Obviously, the major constraint that influenced the treatment of this part came from the settlement of the Solar Challenge of the City; the only source of energy powering the car is solar via battery.

Lead acid batteries called "starters" used in Electro-Solar Vehicle are not well suited to solar energy. In fact, they can be compared to "sprin-ters" to provide common significant start in a very short time (load and rapid discharge). "Solar" battery in turn, rather "Running" will be sought over time to common much lower and the technology is not quite the same (exchange surface

electrolyte / upper electrodes, in particular). Power resources performance at all levels of power; also it will be able to provide the full operation of the battery and motor. We will describe more fully the various bodies in the remainder of this work.

5.2 Influence of Temperature on Cell Efficiency

If the battery is charged directly instead of powering other devices, it is the battery voltage which requires the operation point of the PV panel. The I_{cc} current varies directly with the light radiation (the relationship is proportional) fig 9, the voltage remaining relatively constant. This is interesting, especially for the care of a battery, the temperature also has a significant influence on the characteristics of this panel .When the temperature rises, the voltage decreases and therefore the power too.

Note: that the variation is greater than that provided by simple variation of the exponential. Indeed, the term short circuit current is strongly temperature dependent. The curves in figures 4 and 5 show the drift characteristics this PV panel of crystalline silicon as a function of the temperature.

We see that we move more from an optimal power at 25°C at a deceased power for a temperature 45°C. It is therefore compelled to take into account the temperature of use of the photovoltaic cell in order to apply a reduction coefficient of the optimum at 25°C. Paradoxically, this disadvantage, in very hot climates, becomes an advantage in countries with temperate climate and high brightness fig 10.

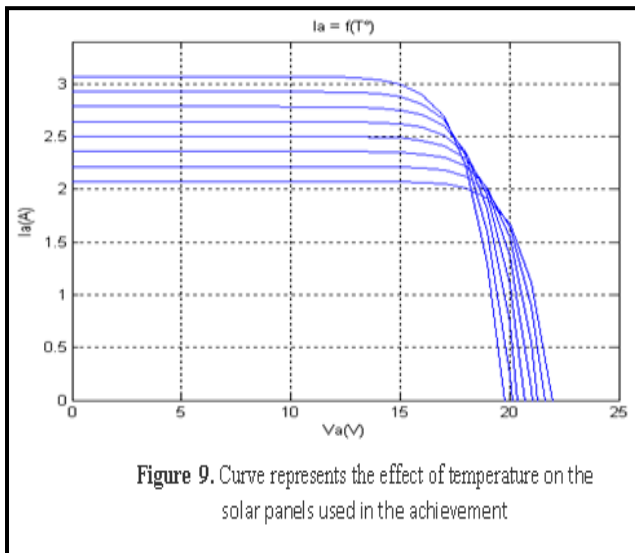


Figure 9. Curve represents the effect of temperature on the solar panels used in the achievement

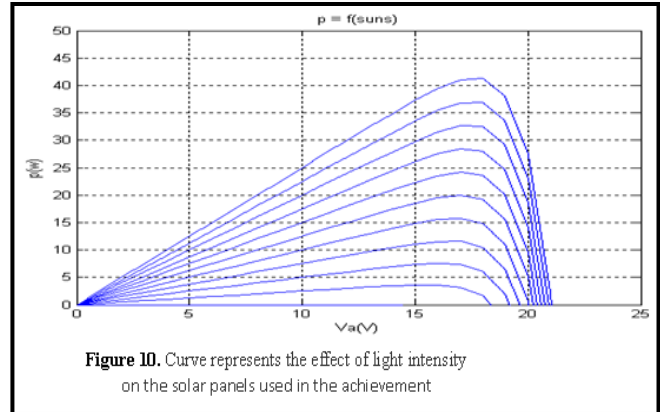


Figure 10. Curve represents the effect of light intensity on the solar panels used in the achievement

5.3 THE SYSTEM DESIGN

Real dimensions of the system are more complex, since there are many additional parameters to consider and many technology choices available. Each step of the design should always seek the best solution and must be performed by considering it with the other steps.

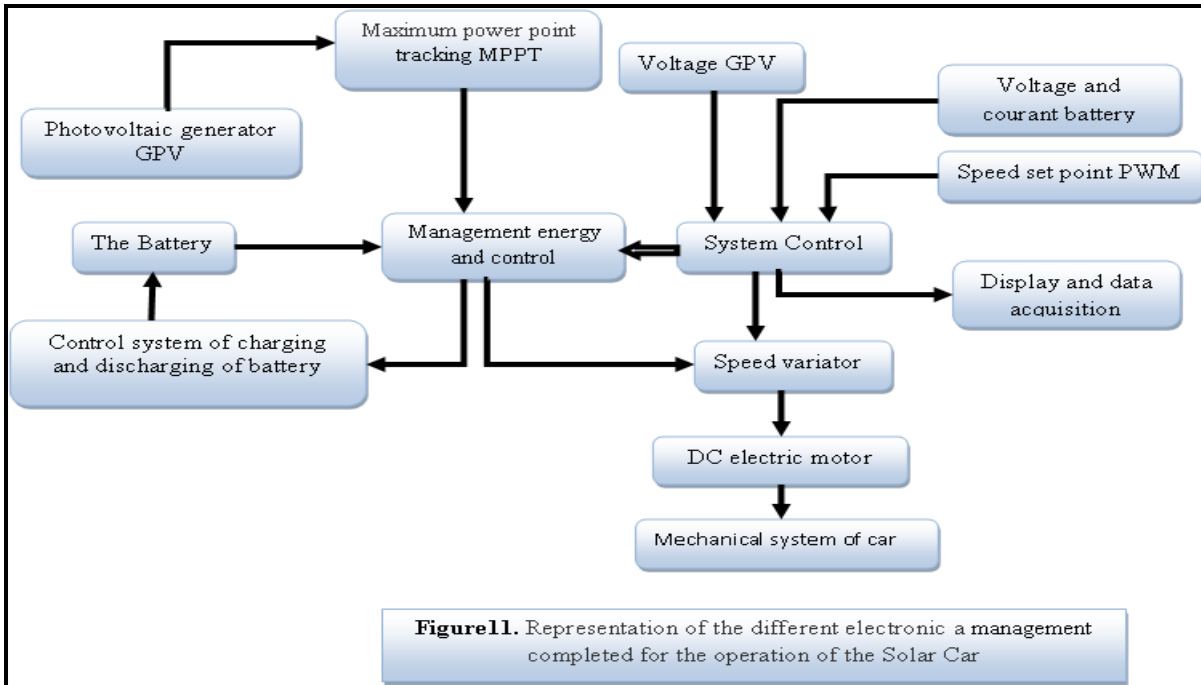
The sizing procedure of the system could be listed as following: Step 1: Identifying the needs: voltage, power and duration of use of equipment ... Step 2: Estimation of solar energy recoverable depending on the location; Step 3: Set the PV module: operating voltage, technology used, total power;

Step 4: Define the capacity and the choice of the battery;

Step 5: Selection of the charge controller; Step 6: Wiring diagram: sections of the cables,...

6. PART ELECTRONICS (PRACTICAL)

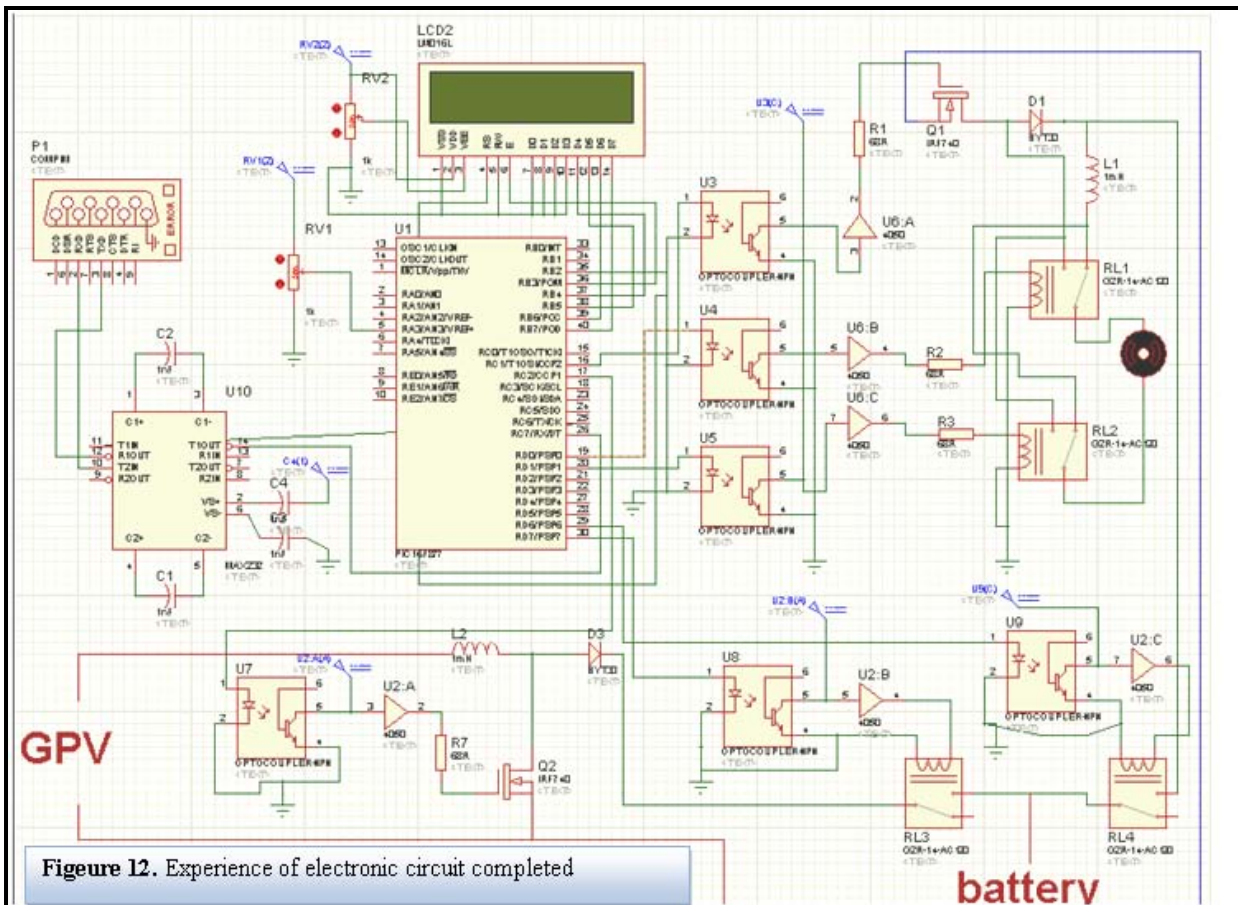
To ensure the effective operation and control of our vehicle, we used all our resources and knowledge. Like all parts of the vehicle fig 11.



6.1

Practical Realization of the Electronics

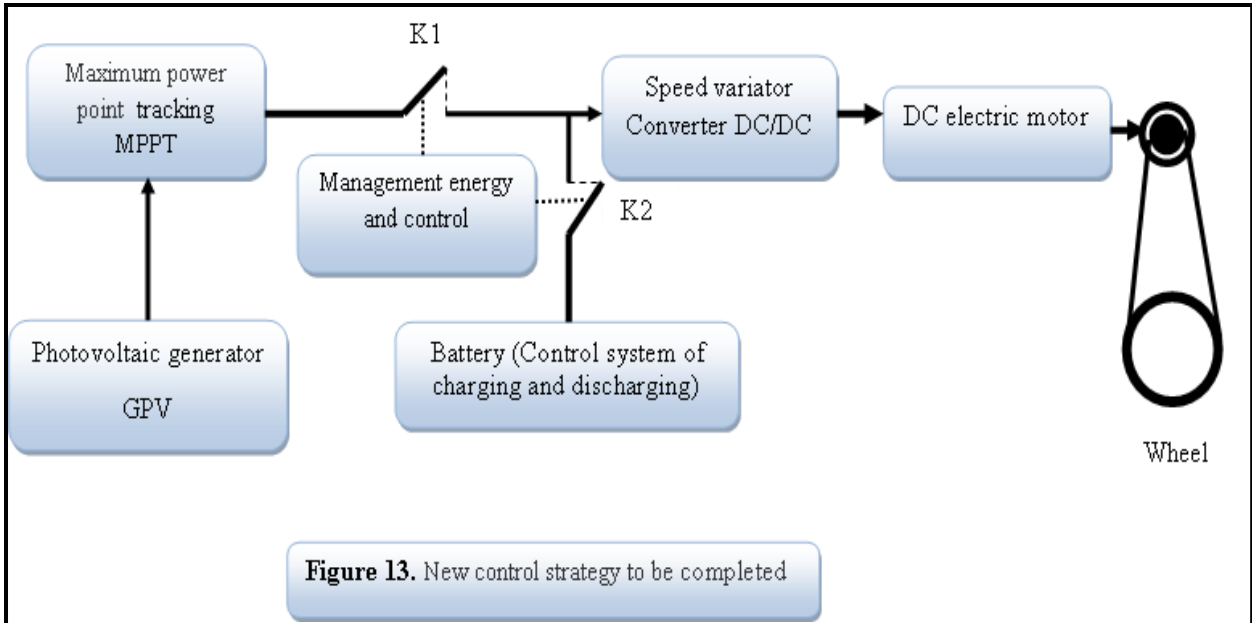
For the implementation, we took into account the synoptic chosen for the desired operation: are related, the failure of one affects all fig12.



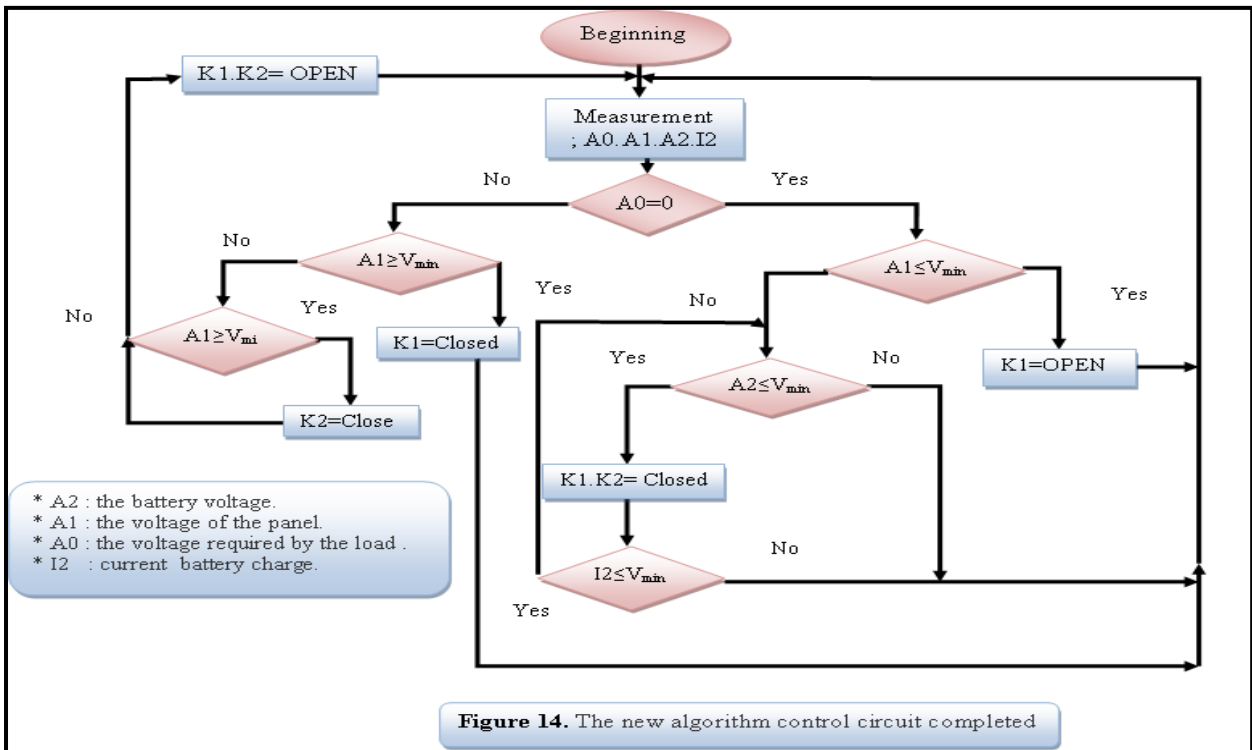
6.2 Operation of Circuit

The vehicle starts with battery mode to provide the current required, after that it rocks to mode panels. Research is going on to develop Brushless DC motor (BLDC motors)

as a prime mover for electric vehicles. These motors possess higher efficiency, lower weight and compact size as compared to others motors fig 13.



The Energy Manager provides load regulation and proper function of the vehicle. The operation manager is described as follows fig 14:



For the proper function of the manager is providing the following algorithm:

- The parameter A2 is the battery voltage;
- The parameter A1 is the voltage of the panel;
- The parameter A0 is the voltage required by the load parameter I2 current battery charge.

6.3 Energy Management of Charge

The energy management strategy aim to full predetermined requirements with no knowledge of future driving conditions. The first step to design the energy management strategy is to find the global strategy

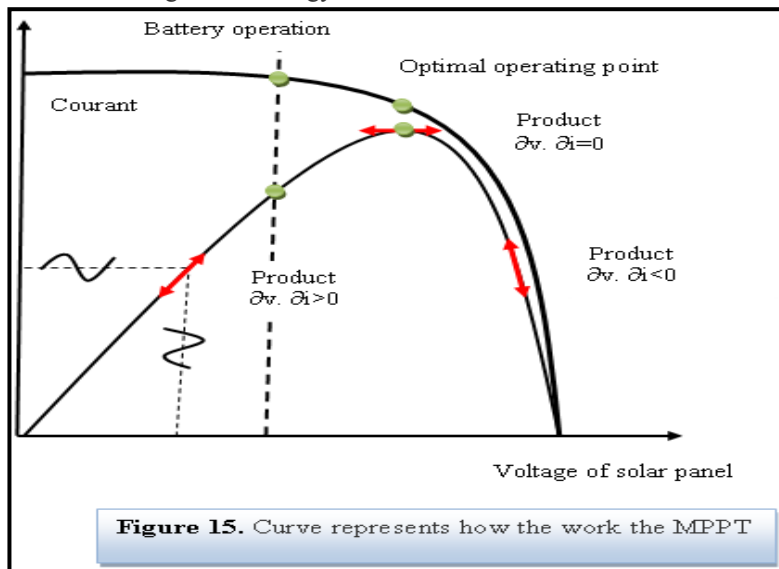
regarding the characteristics and constraints of the vehicle and the hybrid source

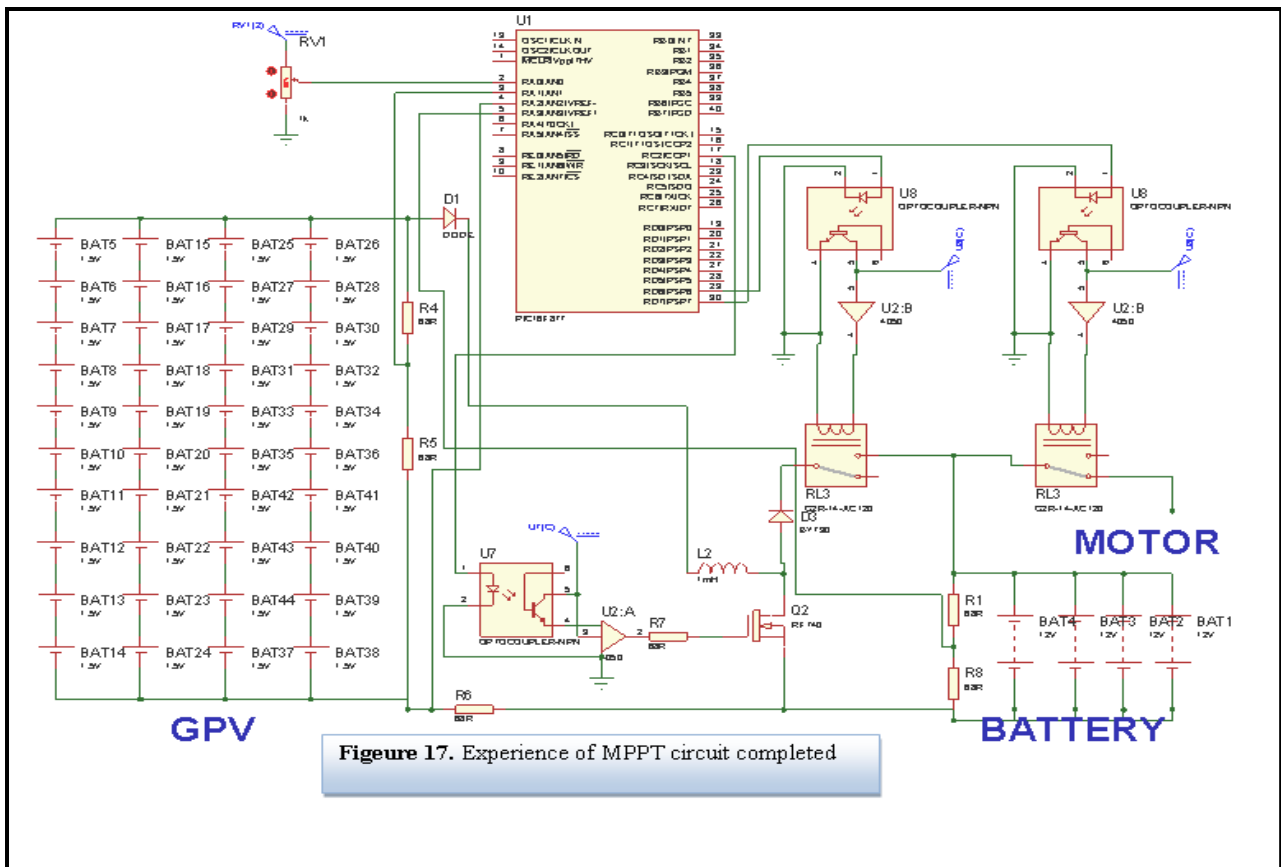
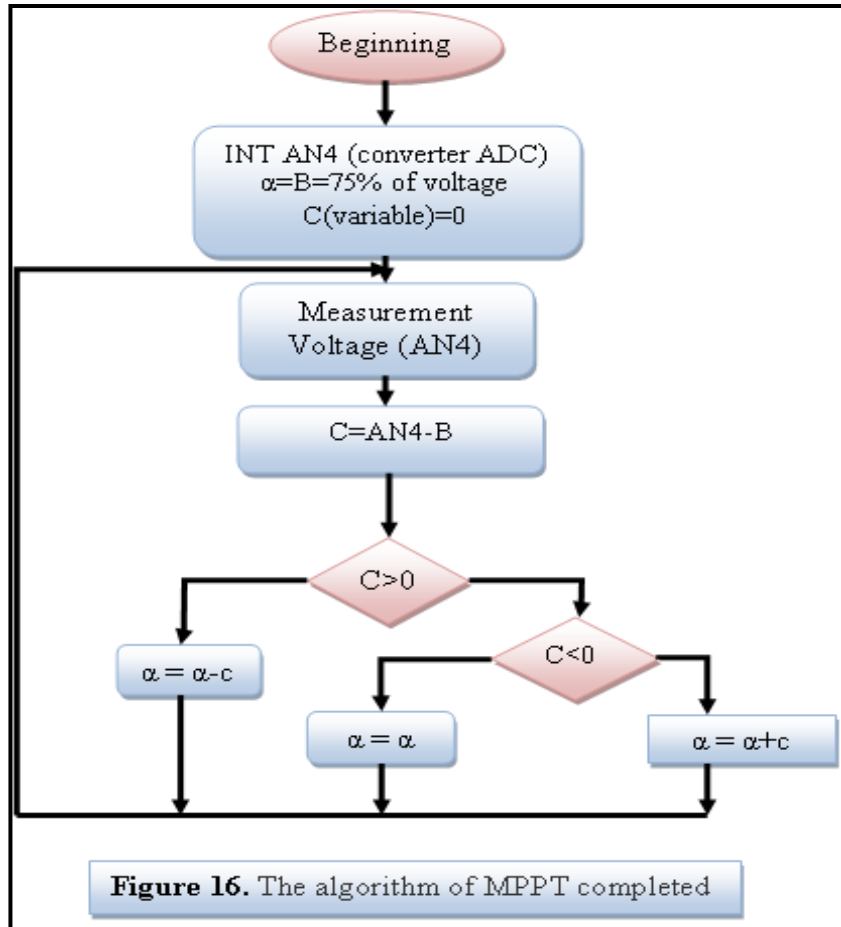
6.4 Mppt

The principle is simple, as we see on the next curve of the characteristic of power, depending on where one is on the curve fig 15, a small voltage change

($dV > 0$) implies either a positive or dI negative, and that's playing on these intensity variations that we will seek to achieve the maximum power point.

For this I have choose the following algorithm for achievement fig 16.





7. EMULATE THE WORK OF THE CAR

In order to study the operation of the car four modes have been considered:

7.1 Case 1 no batteries

we have undertaken this study to see if we can use solar panels as the only source of energy fig 18 as we studied the effect of light intensity on the speed. And in order to show the influence of light on speed fig 19, we have re-

simulated, and this time by using the intensity of light fig 20 constantly changing so the results were expected, where speed is directly related to the strong lighting consequently there was lack of control of the car. Consequently, we reached

the conclusion that we cannot use solar panels as the only source of energy, because to get the speed and capacity required to the work of the car, we need more surfaces of solar panels, which not available in this kind of use.

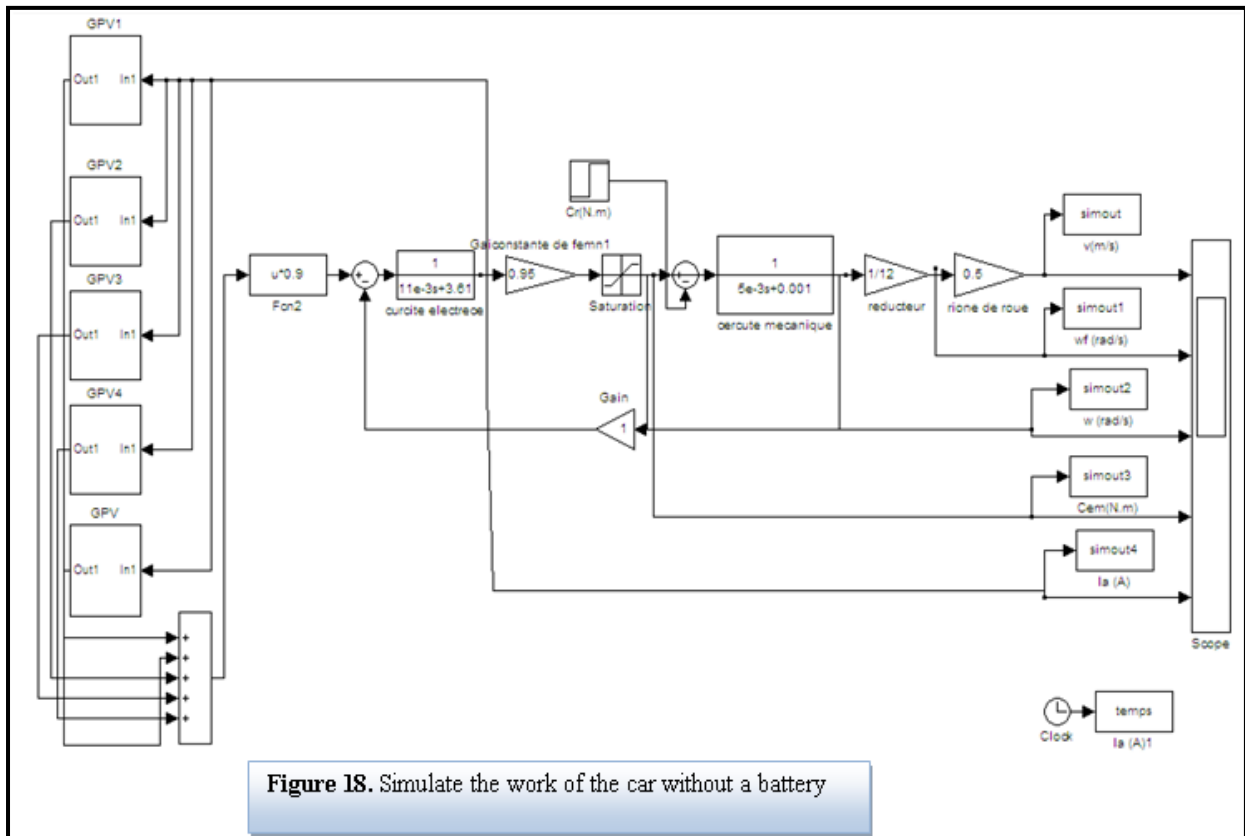


Figure 18. Simulate the work of the car without a battery

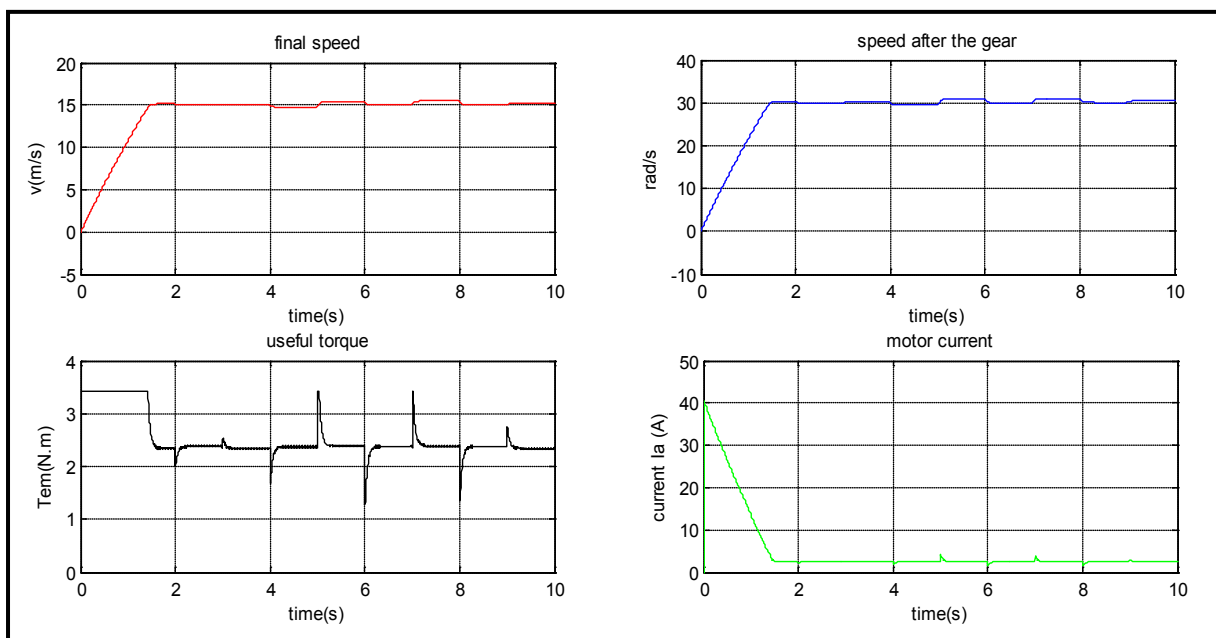


Figure 19 : Case no batteries

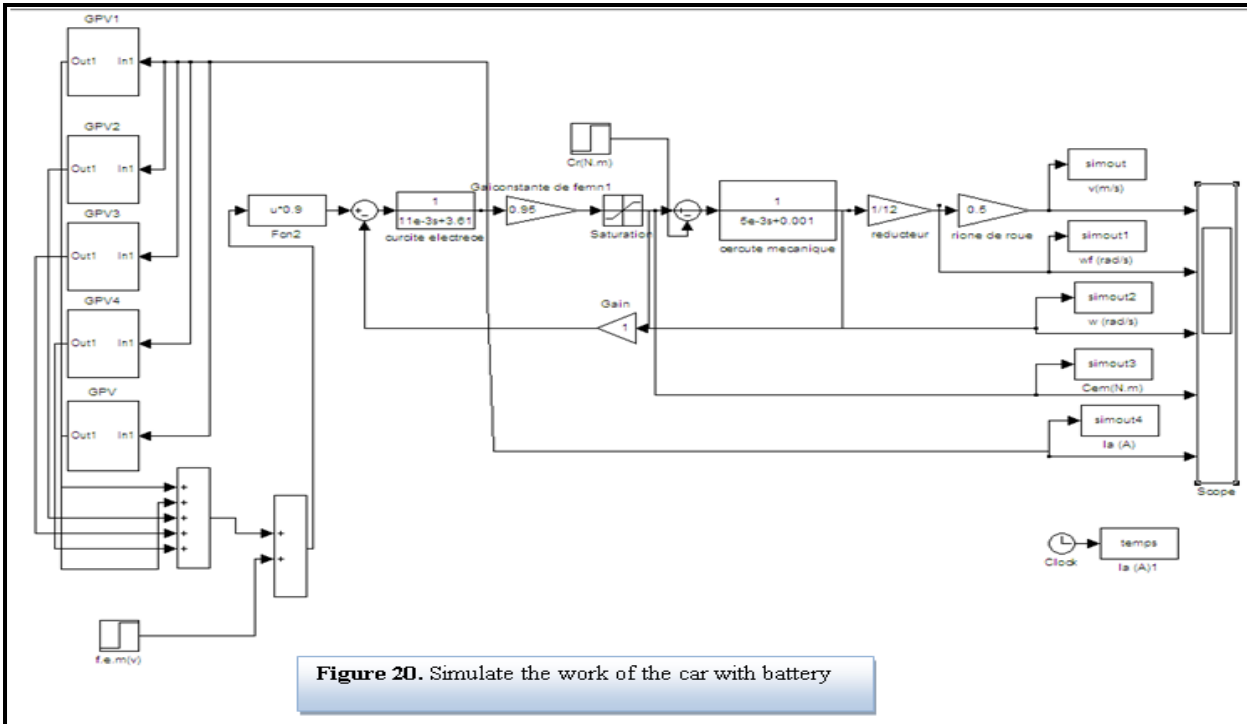


Figure 20. Simulate the work of the car with battery

7.2 Case 2 using the batteries

To solve the problem of changing the speed with changing the climate, we added another source of energy which the batteries fig 21.

Results were that the speed is not related to the climate, to confirm that we did the same simulations again and this time with all the possibilities of function of the car at the same time fig 22.

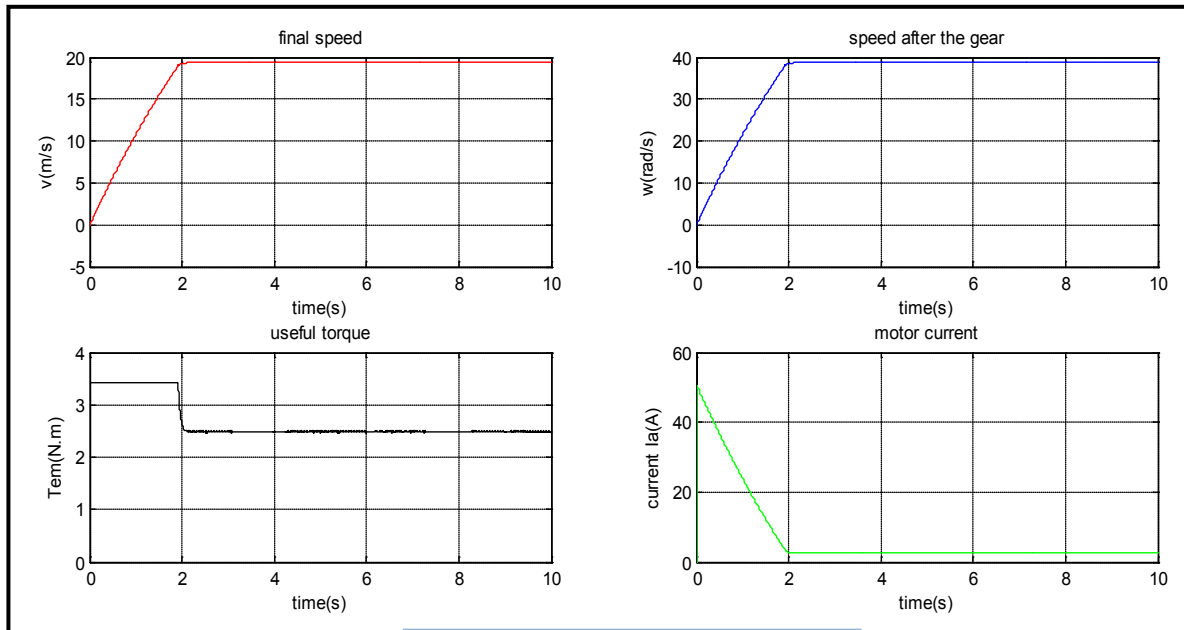


Figure21 : Case no batteries

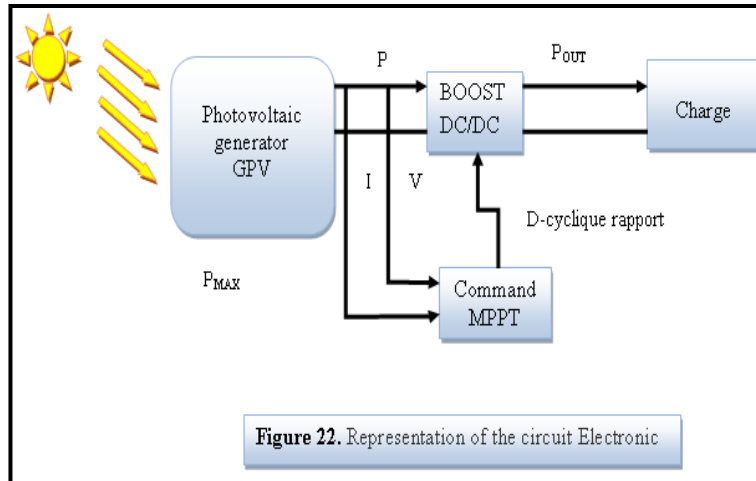


Figure 22. Representation of the circuit Electronic

We noticed that when the car works with batteries it becomes more stable, that the current flowing to the engines is directly related to required speed fig 23.

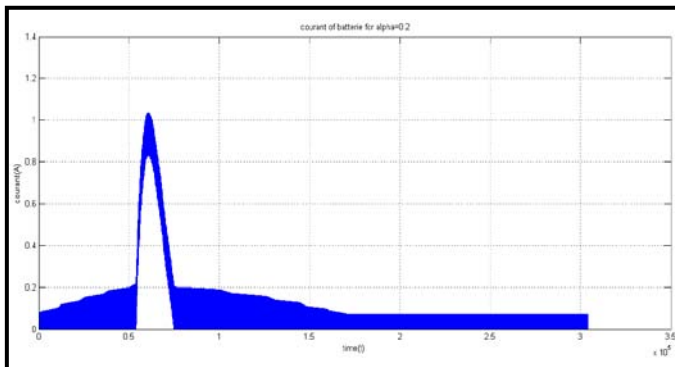


Figure23.Simulationsshow

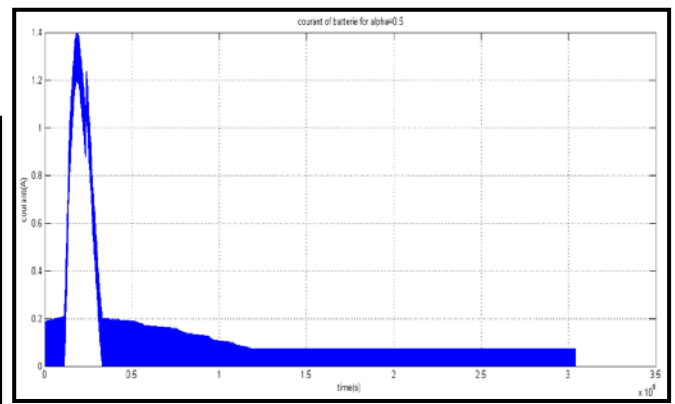


Figure24.Simulationsshowthe courant of the battery for alpha=0.5

7.3 In the case of solar panels and batteries

the situation was more stable, but cannot use this case in the application, because of the difference between the power panels and batteries, according to the total weight, size and maximum speed.

7.4 In the case of solar panels alone

we noticed that the work of the car is related to the factors outside the control, so it cannot be used in practice.

8. SIMULATION OF THE BATTERY CHARGE

This simulation is done by Matlab. We observed the voltage, current, changes in alpha (we took account of all the parameters of the assembly). Simulate the assembly is fig 24:

Notes

we noticed that in all cases the time required to charge the batteries is longer than the duration of the day light fig 25, 26, 27, this stresses that we cannot charge the batteries using the solar panels, and this according to the movement of the car and the charging time, space and the type of solar panels and its output, in relation to each case. In fact there must be another source to charge the batteries and there must be many batteries working in alternation.

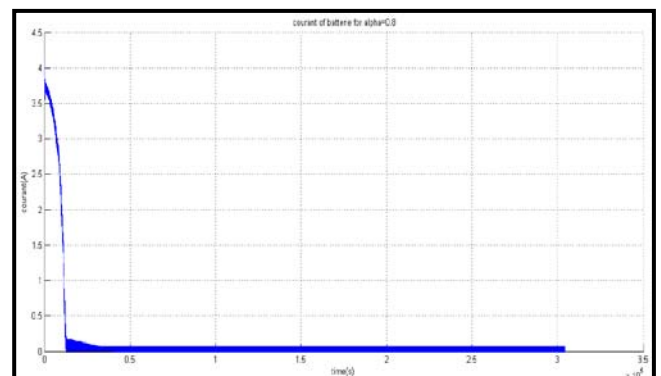


Figure25.Simulationsshowthe courant ofthe batteryfor alpha=0.8

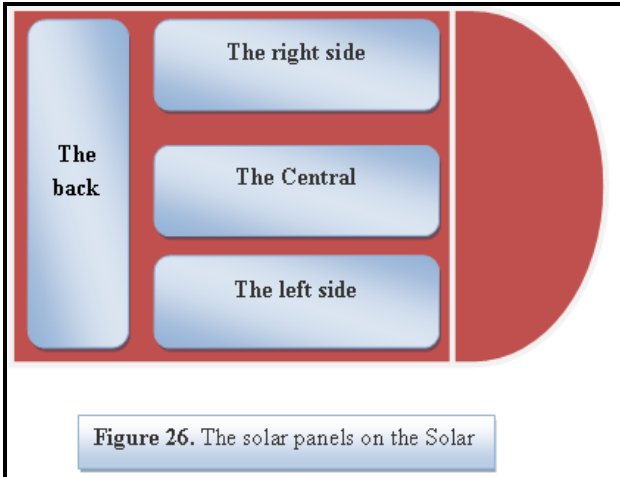


Figure 26. The solar panels on the Solar

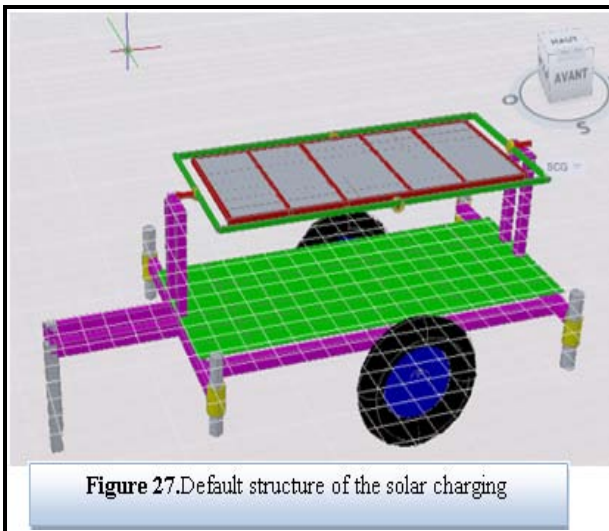


Figure 27. Default structure of the solar charging

9. CLASSIFICATION OF THE VEHICLE ACCORDING TO THE INTERNATIONAL STANDARDS OF THE INTERNATIONAL FEDERATION FOR CARS

We classified our vehicle according to technical criteria for solar power ed vehicles in categories 1 and 4 in the weight class 1 and 8 in the categories of solar electric

propulsion vehicles, and meets the technical regulations of the fourth

10. COMPARISONS WITH OTHER DIRECTORS

If we would like to compare our car with others solar cars, it will better to know even if our car work fully with solar energy. If we look at the cars in the table we note that:

-Engine capacity is greater than the capacity which generate the solar panels, comparing with spacepanels allowed 8 m² (meters square), and the type of panels used.

-In addition to that, the place and the type of the panels does not allow us to use the whole space to produce greater power for energy, because we always have a part which does not produce energy. In the other hand, the solar rays are not perpendicular on the panels, and that decrease its efficiency.

-As well as the battery's type and its capacity; indeed we conclude that the cars are electric -use the batteries to work, the evidence is the total weight and speed and the impossibility to charge the batteries using solar panels only.

-In all cases the time required to charge the batteries is longer than the duration of the day light, this stresses that we cannot charge the batteries using the solar panels, and this according to the movement of the car and the charging time.

Consequently they are not considered as solar cars. And we consider that our results are positive.

11. PROPOSED SOLUTIONS

in order to solve the problems we have the following * the separation of the solar panels from the car and put it in a fixed place fig 29, and make the car work with batteries which, in turn, are charged using solar panels.

For industrialization Follow the following chart fig 30.

This is the unit manufacturer fig 31, 32.

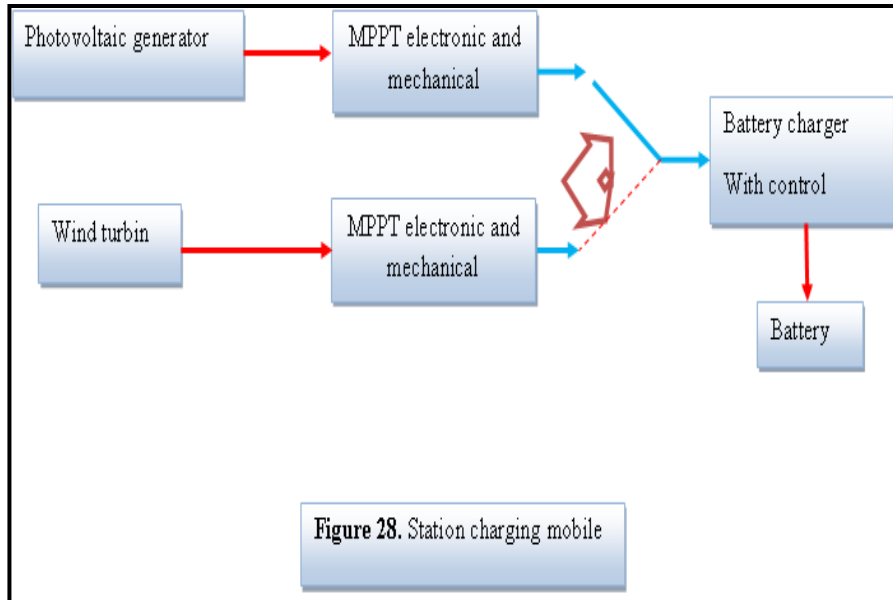
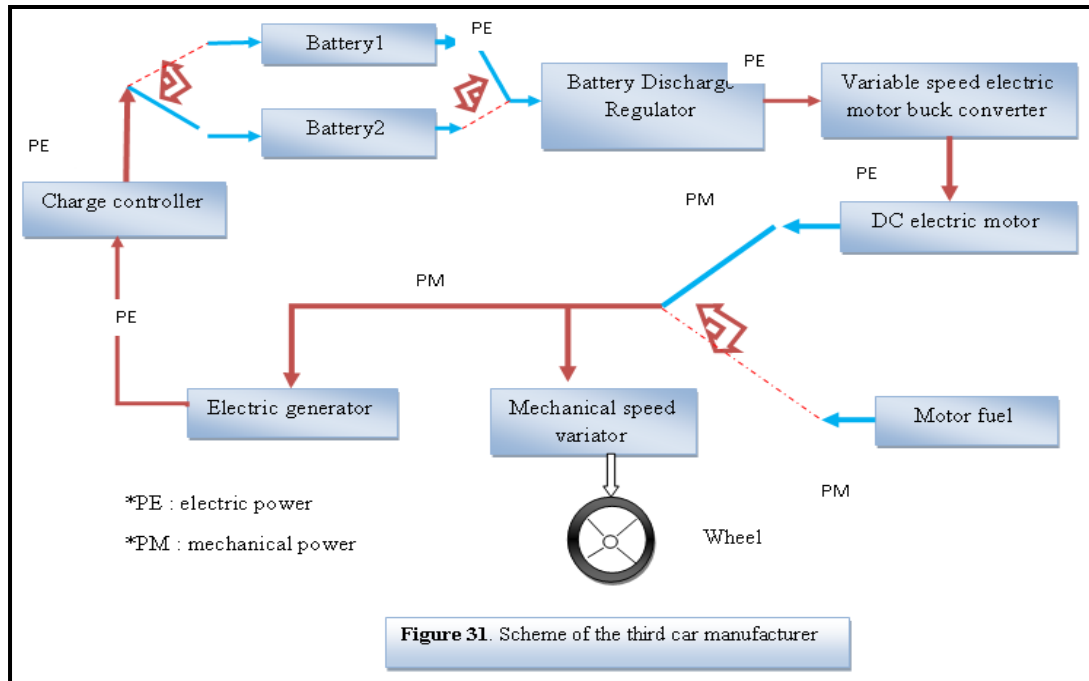


Figure 29. Solar charging unit manufacturer (The front face)



Figure 30. Solar charging unit manufacturer (Back flip)



*As for the time of loading, we've run out of the batteries which are replaced by others charged with solar panels and let the empty to be charged fig 33. The following plans show the mechanism used fig 34.

*We are in the process of experiments in order to replace the batteries by a generator working with the free energy.

12. CONCLUSION

These works aim to design and construct a solar vehicle. This type of engine can be used in open cities (industrial, tourism, golf courses ...). The objective of this work is to achieve a fully autonomous vehicle that is powered by a solar power system equipped with a secondary battery. Our motivations for this project were numerous, but most important was that it is a laboratory for our first confrontation against the design and implementation of such a vehicle.

The implementation of this work needs to study the mechanical and electronic parts; the results obtained are the means for their integration and observation the correlation between them to start up our vehicle. The constraints of this project were numerous. First, it is not easy to build a solar car with little experience; we have established ourselves to achieve a light vehicle and energy optimization. This work was divided into an electronic part and a mechanical part. To do this, we presented the theory, technical problems; the solutions which we thought to solve them, and especially the solutions that we have chosen. But this view was also intended to be reusable, so that our work and our research conserve in the coming years and bring the team to EPES why not win a challenge sun.

A sleek, professional electric vehicle conversion will provide satisfying, economical, and environmentally-friendly transportation.

REFERENCES

- [1] H.C. Lovatt , V.S. Ramsden , B.C. Mecrow “Design of an in-Wheel Motor for a Solar-Powered Electric Vehicle”. IEE Proc-Electr. Power Appl., Vol. 145, No. 5, September 1998, pp 402-408.
- [2] CARICCHI, F., CRESCIMBINI, F., HONORATI, O.,DINAPOLI, A., and SANTINI, E.:“Compact wheel direct drive for EVS”, IEEE Ind. Appl. Mag., 1996, pp. 25-32
- [3]. G. Guo Dong , G. Yu Han, L. Chee Ken ,“studies of electric motors for light-weight electricvehicle”. Proceeding of Malaysian Universities Transportation Research Forum and Conferences 2010 (MUTRFC2010), 21 December 2010, Universiti Tenaga Nasional. ISBN 978-967-5770-08-1 pp.135-148
- [4] J.Connors,“Telemetric development in solar vehicles with synplify pro software,” The Syndicated, vol. 5, no. 1, pp. 1,3–5, 2005.
- [5] K.D.Huang, S.-C. Tzeng, W.-P. Ma, and M.-F. Wu, “Intelligent solarpowered automobile-ventilation system,” Applied Energy, vol. 80, pp.141–154, 2005.
- [6] A. Riisnaes, C. Allen and P. Winkler. ““Dakota Sun” The Next Generation Solar Powered Racing Vehicle”. IEEEAES Systems Magazine, November 1996. Pp.3-6.
- [7] N. Mutoh, Senior Member, IEEE, and T.Inoue “A Control Method to Charge Series-Connected Ultraelectric Double-Layer Capacitors Suitable for Photovoltaic Generation Systems Combining MPPT Control Method”. IEEE TRANSACTIONS ON INDUSTRIAL ELECTRONICS, VOL. 54, NO. 1, FEBRUARY 2007. Pp.374-383.
- [8]<http://www.google.fr/imgres?imgurl=http://webecoist.momtastic.com/wp-content/uploads/2008/11/10-solar-powered-golf-cart->
- [9] Règlement Technique Energie Alternative / Alternative Energy Technical Regulations. FIA Sport / Technical Department. 11.12.2006
- [10]Techniques d’ingénieur (Conversion photovoltaïque de la cellule aux systems par Stéphan ASTIER)

Optimal DFIG Location and Impact of Load Model in Pool Electricity Market

Ashwani Kumar, *Member, IEEE* Manish Kumar and K. S. Sandhu

Abstract-- This paper presents mixed integer nonlinear programming (MINLP) approach for determining optimal location and number of distributed generators in pool electricity market. For optimal location of distributed generation, first the most appropriate zone has been identified based on real power nodal price and real power loss sensitivity index as an economic and operational criterion. After identifying the suitable zone, mixed integer non-linear programming approach has been applied to locate optimal place and number of distributed generators in the obtained zone. The problem of DG location consists of minimization of total fuel cost of conventional and distributed generation sources. The pattern of nodal real and reactive power prices, line loss reduction, and fuel cost saving has been obtained. The results are obtained for pool electricity market model. The proposed MINLP based multi-objective optimization approach has been applied for IEEE 24 bus reliability test system.

Index Terms-- Distributed generation, Loss sensitivity, Nodal price, Mixed integer nonlinear programming, Optimal location.

I. LIST OF SYMBOLS

N_g	set of generators
W	active power pool generator- i
C_i	fuel cost of pool generator- i
a_{gi}, b_{gi}, c_{gi}	cost coefficients in \$/h, \$/MWh, \$/MWh ²
P_i	real power injection at bus- i ;
Q_i	reactive power injection at bus- i ;
P_{gi}, Q_{gi}	real and reactive power generation at bus- i ;
P_{di}, Q_{di}	real and reactive power demand at bus- i ;
P_{GT}, Q_{GT}	Total real and reactive power generation;
P_{DT}, Q_{DT}	Total real and reactive power demand;
P_{LT}, Q_{LT}	Total real and reactive power loss;
V_i	voltage magnitude at bus- i ;
δ_i	load angle at bus- i ;
$Y_{ij} = G_{ij} + B_{ij}$	i - j th element of Y-bus matrix;
N_b	number of buses in the system;
$P_{gi}^{\min}, P_{gi}^{\max}$	minimum and maximum generation limit;
$Q_{gi}^{\min}, Q_{gi}^{\max}$	minimum and maximum generation limit;
V_i^{\min}, V_i^{\max}	upper and lower voltage magnitude limit;
$\delta_i^{\min}, \delta_i^{\max}$	upper and lower angle limit;

$S_{ij}, S_{ij} \leq S_{ij}^{\max}$	Line flow limit;
x	state vector of variables V, δ ;
u	control parameters, $P_{gi}, Q_{gi}, P_{DGi}, Q_{DGi}, P_{gb}, P_{gp}$;
p	fixed parameters $P_{di}, P_{db}, P_{dp}, Q_d, T_{ij}$;
ξ^{int}	an integer variable with values $\{0,1\}$;
N_{DG}	set of distributed generators;
N_l	total number of lines in the network;
P_{DGi}	active power of distributed generator connected at bus- i ;
a_i, b_i, c_i	cost coefficients for conventional generators [24];
$a_{DGi}, b_{DGi}, c_{DGi}$	cost coefficients for distributed generators;
P_{DGi} and Q_{DGi}	real and reactive generation for distributed generators;
$P_{DGi}^{\min}, P_{DGi}^{\max}$	minimum and maximum generation limit;
$Q_{DGi}^{\min}, Q_{DGi}^{\max}$	minimum and maximum generation limit;
N_{DG}^{\max}	maximum number of distributed generator to be located in the network;

II. INTRODUCTION

WITH liberalization of electricity markets there is growing interest in the distributed generation (DG) as an important option of energy production in the near future. With electricity market undergoing tremendous transformation, more price volatility in the market, ageing infrastructure, and changing regulatory environments are demanding users and electric utilities to harness benefits of distributed generation [1-4]. Many definitions of distributed generation have appeared in the literature based on their size, technologies, location, power delivery area and operational constraints with their economical and operational benefits [5-7]. The DG technologies may comprise small gas turbines, micro-turbines, fuel cells, wind and solar energy. Distributed generation can be connected in an isolated or an integrated way in the power system network and issues relating to policy of integrating DGs into power system planning and their impacts in steady state power system operation, contingency analysis, protection coordination as well as dynamic behavior were discussed in [7-8].

With increasing share of distributed generation, the planning of the system in the presence of DGs will require the assessment of several factors such as the number and the capacity of units, best possible location in the network, and impact of DG on the system operation characteristics such as

Ashwani Kumar is with Department of Electrical Engineering at National Institute of Technology, Kurukshetra, India (e-mail: ashwa_ks@yahoo.co.in).

K. S. Sandhu is with the Department of Electrical Engineering at National Institute of Technology, Kurukshetra, India. (e-mail:).

system losses, voltage profile, stability and reliability issues [8].

The optimal placement and sizing of DGs in the distribution network based on different objectives have been reported in the literature. A Lagrangian based approach, Tabu search, Genetic algorithm, was proposed to determine optimal location of DGs considering economic as well as stability limits in [9-11]. Optimal sizing and siting decisions for distributed generation capacity planning using heuristic approach was proposed in [12]. A new integrated model for distributed system planning with an objective of minimizing investment costs, operating costs, and payments for compensation of losses was proposed in [13]. Optimal allocation of embedded generation in distribution network using linear programming approach including short circuit constraints of network was proposed in [14]. A multi-objective optimization approach using evolutionary algorithm for sizing and siting of distributed generation in distribution systems has been presented in [15-18]. A fuzzy multi-objective optimization considering voltage drop, system losses, short circuit capacity, and system operation cost for DG allocation was proposed for a small distribution system in [19]. A theoretical insight to a competitive market integration mechanism for DG in a pool based system, social welfare maximization and multi-objective optimization for DG allocation was proposed in [20-23].

This paper presented a mixed integer nonlinear programming (MINLP) approach for determining optimal location and number of distributed generators for minimization of transmission loss. For optimal location of distributed generation, first the most appropriate zone has been identified based on real power nodal price and real power loss sensitivity index as an economic and operational criterion [24]. After identifying the suitable zone, mixed integer non-linear programming approach has been applied to locate optimal place and number of distributed generators in the obtained zone. The non-linear optimization approach consists of minimization of transmission loss with the presence of DFIG. The impact of wind speed variation has also been incorporated in the optimization model for obtaining the impact of DFIG output on the transmission loss. The total real and reactive power loss, optimal DG location and DG output has been obtained. The effect wind variation is determined on the location and sizes of DG. In this chapter wind turbine DFIG is used as DG source. The proposed MINLP based optimization approach has been applied for IEEE 24 bus reliability test system [25]. The optimization problem has been solved using MATLAB and GAMS interfacing with DICOPT solver in GAMS [25-26].

III. GENERAL OPF FORMULATION IN THE PRESENCE OF DISTRIBUTED GENERATION

A general multi-objective mixed integer non-linear programming approach for hybrid electricity markets considering the cost characteristics of distributed generators together with the fuel cost of other conventional generators and the line loss minimization has been formulated to find optimal location and number of distributed generators.

$$\text{Min } F(x, u, p, \xi^{\text{int}}) \quad (1)$$

Subject to equality and inequality constraints defined as

$$h(x, u, p, \xi^{\text{int}}) = 0 \quad (2)$$

$$g(x, u, p, \xi^{\text{int}}) \leq 0 \quad (3)$$

ξ^{int} an integer variable with values $\{0, 1\}$. The zero value represents absence and one value represents presence of distributed generator in the network.

Objective function F is

$$\text{Min } F(x, u, p, \xi^{\text{int}}) = \left\{ \begin{array}{l} \sum_{i \in N_g} (a_{gi} + b_{gi} P_{gi} + c_{gi} P_{gi}^2) \\ + \xi_i^{\text{int}} * \sum_{i \in N_{DG}} (a_{DGi} + b_{DGi} P_{DGi} + c_{DGi} P_{DGi}^2) \end{array} \right\} \quad (4)$$

The line flows from bus- i to bus- j and bus- j to bus- i are given as:

$$P_{ijl} = V_i^2 G_{ij} - V_i V_j (G_{ij} \cos(\delta_i - \delta_j) + B_{ij} \sin(\delta_i - \delta_j)) \quad (5)$$

$$P_{jil} = V_j^2 G_{ij} - V_i V_j (G_{ij} \cos(\delta_i - \delta_j) - B_{ij} \sin(\delta_i - \delta_j)) \quad (6)$$

A. Equality Constraints: Power flow equations corresponding to both real and reactive power balance equations are equality constraints that can be modified in the presence of distributed generation for all the buses as:

$$\begin{aligned} P_i &= P_{gi} + \xi_i^{\text{int}} * P_{DGi} - P_{di} \\ &= \sum_{j=1}^{N_b} V_i V_j [G_{ij} \cos(\delta_i - \delta_j) + B_{ij} \sin(\delta_i - \delta_j)] \quad \forall i = 1, 2, \dots, N_b \end{aligned} \quad (7)$$

$$\begin{aligned} Q_i &= Q_{gi} + \xi_i^{\text{int}} * Q_{DGi} - Q_{di} \\ &= \sum_{j=1}^{N_b} V_i V_j [G_{ij} \sin(\delta_i - \delta_j) - B_{ij} \cos(\delta_i - \delta_j)] \quad \forall i = 1, 2, \dots, N_b \end{aligned} \quad (8)$$

B. Inequality constraints: The inequality constraints are the voltage and angular limits, limits on power generation of conventional generators and line flow limits. In addition the limits on the distributed generators are also considered.

Power generation limit: This includes the upper and lower real power generation limit of generators at bus- i

a) Real power generation limit

$$P_{DGi}^{\min} \leq P_{DGi} \leq P_{DGi}^{\max}, i = 1, 2, \dots, N_{DG} \quad (43)$$

where, $P_{DGi}^{\min}, P_{DGi}^{\max}$ are the minimum and maximum generation limit.

b) Reactive power generation limit: This includes the upper and lower reactive power generation limit of distributed generators at bus- i

$$Q_{DGi}^{\min} \leq Q_{DGi} \leq Q_{DGi}^{\max}, i = 1, 2, \dots, N_{DG} \quad (44)$$

where, $Q_{DGi}^{\min}, Q_{DGi}^{\max}$ are the minimum and maximum generation limit.

c) Optimal number of distributed generators: This includes the limit on number of maximum distributed generators in the network.

$$N_{DG} = \sum_{i=1}^{N_{DG}} \xi_i^{\text{int}} \leq N_{DG}^{\max} \quad (45)$$

The results have been obtained by solving mixed integer nonlinear programming problem in GAMS using a discrete

continuous optimization package (DICOPT) solver [25].

IV. RESULTS AND DISCUSSIONS

The proposed approach for an optimal distribution generation location has been applied to IEEE 24-bus reliability test system [27]. The results have been obtained for fuel cost, losses, power generation schedule for conventional and distributed generators in the presence of DGs. Five different cases have been considered for loss minimization. Based on number of DGs optimally located at each selected load buses in the candidate zone, five different cases have been considered. The results have also been obtained without presence of DGs for comparison. There can be more than one distributed generators with different possibilities to place in the selected zone at the load buses. The maximum number of DGs is defined in the optimization problem for the different cases. The results are also obtained with zip load considering variation of ZIP load at each bus for comparison. The results are given in tabular form in Tables 4.1 to 4.4

The optimal location of distributed generators among these buses has been obtained using mixed integer based approach. Results have been obtained considering different cases with

different number of distributed generators. The different cases without and with optimally located DGs at the selected buses lying in the most appropriate zone have been categorized as:

- Case 1: without distributed generator
- Case 2: with one distributed generator
- Case 3: with two distributed generator
- Case 4: with three distributed generator
- Case 5: with four distributed generator

A Case 1: with one DG

Table 1 contains the result considering only fuel cost minimization with constant load and Table 2 contains the result for the same problem with zip load. Table 3 contains the result of the minimization fuel cost including DG cost with constant load and Table 4 contains the result of the same problem with zip load. Each table contains the value of fuel cost, DG cost, total active and reactive power loss, optimal location and size of DGs, and conventional generation schedule. The fuel cost is observed lower with ZIP load model and cost reduces with more penetration level of DGs. With inclusions of fuel cost of DGs also, the fuel cost comes out to be slightly higher however, the losses are observed lower.

Tables 1 Results for minimization of fuel cost of conventional generator only with constant load

Case 1:	Without DG	Case 2: With DG =1	Case 3: With DG =2	Case 4: With DG=3	Case 5: With DG=4
Fuel cost	14625.4763 14597.	1046 14573.	3699	14553.3878	14535.0807
DG cost	0	13.3040	30.3070	43.3100 55.	0150
PLT(p.u.MW) 0.	481	0.4797	0.4742	0.4750	0.4567
QLT(p.u.MVar)	-1.4134 -	1.3883 -	1.4932	-1.6224	-1.6692
Total load(p.u.MW)	28.5	28.5	28.5	28.5	28.5
Total load(p.u.MVar)	5.8	5.8	5.8	5.8	5.8
Optimal bus location of DG	0 10		4,10	3,4,10	3,4,6,10
Total DG size(p.u.MW)	0	0.85	1.55	2.2	2.85
Total DG size(p.u.MVar)	0	0.02	0.22	0.37	0.39
Pg(p.u.MW)	28.95589	28.12971	27.42419	26.77498	26.10674
Qg(p.u.MVar)	4.38662	4.391735	4.086795	3.807596	3.740832

Tables 2 Results for minimization of fuel cost of conventional generator only with zip load

Case 1:	Without DG	Case 2: With DG=1	Case 3: With DG=2	Case 4: With DG=3	Case 5: With DG=4
Fuel cost	14620.2096	14592.6458	14566.8815 14542.	3095 14521.	7823
DG cost	0	13.3040	30.3070	43.3100	52.1110
PLT(p.u.MW)	0.5189	0.5177	0.5007 0.	4995 0.	4894
QLT(p.u.MVar)	-0.6873 -	0.8376 -	1.0196	-1.0514	
Total load(p.u.MW)	28.8533	28.2784	28.0313	27.9779	27.9808
Total load(p.u.MVar)	5.8718	5.7548	5.7047	5.694	5.6946
Optimal bus location of DG	0	10	3,10 3,	4,10	3,4,6,10
Total DG size(p.u.MW)	0	0.85	1.5	2.2	2.85
Total DG size(p.u.MVar)	0	0.02	0.17	0.37	0.39
Pg(p.u.MW)	28.95589	28.12971	27.42419	26.77498	26.10674
Qg(p.u.MVar)	4.38662	4.391735	4.086795	3.807596	3.740832

Table 3 Results for minimization of combined cost with constant load

Case 1:	Case 2:	Case 3:	Case 4:	Case 5:
---------	---------	---------	---------	---------

	Without DG	With DG=1	With DG=2	With DG=3	With DG=4
Fuel cost+ DG cost	14625.4763	14614.1076	14603.6769	14594.9085	14588.4696
DG cost		17.0030	30.3070 39.	1080 50.	8130
PLT(p.u.MW)	0.4802 0.	4797 0.	4742	0.4629	0.4509
QLT(p.u.MVar)	-1.4134 -	1.3883 -	1.4932	-1.5802	-1.6241
Total load(p.u.MW)	28.5	28.5	28.5	28.5	28.5
Total load(p.u.MVar)	5.8	5.8	5.8	5.8	5.8
Optimal bus location of DG	0	10	4,10	4,5,10	4,5,6,10
Total DG size(p.u.MW)	0	0.85	1.55	2.1	2.75
Total DG size(p.u.MVar)	0	0.02	0.22	0.234847	0.27
Total Pg(p.u.MW)	28.95589	28.12971	27.42419	26.86289	26.20088
Total Qg(p.u.MVar)	4.38662	4.391735	4.086795	3.984997	3.905931

Table 4 Results for minimization of fuel combined cost with Zip load

Case 1:	Without DG	Case 2: With DG=1	Case 3: With DG=2	Case 4: With DG=3	Case 5: With DG=4
Fuel cost+ DG cost	14620.2096	14606.6187	14595.0530	14585.5858	14576.5256
DG cost		13.3040	22.1050 35.	1080 46.	8130
PLT(p.u.MW)	0.5106 0.	4925 0.	4863	0.4839	0.4710
QLT(p.u.MVar)	-0.6873 -	0.8894 -	0.9478	-1.0101	-1.2091
Total load(p.u.MW)	28.2763	28.02979	27.9758	27.98571	27.98944
Total load(p.u.MVar)	5.7544	5.704481	5.693498	5.695465	5.69624
Optimal bus location of DG	0	3	3,4	3,4,5	3,4,5,6
Total DG size(p.u.MW)	0	0.65	1.35	1.9	2.55
Total DG size(p.u.MVar)	0	0.15	0.35	0.38	0.4
Total Pg(p.u.MW)	28.78695	27.87227	27.1121	26.56962	25.9104
Total Qg(p.u.MVar)	5.067111	4.665085	4.395687	4.305361	4.087112

B. Results with and without DG with constant and zip load (including cost of DGs)

The simulation of combined cost (fuel cost including DG cost) have been determined by solving nonlinear optimization problem. The effect of zip load is obtained from the modification given in section III in the optimization problem that is the modified real and reactive power flow equations. The nodal price variations for both real and reactive power at each bus have been obtained without and with the presence of distributed generation for the different cases with and without zip load. The marginal price variations are shown in Figs.1, 2, 3 and 4. In Figs. 1 and 2 marginal prices for active power are shown with constant and zip load respectively. It is observed from Fig. 3 and 4 that in the presence of DGs, the nodal prices have been considerably reduced and the variation of real power prices has also become uniform at all the buses. It is also observed that with zip load the nodal price are less than with the constant load. With constant load the minimum marginal price occur at bus 8 whereas with zip load minimum marginal price occur at bus 22. With the presence of DGs, it is observed that two price zones can be represented by single price zone. Thus, the consumers in both the zones will pay similar price. The best results have been obtained in Case-5 with four numbers of DGs. With more penetration of DGs in

the network, the improvement in the result is found to be marginal.

It is observed from figures that the reactive power price is high at nodes 6, 10 with constant load and with zip load as compared to other buses. Because at these nodes the reactive power absorption is quite high due to the presence of reactor and transformers. In case 3 with two DG the reactive power marginal price are more with constant as well as zip load.

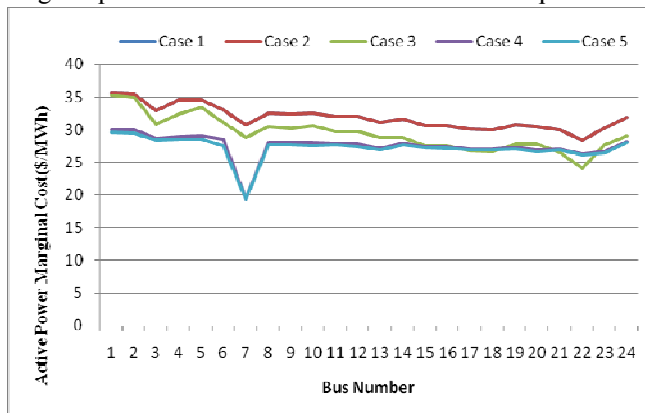


Fig.1. Active power marginal cost (\$/MWh) with constant load

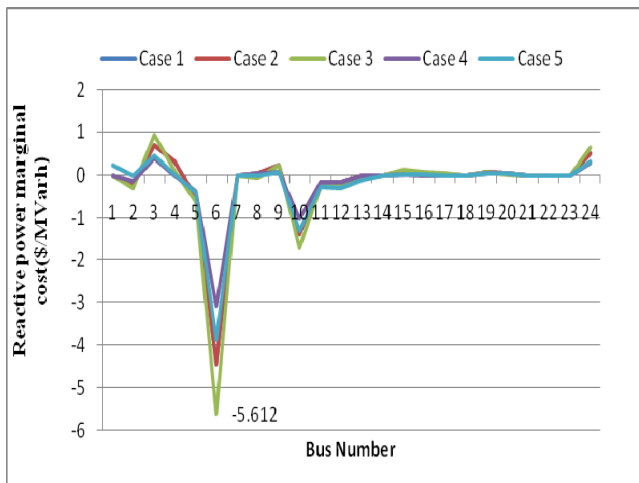


Fig.2. Reactive power marginal cost (\$/MVarh) with constant load

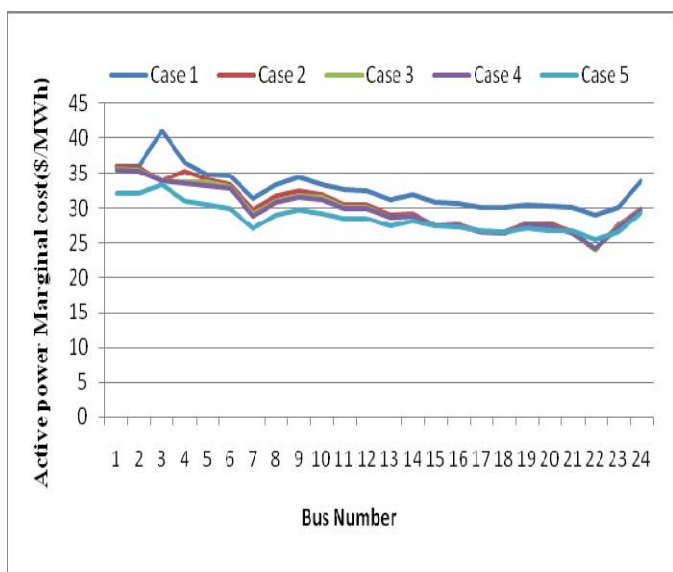


Fig.3. Active power marginal cost (\$/MWh) with zip load

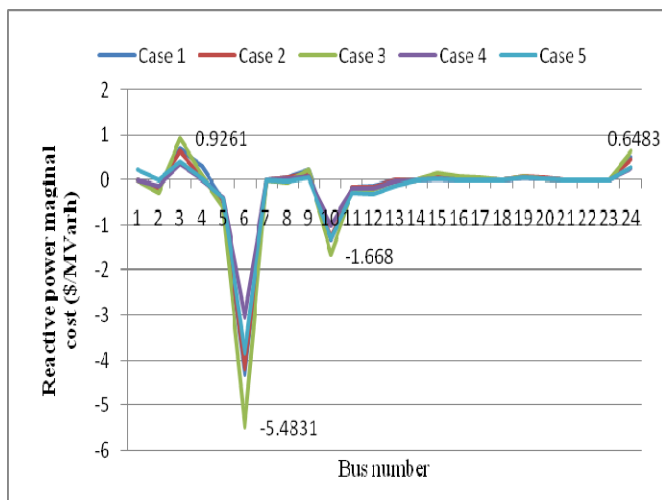


Fig.4. Reactive power marginal cost (\$/MVarh) with zip load

The Lagrangian multiplier for reactive power can be both positive and negative. The reactive power price negative sign

indicates the negative sign associated with Lagrange multiplier corresponding to reactive power balance equation, however, the price has to be paid for reactive power absorption as well as for injecting reactive power in the network. For Case 4, the reactive power price at these nodes reduces considerably due to the reduction of reactive line flows as real power is available locally due to DGs with constant and zip load. Thus, DGs can be help to reduce reactive losses in a system due to power available locally to loads and maintaining better voltage profile. In case 5 with four DGs the reactive power nodal price are slightly lower with constant load whereas with zip load they are slightly higher at most of the buses.

The average nodal price variation for each case is shown in the Fig. 5 for both load cases. It is observed that nodal price reduces considerably in the presence of DGs and become almost uniform. The data series written above is for the constant load and data series written below is for zip load. With DGs, the price of real power is almost uniform in both the zones and customers pay similar price in both the zones. For Case-2 with one DG average real power price with zip load is less than with constant load. It is observed that with constant load there is more reduction than zip load after Case-2. In case 2, 3, 4 there is marginal reduction in average marginal price with zip load whereas with constant P,Q load reduction is considerable. In case 5 average nodal price obtained is minimum. The fuel cost reduction in the presence of DGs with constant as well as zip load is shown in Fig.6. It can be seen that the saving in fuel cost of conventional generator is more with zip load than the saving with constant load for all the cases. Minimum fuel cost is found for Case-5 with four numbers of DGs.

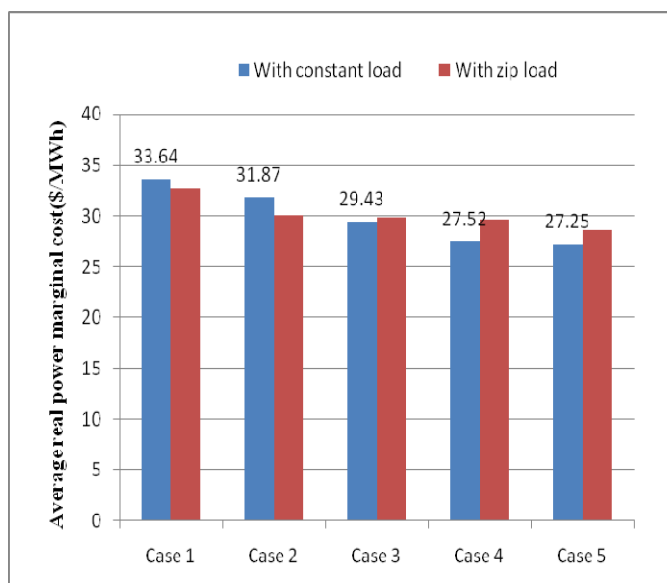


Fig.5. Average real power marginal cost (\$/MWh) with constant and zip load

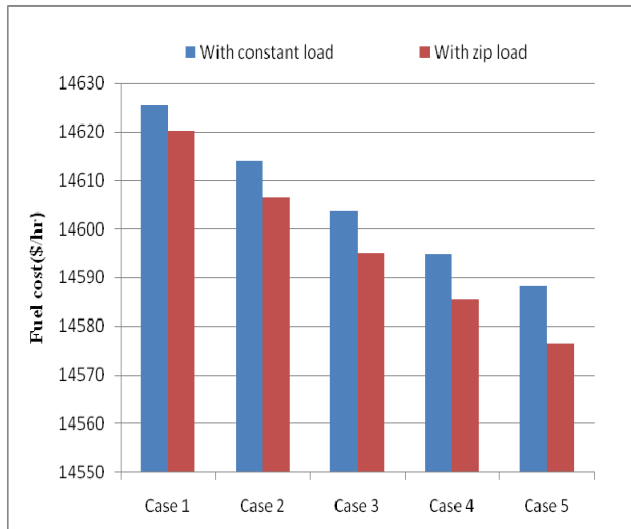


Fig.6. Fuel cost with constant power and zip load

The impact on the real power loss in the presence of DGs is shown in Fig.7. The above data series is given for zip load and below data series is given for constant load. The system total loss without DG with constant load are 0.4802 (MW) and with zip load total loss are 0.5106 (MW). In case-2(with one DG) the system loss are 0.4797 MW (with constant load) and 0.4925 MW (with zip load). In case-3(with two DGs) the total real power loss are 0.4742 MW (with constant load) and 0.4863 MW (with zip load). There is considerable reduction in losses in each case. In case 4(with three DGs) the total real power loss are 0.4629 MW (with constant load) and 0.4839 MW (with zip load). In case- 5 the real power loss are 0.4509 MW (with constant load) and 0.471 MW (with zip load). It is observed that losses are considerably reducing with DG and maximum reduction take place in case 5 (with four DG) for each load model. With zip load losses are more as compared to the constant load.

The optimal size of distributed generators obtained for different cases has been shown in Fig.8 and 9. The number in small parenthesis with Case 1 to 5 (...) in Fig. 8 and 9 represents the optimal bus location of distributed generation. Case 1(0) represents that DG is not added in the system. In case-2 (with one DG) with constant load the optimal bus location is 10 whereas with zip load it is 3. In case-3 (with two DG) with constant load the optimal bus location is 4, 10 whereas with zip load it is 3, 4. In case-4 (with three DG) with constant load the optimal bus location is 4,5,10 whereas with zip load it is 3, 4, 5. In case- 5 (with four DG) with constant load the optimal bus location is 4, 5, 6 and 10 whereas with zip load it is 3, 4, 5 and 6.

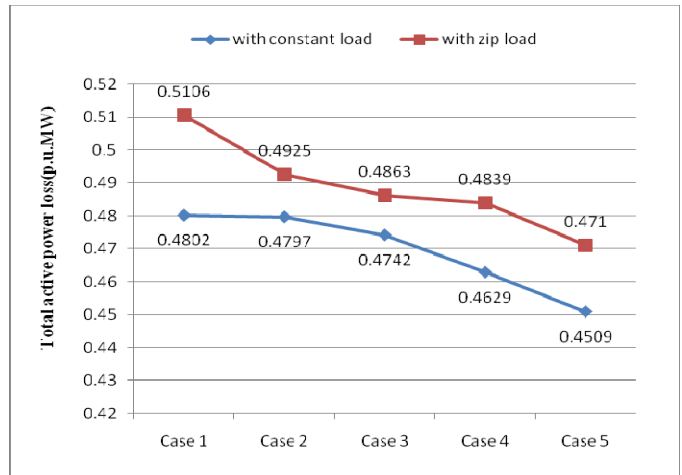


Fig.7. Total Active power loss with constant and zip load

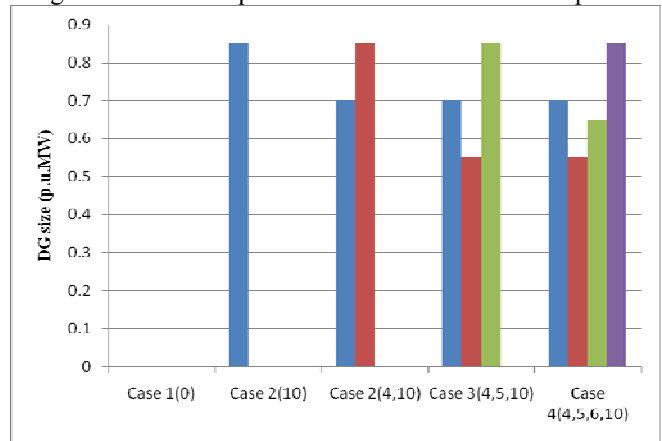


Fig.8. DG size (p.u.MW) with constant load

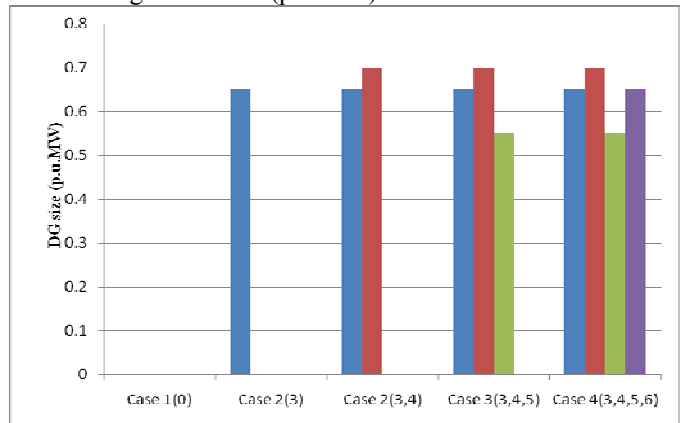


Fig.9. DG size (p.u.MW) with zip load

The penetration level of DGs has been determined as the ratio of DG size to the total demand in the system and has been shown in Fig.10. The penetration level is slightly more in case of constant P,Q load. It is observed that the saving is more with more penetrations. Optimal number of DGs required obtaining best results of fuel cost savings is found to be four with both constant as well as zip load. The voltage profile without and with DG is shown in Fig.11 and 12. It is observed that the voltages are within specified range. It is observed that the voltage profile is improved in each case with DG and it is better with four DGs with constant as well as zip load as compared to all other cases.

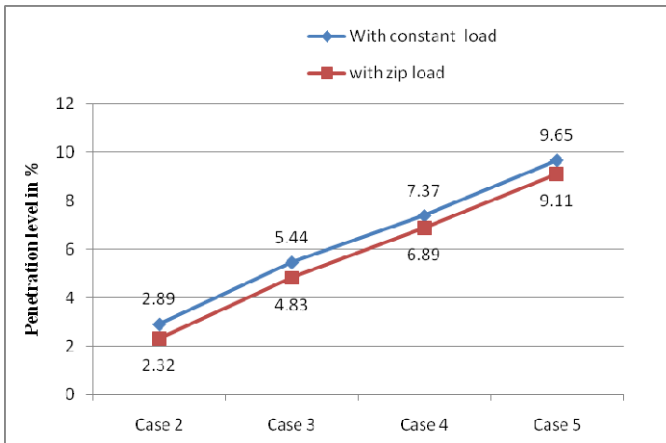


Fig.10. Penetration level of DG with constant and zip load

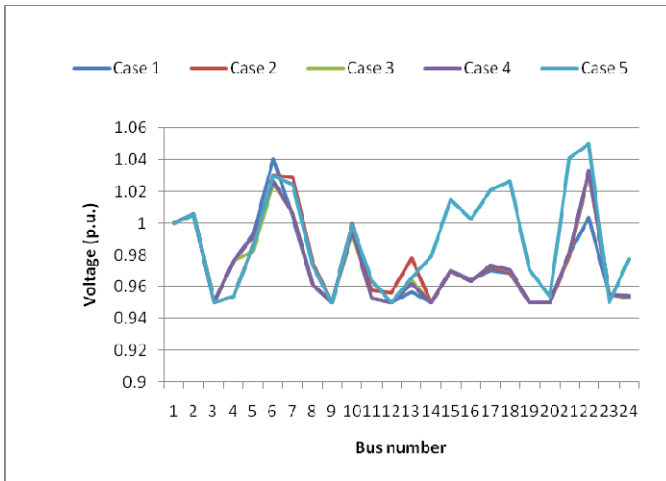


Fig.11. voltage profile without and with DG with constant load

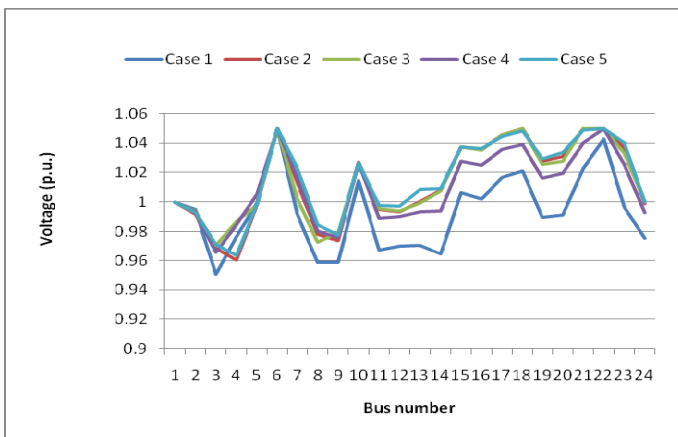


Fig.12. voltage profile without and with DG with zip load

V. CONCLUSIONS

This paper presented the comparison of optimal location and size of distributed generation for minimization of fuel cost with constant P,Q load and zip load. The problems considered here are simple fuel cost minimization of fuel cost of conventional generator without DG cost and minimization of fuel cost of conventional generator including DG cost. Then,

mixed integer non-linear programming approach has been utilized for optimal location and optimal number of distributed generators in the suitable zone. Pattern of real and reactive power nodal price, real power loss, and fuel cost have been determined for constant as well as zip load. The nodal price variations are reduced in both type of problem. It is observed that with DGs, the fuel cost reduces considerably for both type of problem and thus there can be additional saving of fuel cost. Optimal number of DGs were found to be four for constant as well as zip load to obtain maximum fuel cost saving. Saving in fuel cost is more in case of zip load. The minimum fuel cost in case-5 with four DG of conventional generator 14535.0807 \$/hr (with constant load) and 14521.7823\$/hr (with zip load) and for combined cost (fuel cost of conventional generator including DG cost) it is 14588.4696 \$/hr (with constant load) and 14576.5256 \$/hr (with zip load).

VI. REFERENCES

- [1] "Impact of increasing contribution of dispersed generation on power system-Final Report," CIGRE WG 37-23, Sept. 1998.
- [2] R. C. Dugan and S. K. Price, "Issues for distributed generations in the US," in *Proc. IEEE PES, Winter Meeting*, vol.1, Jan. 2002, pp. 121-126.
- [3] *Electric Power Research Institute* web- page, April 2008: <http://www.epri.com/gg/newgen/disgen/index.html>.
- [4] *Gas Research Institute*, Distributed power generation: A strategy for a competitive energy industry, Gas Research Institute, Chicago, USA, 1998.
- [5] T. Ackermann, G. Andersson, and L. Soder, "Distributed generation: a definition," *Electric Power System Research*, vol. 57, 2001, pp. 195-204.
- [6] W. E. El-Khattam and M. M. A. Salam, "Distributed generation technologies, definitions and benefits," *Electric Power System Research*, vol. 71, 2004, pp. 119-128.
- [7] P. Chiradeja and R. Ramkumar, "An approach to quantify for technical benefits of distributed generation," *IEEE Transactions on Energy Conversion*, vol. 19, no. 4, Dec. 2004, pp. 764-773.
- [8] M. Donkelaar, "A survey of solutions and options for integration of distributed generation in electricity supply systems," *Journal of Energy and Environment*, vol. 15, no. 2, 2004, pp. 323-332.
- [9] J. A. P. Lopes, N. Hatziargyriou, J. Mutale, P. Djapic, and N. Jenkins, "Integrating distributed generation into electric power systems: A review of drivers, challenges and opportunities," *Electric Power System Research*, vol. 77, 2007, pp. 1189-1203.
- [10] W. Rosehart and E. Nowicki, "Optimal placement of distributed generation," in *Proc. 14th PSC conference*, Sevilla, 2002, pp. 1-5.
- [11] K. Nara, Y. Hayashi, K. Ikeda, and T. Ashizawa, "Application of tabu search to optimal placement of distributed generators," in *Proc. IEEE PES Winter Meeting*, 2001, pp. 288-294.
- [12] G. Celli and F. Pilo, "Optimal distributed generation allocation in MV distribution networks," in *Proc. IEEE PES conf. on PICA*, Australia: 2001, pp. 81-86.
- [13] W. El-Khattam, K. Bhattacharya, Y. Hegazy, and M. M. A. Salam, "Optimal investment planning for distributed generation in a competitive electricity markets," *IEEE Trans. on Power Systems*, vol. 19, no. 3, Aug. 2004, pp. 1674-1684.
- [14] W. El-Khattam, Y. Hegazy, and M. M. A. Salam, "An integrated distributed generation optimization model for distributed planning," *IEEE Trans. on Power Systems*, vol. 20, no. 2, May 2005, pp. 1158-1165.
- [15] A. Keane and M. O'Malley, "Optimal allocation of distributed generation on distribution networks," *IEEE Trans. on Power Systems*, vol. 20, no. 3, Aug. 2005, pp. 1640-1646.
- [16] G. Celli, E. Ghiani, S. Mocci, and F. Pilo, "A multi-objective evolutionary algorithm for the siting and sizing for distributed generation," *IEEE Trans. on Power Systems*, vol. 20, no. 2, May 2005, pp. 750-757.

- [17] C. L. T. Borges and D. M. Falcao, "Optimal distributed generation allocation for reliability, losses, and voltage improvement," *Electric Power and Energy Systems*, vol. 28, 2006, pp. 413-420.
- [18] N. Acharya, P. Mahat, and N. Mithulananthan, "An analytical approach for DG allocation in primary distribution network," *Electric Power and Energy Systems*, vol. 28, 2006, pp. 669-678.
- [19] G. P. Harrison, A. Piccolo, P. Siano, and A. R. Wallace, "Hybrid GA and OPF evaluation of network capacity for distribution generation connections," *Electric Power and Energy Systems*, vol. 78, 2008, pp. 392-398.
- [20] G. A. J. Estevej, R. P. Behnke, R. T. Avila, and L. S. Vargas, "A competitive market integration model for distributed generation," *IEEE Transactions on Power Systems*, vol. 22, no. 4, Nov. 2007.
- [21] S. Por kar, A. Abbaspour -Tehrani Farid, S. Saadate, "An approach to distribution system planning by implementing distributed generation in a deregulated electricity market," in *Proc. Power System Large Engg. System Conf.* 10-12, Oct. 2007, pp. 90-95.
- [22] D. Gautam and N. Mithulananthan, "Optimal DG placement in deregulated electricity market," *Electric Power System Research*, vol. 77, 2007, pp. 1627-1636.
- [23] M. Sadighzadeh and A. Rezaadeh, "Using genetic algorithm for distributed generation allocation to reduce losses and improve voltage profile," in *Proc. World Academy of Science, Engineering, and Technology*, vol. 27, Feb. 2008, pp. 251-256.
- [24] Ashwani Kumar and Wen Zhong Gao, "Optimal distributed generation location using mixed integer non-linear programming in hybrid electricity markets," *IET Gener. Transm. Distrib.*, pp. 1-18, Vol. 4, No. 2, pp. 281-298, 2010.
- [25] IEEE Reliability Test System, A report prepared by the Reliability Test System Task Force of the Applications of Probability Methods Subcommittee, *IEEE Trans. on Power Apparatus and Systems*, vol. PAS-98, pp. 2047-2054, Nov.- Dec. 1979.
- [26] A User's Guide, GAMS Software, A. Brooke, D. Kendrick, A. Meeraus, R. Raman, R.E. Rasenthal, *GAMS Development corporation*, 1998.
- [27] "MATLAB and GAMS: Interfacing Optimization and Visualization Software", Michael C. Ferris, August 10, 1999.

VII. APPENDIX

BID CURVE DATA FOR DISTRIBUTED GENERATORS AND CONVENTIONAL GENERATORS

Bus No.	Distributed Generators			Bus No.	Conventional Generators		
	a_{DG}	b_{DG}	c_{DG}		a_{gi}	b_{gi}	c_{gi}
3 0.	003	20.0	0.0	1	0.2917	35.07	3591.39
4 0.	004	19.0	0.0	2	.0.0	64.96	306.7
5 0.	010	20.0	0.0	7	0.0322	19.18	1940.98
6 0.	005	18.0	0.0	13	0.0322	19.18	649.99
8 0.	002	15.0	0.0	15	0.0628	27.22	1829.71
10 0.	003	20.0	0.0	16	0.0191	14.86	552.8
18					0.0191	14.86	1105.6
				21 0.	0086	30.0	1992.36
				22 0.	0112	14.17	927.15
				23 0.	0017	17.55	1160.23

MODELING of dislocation evolution in Multi-junction based Photovoltaic devices

Tarek M. Hatem and Mohamed T. Elewa

Abstract—Genuine Processing techniques have been developed to minimize density of dislocations and other defects originating from thermal stresses present in Multi Junction PVs. Embedded Void Approach; (EVA) was used to address the defects evolution in GaAs growth on Si substrates. In attempts to study void effect on dislocation generation; elastic models were prepared for voided and un-voided structures. Stresses and displacements were compared and related to alteration in dislocation density.

Keywords—Dislocation Density, Multi-junction solar cells, Finite Element Modeling, Thermal Stresses

I. INTRODUCTION

THE achievement of a PV device that collects photons in 1.4 eV-1.0 eV range requires considerable effort. It happens to be the main obstacle in achieving cascade solar cells with conversion $\eta > 45\%$. In attempts to address this dilemma, N was added to GaAs forming GaAsN to reduce Eg to ~ 1.0 eV while maintaining the lattice matched conditions to GaAs. The result was poor diffusion length, minority carrier lifetime, and low open circuit voltage [1]. Following the early reports, where an inverted structure of InGaP grown on GaAs substrate, lattice constant is graded to grow $\text{In}_{0.3}\text{Ga}_{0.7}\text{As}$ followed by etching off the GaAs substrate, the problem is in handling ultra-thin film in large scale production [2]. InGaAs/GaAsP strained layered super-lattice (SLS) was lattice matched to GaAs and was reported successful to partially absorb photons in the 1.4 – 1.2 eV range however it required hundreds of SLS periods to fully absorb 1.4 – 1.0 eV, [3]. GaAs growth on Si substrates seem to offer the solution for the 1.0 eV sub cell problem, unfortunately GaAs/Si experiences thermal expansion mismatch of 54%, and a lattice mismatch of 4.1% These mismatches initiate dislocations at the interface that run through the crystalline structure of the films and terminate at free surfaces. Dislocations act as scattering centers affecting carriers' lifetime and setting a limit on the performance, reliability, and lifetime of MJ-PV devices. Voids act as a free surface for inhibiting dislocation propagation, this was the main principle of Embedded Void Approach (EVA) [4] where a high density of micro-voids—a

few micrometers in length and less than a micrometer in diameter—are introduced into the GaAs layer near its interface with Si. Experimentally, the three dimensional void network has an average density of about 10^8 cm^{-2} , dislocations could be reduced uniformly over large area of substrates, by two orders of magnitude from 10^9 cm^{-2} to 10^7 cm^{-2} , [5]. Dislocations propagate to voids in their vicinity or can be redirected to be trapped in the three dimensional networks. Voids act as expansion joints for lattice mismatches as well. In this paper, the problem is parsed numerically where defects evolution is simulated during the processing of GaAs/Si device while accounting for temperature variations. A static study was performed on two elastic models, to confirm effect of void on defect density.

II. PROCEDURE

Void generation process is a three-step process that involves growth, etching and regrowth. It begins with growth of GaAs on a Si substrate by Metal-Organic Chemical Vapor Deposition (MOCVD) at temperatures greater than 600°C , this initiates intrinsic stresses, followed by annealing at elevated temperature around 1000°C for stress relaxation. GaAs is then etched, using mask-less inductively coupled plasma- reactive ion etching mask-less (ICP-RIE), to expose different planes of GaAs and generate Nanowires (NWs). These planes have different growth rates of GaAs facets, thus generating voids filled with low-pressure gas H_2 . In the final step, epitaxial GaAs is overgrown on the GaAs NW template and again followed by annealing for stress relaxation.

Numerically, an Elastic continuum Model was built, GaAs/Si device was modeled with dimensions $30 \mu\text{m} \times 12.5 \mu\text{m}$ for width and length, respectively. The Sketch chiefly focused at the interface region where a partition divided the length into two non-equal parts; GaAs has length of $2.5 \mu\text{m}$ whereas Si length is $10 \mu\text{m}$, voids have random size and vertical orientation with average length of 1 micrometer. Material Properties identified for Si and GaAs are listed in table 1. Simulation was run on ABAQUS software. Unit system used was MPA, as classified by ANSYS, which is similar to SI and CGS unit systems, where mass is in tones; length is in mm and pressure in MPa. Young's Modulus and Poisson's Ratio for both materials were considered for (111) plane; closely packed plane. Material Parameters selected are listed in table 1 in appendix. Static general analysis was performed where maximum number of increments was 1, minimum increment size of $1e^{-5}$ and maximum of 1.

Tarek M. Hatem was with North Carolina State University, Raleigh, NC27695USA. He is now with Mechanical Engineering Department, British University in Egypt, El Sherouk, CA 11837 Egypt.(phone: 202-2689-0000; fax: 202-263-00010; e-mail: tarek.hatem@bue.edu.eg).

Mohamed T Elewa is with the Mechanical Engineering Department, British University in Egypt, El Sherouk, CA11837Egypt. (e-mail: mohamed.elewa@bue.edu.eg).

Thermal stresses occur when structure temperature drops from 1000°C, annealing temperature to 25°C, room temperature. The model experiences two steps each with the assigned temperature. Displacement Constraints were applied by using boundary conditions to the top right node of the substrate in x and y, since all translational and rotational degrees of freedom need to be constrained, i.e. $U_1=U_2=U_3=0$. For inspecting the validity of stress reduction with voids, the previous procedure was carried out for Void and no-Void models. Approximate mesh global seed size of 0.0005. The un-voided model was structure-meshed; voids were free meshed with minimized mesh transition medial axis as complex geometry prevailed. For both models, Element shape was Quadratic and Element type was set to CPS4R, denoting 4-node bilinear, plane stress, quadrilateral, reduced integration. The finite element mesh contained 2171 nodes and 1994 elements for mesh with voids whereas un-voided mesh contained 1586 nodes and 1500 elements. Results based on average element output at nodes, averaging threshold 75%

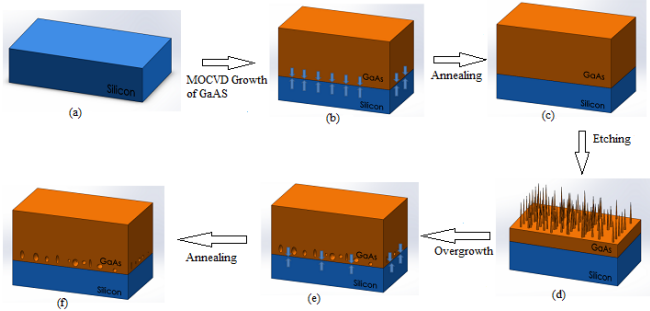


Figure 1 EVA Fabrication process chart a) Silicon Substrate b) MOCVD growth c) Annealing d) Etching e) Overgrowth and creating voids f) Annealing

III. DISCUSSION

After implementing nearly 20 voids in the voided structure, it should be mentioned that obtained interface stress results, measured from silicon substrate, were reduced from 216 MPa, without voids to 186 MPa with voids. Whereas stresses measured from GaAs are 265 MPa with voids and 216 MPa without. Stress value at top of GaAs film was higher for voided structure; stresses peaked at the center of film top with 186 MPa, without voids stress value is 173 MPa. An explanation for raise in stress is that voids act as discontinuities or stress singularities in the structure levitating stresses while annihilating dislocations. It is the main purpose of EVA to reduce defects number which act as barriers for charge carriers in the semiconductors; voids result in higher fatigue and less defects. Lower surface stresses signify less dislocation densities. Stress Contour plots acquired are shown in fig. 1 and 2 for both models. Substrate bottom stresses were reduced significantly from 108 MPa to 79.5 MPa when voids were applied. Maximum Spatial Displacement, 0.141 μm , occurred at top of film left side, for voided model. Same BCs were applied to un-voided model; the displacement had a higher value of 0.158 μm . Spatial displacement plots are

shown in fig. 3 and 4. It was perceived that voids closer to the interface, yielded higher stress values, at that region, than those at a greater distance from the interface. Unfortunately, when voids are shifted upwards, they raise stresses at other regions i.e. GaAs film top. Void network positioning is crucial. Moreover, it was noticed that resulting stresses depend on void density; this was confirmed when a stress of 248 MPa at GaAs and 124 MPa at Si layer were obtained after implementing 40 voids.

Assuming an elastic response from, the effect of raising temperature from T_0 to T initiates thermal stress, σ_T which is given by

$$\Delta\sigma_T = E \Delta\alpha \Delta T \quad (1)$$

Where $\Delta\alpha$ is difference in thermal expansion coefficient in K^{-1} between substrate and film ($\Delta\alpha = \alpha_s - \alpha_f$), ΔT is change in temperature, E is Young's Modulus. For Silicon thermal stress is 431 MPa and 814.3 MPa for GaAs. Since the two materials are considered isotropic ($\varepsilon = \varepsilon_x = \varepsilon_y$, $\sigma = \sigma_x = \sigma_y$), the misfit stress in the upper layer is

$$\sigma^T = \frac{-E_i(\alpha_i - \alpha_s)}{(1 - \nu_i)} * (T - T_0^i) + \sigma_i^I \quad (2)$$

Where i denotes layer number, normally this is the stress present in upper layer when the substrate is ultimately thick compared to film thickness, $h_s/h_f \ll 1$. The equations for top film stress σ and average film stress $\bar{\sigma}$ are related to film/substrate thickness ratio ($\xi = h_f/h_s$) and Biaxial Young's Modulus ratio $\Sigma = \frac{E_2/(1-\nu_2)}{E_1/(1-\nu_1)}$ as seen in (Hutchinson [1996]).

Equations for top film stress σ and average film stress $\bar{\sigma}$ are given by the following relations [6]

$$\frac{\bar{\sigma}}{\sigma^T} = \frac{1 + \Sigma \xi^3}{(\Sigma \xi^2 - 1)^2 + 4 \Sigma \xi (\xi + 1)^2} \quad (3)$$

$$\frac{\sigma}{\sigma^T} = \frac{1 - 3 \Sigma \xi^2 - 2 \Sigma \xi^3}{(\Sigma \xi^2 - 1)^2 + 4 \Sigma \xi (\xi + 1)^2} \quad (4)$$

The curvature of the bilayer could be concluded as

$$\kappa = \frac{1 + \xi}{1 + \Sigma \xi^3} * \frac{6(1 - \nu_1)h_2\bar{\sigma}}{E_1 h_1^2} \quad (5)$$

The curvature of the bilayer could also be calculated. Radius of curvature $\rho = 1/\kappa$, where κ is in mm . Mismatch stress in GaAs layer is 653.9 MPa with a negative sign indicating compression, while stress at film top is 226 MPa, higher by 50 MPa than that obtained from simulation, and average film stress is 286.6 MPa. Curvature Value is 232 corresponding to a curvature radius of 4.32 mm. Applying basic Pythagoras Theorem on nodal displacement on model without voids, curvature of radius was found to be 5.24 mm. While a radius of 7.03 mm was obtained for voided model. Curvature radius indicates the variation of the unit tangent direction, the higher the curvature radius, the less the deflection.

APPENDIX

Table I

Parameter	Si	GaAs	Unit
Young's Modulus	168.9	144	GPa
Poisson's Ratio	0.262	0.31	—
Density	$2.33e^{-9}$	$5.32e^{-9}$	ton/mm ³
CTE (α)	$2.616 e^{-6}$	$5.8 e^{-6}$	K ⁻¹
Slip System	{111}	{111}	—
	$\langle\bar{1}10\rangle$	$\langle 110\rangle$	
Lattice Constant	0.543106	0.56533	nm

ACKNOWLEDGMENT

The support from North Carolina State University Laboratory is greatly appreciated.

REFERENCES

- [1] M. Wanlas *et al.* "Monolithic, ultra-thin GaInP/GaAs/GaInAs tandem solar cells", Photovoltaic Energy Conversion-IEEE 4th World Conference. 1, 2006,729.
- [2] N. Ekins-Daukes *et al.* "Strain balanced GaAsP/InGaAs quantum well solar cells", Appl. Phys. Lett. 75 (26), 1999, 4195.
- [3] T.Katsuyama, S. M.Bedair, N. C.Giles, R. P.Burns, and J. F.Schetzina "Growth and characterization of InGaAs/GaAsP strained layer superlattices", J. Appl. Phys. 62 (2), 1987, 498.
- [4] P.Frajtag *et al.* "Improved light-emitting diode performance by conformal overgrowth of multiple quantum wells and fully coalesced p-type GaN on GaN nanowires", Appl. Phys. Lett. 98, 2011, 143014.
- [5] P.Frajtag, N.A.El-Masry, N.Nepal, S.M.Bedair, Applied Physics Letters 98, 2011, 023115.
- [6] J. W. Hutchinson "Stresses and Failure Modes in Thin Films and Multilayers", Stresses in films and multilayers, 1996.

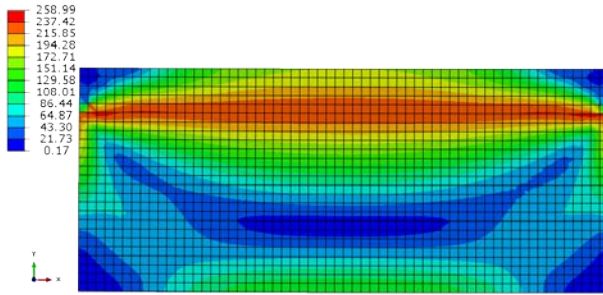


Figure 2 Von Mises Stress Average 75% without voids

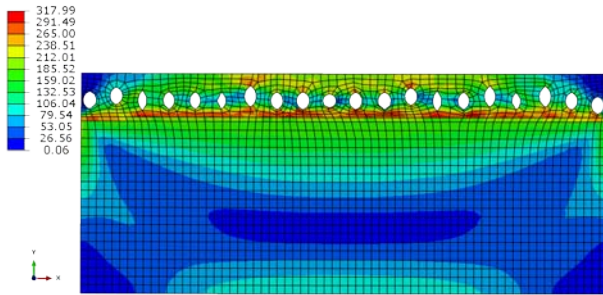


Figure 3 Von Mises Stress with Voids

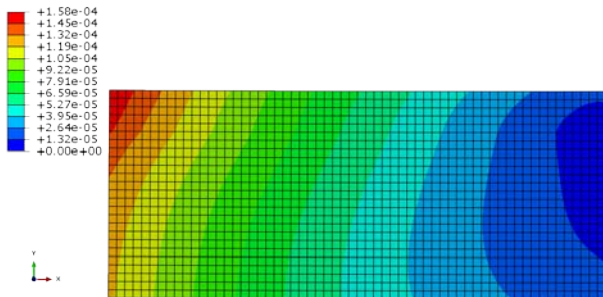


Figure 4 Spatial Displacement without Voids

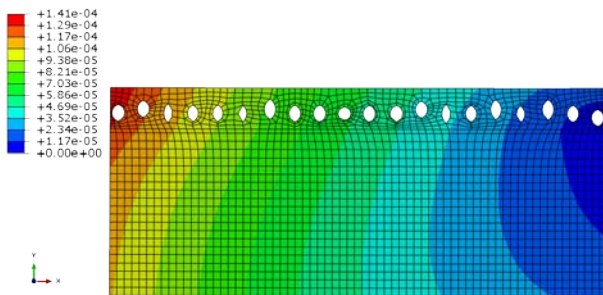


Figure 5 Spatial Displacement with Voids

IV. CONCLUSION

In conclusion, thermal stresses and therefore dislocations have shown reduction when voids were introduced near the interface of GaAs/Si cell. The paper discussed two elastic models illustrating void effect on dislocation density. A reduction in stress at Si layer of 14% while GaAs stresses rose to 18%, reduction in maximum displacement is 11%. The approach may address a solution for the 1.0 eV sub cell problem; permitting an efficiency raise to 45%. Void density and positioning should be controlled for stress reduction.

On an Accurate Estimation of HV Insulators Contamination: Combined Image Statistical Features and Neural Networks Approach

Luqman Maraaba, Hussain Al-Duwaish, Zakariya Al-Hamouz

Abstract— Contaminated insulators in polluted areas may lead to flashovers if they are not cleaned periodically. Flashover in most cases leads to lengthy service outages; hence it has a considerable impact on power system reliability. In this paper, a combined image processing artificial neural networks algorithm has been developed for the estimation of contamination level in high voltage insulators. Image processing has been used to extract needed features from images captured by digital cameras. The type of features which is considered is the “histogram based statistical feature” such as mean, variance, skewness, kurtosis, energy and normalized histogram error. On the other hand, using these features, a neural network has been successfully designed to correlate the insulator captured image and the contamination level. Testing of the developed algorithm showed a high successful rate in estimating the contamination levels of unseen insulators.

I. INTRODUCTION

Electric power is the backbone of development and economy of any country. Demand for electricity is increasing rapidly worldwide and consequently construction of power plants and overhead transmission lines has increased. Overhead transmission lines and substations insulators are one of the cheapest but the most vital part of the power system. Insulators only amount to a small percentage of a new line’s and substations total capital cost, but majority of power outages can be attributed to their bad performance, which directly influence the reliability of the electric power system. They are considered the most significant single piece of hardware item, which can affect the overall performance of high voltage transmission lines and substations. The economic impact of failure of a single insulator in-service can be very high [1]. Insulators are designed to withstand both mechanical and electrical stresses under specified operating conditions and at the same time meeting the user’s applicable economic criteria.

When an insulator is polluted and wetted, its withstand and flashover voltages are reduced. Contaminant particles in the presence of moisture form conducting films on the insulator surface, allowing leakage current to pass. This current will heat the surface leading to formation of dry bands in areas of high current density. High voltages will build up across those bands and may cause partial discharges leading to insulator flashover [2, 3].

This work was supported in part NSTIP (Saudi Arabia) under Grant 11-ENEL1626-04.

Insulator surface contamination and subsequent flow of leakage current have caused operating problems for electric power utilities since electrical power has been in use. The effect of leakage current and insulator flashover is a major practical concern for continuity of electric power supply. Mitigating measures may have to be adopted in order to improve the performance of the power transmission system. The measures to be taken depend on the contamination severity of the region. These include choosing insulator designs that promote minimum deposit accumulations, choosing insulators with longer leakage paths or performing insulator washing etc [4, 5].

The issues concerning determination of the level of contamination of power transmission lines have been studied in different research centers and energy systems for over 50 years. Due to concerns about severe environmental pollution, this issue is still of interest today. Therefore different methods have been developed to monitor and assess the surface contamination level such as Leakage current (LC), Acoustic emission and Digital image processing methods. Under conditions where the relative humidity is less than 90%, it appears that the LC would not be a good indicator [6, 7]. Furthermore, LC measurement can be significantly affected by the presence of other electromagnetic waves in the site. Also, installing LC apparatus required certain arrangement and reconstructing of insulator [8]. While the drawback of the acoustic emission method is that it can be influenced by the background noise [9]. The use of digital image processing method has been adopted by two different groups of researchers. Xin et al. [10] and Zhonglin Xia et al. [11] investigated the use of digital camera in determining the dirty area ratio of insulators using digital image processing. They pointed out that the ratio of the dirty area with respect to the insulator total area may help in determining the contamination severity.

The hereby proposed method is based on digital image processing and artificial neural networks to estimate the contamination level of insulators. The developed method allows electric utilities to prevent catastrophic flashovers and reduces forced outage time by giving accurate information about the contamination level in advance without human

intervention, and to determine when washing is necessary.

II. PROPOSED ESDD ESTIMATION ALGORITHM

In this paper, an algorithm for estimating the contamination level of high voltage insulators based on image processing and artificial neural networks has been developed. Using this algorithm, important extracted features from insulators images will be correlated to the equivalent salt deposited density (ESDD) level and hence the possibility of flashovers can be detected. The flowchart in fig.1 is a complete step by step of the work that has been done. A digital camera has been used to capture images for the naturally polluted collected insulators, after that, ESDD values of the collected insulators have been estimated at the high voltage lab at King Fahd University of Petroleum and Minerals (KFUPM). Edge based segmentation technique as well as matrix manipulation was used to segment captured insulators images. Based on the histogram of the insulator hue segmented image, a number of statistical features have been extracted. After that, a neural network has been successfully designed to correlate the insulator extracted features and its contamination level. Finally, testing of the developed estimation algorithm for estimating the contamination level of unseen insulators has been made.

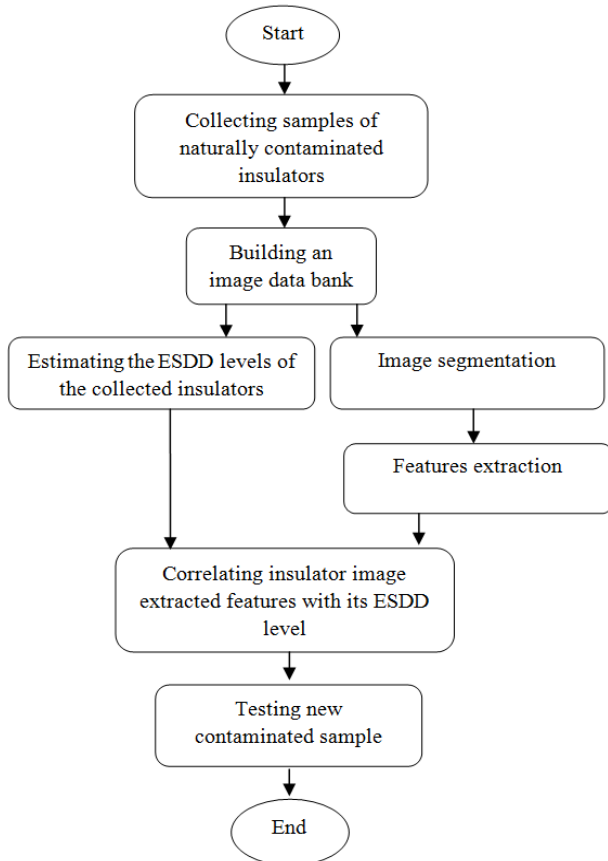


Fig. 1 Proposed ESDD estimation algorithm

The following subsections give a brief discussion on the most important steps in the proposed algorithm.

A. Insulator Image Segmentation and Features Extraction

Segmentation of image is considered as one of the most important preprocessing tasks in image processing. It is used in many applications that depend on computer vision such as hand written recognition, locating objects in images, medical imaging, machine vision, face and finger print recognition and many other applications. In this paper, edge-based segmentation technique has been used to do segmentation. Edge-based segmentation means partitioning an image (separating the objects and background in an image) based on the edge in that image. The edge is defined as the boundaries between two regions in an image having different attributes according to some property such as intensity (gray level), texture or color. Therefore edge based segmentation requires some edge detection techniques before segmentation. Using this method, the boundaries that represent objects in an image are detected, thus these boundaries can be used to specify and identify these objects [12].

In this paper, Sobel operator is used for edge detection. This operator detects the edges by performing a 2D spatial gradient calculation; hence the areas of high gradient values are related to edges [13]. In sobel operator, the calculation of the gradient at each point in a grayscale image is done using two convolution masks (h_x and h_y) with 3x3 sizes, where these masks are convolved with the grayscale image, one of them approximate the gradient in the x-direction $G_x(x, y)$, and the other approximate the gradient in y-direction $G_y(x, y)$.

$$h_x = \begin{bmatrix} -1 & 0 & 1 \\ -2 & 0 & 2 \\ -1 & 0 & 1 \end{bmatrix}, \quad h_y = \begin{bmatrix} -1 & -2 & -1 \\ 0 & 0 & 0 \\ 1 & 2 & 1 \end{bmatrix} \quad (1)$$

$$G_x(x, y) = h_x * f(x, y), \quad G_y(x, y) = h_y * f(x, y) \quad (2)$$

Accordingly, the gradient component $G_x(x, y)$ and $G_y(x, y)$ are produced separately, these can then be combined together to calculate the absolute magnitude of the gradient and the direction of the gradient at each point [13]. The approximate magnitude and direction (θ) of the gradient calculated as follow:

$$|G| = |G_x| + |G_y|, \quad \theta = \arctan\left(\frac{G_y}{G_x}\right) \quad (3)$$

θ : measured with respect to the x-direction.

Image features are of major importance in identification and analysis of regions in an image (image interpretation). They are considered as a distinguishing primitive attributes or characteristics of an image. In this paper, the color model that has been used for features extraction is the HSV (hue, saturation, value) model, especially the hue component. According to that, the RGB segmented insulator was transformed to HSV model. This model was used because it aids in finding numerical differences between insulators of different pollution levels; moreover it helps in reducing the effect of uneven illumination on insulator surface [14].

The histogram of the hue image is a graphical representation of the frequency occurrence of each hue value in the image

[13]. Let $j = 0, 1, \dots, L - 1$, where L is number of hue levels in the image. Therefore, the normalized histogram can be determined as follow:

$$p(r_j) = \frac{n_j}{n} \quad (4)$$

Where $p(r_j)$ is the percentage (probability) of the number of pixels which belongs to level j , while n is the total number of pixels in the image and n_j is the number of pixels at level j . The histogram is usually represented using a bar chart with one bar per hue level. The amplitude of each bar represents the number or percentage of pixels that are related to each level. Fig. 2 shows an insulator image and its hue histogram with 250 levels.

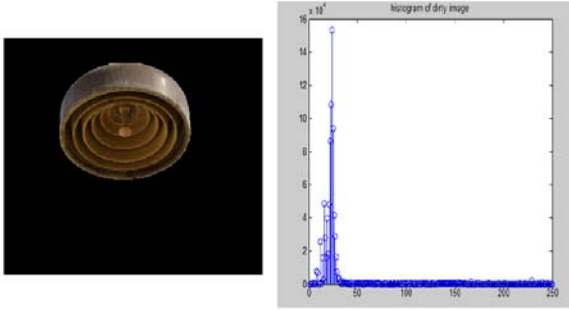


Fig. 2 Image and its hue histogram with 250 levels

Many statistical features, which describe an image or its objects, can be extracted from the hue segmented image histogram [15]. Such as the mean (m), variance, skewness (skew), kurtosis, energy, difference and the normalized histogram error.

The normalized histogram error between two images (have the same view but one of the image has some noise) provides a good measure about the difference between the two images. Hence a high value of the normalized error (Normalized histogram error) means the difference between the two images is high (the image which have noise are highly polluted) and vise versa. In addition to the normalized histogram error feature, the subtraction between the histogram (difference feature) of the two images (clean and dirty) gives a good indication about the variation between the two images. Normalized histogram error and difference features can be calculated as follow

$$\text{Normalized error} = \sum_{j=0}^{L-1} [p_1(r_j) - p_2(r_j)]^2 \quad (5)$$

$$\text{difference} = \frac{\sum_{j=0}^{L-1} [(n_j)_1 - (n_j)_2]}{2 * n} \quad (6)$$

Where r_j is the j th hue level (number of level in histogram is L). Where $p_1(r_j)$ and $p_2(r_j)$ are the percentage (probability) of the number of pixels which belongs to level j for image one and two respectively. $(n_j)_1$ and $(n_j)_2$ are number of pixels which belongs to level j for image one and two respectively.

B. Artificial Neural Networks

Multi-layer Feed-forward Neural Network (MFNN) is considered as one of the most important commonly used method in regression and classification. In general, a MFNN consists of an input layer, several hidden layers, and an output layer. Each layer consists of several numbers of nodes (neuron). Where each node includes a summer and an activation function g . Connecting several nodes in parallel and series, a MFNN network is formed [16]. A typical MFNN network is shown in Fig. 3.

For multi-input multi-output networks in fig. 3 [16], the input vector to the MFNN is given by $R(t) = [r_1(t) \dots r_m(t)]^T$. Therefore, the input to the j th hidden unit is

$$\text{net}_j^h(t) = \sum_{i=1}^{n_y} w_{ji}^h r_i(t) + \theta_j^h \quad (7)$$

where w_{ji}^h are the weights of the hidden layer and θ_j^h is the bias term. The output of the j th hidden neuron is

$$g_j(t) = f_j^h(\text{net}_j^h(t)) \quad (8)$$

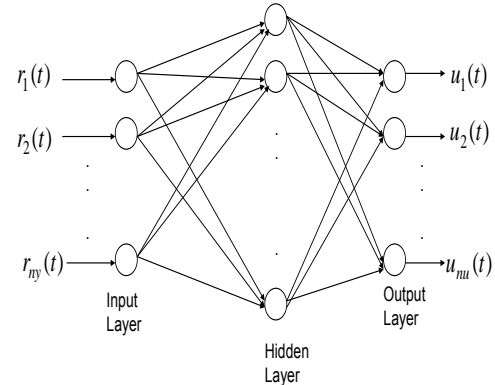


Fig. 3 Typical multi-layer feed-forward neural networks

Where f_j^h is the activation function. The equations for the output nodes with linear activation functions are

$$u_k(t) = \sum_{j=1}^L w_{kj}^o g_j(t) + \theta_k^o \quad (9)$$

Where the “ o ” superscript denotes the output, L is the number of neurons in the hidden layer, $u_k(t)$ denotes the k th output unit where k from $(1, \dots, nu.)$. The neural network is trained using the back-propagation algorithm, which seeks to find optimum weights biases of the neural network along the negative gradient of a cost function. The cost function is described by

$$J = \sum_{i=1}^n [u(i) - u_r(i)] \quad (10)$$

Where u and u_r denote the actual and desired outputs respectively.

III. DESIGN OF A COMBINED IMAGE PROCESSING - NEURAL NETWORK ALGORITHM FOR ESDD ESTIMATION

The statistical features extracted from the processed insulator captured images are used as inputs to the developed neural network. The feature vector was consisted of seven statistical features. Therefore, the number of inputs to the developed neural network is seven and number of outputs is one (contamination level) as shown in fig.4. The used training input matrix looks as follows:

$$\begin{bmatrix} \text{Difference}_1 & \dots & \text{Difference}_n \\ \text{Normalized error}_1 & \dots & \text{Normalized error}_n \\ \text{Mean}_1 & \dots & \text{Mean}_n \\ \text{Variance}_1 & \dots & \text{Variance}_n \\ \text{Skewness}_1 & \dots & \text{Skewness}_n \\ \text{Kurtosis}_1 & \dots & \text{Kurtosis}_n \\ \text{Energy}_1 & \dots & \text{Energy}_n \end{bmatrix} \quad (11)$$

Where, n denotes the number of features patterns for training. The developed neural network has three layers (input, hidden and output) as shown in fig.3. The activation functions that have been used in the hidden layer and the output layer are the nonlinear (Tansig) and linear function (Purelin), respectively.

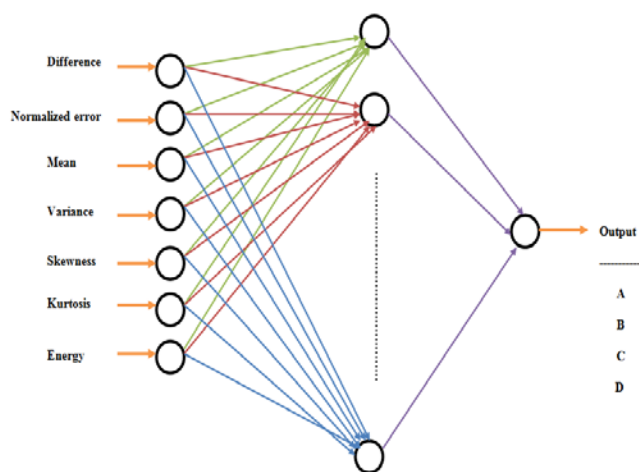


Fig. 4 Developed neural network structure

IV. RESULTS AND DISCUSSION

Fifty one samples of super fog porcelain insulators were collected (each was designated by a code); eleven samples from SEC and the others are from KFUPM Dhahran Electrical Insulator Research Station. The images of insulators were taken at KFUPM Dhahran Electrical Insulator Research Station; this location was selected because it shares similar environmental conditions (may be worst conditions) with many transmission lines and substations in the kingdom. Digital camera (Nikon D7000, 16.9 mega pixels) attached to a fixed stand was used to capture images for the collected insulators.

The International Electro technical Commission (IEC) adopted a standard method to find the ESDD value in case of porcelain insulators [17]. Based on that method, the ESDD levels of the 51 collected insulator samples were estimated at the high

voltage laboratory at the RI-KFUPM. Table I shows the ESDD values of 36 collected insulators while the other 15 ESDD values are listed in table IV. As can be seen, the estimated ESDD values ranges from 0.0001 to more than 0.4 mg/cm². Therefore, the levels of contamination were classified into four ranges: light pollution level ($ESDD < 0.1$), medium pollution level ($0.1 \leq ESDD < 0.2$), heavy pollution level ($0.2 \leq ESDD < 0.3$) and very heavy pollution level ($0.3 \leq ESDD$).

TABLE I
ESDD VALUES OF 36 COLLECTED INSULATORS

Insulator code	ESDD value mg/cm ²	Pollution level	Insulator code	ESDD value mg/cm ²	Pollution level
Clean	0.0009	Light	7G	0.1084	Medium
1F	0.0221	Light	8G	0.0907	Light
2F	0.0227	Light	9G	0.0882	Light
3F	0.0219	Light	10G	0.0357	Light
5AT	0.2107	Heavy	2H	0.1554	Medium
6AE	0.1701	Medium	3H	0.0314	Light
7A	0.1866	Medium	4H	0.1400	Medium
1D	0.2735	Heavy	5H	0.0730	Light
2D	0.2962	Heavy	6H	0.0273	Light
3DE	0.2894	Heavy	C1	0.0007	Light
5DE	0.2738	Heavy	C2	0.0007	Light
10BE	0.4461	Very Heavy	C4	0.0009	Light
11BE	0.4083	Very Heavy	C5	0.0009	Light
12B	0.4134	Very Heavy	C6	0.0008	Light
1G	0.1066	Medium	C8	0.0008	Light
3G	0.0207	Light	C10	0.0009	Light
5G	0.0760	Light	C11	0.0007	Light
6G	0.1659	Medium	C12	0.0009	Light

A. Results of Insulators Images Segmentation and Feature Extraction

Segmentation of insulator image has been done in two stages using Matlab software. In the two stages, segmentation has been done for grayscale insulator image as shown in fig.5-a. In the first stage, the cap of insulator has been excluded from the image using matrix manipulation, where all of the pixels values which is above the edge between the cap and insulators have been changing to zero (The position of that edge is fixed for all insulators images) as shown in fig.5-b. In the second stage, the background of the image has been excluded using edge based segmentation method. Fig.5-c shows the final RGB segmented image.

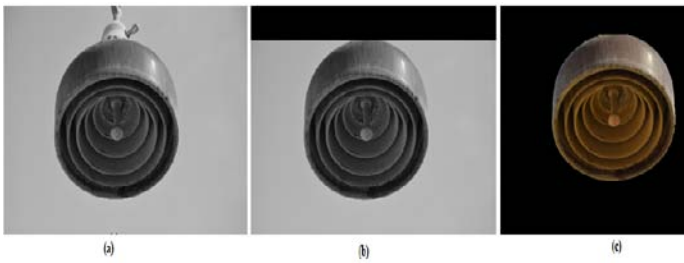


Fig. 5 (a)-Origin grayscale image (b)-First stage segmented image (c) - final RGB segmented image

Based on the histogram of the hue segmented insulator image, statistical features such as mean, variance, skewness, kurtosis, energy, normalized histogram error and the percentage difference between the hue histograms of clean reference image and the collected ones were extracted. Table II shows the statistical feature values of different insulator samples as well as its corresponding ESDD values.

TABLE II
SAMPLE OF STATISTICAL FEATURES AND ITS CORRESPONDING ESDD VALUES OF DIFFERENT POLLUTED INSULATORS

Image code	C9	7A	9AE	12B	6DT	10BE
Difference	8.7138	27.141	27.041	57.111	53.082	59.732
Normalized error	0.2422	2.0792	1.8794	11.249	9.0245	10.067
Mean	19.041	22.384	23.01	23.529	26.264	23.794
Variance	818.05	701.83	748.32	273.26	896.72	312.24
Skewness	6.9847	5.9281	5.7977	9.4155	5.5034	9.1282
Kurtosis	52.149	40.022	38.375	103.46	34.12	95.424
Energy	0.0975	0.0643	0.061	0.1047	0.0816	0.0947
ESDD	0.0009	0.1862	0.1813	0.4138	0.3023	0.4469

B. Training and Validation of the Developed Artificial Neural Network

To train and test the neural network, the collected insulators have been divided into a training group and a testing one. Thirty six insulators with their features patterns and ESDD levels are used for training the developed neural network. The other fifteen insulator samples with their features and ESDD values are used for testing the developed neural network. The insulators groups with their code numbers and corresponding ESDD levels, selected for training and testing the networks, are given in Tables I and IV, respectively. The outputs of the developed neural network are assigned letters as in Table III. The training of the neural network is accomplished using the

most commonly used training algorithm (gradient back-propagation).

TABLE III
NEURAL NETWORK OUTPUTS

Pollution Level	ESDD Range	Output
Light level	$ESDD < 0.1$	A
Medium	$(0.1 \leq ESDD < 0.2)$	B
Heavy	$(0.2 \leq ESDD < 0.3)$	C
Very heavy	$(0.3 \leq ESDD)$	D

Different number of hidden units has been tried such that the performance of the network was optimized. The number of hidden neurons in the optimized neural network was seven, where the mean square error (MSE) for training and testing was the minimum (MSE=0.0011) and (MSE=0.0024), respectively. The validation results of using the testing data given in table IV (for fifteen insulators) indicated that the developed neural network was able to predicate correctly the level of contamination for twelve insulators, while for the other three the pollution level was wrongly estimated. According to that, the performance of the developed network is 80%. Further detail for validation results is given in Table IV. The absolute error column in that table represents the absolute difference between the measured and predicted ESDD value.

TABLE IV
VALIDATION RESULTS

Insulator code	Measured ESDD value mg/cm^2	Actual Pollution level	Predicted ESDD value mg/cm^2	Predicted Pollution level	Absolute Error
4F	0.0234	A	0.0546	A	0.0312
8A	0.2003	C	0.073	A	0.1273
C13	0.0009	A	0.0129	A	0.012
9AE	0.1817	B	0.1435	B	0.0382
4D	0.2765	C	0.3317	D	0.0552
6DT	0.3024	D	0.2546	C	0.0478
13BT	0.4468	D	0.3804	D	0.0664
14B	0.4162	D	0.3992	D	0.017
2G	0.1863	B	0.1821	B	0.0042
4G	0.0217	A	0.0951	A	0.0734
1H	0.0279	A	0.0316	A	0.0037
7H	0.0789	A	0.0477	A	0.0312

C3	0.0007	A	0.0113	A	0.0106
C7	0.0007	A	0.0103	A	0.0096
C9	0.0010	A	0.0053	A	0.0043

V. CONCLUSION

In this paper, an algorithm for estimating the contamination level of high voltage insulators without the intervention of humans has been developed. The developed algorithm is based on a combination of image processing technique and artificial neural networks. Levels of contamination are classified into four categories: light pollution level, medium pollution level, heavy pollution level and very heavy pollution level. Segmentation of insulator image has been done in two stages using Matlab software. In the first stage, the cap of insulator has been excluded from the image using matrix manipulation. In the second stage, edge based segmentation method was used to exclude the background. Image processing has been used to extract needed features from insulators hue segmented images to assess the contamination level that would lead to a flashover. The types of image features were considered is the histogram based statistical feature. Multi-layer Feed-forward Neural Network (MFNN) was used to design a neural network which is capable of predicting the level of contamination (ESDD level) of polluted insulators. The input to the network is the extracted features of insulators images and the output is the pollution levels. The rate of success of the developed algorithm is 80%. It is expected that the developed algorithm, if well implemented, will prevent catastrophic flashovers and reduces forced outage time by giving accurate information about the contamination level in advance. Hence improving the overall reliability of the electrical system.

REFERENCES

- [1] R. S. Gorur, ""Where is Insulator Technology Today:What has been Accomplished, What is still Missing?," in Insulator 2001 World Insulator Congress and Exhibition , Shanghai,China, 2011.
- [2] I. AL-Hamoudi, "Performance of Silicone Rubber Insulators in Eastern Region of Saudi Arabia," Ph.D.Thesis,American University of London, 2002.
- [3] A.-S. H. Hamza, N. M. Abdelgawad and B. A. Arafa, "Effect of desert environmental conditions on the flashover voltage of insulators," Elsevier, Vols. Volume 43, Number 17, November 2002 , pp. 2437-2442(6), 2002.
- [4] K. Siderakis, D. Pylarinos, E. Thalassinakis, I. and E. Pyrgiti, "Pollution Maintenance Techniques in Coastal High Voltage Installations," ETASR - Engineering, Technology & Applied Science Research, Vols. 1,No. 1, 2011, 1-7, 2011.
- [5] The Research Institute of KFUPM, "high Voltage Insulator Performance in the Kingdom of Saudi Arabia," Saudi Arabia ,report prepared for Electricity Corporatin KSA ,1990 pp. 9-127,821-840, 1990.
- [6] C. N. Richard and J. D. Renowden, "DEVELOPMENT OF A REMOTE INSULATOR CONTAMINATION MONITORING SYSTEM," IEEE Transactions on Power Delivery, vol. 12, no. 1, January 1997.
- [7] J. Y. Li, C. X. Sun and S. A. Sebo, "Humidity and contamination severity impact on the leakage currents of porcelain insulators," Generation, Transmission & Distribution, IET, vol. 5, pp. 19- 28, Jan. 2011.
- [8] C. M. Pei, N. Q. Shu, L. L. D. Z. P. Li and D. Wang, "An Acoustic Emission Method for On-line Monitoring the Contamination-causing Flashover of Insulator," in Electrical Machines and Systems, 2008. ICEMS 2008. , 17-20 Oct. 2008.
- [9] R. S. Gorur, E. A. Cherney and J. T. Burnham, "Outdoor Insulators," pp.31,55-56,146,181-191,211, 1999.
- [10] X. Mei, L. Tiecheng, W. Xiaoyun and Z. Bo, "Insulator surface Dirty Image Detection Technology Based on Improved Watershed Algorithm," in IEEE, 2012.
- [11] Z. Xia, D. Hu, X. Hu, W. Xie, Z. Yuan and Q. Qin, "Application of an improved watershed algorithm in the insulator contamination monitoring," in IEEE, 2011.
- [12] S. B. Wesolkowski, "Color Image Edge Detection and Segmentation: A Comparison of the Vector Angle and the Euclidean Distance Color Similarity Measures," Waterloo, Ontario, Canada, 1999.
- [13] O. Marques, PRACTICAL IMAGE AND VIDEO PROCESSING USING MATLAB®, Wiley Press.
- [14] P. Sebastian, Y. Voon and R. Comley, "Colour Space Effect on Tracking in Video Surveillance," International Journal on Electrical Engineering and Informatics, Volume 2, Number 4, 2010.
- [15] W. K. Pratt, Digital Image Processing: PIKS Inside, Third Edition., John Wiley & Sons, Inc.ISBNs: 0-471-37407-5 (Hardback); 0-471-22132-5 (Electronic), Copyright © 2001.
- [16] A. P. Engelbrecht, Computational Intelligence: An Introduction, 2nd Edition, WILEY.
- [17] "Artificial pollution tests on high-voltage insulators to be used on a.c. system".IEC 60507, International Electro technical Commission (IEC) document.

Intelligent Control of DFIG based Variable Speed Wind Turbine System using Artificial Neural Network

Sathans^a and Jitender Rohilla^b

- a. is Professor with the Department of Electrical Engineering, National Institute of Technology, Kurukshetra-136119, INDIA (phone: +91-1744-233390; fax: +91-1744-238050; e-mail: sathans@rediffmail.com).
- b. Jitender Rohilla was M. Tech. Student with the Department of Electrical Engineering, National Institute of Technology, Kurukshetra-136119, INDIA (e-mail: jiturohilla@gmail.com).

Abstract— In this paper, intelligent control scheme using artificial neural network (ANN) is proposed for doubly fed induction generator (DFIG) based variable speed wind turbine system. ANN based rotor loop design is developed for variable speed wind turbine and the rotor side controller is proposed for DFIG to improve its transient performance in all wind speed conditions. For comparative analysis, the conventional vector control scheme is also implemented for the system under investigation. It is observed, from the results, that the dynamic performance of the DFIG is improved with the proposed intelligent control scheme, as compared to the conventional control. The simulations are carried out using MATLAB platform.

Keywords— Artificial neural network (ANN), Doubly fed induction generator (DFIG), Intelligent control, Variable speed wind turbine, Vector control.

I. INTRODUCTION

IN recent years, exploitation of fossil fuel is on the rise leading to the increased air pollution by greenhouse gases. As an alternative, renewable energy systems, especially wind energy generation, have attracted great interests. Large wind farms have been installed or planned across the globe and the power ratings of the wind turbines are increasing. Wind power installed capacity is growing at the rate of 20% annually on the average around the world, and its cost has decreased 50% in the last 10 years [1]. In wind farms, wind turbines based on DFIG, with converters rated at 25% - 30% of the generator rating, are used as compared to wind turbines using a fixed speed induction generator, due to variable speed operation, four-quadrant active and reactive power capabilities, lower converter costs, lower power losses, higher efficiency, reactive power production, and flexible control of DFIG [2-4]. Many researchers have attempted to improve DFIG transient performance by developing different control schemes in the past. In [5], the authors investigated and compared the different crow bar protections and rotor side converter restart schemes to improve DFIG transient performance. A new series and parallel connected grid side converters with conventional DFIG was developed to damp out the stator and rotor currents oscillations in [6]. The authors in [7] used

particle swarm optimization (PSO) to design the optimal PI controllers for the rotor side converter and grid side converter of DFIG for a particular wind speed. In [8], the authors used intelligent control techniques for the variable speed cage machine used for the wind generation system, in which a cage induction machine is considered and a fuzzy control system is used to drive the wind energy conversion system to the point of maximum energy capture for a given wind velocity. Fuzzy logic is used to develop an advanced and intelligent control strategy for a line excited cage generator system used for wind power applications in [9]. In [10], ANN control technique has been developed for DFIG based wind energy generation system.

This paper presents the design and implementation of intelligent control scheme using ANN for DFIG based variable speed wind turbine system. The first part of the paper explains the modeling of wind turbine and ANN based rotor loop design and the second part illustrates the modeling and implementation of ANN based intelligent rotor control of DFIG. The conventional vector control scheme is also implemented on the same system to present the comparative analysis of performance with the proposed ANN based control scheme. It is demonstrated through results that the ANN based control scheme ensures better stability and regulation of the power generated by the DFIG based wind turbine system.

II. MODELING OF WIND TURBINE

Wind turbines produce electric power by using the power of the wind to drive an electrical generator. The power contained in the wind is given by the kinetic energy of the flowing air mass per unit time [11] and is given as:

$$\begin{aligned}
 P_{\text{air}} &= \frac{1}{2} (\text{air mass per unit time})(\text{wind velocity})^2 \\
 &= \frac{1}{2} (\rho AV)V^2
 \end{aligned}$$

$$P_{\text{air}} = \frac{1}{2} \rho A V^3 \quad (1)$$

Although Eq. (1) gives the power available in the wind, the power transferred to the wind turbine rotor is reduced by the power coefficient, C_p ,

$$C_p = \frac{P_{\text{wind}}}{P_{\text{air}}} \quad (2)$$

$$P_{\text{wind}} = C_p P_{\text{air}}$$

$$P_{\text{wind}} = \frac{1}{2} \rho A C_p V^3 \quad (3)$$

Where, P_{air} is the power contained in wind (in watts) , ρ is the air density (1.225 kg/m³ at 15°C and normal pressure), A is the swept area in square meter, and V is the wind velocity in m/sec. Fixed pitch wind turbine has been modeled to drive the DFIG. The number of blades are considered as 3, blade radius is considered as 13m with fixed pitch as ($\beta = 0$) [12]. C_p is calculated as

$$C_p(\lambda, \beta) = C_1 \left(\frac{C_2}{\lambda_i} - C_3 \beta - C_4 \right) e^{\frac{-C_5}{\lambda_i}} + C_6 \lambda \quad (4)$$

Where,

$$C_1=0.5176, C_2=116, C_3=0.4, C_4=5, C_5=21, C_6=0.0068$$

$$\frac{1}{\lambda_i} = \frac{1}{\lambda + 0.008\beta} - \frac{0.0035}{\beta^3 + 1} \quad (5)$$

And turbine torque is

$$T_{wt} = \frac{P_{\text{wind}}}{\omega} \quad (6)$$

Where, ω = rotational speed of rotor

The relationship of C_p , λ and β is nonlinear. The tip speed ratio λ is given by:

$$\lambda = \frac{\omega R}{V} \quad (7)$$

Where, R = radius to tip of rotor

Under rated wind speed conditions, pitch angle β is considered zero. Therefore, the three-dimensional relationship of C_p , λ and β turns to the two-dimensional relationship of C_p and λ , and for wind speed conditions above rated speed, pitch angle β is controlled to get steady output power. Because the wind power generation is a complex nonlinear system, ANN based control method is proposed in this paper. ANN offers many advantages over nonlinear adaptive controllers in terms of robustness, improved performance, learning capabilities, and increased flexibility [13]. Fig. 1 shows the systematic diagram of ANN implementation to obtain C_p vs. λ characteristics of wind turbine at different β .

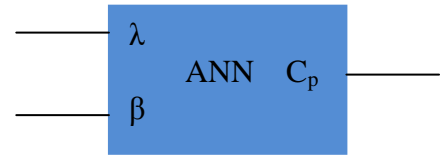


Fig 1 ANN block for C_p vs. λ characteristics

The C_p (λ , β) curves are known for some discrete values of β ($\beta = 0 \dots 20$). The discrete values are used as training data for the ANN. The neural network has two inputs, λ and β , and one output C_p , and it consists of two hidden layers. The standard back-propagation algorithm is used for learning. The neural network, so designed, is able to produce a power coefficient for any value of tip speed ratio in the range $[0 \dots 20]$ and for any continuous pitch value in the range $[0 \dots 20]$. Obtained with ANN, the Fig 2 shows the C_p vs. λ characteristics of wind turbine at different β .

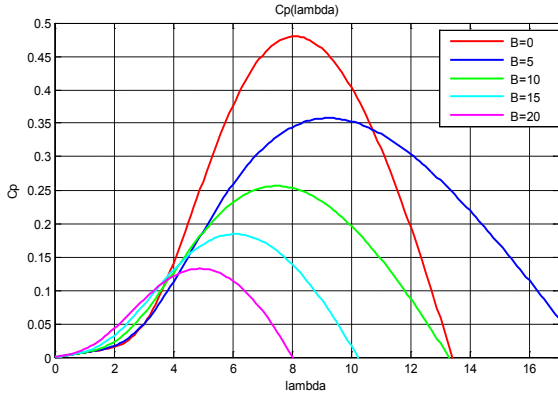


Fig 2. C_p vs. λ characteristics of wind turbine at different β .

III. MODELLING OF DFIG

DFIG is basically a wound rotor induction machine in which stator is directly connected to the grid, and the connection of the rotor to the grid is via a back-to-back (PWM) converter as shown in Fig. 3.

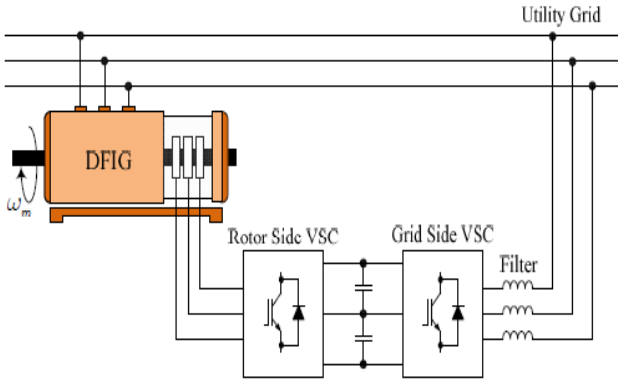


Fig.3 Schematic diagram of a DFIG-based wind energy generation [14].

The DFIG is modeled same as induction machine. Stator and rotor windings are identical, sinusoidally distributed and displaced 120 degree apart. In order to explain the actual behavior of the DFIG, dynamic equations are considered for more realistic observation. From the control point of view of the machine, the d-q representation of an induction machine leads to control flexibility. The dynamic behavior of the DFIG in synchronous reference frame can be represented by the Park equations provided all the rotor quantities are

referred to the stator side. The stator and rotor voltages are expressed as [15]:

$$V_{ds} = R_s i_{ds} + \frac{d\phi_{ds}}{dt} - \omega_e \phi_{qs} \quad (8)$$

$$V_{qs} = R_s i_{qs} + \frac{d\phi_{qs}}{dt} + \omega_e \phi_{ds} \quad (9)$$

$$V_{dr} = R_r i_{dr} + \frac{d\phi_{dr}}{dt} - (\omega_e - \omega_r) \phi_{qr} \quad (10)$$

$$V_{qr} = R_r i_{qr} + \frac{d\phi_{qr}}{dt} + (\omega_e - \omega_r) \phi_{dr} \quad (11)$$

The flux linkage equations of the stator and rotor can be related to their currents and are expressed as:

$$\phi_{ds} = L_{ss} i_{ds} + L_m i_{dr} \quad (12)$$

$$\phi_{qs} = L_{ss} i_{qs} + L_m i_{qr} \quad (13)$$

$$\phi_{dr} = L_{rr} i_{dr} + L_m i_{ds} \quad (14)$$

$$\phi_{qr} = L_{rr} i_{qr} + L_m i_{qs} \quad (15)$$

Where $L_{ss} = L_s + L_m$ and $L_{rr} = L_r + L_m$

The electromagnetic torque developed is expressed as:

$$\begin{aligned} T_e &= 1.5p(\phi_{ds} i_{qs} - \phi_{qs} i_{ds}) \\ &= 2H \frac{d\omega_m}{dt} + B\omega_m + T_m \end{aligned} \quad (16)$$

Where, T_m is positive for motoring operation and negative for generator operation. Equations (8) to (16) are the set of differential equations which represent a 4th order model for describing the dynamic behavior of DFIG. These equations are simulated in MATLAB to develop a model of the DFIG for analysis. In the simulated model, the mechanical torque, the stator and rotor input voltages and the synchronous speed are the inputs and the electromagnetic torque, the stator and rotor currents and the rotor speed act as the outputs. The model can be run in sub-synchronous as well as in super-synchronous mode. In sub-synchronous mode ($\omega_e > \omega_r$) positive load torque will operate the model as a motor while in super-synchronous mode ($\omega_r > \omega_e$) a negative load torque will operate the model as a generator. The power flow scheme of both operating modes is shown in Fig 4 [16].

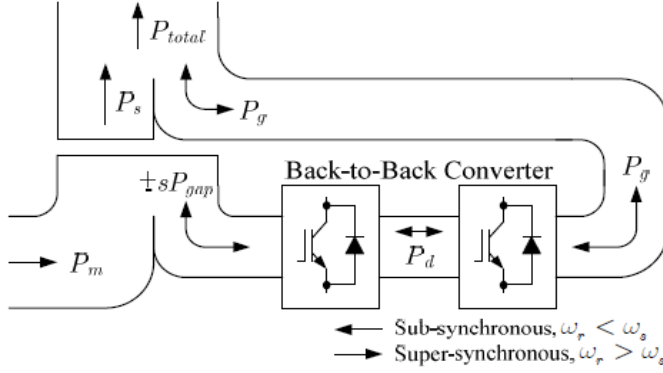


Fig.4 Power flow of a DFIG system [16].

IV. CONTROL SCHEME OF DFIG

Power regulation between the generator and the grid is an essential requirement when DFIG is connected to an existing grid [17]. The control technique can be applied on both rotor side converter (RSC) and grid side converter (GSC). The objective of the RSC is to control both the active and reactive powers independently; while the objective of the GSC is to keep the dc-link voltage constant, regardless of the magnitude and direction of the rotor power. This control technique is called vector control technique and is a conventional technique. In this paper, the main focus is the design of the ANN based RSC controller.

A. Conventional RSC Controller Design

In order to achieve a decouple control of active and reactive power; stator flux oriented vector control scheme is adopted. In the stator-flux oriented reference frame, the d-axis is aligned with the stator flux linkage vector φ_s , namely, $\varphi_{ds} = \varphi_s$ and $\varphi_{qs} = 0$. Stator voltage drop across resistance has been neglected [18]. The frequency and amplitude of the stator or grid voltage is assumed constant. Thus $V_{ds} = 0$, $V_{qs} = V_s$ and $\varphi_{ds} = \varphi_s$, $\varphi_{qs} = 0$. Neglecting the stator resistance, $R_s = 0$, then eq. (8) to (15) become

$$V_{ds} = 0 = \frac{d\varphi_{ds}}{dt} - \omega_e \varphi_{qs} \quad (17)$$

$$V_{qs} = \omega_e \varphi_{ds} = V_s = \frac{d\varphi_{ds}}{dt} + \omega_e \varphi_{ds} \quad (18)$$

$$V_{dr} = R_r i_{dr} + \frac{d\varphi_{dr}}{dt} - (\omega_e - \omega_r) \varphi_{qr} \quad (19)$$

$$V_{qr} = R_r i_{qr} + \frac{d\varphi_{qr}}{dt} + (\omega_e - \omega_r) \varphi_{dr} \quad (20)$$

And

$$\varphi_s = L_{ss} i_{ds} + L_m i_{dr} \quad (21)$$

$$0 = L_{ss} i_{qs} + L_m i_{qr} \quad (22)$$

$$\varphi_{dr} = L_{rr} i_{dr} + L_m i_{ds} \quad (23)$$

$$\varphi_{qr} = L_{rr} i_{qr} + L_m i_{qs} \quad (24)$$

Now by using eq. (21-24) the eq. (19-20) are:

$$V_{dr} = R_r i_{dr} + \left(L_{rr} - \frac{L_m^2}{L_{ss}} \right) \frac{di_{dr}}{dt} - [(\omega_e - \omega_r) \{ L_{rr} - \frac{L_m^2}{L_{ss}} \}] i_{qr}$$

$$V_{qr} = R_r i_{qr} + \left(L_{rr} - \frac{L_m^2}{L_{ss}} \right) \frac{di_{qr}}{dt} + [(\omega_e - \omega_r) \{ L_{rr} - \frac{L_m^2}{L_{ss}} \}] i_{dr} + \frac{L_m V_s}{\omega_s L_{ss}}$$

by solving these eq. we have:

$$V_{dr} = V'_{dr} + V_{dr}^{comp} \quad (25)$$

$$V_{qr} = V'_{qr} + V_{qr}^{comp} \quad (26)$$

$$v_{dr}^{comp} = - \left[(\omega_s \omega_r) \left(L_r \frac{L_m^2}{L_s} \right) \right] i_{qr} \quad (27)$$

$$v_{qr}^{comp} = (\omega_s - \omega_r) \left[\left(L_r - \frac{L_m^2}{L_s} \right) i_{dr} \frac{L_m V_s}{\omega_s L_s} \right] \quad (28)$$

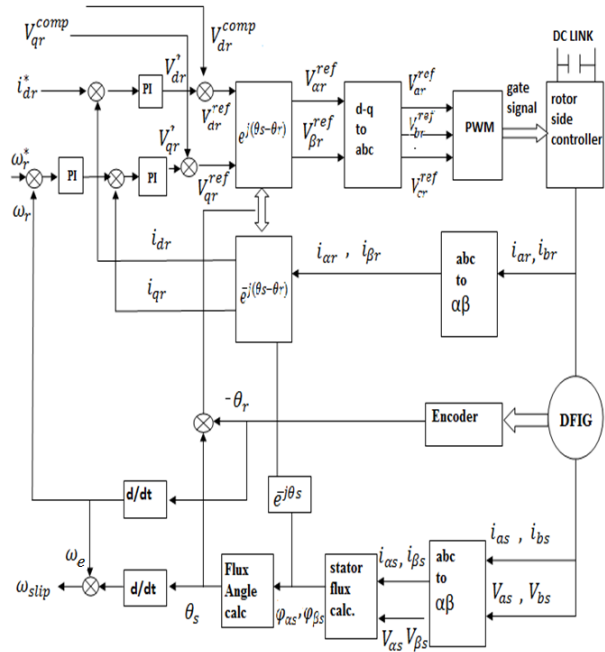


Fig.5 Vector control scheme of RSC

B. Proposed ANN controller

ANNs are powerful tools for modelling. ANNs can identify and learn correlated patterns between input data sets and corresponding target values. After training, ANNs can be used to predict the outcome of new independent input data [19].

In this paper, the data set from Conventional PI controller is used to train ANN structure, with one input layer and one output layer and number of hidden neurons as two, using Levenberg-Marquardt back propagation method. In the training process, 70% data is used for training, 15% is used for validation and 15% is used for testing. The ANN speed control technique block in a vector controlled drive system is shown in Fig. 6. The controller observes the pattern of speed loop error signal and correspondingly updates the output so that actual speed ω_r matches the reference speed ω_{r_ref} .

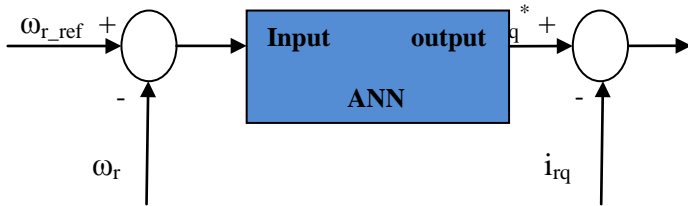


Fig.6 Proposed ANN control structure.

V. RESULTS AND DISCUSSION

Simulation studies are carried out on a 3hp DFIG and its control scheme is implemented in MATLAB environment. The parameters used are given in Appendix. When, after 5 sec, there is a step change in wind velocity from 12 m/s to 10 m/s, the simulation results with conventional PI tuned controller are shown in Fig. 9-12.

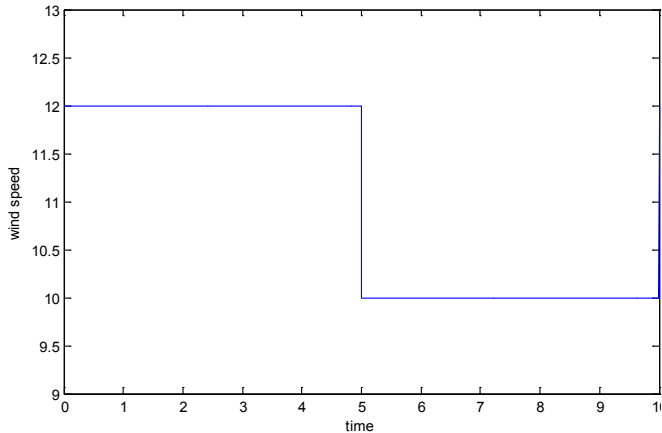


Fig. 7 Wind velocity

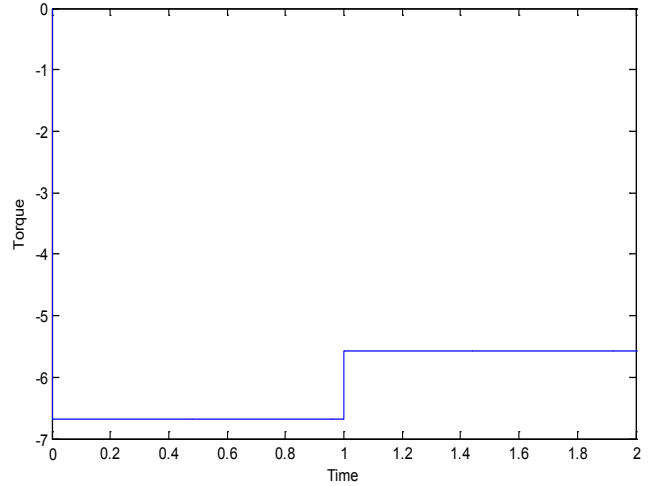


Fig. 8 Mechanical input torque

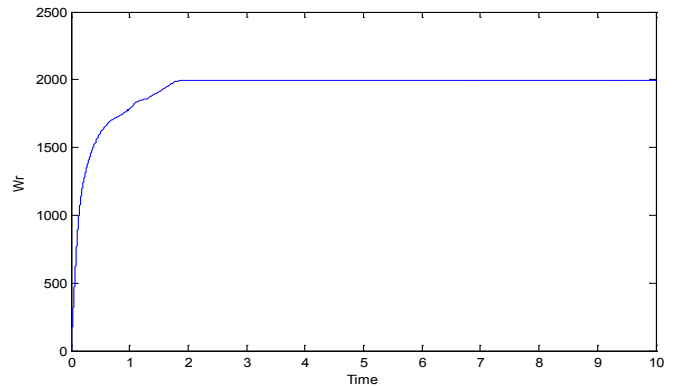


Fig. 9 Rotor speed with conventional PI controller

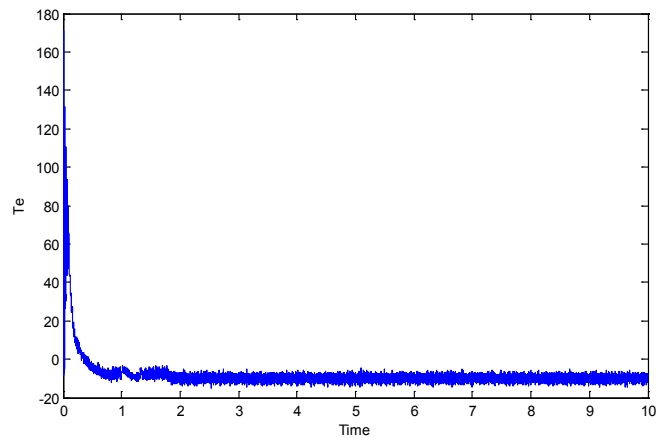


Fig.10 Torque with conventional PI controller

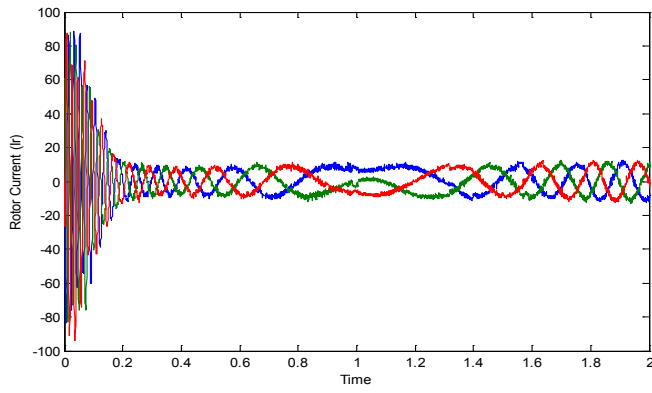


Fig.11 Rotor current without ANN

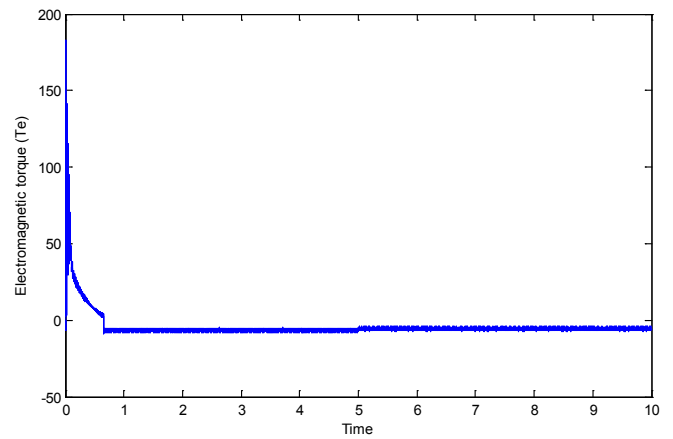


Fig. 14 Torque with ANN control scheme

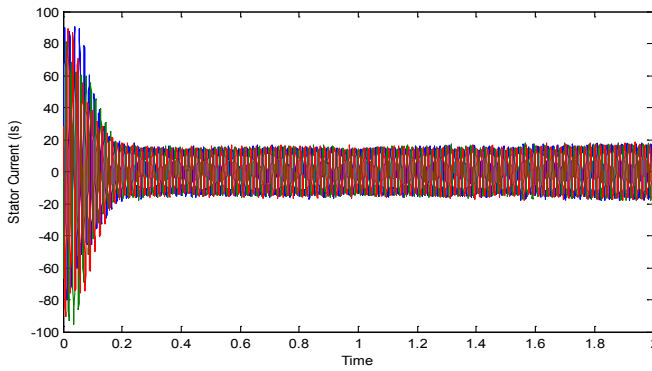


Fig.12 Stator current with conventional PI controller

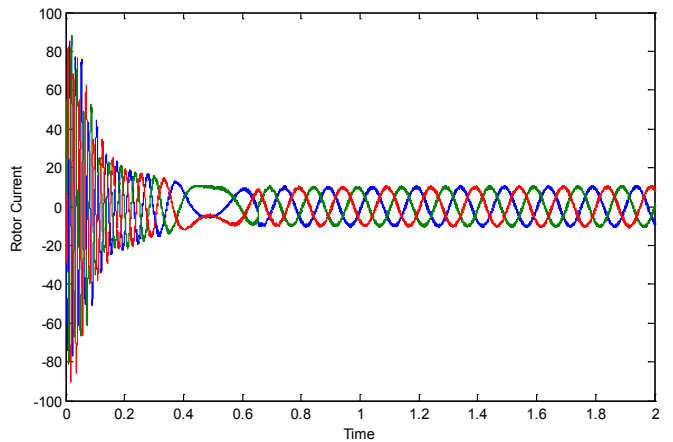


Fig. 15 Rotor current with ANN control scheme

The results with the proposed ANN control scheme are shown in Fig. 13-16.

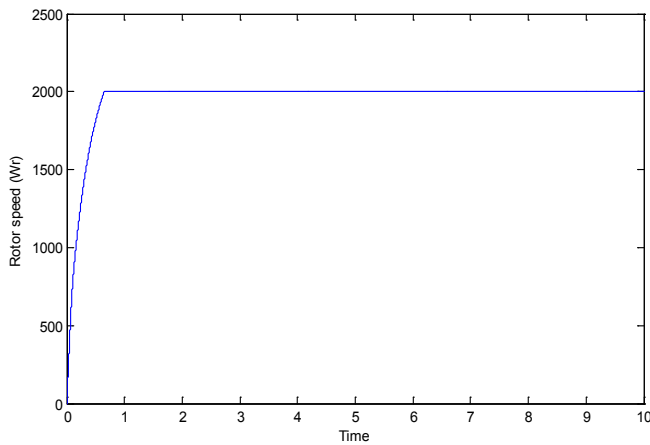


Fig.13 Rotor speed with ANN control scheme

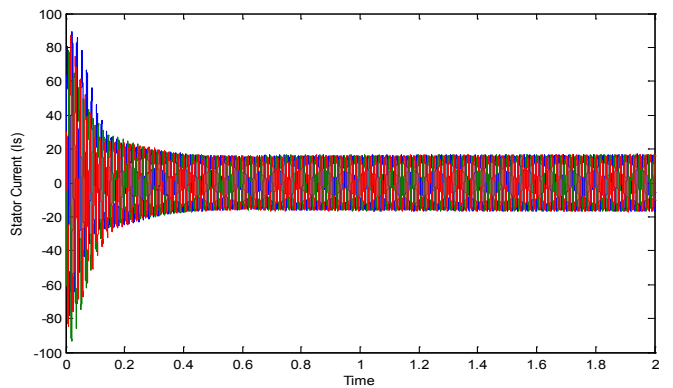


Fig. 16 Stator Current with ANN control scheme

From Fig. 9-16, it is evident that the disturbances caused in the rotor speed, electromagnetic torque, stator and rotor current

are smoothened and with the use of the ANNs and less oscillatory as compared to conventional PI controller.

VI. CONCLUSION

An ANN based speed control scheme of DFIG, driven by a wind turbine, has been developed. The developed ANN control scheme has reasonable accuracy and simple structure. The comparative analysis of the performance with the intelligent and conventional controllers shows that ANN is very effective on the stabilization of the system.

APPENDIX

Stator Voltage	220V
R_s	0.435 ohm
R_r	0.816 ohm
X_s	0.446 ohm
X_m	0.43 ohm
X_r	0.446 ohm
No of pole pair	2
J (Inertia constant)	0.08 kg.m ²

REFERENCES

[1] "Global wind energy outlook 2008", Global Wind Energy Council, Oct. 2008(available online at [http://www.gwec.net /index.php?id=92](http://www.gwec.net/index.php?id=92)).

[2] Lie Xu, Phillip Cartwright, "Direct Active and Reactive Power Control of DFIG for Wind Energy Generation", IEEE Transactions on Energy Conversion, Vol. 21, No.3, September 2006.

[3] Muller S., Deicke M. "Doubly fed induction generator systems for wind turbines," IEEE industry application magazine, May /June 2002.

[4] F. Mei and B. C. Pal, "Modeling analysis of grid connected doubly fed induction generator", IEEE Transactions on Energy Converse., Volume 22, No. 3, pp. 728-736, Sep 2007.

[5] Mustafa Kayikçi, J.V.Milanovic, "Assessing Transient Response of DFIG-Based Wind Plants—the Influence of Model Simplifications and Parameters," IEEE Transactions on power systems, Vol. 23, No. 2, pp. 545-554, May 2008.

[6] Singh B., Emmoji V., Singh S.N., "Performance evaluation of series and parallel connected grid side converters of DFIG," Power and Energy Society General Meeting - Conversion and Delivery of Electrical Energy in the 21st Century, 2008 IEEE, pp. 1-8, 20-24 July 2008.

[7] F. Wu, X. P. Zhang, K. Godfrey, "Small Signal Stability Analysis and Optimal Control of a Wind Turbine with Doubly Fed Induction Generator," IET Generation, Transmission & Distribution, Volume 1, Issue 5, pp. 751-760, 2007.

[8] M. G. Simoes, B. K. Bose, R. J. Spiegel, "Design and performance evaluation of a fuzzy logic based variable speed wind generation system," IEEE Trans. Ind. Appl., vol. 33, no. 4, pp. 956-965, Aug. 1997.

[9] M. G. Simoes, B. K. Bose, R. J. Spiegel, "Fuzzy logic based intelligent control of a variable speed cage machine wind generation system," IEEE Trans. Power Electron., vol. 12, no. 1, pp. 87-95, 1997.

[10] G. Venu Madhav and Y. P. Obulesu "Artificial Neural Network based control of Double Fed Induction Generator" International Journal of Emerging Trends in Electrical and Electronics (IJETEE) Vol. 1, Issue. 1, March-2013.

[11] O. A. Lara, N. Jenkins, J. Ekanayake, P.Cartwright, M. Hughes, "Wind energy generation: Modeling and Control", John Wiley and Sons, UK, 2009.

[12] K. Trinadha, A. Kumar, K. S. Sandhu, " Study of Wind Turbine based SEIG under Balanced/Unbalanced Loads and Excitation" International Journal of Electrical and Computer Engineering (IJECE) Vol.2, No.3, June 2012, pp. 353-370 ISSN: 2088-8708

[13] WEI Zhi-nong, YU Xiao-yong, WU Jia-jia, HAN Lian-shan, XIE Xiang, CHE Dan, WANG Yue "The Intelligent Control of DFIG-Based Wind Generation".

[14] Tarek Medalel Masaud1, Student Member, IEEE And P.K. Sen2, Fellow IEEE"Modeling And Control Of Doubly Fed Induction Generator For Wind Power"

[15] Md. Arifujjaman, m.T. Iqbal,John E. Quicoe "Vector Control Of A Dfig Based Wind Turbine" Istanbul University Journal Of Electrical & Electronics Engineering.

[16] Srirattanawichaikul,W, Kumsuwan Y, Premrudeepchacharn S,and Wu B,,"A Vector Control of A Grid Connected 3L-NPC-VSC with DFIG Drives."(ECTI-CON) International Conference, pp .828,May 2012.

[17] Lie Xu, Cartwright P, "Direct Active and Reactive Power Control of DFIG for Wind Energy Generation", IEEE Transactions on Energy Conversion, Vol. 21(3), September 2006.

[18] Mohamed, M.B., Jemli, M., Gossa, Jemli, K., "Doubly fed induction generator (DFIG) in wind turbine modeling and power flow control," Proceedings of the IEEE International Conference on Industrial Technology 2004, AL; USA, Vol: 2, pp. 580-584, 2004.

[19] S. Haykin, "Neural Networks: A Comprehensive Foundation," New Jersey: Prentice-Hall, 1999.

Daylighting Rules of Thumb and a Comparison of Different Floor Depth under Overcast and Intermediate Sky Without Sun

M. F. M. A. Sadin, N. L. N. Ibrahim, K. Sopian, E. Salleh

Abstract—Daylighting rules of thumb are simple and comprehensive principles, which can be readily applied in the design process to predict or achieve daylight conditions deemed appropriate for an interior. They have been expressed in a variety of modes in architectural and can be divided into categories based on the parameters which constitute them. One of the categories is floor depth. This paper presents the impact of different floor depth on daylighting performance of the simulated office room using 1 meter shading device under overcast sky and intermediate sky without sun. Several parameters such as shading device, ceiling height, and material reflectance have been appointed. Models then were simulated and analyzed using an application of IES_VE software called RADIANCE. Existing daylighting rules of thumb has been modified and thus create new formula for Kuala Lumpur sky based on the smallest academic office as a lecturer room in public university. All these successfully resulted equations can be considered as simple formulas that can ease everybody to estimate daylighting based on parameters mentioned above.

Keywords— daylighting, floor depth, radiance, rules of thumb.

I. INTRODUCTION

There are many reasons for the renewed interest in daylighting, with the increasing cost of fossil fuels and the realization that sources of electricity have a finite life, being quoted as most cogent; but perhaps even more important are the less tangible aspects of daylighting which relate more to the human spirit and the need for a quality of life [1]. Daylight, by displacing electric light use, reduces carbon dioxide emission and, in turn, the greenhouse effect [2].

Daylighting became a minor architecture issue because of the availability of efficient electric light sources, cheap, abundant electricity and the perceived superiority of electric

lighting [3]. Daylighting should be adopted to overcome the excessive use of electrical energy in office space. There are many benefits for using natural light, for examples reduction in electrical energy consumption and a better indoor quality as often been quoted in the literature.

The use of artificial lighting not only consumed energy but also produced waste heat inside the building that eventually contributed to the heating or cooling load [4]. The use of natural light has been seen as important in improving the environmental quality and energy efficiency of buildings [5].

II. DAYLIGHTING RULES OF THUMB AND FLOOR DEPTH

The Cambridge International Dictionary of English defines *Rules of thumb* as a practical and approximate way of doing or measuring something [6]. Or in other word, rule of thumb in daylighting is an attempt towards simplification of a complex reality. According to [7], rules of thumb have been regarded by some authors as a form of knowledge which has no theoretical reasoning and is therefore unreliable. This perception can be dispelled by adapting a typological approach in dealing with rules of thumb in daylighting. Daylighting rules of thumb can be scientifically examined if their typological limitations are determined and addressed [8]. One of these is floor depth.

A limiting depth of not more than 4 meters for unilateral sidelit room has been proposed by [9] and [10]. According to [9], suggests a limiting depth of 4 meters for office space with a normal ceiling height as a condition for achieving a 2% daylight factor at the back of the room. A slightly higher limiting depth of 4.5 meters for a ‘primarily daylight’ or a ‘fully daylight’ zone was proposed by [11] and [3] for non-residential buildings. According to [11], this distance allows the space to be fully daylight and especially suitable for clerical work. It was [12] and [13] who prescribe sufficient daylight penetration into room of about 4 to 6 meters from window could possibly be considering partially daylight area between the limiting dimensions. Reference [14] claims that a typical office building could provide full illumination to task areas between 3.5 to 4.5 meters from window and partial illumination to areas not more than 7.5 to 9 meters from window. In general, beyond 6 meters from a window, the area can be considered as ‘partially daylight’ which means the area could still be daylight but it may have to rely on artificial light for a considerable period

This work was supported by the Ministry of Higher Education of Malaysia.

M. F. M. A. Sadin is with the Solar Energy Research Institute, National University of Malaysia, 43600 Bangi, Selangor, Malaysia (e-mail: fadlie.as@gmail.com).

N. L. N. Ibrahim is now with the Department of Architecture, Faculty of Engineering and Built Environment, National University of Malaysia, 43600 Bangi, Selangor, Malaysia (e-mail: n.lukman@gmail.com).

K. Sopian is with the Solar Energy Research Institute, National University of Malaysia, 43600 Bangi, Selangor, Malaysia (e-mail: ksopian@vlsi.eng.ukm.my).

E. Salleh is with the Solar Energy Research Institute, National University of Malaysia, 43600 Bangi, Selangor, Malaysia (e-mail: elias@ukm.my).

during daytime.

III. EXTERNAL SHADING DEVICES AND BENEFITS

In office buildings, an appropriate selection of solar shading devices can control indoor illumination from daylight, solar heat gains, and glare while maintaining view out through windows, thus saving lighting and thermal energy while maintaining visual comfort [15]. In another study by [16], it was discovered that an effective passive design strategy to control solar heat gain in buildings is the application of external shading devices, which can reduce solar heat gain more effectively than interior devices. According to [17], 1 meter shading device is the most suitable choice that meets the criteria for daylighting inside the room.

IV. DAYLIGHT FACTOR

The use of the daylight factor has persisted to the present day. The daylight factor has an important characteristic which is a good indicator of the overall appearance of a room. This is because the brightness appearance of a place depends at least as much on the relative luminance of surfaces within the field of vision as on absolute values. By definition, the daylight factor is a measure of the contrast between inside and outside [18]. Daylight factor defined as the proportion of the unobstructed external daylight illuminance that reaches a point inside the room. That is, if the room is removed, the point of interest would receive all the available daylight. That point would be having the daylight factor of 100% [19]. The standard also outlined illuminance levels recommendations for various applications and the recommended daylight factor (DF) for an effective daylight-lit office space is 1.5%. In Table I, daylight levels with the associated visual tasks are outlined in more detail by [20].

IESNA and CIBSE has recommended of 100 – 200 lux for minimum working space illuminance where visual tasks are only occasionally performed [21].

Table I: Amount of daylight levels for adequate visual performance

Visual Tasks	Illumination Levels (Lux)	Daylight Factor (%) (based on overcast sky which provides 5000 lux on horizontal plane)
Casual reading, ordinary factory bench work, etc.	75 – 100	1.5 – 2
Prolonged reading, school and office work, etc.	100 – 150	2 – 3
Sewing, typing and other difficult visual work.	150 – 250	3 – 5

Very fine work or in poor contrast	250 – 500	5 – 10
------------------------------------	-----------	--------

V. EXPERIMENTAL PROCEDURE

For the purpose of investigating the effects of different length of floor depth on daylighting and rules of thumb, this study use a series of simulations by an energy analysis program, IES_VE. A model designed based on the smallest academic office room (a lecturer room) in National University of Malaysia was simulated. The room size is approximately 3.5m wide and 2.6m high with a full width window facing north. The window glass transmittance is set at 0.9 (being a normal clear glazed window). This room use 1m horizontal shading device. The variable parameter in this experiment is floor depth, which ranged from 3m to 10m with gradual 1m interval. Interior room surfaces reflectance in the simulation has been designated as 0.3 for floor surface reflectance, 0.6 for wall surface reflectance and 0.8 for ceiling surface reflectance. This is based on [22], the reflection surface recommended for general systems are from 0.7 to 0.9 for ceiling finishes, from 0.4 to 0.7 for wall finishes and from 0.1 to 0.4 for floor finishes. Approximately, this is similar to reflectance criteria for best visual comfort in office interior proposed by [23]. The daylight illuminance was measured at the work plane 0.85m above the floor surface. Refer to Fig. 1 for the section diagram.

The original Littlefair's formula was used to calculate daylight factors which were then correlated to the simulation's daylight factors obtained under an overcast sky. Meanwhile, an intermediate sky without sun type is the one that suitable for Malaysia sky. The original Littlefair's daylight factor formula [24] is shown below:

$$DF_{avg} = \frac{\tau_w A_g \theta}{A_s (1-R^2)} \quad (1)$$

- DF_{avg} average daylight factor
 A_g window glazing area (m²)
 τ_w transmission of window glazing
 θ sky angle measured at the center of the window in degrees
 A_s total area of the room surfaces ceiling, floor, walls and window (m²)
 R the average reflectance. For fairly light colored rooms such as in the case studies, a value of 0.5 is normal

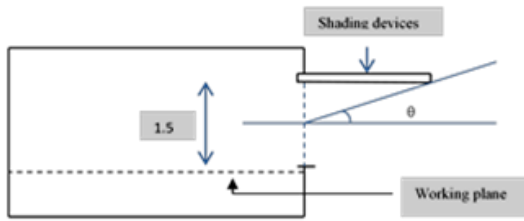


Fig. 1 showing the section diagram of the simulated room model

VI. RESULT AND DISCUSSION

Fig. 2(a) and 3(b) show that illuminance at the back of the rooms were generally lower than rear due to increase room depth. Maximum illuminance obtained under overcast sky was higher than the one which was under intermediate sky without sun. Furthermore, centreline illuminance of not less than 100 lux can be maintained under overcast sky at limiting depth 3 meter meanwhile 2.5 meter for intermediate sky without sun.

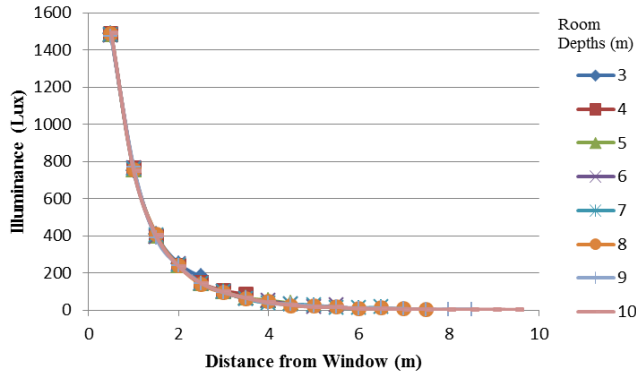


Fig. 2(a) showing centreline illuminance of floor depth under overcast sky

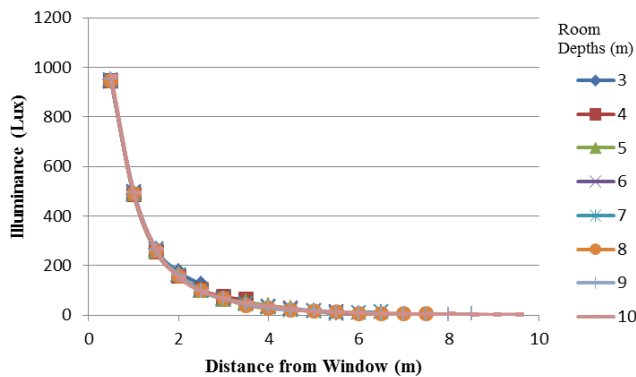


Fig. 2(b) showing centreline illuminance of floor depth under intermediate sky without sun

Fig. 3(a) and 3(b) show that average illuminance increased inside rooms with a larger percentage of window area to floor area. Average illuminance of about 380 lux was achieved inside a room with a window to floor area ratio of 20% under

overcast sky and about 240 lux for same ratio under intermediate sky without sun. The linear correlation between average illuminance and the percentages of window area to floor area as shown below:

$$E_{avg} \approx 20 A_w/A_f \quad (\text{overcast sky}) \quad (2)$$

E_{avg} average illuminance
 A_w window area (m^2)
 A_f floor area (m^2)

$$E_{avg} \approx 10A_w/A_f \quad (\text{intermediate sky without sun}) \quad (3)$$

E_{avg} average illuminance
 A_w window area (m^2)
 A_f floor area (m^2)

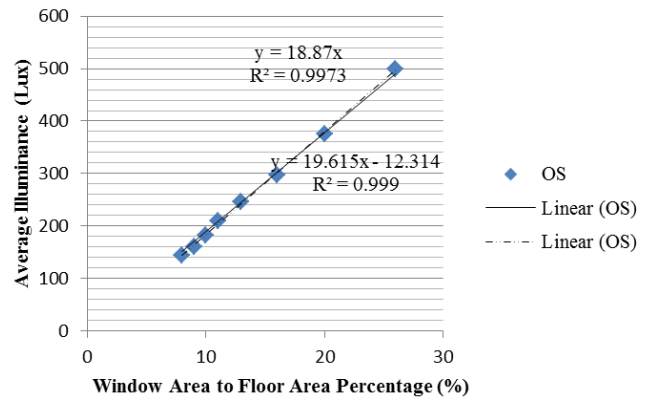


Fig. 3(a) showing average illuminance vs. window area to floor area under overcast sky

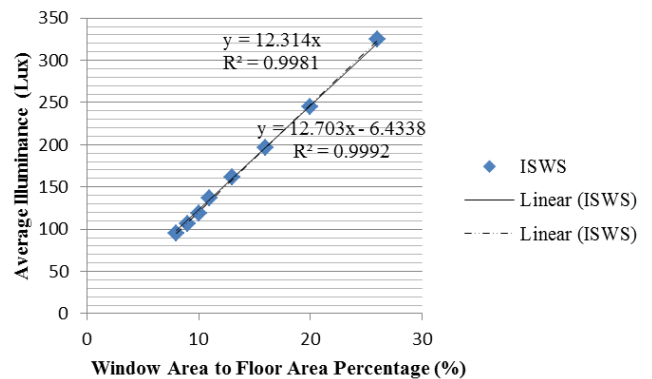


Fig. 3(b) showing average illuminance vs. window area to floor area under intermediate sky without sun

Analyses were carried out to determine further correlations between the simulation daylight factors and the formula daylight factors. However, the Littlefair’s daylight factors formula is modified by substituting A_s with A_f as shown in Fig. 4(a) and 4(b). Therefore, the generated correlative equations

are much easier to calculate. The objective is for increased usability of the daylighting rules of thumb.

The correlation can be represented by the following rules of thumb:

$$DF_{avg} = 10 \text{ Ag/Af } \% \quad (R^2 = 0.999) \quad (4)$$

$$DF_{avg} = 7 \text{ Ag/Af } \% \quad (R^2 = 0.999) \quad (5)$$

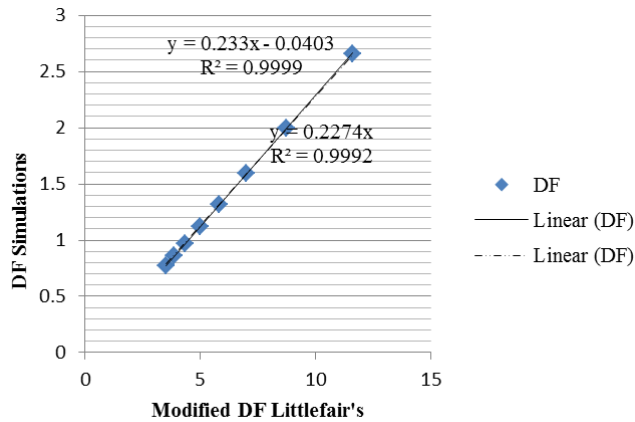


Fig. 4(a) showing simulation daylight factor vs. modified Littlefair daylight factor under overcast sky

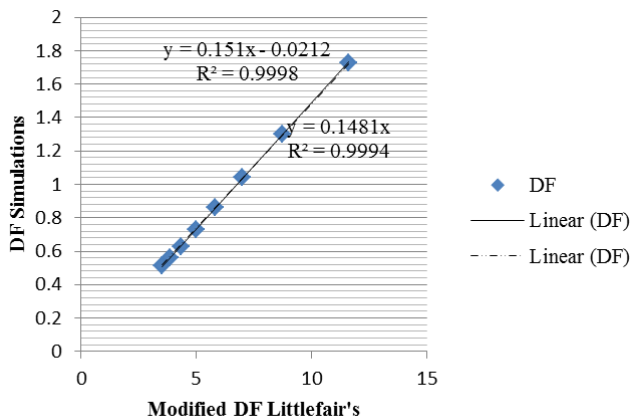


Fig. 4 (b) Simulation daylight factor vs. modified Littlefair daylight factor under intermediate sky without sun

I. CONCLUSION

The simplified equations or rules of thumb produced in this article are applicable for small size office rooms in public university of Malaysia with standard glazing transmittance, standard ceiling high, and 1m shading device under both an overcast sky and intermediate sky without sun. These equations can be considered as rules of thumb to estimate daylighting for a standard office room. These rules of thumb can aid architects in designing sufficiently daylit office space with shading device. The experiments show that small office room, 3.5 meter width with full width window and 1 meter horizontal external shading can provide sufficient interior

illumination for both under overcast sky and intermediate sky without sun.

REFERENCES

- [1] D. Phillips, *Daylighting: Natural Light in Architecture*, Architectural Press, Oxford: Elsevier, 2004.
- [2] N. Baker, A. Fanchiotti, and K. Steemers, *Daylighting in Architecture: A European Reference Book*. James & James (Science Publishers Ltd), 1993.
- [3] N. Lechner, *Heating, Cooling, Lighting: Sustainable Design Methods for Architects*, 3rd ed. John Wiley & Sons Inc, 2009.
- [4] A. Zain-Ahmad, K. Sopian, M. Y. H. Othman and A. Z. Zainol, "The availability of daylight from tropical skies: a case study of Malaysia," *Renewable Energy*, vol. 25, pp. 21-30, 2002.
- [5] C. Aghemo, A. Pellegrino, and V. R. M. Loverso, "The approach to daylighting by scale models and sun and sky simulators: a case study for different shading systems," *Build Environment*, vol. 43, no. 5, pp. 917-927, 2008.
- [6] *Cambridge International Dictionary of English*, Cambridge: Cambridge University Press, 1995.
- [7] G. Stevens, *the Reasoning Architect*, 3rd ed., Sydney: The University of Sydney, 1988.
- [8] N. L. N. Ibrahim, S. Hayman, and R. Hyde, "A typological approach to daylighting analysis," in *44th Annual Conference of The Architectural Science Association (ANZAScA)*, Unitec Institute of Technology, 2010.
- [9] P.R. Boyce, *Human Factors in Lighting*. London: Applied Science Publishers (1981).
- [10] C. Day, *Spirit and Place*. Oxford: Architectural Press, 2002.
- [11] P. Manning, *Office Design: A Study of Environment*, Ed. Liverpool: The Pilkington Research Unit & Dept. of Building Science, University of Liverpool, 1965.
- [12] P. F. Smith, *Architecture in a Climate of Change*, 2nd ed. Oxford: Architectural Press/Elsevier, 2005.
- [13] P. Guthrie, *the Architect's Portable Handbook: First Step Rules of Thumb for Building Design*. New York: Mc-Graw-Hill, 1995.
- [14] E. Allen and J. Lano, *the Architect's Studio Companion: Rules of Thumb for Preliminary Design*, 3rd ed. New York: John Wiley & Sons, 2002.
- [15] A. Laouadi, and A. D. Galasiu, "Effective Solar Shading Devices for Residential Windows Save Energy and Improve Thermal Conditions," *Lighting Design + Application: LD + A*, vol. 39, no. 6, pp. 18-22, 2009.
- [16] G. C. R. Gutierrez and L. C. Labaki, "An experimental study of shading devices: orientation typology and material," presented at the 2007 Thermal Performance of Exterior Envelopes of Whole Buildings X.
- [17] M. C. Dubois, "Impact of solar shading devices on daylight quality: measurements in experimental office rooms," research report, Lund University, Sweden, 2001.
- [18] P. Tregenza and M. Wilson, *Daylighting Architecture and Lighting Design*, Routledge Taylor & Francis Group, 2011.
- [19] A. M. A. Rahman, M. H. A. Samad, A. Bahauddin, and M. R. Ismail, *Towards A Low-Energy Building for Tropical Malaysia*. Malaysia: Penerbit Universiti Sains Malaysia, 2009.
- [20] Building Research Station (B. R. S), *Principles of Modern Building*, vol.1. London: Her Majesty's Stationery Office (HMSO), 1956.
- [21] P. Michel, "Applied Lighting Technology for Urban Building" in *Energy and Climate in the Urban Built Environment*, M. Santamouris, Ed. James & James (Science Publishers Ltd), 2001.
- [22] J. E. Flynn, J. A. Kremers, A.W. Segil and G.R. Steffy, "Chapter 5: Light Generation and Control" in *Architectural Interior Systems: Lighting, Acoustics, Air Conditioning*, 3rd ed. New York: Van Nostrand Reinhold, 1992.
- [23] B. Boylan, *the Lighting Primer*. Ames: Iowa State University, 1987.
- [24] J.A. Lynes, "Chapter 3: Daylight and Energy" in *Energy Efficient Building A Design Guide*, S. Roaf and M. Hancock, Ed. Oxford: Blackwell Scientific Publications, 1992.

Muhamad Fadle Bin Mohamad Abu Sadin was born in Kelantan, Malaysia on 10th of February 1977. He earned his Degree (Honor) in Mathematics from National University of Malaysia in 2000 and later pursued a Master Degree (Energy Technology) from same university in 2004. Currently he is pursuing a PhD in Renewable Energy, majoring in daylighting in Solar Energy Research Institute (SERI), National University of Malaysia.

Ecological refrigerants used in refrigeration, air-conditioning and heat pump systems

Ioan Sarbu and Emilian Stefan Valea

Abstract—The paper presents conditions in order to assure comfortable temperatures in working and living environments using cooling systems in sustaining life quality. They are treated aspects of the environmental pollution through the working fluids of the refrigeration, air-conditioning and heat pump systems and it is described the new strategy in using refrigerants in accordance with the international legislation. It is described the selection of refrigerants adapted to each utilization, based on the thermodynamic and -physical properties, the technological behaviour, costs and use constraints as principal aspects of the environmental protection. Also, it is performed a comparative analysis in function of the total equivalent warming impact (TEWI) for some possible substitutes of refrigerant R22 used in various refrigeration and heat pump systems.

Keywords—Environmental protection, Cooling, Refrigerants, Pollution, Ecological substitutes

I. INTRODUCTION

THE environment pollution represents a major risk for all that means life on our planet (men, flora, fauna), it consist not only in the local noxious effect of different pollutants but in the unbalances produced in a large scale on the whole planet. Environmental protection represents the fundamental condition of the society's sustainable development, a priority purpose of national interest that is realized in institutional frame where the legal norms authoresses the development of activities with environmental impact and exert the control upon these.

The purpose of environmental protection is to maintain the ecological balance, to maintain and improve the natural factors, to prevent and control pollution, the development of natural values, to assure better life and work condition for the present and future generations and it refers to all actions, means and measures undertaken for these purpose.

One of the minor components of atmosphere, the ozone has a special importance in maintaining the ecological balance. It is distributed in principal between the stratosphere (85-90%) and troposphere. Any perturbation of the atmospheric ozone concentration (it varies between 0 and 10 ppm, in function of the regions) has direct and immediately effect upon life.

For most of the states the problems of forming and maintaining the earth ozone layer, represents a major priority. In this context during the last 30 years, the European Union has adopted a great number of laws and regulations concerning environmental protection, to correct the pollution effects, frequently by indirect directives, imposing allowable concentrations, asking for government collaboration, programs and projects for regulation of industrial activities and productions. The Alliance for Responsible Atmospheric Policy [1] maintains a brief summary of regulations for some countries.

In this paper are treated aspects of the environmental pollution through the working fluids of the refrigeration, air-conditioning and heat pump systems and it is described the new strategy in using refrigerants in accordance with the international legislation. Additionally, it is performed a comparative analysis concerning the environmental impact of some possible substitutes for refrigerant R22 used in different refrigeration, air-conditioning and heat pump systems.

II. ACTION OF REFRIGERANTS ON ENVIRONMENT

Refrigerants are the working fluids in refrigeration, air-conditioning, and heat pump systems [2]. The phase changes occur both in absorption and mechanical vapour compression systems, but not in systems operating on a gas cycle using a fluid such as air. The design of the refrigeration equipment depends strongly on the properties of the selected refrigerant.

Refrigerant selection involves compromises between conflicting desirable thermo physical properties. A refrigerant must satisfy many requirements, some of which do not directly relate to its ability to transfer heat. Chemical stability under conditions of use is an essential characteristic. Safety codes may require a non-flammable refrigerant of low toxicity for some applications. Cost, availability, efficiency, and compatibility with compressor lubricants and equipment materials are other concerns [3].

Minimizing all refrigerant releases from systems is important not only because of environmental impacts, but also because charge losses lead to insufficient system charge levels, which in turn results in suboptimal operation and lowered efficiency.

Working fluids escaped through leakages from refrigeration equipments, during the normal operating (filling, emptying) or accidental (damages), gathers in significant quantities in high levels of the atmosphere (stratosphere). There, through catalytically decomposing they deplete the ozone layer that normally is filtering the ultraviolet sun

Ioan Sarbu is currently a Professor at the Civil Engineering and Building Services Department, Polytechnic University Timisoara, 300006 ROMANIA, e-mail address: ioan.sarbu@ct.upt.ro

Emilian Stefan Valea is currently a Lecturer at the Civil Engineering and Building Services Department, Polytechnic University Timisoara, 300006 ROMANIA, e-mail address: emilian.valea@ct.upt.ro

radiations, dangerous for living creatures and plants on earth. Stratospheric ozone depletion has been linked to the presence of chlorine and bromine in the stratosphere. In addition, refrigerants contributed to the global warming of atmosphere, as gases with greenhouse effect.

The average global temperature is determined by the balance of energy from the sun heating the earth and its atmosphere and of energy radiated from the earth and the atmosphere space. Greenhouse gases (GHGs), such as carbon dioxide (CO₂) and water vapour, as well as small particles trap heat at and near the surface, maintaining the average temperature of the Earth's surface about 34 K warmer than would be the case if these gases and particles were not present (the greenhouse effect).

Global warming is a concern because of an increase in the greenhouse effect from increasing concentrations of GHGs attributed to human activities. Thus, the negative influences of refrigerants, especially of Freon's upon environment, can be synthesized by the two effects [4]:

- depletion of the ozone layer;
- contribution to global warming at planetary level by the greenhouse effect.

The measure of a material's ability to deplete stratospheric ozone is its *ozone depletion potential* (ODP), a value relative to that of R11, which has an ODP of 1.0.

The *global warming potential* (GWP) of a GHG is an index describing its relative ability to trap radiant energy compared to CO₂ (R744), which has a very long atmospheric lifetime. Therefore refrigerants will be select so that the ozone depletion potential will be zero and with a reduced atmospheric global warming potential.

The most utilized refrigerants are those who derivate from methane and ethane and there toxicity and flammability is according to the number of Cl and H atoms.

Concerning the polluting action upon environment, for the atmospheric ozone, presented through the Montreal protocol (1987) and the further amendments, as well as for the green house effect according to the Kyoto protocol (1997), refrigerants can be classified as follows:

- having strong destructive action on the ozone layer and with significant amplification of the greenhouse effect upon the earth (Chlorofluorocarbons-CFCs);
- having reduced action on the ozone layer and with moderate amplification of the greenhouse effect (Hydrochlorofluorocarbons-HCFCs);
- being harmless to the ozone layer, with less influence upon the greenhouse effect (Hydro-fluorocarbons-HFCs);
- being harmless to the ozone layer, with no influence upon greenhouse effect (ammonia - NH₃, carbon dioxide - CO₂, natural hydrocarbons).

Refrigerants as Chlorofluorocarbons had been used since the 1930s because of their superior safety and performance characteristics. However, their production for use in developed countries has been eliminated because it has been shown that they deplete the ozone layer [5]. Production for use in developing countries hat to be eliminated by 2010, except as allowed under essential use exemptions or in feedstock applications.

Hydro-chlorofluorocarbons also deplete the ozone layer, but to a much lesser extent than CFCs. Their production for use as refrigerants is scheduled for elimination by 2030 for developed countries, and by 2040 for developing countries.

Hydro-fluorocarbons do not deplete the ozone layer and have many of the desirable properties of CFCs and HCFCs. They are being widely adopted as substitute refrigerants for CFCs and HCFCs. The HFC refrigerants have significant benefits regarding safety, stability and low toxicity, being proper for large applications.

A second influence of refrigerants upon the environment, preciously mentioned, guided to a new classification of refrigerants according to their contribution to the atmosphere warming. Comparison of this specific contribution to the greenhouse effect is realized even for R11 (the most noxious even from point of view of ozone layer depletion) as well as for CO₂. Freon's placed on the undesirable position 3 (14%) between the gases with green house effect, could be explained by their great absorption capacity of infrared radiation.

In the case of the refrigeration and heat pump systems, supplementary with direct action to the green house effect, because of the refrigerants leakage in the atmosphere, it must be considered even the indirect action to global warming by the CO₂ quantity released in atmosphere during the transport of energy produced by the installation, obviously greater than the associated direct action [6]. While the refrigerant quantity increases in the installation, the effect of direct action rises.

The *total equivalent warming impact* (TEWI) of an HVAC&R system is the sum of direct refrigerant emissions expressed in terms of CO₂ equivalents, and indirect emissions of CO₂ from the system's energy use over its service life.

The *life-cycle climate performance* (LCCP) of an HVAC&R system includes TEWI and adds direct and indirect emissions effects associated with manufacturing the refri-gerant. The analysis of TEWI index for refrigeration systems operating with different refrigerants (CO₂, R22, NH₃, R134a, R404A) shown that the direct effect generated by CO₂ is negligible comparing with the other refrigerants [7]. The indirect effect generated by CO₂ is great because of the high condensation pressures that determine great energy consumption and in consequence the maximum value of TEWI for CO₂.

Environmentally preferred refrigerants have:

- low or zero ODP;
- relatively short atmospheric lifetimes;
- low GWP;
- provide good system efficiency;
- appropriate safety properties;
- ability to yield a low TEWI or LCCP in system applications.

In Table 1 is presented the refrigerants effect upon the environment [8]. Because HFCs do not contain chlorine or bromine, their ODP values are negligible and represented through 0 in this table.

Table 1. Effect of refrigerants on environment

Group	Fluid	ODP	GWP (R11=1)	GWP (CO ₂ =1)	Atmospherically lifetime (years)
0	1	2	3	4	5
CFC	R11	1	1	4000	50...60
	R12	1	2.1...3.05	10600	102...130
	R113	0.8-1.07	1.3	4200	90...110
	R114	0.7-1.0	4.15	6900	130...220
	R12B ₁	3-13	–	1300	11...25
HCFC	R13B ₁	10-16	1.65	6900	65...110
	R21	0.05	0.1	–	<10
	R22	0.055	0.034	1900	11.8
	R123	0.02	0.02	120	1.4...2
HFC	R142b	0.065	0.3...0.46	2000	19...22.4
	R23	0	6	14800	24.3
	R32	0	0.14	580	6...7.3
	R125	0	0.58...0.85	3200	32.6
	R134a	0	0.28	1600	14...15.6
	R143a	0	0.75...1.2	3900	55...64.2
Azeotropic blends	R152a	0	0.03...0.04	140	1.5...8
	R500(R12/R152a)	0.63-0.75	2.2	6000	–
	R501(R12/R22)	0.53	1.7	4200	–
	R502(R22/R115)	0.3-0.34	4.01...5.1	5600	>100
Quasi-azeotrope blends	R507(R125/R143a)	0	0.68	3800	–
	R404A(0.44R125/0.52R143a / 0.04R134a)	0	0.6...0.94	3750	–
	R410A(0.5R32/0.5R125)	0	0.5	1890	–
Zeotropic blends	FX40(0.1R32/0.45R125/ 0.45R143)	0	0.6	3350	–
	R407A(0.2R32/0.4R125/ 0.4 R134a)	0	0.14...0.45	1920	–
	R407B(0.1R32/R0.7R125/ 0.2R134a)	0	0.1...0.5	2560	–
	R407C(0.23R32/0.25R125/ 0.52R134a)	0	0.29...0.37	1610	–

A major contribution against the climate changes has the European Union through regulations regarding some fluorinated gases with green house effect and it is a real support in the emission reducing resulted from these fluorinated gases all over Europe. All regulations establish a high protection level of the environment as well as an inside market for equipments containing fluorinated gases and for the members involved in this activities.

III. STRATEGY CONCERNING NO-ECOLOGICAL REFRIGERANTS

After the finding that CFCs, HCFCs and some other human-produced compounds deplete the ozone layer, most countries agreed to the Montreal protocol. This protocol is an international treaty, administered by the United Nations Environment Programs (UNEP) that controls consumption and production of ozone-depleting substances, including CFCs and HCFCs [5].

Hydro-fluorocarbons (HFCs) do not deplete the ozone layer and have many of the desirable properties of CFCs and HCFCs. They are being widely adopted as substitute refrigerants for CFCs and HCFCs. However, HFCs are also associated with an environmental issue; they contribute to global warming if released into the atmosphere [2]. Countries, trade associations and companies are increasingly adopting regulations and voluntary programs to minimize these releases and, hence, minimize potential environmental effect while continuing to allow use of these refrigerants.

Consequently a new orientation appeared upon the utilization of working fluids. Thus, CFC refrigerants as R11 and R12 were substituted by simple compound refrigerants R123 (HCFC) and R134 (HFC) with a reduced even zero action upon the depletion of the ozone layer. This alternative is attractive because the substitutes have similar properties (temperature, pressure) with the replaced one [9] and the

changes that took place directly on the existent installations will be realized with minimum of investments.

For other refrigerants it were not found simply compound fluids as for example for R502 that could be replaced with a mixture of R115 (CFC) and R22 (HCFC) or in some cases only with R22, that is a fluid for temporary replacement, conform with the international legislation.

By blending two or three pure Freon's we obtain new substances, better adaptable for desired cooling application. The first blends are named azeotropes while the others are named zeotropes [10]. The use of blends could generate undesired aspects, especially by leakages of the working fluid, accidentally or during the installations filling.

Figure 1 presents the strategy concerning the refrigerants.

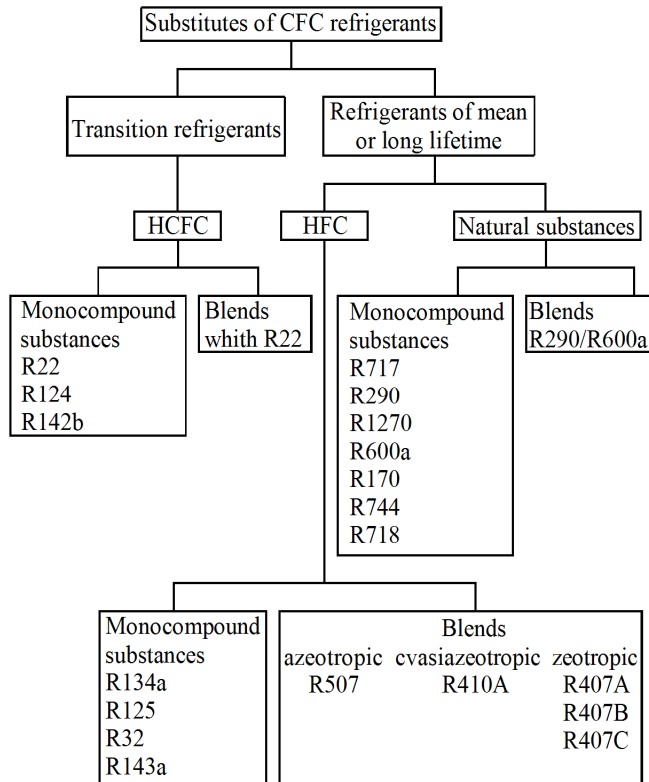


Fig. 1 Strategy concerning the refrigerants

The substitutes for refrigerant R22 could be R134a, R290, R600a and R744, the HFC blends (R407C, R410A, R417A, and FX 90) and the ammonia (R717) [11].

None of these substances can efficiently substitute R22, presenting a specific cooling power or a different saturation pressure, restricted application and specially demands in the installation design.

In new installations, for certain applications, R143a is a good substitute, having a reduced delivering compressor pressure and temperature, but also an inferior specific cooling power being necessary a greater cylinder of the compressor.

The HFC zeotropic blends are considered substitutes for a short period. Between the natural fluids, the ammonia is the best substitute for R22, having favourable thermodynamic properties, high heat transfer coefficient (3-4 times superior to R22) and a performance coefficient similarly good for many applications, especially industrial one, with great cooling powers. It is cheap and ecological (ODP=0, GWP=0).

Carbon dioxide (R744) is a possible substitute for all refrigerants, being used even by low and high temperatures (cascade system, commercial cooling and air-conditioning). It is accessible, has a low cost and doesn't impact upon ozone, while his heating potential is negligible. His low critical temperature involves the use in supercritical cycles. The high saturation pressure and isotherm compression coefficient are considered as inconvenient.

Because thermodynamic and thermo-physic properties influences the energetically performances of refrigeration systems and produces meantime the environmental impact, they must be carefully analyzed and take in account by the installations conception and planning.

In Table 2 are presented the principal thermodynamic properties of CO₂ and other natural refrigerants [12], [13]. These properties determine the advantages and also the disadvantages by using CO₂.

Table 2. Thermodynamic properties of principal natural refrigerants

Property	Carbon dioxide (R744)	Ammonia (R717)	Water (R718)	Propane (R290)	Isobutene (R600a)
0	1	2	3	4	5
Molecular mass [g/mol]	44	17	18	44.1	58.1
Critical temperature [°C]	30.98	132.4	374	96.8	135
Critical pressure [bar]	73.75	113.5	221	44.1	36.5
Normal boiling point [°C]	-37.00	-33.5	100	-42.2	-11.7
Freezing point [°C]	-56.57	-77.9	0	-187.1	-159.6
Adiabatic compression index (c_p/c_v)	1.7015	1.400	-	1.140	1.110
Compression ratio (-15/35 °C)	3.147	5.72	-	4.21	-
Refrigeration volumetric capacity [kJ/m ³] (-15/35 °C)	4922	2156.4	-	450	130

IV. ENVIRONMENTAL IMPACT OF SUBSTITUTE REFRIGERANTS

The TEWI index is comparatively analyzed for three types of refrigeration systems operating with various refrigerants [11], possible substitutes of R22, as follows:

- air-conditioning device with cooling power of 10.55 kW ($t_i=25\text{ }^\circ\text{C}$, $t_e=35\text{ }^\circ\text{C}$);
- liquid cooler with air cooled condenser having refrigeration power of 11.3 kW ($t_{cold\ water\ in/out}=7/12\text{ }^\circ\text{C}$, $t_e=35\text{ }^\circ\text{C}$);
- refrigerator/freezer with direct and indirect evaporation and air-cooled condenser for cold storage (refrigeration space with $t_i=0\text{ }^\circ\text{C}$ and congelation space with $t_i=-20\text{ }^\circ\text{C}$ and $t_e=35\text{ }^\circ\text{C}$), with refrigeration power of 11.3 kW.

For calculation of TEWI index has been used the following equation [14]:

$$TEWI = n/GWP + M(1 - \alpha_{rec})GWP + n\beta E_D \quad (1)$$

where:

$$E_D = P_i \tau \quad (2)$$

in which: n is the operation years number of system (10 years), l – annual rate of system leakages (3-8%); GWP – global warming potential for a period of 100 years compared to CO_2 ; M – refrigerant charge of the system, in kg; α_{rec} – refrigerant recycling factor (0.70-0.85%); β – the CO_2 emission factor (0.41435 for Romania); E_D – annual energy consumption, in kWh; P_i – compressor power, in kW; τ – system running time per year, in h (610 h/year).

The comparative analysis is performed for refrigerant vapour superheat of 5 K and an isentropic efficiency of 0.8.

Mass flow rate, corresponding to each refrigerant, is determined considering the compressor displacement constant during operation, for refrigerant and evaporation temperature

change. The consumed electric power in installation is determined as a sum of electric powers consumed by compressor, fans and circulation pumps (for direct evaporation installations).

After the calculation result the values for the refrigerant mass flow rate (m), refrigeration power (Q_0), total electric power (P_i) and performance coefficient (EER). These values, corresponding to the above-mentioned operating modes are summarized in Table 3, from which it is seen that under the same operating conditions of the system, mass flow rates have different values depending on the used refrigerant. Also, it is found that with decreasing evaporation temperature the mass flow rate for the same refrigerant decreases. This decrease is due to this increase in specific volume.

For indirect evaporation system, the total electric power values are reduced compared with the direct evaporation system, although the evaporation temperature decreases. This trend is explained by the fact that the refrigerant mass flow rate decreases more compared to increase of specific mechanical work.

The TEWI index variation is summarized in Table 4. The obtained results shown that possible substitutes for refrigerant R22 can be grouped into three categories:

- a) with deviations of approx. 2% (R417A, R407C, R427A, R424A);
- b) with deviations of approx. 30-45% (R134a, R410A, R290, R600a, R152a);
- c) with deviations of approx. 50-70% (R507, R404A, R428A, R422A).

For substitutes involved in b) and c) group, their use is not recommended because the plant will operate with a significant decrease of refrigeration power. Their use is possible only if some changes in components of the installation are made.

Table 3. Characteristics of air-conditioning, refrigeration, and congelation systems

Refrigerant	Air-conditioning system								Refrigeration system								Congelation system							
	Direct cooling				Liquid cooler				Direct evaporation				Indirect evaporation				Direct evaporation				Indirect evaporation			
	m [kg/s]	Q_0 [kW]	EER [-]	P_i [kW]	m [kg/s]	Q_0 [kW]	EER [-]	P_i [kW]	m [kg/s]	Q_0 [kW]	EER [-]	P_i [kW]	m [kg/s]	Q_0 [kW]	EER [-]	P_i [kW]	m [kg/s]	Q_0 [kW]	EER [-]	P_i [kW]	m [kg/s]	Q_0 [kW]	EER [-]	P_i [kW]
0	1	2	3	4	5	6	7	8	9	10	11	12	13	14	15	16	17	18	19	20	21	22	23	24
R22	0.061	9.8	8.0	1.71	0.059	9.0	6.6	1.69	0.049	7.3	2.7	3.10	0.044	6.4	2.4	3.11	0.030	4.3	2.5	2.08	0.024	3.3	2.2	1.87
R134a	0.080	12.0	10.0	1.68	0.077	10.9	7.3	1.81	0.033	4.3	3.5	1.61	0.026	3.3	3.1	1.45	0.018	2.2	2.4	1.29	0.015	1.8	2.1	1.21
R290	0.032	9.2	9.8	1.41	0.032	8.8	8.3	1.38	0.025	6.2	3.5	2.15	0.021	5.1	3.1	2.05	0.015	3.5	2.4	1.83	0.012	2.8	2.1	1.71
R600a	0.051	14.4	10.3	1.87	0.049	13.6	8.7	1.89	0.010	2.4	3.7	1.02	0.008	1.9	3.2	0.97	0.005	1.2	2.5	0.86	0.004	1.0	2.2	0.81
R152a	0.050	12.6	10.4	1.89	0.049	11.8	8.5	1.72	0.019	4.3	3.8	1.52	0.016	3.5	3.4	1.43	0.011	2.3	2.7	1.25	0.009	1.9	2.4	1.17
R407C	0.061	10.1	7.8	1.78	0.059	9.3	6.1	1.84	0.056	8.3	2.6	3.62	0.047	6.8	2.2	3.42	0.033	4.6	2.3	2.33	0.027	3.7	2.1	2.17
R404A	0.070	7.8	6.7	1.64	0.068	6.9	4.9	1.74	0.071	6.7	2.2	3.45	0.061	5.6	1.9	3.33	0.042	3.6	1.9	2.21	0.036	2.9	1.7	2.05
R410A	0.050	7.8	7.2	1.56	0.049	7.2	5.7	1.59	0.070	10.1	2.4	4.65	0.059	8.3	2.1	4.40	0.041	5.6	2.3	2.77	0.034	4.6	2.1	2.54
R507	0.071	8.2	7.0	1.65	0.068	7.3	5.1	1.74	0.075	7.7	3.2	2.77	0.063	6.4	2.1	3.43	0.045	4.3	2.2	2.34	0.037	3.5	1.9	2.15
R417A	0.060	7.7	6.0	1.76	0.058	6.9	4.6	1.82	0.048	5.5	3.2	2.08	0.039	3.9	2.5	1.94	0.026	2.6	2.0	1.69	0.022	2.1	1.8	1.58
R422A	0.100	10.1	7.4	1.84	0.094	8.7	5.2	2.02	0.073	6.4	2.8	2.72	0.063	5.1	2.3	2.55	0.045	3.3	1.7	2.34	0.037	2.7	1.2	2.54
R424A	0.054	9.7	8.1	1.67	0.062	8.8	6.2	1.75	0.041	5.3	3.2	2.02	0.042	5.2	2.5	2.42	0.022	2.5	1.7	1.82	0.020	2.2	1.6	1.73
R427A	0.063	7.9	8.2	1.43	0.051	7.2	6.3	1.48	0.046	6.3	6.0	1.43	0.037	4.9	2.9	2.06	0.024	3.2	4.7	1.06	0.021	2.6	4.2	0.99
R428A	0.101	11.6	9.6	1.68	0.095	10.2	6.6	1.88	0.069	6.9	4.8	1.82	0.066	6.3	2.9	2.53	0.033	3.0	2.0	1.86	0.026	2.2	1.7	1.69

Table 4. TEWI index for analyzed systems

Refrigerant	Air-conditioning system			Refrigeration system			Congelation system		
	Direct cooling	Liquid cooler	Variation [%]	Direct evaporation	Indirect evaporation	Variation [%]	Direct evaporation	Indirect evaporation	Variation [%]
0	1	2	3	4	5	6	7	8	9
R22	6712.14	6593.167	-1.77	10936.271	10758.251	-1.66	7649.71	6867.16	-10.23
R134a	6592.85	6825.870	3.53	6030.105	5418.592	-11.29	4780.63	4504.75	-5.77
R290	3576.38	3493.949	-2.30	5428.709	5184.069	-4.72	4626.12	4315.25	-6.74
R600a	4737.29	4790.571	1.12	2584.504	2460.577	-5.04	2187.29	2046.10	-6.45
R152a	4418.23	4477.189	1.33	3966.865	3745.511	-5.91	3282.83	3055.91	-6.91
R407C	6841.98	6926.828	1.24	12422.319	11607.347	-7.02	8344.42	7731.60	-7.34
R404A	9918.05	9970.406	0.53	17192.790	16081.480	-6.91	11754.72	10760.23	-8.46
R410A	6309.27	6327.940	0.29	16227.552	15116.969	-7.35	10222.35	9354.25	-8.49
R507	10046.62	10096.46	0.49	15943.355	16618.822	4.06	12355.41	11238.14	-9.04
R417A	6746.13	6823.021	1.14	8245.918	7572.605	-8.89	6486.09	6047.81	-6.76
R422A	9598.11	9817.999	2.29	12459.793	11529.942	-8.07	9993.82	10089.46	0.96
R424A	7578.52	7666.723	1.16	8892.173	9950.639	10.64	7434.57	7093.74	-4.58
R427A	6613.22	6650.369	0.56	7765.200	8885.685	12.61	5718.89	5354.30	-6.38
R428A	11365.36	11508.68	1.26	12202.633	13793.359	11.53	9660.66	8755.44	-9.37

V. CONCLUSIONS

Scientific research based on mono-compound substances or mixtures, will lead to find adequate substitutes for cooling applications, that will be ecological (ODP=0, reduced GWP), non-flammable and non-poisonous, but also with favourable thermo-dynamic properties.

A possible solution is the use of inorganic refrigerants (NH₃, CO₂) and hydrocarbon refrigerants (propane, isobutene, ethylene, propylene) for industrial applications, in air-conditioning or food and household cooling. Because the hydrocarbon refrigerant presents a high risk of flammability and explosion, these substances will not be often used as refrigerants comparative with CO₂ or NH₃. On other advantage of these two substances represents the fact that they were used for a long time as refrigerants.

The European Partnership for Energy and Environment considers the HFC refrigerants as the best alternative for the refrigerant CFC and HCFC in most of the applications. The HFC refrigerants allow the use energetically efficient applications, offering significant benefits comparing with the existent alternatives. In average over 80% of the gases with green house effect used in cooling equipments have the indirect emissions as sources. The high energy efficiency resulted by the use of HFC refrigerants balances in a great measure the global warming potential.

The TEWI index values computed for all the three analyzed installation types are lower for indirect evaporation than direct evaporation. Maximal deviation of 20% is obtained for refrigeration system.

The decrease of evaporation temperature by 15 K for refrigeration and congelation systems determine TEWI index decrease by 15-37%. Direct effect of TEWI index represents 33-60% from total value for most of analyzed refrigerants. Minimal values are for R290, R600 and R152. The direct effect of these refrigerants is of 2%.

There are cases with more options for an alternative refrigerant and the problem is to choose the economical variant. The replacement of some refrigerants with other non-polluting influences the operating conditions of the cooling installations, by a rapid degradation of components made from elastomers [4, 15] or plastic materials [3], or it is necessary to replace mineral oils with some other oils adequate to the new refrigerants. Some problems of materials endurance and compatibility can be solved only during many testing, but the estimation of energetically performances and expenses that results by modification of operational characteristics when replacing the refrigerant can be solved with numerical modelling.

It is imposed a new conception in execution the refrigeration systems: it must be realized very tight, with refrigerants having a reduced atmospheric warming potential, but as possible efficient energetically.

REFERENCES

- [1] <http://www.arap.org>
- [2] UNEP, *Report of the refrigeration, air conditioning, and heat pumps technical options committee*, United Nations Environment Programme, Nairobi, Kenya, 1994.
- [3] R.C. Cavestri, *Compatibility of refrigerants and lubricants with engineering plastics, Air-Conditioning and Refrigeration Technology Institute Report*, Arlington, 1993.
- [4] ASHRAE, *Fundamentals Handbook*, American Society of Heating, Refrigerating and Air Conditioning Engineers, Atlanta, 2009.
- [5] UNEP, *Handbook for the international treaties for the protection of the ozone layer*, United Nations Environment Programme, Nairobi, Kenya, 2003.
- [6] I. Sarbu, C. Sebarchievici, *Heat pumps*, Polytechnic Publishing House, Timisoara, 2010 (in Romanian).
- [7] G.V. Dragos, R. Dragos, *Use of CO₂ in non-polluting refrigerating systems, Proceedings of the 28th Conference "Modern Science and Energy"*, Cluj-Napoca, 2009, pp. 149-157.
- [8] I. Sarbu, O. Bancea, *Environment global protection to the polluting action of refrigerants, WSEAS Transaction on Environment and Development*, vol. 5, no. 6, pp. 425-434, 2009.
- [9] Ricardo, R.Q. *Analysis of the behaviour of ternary hydrocarbon mixture as substitutes of the CFC-12, Proceedings of the 2nd IASME/ WSEAS Int.*

- Conference on Energy & Environment*, Portoroz, Slovenia, May 15-17, 2007, pp. 91-94.
- [10] D. Hera, G. Ivan, A. Pirvan, Use of azeotropic and zeotropic blends as substitutes of the R22, *Proceedings of the 20th Conference "Modern Science and Energy"*, Cluj Napoca, 2001, pp. 120-126.
- [11] A. Girip, A. Ilie, L. Drughean, D. Hera, Environmental impact of some possible substitutes for R22 in refrigeration and heat pump systems, *Proceedings of the Nat. Conference "Installations for beginning of three millennium"*, Sinaia, Romania, 13-15 November, 2013, pp. 195-205.
- [12] Proprietes thermodynamiques des fluides frigorigenes, Dehon Service, 1977.
- [13] A. Cavallini, F. Steinle, Natural working fluids in a historic perspective, *Naturals actives fluids, Conference of l'IIF*, Gustav Lorentzen, Oslo, 1998, pp. 37-42.
- [14] Australian Institute of Refrigeration, Air-conditioning and Heating, *Methods of calculating total equivalent warming impact (TEWI)*, Best practice guidelines, 2012.
- [15] B.J. Eiseman, Effect on elastomers of Freon compounds and other halo-hydrocarbons, *Refrigerating Engineering*, no. 12, pp. 1171, 1949.

Ordinal Optimization Approach to Power System objectives in the Presence of SVC and TCSC

K.Srikumar, Ch.V.Suresh, S.Sivanagaraju, V.Ganesh

Abstract— Due to the continuous growth in electricity demand and transactions of the power through existing transmission system needs to be enhancing their loading capacity. The modern technology based power semiconductor devices known as Flexible AC Transmission System (FACTS) devices are utilized. In this paper, most popularly used devices, Static VAR Compensators (SVC) and Thyristor Controlled Series Compensator (TCSC) are used to increase the loadability on a given system and to calculate the corresponding minimized device cost. Finding an optimal location for these devices is a tedious task and needs a lot of expertise. Because of the inconvenience with the conventional methods, an ordinal optimization methodology is proposed. This ordinal optimization technique mainly concentrates on selecting better solutions than the best solution, for this, the entire solution space needs to be optimized to reduce computational burden. This approach makes use of rough analysis and selection of subset locations from ordered performance curve. Finally by using refining process exact size of the devices towards objective is estimated. The proposed methodology is tested on standard IEEE-14 bus test system, numerical results based on the test system confirms that a proposed OO-based approach is suitable for finding good enough solutions.

Keywords— Ordinal Optimization, Ordered Performance Curve, Optimal Location, SVC, TCSC.

I. INTRODUCTION

AS the needs of the electricity and the utilization of the FACTS devices increase the system performance. The optimal configuration will be the one that maximizes the system loadability while keeping the power system operating within appropriate limits. Because of increase in electrical power demand has grown rapidly, needs the expansion of already existing transmission system to avoid the overloading of the transmission corridors. The importance of FACTS devices provides the ability in controlling power flow rapidly, continuously, and accurately.

Three important aspects to be considered throughout the optimization of these devices are their location and their

corresponding settings to maximize the system loadability and to calculate the appropriate minimized cost. FACTS controller is a power electronic based system and other static equipment that provides control of one or more of the AC transmission system parameters [1]. By controlling or adjusting one or more of these parameters, FACTS controllers can increase the loading capability of lines, provides greater flexibility in control, reduce reactive power flows, increase utilization of lowest cost of generation [2]. There are many FACTS controllers, which can be categorized by the parameters they control. This means that, different types of FACTS deal with different problems. Therefore, the choice of the controller to be used is greatly impacted by the desired effect [3].

A new methodology for combined optimal location of TCSC and Thyristor Controlled Phase Angle Regulator (TCPAR) has been proposed using Mixed Integer Linear Programming Approach. This methodology is based on DC load flow equations taking constraints on generation and line flows [4]. An algorithm for optimal location of FACTS controllers using evolutionary strategies is proposed in [5], based on maximizing the system loadability while keeping the power system is operating within appropriate security limits. Three important aspects like type of FACTS controllers used, their location and their settings are optimized using evolutionary approaches [5]. A possible method to determine the best arrangement is by performing a separate power flow study for each of the possible scenarios [6]. However, this would be quite time consuming, even for a power system of moderate size. The simultaneous solution of the three issues mentioned above represents a very complex and difficult optimization problem. Traditional optimization methods may not be the best option for finding the solution to problems of this nature [7-8].

Aiming at various objectives, different methods have been proposed to determine optimal locations and controls of FACTS devices. Continuation Power Flow (CPF) method was used in [9] and [10] to derive the control schemes of FACTS devices to improve system security and system loadability. A novel method was proposed in [11] to determine the locations, size, and control modes for SVC and TCSC to achieve a bifurcation point-based maximum loadability.

Linear programming and mixed integer linear programming-based optimal power flow (OPF) methods were used in [12] and [13] to determine FACTS controls and load shedding in order to relieve overload and irregular voltages after outages in pool and hybrid electricity markets. Authors

K.Srikumar, Ch.V.Suresh, S.Sivanagaraju is with the Electrical & electronics Engineering Department, Jawaharlal Nehru Technological University Kakinada, Kakinada, Andhra Pradesh, India, 533 003. (*kotni.77@gmail.com, 07702862555).

V.Ganesh is with the Department of Electrical & Electronics Engineering, JNTU ACE, Pulivendula, YSR District, A.P, India.

of [14] studied the impact of FACTS devices on available transfer capability (ATC). The best location for an SVC installation was determined based on improved voltage profile and total transmission capability (TTC) of the system. Intelligent techniques such as genetic algorithm, hybrid tabu search, simulated annealing [15]-[17], and particle swarm optimization (PSO) [18-19] techniques are also proposed to solve the system loadability problem.

In general, computational effort increases in an optimization problem as the size of the problem becomes larger. Ordinal Optimization (OO) algorithm was proposed aiming to speed up computation of complicated optimization problems while maintaining solution accuracy. It is one of the probabilistic optimization methods that focus on good enough solution rather than the best. This is referred to as goal softening [20]. OO technique was used to determine a good enough solution in optimal system operations problems that involve discrete control variables such as switching shunt capacitor banks and transformer taps [21]. Crude models and rough estimates are used to derive a small set of plans for which simulations are necessary and worthwhile to find good enough solutions[22]. Descriptions of OO-based technique and its applications in power system planning and control can also be found in [23] and [20].

An OO-based approach is adopted in this paper to search for good enough solutions for system loadability enhancement with an acceptable alignment probability. Instead of searching the best for sure, the proposed method aims to reduce the number of search samples in the solution space formed by all discrete variables, and seek candidates of good enough solutions in the set of, say top 1%-5%, best solution for the original problem.

II. POWER SYSTEM IN THE PRESENCE OF FACTS

FACTS devices are being increasingly utilized in many electric power systems to enhance voltage control, to increase power transfer capability, to improve system dynamic performance. Among the existing devices, SVC has been found to improve the voltage stability limits and TCSC can be used to improve power transfer.

A. Effect of SVC [14]

The SVC shown in Fig.1., is a shunt connected static VAR generator or absorber whose output is adjusted to exchange capacitive or inductive current to as to maintain or control specific parameters of the electrical power system, typically bus voltage. The SVC can be represented as a conventional generator based on the variable shunt susceptance concept. SVC state variables are combined with the nodal bus voltage magnitudes and angles of the network in a single frame of reference for unified iterative solutions using NR method. An assumption that may be acceptable as long as the SVC operates within its design reactance limits.

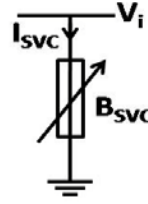


Fig.1. SVC Model

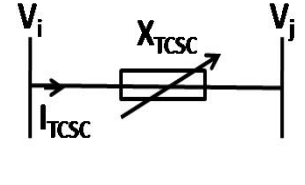


Fig.2 TCSC Model

The reactive power drawn by the SVC, which is the reactive power injected at bus 'i' is

$$Q_{SVC} = Q_K = -V_K^2 B_{SVC} \quad (1)$$

The changing susceptance represents the total SVC susceptance necessary to maintain the nodal voltage magnitude at the specified value. The acceptable values for the SVC are between $-Q_{SVC}$ and Q_{SVC} , corresponding to the reactive power injected or absorbed at a nominal voltage of 1 p.u.

B. Effect of TCSC[5]

The simpler TCSC model shown in Fig.2, exploits the concept of a variable series reactance. The series reactance is adjusted within limits, to satisfy a specified amount of active power flows through it. The value of the reactance represents the equivalent reactance of all series connected modules making up the TCSC, when operating either in inductive or capacitive regions.

The reactance between buses 'i' and 'j' is given as,

$$X_{ii} = X_{jj} = X_{TCSC} \text{ \& } X_{ij} = X_{ji} = -X_{TCSC}; \quad (2)$$

for inductive operation

$$X_{ii} = X_{jj} = -X_{TCSC} \text{ \& } X_{ij} = X_{ji} = X_{TCSC}; \quad (3)$$

for capacitive operation

The TCSC is modeled as an element, which can either decrease or maintain fixed the fixed reactance of line X_L , respectively. The range of values that the TCSC may take is a function of $0.8/B_{line}$. Hence, the apparent value of the line reactance is given by: $X_{L,app} = (1-k)/B_{line}$, where $0 \leq k \leq 0.8$.

C. Device Limits

The following device constraints are considered as

The rating of SVC device is

$$Q_{c,min}^{SVC} \geq Q_c^{SVC} \leq Q_{c,max}^{SVC} \quad (4)$$

where

$$Q_{c,min}^{SVC} = -1.0 \text{ p.u or } -100 \text{ MVAR}$$

$$Q_{c,max}^{SVC} = 1.0 \text{ p.u or } 100 \text{ MVAR}$$

The rating of TCSC device is

$$x_{min}^{TCSC} \leq x^{TCSC} \leq x_{max}^{TCSC} \quad (5)$$

where

$$x_{min}^{TCSC} = -0.8x_{line},$$

$$x_{max}^{TCSC} = 0.2x_{line}$$

D. FACTS device Cost

According to [24], the investment costs of TCSC and SVC can be formulated as follows:

$$C_{TCSC} = 0.0015.S_{TCSC}^2 - 0.713.S_{TCSC} + 153.75 \quad (6)$$

$$C_{SVC} = 0.0003.S_{SVC}^2 - 0.3051.S_{SVC} + 127.38 \quad (7)$$

$$IC_{dev} = \sum_{m \in M} S_{TCSC,m} \cdot C_{TCSC,m} + \sum_{n \in N} S_{SVC,n} \cdot C_{SVC,n} \quad (\$)$$

Here $S = |Q_2| - |Q_1|$,

where

Q_2 is the reactive power flow in the line after installing FACTS device in MVAR.

Q_1 is the reactive power flow in the line before installing FACTS device in MVAR.

'M' and 'N' are respective number of TCSC and SVC devices.

The general PSO technique is used to find the minimized device cost corresponding to the loadability increments. The system and device control parameters are processed subjected to the system constraints.

III. PROBLEM FORMATION

A. Conventional Problem Formulation

The system real and reactive power balance equations can be expressed as

$$\sum_{\forall i} P_{G_i} - \sum_{\forall j} (1 + \lambda) P_{Load_j} - \sum_{\forall k} P_{Losses_k} = 0 \quad --(9)$$

$$\sum_{\forall i} Q_{G_i} - \sum_{\forall j} (1 + \lambda) Q_{Load_j} - \sum_{\forall k} Q_{Losses_k} = 0 \quad --(10)$$

where P_{G_i} and Q_{G_i} are the active and reactive power generations at i^{th} generator, P_{Load_j} and Q_{Load_j} are the real and reactive power loads at j^{th} bus under base case condition ($\lambda=0$), P_{Losses_k} and Q_{Losses_k} are real and reactive power losses in k^{th} transmission line and ' λ ' is the loadability factor

The system loadability objective can be formulated as:

$$\text{Max}(\lambda) \quad --(11)$$

Subject to equality and inequality constraints given in Eq (12) and Eqs (13) – (17).

B. Equality constraints:

The equality constraints $g(x,u)$ are the nonlinear power flow equations which are formulated as follows

- Power balance constraint

$$\sum P_G = \sum P_{Load} + \sum P_{Losses} \quad --(12)$$

C. In-equality constraints:

The inequality constraints for control variables and state variables are given as; Generator active power (P_G), reactive power (Q_G), and Voltage (V_G) are restricted by their limits as follows:

$$\left. \begin{aligned} P_{G_i}^{min} &\leq P_{G_i} \leq P_{G_i}^{max}, & \forall i \in N_G \\ Q_{G_i}^{min} &\leq Q_{G_i} \leq Q_{G_i}^{max}, & \forall i \in N_G \\ V_{G_i}^{min} &\leq V_{G_i} \leq V_{G_i}^{max}, & \forall i \in N_G \end{aligned} \right\} --(13)$$

The constraints of voltages at load buses V_L and transmission loading S_L are represented as:

$$V_{L_i,min} \leq V_{L_i} \leq V_{L_i,max}; \quad i = 1,2,3, \dots \dots n_L \quad --(14)$$

$$S_{L_i} \leq S_{L_i}^{max}; \quad i = 1,2,3, \dots \dots n_l \quad --(15)$$

where n_L is the number of transmission lines and n_l is the number of load buses.

The inequality constraints on control (independent) variable limits are given by

$$T_i^{min} < T_i < T_i^{max}; \quad i = 1,2,3, \dots \dots n_t \quad --(16)$$

$$Q_{C_i}^{min} < Q_{C_i} < Q_{C_i}^{max}; \quad i = 1,2 \dots \dots n_c \quad --(17)$$

where n_t is the number of tap changing transformers and n_c is the number of switchable VAr sources.

D. Difficulty with the conventional method

The problem given in Eq. (11) can be solved through extensive simulations. For a large power system the solution space would be large. Using a system with 50 buses and 100 branches as an example, to select nv is the number of load buses and ns is the number of transmission lines for SVC and TCSC installations, there are at most $(50!)/((50 - nv)! \cdot nv!) \times (100!)/((100 - ns)! \cdot ns!)$ options. It would require extensive efforts to conduct the search for the best solution.

IV. ORDINAL OPTIMAL APPROACH

The Ordinal Optimization theory proposed in [18], [22] is to find good enough solutions. More specifically, it is to find good enough solutions in a given high alignment probability. A good enough subset is the subset consisting of the top best solutions, say, top 5% in the solution space. Good enough subset is easy to specify, but difficult to obtain. Selected subset is defined practically in ordinal optimization theory to find the good enough solutions. The principle of defining a selected subset is to be sure that the selected subset has intersection with the good enough subset.

A. Solution Methodology

The proposed OO method consist the following stages.

1) Rough Analysis

First, a large set of candidate solutions are selected randomly, each with different sites for FACTS device installations, and then crude models described above and a PSO method are used to quickly determine a subset of most promising solutions from the candidate solutions. Exact models are then used in the second stage to obtain a good enough solution from the subset.

2) Ordered performance curve

Once the solution for each candidate is obtained, all candidates are ranked according to the value of $-\lambda'$ in ascending order. And then, the ranking distribution is compared with the standard ordered performance curve (OPC) [28]. The shape of the OPC determines the nature of the underlying the optimization problem.

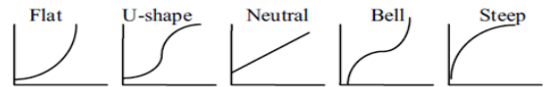


Fig.3. Five types of OPCs

The shape of the curve shows the density and distribution of the top solutions for an optimization problem. Usually the curve follows on the five shapes shown in Fig.3, Flat (many good schemes), U-shape (many good and bad schemes), Neutral (good and bad schemes equally distributed), Bell (many intermediate schemes), and Steep (many bad schemes).

3) *Decide the Size of Selected Subset(S)*

The selected subset candidates are promoted to the second stage of the Ordinal Optimization method, these are obtained from the ordered performance curve, the size of the subset candidates are determined from the slope of the ordered performance curve and nearer to the origin. Finally, exact models are formulated for the candidates in ‘S’, and PSO is used to determine the best solution in the subset.

The selected candidates in ‘S’ with tentative generation outputs and SVC and TCSC at specific installation locations obtained at the first stage is used as the starting point for next stage that uses exact model to determine refined generation outputs P_G and capacity settings, Q_c for SVC and X_c for TCSC in the installation locations.

4) *Particle Swarm Optimization*

To proceed, in the first few iterations of PSO, 30 particles are initialized randomly with smaller searching ranges around the tentative capacity settings and a load flow computation is executed for each particle. PSO conducts its search using a population of particles. Each particle in PSO changes its position according to new velocity and the previous positions in the problem space.

Because of the advantages of the PSO, like simple concept and implementation mechanism, handling of control parameters, finding procedure of the global best solution is chosen to implement the defined solution methodology.

In PSO, the particle velocity and the position in $(k+1)^{th}$ iteration is updated using Eq's (18) and (19)

$$V_j^{k+1} = \omega \cdot V_j^k + C_1 \cdot rand1(.) \cdot (P_{best,j} - X_j^k) + C_2 \cdot rand2(.) \cdot (G_{best} - X_j^k) \quad - (18)$$

$$X_j^{k+1} = X_j^k + V_j^{k+1} \quad \forall j = 1,2,3, \dots, n \quad - (19)$$

where k is the iteration count, C_1 and C_2 are acceleration coefficients, $rand1$ and $rand2$ are uniformly distributed random numbers in $[0, 1]$. $P_{best,j}$ is the best position found by the particle j so far, G_{best} is the position among all particles. Here, the second part is a cognitive part and has its own thinking and memory. The third term is the social parameter on which the particle changes its velocity. ' ω ' is the inertia weight and can be calculated as follows

$$\omega^{k+1} = \omega_{max} - \frac{\omega_{max} - \omega_{min}}{k_{max}} \cdot k \quad - (20)$$

Equations (18) and (19) have three tuning parameters ω , C_1 and C_2 that greatly influence the PSO algorithm performance. The value of ' ω ' was proposed linearly with time from a value of 1.4–0.5 [25]. As such global search starts with a large weight value and then decreases with time to favor local search over global search [26]. In this paper, the methodology to find values for the tuning parameters and the procedure of updating dynamic inertia weight is implemented [27]. Because this provides a balance between global and local explorations, thus it needs less number of iterations to get an optimal solution.

5) *Algorithm*

The detailed algorithm to solve Ordinal Optimization based problem is given below.

Step. 1: Identify all possible locations to install SVC and TCSC devices.

Step. 2: Choose any size value for SVC and TCSC within its limits.

Step. 3: Perform load flow by incorporating SVC and TCSC in a given system.

Step. 4: Calculate the objective function values in all locations.

Step. 5: Plot the ordered performance curve using the procedure in subsection ‘ii’.

Step. 6: Select the subset of candidates to perform refining process given in subsection ‘iv’

V. RESULTS AND ANALYSIS

To investigate the proposed methodology, IEEE – 14 bus system with 3 generators and 20 lines is considered. For base case the maximum loadability factor on this system is 0.445.

Case -1: Initially from the above mentioned procedure to identify the possible installation locations for SVC and TCSC are identified. For this system there are 200 possible locations to install device. The loadability is calculated in each location with fixed SVC and TCSC sizes. Here it is considered that, the reactive power injected by SVC is $0.2p.u$ ($-1p.u \leq Q_{SVC} \leq 1p.u$) and the TCSC value is $-0.5X_{ij}$ ($-0.8X_{ij} \leq X_{TCSC} \leq 0.2X_{ij}$).

Case 2: After completion of calculating loadability in each location, the ordered performance curve is plotted by taking the variation of loadability with respect to the locations, is shown in Fig.4.

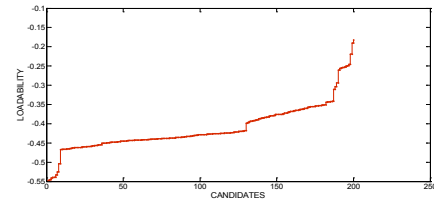


Fig.4: OPC for IEEE-14 bus system

From this figure it is observed that, the curve is very much identical to the U-shaped curve described in section V. Hence the entire set of candidates consist many good and bad schemes. So it is assumed that the top 5% of the candidates are the better candidates to install devices. From this assumption, the top 10 candidates given in Table.1 are considered for refining process.

Table.1: Selected Subset Candidates

S.NO	SVC bus no	TCSC line no	Loadability
1	13	9	0.5465
2	6	9	0.5452
3	11	9	0.541
4	12	9	0.5394
5	14	9	0.5392
6	10	9	0.5326
7	9	9	0.5249
8	7	9	0.5035
9	11	17	0.4666
10	10	17	0.4659

Case 3: The identified subset candidates are passed to refining process to identify the proper size of the devices. Using PSO by generating the size of the devices randomly within limits and solved towards maximizing the loadability is performed for each candidate. After completion of the process, the candidate having the highest loadability is the best candidate with the corresponding size. Hence, the best location to install SVC is 13 and TCSC is line-9 (4-9). With

this the maximum loadability factor is improved from 0.445 to the value of 0.6669.

The variation of the voltage magnitudes is given in Table.2 for without and with FACTS devices. From this table it is observed that, the magnitude of voltages increases as loadability increases. It is also observed that the voltage magnitude at SVC installed bus (Bus-13) is increased from 0.9665p.u to 1.0346p.u, this is about 7.046%. The variations are shown Fig.5.

Table.2: Variation of bus voltage magnitudes for base case and with FACTS devices (during loadability)

S.No	Bus No	Base Case (without FACTS) With loadability ($\lambda=0.445$)	With FACTS ($\lambda=0.6669$)
1	1	1.1	1.1
2	2	1.0761	1.0708
3	3	1.047	1.0335
4	4	1.0103	1.0091
5	5	1.0181	1.0213
6	6	0.992	1.0326
7	7	1.0312	1.0484
8	8	1.0602	1.0863
9	9	1.0067	1.0351
10	10	0.9928	1.0222
11	11	0.9873	1.0217
12	12	0.9712	1.0258
13	13	0.9665	1.0346
14	14	0.961	1.0036

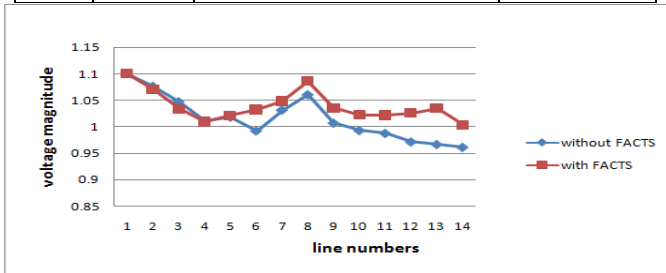


Fig.5. Variation of bus voltage magnitudes

The variation of the generated active powers is given in Table.3 for without and with FACTS devices. From this table it is observed that, the active power generated at slack bus is increased from 186.6497 MW to 249.9942 MW, this is about 33.93%.

Table.3: Variation of generated active powers for base case and with FACTS devices (during loadability)

S.No	Bus No	Base Case (without FACTS) With loadability ($\lambda=0.445$)	With FACTS ($\lambda=0.6669$)
1	1	186.6497	249.9942
2	2	100	100
3	3	100	100
4	8	0	0

The variation of the generated reactive powers is given in Table.4 for without and with FACTS devices. From this table it is observed that, the reactive power generated at slack bus is decreased from 31.2711 MVar to 26.613 MVar, this is about 17.50%. Similarly, the reactive power generated at bus-8 (synchronous condenser) is increased from 17.4885 MVar to 23.3879 MVar., this is about 33.73%.

Table.4: Variation of generated reactive powers for base case and with FACTS devices (during loadability)

S.No	Bus No	Base Case (without FACTS) With loadability ($\lambda=0.445$)	With FACTS ($\lambda=0.6669$)
1	1	31.2711	26.613
2	2	50	50
3	3	40	40
4	8	17.4885	23.3879

1	1	31.2711	26.613
2	2	50	50
3	3	40	40
4	8	17.4885	23.3879

The variation of the lines apparent power flow is given in Table.5 for without and with FACTS devices. From this table it is observed that, the apparent power flow in all lines increases as loadability increases. It is also observed that the apparent power flow in TCSC installed line (line-9) is increased from 36.61MVA to 55.4309 MVA, this is about 51.409%. The variations are shown in Fig.6.

Table.5: Variation of lines apparent power flows for base case and with FACTS devices (during loadability)

S.No	Line (i-j)	Base Case (without FACTS) With loadability ($\lambda=0.445$)	With FACTS ($\lambda=0.6669$)
1	1-2	112.9394	156.77
2	1-5	77.7506	95.6418
3	2-3	52.3851	68.6224
4	2-4	72.6788	84.0443
5	2-5	59.2771	65.9207
6	3-4	21.9078	14.0365
7	4-5	57.1744	75.5368
8	4-7	45.1852	40.7721
9	4-9	36.61	55.4309
10	5-6	64.9712	63.7403
11	6-11	6.972	6.5767
12	6-12	11.0912	11.4384
13	6-13	24.9546	31.2362
14	7-8	17.0092	22.5714
15	7-9	49.9994	42.5815
16	9-10	16.6564	18.1589
17	9-14	19.0366	20.4735
18	10-11	4.0471	0.2673
19	12-13	1.7452	5.4872
20	13-14	5.6161	8.4419

The variation of system active and reactive power losses is given in Table.6 for without and with FACTS devices. From this table it is observed that, the active power losses are increased from 12.3688MW to 18.2670MW this is about 47.686% and similarly, reactive power losses are increased about 55.56%.

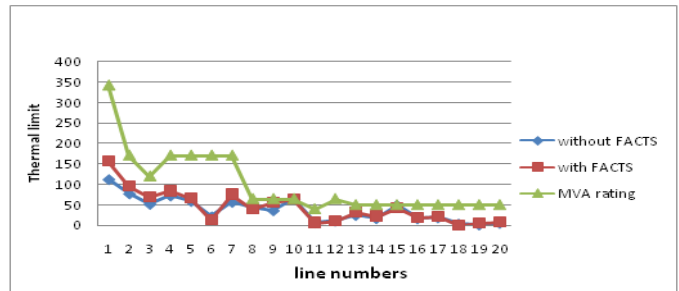


Fig.6. Variation of line apparent power flows

Table.6: Variation of system active and reactive power loss for base case and with FACTS devices (during loadability)

Description	Base Case (without FACTS) With loadability ($\lambda=0.445$)	With FACTS ($\lambda=0.6669$)
P loss (MW)	12.3688	18.2670
Q loss (MVar)	37.5447	58.4046

Case 4: The device minimized cost is calculated for each loadability step, and is given in Table.7. It is observed that device cost is increased for increase in loadability. The same is shown in Fig.7.

Table.7: Variation of device minimized cost

Loadability Steps	Loadability (λ)	Minimized Device Cost (\$/h)
1	0.1	0.0500
2	0.2	0.1162
3	0.3	0.17683
4	0.4	0.1834
5	0.5	0.2668
6	0.6	0.27045

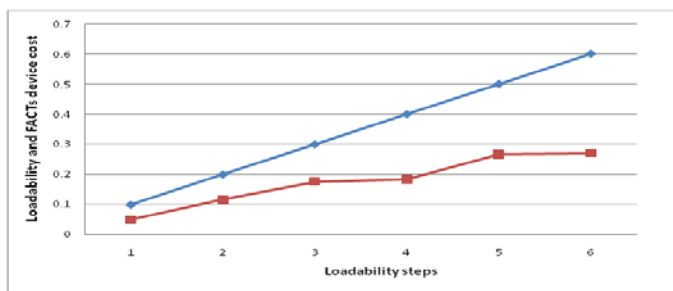


Fig.7. Variation of device cost with loadability

VI. CONCLUSION

In this paper, a procedure to choose suitable locations to install FACTS devices is proposed. The enhancement of loadability by incorporating SVC and TCSC devices in a given system is implemented. The optimal location to install SVC and TCSC is identified by using Ordinal Optimization approach through the selection of subset locations. Using appropriate crude models, the number of search samples in the solution space formed by all variables can be reduced to a much smaller set of candidates contain good enough solutions. The refining process to select optimal device settings through PSO has been implemented. The total minimized device cost is calculated for loadability increments. The proposed methodology is tested on standard IEEE-14 bus test system. The obtained results demonstrate the best option to increase the loadability of the system is by using optimal control of FACTS devices simultaneously. It is known that the maximum settings of the FACTS controllers in an optimal location beyond which it is impossible to improve the system loadability.

REFERENCES

- [1] A Oudalov, R Cherkaoui, A J Germond., "Application of fuzzy logic techniques for the coordinated power flow control by multiple series FACTS devices", Proceedings of the 22nd IEEE power engineering society international conference, 2001, pp.74-80
- [2] B M Zhang, Q F Ding., "The development of FACTS and its control", Proc. Of the 4th International Conf. on advances in power system control, operation and management, Hong Kong., 1997, pp.48-53.
- [3] H C Leung, T S Chung., "Optimal placement of FACTS Controllers in power system by a genetic based algorithm", Proc. of the IEEE international conference on power electronics and drive systems, 1999, pp.833-836.
- [4] Ashwani Sharma, Saurabh Chanana, Sanjoy Parida., "Combined Optimal Location of FACTS Controllers and Loadability Enhancement in Competitive Electricity Markets Using MILP", IEEE Power Engineering Society General Meeting, 2005, Vol.1, pp. 670-677.
- [5] M Santiago-Luna, J R Cedeno-Maldonado., "Optimal Placement of FACTS Controllers in Power Systems via Evolution Strategies", IEEE Transmission & Distribution Conference and Exposition: Latin America, 2006. TDC '06, pp.1-6.
- [6] D J Gotham, G T Heydt., "Power flow control and power flow studies for systems with FACTS devices", IEEE Trans. on Pwr. Sys., Vol.13, No.1, 1998, pp.60-65.
- [7] J H Kim, H Myung., "Evolutionary programming techniques for constrained optimization problems", IEEE Trans. on Evolutionary Computation., Vol.1, No.2, 1997, pp.129-140.
- [8] A P Alves, P J Abrao., "Applications of evolutionary computation in electric power systems", Proc. Congress on Evolutionary Computation, 2002, pp.1057-1062.
- [9] A. R. Messina, M. A. Per`ez, and E. Heman`dez, "Coordinated application of FACTS devices to enhance steady-state voltage stability," *Int. J. Elect. Power Energy Syst.*, Vol. 19, No. 2, 2003, pp. 259-267,
- [10] A. Kazemi and B.Badraheh, "Modeling and simulation of SVC and TCSC to study their limits on maximum loadability point," *Int. J. Elect. Power Energy Syst.*, Vol. 26, No. 5, Jun. 2004, pp. 381-388.
- [11] T. T. Ma, "Enhancement of power transmission systems by using multiple UPFC on evolutionary programming," in *Proc. IEEE Bologna Power Tech Conf.*, Jun. 2003, Vol. 4.
- [12] S. Gerbex, R. Cherkaoui, and A. J. Germond, "Optimal location of multi-type FACTS devices in a power system by means of genetic algorithm," *IEEE Trans. Power Syst.*, vol. 16, no. 3, pp. 537-544, Aug.
- [13] P.Bhasaputra and W. Ongsakul, "Optimal power flow with multi-type of FACTS devices by hybrid TS/SA approach," in *Proc. IEEE Int. Conf. Industrial Technology*, Dec. 2002, vol. 1, pp. 285-290.
- [14] M. Saravanan, S. M. R. Slochanal, P. Venkatesh, and J.P.S.Abraham, "Application of PSO technique for optimal location of FACTS devices considering system loadability and cost of installation," in *Proc. 7th Int. Power engineering Conf(IPEC)*, Dec. 2005, vol. 2, pp. 716-721.
- [15] K. Y. Lee, M. Farsangi, and H. Nazambadi-Pour, "Hybrid of analytical and heuristic techniques for FACTS devices in transmission systems," in *Proc. IEEE PES General Meeting*, Jun. 24-28, 2007, pp. 1-8.
- [16] S. Y. Lin, Y. C. Ho, and C.H. Lin, "An ordinal optimization theory-based algorithm for solving the optimal power flow problem with discrete control variables," *IEEE Trans. Power Syst.*, vol. 19, no. 1, pp. 276-286, Feb. 2004.
- [17] M. Xie, J. Zhong, and F. F. Wu, "Multiyear transmission expansion planning using ordinal optimization," *IEEE Trans. Power Syst.*, vol. 22, no. 4, pp. 1420-1428, Nov. 2007.
- [18] T.W. E. Lau and Y. C. Ho, "Universal alignment probabilities and subset selection for ordinal optimization," *J. Optim. Theory Appl.*, vol. 93, no. 3, pp. 445-489, Jun. 1997.
- [19] W. F. Tinney, J. M.Bright, K. D. Demaree, and B. A. Hughes, "Some deficiencies in optimal power flow," *IEEE Trans. Power Syst.*, vol. 3, no. 2, pp. 676-682, May 1988.
- [20] J. Kennedy and R. Eberhart, "A new optimizer using particle swarm theory", Proc. 6th International Symposium on Micro Machine and Human science, Vol.4, 1995, pp.1942-1948.
- [21] Y. C. Chang and R.F. Chang, "Utilization performance based FACTS devices installation strategy for transmission loadability enhancement," in *Proc. 4th IEEE Conf. Industrial Electronics and Applications (ICIEA 2009)*, May 25-27, 2009, pp. 2661-2666.
- [22] F. Li, "Application of ordinal optimization for distribution system reconfiguration," in *Proc. IEEE/PES Power Systems Conf. Expo.*, 2009.
- [23] Y. C. HO, R. S. Sreenivas, and P. Vakili, "Ordinal Optimization in DEDS," *Journal of Discrete Event Dynamic Systems*, vol. 2, pp.61-68, 1992.
- [24] Rony Seto Wibowo, Naoto Yorino, et al., "FACTS Devices Allocation with Control Coordination Considering Congestion Relief and Voltage Stability", IEEE Trans.on Pwr. Syst. Vol.26, No.4, 2011, pp. 2302-2310.
- [25] Shi.Y, Eberhart.R., "A modified particle swarm optimizer," Proceedings of the IEEE international conference on evolutionary computation., Piscataway, NJ: IEEE Press., 1998, pp. 69-73.
- [26] Eberhart. R, Shi. Y., "Computation between genetic algorithms and particle swarm optimization," Proceedings of the 7th annual conference on evolutionary programming., Berlin: Springer; 1998, pp. 611-618.
- [27] Caponetto. R, Fortuna. L, Fazzino. S, Xibilia. M.G., "Chaotic sequences to improve the performance of evolutionary algorithms," IEEE Trans. Evol. Comput., Vol. 7, No. 3, 2003., pp. 289-304.
- [28] Ya Chin Chang, Rung Fang Chang, Tsun Yu Hsiao, Chan Nan Lu., "Transmission System Loadability Enhancement Study by Ordinal Optimization Method", IEEE Trans. on Pwr. Syst., Vol.26, No.1, 2011, pp.451-459.

Removal of Anionic Dyes from Aqueous Solutions using Local Activated Kaolins as Adsorbers

F.Z. EL BERRICHI^{1*}, S.ZEN²

1 Laboratoire de Chimie Physique, University 8Mai45, BP 401, Guelma, Algeria * corresponding author :zora172001@yahoo.fr

2 Laboratoire de Chimie Appliquée, University 8Mai45, BP 401, Guelma, Algeria

Abstract— There are significant amounts of unused dyes remaining in wastewater from dyeing industry. The release of these effluents causes abnormal coloration of surface waters and there is a risk of toxicity. This research involved the efficient adsorption of anionic dyes (coriacide bordeau 3B, derma blue R67 and the coriacide brown 3J) used in tanning industry by local natural and treated clays; DD3 and KT2, a low-cost material abundant in highly weathered soils from Algerian East. The activated kaolins were characterized by chemical analyses (XRF), X-ray diffraction, Fourier Transform IR, Scanning Electron Microscopy (SEM) to obtain information about their structure and surface texture. The adsorption kinetics was investigated using the parameters such as contact time, amount of clay, solution initial dye concentration and acid activation. The adsorption capacity of all three dyes on local kaolinite clays exceeds 90 % observed after 40 to 80 min. Compared to adsorption experiments on bentonite, the results show that the kaolin has the best adsorption capacity for anionic dyes under the experimental conditions of this work.

Keywords— Kaolin, Bentonite, acid activation, anionic dyes, adsorption kinetics

I. INTRODUCTION

The presence of dyes in aqueous effluent such as in river stream can be noticed easily because dyes are colored and highly visible. The discharge of dyes directly into aqueous effluent can endanger living organism and its aquatic ecology because most dyes are toxic. They have negative environmental effects, causing oxygen impoverishment and light transmission attenuation in aquatic ecosystems affecting both fauna and flora [1]. Various physical, chemical and biological decolorization methods such as coagulation, reverse osmosis, electrochemical, dilution, filtration, flotation, and reverse osmosis technologies have been proposed [2]. Several conventional methods for the treatment of effluents containing

dyes are available [3], and the most efficient one is the adsorption process, because it is simple in terms of operation and can remove the contaminant even at very low concentration. However, the choice of the adsorbent is based on economical and practical reasons and clay minerals are natural materials with low cost. Kaolinite is the most abundant

phyllosilicate mineral in highly weathered soils and its use as adsorbent would be very convenient for removing organic pollutants and of heavy metal ions [4], [5]. Kaolinite has a low-cation exchange capacity (CEC) (3-15mequiv./100 g) and the adsorption properties may play an effective role in scavenging inorganic and organic pollutants from water [6], [7]. Therefore, the aim of this study was to determine the adsorption kinetics of anionic dyes widely used in the tannery, such as: derma blue R67, coriacide brown 3J and coriacide bordeau 3B on kaolinite over a range of physicochemical conditions that are important to identify various natural environmental systems., on Algerian kaolinite from Djebel Debagh “DD3” and EL Milia “KT2” in which Algeria possesses estimated at millions of tons, in the East, and that need to be valorised. A number of experimental parameters in this study are considered, including the effect of initial dye concentration, acid activation, and nature of clay. To explore the feasibility of this clay, bentonite was chosen to test the adsorption capacity to release the anionic dyes after treatment.

II. EXPERIMENTAL

A. Materials

Two commercial clays, DD3 and KT2, were chosen to represent abundant raw materials without special degree of purity. The kaolin (DD3), gray in color, was obtained from the Guelma region (Djebel Debagh) in Algeria and supplied by ETER (ceramic company, Guelma, Algeria). The type of kaolin is much rarer other clay minerals [8]. The second kaolin used “KT2” is an Algerian kaolin treated and enriched by ceramic company (ETER). The kaolin “KT2” came from the original EL Milia deposit “TAMAZERT” in the region of Jijel (Algeria). In order to obtain the acid-activated clays (DD3)

and KT2, the acid treatment was carried out with 0.1N H₂SO₄ acid [9]. The cation-exchange capacity (CEC) was measured in order to evaluate the potential use of these clays for adsorption. It was determined using the cobalt hexaammine chloride saturation method using a UV-VIS spectrophotometer. The decrease CEC values after

deactivation from 13.87 meq/100 g to 10.5 of DD3 and 27.62 meq/100g to 21.17 of KT2, previously air-dried overnight at 120 °C mainly due to dealumination.

Chemical compositions in mass % of natural KT2 and DD3 obtained by X-ray fluorescence (XRF) are listed in Table I.

Table I. X-ray fluorescence analysis: oxide composition (%) of natural “KT2” and “DD3” kaolins

Kaolins	Components (mass %)												
	SiO ₂	Al ₂ O ₃	Fe ₂ O ₃	MgO	CaO	Na ₂ O	K ₂ O	NO ₂	TiO ₂	BaO	SO ₃	MnO	LOI
DD3	41.97	38.00	0.12	0.07	0.20	-	-	-	-	-	0.75	1.34	16.80
KT2	49.30	33.50	1.59	0.40	0.08	0.09	2.75	-	0.24	-	-	-	10.50

LOI: Loss on ignition at 1000°C

B. Characterisation

Mineralogical compositions of representative clays samples were determined by XRD using air-dried. XRD patterns of DD3 and KT2 clays (before and after activation) were collected on a X-Pert Proanalytical diffractometer using Ni filtered Cu-K α radiation ($\lambda=1.5406\text{\AA}$, 30 kV, 30 mA and automatic monochromator). The diffractograms were recorded in the range $2\theta = 6-65^\circ$. The scanning speed was 1°/min. The FTIR spectra of natural and treated KT2 and DD3 with H₂SO₄ acid were obtained in the region 4000–500 cm⁻¹ by using FT-IR spectrometer, type Perkin Elmer Spectrum one model, at room temperature dispersed in KBr discs. The morphologies of natural and activated bentonite were examined using a scanning electron microscopy (Model JEOL JSM 6390 LU).

C. Dyes Solutions

The reactive dyes used as adsorbates are bifunctional dyes, they were provided by the Stahl Iberica of Spain and they were simulated by aqueous solutions of organic anionic dyes industrially used in tanning industry, with commercial names: coriacide bordeau 3B, derma blue R67 and coriacide brown 3J. Synthetic test dye solution was prepared by dissolving an accurately weighed amount of dye (1 g/L) in distilled water and subsequently diluted to required concentrations. Analytical samples were taken from the reaction suspensions at various time intervals during the reaction, then centrifuged the samples to remove the suspended particulates, and the equilibrium concentrations of dye were determined by measuring the absorbance at 510, 610 and 430 nm of the coriacide bordeau 3B (pH was 6.1), derma for blue R67 (5.6) and coriacide brown 3J (6.3), respectively with an UV-vis spectrophotometer (Photolab Spektral WTW). The complete structure diagrams of three dyes are not available. Intrinsic pH values of 6.1, 5.6 and 6 were measured at 25 °C with a Consort C831 potentiometer. These pH values did not vary immediately after addition of clay but only after few minutes once dye adsorption started.

D. Adsorption Studies

Adsorption of tanning dyes by the different kaolin fractions was carried out in batch. Batch adsorption is a simple technique commonly utilized to assess the adsorptive capacities of natural and synthetic sorbents. In the present study, the Algerian bentonite, supplied by ENOF (mining products company), was chosen to test the adsorption capacity to release the anionic dyes after treatment in addition to Djebel Debagh “DD3” and treated Tamzert “KT2” kaolins.

The adsorption process was conducted by adding a known amount of activated clays Tamazert “KT2” or Djebel Debagh “DD3” or bentonite into 500 mL of 100 mg/L dye solution at a constant stirring speed of 450 rpm. Dye adsorption kinetics was investigated at 20 °C and natural pH=4 for 200min. Two milliliters of samples were drawn at suitable time intervals. The samples were then centrifuged for 15min at 5000rpm and the left out concentration in the supernatant solution were analysed through UV visible at maximum wavelength. In order to characterize the adsorption process of dye on clay, we have discussed the effect of parameters such as contact time, initial dye concentration, and acid activation on the removal rate of dye onto clay from aqueous solution.

In the kinetic experiments the amount of dye adsorbed at a time interval t , Q_t (mg/g) or the percentage removal (P %) were calculated using the following equations:

$$Q_t = (C_0 - C_t) V/m \quad (1)$$

$$P\% = 100(C_0 - C_t)/C_0 \quad (2)$$

where C_0 and C_t are the initial and liquid-phase concentrations at any time t of dye solution (mg/L), respectively; q_t is the dye concentration on adsorbent at any time t (mg/g), V the volume of dye solution (L), and m is the mass of kaolinite sample used (g).

III. RESULTS AND DISCUSSION

A. Characterisation of DD3 and KT2 kaolins

The raw kaolins were rich in SiO₂ (>40%), in Al₂O₃ (>30%) and contained only small amounts of Ca²⁺, Mg²⁺, Na⁺ ions

(Table I). However, titanium oxide (TiO₂) is present in traces amounts for KT2 in all their crystalline forms such as the anatase and the rutile and the low manganese oxide content is present in DD3. The low concentrations of these minerals generate the rheological and physico-chemicals properties which are direct influence on quality of raw material. Physical characterization of layer structure for DD3 and KT2 before and after activation was conducted by X-ray diffraction. The XRD results for kaolins before and after activation shown in Fig. 1. The interlayer spacing or d₀₀₁ spacing is measured from the top of the corresponding Si tetrahedral silica sheet (T) to the top of the Si tetrahedral sheet of the following layer [10]. The KT2 and DD3 clays yielded, 5 to peaks in the range of 6–40° (2θ). The basal spacing (d₀₀₁) of DD3 and KT2 natural kaolins are 7.26, 3.50 Å, respectively attributed to kaolinite (Figure 1a and c). Other reflections attributed to quartz, calcite as impurities are observed for both natural kaolins. The increase of basal spacing in DD3 (7.33 Å) and KT2 (3.59 Å) activated (Fig. 1b and d) indicate the acid treatment affect slightly the structure of the components and expanded the interlayer spaces. Furthermore, acid treatment with H₂SO₄ 0.1N, dissolves major impurities such as calcite, quartz and dolomite for both materials.

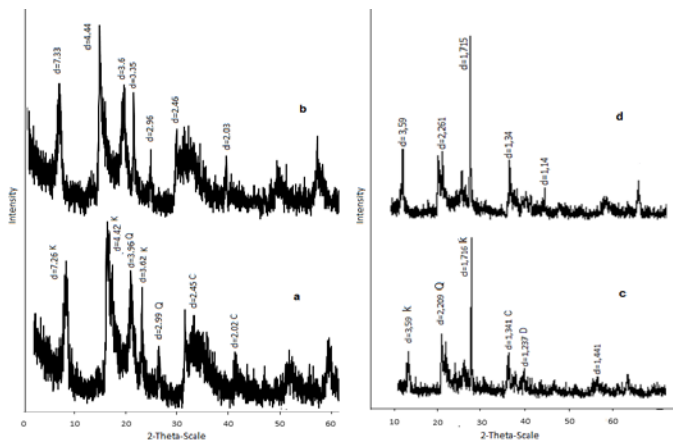


Fig. 1 XRD analysis results for the natural and activated kaolins; (a and c): natural DD3 and KT2; (b and d): activated DD3 and KT2; K= kaolinite and impurity phases (C= Calcite, D= Dolomite and Q= Quartz) are shown.

The infrared spectroscopy constitutes for the mineralogists a tool for characterization of the crystallinity of clays by the observation of the relative intensities of the bands of vibrations of hydroxyls of structure. The FTIR spectrums of natural and activated clays are shown in Fig. 2. As we can see, all clays natural and activated exhibit two moderately intense bands between 3620.64 and 3750cm⁻¹, which might be ascribed to the stretching frequencies of the OH functional groups of coordination water and of the hydration OH stretching. The absorption peaks between 1620 and 1630.53cm⁻¹ can be taken as both due to OH stretching vibration and δ(H₂O) deformation. The rest of the bands between 450 and 1095 cm⁻¹

in natural clays are due to stretching vibration of Si–O, Si–O–Si, OH attached to (Al³⁺, Fe³⁺, and Mg²⁺) groups, and the silica quartz impurities.

After acid treatment, a significant difference is not observed between original and activated KT2 and DD3. Under these mild conditions, the FTIR curves showed that a weak destruction of the layers and interlayer space of activated clay was carried [11].

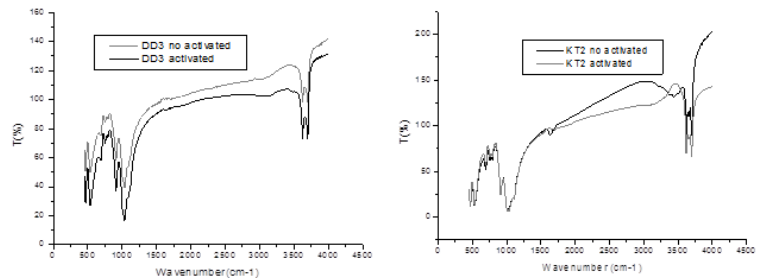


Fig. 2 Infrared Spectra of natural and activated kaolins DD3 and KT2

SEM was used to probe the change in morphological features of natural and activated kaolins DD3 and KT2. Fig. 3 shows the SEM micrographs of DD3 and KT2. The surface morphology of natural kaolin is different from that of the treated kaolin. DD3 activated has larger pores between particles than DD3 non activated (Fig. 3 a and b). Also, natural KT2 appears to be highly compact than activated KT2 (Fig. 3c and d). It is seen that in all non activated kaolins the inter-particle pores are smaller compared to the activated kaolins.

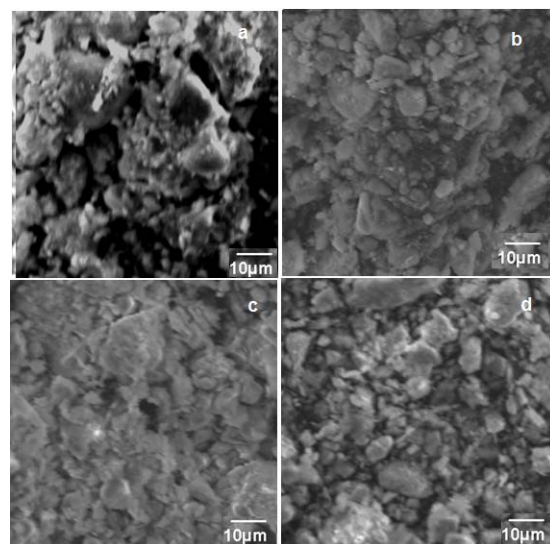


Fig. 3 SEM image of DD3 and KT2 kaolins: (a and c): natural DD3 and KT2; (b and d): activated DD3 and KT2

B. Adsorption studies

B.1 Effect of contact time

The influence of contact time on removal of blue derma R67, coriocide bordeaux 3B and coriocide brown 3J by 4g of

activated Tamazert "KT2", Djebel Debagh "DD3" kaolins or bentonite at pH 4 and 20°C with an initial dye concentration 20mg/l are shown in Fig. 4. It is evident that all clays are efficient to adsorb dyes with different efficiencies and the removal of dyes was rapid and strong in the initial stages of contact time (2 min) followed by a slow increase until reaching equilibrium, due to the abundant availability of active sites on the clay surface, and with the gradual occupancy of these sites, the sorption becomes less efficient. The shape of the curves for DD3, KT2 and bentonite clays are similar. This indicates a monolayer formation of the dye on the external surface [12]. The adsorption of the activated DD3 and KT2 is faster than

that of activated bentonite for three dyes. Moreover, the maximum removal percentage of three dyes adsorbed (P%) is higher for the activated DD3 (98%) and for the activated KT2 (97%) than for activated bentonite (82%). To reach equilibrium for anionic dye as blue derma R67, it takes 10, 25 and 80 min for activated DD3, KT2 and bentonite, respectively. At the equilibrium, the activated DD3, KT2 and bentonite fixes more blue derma R67 than the coriacide brown 3J and coriacide bordeaux 3B.

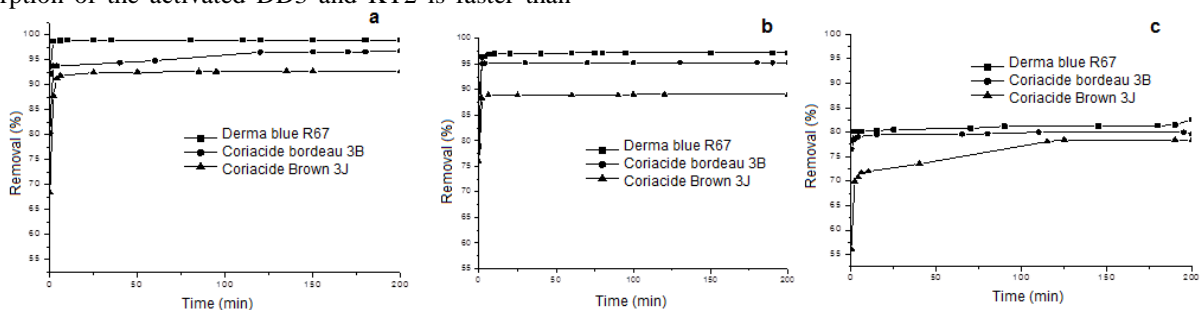


Fig.4 Effect of contact time on the removal of three anionic dyes on activated DD3 (a), KT2 (b) and bentonite (c).

B.2 Effect of clay nature

Fig. 5 shows the effect of clay nature on the anionic adsorption dye at initial dye concentrations of 20mg/L at pH=4 for derma blue as function of contact time on 4g of activated bentonite or DD3 or KT2. In order to characterise the adsorption capacity on kaolin of the anionic dye "blue derma R67" which was fixed more than coriacide bordeaux 3B and brown 3J, we have compared with activated bentonite. The removal of derma blue R67 was rapid in the initial stages of contact time (Fig. 5) and gradually decreased with lapse of time until equilibrium. The rapid adsorption observed during the first 2 min is probably due to the abundant availability of active sites on the kaolinite surface, and with the gradual occupancy of these sites, the sorption becomes less efficient. The time necessary to reach the equilibrium is about 10 min for DD3 and KT2 with higher removal percentage (98%) than that of bentonite (80%). Thus the main process involved in anionic derma blue dye adsorption on activated DD3 and KT2 kaolins may be the attraction on the broken edges of clay particles where charges become positive at acidic pH.

The effect of clay nature on dye adsorption observed in this study was explained by electrostatic interaction between kaolinite or bentonite and dye molecules. As the pH of the system (dye +kaolinite) is acid (pH=4), knowing that the pH has a relatively high value for kaolinite (2–4.6) [13], the number of negatively charged sites decreases and the number of positively charged sites increases in activated DD3 and KT2. The lower adsorption of anionic dyes on activated bentonite is because of the low presence of H⁺ ions competing with dye anions for the adsorption sites.

B.3 Effect of initial dye concentration

The amount of dyes adsorbed, removal percentage (P%), increases with time for all initial concentration at pH=4 for derma blue as function of contact time on 4g of activated clay. When the equilibrium conditions are reached the adsorbate molecules in the solutions are in a state of dynamic equilibrium with the molecules adsorbed by the adsorbent. The adsorption capacity increased with increasing initial dye concentration and the process was faster at low concentrations (20mg/L) than high concentration (200mg/L) because the adsorption sites took up the available dye more quickly (Fig. 6). However, at higher concentrations, dye needed to diffuse to the sorbent surface by intraparticle diffusion. Also, the steric repulsion between the solute molecules could slow down the adsorption process.

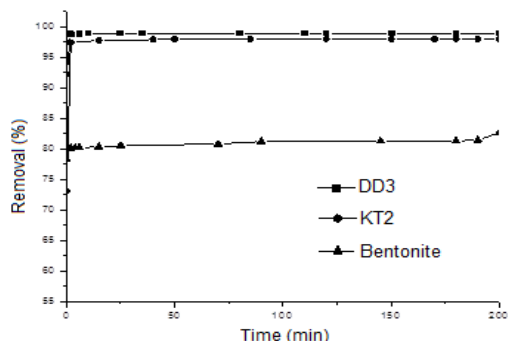


Fig. 5 Effect of clay nature on the removal of derma blue R67 on activated "DD3", KT2 and bentonite.

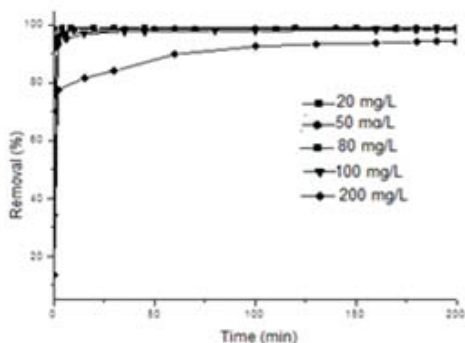


Fig. 6 The effect of initial dye concentration on the removal of blue derma on activated DD3

The high adsorption indicates that the low initial concentration provided a powerful driving force to overcome the mass transfer resistance between the aqueous and solid phases [14]. On the other hand, the shapes of the curves are similar and approximately independent on the initial dye concentration (Fig. 6). This indicates a monolayer formation of the dye on the external surface [12].

B.4 Effect of acid-activation

The adsorption rate of derma blue R67 on the acid activated and no activated DD3 kaolin was investigated at 20°C and pH =4 as a function of time (Fig. 7). The removal percent of derma blue on the kaolinite surface increased with kaolinite treated. The fact that the adsorption of tanning dye increase with DD3activated, may be due to transforming of SOH groups to SOH₂⁺ groups on kaolinite surface according to the following reaction [15]:

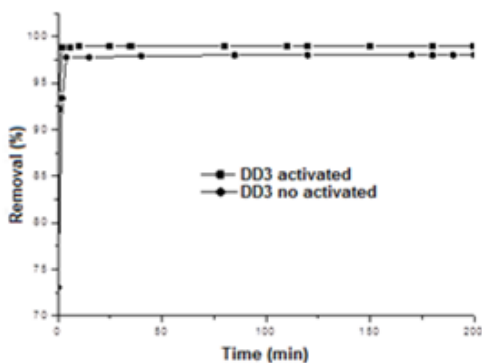


Fig. 7 The effect of acid activation on the removal of blue derma on DD3.

IV. CONCLUSION

Algerian kaolins, DD3 from Djebel Debagh (Guelma) and KT2 from Tamazert (El Milia region), activated by acid treatment can be employed as an effective and promising low cost alternative adsorbents for the removal of anionic dyes from tannery wastewater. The adsorption of derma blue R67, coriacide brown 3J and coriacide bordeaux 3B was highly

dependent on initial dye concentration and acid-activation. A comparative study of adsorption evidences the high adsorption capacity of the three tanning dyes on the activated DD3 and KT2 than activated bentonite. An increase in the initial dye concentration enhances the interaction between tanning dyes and kaolins "DD3 and KT2", resulting in greater and fast adsorption capacity with the equilibrium was attained after 10 to 80min for anionic dyes by comparison with activated bentonite, the adsorption capacity is low for all the three anionic dyes and the time to reach equilibrium was 80 to 140min. These results could be explained by the electrostatic attraction between the positively charged surface and the negatively charged dye molecule in the acidic medium (natural pH=4). Compared to standard bentonite clay, activated DD3 and KT2 have a good and high potential for adsorption removal of anionic dye from aqueous solution.

REFERENCES

- [1] M.Maes, « Les résidus industriels, traitement valorisation et législation ». Entreprise Moderne d'Édition Technique et Documentation, Paris, 1994.
- [2] K.P.Singh., D.Mohan, S.Sinha., G.S.Tondon, D.Gosh, « Color removal from wastewater using low-cost activated carbon derived from agricultural waste material », Industrial and Engineering Chemistry Research, vol.42, Apr. 2003, pp.1965–1976.
- [3] T. Akar, T.A. Demir, I. Kiran, A. Ozcan, A.S. Ozcan, and S. Tunali, "Biosorption potential of *Neurospora crassa* cells for decolorization of Acid Red 57 (AR57) dye", Journal of Chemical Technology and Biotechnology, vol.81, Feb.2006, pp.1100–1106.
- [4] S.P.Dubey, K.Gopal, and J.L. Bersillon, "Utility of adsorbents in the purification of drinking water: A review of characterization, efficiency and safety evaluation of various adsorbents", Journal of Environmental Biology, vol. 30, May. 2009, pp. 327–332.
- [5] V.K.Gupta, N. Suha, "Application of low-cost adsorbents for dye removal - A review », Journal of Environmental Management, vol.90, Mar. 2009, pp. 2313–2342.
- [6] P.Turan, M. Dogan, M. Alkan, "Uptake of trivalent chromium ions from aqueous solutions using kaolinite", Journal of Hazardous Materials, vol. 148, Sept. 2007, pp. 56–63.
- [7] M.Alkan, O. Demirbas, M. Dogan, "Electrokinetic properties of kaolinite in mono and multivalent electrolyte solutions", Microporous and Mesoporous Materials, vol.83, Sept. 2005, pp.51–59.
- [8] K.G. Papke, "Halloysite deposits in the Terraced Hills Washoe County, Nevada": Clays and Clay Minerals, vol.19, May. 1971, pp. 71-74, .
- [9] B. Benguella, A. Yacouta-Nour, "Adsorption of Bezanyl Red and Nylomine Green from aqueous solutions by natural and acid-activated bentonite", Desalination, vol. 235, Jan. 2009, pp. 276–292.
- [10] M. Majdan, S. Pikus, Z. Rzaczyńska, M. Iwan, O. Maryuk, R. Kwiatkowski, and H. Skrzypek, "Characteristics of chabazite modified by hexadecyltrimethylammonium bromide and of its affinity toward chromates". Journal of Molecular Structure, vol.791, June 2006, pp. 53–60.
- [11] A. Salem, and L. Karimi, "Physico-chemical variation in bentonite by sulfuric acid activation". Korean Journal of Chemical Engineering, vol. 26, no.4, Jan. 2009, pp. 980-984.
- [12] M.A. Al-Ghouti, M. Khraish, S.J. Allen, and M.N. Ahmad, "The removal of dyes from textile wastewater: a study of the physical characteristics and adsorption mechanisms of diatomaceous earth", A review of Journal Environmental Management, vol. 69, Nov. 2003, pp. 229–235.
- [13] B.K. Schroth, G. Sposito, "Surface charge properties of kaolinite", Clays. Clay. Min., vol.45, no.1, 1997, pp. 85–91.

- [14] W.-T. Tsai., H.-C. Hsub, T.-Y. Su, K.-Y. Lin, K.-Y., C.-M. Lin, T.-H. Dai, « The adsorption of cationic dye from aqueous solution onto acid-activated andesite”, *Journal of Hazardous Materials*, vol. 147, Aug. 2007, pp. 1056–1062.
- [15] M.Alkan, B. Kalay, M. Dogan, O. Demirbas, “Removal of copper ions from aqueous solutions by kaolinite and batch design”, *Journal of Hazardous Materials*, vol. 153, May. 2008, pp. 867–876.

Plasma-assisted ignition and combustion of pulverized coal at thermal power plants of Kazakhstan

V. E. Messerle, A. B. Ustimenko, and O. A. Lavrichshev

Abstract—Application of direct-flow and vortex plasma-fuel systems (PFS) for coal-fired boilers of thermal power plants (TPP) at Ust-Kamenogorsk, Shakhtinsk, and Almaty (TPP-2 and TPP-3) (Kazakhstan) is discussed. In the plasma technology coal replaces traditionally used for the boiler start up and pulverized coal flame stabilization fuel oil or natural gas. Part of coal/air mixture is fed into the PFS where the plasma-flame from plasma torch induces gasification of the coal and partial oxidation of the char carbon. As coal/air mixture is deficient in oxygen, the carbon being mainly oxidized to carbon monoxide. As a result, a highly reactive fuel (HRF) composed of mixture of combustible gases and partially oxidized char particles is obtained at the exit of the PFS. On entry to the furnace, this HRF is easily ignited.

Simulation and testing of PFS at existing pulverized coal-fired boilers of TPP confirmed the technical feasibility, environmental and energy efficiency of no-fuel oil boilers start-up and pulverized coal flame stabilization using PFS.

Keywords—Coal, plasma torch, ignition, combustion, furnace, efficiency, environment.

I. INTRODUCTION

THE technology of plasma ignition of coal and its realizing plasma-fuel systems (PFS) is electro-thermo-chemical preparation of fuel to burning (ETCPF) [1] – [6]. In this technology pulverized coal is replaced traditionally used for the boiler start up and pulverized coal flame stabilization fuel oil or natural gas. Part of the coal/air mixture is fed into the PFS where the plasma-flame from plasma torch, having a locally high concentration of energy, induces gasification of the coal and partial oxidation of the char carbon. As coal/air mixture is deficient in oxygen, the carbon being mainly oxidized to carbon monoxide. As a result, a highly reactive

This work was supported in part by the Ministry of Education and Science of the Republic of Kazakhstan under Grants 0112PK02834, 0112PK01824, 0112PK01825, 0112PK01466.

A. B. Ustimenko is with Research Institute of Experimental and Theoretical Physics of al-Farabi Kazakh National University, Almaty, Kazakhstan (corresponding author to provide phone: 7727-377-3369; fax: 7727-377-3174; e-mail: ust@physics.kz).

V. E. Messerle is with Combustion Problems Institute, Almaty, Kazakhstan, and with Institute of Thermophysics of Russian Academy of Science, Novosibirsk, Russia (e-mail: ust@physics.kz).

O. A. Lavrichshev is with the Research Institute of Experimental and Theoretical Physics of al-Farabi Kazakh National University, Almaty, Kazakhstan (e-mail: lavr@physics.kz).

fuel (HRF) composed of mixture of combustible gases (at a temperature of about 1300 K) and partially oxidized char particles is obtained at the exit of the PFS. On entry to the furnace, this HRF is easily ignited.

II. BOILERS PLASMA START UP

75 ton steam productivity boiler (Fig. 1) of Ust-Kamenogorsk TPP has three main pulverized coal turbulent burners and two kindling muffle burners. The last two were transformed to PFS. Kuznetsk bituminous coal of 17.7 % ash content and 4878 kcal/kg calorific value was incinerated in the boiler. During the PFS tests at this boiler the pulverized coal flow through each PFS was 1.5 t/h and the primary air - 2.6 t/h. The pulverized coal flow through the main burners was 11.5 t/h. Plasma torch power was varied from 60 to 70 kW and its heat efficiency was 85-86 %. HRF flame temperature at the PFS exit was in interval 1040-1240°C. Plasma torch's relative power consumptions were 0.5 – 0.7 % of the muffle burner heat power. NO_x concentration on the PFS exit was not more than 20 mg/Nm³ and synthesis gas (CO+H₂) yield exceeded 60 %. In 35 minutes of the PFS start stationary heat regime of the muffle burner was achieved, plasma torches were turned off and heated muffles went on stabilizing the flame combustion. The flames from muffle burners were 3 m in length. The boiler oil-free start-up lasted 3.25 h after which the boiler was linked up with the main steam pipeline of the TPP.

75 ton steam productivity boiler of Shakhtinsk TPP has four burners (Fig. 2), two on the front and rear in one layer. Bituminous coal of 30% ash content with the flow through the burner (or PFS) 3200 kg/h is incinerated in the boiler. Primary air flow through the burner is 6400 kg/h, plasma torch power is 200 kW and PFS length is 2.3 m (Fig. 3). Numerical modeling of the ETCPF in PFS is performed using a one-dimensional mathematical model Plasma-Coal. The calculation results allowed defining the geometric dimensions of PFS, the required power of plasma torch, temperature, velocity and composition of the products of ETCPF. These results can be used as initial conditions for numerical simulation of HRF combustion in the boiler furnace using Cinar ICE code. 3D modeling results showed that when operating PFS ignition of pulverized coal flame starts earlier, the combustion front moves to the installation location of the PFS on the boiler, resulting in lower temperature of the exhaust gases, the

concentration of nitrogen oxides in them and unburned carbon, compared with the traditional mode of coal incineration without plasma activation in PFS.

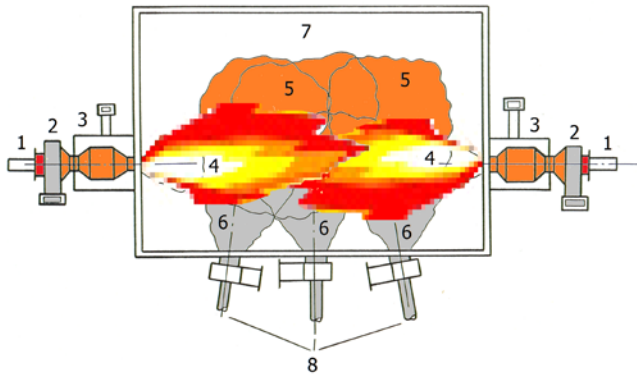


Fig. 1. PFS layout at a boiler of 75 ton steam productivity of Ust-Kamenogorsk TPP (cross-section view of the furnace with PFS): 1) plasmatron, 2) chamber for plasma assisted incineration, 3) muffler burner, 4) flame of high reactive two component fuel from PFS, 5) pulverised coal flame, 6) air-coal mixture from the main burners, 7) furnace, 8) the main pf burners

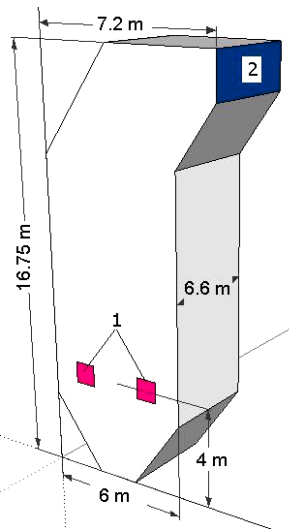


Fig. 2. Layout of the furnace of BKZ-75 power boiler: 1) burner throat, 2) section of the swiveling chamber of the boiler

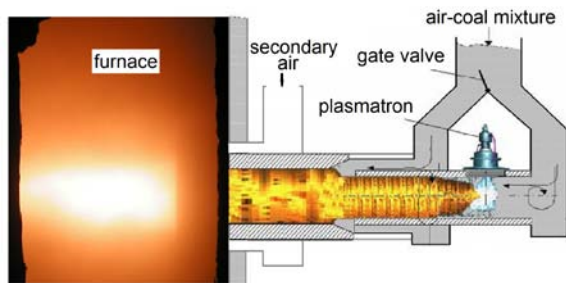


Fig. 3. Sketch of the PFS for replacement of the traditional burners of the boiler BKZ-75

Almaty TPP-3 boiler of 160 t/h steam productivity (Fig. 4) has four coal-fired blocks of two-layer slot burners (Fig. 5).

Consumption of 45 % ash content and 3800 kcal/kg calorific value Ekibastuz bituminous coal was 4 t/h through each burner. Two PFS were installed in the lower layer of the burners diagonally. Plasma torches were running on the power of 120-140 kW (350-450 A current, and 300-350 V voltage). Ignition of the flames in the furnace was observed in 2-3 seconds after submitting of pulverized coal at a rate of up to 3 t/h through each PFS. Coal-dust flame temperature at the exit of the PFS reaches 1200-1300°C, and is 5-6 m in length. Using these parameters, the formation of the bright yellow core flame in the center of the furnace was observed. In 3.5 hours from the kindling start parameters of the boiler reached operating values, and it was connected to the steam main, after which air/coal mixture was filed to all the burners. According to the rule one start-up of the boiler consumes 12 tons of fuel oil that by calorific value is equivalent to 30 tons of the coal. Instead, one start-up on average consumed about 16.5 tons of coal that confirms ETCPF energy efficiency. The specific power consumptions for plasma torches were 1.2-1.4% of the heat capacity of pulverized coal burners.

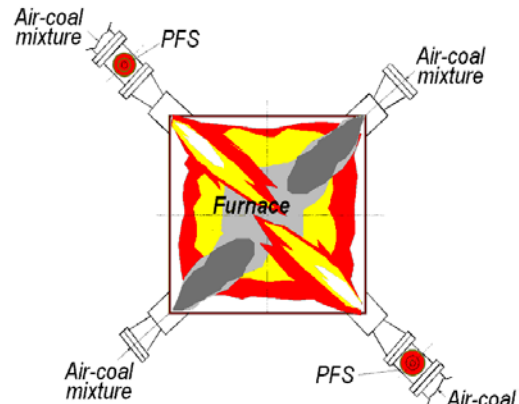


Fig. 4. BKZ-160 boiler furnace of 160 ton steam productivity (Almaty TPP-3) equipped with two PFS (top view)

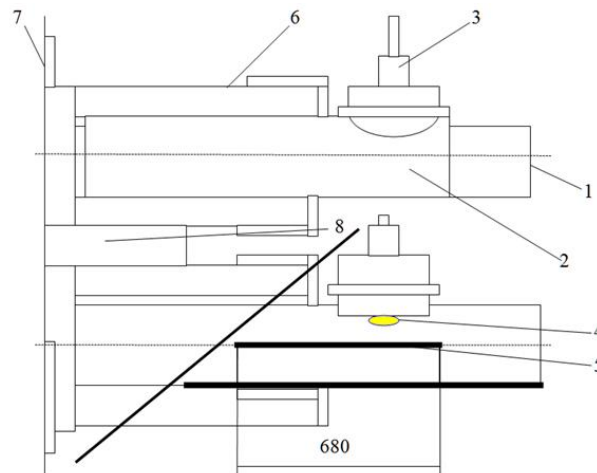


Fig. 5. Sketch of direct flow PFS – burner assembly with plasma torches: 1) dust flue, 2) chamber of plasma ignition, 3) plasma torch, 4) plasma flame, 5) partition plate, 6) secondary air duct, 7) furnace border, 8) oil fuel nozzle channel

III. COMPUTATION OF PFS AND FULL-SCALE INDUSTRIAL BOILER'S FURNACE

The fulfilled verification of CINAR ICE code for plasma assisted coal combustion in the experimental furnace of 3 MW power confirmed legitimacy of the used codes complex (PLASMA-COAL and CINAR ICE) for simulation of the furnaces equipped with PFS. Thus in this part the numerical study was performed for a power-generating boiler with a steam productivity of 75 t/h. The boiler's furnace (Fig. 2) is equipped with four swirl burners arranged in one layers, by two burners, on the boiler front and backside. Low-rank bituminous coal of 35.1 % ash content, 22 % devolatilization and 18550 kJ/kg heat value was incinerated in the furnace. Averaged size of the coal particles was 75 micron. All the calculations were performed in accordance to the aforementioned technique.

Three modes of the boiler operation were chosen for the numerical studies. The first one was traditional regime, using four pulverized coal burners, the second one was regime with plasma activation of combustion, using the replacement of two burners onto PFS (Fig. 3), and the third one was regime of the boiler operation using four PFS instead of all burners.

PLASMA-COAL computer code has been used for calculation of ETCPF in the volume of PFS of 2.3 m length. The following initial parameters were used for calculations: plasma torch power was 200 kW, initial temperature of pulverized coal (coal/air mixture) was 90°C, coal and primary air consumptions through PFS were 3200 and 6400 kg/h correspondingly.

The results of numerical simulation by the PLASMA-COAL code are summarized in Table I. Heat value of the coke residue was 8580 kJ/kg. These data were taken as initial parameters for 3-D computation of the furnace of the power-generating boiler equipped with PFS. This computation was performed using CINAR ICE code to demonstrate advantages of plasma aided coal combustion technology.

Table I. Characteristics of ETCPF at the PFS exit

Content of gas phase, vol.% & kg/h							
H ₂	CO	CH ₄	C ₆ H ₆	CO ₂	H ₂ O	N ₂	O ₂
14.2	18.4	0.3	0.6	6.8	2.9	56.4	0.3
88.5	1599.0	14.0	133.8	931.2	162.8	4911	31.0
Ash, kg/h		Char carbon, kg/h		T _{HRF} , °C		V _{HRF} , m/s	
1123.2		435.0		997		189	

Initial parameters for calculations of the furnace (Fig. 2) in different operational regimes were the following: temperature of the secondary air was 290°C, coal productivity of the burner was 3200 kg/h and primary air flow rate through the burner was 10260 kg/h. Secondary air flow rate to the boiler was 78160 kg/h. The grid is defined by 85 x 69 x 116 grid

lines in three directions (x, y and z).

The calculations results are shown in Figs. 6 - 10. Fig. 6 visualizes the difference between temperature fields in three regimes of coal incineration. In the traditional regime (Fig. 6 a), with maximum temperature of 1852°C, four symmetrical flames are generated. In central space of the furnace they form overall body of flame with the temperature about 1300°C. In Fig. 6 b two PFS are on top. The PFS impact appears as increase of temperature maximum up to 2102°C and transformation of HRF flame shape, it becomes narrow and longer. When the furnace operates with four PFS (Fig. 6 c) the flames length increases but maximal temperature decreases to 1930°C.

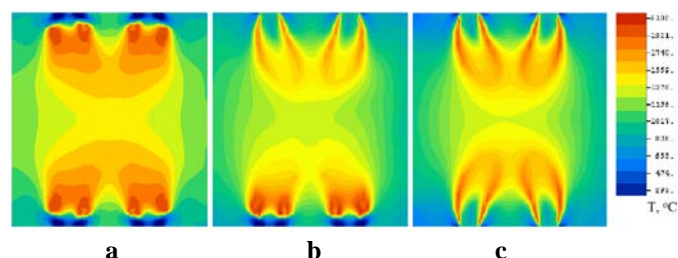


Fig. 6. Temperature field within the combustion chamber at the level of the pulverized coal burners: a) standard operational regime, b) plasma operational regime with two PFS, c) plasma operational regime with four PFS

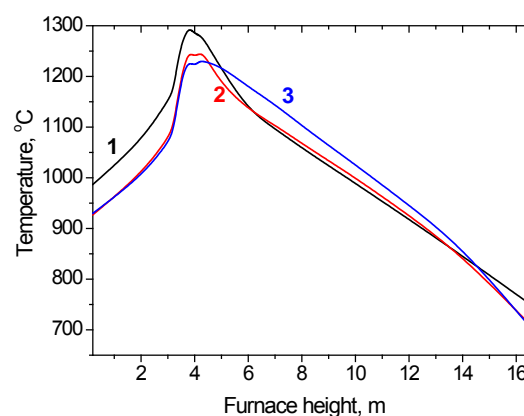


Fig. 7. Furnace height distribution of mass average temperature: 1) standard operational regime, 2) regime with two PFS, 3) regime with four PFS

Average characteristics of the boiler are compared in Figs. 7 - 10 for three modes of the boiler operation. The temperature curves have a characteristic maximum in the zone of the burners arrangement at a height of 4 m (Fig. 7). In the traditional mode of combustion level of the average temperature in the furnace at a height of up to 6 m higher than that for the boiler operating with PFS. The temperature difference reaches 75 degrees (height between 2 and 3 m), due to more intense radiation from the coal particles having a higher concentration and the total surface at the traditional combustion, compared to the operation mode with PFS. From the PFS HRF enters the combustion chamber, consisting of

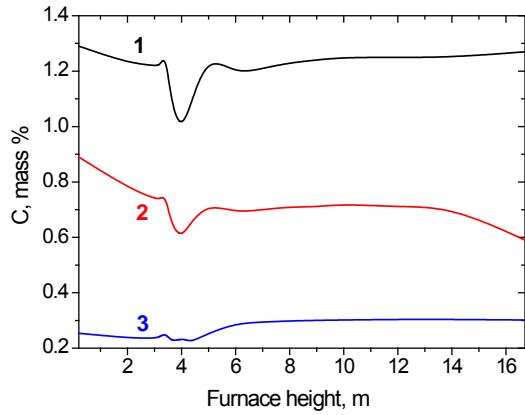


Fig. 8. Furnace height distribution of carbon mean concentrations: 1) standard operational regime, 2) regime with two PFS, 3) regime with four PFS

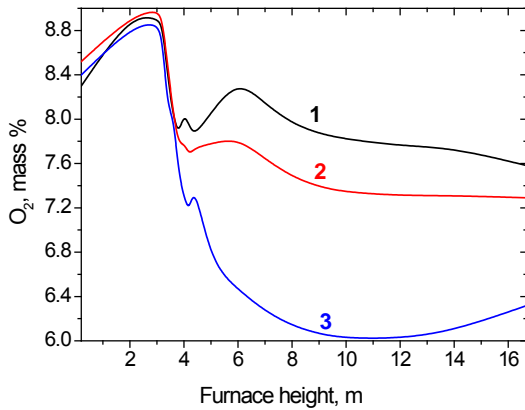


Fig. 9. Furnace height distribution of oxygen mean concentrations: 1) standard operational regime, 2) regime with two PFS, 3) regime with four PFS

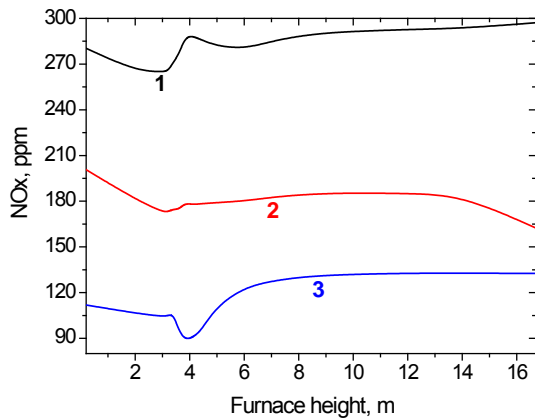


Fig. 10. Furnace height distribution of NOx mean concentration: 1) standard operational regime, 2) regime with two PFS, 3) regime with four PFS

fuel gas and coke residue particles, whose mass does not exceed 30 % of the consumption of raw coal, which leads to a threefold reduction in the total surface of the radiating particles. Further, the section of the furnace from 4.5 to 16.75 m, the temperature in the regime with PFS higher than that for the traditional burning by 10 and 32 degrees in the case of 2 and 4 PFS respectively. This is due to more complete fuel burnout (Fig. 8) by ETCPF confirmed by decreased oxygen concentration in the furnace at the same location (Fig. 9). PFS improves the environmental characteristics of the combustion of solid fuels. Compared with the traditional mode of coal incineration use of four PFS reduces the unburned carbon at the outlet of the furnace (height of 16.75 m) 4 times, and nitrogen oxide emissions by more than 2.2-fold (Fig. 10).

IV. COMPUTATION OF 420 T/H STEAM PRODUCTIVITY BOILER'S FURNACE EQUIPPED WITH PFS

The boiler of 420 t/h steam productivity (Fig. 11) is equipped with 6 swirl burners arranged in two layers, three burners each, on faced wall of the furnace. As it is seen from the figure three PFS (Fig. 12) are installed instead of two burners of the lower layer and one of the upper layer. Low-rank Ekibastuz bituminous coal of 40 % ash content, 24 % devolatilization, 5 % humidity and 16700 kJ/kg heat value was incinerated in the furnace. The coal grinding fineness is $R_{90}=15\%$. All the calculations were performed in accordance to the aforecited technique.

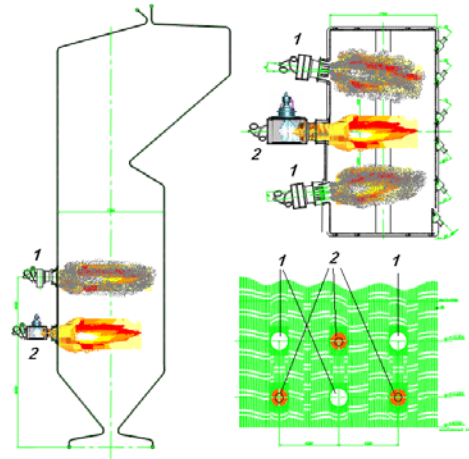


Fig. 11. Scheme of industrial 420 t/h steam productivity boiler in Almaty TPP-2 (Kazakhstan) retrofitted with PFS: 1) standard pulverized coal swirl burner, 2) PFS

PLASMA-COAL computer code has been used for calculation of ETCPF in the volume of PFS of 3.687 m length. The following initial parameters were used for calculations: plasma torch power was 200 kW, initial temperature of pulverized coal (coal/air mixture) was 90°C, coal and air consumptions through PFS were 6000 and 8955 kg/h correspondingly.

The results of numerical simulation by the PLASMA-COAL code are summarized in Table II. Heat value of the coke residue

was 6165 kJ/kg. These data obtained for the PFS exit were taken as initial parameters for 3-D computation of the furnace of a power-generating boiler equipped with PFS. This computation was performed using CINAR ICE code to demonstrate advantages of plasma aided coal combustion technology.

Table II. Characteristics of ETCPF at the PFS exit

Content of gas phase, vol.% & kg/h							
H ₂	CO	CH ₄	C ₆ H ₆	CO ₂	H ₂ O	N ₂	O ₂
1.05	7.75	0.3	0.77	15.6	3.55	70.84	0.15
7.272	751.4	16.75	207	2378	220.5	6870	16.49
Ash, kg/h		Char carbon, kg/h		T _{HRF} , °C		V _{HRF} , m/s	
1518		261		1025		48.2	

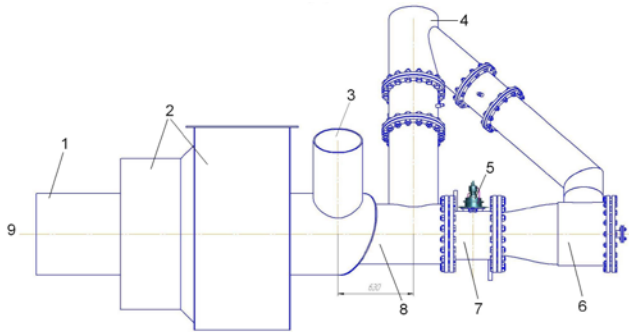


Fig. 12. Layout of the PFS for the boiler of Almaty TPP-2: 1) channel of the external flow of pf, 2) secondary air duct, 3) inlet of pf external flow, 4) inlet of pf internal flow, 5) plasmatron, 6) chamber for pf flow turning, 7) chamber for plasma chemical preparation of fuel for combustion, 8) chamber for mixing and thermochemical preparation of fuel, 9) furnace

Initial parameters for calculations of the furnace (Fig. 11) in different operational regimes were the following: temperature of the secondary air was 280°C, coal productivity of the burner was 12000 kg/h and primary air flow rate through the burner was 17900 kg/h. Secondary air flow rate to the boiler was 446412 kg/h. Averaged size of the coal particles was 60 micron. The furnace size is as follows: 27 m height, 7.7 m depth and 14.5 m width. The x, y, z grid size was, respectively: 106 x 38 x 104.

The model predictions are presented in Figs. 13 - 17 which show results for the plasma-activated coal combustion in comparison with conventional coal combustion. Figs. 13 and 14 show temperature fields along the furnace height in the mean cross-sectional plane for two regimes of the furnace operation, traditional (Fig. 13) and plasma activated coal combustion (Fig. 14). The figures visually demonstrate the difference between the temperature fields for the two modes of coal combustion. When the coal combustion is in conventional

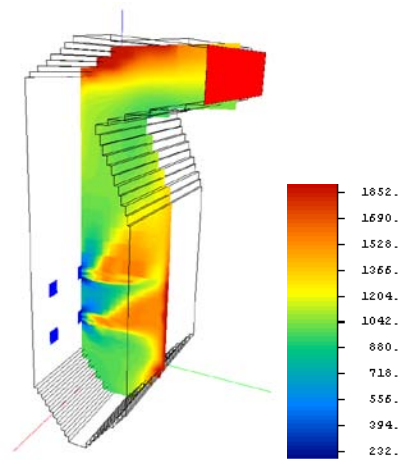


Fig. 13. Temperature field (°C) along the furnace height in the mean cross-sectional plane of the furnace when it works in conventional mode of coal combustion

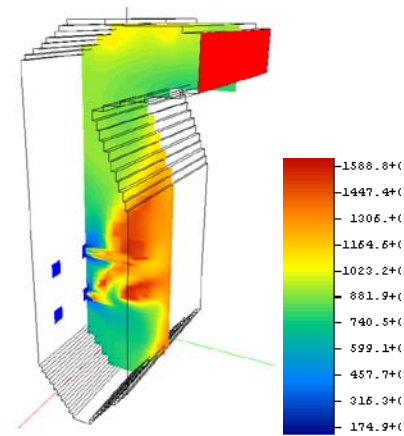


Fig. 14. Temperature field (°C) along the furnace height in the mean cross-sectional plane of the furnace when it works in plasma-assisted mode of coal combustion using 3 PFS

mode, six symmetric pulverized coal flames are formed. Maximum temperature of these flames is 1852°C. In Fig. 14 one can see influence of PFS on to the shape of the ETCPF flame and its maximal temperature. In the presented plane PFS is upwardly. High temperature body of the flame is moved closer to the PFS exit and upper in the furnace. Its maximal temperature is 1588°C.

Averaged temperature curves (Fig. 15) have their maxima. The first one ($H = 3$ m) is generated by overheating of the furnace back wall by the pulverized fuel flame. The second maximum is above level of the burners of the upper layer due to common forming of the flame body and observed moving as a result of natural convection. Averaged temperatures in the furnace operated in conventional mode are higher one for the furnace operated in plasma assisted regime using PFS. The difference achieves 350 degrees at the furnace exit. The reason of this is more intensive radiation of coal particles which have higher concentration and total reacting surface when the furnace operates in conventional mode in comparison with plasma assisted coal combustion. When PFS operates two component fuel of combustible gas and particles of coke

residue enters the furnace. Mass of this fuel does not exceed 30 % of the initial coal mass. That decreases total surface of the radiative particles.

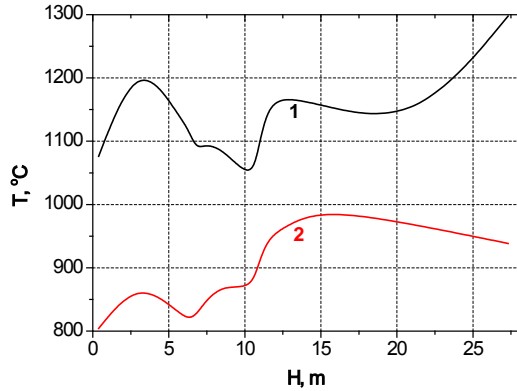


Fig. 15. Temperature (T) along the furnace height (H): 1) conventional incineration of coal, 2) incineration of coal when 3 PFS operate

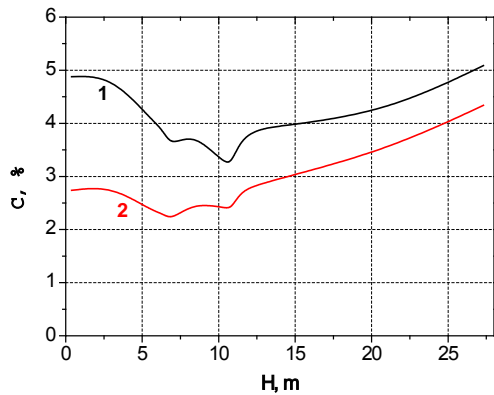


Fig. 16. Mean concentration of unburned carbon (C) along the furnace height: 1) conventional incineration of coal, 2) incineration of coal when 3 PFS operate

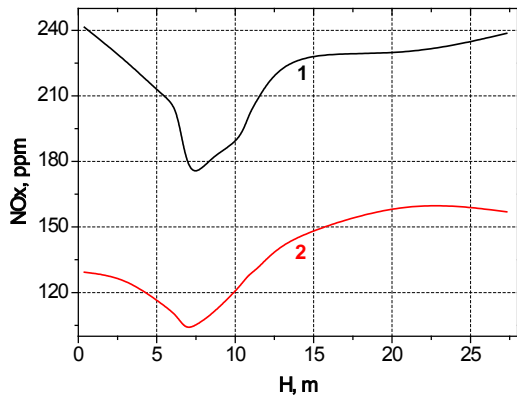


Fig. 17. NO_x mean concentration along the furnace height: 1) conventional incineration of coal, 2) incineration of coal when 3 PFS operate

At the furnace exit when three PFS operate concentration of unburned carbon (Fig. 16) is 16 % less one when the furnace works in traditional mode of coal combustion. Use of PFS improves ecological characteristics of the process of solid fuel combustion. Fig. 17 demonstrates more than 33 % decrease of nitrogen oxides concentration. Evidently decrease of unburned carbon and NO_x concentrations at the furnace exit improves ecology-economic indexes of TPP.

V. CONCLUSION

Simulation and testing of PFS at existing coal-fired boilers of TPP confirmed the technical feasibility, environmental and energy efficiency of fuel oil free boilers start-up and pulverized coal flame stabilization using PFS.

PFS tests at the boilers BKZ-160 and BKZ-420 of Almaty Power System in the mode of the boilers start-up from cold confirmed possibility of high ash Ekibastuz coal ignition.

Inculcation of PFS gives economical effect, which depends on coal/fuel oil price ratio (Table III). Pay back period varies from 12 to 18 months. Economical effect for TPP of Kazakhstan is 400 mln. of US dollars a year.

Table 3. Economical comparison of the PFS technology with traditional one

Conventional technology	Plasma technology
1. Fuel Oil Rate for Russian TPP	
5.1 mln. t/year (cost is more than \$ 2 billion)	0
2. Fuel Oil Rate for Kazakhstan TPP	
~1 mln. t/year (cost is about \$ 400 mln.)	0
3. Investments for TPP	
100%	3-5%
4. Operating costs	
100%	28-30%
5. Electric power consumption for TPP auxiliary	
3-5%	0.5-1.0%

REFERENCES

- [1] Sakipov, Z.B.; Messerle, V.E.; Ibraev, Sh.Sh., Electrothermochemical preparation of coal to burning. (in Russian). Almaty: "Nauka", 1993, 259 p. (in Russian)
- [2] Messerle, V.E.; Ustimenko, A.B., Plasma ignition and combustion of solid fuel. (Scientific-and-technological basics). (in Russian). Saarbrucken, Germany: Palmarium Academic Publishing (ISBN: 978-3-8473-9845-5), 2012, 404 p. Available: <http://ljubljuknigi.ru/>
- [3] Gorokhovski, M.A.; Jankoski, Z.; Lockwood, F.C.; Karpenko, E.I.; Messerle, V.E.; Ustimenko, A.B., Enhancement of Pulverized Coal

- Combustion by Plasma Technology. *Combustion Science and Technology*, 179 (10), 2007, 2065–2090.
- [4] Karpenko, E.I.; Messerle, V.E.; Ustimenko, A.B., Plasma-aided solid fuel combustion. *Proceedings of the Combustion Institute*. Elsevier. 31 (part II), 2007, 3353-3360.
 - [5] Karpenko, E. I.; Karpenko, Yu. E.; Messerle, V. E.; Ustimenko, A. B., Using Plasma-Fuel Systems at Eurasian Coal-Fired Thermal Power Stations. *Thermal Engineering*. 56, N 6, 2009, 456-461.
 - [6] Askarova, A.S.; Karpenko, E.I.; Lavrishcheva, Y.I.; Messerle, V.E.; Ustimenko, A.B., Plasma-Supported Coal Combustion in Boiler Furnace. *IEEE Trans. Plasma Sci.* 35 (6), 2007, 1607–1616.
 - [7] Kalinenko, R.A.; Kuznetsov, A.P.; Levitsky, A.A.; Messerle, V.E.; Mirokhin, Yu.A.; Polak, L.S.; Sakipov, Z.B.; Ustimenko, A.B., Pulverized Coal Plasma Gasification, *Plasma Chemistry & Plasma Processing*. 13 (1), 1993, 141-167.
 - [8] Gorokhovski, M.; Karpenko, E.I.; Lockwood, F.C.; Messerle, V.E.; Trusov, B.G.; Ustimenko, A.B., Plasma Technologies for Solid Fuels: Experiment and Theory. *Journal of the Energy Institute*. 78 (4), 2005, 157-171.
 - [9] Jankoski, Z.; Lockwood, F.C.; Messerle, V.E.; Karpenko, E.I.; Ustimenko, A.B., Modelling of Plasma Pre-Treatment of Powdered Coal for Combustion. *Thermophysics and Aeromechanics*. 11, (3), 2004, 461-474.
 - [10] Lockwood, F.C.; Salooja, A.P.; Syed, A.A., A prediction method for coal-fired furnaces. *Combustion and Flame*. 38, (1), 1980, 1-15.
 - [11] Lockwood, F.C.; Mahmud, T.; Yehia, M.A., Simulation of pulverised coal test furnace performance. *Fuel*. 77, (12), 1998, 1329.
 - [12] Lockwood, F.C.; Mahmud, T., The Prediction of Swirl Burner Pulverised Coal Flames. *Twenty-Second Symposium (International) on Combustion*, Pittsburgh, PA: The Combustion Institute. 1988, 165.
 - [13] Lockwood, F.C.; Shan, N.G., Evaluation of an efficient radiation flux model for furnace prediction procedures. *Proc. Sixth Intern. Heat Transfer Conference*. 1978, 1405-1413.
 - [14] Lockwood, F.C.; Shan, N.G., A new radiation solution method for incorporation in general combustion prediction procedures. *Proc. 18th Intern. Symp. On Combustion*. Pittsburg, PA: The Combustion Institute. 1981, 1405-1413.
 - [15] Launder, B.E.; Spalding, D.B., The numerical computation of turbulent flows. *Comput. Meth in Appl. Mech. and Eng.* 3 (2), 1974, 269-289.
 - [16] Messerle, V.E.; Karpenko, E.I.; Ustimenko, A.B.; Lavrichshev, O.A., Plasma preparation of coal to combustion in power boilers. *Fuel Processing Technology*. 107, 2013, 93–98.

Research Department of Plasmotechnics (Kazakhstan) as CEO and since 2002 he is a leading staff scientist and head of thermal physics department of Research Institute of Experimental and Theoretical Physics of al-Farabi Kazakh National University.

Oleg A. Lavrichshev was born on August 5, 1956, in Azerbaijan. He graduated from Kazakh State University, Physical department in 1979. He has Candidate Degree on physical and mathematical sciences (equivalent to Ph.D.), topic of the Thesis is "Heat-mass exchange in circular wall boundary streams", Moscow, 1987. From 1979 he is with the Kazakh National University. Since 2000 he is a leading staff scientist and since 2006 he is director of Research Institute of Experimental and Theoretical Physics of al-Farabi Kazakh National University.

Vladimir E. Messerle was born on June 10, 1947 in Alma-Ata, Kazakhstan. In 1970 he graduated from Physical department of Kazakh State University. He has Candidate Degree on physical and mathematical sciences (equivalent to Ph.D.), Moscow, 1979, Doctor Degree on technical sciences, Moscow, 1991, Professor, Moscow, 1997, academician of International Energy Academy, Moscow, 1997, academician of International Informatization Academy, Moscow, 2003. He is Professor of the Chair "Thermal Power Plants" of East-Siberian State Technological University, Ulan-Ude, 1998, and Professor of the Chair of Thermal Physics and Technical Physics of the Physicotechnical Department of Kazakh National University after al-Farabi, 2002. He is a head of the laboratory of Plasma Chemistry of the Combustion Problems Institute, 2001, and leading staff scientist of Institute of Thermophysics of Russian Academy of Science, Novosibirsk, Russia. Vladimir Messerle is the main author of the technology of electrothermochemical preparation of the solid fuel for burning. Under the direction of Professor Messerle 13 Ph.D. theses and 2 doctoral theses were prepared and defended. From 2011 he is co-chairman of National Scientific Council of the Republic of Kazakhstan on «Energetics».

Alexander B. Ustimenko was born on August 24, 1962, in Alma-Ata, Kazakhstan. He graduated from Kazakh State University, Physical department in 1984. He has Candidate Degree on physical and mathematical sciences (equivalent to Ph.D.), topic of the Thesis is "High-temperature heating and gasification of coal particles", Moscow, 1991, Doctor Degree on technical sciences, topic of the Thesis is "Plasma-fuel systems for fuel utilization efficiency increase" Moscow, 2012. From 1984 to 2001 he was a researcher of the Kazakh Scientific-Research Institute of Energetics. From 2001 to 2007 he was a leading staff scientist of Combustion Problems Institute at al-Farabi Kazakh National University. Since 1991 he is with

A novel STATCOM wide area feedback controller for improving stability in multimachine system

Aman Ganesh, Ratna Dahiya and G. K. Singh

Abstract—The paper presents a hybrid scheme to enhance the stability of the multimachine power system. The voltage regulation and the angular stability of the power system are improved with the help of STATCOM. A novel robust regulator for the STATCOM with a wide area multi frequency band supplementary controller is used to improve the voltage profile of the power network and to damp the inter area low frequency oscillation. The selection of the wide area control signals is done by using eigenvalue sensitivity expressed in terms of participation factor. The effectiveness of the proposed scheme is tested on IEEE 12 bus benchmark system to cover a wider range of operating conditions. The simulation results show that the proposed scheme stabilizes the system at multiple operating points.

Keywords— STATCOM, Robust Control, Voltage Regulation, Low Frequency Oscillation

I. INTRODUCTION

DU E to economical, geographical and environmental reasons, the transmission and generation networks of the power system are being operated close to their safety limit. This in turn weakens the system against transient and dynamic disturbances. The static synchronous compensator (STATCOM) under steady state condition can control the voltage and the reactive power exchange with the network at the point of common coupling (PCC) and is also capable of improving the damping of power system during dynamic and transient disturbances. Many control schemes have been reported in literature for improving the regulation property of the STATCOM in terms of voltage and power under different applications with the use of PI controller as regulator for ac system voltage, the dc voltage and the current regulators [1-7] under dynamic conditions of fault and loading. A typical double loop PI control strategy using fixed gain was employed for regulating the voltage at the PCC. Due to fault or switching there is change in system matrix and eigenvalue; also the controller can give uncertain

or indefinite results, if the integrator of the controller saturates in presence of the control error which becomes too large under the condition of sudden changes in load, power system configuration. To have the satisfactory dynamic response, some non linear techniques using ANN and fuzzy logic have been forwarded for adapting the PI controller gain of the STATCOM during dynamic disturbances [8-11].

The main contribution of the reported work is in highlighting a novel PI regulator scheme which have the advantage of being inexpensive, robust and provides better reactive power support in comparison to conventional STATCOM PI regulator while performing its main task of voltage regulation and it does not involve the use of intelligent or non linear control technique which requires the rule base or the training which is a tedious and expensive method of implementation.

Change in power system operating conditions and dynamic disturbances such as loss of line, occurrence of fault and load change can trigger oscillations in power systems which are due to relative angular motion between the rotors of synchronous machines. Under certain operating conditions, the oscillations may be poorly damped or unstable. In order to improve the angular stability methods such as fast acting excitation system and use of power system stabilizer (PSS) are prevalent. PSS are generally tuned for narrow operative range to provide damping torque component used for controlling generator excitation to damp the oscillations. In multimachine system each machine is generally equipped with such exciters and PSS to damp the local mode of oscillation. STATCOM besides regulating the voltage and the power flow at the point of common coupling to the grid can also be used to damp these oscillations. However the angular stability controllability depends upon the location of the device i.e. STATCOM in the grid and the quantity viz. bus voltage or angle, line current, line active or reactive power to be controlled. In literature one can find the use of supplementary controllers for the STATCOM linear and non linear, intelligent and optimized controllers are used for damping the oscillations [12-17]. Earlier paper used the local signals as the input to the auxiliary or the supplementary controller but wide area signals can also be used to damp the inert area oscillations but in this paper both the local and global feedback signals are used as the input to the proposed supplementary controller and its output is used as the stabilization signals to the STATCOM line voltage controller for damping out the low frequency oscillations.

Aman Ganesh is with MMU, Mullana, India and is pursuing his Ph.D from National Institute of Technology Kurukshetra, India. (phone: +91-9671251070, e-mail: raman_ganesh@rediffmail.com).

Ratna Dahiya did her Ph. D from NIT Kurukshetra. Presently she is serving as Professor in the Department of Electrical Engineering at NIT Kurukshetra. Her interest area includes electrical machines, Power systems, Electric Drives, Power Electronics & FACTS

G. K. Singh received the Ph. D degree from BHU, Varanasi, India. Presently he is a Professor in the electrical Engineering Department, IIT Roorkee, India. He has been involved in design and analysis of electrical machines, in particular, high-phase-order ac machines, and has coordinated a number of research projects sponsored by the CSIR and UGC, Government of India. He received the Pt. Madan Mohan Malaviya Memorial Medal and the Certificate of Merit Award 2001–2002 of The Institution of Engineers (India).

II. STATCOM STRUCTURE

Usually a STATCOM is installed to support power system networks that have a poor power factor and often poor voltage regulation. It controls the line voltage at the point of common connection to the electric power network by generating or absorbing reactive power at a faster rate. It is based on a power electronics voltage-source converter. The nonlinear STATCOM equation of the VSC based STATCOM described in d-q reference frame [18] are given by (1) and (2)

$$\begin{bmatrix} V_d \\ V_q \end{bmatrix} = \begin{bmatrix} R & -\omega L \\ \omega L & R \end{bmatrix} \begin{bmatrix} i_d \\ i_q \end{bmatrix} + L \begin{bmatrix} \frac{di_d}{dt} \\ \frac{di_q}{dt} \end{bmatrix} + \begin{bmatrix} V \\ 0 \end{bmatrix} \quad (1)$$

$$C \frac{dV_{dc}}{dt} = \frac{3}{2} (S_d i_d + S_q i_q) \quad (2)$$

where V_d and V_q are the VSC side voltage i_d and i_q are injected STATCOM currents, C is the equivalent capacitance of the dc bus capacitors, V_{dc} is the voltage across the DC capacitor, R and L represent the coupling transformer resistance and inductance, ω : synchronous angular speed of the network voltage at the fundamental system frequency f and V represents the grid side voltage.

In order to determine the power exchange between the STATCOM and the power system the frequency control and the voltage control has to be exercised. The frequency control is achieved by modulating the active (id) and reactive output current (iq) while the voltage control is done by generating the voltage reference signal V_r by controlling iq which is varied in accordance to the frequency deviation which directly represents the power oscillation of the power system. The frequency signal is derived from the positive sequence components of the ac voltage vector measured at the PCC of the STATCOM, through a phase locked loop. The actual power exchange is done by tracking the reference values V_r^* or in actual i_q^* and this is achieved by injecting the voltage in phase with the line voltage at PCC. This synchronization is done with the help of PWM based switching of VSC module for which the voltage v_{dq}^* generates the modulation index and phase.

A. Transfer Function of Voltage Source Converter of the STATCOM and Current Controller

Considering the multiple input multiple output system described by (1) two identical single input single output system for d and q axis transfer function is derived and is given by (3)

$$\frac{i_d(s)}{v_d(s)} = \frac{1}{(R + sL)} \quad (3)$$

For the obtained plant transfer function a first order PI controller is sufficient so that the closed transfer function of the plant and the PI controller together depicts a low pass filter with bandwidth α and time constant τ . The desired PI obtained is represented in (4)

$$G_i(s) = k_p + \frac{K_i}{s} \quad (4)$$

The mapped controller parameters are $k_p = \alpha L$ and $k_i = \alpha R$.

From (3) and (4) it is clear that the VSC transfer function is based on the impedance seen by the VSC to the grid side. So the controller is also mapped on the same basis. For proper synchronization the impedance too has to be

represented in synchronous frame too. If y^s is a general space vector with $\theta = \omega t$, its transformation in synchronous coordinates is

$$y_{dq} = y^s e^{-j\theta} \quad (5)$$

The time derivative of (5) is transformed as (notations, derivative operation $p = d/dt$)

$$\frac{dy^s}{dt} = \frac{d(e^{j\theta} y_{dq})}{dt} = e^{j\theta} (p + j\omega) y_{dq} \quad (6)$$

In the Laplace domain, the following substitution is made as $s \rightarrow s + j\omega$. This implies that the complex impedance of an inductor in synchronous coordinates is represented as

$$Z(s) = (s + j\omega)L \quad (7)$$

So the modified identical d-axis (as is q-axis) transfer function in reference to (3) obtained is

$$\frac{id(s)}{vd(s)} = \frac{1}{(R + sL + j\omega L)} \quad (8)$$

Now the aim is to find the synchronous coordinate equation for this (1) has to be modified

(notations, $\underline{x} = x_{dq} = xd + jxq$, $\underline{E} = v_{dq}$, $\underline{v} = v_{indq}$)

$$L \frac{di}{dt} = \underline{E} - (R + j\omega L) \underline{i} - \underline{v} \quad (9)$$

And the system transfer function $\underline{G}(s)$ is given by

$$\underline{G}(s) = \frac{\underline{i}}{\underline{v}} = -\frac{1}{R + sL + j\omega L} \quad (10)$$

Cross coupling is initiated by the term $j\omega Li$ (since multiplication by j maps the d axis on q axis and vice versa).

With the accurate estimation of L this can be achieved. \bar{L} is estimated for L . For high performance and accuracy current tracking we need to cancel this cross coupling. Selecting \underline{v} as (9) and estimating the value of \underline{E} as \bar{E} we have

$$\underline{v} = -\underline{v}' + \bar{E} - j\omega \bar{L} \underline{i} \quad (11)$$

If $\bar{L} = L$ and $\bar{E} = E$, then

$$\underline{i} = \frac{\underline{v}'}{R + sL} \quad (12)$$

The decoupled system transfer function obtained is

$$\underline{G}'(s) = \frac{\underline{i}}{\underline{v}'} = \frac{1}{R + sL} \quad (13)$$

B. Decoupled Current Control

To establish the decoupled current control consider (9) as reference and continuing with it. We define \underline{I} , complex

integrator state variable as $\frac{dI}{dt} = \varepsilon$, we have

$$\underline{v} = (\bar{E}_d + j\bar{E}_q) - k_p(\varepsilon_d + j\varepsilon_q) - ki(I_d + jI_q) - j\omega \bar{L}(i_d + ji_q) \quad (14)$$

The reference voltage is then computed by writing the real and the imaginary part

$$v_d^* = \bar{E}_d - k_p \varepsilon_d - k_i i_d + \omega \bar{L} i_q \quad (15)$$

$$v_q^* = \bar{E}_q - k_p \varepsilon_q - k_i i_q + \omega \bar{L} i_d \quad (16)$$

where i_d and i_q determines the active and reactive power flows.

C. Proposed Robust Control Scheme

For large step variation of the d-current, the controller might demand a too large voltage. Considering v as the reference voltage, the PI controller output is expressed as

$$v(t) = k_p \varepsilon(t) + k_i \int \varepsilon(t) dt, \text{ where } \frac{dI}{dt} = \varepsilon \quad (17)$$

The difficulty arises once v becomes limited. In order to avoid this, the integrator part I should not be updated with too large error ε . For this the integrator is fed with another error $\bar{\varepsilon}$, so that $v = \bar{v}$.

$$\bar{v}(t) = k_p \bar{\varepsilon}(t) + k_i \int \bar{\varepsilon}(t) dt \quad (18)$$

Then by writing the difference $\bar{v} - v$ the error is

$$\bar{\varepsilon} = \varepsilon + \frac{\bar{v} - v}{k_p} \quad (19)$$

For the decoupled controller (15) and (16) can be expressed as

$$v_{dq}^* = \bar{E}_{dq} - k_p \varepsilon_{dq} - k_i \int \varepsilon_{dq} dt + \omega \bar{L}i_d + \omega \bar{L}i_q \quad (20)$$

The value of v_{dq}^* after some saturation is expressed as

$$v_{dq}^* = \bar{E}_{dq} - k_p \bar{\varepsilon}_{dq} - k_i \int \bar{\varepsilon}_{dq} dt + \omega \bar{L}i_d + \omega \bar{L}i_q \quad (21)$$

By writing the difference $v_{dq}^* - \bar{v}$ the error fed to the controller is

$$\bar{\varepsilon}_{dq} = \varepsilon_{dq} + \frac{v_{dq}^* - \bar{v}}{k_p} \quad (22)$$

The advantage of using this robust signal is that it continuously updates the new reference value of voltage and hence the control scheme efficiently generates the new reference value for the active and the reactive component of current (i_d and i_q) which is aimed to achieve better power flow or in turn result in better voltage regulation. The validation of the proposed scheme is done on IEEE 12 bus system shown in fig. 1.

The system considered is a standard IEEE 12 bus benchmark power system. After completing load flow study for the selected network bus 4 has the lowest bus voltage of 0.95 p.u. The STATCOM is connected to bus 4 for the purpose of improving the voltage stability and to control the voltage and the active reactive power flow during the dynamic disturbances..

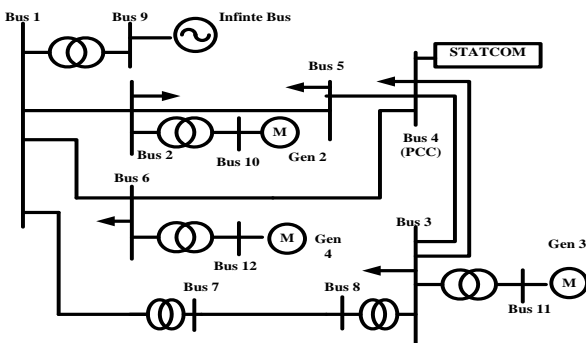


Fig. 1 IEEE 12 bus benchmark system

III. INTER AREA LOW FREQUENCY OSCILLATION DAMPING

A multimachine power system is characterized with low frequency oscillations owing to the presence of group of

generators because of which interplant/local mode of oscillation and interarea mode of oscillations can be present. To overcome the local mode of oscillations the synchronous machine are provided with fast exciters and locally tuned PSS. But they fail to damp the interarea oscillations. Although STATCOM is already installed in the selected power system to improve the voltage profile which is its primary objective but the same can be used to damp the present interarea low frequency oscillations.

A. Signal Selection

For the purpose of stabilizing the oscillations any of the available measured signals such as frequency and speed deviations of the generators, bus voltage, bus angle, line current, line active, and reactive power can be used as feedback signal. But in this paper both the speed deviation has been taken as input signal to the controller which helps in generating a new voltage reference control signal. There speed signals can be treated as feedback signal which forms the input of the proposed controller.

A simplified linearized method, dependent on the operating condition of the power system, is applied for introducing auxiliary signals to the STATCOM controller for improving the transient and dynamic behavior of the power system, by controlling the network parameters in its neighborhood. The state space representation of the power system can be expressed as

$$\begin{aligned} \dot{\Delta x}(t) &= A\Delta x(t) + B\Delta u(t) \\ \Delta y(t) &= C\Delta x(t) + D\Delta u(t) \end{aligned} \quad (23)$$

where $\Delta x(t)$ and $\Delta y(t)$ are the state and output vector of dimension n and m respectively, A is the state matrix of dimension $n \times n$. The method of modal analysis of the given power system is conventionally done to find out the dominant machine of each area. The right eigenvector gives the system mod of oscillation. The participation factor helps to relate the participation of the respective state variable to the selected mode or in other words it relates the left and the right eigenvectors for identifying the relationship between the states and the modes. For any given eigenvalue λ_i of the state matrix A , assume ϕ_i and ψ_i to be the left and the right eigenvectors respectively. Then the participation factor p_k , for the k th element is defined as

$$p_{ki} = \phi_{ki} \psi_{ik} \quad (24)$$

The eigenvalue analysis of the system shows that there are three modes of oscillations oscillating at different frequency owing to the presence of three synchronous generators. as shown in table 1. The participation of the generator speed deviations ($\Delta\omega_2, \Delta\omega_3, \Delta\omega_4$) and in the three oscillating modes is also shown in table 1.

Table 1 Critical mode of oscillation of IEEE 12 bus System

System modes	Damping (%)	Frequency (Hz)	Participation Factor		
			ω_2	ω_3	ω_4
-0.19 ± 4.982	3.81	0.792	0.459	0.0002	0.0021
$-0.318 \pm j7.436$	4.27	1.183	0.0049	0.426	0.0451
$-0.143 \pm j4.449$	3.21	0.708	0.016	0.0978	0.311

It is clear that the participation of $\Delta\omega_3$ and $\Delta\omega_4$ in first

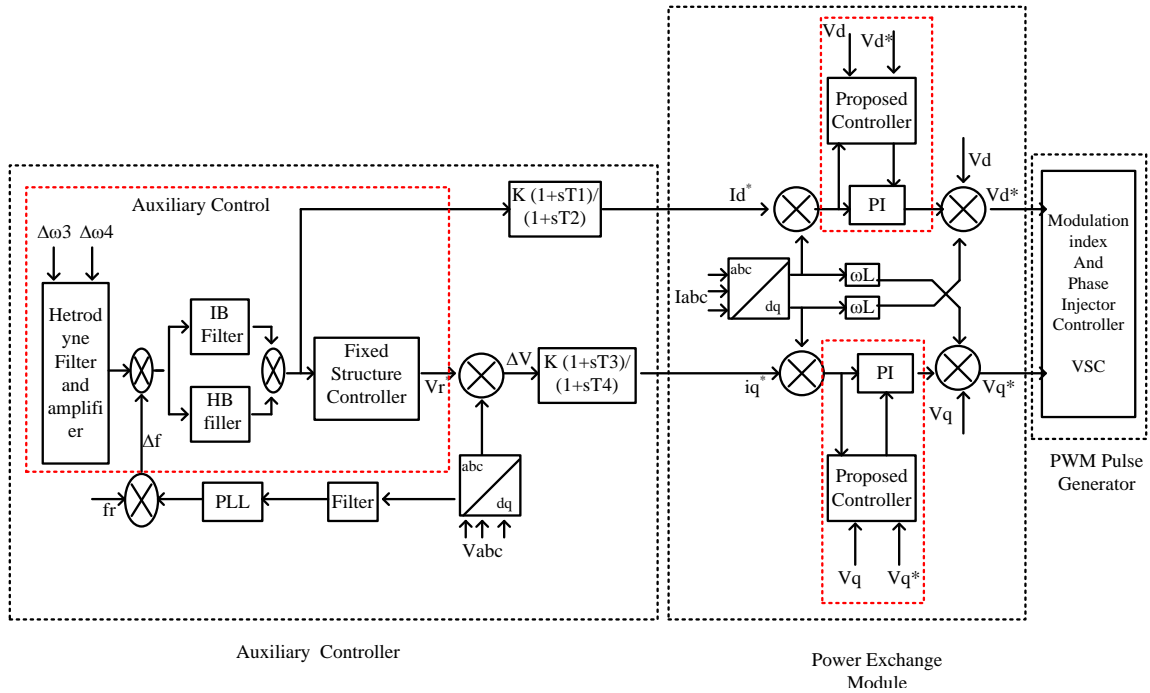


Figure 2: Complete proposed control Scheme

mode oscillating at frequency 0.792 Hz is low. While the participation of $\Delta\omega_2$ in other two modes oscillating at the frequency of 1.183 Hz and 0.708 Hz respectively is relatively low in comparison to $\Delta\omega_3$ and $\Delta\omega_4$.

It can be attributed that generator 2 considerably being in the vicinity of the infinite bus has sufficient damping whereas damping is required for the other modes. For this $\Delta\omega_3$ and $\Delta\omega_4$ are selected as input for the supplementary controller for damping these local mode oscillations.

B. Supplementary Controller Design for Damping Low Frequency Oscillation

The external controller is supplemented to first level control helps in generating a new voltage reference control signal V_r^* proportional to the generator speed deviations (of generators 3 and 4). This added signal causes the i_q , to vary around the operating point defined by V_r^* , to damp the power oscillations. The voltage at PCC is forced to decrease/increase when the frequency deviation Δf is positive/negative aiming at reducing/increasing the transmitted power thus providing reserve that opposes the deceleration/acceleration of the generator in power system. The fixed structure controllers are designed for the desired gain and phase characteristics of the frequency stabilizer for the case of modulating the output current i_q . The power system oscillations are damped out by rapidly exchanging active power with the utility system i.e. by controlling the output direct current i_d . Thus the reference of the STATCOM output current, i_d^* , is directly derived from Δf . For this a band pass filter is used where tuning of the intermediate band filter is done at 0.7 Hz and high pass filter is tuned at 7 Hz which provides zero gain at high frequency and phase leading up to the resonant frequency. The resulting compensator controllers are combined to obtain frequency stabilizer with an adequate phase characteristic for all small frequency deviation modes. The resulting

stabilizer signal is then passed through a final limiter for setting the reference i_d^* . The complete proposed control scheme is shown in fig.2. The frequency response of the proposed multiband tuned filter structure is shown in fig. 3

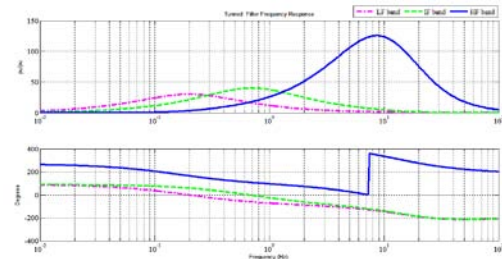


Fig. 3 Frequency response of tuned filter structure

IV. RESULTS AND DISCUSSION

The system considered is a standard IEEE 12 bus benchmark power system. The selected power system is divided into three areas. (a) Area 1 which consist of generator 2 and buses 1,2,7,9 and 10. (b) Area 2 consist of generator 3 and bus 3,4,5,8 and 11 and (c) Area 3 consist of generator 4 and buses 6 and 12 basically it connects the area 1 and area 2. Simulations for the Load flow and dynamic stability studies for the selected power system were carried out in PSAT toolbox in MatLab and it was observed that area 2 is the weakest and needs voltage support at buses 4 and 5. So shunt compensation in form of STATCOM is applied at bus 4 which considerably improves the voltage level, as suggested by the simulation results

A. Transient Stability Test

A general 3phase to ground fault is applied to the middle of the parallel transmission lines connecting the STATCOM to the generator at $t=0.4s$ for 100 ms (6 cycles) and the bus

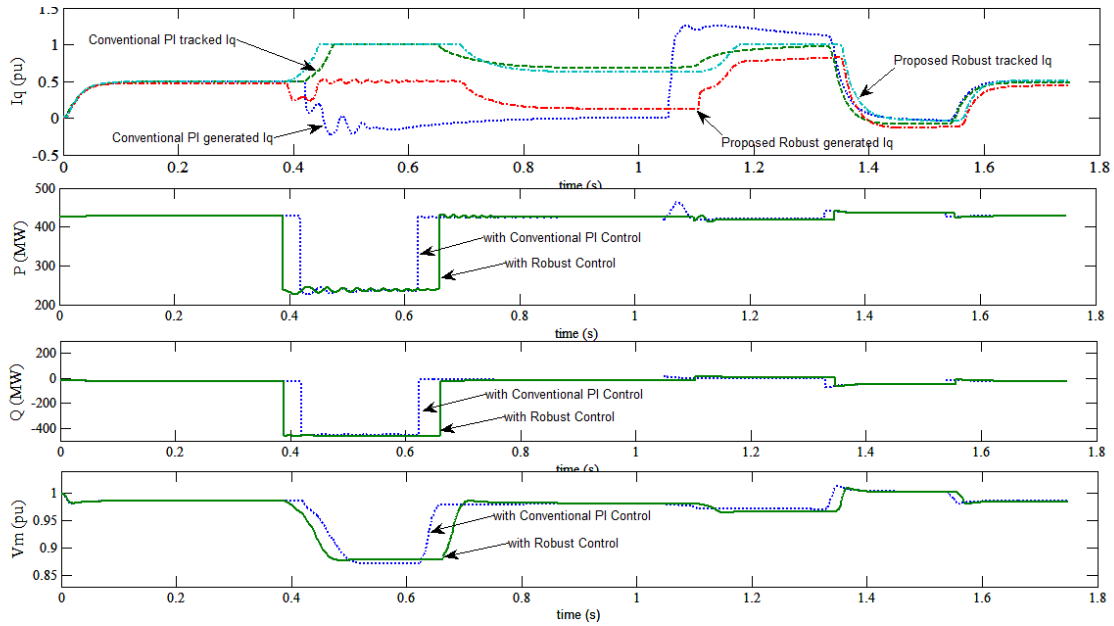


Figure 4 Case-I (a) reference current tracking (b) active power oscillation (c) injected reactive power (d) voltage at PCC

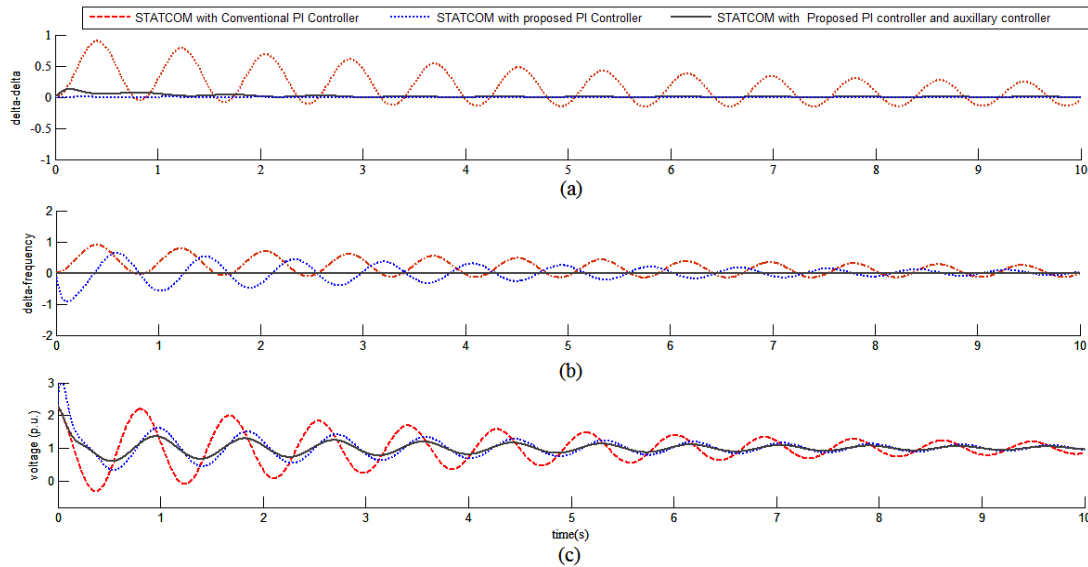


Figure 5: case-I (a) rotor angle variation (b) frequency (c) voltage profile

is loaded with switch capacitive and inductive load from $t=1.15$ to 1.55 with a span switching of point twenty. The STATCOM operates in the reactive current reference control mode. Figure 4(a), shows the reactive current tracking. The good performance of the voltage regulation at the PCC of the STATCOM is evidently depicted, fig. 4(d), by the compensators ability to inject or withdraw reactive power, fig 4(c), into the network in response to the active oscillation in active power viz. load angle fig 4(b). During the time when the transmission line active power (load angle) is increasing, reactive power injection into the network causes an increase in PCC voltage which opposes the change in active power. The power compensation depends upon the severity of the fault and loading conditions.

B. Dynamic response of the controller for power oscillation damping

1) Case I

The performance of the proposed auxiliary controller is discussed under the condition of three phase short circuit at bus 3-4 for 100 ms after this the line is reconnected . This causes electromechanical oscillations of the generator which have effect on the rest of the electric system. To maintain the system stability these oscillations have to be damped out by the proposed control scheme. The results are shown in fig.5

2) Case-II

The operating condition of the selected power system is changed by changing the active power of generator 3 and 4. After reaching the steady state condition fault is applied at bus-4. The obtained simulation results are shown in fig 6.

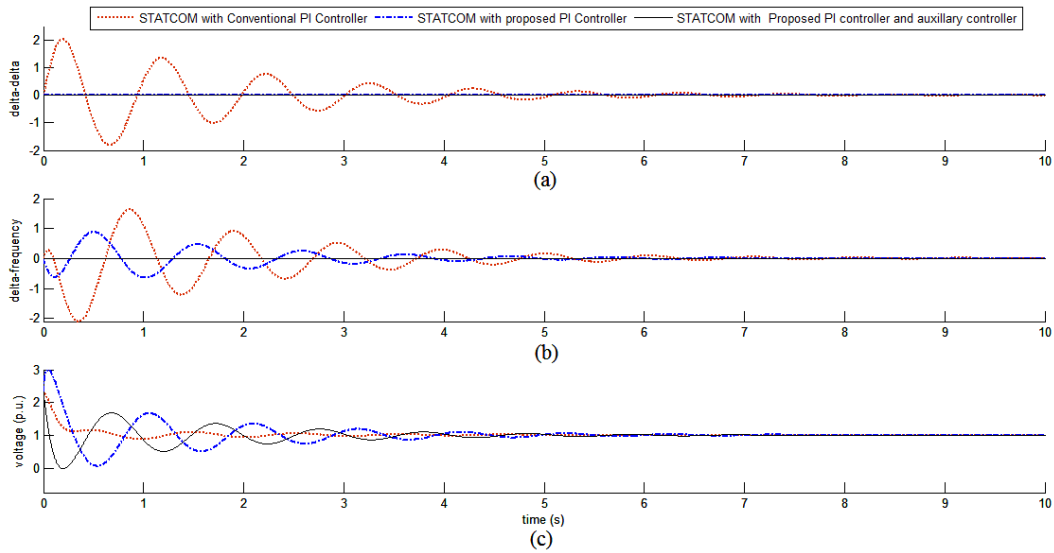


Figure 6: case-II Change in active power (a) rotor angle variation (b) frequency (c) voltage profile

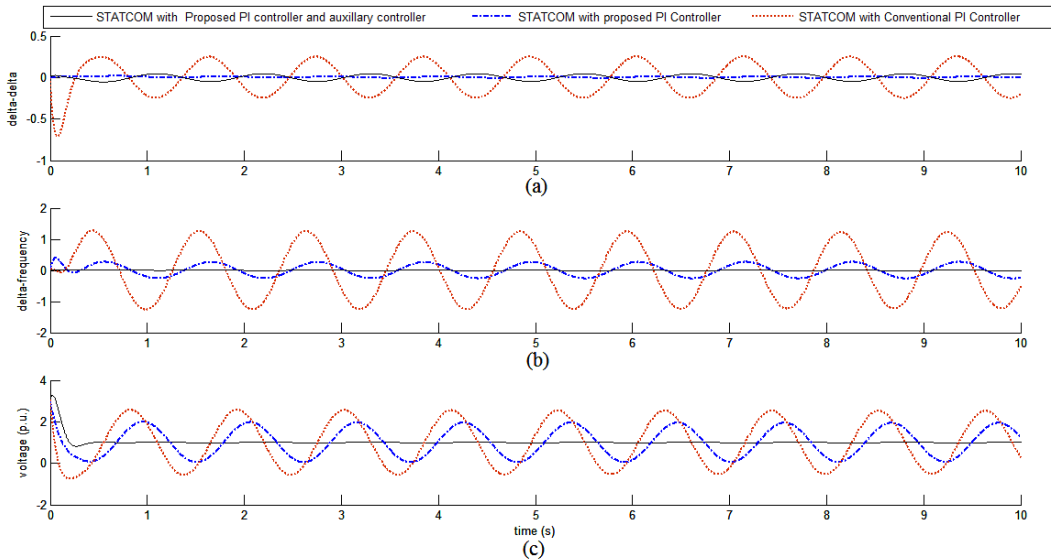


Figure 7 case-III Loss of line (a) rotor angle variation (b) frequency (c) voltage profile

3) Case-III

The STATCOM at bus 4 loses impact if the transmission line 4-6 is disconnected the effect is more severe the result is shown in fig. 6

V.CONCLUSION

This paper presented the stability enhancement ability of the STATCOM connected to a multimachine system. The mathematical model of PI regulator is developed to provide reactive power support during various operating conditions. An auxiliary controller in addition to STATCOM line voltage controller is also proposed which efficiently damps out the low frequency oscillations and provides improved performance as compared to conventional STATCOM scheme using fixed structure controller. The wide area signal selection for the auxiliary controller was done on the basis of eigenvalue sensitivity expressed in terms of participation factor of the network parameter.

REFERENCES

- [1] Keyou Wang and Mariesa L. Crow, "power system voltage regulation via STATCOM internal nonlinear control" *IEEE Trans. Power Sys.*, vol. 26, no. 3pp. 1252-1262, Aug. 2011
- [2] Y. Han, Y.O. Lee and C.C. Chung, "Modified non-linear damping of internal dynamics via feedback linearisation for Static Synchronous Compensator" *IET Gener. Transm. Distrib.*, vol. 5, iss. 9, pp. 930-940., 2011
- [3] W.-L. Chen, Z.-C. Li and C.-Z. Xie, "Control of static synchronous compensator with supplementary damping enhancement for wind farm voltage regulation" *IET Gener. Transm. Distrib.*, vol. 5, iss. 12, pp. 1211-1220, 2011.
- [4] H. Zhou, G. Yang, J. Wang and H. Geng, "Control of a hybrid high-voltage DC connection for large doubly fed induction generator-based wind farms" *IET Renew. Power Gener.*, vol. 5, Iss. 1, pp. 36-47, 2011.
- [5] Vitaly Spitsa, Abraham Alexandrovitz and Ezra Zeheb, "Design of a Robust State Feedback Controller for a STATCOM using a zero set concept" *IEEE Trans. Power Del.*, vol. 25, no. 1, pp. 456-467, Jan. 2010.
- [6] B. S. Chen and Y. Y. Hsu, "A minimal harmonic controller for a STATCOM," *IEEE Trans. Ind. Electron.*, vol. 55, no. 2, pp. 655-664, Feb. 2008.
- [7] B. S. Chen and Y. Y. Hsu, "An analytical approach to harmonic analysis and controller design of a STATCOM," *IEEE Trans. Power Del.*, vol. 22, no. 1, pp. 423-432, Jan. 2007.

- [8] S. Mohagheghi, Y. del Valle, G. K. Venayagamoorthy, and R. G. Harley, "A proportional-integral type adaptive critic design-based neuro controller for a static compensator in a multimachine power system," *IEEE Trans. Ind. Electron.*, vol. 54, no. 1, pp. 86–96, Feb. 2007.
- [9] V.K.Chandrakar and A.G. Kothari, "Comparision of RBFN and Fuzzy based STATCOM for Transient stability improvement" *International Aegean conference on electrical machines and Power Electronics*, pp. 520-525, Sept. 2007
- [10] S. Mohagheghi, G. K. Venayagamoorthy, and R. G. Harley, "Fully evolvable optimal neurofuzzy controller using adaptive critic designs," *IEEE Trans. Fuzzy Syst.*, vol. 16, no. 6, pp. 1450–1461, Dec. 2008.
- [11] S. Mohagheghi, R. G. Harley, and G. K. Venayagamoorthy, "An adaptive Mamdani fuzzy logic based controller for STATCOM in a multimachine power system," in Proc. ISAP, Nov. 2005, pp. 228–233. R. Cimbals, O. Krievs and L. Ribickis, "A Static Synchronous Compensator for Displacement Power Factor Correction under Distorted Mains Voltage Conditions" *Electronics and Electrical Engineering*. – Kaunas: Technologija, 2011. – No. 4(110). ,pp. 71-76.
- [12] Li Wang and Dinh-Nhon Truong, "Dynamic stability improvement of four parallel-operated PMSG-based offshore wind turbine generator fed to a power system using STATCOMs" *IEEE Trans. Power Del.*, vol. 28, no. 1, p p. 111-119, Jan. 2013
- [13] Li Wang and Chia-Tien Hsiung, "Dynamic stability improvement of an integrated grid-connected offshore wind farm" *IEEE Trans. Power Sys.*, vol. 26, no. 2, pp. 690-698, May 2011.
- [14] A. H. Norouzi and A. M. Sharaf, "Two control schemes to enhance the dynamic performance of the STATCOM and SSSC," *IEEE Trans. Power Del.*, vol. 20, no. 1, pp. 435–442, Jan. 2005.
- [15] N. Mithulananthan, C. A. Canizares, J. Reeve, and G. J. Rogers, "Comparison of PSS, SVC, and STATCOM controllers for damping power system oscillations," *IEEE Trans. Power Syst.*, vol. 18, no. 2, pp. 786–792, May 2003.
- [16] Ahmad Rohani, M. Reza Safari Tirtashi, and Reza Noroozian, "Combined Design of PSS and STATCOM Controllers for Power System Stability Enhancement" *Journal of Power Electronics*, Vol. 11, No. 5, pp. 734- 742 , Sept. 2011.
- [17] D Harikrishna, Kamal Narayan Sahu and N V Srikanth, "Power System Dynamic Stability Enhancement Using Fuzzy Controlled STATCOM" *Electrical and Electronic Engineering*, Vol. 1, No. 2, pp. 72-78, 2011.
- [18] Schauder and H. Mehta, "Vector analysis and control of advanced static VAR compensators," *Proc. Inst. Elect. Eng.—C*, vol. 140, no. 4, pp. 299– 306.1993.

Sliding mode Control of Chopper Connecting Wind Turbine with Grid based on synchronous generator

Ahmed TAHOUR¹, Abdel Ghani AISSAOUI², Mohamed ABID, Najib ESSOUNBOULI, Frederic NOLLET

Abstract: In this chapter we propose to design a robust control using sliding mode for chopper control of synchronous generator. The purpose is therefore to make the voltage and the current control resist to speed variations, because the variation of speed degrades the performance of the voltage produced to the networks. The use of the nonlinear sliding mode method provides very satisfactory performance for chopper control of synchronous generator, and the chattering effect is also eliminated by the function “sat”. Simulation results show that the implementation of the sliding mode controllers leads to robustness and dynamic performance satisfaction. Conclusions are summarized in the last section.

Keys words: synchrone generator, wind turbine, sliding mode control and voltage control.

I. INTRODUCTION

Global consumption of energy has increased in recent years because of massive industrialization which tends to grow more and more, specifically in certain geographic areas as Asian countries [1].

The risk of shortages of fossil fuels and their effects on climate change, indicate once again the importance of renewable energy. Following this awareness, economic development that takes care of the environment becomes absolutely necessary [2].

Several sources of renewable energy are object of advanced researches, which aim to develop techniques for extracting power with high reliability, lower cost and increase energy efficiency [2-3].

In this paper, we focus on the conversion of wind energy into electrical energy that has become competitive due to three main factors [4]:

- Wind energy is clean, renewable and naturally replenished by nature,
- The development of the wind turbine industry,
- The evolution of semiconductor technology, and new methodologies for control of variable speed turbines.

However, several problems, related in part to the complexity of wind conversion systems as the need for speed multiplier between the turbine and generator, and the instability of wind speed on the other hand [5].

The use of wind turbine structures with synchronous generator of high poles number make of wind conversion systems with variable speed more attractive than those with fixed speed, because of the possibility of extracting the optimal energy for different wind speed, reducing mechanical stresses by eliminating the multiplier which

improves system reliability, and reduce the maintenance costs [1, 6].

This paper deals with a variable-speed system consisting of synchronous generator, diode rectifier and thyristor inverter. The advantages of the synchronous generator and a diode rectifier are the high efficiency of the rectifier and the low price. There are two disadvantages that can be important in wind turbine generator systems. Motor start of the turbine is not possible without auxiliary equipment and the torque control is normally not faster. The aim of this report is to describe an efficient variable-speed system and to model the generator and converter losses [1].

In this context, the present study focuses on wind energy, which seems to be one of the most promising. The aim of this paper is to present a comprehensive model of a synchronous generator based on a proposed structure and control strategies to optimize power output, to regulate the DC bus voltage, and to control voltage transmitted to the network [1, 7].

To control the Wind Energy Conversion System (WECS) we need robust controller. Sliding Mode Control (SMC) is a nonlinear control technique derived from variable structure control system theory and developed by Vladimir UTKIN. Such control solution has several advantages such as simple implementation, robustness and good dynamical response. Moreover, such control complies with the nonlinear characteristic of the switch mode power supplies [4, 11, 12]. The organization of this chapter is as follow: in the first section, we establish the model of the turbine. The second section is devoted to modeling the synchronous machine with their equivalent electrical model. Global model of the chain of wind conversion device and associated controller are developed in an equivalent continuous model that takes into account relevant parts of the voltages at the generator, the DC bus and the network is started at third Section.

The last section is devoted to the simulation results. All models developed in this study are simulated by the Matlab-simulink.

II. WIND CONVERSION SYSTEM MODEL

The WECS described in this article includes the wind turbine, synchronous generator, a transformer, a diode rectifier, a filter and an inverter. In this system, the wind energy is transmitted through the turbine to the three-phase synchronous machine and generated in electrical form. This energy is transmitted directly through a transformer, a bridge rectifier and inverter to the electrical

¹ University of Mascara, 29000, Algeria

Corresponding author e-mail: tahourahmed@yahoo.fr

² IRECOM Laboratory, University of Sidi Bel Abbes, 22000, Algeria,

network (Figure 1). We consider in this study that the transformer is perfect. The main assumption in this simplified study is that the currents are sinusoidal and semiconductors are ideal [6-7]. Figure (1) shows the equivalent diagram of the WECS.

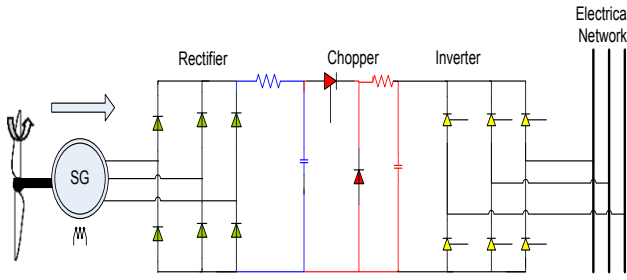


Fig.1. Wind electrical conversion system based on synchronous machine

A. Turbine Model

The turbine model is to present the power and the torque developed by the turbine, and which can be defined by the following equations [2-3, 8]:

$$P_m = \frac{1}{2} \rho \pi R^2 v^3 C_p(\lambda) \quad (1)$$

$$T_m = \frac{P_m}{\Omega} = \frac{1}{2\lambda} \rho \pi R^3 v^2 C_p \quad (2)$$

Which λ presents the ratio between the turbine angular speed and the wind speed. This ratio called the tip speed ratio and is defined as:

$$\lambda = \frac{\Omega R}{v} \quad (3)$$

Where: ρ is the air density, R is the blade length, v is the wind speed, C_p is the power coefficient, Ω is the turbine angular speed.

The power coefficient (C_p) presents the aerodynamic efficiency of the turbine and depends on the specific speed λ and the angle of the blades.

It is different from a turbine to another, and is usually provided by the manufacturer and can be used to define a mathematical approximation. A model of wind is developed and it's presented on figure (2).

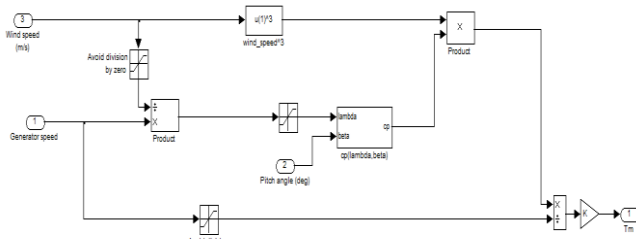


Fig.2. Model of Wind

Figure (3) represents the power coefficient C_p as a function of β and λ .

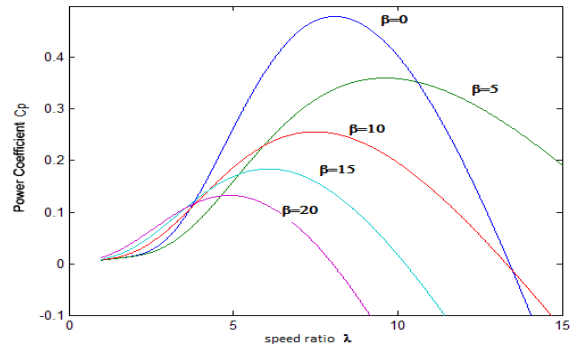


Fig.3. Power coefficient C_p as a function of β and λ

Figure (4) shows the mechanical power as a function of rotor speed of the turbine for different values of wind speed [4].

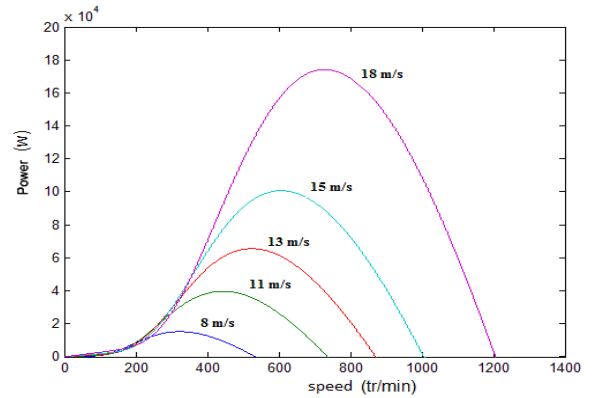


Fig.4. The characteristics of the mechanical power as function of the turbine speed.

B. Generator Model

The generator chosen for the conversion of wind energy is the synchronous generator [6, 9-10]. The dynamic model of synchronous generator in d-q frame can be represented by the following equations:

Electrical equations:

$$\begin{aligned} V_{ds} &= -R_s i_{ds} - \omega \varphi_{qs} + \frac{d\varphi_{ds}}{dt} \\ V_{qs} &= -R_s i_{qs} - \omega \varphi_{ds} + \frac{d\varphi_{qs}}{dt} \end{aligned} \quad (4)$$

$$V_{fd} = R_f i_{fd} + \frac{d\varphi_{fd}}{dt}$$

The flux linkage equations are:

$$\begin{aligned} \varphi_{ds} &= -L_d i_{ds} + M_{fd} i_{fd} \\ \varphi_{qs} &= -L_q i_{qs} \\ \varphi_f &= L_f i_{fd} - M_{fd} i_{ds} \end{aligned} \quad (5)$$

The dynamic behavior of synchronous generator can be defined by:

$$T_m - T_{em} - f\omega = J \frac{d\omega}{dt} \quad (6)$$

Where R_s – stator resistance, R_f is the field resistance, L_{ds}, L_{qs} – respectively direct and quadrature stator inductances, L_f is field inductance, T_w – Wind torque

applied to SG rotor, T_{em} – electromagnetic torque, p – pair number of poles, f – is the damping coefficient, J – is the moment of inertia, ω – electrical angular speed of motor.

III. Sliding Mode Controller

A. Sliding mode principle

Sliding modes is phenomenon may appear in a dynamic system governed by ordinary differential equations with discontinuous right-hand sides. It may happen that the control as a function of the system state switches at high frequency, this motion is called sliding mode. It may be enforced in the simplest tracking relay system with the state variable $x(t)$ [7, 8]:

$$\frac{\partial x}{\partial t} = f(x) + u \quad (7)$$

With the bounded function $f(x)$ $|f(x)| < f_0$ f_0 constant and the control as a relay function (figure(5)) of the tracking error $e = r(t) - \frac{\partial x}{\partial t}$ $r(t)$ is the reference input and u is given by :

$$u = \begin{cases} u_0 & \text{if } e > 0 \\ -u_0 & \text{if } e < 0 \end{cases} \quad \text{or} \quad u = u_0 \text{sign}(e) \quad u_0 = \text{constant}$$

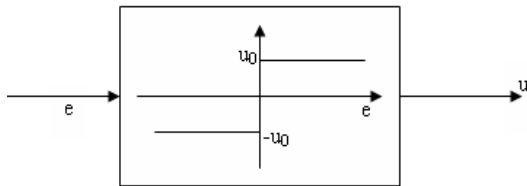


Fig. 5 – relay control

The values of e and $\frac{\partial e}{\partial t} = \frac{\partial r}{\partial t} - f(x) - u_0 \text{sign}(e)$ have different signs if $u_0 > f_0 + \left| \frac{\partial r}{\partial t} \right|$.

B. CONTROL STRATEGY

It is possible to control the load voltage, by the control of the converter associated. The all system is shown in Figure (6). The control of the system is based on the control of the PWM inverter and the chopper [15-16].

The DC-Link is made by using buck DC/DC converter.

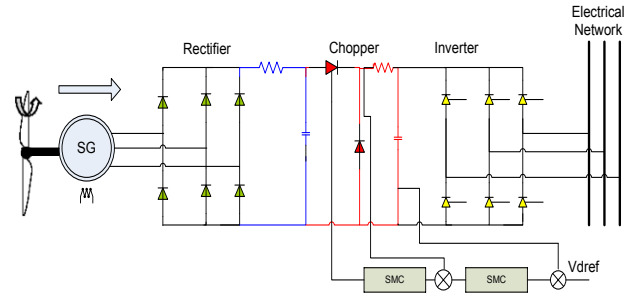


Fig.6. Control of the WECS.

For the Buck converter we consider the following sliding surface S :

$$S = \left(\lambda + \frac{\partial}{\partial t} \right) . e \quad (8)$$

where k is the sliding coefficient and e is the output voltage error defined as follows :

$$e = V_{dcref} - V_{dc} \quad (9)$$

By considering the mathematical model of the Buck converter, the surface can be expressed by the following expression (Tan, et al, 2006; Ben Saad et al 2008):

$$S = \frac{\partial V_{ref}}{\partial t} - \frac{1}{C} . i_L + \lambda . (V_{dcref} - V_{dc}) \quad (10)$$

and its derivative is given by :

$$\frac{\partial S}{\partial t} = \lambda . \frac{\partial V_{ref}}{\partial t} + \frac{\partial^2 V_{ref}}{\partial t^2} - \frac{1}{C} . i_L + \left(\frac{1}{L.C} \right) . V_{dc} - \left(\frac{V_{red}}{L.C} \right) . u \quad (11)$$

The next step is to design the control input so that the state trajectories are driven and attracted toward the sliding surface and then remain sliding on it for all subsequent time. The SMC signal u consists of two components a nonlinear component u_s and an equivalent component u_{eq} , [13].

$$u_{eq} = \frac{\lambda . L.C}{V_{red}} . \frac{\partial V_{ref}}{\partial t} + \frac{L.C}{V_{red}} . \frac{\partial^2 V_{ref}}{\partial t^2} - \frac{L}{V_{red}} . i_L + \left(\frac{1}{V_{red}} \right) . V_{dc} \quad (12)$$

Let us consider the positive definite Lyapunov function V defined as follows:

$$V = \frac{1}{2} . S^2 \quad (13)$$

The time derivative $\frac{\partial V}{\partial t}$ of V must be negative definite

$$\frac{\partial V}{\partial t} < 0 \quad \text{to insure the stability of the system and to make}$$

the surface S attractive. Such condition leads to the following inequality:

$$S . \frac{\partial S}{\partial t} = S . \left(\frac{-V_{red}}{L.C} . u_s \right) < 0 \quad (14)$$

To satisfy such condition, the nonlinear control component can be defined as follows:

$$u_s = \text{sign}(S)$$

Where V_{dc} output voltage of chopper, V_{red} input voltage of chopper, V_{dref} reference voltage, L and C is the inductance and capacitance of chopper.

C. SIMULATION DES RESULTATS

In this part we have simulated, the system described in Figure (6), taking into account of the real waveforms. The wind speed taken is 3m/s and that change to 6m/s at $t=20s$ (Fig. 7). The reference DC-link voltage taken is $V_{dcref} = 580v$ and which corresponds to the voltage applied in the network with a value of 220v and a frequency of 50Hz .

Figures 8.a and 8.b present the simulation results using a sliding mode controller voltage. It can be shown that the voltage generated will influence the energy consumption figure (8.a). In figure (8.b), the voltage given by the chopper follows the reference voltage needed for the voltage requested by the network.

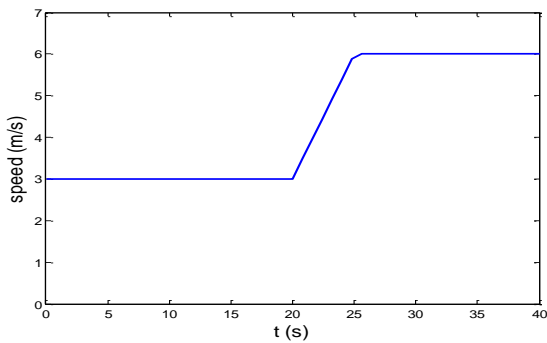
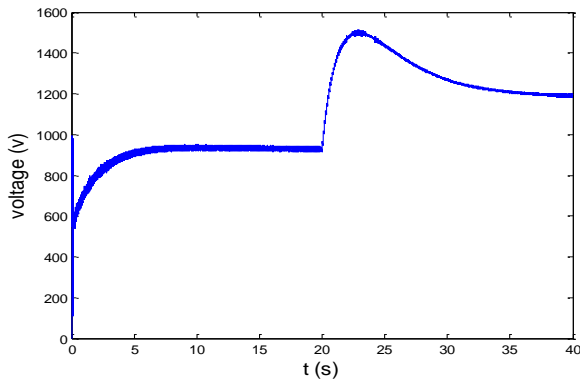
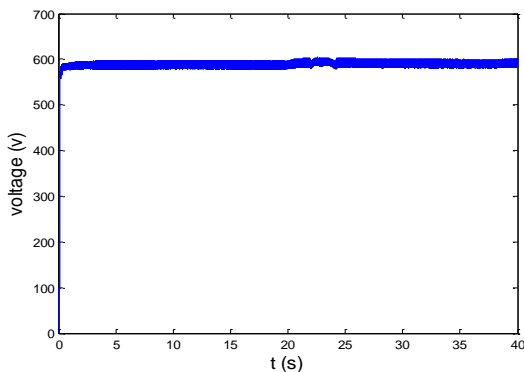


Fig. 7. The curve of wind speed



-a-



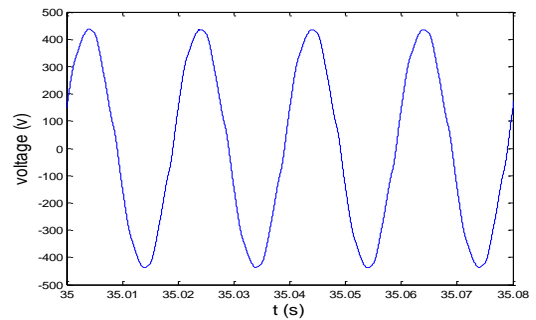
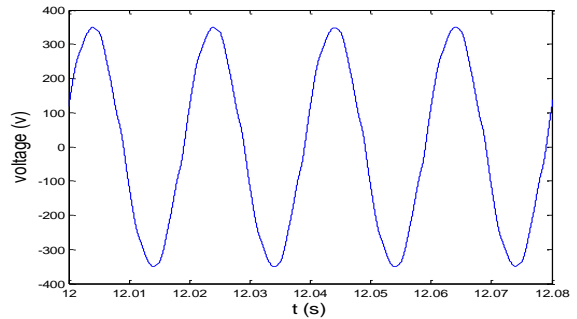
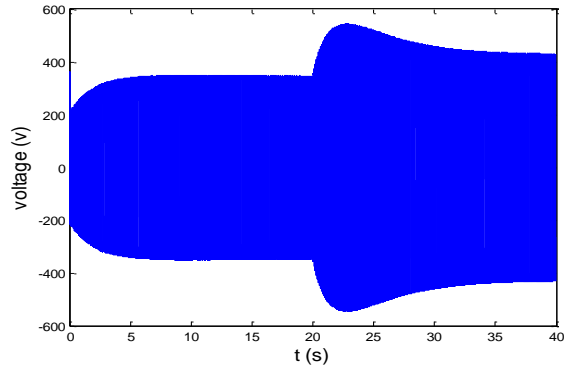
-b-

Fig. 8. The voltages in the output of: a- Rectifier, b- Chopper

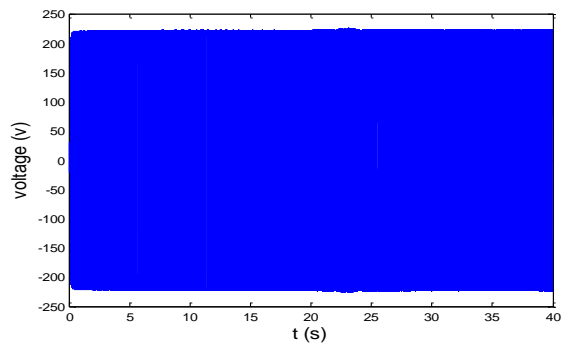
In the grid side, we have simulated the WECS in two cases: without using controllers and with using controllers.

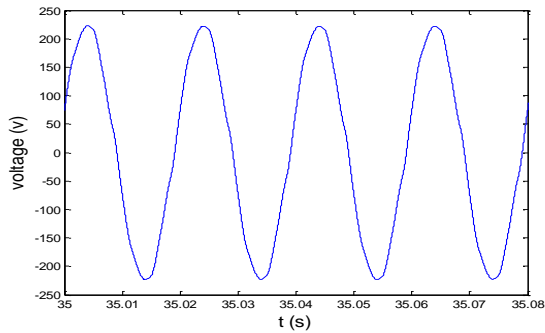
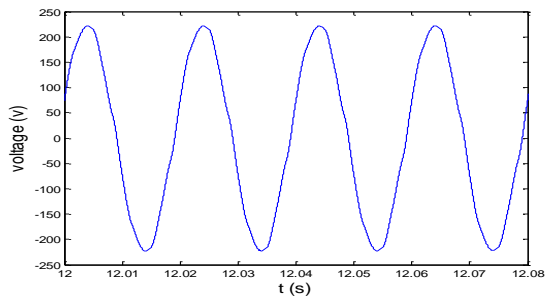
In the first case, the voltages in the grid phases vary with the variation of wind speed (Figure 9.a). In the second case, the voltages in the grid phases are constant in different variations of wind speed (figure 9.b).

Figure (10) shows the voltages in three grid phases. The use of SM gives good result in control of voltages transmitted to the grid.



a





-b-

Fig. 9. The voltage in the grid phase A : a- Without controller, b- In the presence of controller

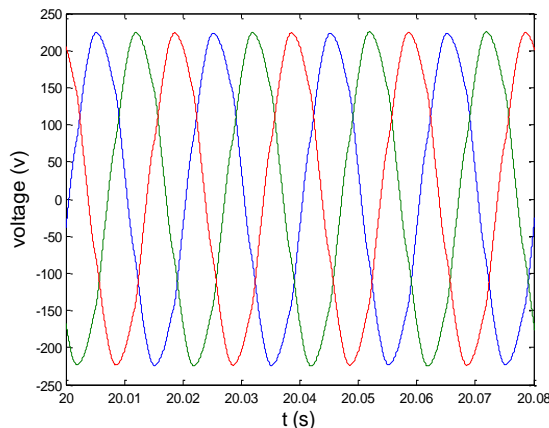
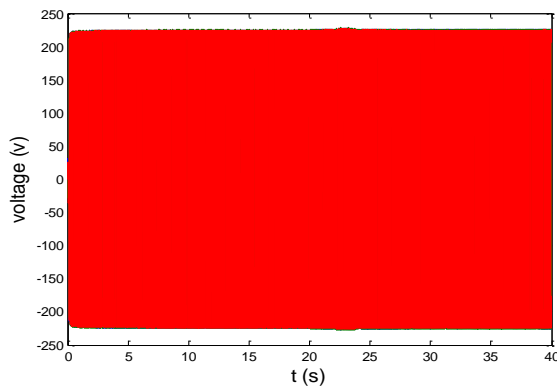


Fig. 10. The voltages in the three phases grid

D. CONCLUSION

In this chapter, we have described the different structures of wind turbines based on the synchronous generator; we have established a model of the wind conversion chain,

consisting of a synchronous generator, a three-phase diode rectifier, a Buck chopper and a PWM Inverter. We have subsequently built a device for controlling the chain of the proposed conversion.

The all system is simulated in two different wind speed. The simulation results show the possibility of extracting the maximal of wind power, and the control of the chopper output voltage and the inverter in order to regulate the grid voltages to the desired values.

REFERENCES

- [1] A. MIRECKI, Etude comparative de chaînes de conversion d'énergie dédiées à une éolienne de petite puissance, Thèse de doctorat de L'institut national polytechnique de Toulouse le 5 avril 2005.
- [2] F. Poitiers "Etude et Commande de Génératrice Asynchrone pour L'utilisation de L'énergie Eolienne ", Thèse de Doctorat de l'Université de Nantes, 19 décembre 2003.
- [3] G. A. Smith, K.A. Nigim, Wind-energy Recovery by a Static Scherbius Induction Generator", Proc. IEE, 1981, 128, pp. 317-324.
- [4] Nguyen, V.M. & Lee, C.Q. (1996). Indirect implementations of sliding-mode control law in buck-type converters, *Proceedings of the IEEE Applied Power Electronics Conference and Exposition*, pp. 111–115, Vol. 1, March, 1996.
- [5] A. Rachid, " Systèmes de régulation", Masson, paris, 1996.
- [6] Chunting Mi, Mariano Filippa, Johan Shen and Narashim Natarajan, Modeling and Control of Variable Speed Constant Frequency Synchronous Generator With brushless Exciter, *IEEE Transactions on industry application*, vol. 40, No. 2, pp565-573, March/april 2004.
- [7] E. S. Abdin, W. Xu, Control design and Dynamic Performance Analysis of a Wind Turbine- Induction Generator Unit, *IEEE Trans. on Energy conversion*, vol.15, No1, March 2000.
- [8] H. Camblong, Minimisation de l'impact des perturbations d'origine éolienne dans la Génération d'électricité par des aérogénérateurs à vitesse variable, Thèse de doctorat, ENSAM Bordeaux, 2003.
- [9] L. Refoufi, B.A.T. Al Zahawi, A.G. Jack "Analysis and modelling of the steady state behavior of the static Kramer induction generator", *IEEE Transactions on Energy Conversion*, Volume 14, Issue 3, 1999, pp 333-339.
- [10] S. El Aimani, Modélisation de différentes technologies d'éoliennes intégrées dans un réseau de moyenne tension », Thèse de doctorat de l'Ecole Centrale de Lille (ECL) Cohabité avec L'université des sciences et technologies de Lille 1 (USTL), 06 décembre 2004.
- [11] Tan, S.C.; Lai, Y.M.; Cheung, M.K.H. & Tse C.K. (2005). On the practical design of a sliding mode voltage controlled buck converters, *IEEE Transactions on Power Electronics*, Vol. 20, No. 2, pp. 425-437, March 2005, ISBN 0-13-040890-5.
- [12] Tan, S.C.; Lai, Y.M. & Tse, C.K. (2006). An evaluation of the practicality of sliding mode controllers in DC-DC Converters and their general design issues, *Proceedings of the IEEE Power Electronics Specialists Conference*, pp.187-193, June 2006.
- [13] Ben Saad, K.; Sahbani, A. & Benrejeb M. Design Procedure and Implementation of a Robust Fuzzy Sliding Mode Controller for Buck Converters, *International Review of Automatic Control*, Vol.1, No.3, pp. 303-310, September 2008, ISSN 1974-6059.
- [14] S.R.Guda, « Modeling and power management of a hybrid wind-microturbine power generation », thèse de master de l'université de Bozeman, Monata. Juillet 2005.
- [15] A.D. Hansen, C.Jauch, P.Sørensen, F.Iov, F. Blaabjergm, Dynamic wind turbine models in power system simulation tool DIGSILENT, projet de recherche, laboratoire national de Riso, Roskilde. Décembre 2003.
- [16] K. Amei, Y. Igkayasu, T. Ohji, M. Sakui, A Maximum Power Control of Wind Generator System Using a Permanent Magnet synchronous Generator and a Boost Chopper Circuit, 0-7803-7 156-9 2002.

The Fundamental Problems of Transmission of Data and Voice by Using PLC via High Voltage Lines

Javad Abdi¹, Azam FamilKhalili²

¹ Department of Electrical and Computer Engineering, NazarAbad Center, Islamic Azad University, Alborz, Iran
E-mail: javad.abdi@kia.ac.ir

² Department of Information Technology & Computer Engineering, Amirkabir University of Technology, Tehran, Iran
E-mail: a.familkhalili@aut.ac.ir

Abstract- This paper, dealing with T-Off, would focus on the fundamental problems of high Voltage Lines and the procedures for fixing them.

Key words:

High Voltage Lines, Information Transmission Systems, T-Off.

I. INTRODUCTION

If a high Voltage Line is used for voice and data transmission too, the PLC communication link should have a proper response in the defined range. It is obvious that if the Line does not transfer a proper frequency signal, communication would be undesirable especially for data.

This paper is organized as follows: a brief review of T-off in section two. Section three focuses on the effect of T-off existence. Section four gives some practical simulation. Issues on T-off issues on frequency domain and line improper impedance analysis are presented in section five and six, respectively. Finally, the simulation results and drawn conclusions are summed up in sections Seven.

II. T-OFF

In Particular, for assigning a frequency to a PLC link in point-to-point lines consisting one or more T-off, a range of PLC frequency band should be considered which has the perfect frequency behavior. It's obvious that existence of any Notch in a Line frequency signal would disturb proper usage of PLC in that area. Creation of notch in frequency signal is depending on T-Off that easily could be explained.

For instance: suppose the distance of a T-Off up to transmission Line (data) is equal to 2Km ; the end of the T-Off is open and the PLC wave transmission rate on the Line is equal to 2×10^8 m/s. According to transmission theory if the T-Off length is equal to multiple of $\lambda/4$ and the end of the Line is open ,therefore in Line frequency signal the frequency of 25 kHz, 75 kHz, 125 kHz and etc Notch are seen. Whatever the length of T-OFF become more the number of Notch frequency in PLC band will increase. Indeed all the Notch will close to each other and capability of Line usage in a very shorter limited area would be possible.

However environmental term especially humidity will cause Line weakness, specific Lines Impedance and change in all the frequency Notch.

III. EFFECT OF T-OFF EXISTENCE

Significant problem on transmission Line will occur if the T-Off length (ℓ) is noticeable than message signal wave length (λ).

According to figure 1, amount of Z_{in} compute from ℓ , Z_0 and Z_T

$$Z_{in} = Z_0 \frac{Z_T + jZ_0 \tan \beta \ell}{Z_0 + jZ_T \tan \beta \ell} \tag{1}$$

where: $\beta = \frac{2\pi}{\lambda}$.and Z_0 is specific Line Impedance.

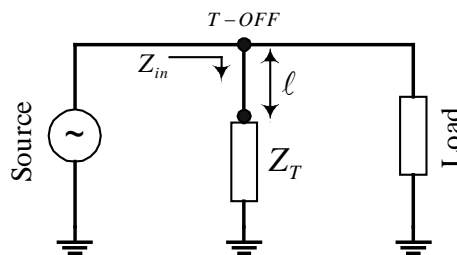
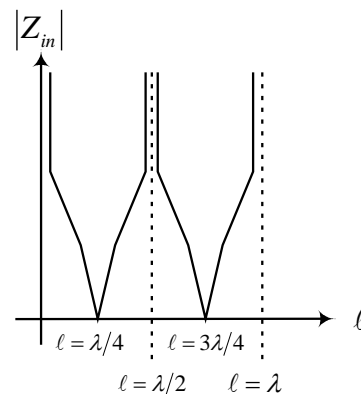


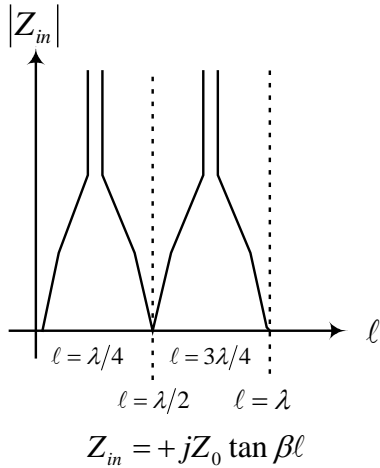
Fig. 1. Modeling transmission Line that include T-Off

III-1- Example No. 1: $Z_T = \infty$



$$Z_{in} = -jZ_0 \cot \beta \ell$$

III-2- Example No. 2: $Z_T = 0$



IV. PRACTICAL RESULTS

One T-Off with the length of 1 m & 4 m in situation of $Z_T = 0$ and $Z_T = \infty$ in the frequency range of 0 up to 400 have been simulating in lab. As regards to below figures in specific frequencies Line weakness is 25 db more than other frequencies.

IV-1- In figure 2, $l = 1m$ and $Z_T = 0$

As you see Line signal is similar to band pass filter signal that this transmission Line is useless in frequencies about 115 MHz, 230 MHz and 345 MHz.

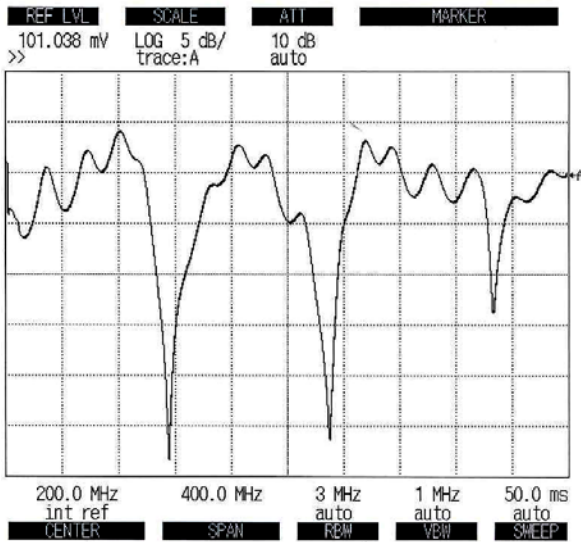


Fig. 2. Line signal if $l = 1m$ and $Z_T = 0$, short circuit

IV-1- In figure 3 $l = 1m$ and $Z_T = \infty$

As regards Line signal is similar to band pass filter signal that this transmission Line is useless in frequencies about 180MHz, 240 MHz and 300 MHz.

In figures 4 and 5, $l = 4m$, $Z_T = 0$ and $Z_T = \infty$, respectively.

As been considered whenever the T-Off length increase the useless frequencies will increase too. So the canal frequency should be elected punctuality.

In above simulated circuits if we thousand fold the T-Off length and wave length the above frequencies will change from MHz to kHz.

So in figure (1) if we change the frequencies from MHz to kHz (that is in PLC duty) despite the length of T-Off that is 1 km Line signal is equal to high Voltage Line signal. This matter is accurate in other simulated figures and circuits.

IV-3- Practical Solutions

While there is T-Off in transmission Line before specifying a frequency a team should be send to purposed sites for Line scan and election of proper canal.

V. SPECIFYING A FREQUENCY

V-1 - Problem/ Question

Existence of PLC Line filter creates the ability that several PLC could use from one transmission Line in common. But there are some limitations.

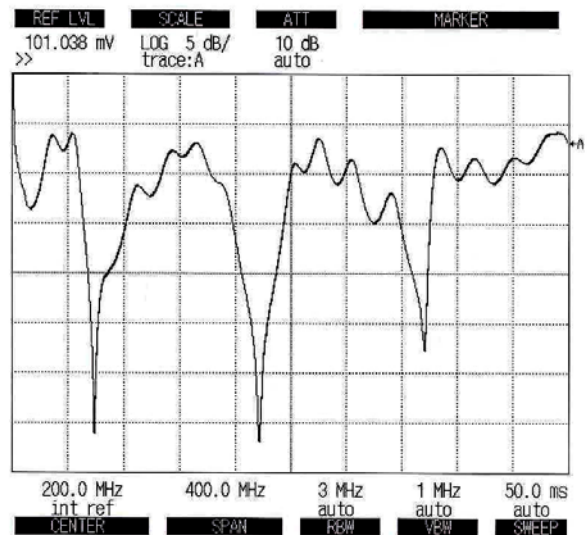


Fig. 3. Line signal if $l = 1m$ and $Z_T = \infty$, open circuit

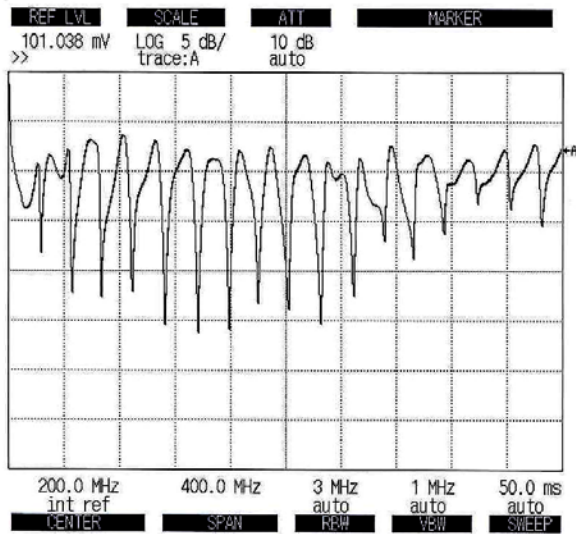


Fig. 4. Line signal if $\ell = 1m$ and $Z_T = \infty$, short circuit

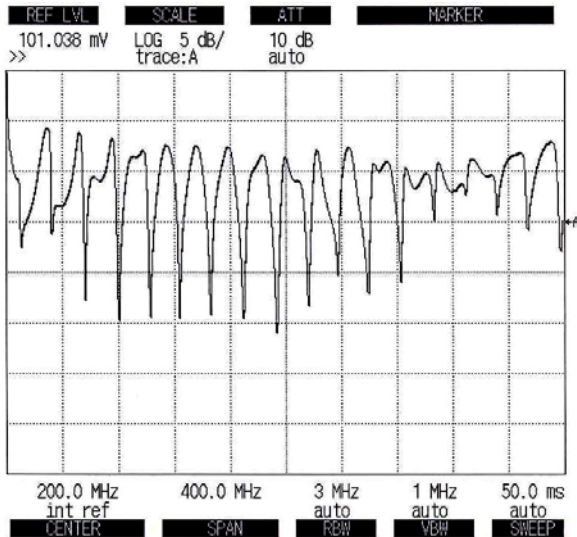


Fig. 5. Line signal if $\ell = 1m$ and $Z_T = \infty$, open circuit

Suppose that PLC second link want to use from one canal so the send and receive frequencies will be RX_1 , TX_1 , RX_2 and TX_2 , respectively.

In international standard IEC 60495 exactly these limitations has been mentioned.

$$|TX_i - TX_j| \geq 8KHz$$

$$|TX_i - RX_j| \geq 8KHz$$

$$|RX_i - RX_j| \geq 8KHz$$

There is no limitation for RX_i and TX_i so the frequency subtraction of RX_i and TX_i even can be equal to zero.

Exactly this limitation is because of Line filter band width and receiver. Line filter designed in a way that has short circuit in favorite band width and high Impedance out of band with the distance of 12 kHz (accordingly PLC Impedance could be ignore/forget in frequencies higher than limited area).

V-2 - Practical solutions

All PLCs that violate above limitation by adding new PLC should be adjusted again when disrespect above limitations. And also should be adjusted again after PLC deletion.

VI. LINE IMPROPER IMPEDANCE

VI-1 - Question

Line improper Impedance can be because of: lacking or mismatching Line Trap, mismatching LMU, existence of T-Off and existence of the PLCs that are in neighbor canals.

VI-2 - The problem that occur because of improper Line Impedance

- Improper Line frequency signal;
- Improper adjust of Hybrid circle;
- Returning capability in amplifier;
- Changing Line filter signal.

VI-3 - Practical solutions

In all above mentioned conditions frequency specifying should be done punctuality and before specifying a frequency an expert team should be send to purposed sites for Line scan.

VII. RESULTS

Having strong Data Base consist of below information for optimizes use of High Voltage Lines and data transmission is strongly needed and this information and data should be updated continually.

1. The posts manner of connection with High Voltage network.

2. Existence or lack of Line Trap and Line Trap Band Width in all of the posts

3. Plc's send & receive frequency canal using in any post and in any High Voltage Line.

REFERENCES

- [1] A. Ohman, and S. Mineka, "Fears, Phobias, and Preparedness: Toward and Evolved Module of Fear and Fear Learning," *Journal of Psychological Review*, vol. 108, no. 3, pp. 483-522, 2001002E
- [2] R.M. Viens, H.J.Trussel, L.J.Gate and J.B.O'Neal, "Noise on residential power distribution circuits", *IEEE Trans. on Electromagnetic Compatibility*, Vol.EMC-26, no.4, Nov. 1994, pp 161-168
- [3] J.A.Malac and J.R.Engstrom, "RF Impedance of United States and European Power Lines ", *IEEE Trans. on Electromagnetic Compatibility*, Vol.EMC-18, no.1, Feb. 1976, pp 36-38.
- [4] R.M.Vines, H.J.Trussel, K.S.Shuey and J.B.O'Neal, "Impedance of the residential power distribution circuit", *IEEE Trans. on Electromagnetic Compatibility*, Vol.EMC-27no.1, Feb. 1985, pp 6-12.
- [5] P.K.Gracht and R.W.Donaldson, "Communication using pseudo noise modulation on electric power disturbance circuit ", *IEEE Trans. On Communications*, Comm-33, no.9, Sept. 1985, pp 964-974
- [6] J.B.O'Neal, "Substation noise at distribution Line communication frequencies ", *IEEE Trans. On Electromagnetic Compatibility*, Vol.30, no.1, Feb. 1988, pp. 71-77.
- [7] Matthias Karl and Klaus Dastert, "Selection of an Optimal Modulation Scheme for Digital Communications over Low Voltage Power lines ", *IEEE Aug.1996*, pp.1087, 1091
- [8] Chassaing, R., Horning, D.W., "Digital Signal Processing with Fixed and Floating-Point Processors." CoED, USA, Volume 1, Number 1, pages 1-4, March 1991
- [9] Antoniou, A., *Digital Filters: Analysis and Design*, New York, NY: McGraw-Hill Company, Inc., 1979
- [10] Defatta, David J., Joseph G. Lucas, and William S. Hodgkiss, *Digital Signal Processing: A System Design Approach*, New York: John Wiley, 1988
- [11] User's Guide of DSP Processor "TMS320C25/26 ", 2000
- [12] Erskine, C., and S. Magar, "Architecture and Applications of a Second-Generation Digital Signal Processor." *Proceedings of IEEE International Conference on Acoustics, Speech, and Signal Processing*, USA, 1985
- [13] "Signaling on Low Voltage electrical installation in the frequency range 3kHz to 148.5kHz", *European standard EN 50065*, VDI-Verlag, Berlin, Jan, 1991

Economic Analysis of Wind Turbine Using New Cost Model

Sahil Bajaj, Kanwarjit Singh Sandhu

Abstract—Wind energy is considered to be a clean and green source of energy. Among various renewable energy sources wind energy is found to be most efficient in nature. Production of wind energy is associated with a huge capital cost followed by maintenance cost. In the present paper a new cost model is proposed. Model as proposed is found to be effective for the economic analysis of wind turbine, in addition to the computation of its total cost. The developed cost model has been used to determine the rating of wind turbine, which results in a maximum saving due to certain reduction in cost effecting parameter.

Keywords— Cost model, Economic analysis, Renewable energy sources, Wind energy, Wind turbine

I. INTRODUCTION

Generation of energy mainly follows the use of conventional sources like coal, petroleum etc. But these sources are depleting with time, moreover use of these sources also leads to environmental effects like climate change, global warming to some extent. With increase in population and considering the environmental changes there is a huge need to shift to renewable energy sources. There are many renewable energy sources that can be exploited efficiently and effectively, these include solar energy, wind energy, tidal energy etc. As per the statistics available due to many reasons wind energy seems to be effective in contrast to others. The contribution of wind power to the energy supply has reached a substantial share even on the global level. Total power generated worldwide by the use of wind energy conversion system is around 282275 MW.

There are many factors affecting the cost of energy produced using a wind farm. No doubt there is negligible fuel cost associated with wind energy but installation of wind turbine requires great capital cost and in addition to that also the operational and maintenance cost. Wind power plants appear to be a viable alternative in contrast to other renewable energy resources due to clean and never ending fuel. Generating electricity from wind makes economic as well as environmental sense; the wind is a free, clean and renewable fuel which will never run out. Even though wind is free its cost of electricity however, is not free. There are initial capital costs of purchasing wind turbines, towers, transportation of

materials, labor charge, expertise charge, operational and maintenance cost etc. Wind turbines are becoming cheaper and more powerful, with larger blade lengths which can utilize more wind and therefore produce more electricity, bringing down the cost of renewable power generation.

Many researchers tried to explore wind energy economics. Milborrow [1] studied the economics of wind power and its comparison with conventional thermal plant. It includes the expected prices and of wind energy up to year 2000. In 1997, national wind coordinating committee [2] published a paper which reviewed the measures of cost used for electricity-generating systems employing wind turbines. Peter fugslang and Kenneth thomson [3] tried to optimized the cost of wind turbines for large scale offshore wind farms. Optimizations were carried out to find out the optimum overall wind turbine design. They also analyzed that wind turbines for offshore wind farms should be different compared with a standalone system. In 2001 they [4] presented a method for site-specific design of wind turbines where cost of energy is minimized. Hani [5] described several optimization models for the design of a typical wind turbine tower structure by considering cross sectional area radius of gyration and height as effective design variable. Neils [6] studied the development of methods and guidelines for the use of wind energy in isolated communities and presented an approach in order to support a fair assessment of the technical and economic feasibility of wind energy. In 2008, Maria [7] observed the capital cost and the variable cost associated with generation of wind energy. In the same year Sangmesh [8] presented a new methodology to select a wind turbine generator from the view point of performance and economic consideration. Many new technologies as emerged to lower the wind energy were examined by Hoffman [9]. Dai [10] studied the wind energy resources assessment in wind power generation and described various wind energy resources assessment methods. Stannard [11] found energy yield and cost analysis of small scale wind turbines. A further attempt was made by Thomas [12] to analyze the development in large blades for lowering cost of wind turbines. IRENA issued a cost analysis series [13] focusing mainly on cost associated with renewable energy technology. Eric [14] presented a technical report that identified and summarized the past and future cost of wind energy. John [15] formulated the design of an integral wind turbine tower and foundation system as a multiobjective optimization problem using the process automation and design exploration software insight. In the present work a model has been developed for determining total cost for a wind turbine at a given power rating considering cost of transportation, manufacturing and percentage value of other cost associated.

Sahil Bajaj is doing M.Tech in School of Renewable Energy and Efficiency, National Institute of Technology Kurukshetra, Haryana-136119 India (phone: +91-9802792002; email: sahil_bajaj1990@yahoo.com).

Kanwarjit Singh Sandhu is Professor in the Department of Electrical Engineering, National Institute of Technology Kurukshetra, Haryana-136119 India (phone: +91-1744-9416314445; e-mail: kjssandhu@rediffmail.com).

II. ECONOMICS OF WIND TURBINE

As shown in fig. 1 cost of wind power plant may be distributed among the major works as given below.

1. Planning and project costs (9%)
2. Turbine cost (64%)
3. Civil works (16%)
4. Grid connections (11%)
5. Others (1%)

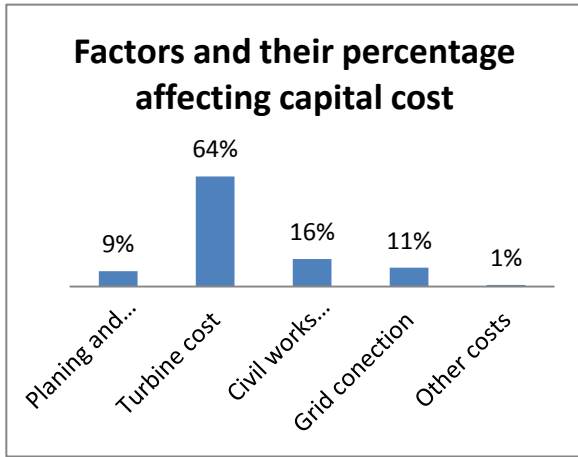


Fig. 1 Factors and their percentage affecting capital cost

On the basis of facts as shown in fig. 1, Cost of wind turbine, which accounts for the major share, needs analysis to derive the total cost of the plant. A typical wind turbine may consist of number of constituting parts and cost of its major components is as shown in fig. 2.

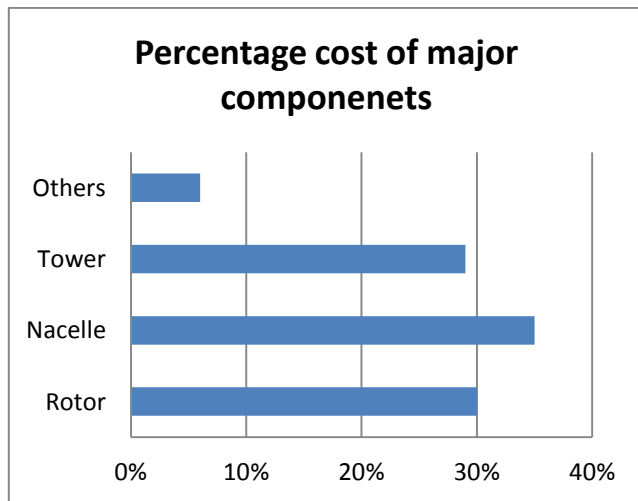


Fig. 2 Main components of wind turbine

From above figure, it is observed that cost of nacelle, cost of rotor and cost of tower accounts 94% of the total cost of the wind turbine. This is dependent upon the rating and weight of the complete structure. In the next section an attempt has been made to estimate the total cost of wind turbine with a focus on nacelle, tower, rotor and other components such as rate of interest on loan, consultancy, commission, maintenance etc. A new cost model has been proposed for the economic analysis of wind turbine.

III. COST MODEL

The total cost, (C), of the wind turbine may be calculated as a sum of following components:

- Manufacturing cost of the component
- Cost of material used for manufacturing the various components
- Transportation cost
- Other cost such as rate of interest on finance, consultancy commissions, maintenance cost etc.

Using the facts as mentioned above, following model may be developed to analyze the effect of many factors on the cost of wind turbine.

$$C = \frac{c_i \left[\sum_{i=1}^n W_i(p) \right] + \sum_{j=1}^n c_j W_j(p)}{\left[1 - \left(\sum_{i=1}^n R_i b_i \right) - k_0 \right]}$$

Where

C= Total cost of wind turbine(Rs.)

C_i=Transportation cost/ton (Rs).

C_j=Price of the jth material/ton (Rs).

R_i =Per unit cost of ith component.

b_i=Per unit manufacturing cost of ith component.

k₀=percentage value of cost which includes rate of interest on loan, consultancy, commission, maintenance etc.

W_i(p)=weight of ith component in tons as a function of turbine rating.

W_j(p)=weight of jth material used in construction in tons as a function of turbine rating.

In the above model for finite positive value of total cost, the term which appears in the denominator should have a range as below.

$$1 \geq \left[1 - \left(\sum_{i=1}^n R_i b_i \right) - k_0 \right] > 0.$$

Its maximum value may be one, which is true if

$$\left[- \left(\sum_{i=1}^n R_i b_i \right) - k_0 \right] = 0, \text{ which is not possible. However its}$$

maximum possible value is desirable to reduce the cost of generation. This can be achieved by the maximum feasible reduction of b_i & k₀ & it is true also.

IV. RESULTS & DISCUSSIONS

The model developed was used to analyze the effect of k₀ on the total cost of wind turbine. For such analysis MATLAB coding is employed and cost model as proposed is used for reflecting the effects of variation of k₀ from 0.1 to 0.09. Values of other parameters as used in cost model are shown in Appendix-I. Fig. 3 shows the effect of variation of k₀ on the total cost of wind turbine. Further, simulated results as shown in tables 1 to 6, are sufficient to describe the effect of such changes on the total cost of the turbines and resultant savings.

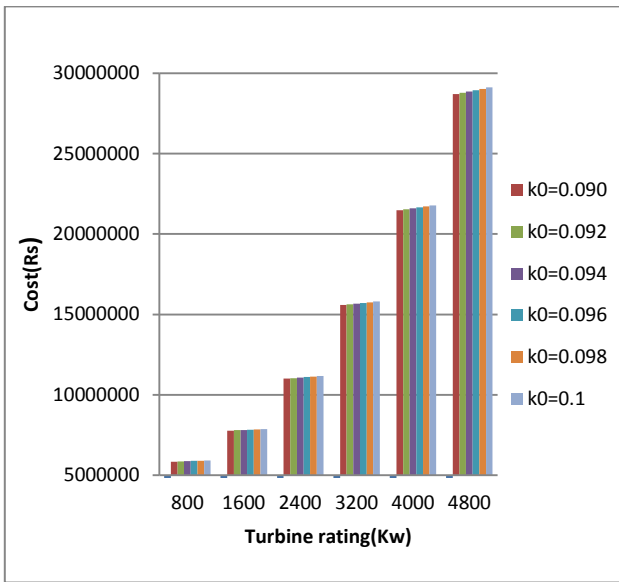


Fig.3 Effect of K_0 on total cost of wind turbine.

Table 1 Effect of k_0 on cost when turbine rating is 800kw

k_0	Cost	Percentage reduction in cost	Saving (Rs/Kw)
0.1	5919400	0	0
0.098	5902700	0.282123188	20.87
0.096	5886000	0.564246376	41.75
0.094	5869500	0.842990844	62.37
0.092	5853000	1.121735311	83.00
0.090	5836600	1.398790418	103.50

Table 2 Effect of k_0 on cost when turbine rating is 1600kw

k_0	Cost	Percentage reduction in cost	Saving (Rs/Kw)
0.1	7868000	0	0
0.098	7845800	0.282155567	13.87
0.096	7823600	0.564311134	27.75
0.094	7801600	0.843924759	41.50
0.092	7797700	0.893492628	43.93
0.090	7758000	1.398068124	68.75

Table 3 Effect of k_0 on cost when turbine rating is 2400kw

k_0	Cost	Percentage reduction in cost	Saving (Rs/Kw)
0.1	11162000	0	0
0.098	11130000	0.286686974	13.33
0.096	11099000	0.564414979	26.25
0.094	11068000	0.842142985	39.16
0.092	11037000	1.119870991	52.08
0.090	11006000	1.397598997	65.00

Table 4 Effect of k_0 on cost when turbine rating is 3200kw

k_0	Cost	Percentage reduction in cost	Saving (Rs/Kw)
0.1	15801000	0	0
0.098	15757000	0.278463388	13.75
0.096	15712000	0.56325549	27.81
0.094	15668000	0.841718879	41.56
0.092	15624000	1.120182267	55.31
0.090	15580000	1.398645655	69.06

Table 5 Effect of k_0 on cost when turbine rating is 4000kw

k_0	Cost	Percentage reduction in cost	Saving (Rs/Kw)
0.1	21786000	0	0
0.098	21725000	0.279996328	15.25
0.096	21663000	0.56458276	30.75
0.094	21602000	0.844579087	46.00
0.092	21542000	1.119985312	61.00
0.090	21482000	1.395391536	76.00

Table 6 Effect of k_0 on cost when turbine rating is 4800kw

k_0	Cost	Percentage reduction in cost	Saving (Rs/Kw)
0.1	29117000	0	0
0.098	29034000	0.28505684	17.29
0.096	28952000	0.56667926	34.37
0.094	28871000	0.84486726	51.25
0.092	28790000	1.12305526	68.12
0.090	28709000	1.40124326	85.00

Results as given above may be used to draw the fig. 4, which shows the saving per Kw, when K_0 varies from 0.1 to 0.09. It is also evident the savings per Kw comes out to be highest for a turbine rating for 800Kw as Rs. 103.50. Whereas, it's value is always less than 103.5 for other ratings. Such analysis shows that for maximum saving for such variation of k_0 , selection of rating of wind turbine should be 800 Kw or it's multiple. For example it is economical to install six units of 800 Kw instead of single unit with 4800 Kw.

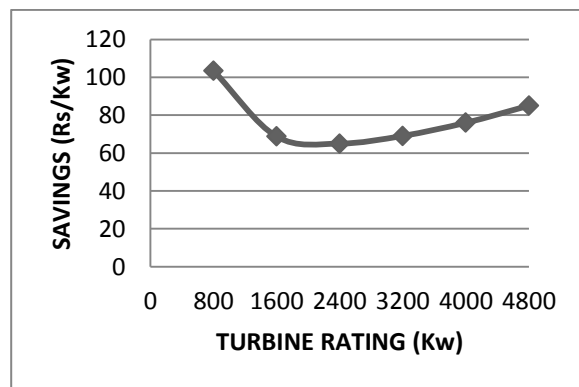


Fig.4 Saving per Kw, when K_0 varies from 0.1 to 0.09

V. CONCLUSIONS

In the present paper a new cost model as proposed is found to be effective for the economic analysis of wind turbine, in addition to the computation of its total cost. It is observed that the denominator of the cost model which depends upon k_0 may be controlled by controlling this parameter, which in turn depends upon the interest rate of finance involved for the wind power plant. A small change in this parameter may be effectively utilized for maximum saving by using proposed model. This has also been proved in the result and discussion section of the paper.

APPENDIX-I

$$C_t = \text{Rs.}3375 / \text{ton}$$

$$C_j \text{ for iron} = \text{Rs } 3600/ \text{ ton}$$

$$C_j \text{ for steel} = \text{Rs } 4500/\text{ton}$$

$$C_j \text{ for copper} = \text{Rs } 209400/\text{ton}$$

$$C_j \text{ for resin} = \text{Rs } 62230/\text{ton}$$

$$C_j \text{ FOR GLASSFIBER} = 61130/\text{TON}$$

$$R_i \text{ for nacelle} = 0.35$$

$$R_i \text{ for rotor} = 0.30$$

$$R_i \text{ for tower} = 0.29$$

$$b_i \text{ for nacelle} = 0.3$$

$$b_i \text{ for rotor} = 0.1$$

$$b_i \text{ for tower} = 0.3$$

Total weight of all components

$$= 67.73 + 0.02167p + 0.00001341p^2$$

$$W_j(p) \text{ for steel} = (10.038 + 0.045269p + 0.0000020115 * p^2)$$

$$W_j(p) \text{ for copper} = (14.7224 - (0.0069388 * p) + 0.0000029502 * p^2)$$

$$W_j(p) \text{ for iron} = (38.144 - 0.0179778 * p + 0.0000076437 * p^2)$$

$$W_j(p) \text{ for resin} = (2.4876 + 0.0183138 * p + 0.0000004023 * p^2)$$

$$W_j(p) \text{ for resin} = (1.6224 + 0.0006532 * p + 0.0000002682 * p^2)$$

REFERENCES

- [1] David Milborrow "Economics of Wind Power and Comparisons with Conventional Thermal Plant", Elsevier Science Ltd, Renewable Energy, vol 5, part 1, pp692- 699, 1994.
- [2] National wind coordinating Committee "Wind Energy Series", no.11, January 1997.
- [3] Peter fugslang and Kenneth Thomson, "cost optimization of wind turbines for large scale offshore wind farms", Riso national laboratory, Roskilde, February 1998.
- [4] Peter fugslang and Kenneth Thomson, " Site-Specific Design Optimization of 1.5–2.0 MW Wind Turbines "Riso national laboratory, Roskilde, journal of solar energy engineering, , vol 123, November 2001.
- [5] Hani m negam "structural design optimization of wind turbine towers", Pergamon, Computers and structures, 2000, 649-666.
- [6] Niels-Erik Clausen, Henrik Bindner, Sten Frandsen, Jens Carsten hansen, Lars Henrik Hansen, Per Lundsager "isolated systems with wind power, an implementation guide"riso national laboratory, Roskilde, june 2001
- [7] Maria Isabel Blanco "Renewable and Sustainable Energy" Reviews 13 (2009), pp. 1372– 1382.
- [8] Sangmesh S Soddamani, "economic index for selection of wind turbine generator at site", IEEE 978-1-4244-1888 -6/08, 2008.

- [9] D.L Hoffman and T.S molinski "How New Technology Developments will Lower Wind Energy Costs, CIGRÉ Canada, Symposium, Calgary, July 29th – July 31st, 2009 .
- [10] Dai ting, "study on the wind energy resource assessment in wind power generation", IEEE 978-1-4577- 0536-6/11/, 2008.
- [11] N J stanard "Energy Yield and Cost Analysis of Small Scale Wind Turbines" Durban University, UK, 2006.
- [12] Thomas,D,ashwil, "Development in Large Blades for Lower Cost of Wind Turbines" Sandia National Laboratories.
- [13] Renewable energy technology, "Cost Analysis Series" IRENA, Volume: Power Sector, Issue 5/5, 2012.
- [14] Eric lanz "The Past and Future Cost of Wind Energy" IEA Wind Task 26, 2012.
- [15] John c Nichols, "Multiobjective structural optimization of wind turbine tower and foundation system using insight", 10th world congress on structural and multidisciplinary optimization, Orlando,florida, USA, may 19- 24, 2013.

BIOGRAPHIES



Sahil Bajaj was born in Delhi, India on 29th October 1990. He did his B.Tech (Mechanical Engg.) from Sikkim Manipal Institute Of Technology, Sikkim, India. At present he is doing M.Tech (Renewable Energy System) from National Institute of Technology, Kurukshetra. His areas of Interest are wind energy, optimization theory , Research methodologies and Renewable Energy Systems.



Kanwarjit Singh Sandhu was born in Haryana, India on 21st December 1957. He received the B.Sc. Engg. (Electrical), M.Sc. (Power System) and Ph.D (Electrical Machines) degrees from Regional Engineering College, Kurukshetra University, Kurukshetra, India in 1981, 1985 and 2001, respectively. He joined the Electrical Engineering Department of Regional Engineering College, Kurukshetra, as Lecturer in January 1983. Currently, he is Professor in Electrical Engineering Department, National Institute of Technology, Kurukshetra (Formerly Regional Engineering College, Kurukshetra), India. He has more than 60 international journals and about 70 conference publications in the area of Machines & Energy. His areas of interest include electrical machines, wind energy conversion, power quality, artificial intelligence and power systems.

Comparative germination studies in mature seeds of *Haloxylon salicornicum*

L.Almulla

Kuwait Institute for Scientific Research
P. O. Box 24885, 13109 Safat, Kuwait
e-mail: lmulla@kisir.edu.kw

Abstract— As native plants are better adapted to the local environment, can endure long spells of drought, withstand high soil salinity levels and provide a more natural effect to landscape projects, their use in landscape projects are gaining popularity. Standardization of seed germination methods and raising the hardened plants of selected native plants for their use in landscape projects will both conserve natural resources and produce sustainable greenery. In the present study *Haloxylon salicornicum*, a perennial herb with a potential use for urban greenery was selected for seed germination tests as there is an urgent need to mass multiply it for its large-scale use. The main outcome of this study is to provide information about the best propagation methods of *Haloxylon salicornicum* native plants to enhance the use of native plants in landscaping.

Keywords— dormancy, gibberelic acid, germination trays, vigor index s.

I. INTRODUCTION

THE world's arid ecosystems support only plants with minimum water requirement that are drought and salt tolerant. An ongoing program to introduce and screen plants from different regions of the world that have agro-climatic conditions which are similar to Kuwait is essential in developing and continually updating the plant palette. Over the years, the Kuwait Institute for Scientific Research has introduced and evaluated several plants from various sources for their adaptability and growth performance under Kuwait's harsh environmental conditions. Some of them were found to be promising in enhancing plant diversity, thereby allowing greater flexibility in plant selection, preventing visual monotony and increased aesthetic appeal to the local landscape and greenery activities. Water-efficient plants play an important role in conserving natural resources in the world's arid regions.

The author is grateful for the financial support of Kuwait Institute for Scientific Research (KISR) provided for this project.

Water conservation is a vital issue that is not only restricted to the desert countries but is also of international significance [5]. The native plants are disappearing from their habitat at an alarming rate. Although the introduced ornamental plants are essential in providing diversity in urban and suburban landscape projects, a majority of them require excessive irrigation water and maintenance to cope with the harsh summer weather conditions. Therefore, the use of a proper blend of exotic and native plant species could lead to the establishment of sustainable greenery in urban and sub-urban areas. The use of native plants in urban landscape/greenery will also reduce fertilizer, pesticide and insecticide usage, thereby minimizing threats to the local environment. It will also promote wildlife, and at the same time, conserve native vegetation. Therefore, the evaluation of native plants for their suitability for urban landscape has obtained very promising results. The ornamental introduction program, together with the evaluation of native plants, has led to the selection of several promising plants. These plants need to be mass multiplied for use in large-scale landscaping and greenery projects. Several native desert environment plants are being threatened and are facing danger of extinction due to anthropogenic causes [4].

Because sustainable greenery and landscaping are the needs of the day, particularly in countries that have limited natural resources, the propagation of native perennial vegetation makes efficient utilization of available natural resources in greenery. The natural designs are best adapted to the local conditions, require less maintenance, reduce environmental damage, benefit wildlife and require little maintenance. Moreover, the use of desert plants will expand the plant species' diversity, offering greater flexibility in urban landscape projects. Utilizing the native desert plants will also minimize the need for introducing the exotic ornamental plants, thereby reducing the chances of accidental introduction of new pests and diseases along with exotic plants. The desert plants provide seasonal interest and help preserve the local wildlife habitat. Sustainable landscape has long-term benefits as the plant species reseed themselves every season. Native plants in gardens can potentially aid conservation by contributing to the genetic diversity and buffer small and otherwise isolated populations from extinction [6].

Haloxylon salicornicum is a perennial shrub with a great potential for dune fixation, it promotes the biodiversity, as lizards and different kind of Fauna and flora are coexisting naturally with it. Flowering is during October to November, it is distributed in areas northeast of Kuwait and south of coastal areas[1],[3]and [7]. Seed germination of halophytic species is regulated by factors such as water, temperature, light, soil salinity, and their interactions [2] . *Haloxylon salicornicum* was selected for germination studies for its mass propagation through seeds. *Haloxylon* plant is an excellent sand binder [3] and is a native plant with a potential for urban greenery in Kuwait.

II. MATERIALS AND METHODS

The seeds of *Haloxylon salicornicum* used in this experiment were collected from Kuwait desert during December 2012 from Wadi Al-Batin, and it was stored in the seed bank of Kuwait Institute for Scientific Research from that time at 4°C temperature, another seed lot collected from National park on December 2012 was used directly without storing it in the seed bank.

Our experiment started on May 2013, The seeds of *Haloxylon salicornicum* underwent nine treatments with five sets of replications of each treatment. A total number of ten seeds were used in each replication and, hence, fifty seeds were used in each treatment. The seeds were incubated at 22°C, under continuous light and, 40% humidity. The nine treatments are:

- T1 -10 days dry heat (50°C)
- T2- 10 days dry heat (50°C) + 250 GA₃
- T3-10 days dry heat (50°C) + 500 GA₃
- T4-20 days dry heat (50°C)
- T5-20 days dry heat (50°C) + 250 GA₃

- T6-20 days dry heat (50°C) + 500 GA₃
- T7-250 GA₃
- T8-500 GA₃
- T9-Control

Pre-treated seeds were germinated in Petri dishes with moistened filter paper, thin layer of water was always maintained. Observations of seed germination and seedling vigor on 1 to 5 subjective scales with five being the most vigorous seedling were recorded. Data were compiled and analyzed using the Analysis of Variance procedures (ANOVA). As germination was poor, the same treatments were repeated with seed lot 2 after removing the wings. The results of the experiments are discussed below.

III. RESULTS AND DISCUSSIONS

The germination percentage and vigor index is presented in Table 1. Control/untreated seeds exhibited highest germination with highest number of vigor 5 seedlings. Treatment with 250 GA₃ also produced similar results. This indicates that germination of *Haloxylon salicornicum* was slightly reduced by pretreatment with 10d, 20d heat and GA₃ other than 250GA₃. Untreated seeds of *Haloxylon salicornicum* can germinate readily without any pretreatment

The seeds of *Haloxylon salicornicum* exhibited less germination rate and percentage with high temperature treatments and high GA concentrations. Seed lot that was collected from the National Park, and wasn't stored in the seed bank, did not germinate easily because of dormancy.

Among the different treatments in *Haloxylon salicornicum* after the wings were removed, the control and 250 GA₃ produced the maximum germination (86%). The removal of wings in *Haloxylon salicornicum* before pretreatment is found to improve the germination.

Table 1. Germination and the Vigor Index Observed in *Haloxylon salicornicum* from Seed lot 2(Seed Bank) under Different Treatments

Treatment	V1	V2	V3	V4	V5	Total Vigor	Germination (%)
T1 10 d heat (50°C)	0	1	3	8	22	34	68ab
T2 10 d heat (50°C) + 250 GA ₃	1	0	1	6	13	21	44.7c
T3 10 d heat (50°C) + 500 GA ₃	1	1	4	5	19	30	60bc
T4 20 d heat (50°C)	1	0	6	0	30	37	74ab
T5 20 d heat (50°C) + 250 GA ₃	1	1	1	5	29	37	74ab
T6 20 d heat (50°C) + 500 GA ₃	1	1	4	1	26	33	66ab
T7 250 GA ₃	0	1	1	0	41	43	86a
T8 500 GA ₃	0	0	0	2	36	38	76ab
T9 Control	0	0	0	1	42	43	86a

Note: V5:Excellent; V4: Very Good; V3: Moderately Good; V2:Average; V1: Poor. The means in the column followed by similar letters within column are not significant at p≤0.01.

ACKNOWLEDGMENT

The author thanks the Kuwait Institute for Scientific Research (KISR) and the Kuwait foundation for the advancement of sciences for supporting and publishing this research. Assistance provided by the biodiversity of terrestrial ecosystem program staff in executing this study is gratefully acknowledged.

REFERENCES

- [1] M. A. Clor., T. A. Al-Ani, and F. Charchafchy. 1976. Haloxylon salicornicum as affected by storage and seed size. *Journal of Range Management*. (29)1, pp. 60 – 62.
- [2] G B Noe, and J. B. Zedler. 2000. Different effects of four abiotic factors on the germination of salt marsh annuals. *American Journal of Botany*.87: 1679–1692.
- [3] S.Omar.,Y.Al-Mutawa and S.Zaman,2000.Vegetation of Kuwait. Kuwait Institute for Scientific research, Al-Assriya Printing press, publishing and distribution company,Kuwait,pp:159.
- [4] C.Sudhersan, , M. AboEl-Nil and J. Hussain, 2003. Tissue Culture Technology for the Conservation and Propagation of Certain Native Plants. *J. Arid Environ.*, 54: 133-147.
- [5] M.K.Suleiman,.; N. R .Bhat; M. S. Abdal; S. Zaman; S .Jacob; and R.R. Thomas. 2009. Germination studies in *Rhanterium epapposum* Oliv. *World Applied Sciences Journal*, (7) 4; 468 – 471.
- [6] R.J.Whelan,.; D.G.Roberts; P.R.England; and D.J.Ayre. 2006. The potential for genetic contamination vs. augmentation by native plants on urban gardens. *Biological Conservation*, (128), 4: 493 – 500.
- [7] S.Zaman,., S.Padmesh, N.R.Bhat and H.Tawfiq. 2006. Germination of some Kuwait's native plants under Saline conditions. *Aurasian J.Agric& Environ.Sci.*,1(2):146-148,2006.

Applying GIS to assessment of ecosystems in the landscape level

Case study from the Czech Republic

Vilém Pechanec, Ivo Machar, Aleš Vávra, Helena Kiliánová

Abstract - Remote sensing and GIS are very important methods for assessment of changes and development of ecosystems in the landscape level. The aim of this work was to identify and evaluate the state and development of the permanent grass herbage in the Horňácko region (Czech Republic) on the basis of historical and present geodata, aerial and satellite images and other available materials. With the help of the landscape-ecological indices, we are able to describe the state and structure of the permanent grass of geoinformation technologies, especially by employing the geographical information systems and remote sensing. We used

two GIT types which are closely connected and supplement each other. The values of the ecological indices were obtained by application of the Vector-based Landscape Analysis Tools extension and Patch Analyst extension and Image/Spatial Analyst extension for processing of the LANDSAT image.

Keywords - GIS, ecosystem, land-use, landscape indicators, remote sensing.

I. INTRODUCTION

Geoinformation technologies are specific information technologies used for processing of geodata and geoinformation. At present, they become very important tools in geoanalysis and are integral parts of all scientific disciplines that work with spatial data. The fundamental geoinformation technologies include geographical information systems (GIS), remote exploration of the Earth, digital relief models, positional and navigational systems, computer cartography, digital photogrammetry and spatial modeling.

This article deals with applying of remote sensing and GIS methods to assessment of ecosystems in agricultural landscape in the Horňácko region, extending to the White Carpathians Mountains Protected Landscape Area (Czech Republic). The the structure of ecosystems and their land cover have dramatically changed since the last hundred years due to the political and economical changes in the central Europe (changes in the ownership and the transfer of the small-scale production to the mass production). The aim of this article is to identify and evaluate these changes of ecosystems in the landscape level.

II. METHODS AND PROCEDURES

A. Data collection and pre-processing

The aim was to acquire various types of background data which were subsequently used as input data in the

process of finding solutions of various types of spatial operations, analyses and evaluation of changes in the development of permanent herbage (abbreviated in the article as "TTP").

A.1 Tabular data

The data originated from the project called "Motive Powers of Changes in Differentiation of Usage of Landscapes of the Czech Republic and Neighbouring Countries - Perspectives after Acceptance to EU". According to [1] the attribute table, based on the cadastral data from years 1845-1948-1990-2000, constitutes the groundwork of these data. Since the area of particular land registers changed, some land registers were formed and others ceased to exist, the land registers were therefore added to so-called the Basic Territorial Units, whose area was almost constant in the given years (i.e. the area changed within 1 % tolerance). In the tabular and map form, the stable land register represents well-established, detailed background for all procedures ending with the detailed knowledge on the development of the landscape structure. One can say that it is a comprehensive, up-to-date ultimately objective and precise piece describing quantitative and qualitative state of land reserves and economics in the Czech lands, Moravia and Silesia. For each time interval, an individual table was constructed characterizing the evolution of land exploitation in the particular cadastral territories in terms of hectares and percentages.

A.2 Satellite images

CORINE Land Cover (CLC) - We used data sets from two time periods, namely CORINE Land Cover CLC90 and CORINE Land Cover CLC2000. Both covers were in SHP data format and provided data on the whole territory of the Czech Republic. For further processing, it was necessary to modify these two covers with respect to the extent of interested territory with the use of ArcGIS program (function "Clip"). In order to have individual categories matched with the legend defined for tabular data, new categories of landscape exploitation were determined: woods, grasslands, non-

forest green, arable land, gardens and vineyards and built-up area. By this process, two new covers were formed, which became a basis for following operations and analysis of changes in TTP areas.

LANDSAT - From the beginning of seventies of the 20th century, satellites of LANDSAT system and image data, which are produced by this system, are widely recognized as the most important source of information on natural sources of the Earth. For the need of our study, the satellite image was taken by a LANDSAT 7 satellite with an ETM+ (Enhanced Thematic Mapper Plus) sensor. The image was downloaded from the webpage belonging to Global Land Cover Facility (CLCF). The image is related to the time period in the year 2000.

In the working environment of the ArcGIS software program (using "Clip" function), the image was cut along to the outermost points enclosing the interested territory. We then worked only with these layers (covers).

Thanks to the high number of contained spectral zones, it is possible to visualize the interested territory in various combinations of spectral zones when each of these combinations brings a slightly different view and highlights certain properties of the land surface.

A.3 Vector data

The vector data comes from the Fundamental Basis of Geographical Data (ZABAGED®). ZABAGED® is a digital geographical model of the territory of the Czech Republic, which, with its characteristic accuracy and particulars of imaging of geographical reality, corresponds to the accuracy and particulars of the Basic Map of the Czech Republic with the 1:10000 scale [2]. These data were in the SHP data format and related to the year 2001. For finding the changes in the landscape, the second cover of ZABAGED® was created, this time for the year 2007 when it was updated by the combination usage of following programs: Janitor and ArcGIS. For subsequent comparison with the CORINE Land Cover data, the legend was reduced from 10 categories of land exploitation to seven categories.

B. Software and methods

The basic analytic procedure of used data lies in the analysis of the time series, which enables to judge the initial state of the landscape in comparison with the existing landscape state by means of monitoring a change in the exploitation of parcels, change in areas, change in arrangement of the landscape and change in natural and naturally close structures. In addition to the ArcGIS 9.x extended of Spatial Analyst we used two special extensions. For monitoring the changes in the exploitation of the landscape, "Change Detection" extension is used for satellite images, especially for CORINE Land Cover images. The resulting data are supplemented with maps, tables, graphs of state and development of permanent herbages and with a series of ecological indices, all acquired with the use of V-LATE

and Patch Analyst extension. From LANDSAT satellite image, we find out information on a change in the areas in the landscape, vegetation and health state of vegetation by means of defined vegetation indices and ImageAnalysis/Spatial Analyst function.

B.1 Vector-based landscape analysis tools extension

Vector-based Landscape Analysis Tools (V-LATE) provides a set of the most frequently used metric functions (landscape indices) for the study and determination of the landscape structure. It can be freely downloaded in two versions, namely 1.0 version intended for ArcGIS 8.x program and 1.1 version for ArcGIS 9.x. As it is evident, the extension works with vector-based data [3]. V-LATE works only with polygons of shapefile data format. GRID and geodatabase files are not supported. The extension button is inactive until the polygon layer is loaded into the ArcMap project. The on-the-fly projection is not supported by this extension so far and it works only with the projected data. When working with a large amount of polygons (more than 1500 polygons), the process of calculation becomes significantly time consuming. If the appropriate classes are not explicitly expressed in the attribute table, they are automatically generated by the extension [3].

B.2 Patch Analyst

The Patch Analyst extension enables to perform spatial analyses of the landscape, supports modeling of standpoints, maintenance of biodiversity and woods management. The extension is available at the webpage of the Center for Northern Woods Ecosystems Research located at the Lakehead University. It is available in two versions, namely 3.12 version intended for the ArcGIS 3.x version program and 4.0 version for the ArcGIS 9.1 version program [4]. The menu of the 3.12 version Patch Analyst consists of 12 functions, which are divided into four thematic groups.

The first group involves the creation of new layers. Compared to V-LATE, this group offers two extra functions, namely "Intersect" function (crossing of polygons) and "Make Hexagon Regions" function (creation of regions of a regular hexagonal shape). The second thematic group deals with the setting of the parameters: Add/Refresh Area and Perimeter to shapefile and Parse Species Composition String (this function divides the column with the date of one attribute into a given number of columns), The third thematic group enables attribute modelling, which allows editing the attribute algorithms, i.e. questioning, searching and adding the information in the attribute table. The fourth thematic group works with the spatial operations: Neighbourhood mean (this function defines the landscape regions, where the polygons have similar values), Analysis by Regions (analysis of the individual categories, e.g. age analysis according to a given region) and Spatial Statistics.

At this points, it is worthwhile to mention following indices: Area Weighted Mean Patch Fractal Dimension – AWMPFD and Area Weighted Mean Shape Index – AWMSI belonging to the “Shape Index” group and Core Area Density – CAD from “Core Area Metrics” group [4]. These indices are present only in the Patch Analyst extension; they are missing in the V-LATE extension.

B.3 Study area

The Horňácko region is a small ethnical region that is situated in the eastern part of Moravia, close to the boundary with the Slovak Republic, in so-called the Moravian-Slovak borderland and at the foothill of Bílé Karpaty mountain range. The prevailing part of the model territory belongs to the CHKO Bílé Karpaty unit.

The total area of the territory is 14 312 hectares. The structure of the agricultural landscape of Horňácko region changes crucially during last one hundred years due to the political and economical changes, changes in the ownership and the transfer of the small-scale production to the mass production. The first stage of changes took place in the 1950s and 1960s due to the process of collectivization resulting in ploughing of balks and creation of large fields. The second stage of changes took place in the 1970s when more land was converted into arable land. This resulted in an increase of arable land at the expense of permanent herbage and entire environmental disturbance of the structure and function of the landscape. After 1989, there was a significant step towards development of permanent herbage when big parts of the arable lands got grassed [5].

The studied territory is unique for its characteristic landscape structure which, for the last 160 years, was not so devastated and disturbed by the process of intensification of agricultural production and process of collectivization compared to the other territories of the Czech Republic. Thus, one can say that the Horňácko region exhibits a so-called harmonic landscape [6].

III. RESULTS

A. TTP development

A complete comparison of the acquired results is somewhat complex. The only one year, for which we have all the three types of data, is 2000 (or 2001 in the case of ZABAGED data if we assume that during one year, there was no significant change in the development of TTP areas). As far as the year 1990 is concerned, it is possible to carry out a comparison only within tabular data and CORINE Land Cover (CLC) data. Other values, i.e. those from the years 1845, 1948 and 2007, can be evaluated in dependence on assumed TTP development.

We encountered a problem in the case of the tabular data when the values of the land areas of the individual categories are related to the BTU (Basic Territorial Units) and do not carry any information on the number of lands and their distribution within the territory. Thus,

from these data, it is impossible to evaluate any landscape-ecological indices except the index of change, the coefficient of ecological stability (KES) of territory and the absolute and relative presence of individual categories of land exploitation.

The whole period of 165 years is characterized by a decrease in the TTP area. In the years 1845-1948, almost 33 % of the total area of TTP was converted arable land. The decrease in the TTP area continued also in the years 1948-1990, when the drop in the TTP area was not so striking (less than 10 %). From the year 1990, an increase in the TTP area is observed in the period from 1990 to 2000. For this increase, the values derived from the tabular data and CLC data differ, the trend of the increase is the same, but the change in the TTP area is 15.50 hectares (0.43 %) and 901.97 hectares (i.e. 2/3 increase) from the tabular data and CLC data, respectively. In the last monitored time interval from 2000 (or 2001) to 2007, the increase in the TTP area still persists, however, this increase is not so dramatic (about 44.90 hectares – 1.28 %) as in the case of the previous time interval.

If we concentrate on the resulting values of the area of the grasslands for the mentioned year 2000 (or 2001), one can see from Table 1 that the values of the tabular data and CLC data are very close to each other but are not similar with the ZABAGED data as the difference between them is approximately 823.13 hectares.

Table 1. Area of TTP in the Horňácko region from particular data in the year 2000 (or 2001).

Data	Area of TTP (ha)
Tabular data	2679
CORINE Land Cover	2667,94
ZABAGED	3496,6

Such a trend evolution in the TTP area is also implied by the index of change when the lowest value ($IZ = -0.86$) corresponds to the time interval from 1845 to 1948 which is period of the highest decline in TTP area at the expense of the arable land due to developing agriculture. In the years 1848-1990, $IZ = -0.30$, signaling further decrease in the TTP area. On the contrary, an increase in the TTP area is evidenced in the years 1990-2000 ($IZ = 0.03$ from the tabular data and $IZ = 0.5$ from CLC data). In the years 2000(or 2001)-2007, the value of the index of change decreased to $IZ = 0.01$, which confirms that in this time interval, there was not so significant change in the area of individual categories.

The evolution of the landscape-ecological indices is different comparing the time periods of 1990-2000 and 2001-2007. In both monitored periods, we see an increase in the TTP area at the expense of the decrease in the area of the arable land, increase in the number of TTP parcels, increase in the index of mean size of the parcel (MPS), total length of edges (TE), density of parcel edges (ED), average shape of the parcel (MSI), Shannon index of diversity (SDI) and Shannon index of equilibrium (SEI), all being similar. The differences are

observable for the index of mean parcel edge (MPE), fractal dimension (FD), dominance (D) and for other indices. According to the index of polygon shape (SI), [5] TTP are in a leading position, immediately after the category of non-forest greens over the CLC data and category of water areas over the ZABAGED data. This is caused by the prevailing line character of the mentioned categories.

The number of types of changes in the land exploitation shows evidence of the accuracy and punctuality of the data of landscape structure of Hornácko region. The ZABAGED data are recorded with more detailed landscape structure than those coming from CORINE Land Cover. Therefore, much more types have been recorded for the ZABAGED data than for the CLC data when analyzing the change in the land exploitation. For CLC data, there are only three types of changes: non-forest greens to woods, woods to non-forest greens and arable land to TTP. For ZABAGED data, there are 11 types of changes recorded: woods to TTP, woods to arable land, TTP to woods, TTP to non-forest greens, TTP to arable land, non-forest greens to TTP, arable land to woods, arable land to TTP, arable land to non-forest greens, arable land to gardens and vineyards, and arable land to build-up area.

By analysis of the LANDSAT 7 satellite image, we defined the most suitable zone for detection of TTP in grey tones, i.e. zone No.4 and No.5. In the colour combination, the most suitable was a combination of zones No.4, No.3 and No.2. The majority of parcels with maximum density of vegetation are found in the highest altitudes, i.e. in the cadastral territory of Nová Lhota and Suchov. On the other hand, parcels with little vegetation or without vegetation are found in the cadastral territory of Lipov, Louka and in middle part of Hornácko region.

B. Evaluation of calculation accuracy

The landscape-ecological indices were possible to be applied only to CLC and ZABAGED data. Their calculations carried out in the Patch Analyst extension have been compared with the selected indices in V-LATE extension and their accuracy has been then evaluated. As one can see in Table 2 and 3, the values of indices from the CLC data are accurate within two decimal digits. The difference is only observed for the ZANAGEB data when the value of the index of density of parcel edges (ED) and the index of core land area (TCAI) differs by decimal digit. By this process, we confirmed the consistency and accuracy of the calculation of both extensions. When comparing the CLC and ZABAGED data, the resultant landscape-ecological indices are different from year other. The increase trend persists, the area of the TTP again slightly increases by a few percent in the time period of 2000(or 2001)-2007.

Table 2. Comparison of accuracy of results of selected landscape indices derived from the CLC data.

Tool	Year	MPS	PSSD	ED	SDI*	TCAI
Patch	1990	65,05	68,34	6,73	1,36	93,05

Anal.	2000	81	76,76	10,18	1,44	93,65
V-	1990	65,05	68,34	6,73	1,36	93,05
LATE	2000	81	76,76	10,18	1,44	93,65

*SDI of all categories of land-use

Table 3. Comparison of accuracy of results of selected landscape indices derived from the ZABAGED.

Tool	Year	MPS	PSSD	ED	SDI*	TCAI
Patch	2000	17,31	55,59	29,42	1,35	89,78
Anal.	2007	15,33	51,8	30,91	1,36	89,54
V-	2000	17,31	55,59	29,41	1,35	88,49
LATE	2007	15,33	51,8	30,91	1,36	88,09

* SDI of all categories of land-use

The resultant values of TTP indices are different when comparing the year 2000 (CLC) and 2001 (ZABAGED). Especially, the number of land parcels is several fold higher for ZABAGED data (more than 622 %). This value thus influences other landscape-ecological indices.

The reason lies in the primary processing of these data. CORINE Land Cover data are not so accurate compared to the ZANAGED data. The 1:100 000 scale is too small for a study of more detailed landscape structures. The CLC data consist predominantly of middle and larger land parcels but do not include small and line-shape land parcels as during the generation, the small land parcels have joined up the neighbouring larger categories. Here, the minimum area of the land parcel is 25 hectares with a minimum width of 100 meters. Therefore, for the CLC data, we do not register the category of water area and we only occasionally register the non-forest greens of a line character. This is also reflected in the update from the year 2000 when a plenty of errors were found out and a change in the land exploitation was registered if the change was higher than 5 hectares. This influences not only the number of land parcels but also other landscape-ecological indices.

On the other hand, for ZABAGED data, the structure of the landscape is detailed as a whole, the most detailed out of the mentioned data. Again, the scale plays an important role, but this time, it is ten times smaller than 1:10 000. This is then reflected in much more detailed landscape structure of individual categories and in the overall accuracy.

For further investigation, it would be suitable to also include the aircraft image from the time period of 1960-1970 in order to get a more comprehensive view on the development of the TTP area, or to also have the prepared CLC2008 data.

IV. CONCLUSION

The resulting values, obtained from the used data, confirmed that the trend of the TTP development at the Hornácko region is identical with the trend of the TTP development in the Czech Republic. The TTP area was the highest in 1845, then the TTP area decreased in dependence on the expansion of the arable land until 1990 after when, thanks to the decline of the agricultural production mainly in the under-mountains regions, the

renewal of the function of the grass growths takes place which is also reflected in the increase in the biological diversity of the whole territory. The most dramatic changes happened in the years 1845-1945 which was caused not only by the proceeding agricultural revolution but also duration length of the monitored period. This trend of decline continued in the following time interval of 1948-1990. In 1990, the mentioned turnover is observed in the development of the grasslands. From Table 1, one can see that the TTP values differ in the year 2000 (or 2001). The difference is 11.60 hectares between the tabular data and CLC data, which is not such a big discrepancy if we take into account the larger territory of BTU with a part of Uherské Hradiště district. However, in 1990, the acreage difference is more significant and is 2215.03 hectares (in favour of the tabular data, i.e. 62 % more compared to the CLC data). Inadequacy of the tabular data lies in the fact that they are related to the area of BTU and do not carry any information on the number of land parcels and their distribution within the studied territory. Therefore, for these data, it is not possible to evaluate other landscape-ecological indices except the fundamental ones, mentioned in the text.

For landscape-ecological indices, we observe an increase in the TTP area at the expanse of the arable land, increase in the number of land parcels, length of land parcels edges and their density, fractal dimension, shape of polygons, geological diversity (the Shannon indices). The usage of Patch Analyst and V-LATE extensions for the landscape-ecological studies and changes of the landscape structure represents a very suitable and powerful tool to get a comprehensive view on the landscape. It is obvious that the TTP state is getting much more better which is in a close connection with the structural changes within the agricultural land, support of grassing in the under-mountains regions, agro-environmental programs, support to local farmers and initiatives of Ministry of Agriculture and Ministry of Environment of the Czech Republic together with the grants of the European Union. Thanks to these financial supports, one can assume that the increase in the grass areas will continue in the forthcoming years.

The authors make available the detailed results together with the table appendices with the area of individual categories of the land exploitation and their changes, appendices with resulting landscape-ecological indices and map appendices documenting the TTP state and its evolution at the Horňácko region in the monitored time periods.

REFERENCES

- [1] Bičík, I., Jeleček, L. Land use and landscape changes in Czechia during the period of transition 1990-2007. *GEOGRAFIE*. Volume: 114 Issue: 4, 2009, pp. 263-281.
- [2] ZABAGED. Technical documents of Central Institute of Surveying and Land Register, Czech Republic: [online]. c2006, [cit.2008-2-1]. Available at: <http://www.cuzk.cz/>.
- [3] University of Salzburg: V-LATE - Vector-based Landscape Analysis Tools Extension [online]. Last revision 10.01.2006 [cit. 2008-01-27]. Available at: <http://www.geo.sbg.ac.at/larg/vlate.htm>.

- [4] Patch Analyst 4: Download Page [online]. c2008, last revision: 18. 01. 2008 [cit. 2008-01-26]. Available at: <http://flash.lakeheadu.ca/~rrempel/patch/download.htm>.
- [5] Pechanec, V., Janíková, V., Brus, J., Kilianová, H. Typological data in the process of landscape potential identification with using GIS. *Moravian geographical reports*. Vol. 17, 4, 2009, pp. 12-24.
- [6] Otýpková, Z., Chytrý, M., Tichý, L., Pechanec, V., Jongepier, J.W., Hájek, O. Floristic diversity patterns in the White Carpathians Biosphere. *BIOLOGIA*. Volume: 66, Issue: 2, 2011, pp. 266-274.
- [7] Machar, I., Pechanec, V. Application of geocological concept of the alluvial landscape in the creation of nature reserve (case study from CR). *Acta Universitatis Agriculturae et Silviculturae Mendelianae Brunensis*. Volume 59, Issue 3, 2011, pp. 123-135.

Controlled Output of Wind Turbine during Wind Variations

Navjot Singh Sandhu, Shelly Vadhera and Kanwarjit Singh Sandhu

Abstract— In a wind power plant, wind turbine is used to capture the wind energy associated with the wind for driving the electrical generator, which in turn feeds the load. Power output of wind turbines changes in accordance with the wind disturbances, which are uncontrollable. In the present paper, the Matlab/Simulink based model as developed for a wind turbine is used to control the output power during such wind variations. A new methodology as proposed is found to be very effective to control its power output. Simulated results as obtained are found to be superior in contrast to other schemes.

Keywords— Energy, MATLAB/ Simulink, Renewable Energy, Wind turbine

I. INTRODUCTION

Due to the harmful effects and fast depletion of conventional fossil fuels now researchers are looking for renewable sources of energy which are ecofriendly such as wind power, solar power, tidal power etc. Out of these wind power is the fastest-growing source and is expected to be the leading source in future also. Wind energy is found to be viable source of energy and its installation capacity is continuously increasing and presently reached at a significant level across the world. Total power generated worldwide by the use of wind energy conversion system is around 296225 MW. On the other hand India is considered to be the 5th largest country in producing energy from wind with total installed capacity of 19546MW. The worldwide market of wind energy has been driven by mainly by the five big countries that are China, USA, Germany, Spain, and India. Fig.1 shows the assembly of a turbine and generator.

Wind turbine captures the energy associated with the wind for driving generator, which in turn generates electric power. Many researchers [1]-[12] tried to analyze the behaviour of wind energy conversion system. Major issues and challenges related to wind turbine aerodynamics were discussed by [1].

Navjot Singh Sandhu is doing M.Tech in School of Renewable Energy and Efficiency, National Institute of Technology Kurukshetra, Haryana-136119 India (phone:9416528979;email:navjot_singhsandhu@yahoo.com).

Shelly Vadhera is Associate Professor in the Department of Electrical Engineering, National Institute of Technology Kurukshetra, Haryana-136119 India phone: +919416377796; e-mail: shelly_vadhera@rediffmail.com).

Kanwarjit Singh Sandhu is Professor in the Department of Electrical Engineering, National Institute of Technology Kurukshetra, Haryana-136119 India (phone: +91-1744-9416314445; e-mail: kjssandhu@rediffmail.com).

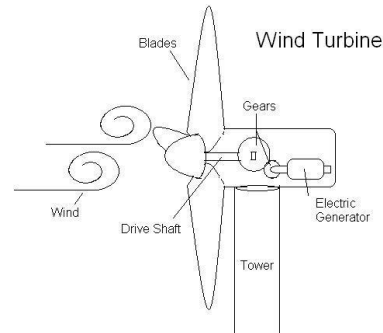


Fig 1 Wind Turbine with generator

Reference [2] tried to investigate the wind turbine resource potential with the help of seven small wind turbines and it was found that even for the same power rating, aerodynamic characteristics of selected wind turbine effects its production. New models to predict the mechanical torque of a wind turbine were proposed by [3]. Few researchers [4]-[11] tried to investigate the performance of wind turbine with wind speed variations. It was observed that rotor speed control by any technique may be helpful to control the performance of wind turbines, when subjected to wind variations.

Efforts have been made for the comparison of different structures for wind energy system, as well as their mechanical, electrical and economical aspects. Reference [4] gave the comparison of variable-speed against constant speed wind turbine systems. In terms of energy capture, every researcher concluded that variable speed turbine will produce more energy than constant speed turbines. Based upon this fact, [5] proposed maximum power tracking algorithm for operating a wind turbine in variable speed mode. Some of the researchers [6]-[7] adopted the Matlab/Simulink models for the analysis of wind turbines when subjected to wind variations. Whereas [8]-[10] discussed the pitch control strategies for variable speed wind turbines. However such control when incorporated makes the system costly and complicated. Reference [11] discussed the analysis of a variable blade length wind turbine, which includes the effect of extending turbine blade when wind speed falls. Similarly [12] presents a review of the state of the art and present status of active aero elastic rotor control research for wind turbines. With the increasing size of wind turbine blades, the need for more sophisticated load control techniques has induced the interest for locally distributed aerodynamic control systems with build in intelligence on the blades. Such concepts are often named in popular terms 'smart structures' or 'smart

rotor control'. The review covers the full span of the subjects, starting from the need for more advanced control systems emerging from the operating conditions of modern wind turbine and current load reduction control capabilities. Such controls may require special designs for blades, accounting the stresses upon the flexible parts.

In the present paper, the Matlab/Simulink based model as developed for a wind turbine is used to control the output power during wind disturbances/variations. A new scheme as proposed is found to be effective to control the performance of wind turbine. Simulated results as obtained are found to be effective for controlled output.

II. WIND TURBINE MODELING

Following equations are used to develop the wind turbine model as shown in fig 2.

$$P = 1.963 C_p R^2 v^3 \text{ ----- (1)}$$

Where

- C_p = Power coefficient
- v = Wind speed (m/sec)
- R = Blade radius (m)

The power coefficient (C_p) is a function of blade pitch angle β and tip speed ratio λ . Equation (1) may be used to define the power coefficient as:

$$C_p = f(R, v, P) \text{ ----- (2)}$$

The tip speed ratio as defined as the ratio between wind speed and rotor speed, and is expressed as:

$$\lambda = \frac{\omega R}{v} \text{ ----- (3)}$$

This gives:

$$\omega = f(R, v, \lambda) \text{ ----- (4)}$$

The general equation which may be used to define the power coefficient C_p is:

$$C_p(\lambda, \beta) = C_1 \left(\frac{C_2}{\lambda_1} - C_3 \beta - C_4 \right) \cdot e \left(-\frac{C_5}{\lambda_1} \right) + C_6 \lambda$$

With

$$\frac{1}{\lambda_1} = \frac{1}{\lambda + 0.08\beta} - \frac{0.035}{\beta^3 + 1}$$

Coefficient C_1 to C_6 , depend on the design wind turbine.

Fig. 3 shows the variation of power coefficient with tip speed ratio for different values of pitch angle. However in the present paper pitch angle is assumed to be constant as zero degree.

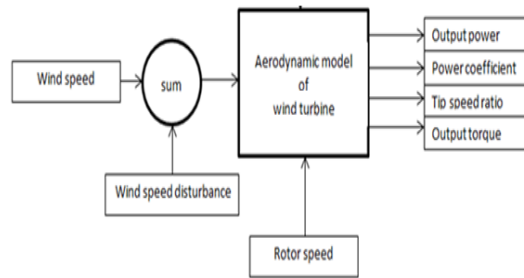


Fig.2 Wind turbine model

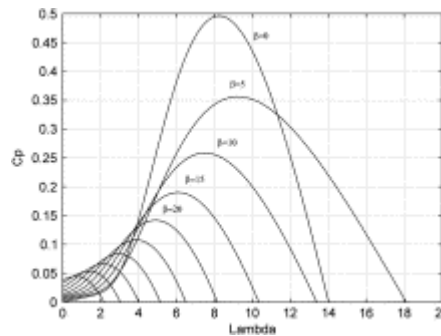


Fig. 3 Variation of Cp with λ

III. RESULTS AND DISCUSSIONS

The Matlab/Simulink model of wind turbine as developed is shown in fig.4. The model as shown may be used to control the output power during wind disturbances/variations, with constant blade pitch angle as zero degree.

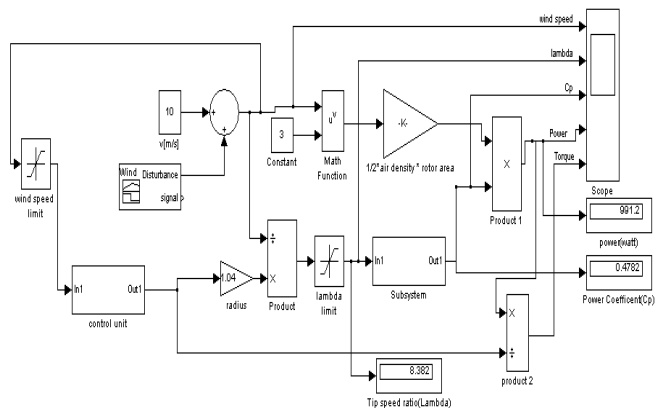


Fig.4 Simulink model of wind turbine

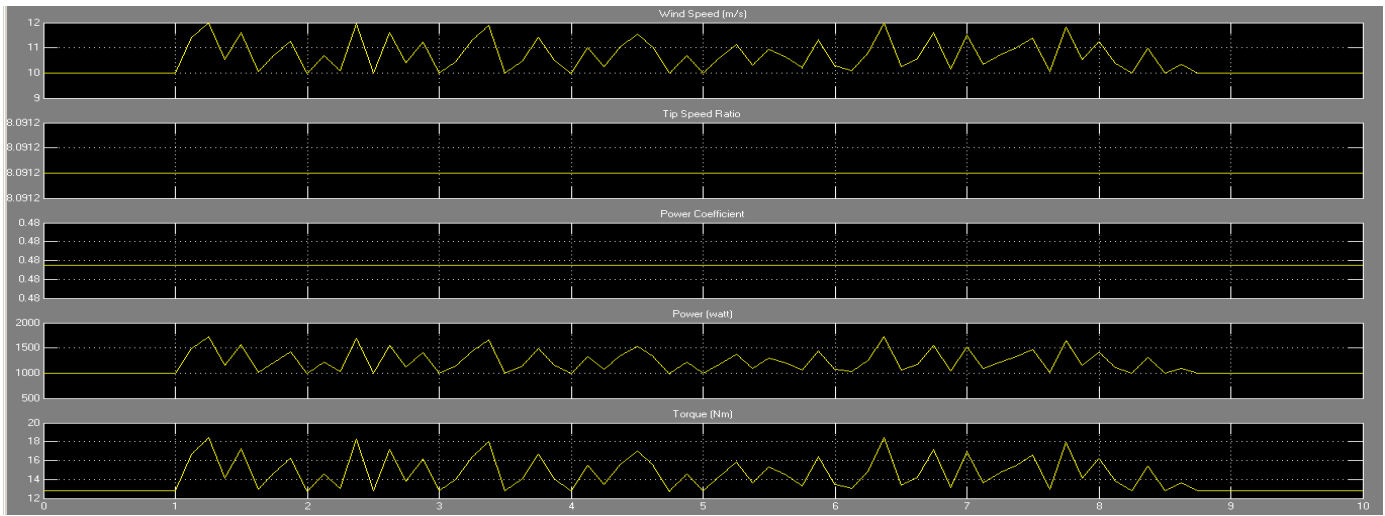


Fig.5 Effect of wind disturbances when rotor speed varies in proportion to wind speed

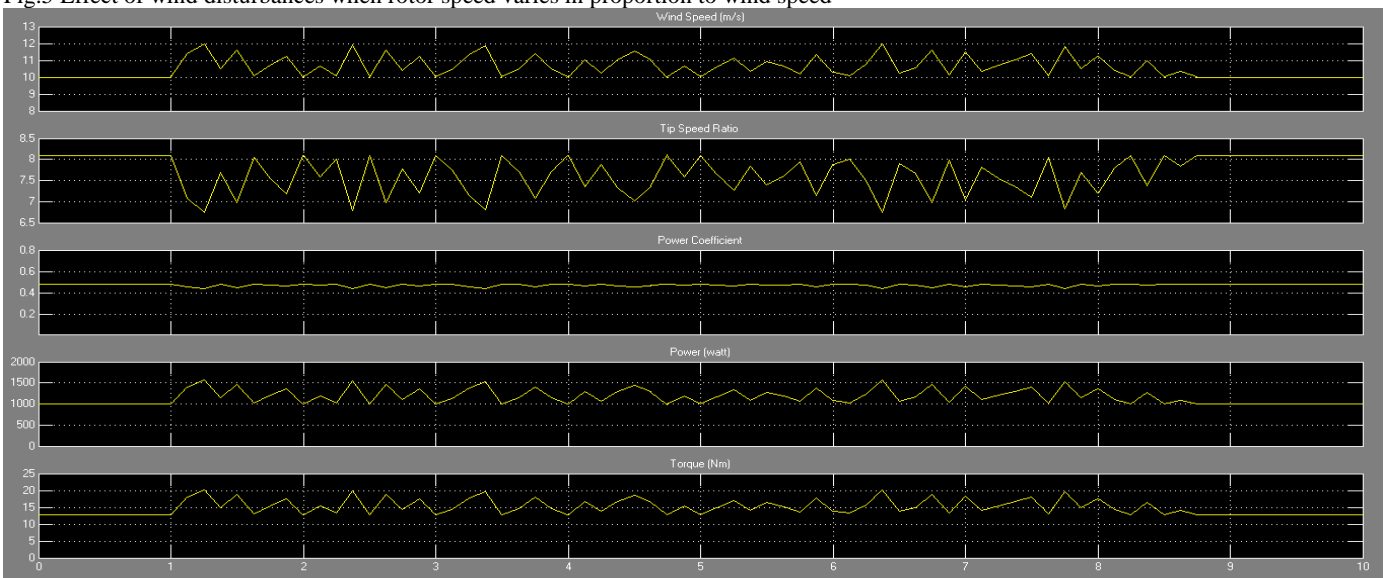


Fig. 6 Effect of wind disturbances when rotor speed is maintained constant

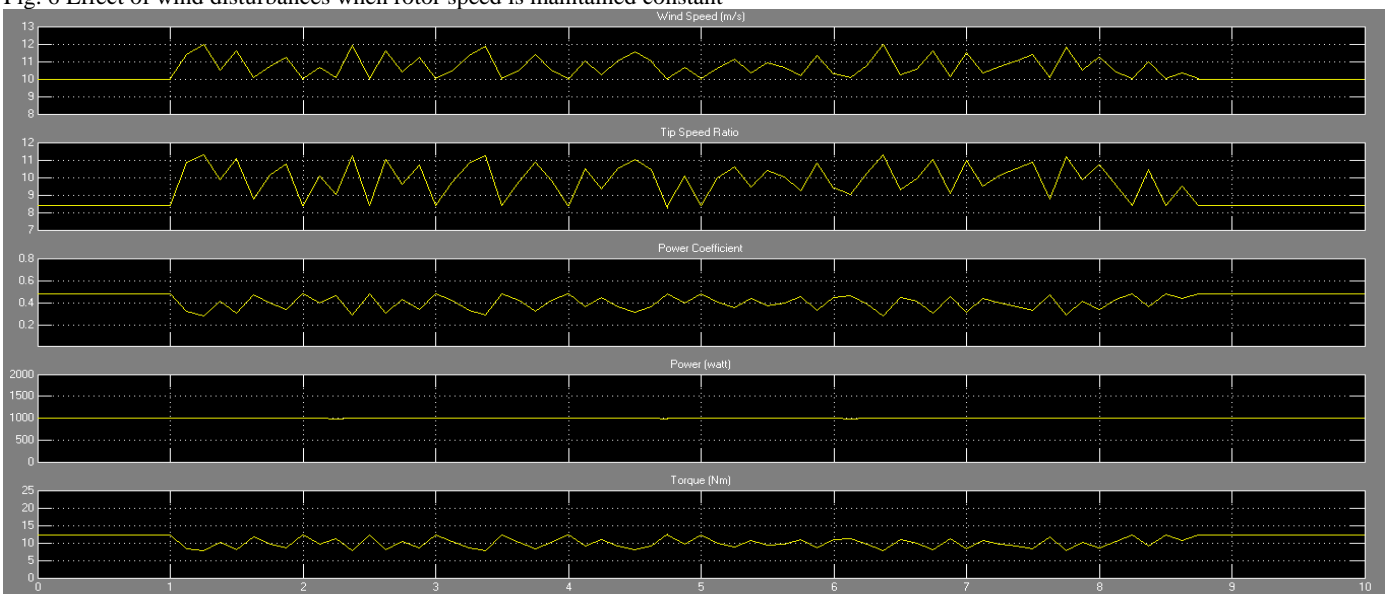


Fig. 7 Effect of wind disturbances when rotor speed is varied in a controlled manner

Fig.5 to Fig.7 shows the simulated result on a wind turbine with Rated Power 1KW, Wind Blade Radius 1.04m, Cut-in Speed 4m/s and Rated Wind Speed 10m/s. Turbine when run at the rated wind speed of 10 m/sec and blade speed of 77.8 rad/sec, results in to the rated power output.

Fig.5 shows the simulation results for Tip Speed Ratio, Power Coefficient, Power and Torque in case wind varies randomly between 10m/s to 12m/s. During simulation, rotor speed goes on changing in proportion to wind. As observed it results in to the large variations in output power and torque, even lambda and power coefficients are maintained. This shows the uncontrolled behaviour of the turbine.

Fig.6 shows the simulated results during wind disturbance, when rotor movement is controlled and it is kept constant as 77.8 rad/sec. Such control i.e constant speed operation does not lead to satisfactory operation in terms of output power and torque. It is due to the large variations in lambda, which depends upon wind speed.

However simulated results as obtained using the proposed scheme, which involves the speed variation in a specific manner as defined by equations (1) to (4), are shown in fig. 7. As shown the output power of the turbine can be maintained as rated one, even during random wind disturbances. A comparison of the simulation results as shown in fig. 5 to 7 indicates the effectiveness of scheme as proposed. Power output is controlled using simultaneous control of lambda and power coefficient by controlling the rotor speed in a specific manner.

IV. CONCLUSIONS

In the present paper, the Matlab/Simulink based model as developed for a wind turbine is used to predict the behaviour of wind turbine, with randomly varying wind disturbances. Two control schemes as described are adopted to control the output power during such operations. The new scheme as proposed is found to be superior in contrast to other scheme. Comparison of simulated results as shown proves the effectiveness of proposed scheme.

REFERENCES

[1] Williams E. Holley “Wind Turbine Dynamics and Control – Issues and Challenges” IEEE American Control Conference Denver, Colorado June 4-6, 2003.

[2] Zdenko imic, Maja Bo icevic Vrhovcak and Damir Ijivac “Small Wind turbine Power curve Comparison” IEEE Conference, AFRICON Nairobi, Kenya September 23-25, 2009.

[3] J. Villanueva and L. Alvarez – Icaza “Modeling Mechanical Torque in Wind Turbine” 18th IEEE International Conference on Control Applications, Saint Petersburg, Russia, July 8-10, 2009.

[4] O. Carlson, J. Hylander and K. Thorborg; “Survey of Variable Operation of Wind Turbines”, European Union Wind Energy Conference, Goeteborg, Sweden, May 1996, pp. 406-409.

[5] Shibashis Bhowmik and Rene Spee; “Wind Speed Estimation Based Variable speed Wind Power Generation”, Proc. 24th Annual Conference of the IEEE, Vol. 2, 31st Aug- 4th Sept 1998, pp. 596-601.

[6] Phlearn Jansuya and Yuttana Kumsuwan; “Design of Matlab/Simulink Modeling of Fixed-Pitch Angle Wind Turbine Simulator” 10th Eco-

Energy and Materials Science and Engineering, Elsevier, Energy Procedia (34, 2013, pp. 362-370).

[7] Ph. Delarue, A. Bouscayrol, A. Tounzi, X. Guillaud and G. Lancigu; “Modeling, Control and Simulation of an Overall Wind Energy Conversion System” Elsevier, Renewable Energy 28, pp. 1169-1185, 2003.

[8] E. Muljadi, K. Pierce and P. Migliore; “Control Strategy for Variable-Speed, Stall-Regulated Wind Turbines” American Controls Conference, Philadelphia, PA, June 24-26, 1998.

[9] Engr.G. Ofualagba and E.U. Ubeku; “Wind Energy Conversion System-Wind Turbine Modeling”, IEEE Power and Energy Society General Meeting- Conversion and Delivery of Electrical Energy in the 21st Century, Pittsburgh, PA, 20-24 July, 2008.

[10] Luncian Mihet-Popa, Frede Blaabjerg and Ion Boldea; “Wind Turbine Generator Modeling and Simulation where Rotational Speed is the Controlled Variable”, IEEE Transactions on Industry Application, Vol. 40, No. 1, Jan/Feb 2004.

[11] R.N. Sharma, U.K. Madawala; “The Concept of a Smart Wind Turbine System”, Elsevier, Renewable Energy 39, 2013, pp. 403-410.

[12] T.K. Barlas and G.A.M. Van Kuik; “Review of State of the Art in Smart Rotor Control Research for Wind Turbines”, Elsevier, Progress in aerospace Sciences 46, 2010, pp. 1-27.

BIOGRAPHIES



Navjot Singh Sandhu was born in Haryana, India on 28th March 1990. He did his B.Tech (Mechanical Engg.) from UIET, Kurukshetra University, Kurukshetra. At present he is doing M.Tech (Renewable Energy System) from National Institute of Technology, Kurukshetra. His areas of Interest are wind energy, optimization techniques and energy auditing.



Shelly Vadhera was born on 01 September, 1972. She received the B.E. (Electrical) degree from Thapar Institute Of Engineering and Technology, Patiala Deemed University, Patiala, M. Tech. (Power System) degree from Regional Engineering College, Kurukshetra University, Kurukshetra, India in 1994, 1998, respectively. She joined the Electrical Engineering Department of Regional Engineering College, Kurukshetra, as Lecturer in August 1998. Currently, she is Associate Professor in the Electrical Engineering Department. Her areas of interest are electrical machines, high voltage and power systems.



Kanwarjit Singh Sandhu was born in Haryana, India on 21st December 1957. He received the B.Sc. Engg. (Electrical), M.Sc. (Power System) and Ph.D (Electrical Machines) degrees from Regional Engineering College, Kurukshetra University, Kurukshetra, India in 1981, 1985 and 2001, respectively. He joined the Electrical Engineering Department of Regional Engineering College, Kurukshetra, as Lecturer in January 1983. Currently, he is Professor in Electrical Engineering Department, National Institute of Technology, Kurukshetra (Formerly Regional Engineering College, Kurukshetra), India. He has more than 60 international journals and about 70 conference publications in the area of Machines & Energy. His areas of interest include electrical machines, wind energy conversion, power quality, artificial intelligence and power systems.

Comparison for Performance and Exhaust Emissions of Steam Injected and Thermal Barrier Layer (TBL) Coated Piston Spark Ignition Engine

Adnan Parlak, Idris Cesur, Vezir Ayhan, Barış Boru and Görkem Kökkülünk

Abstract—In this study, steam injected SI engine, TBL coated piston (MgO-ZrO₂ ceramic component) SI engine and TBL coated piston SI engine with steam injection have been compared in terms of performance and exhaust emissions with standard SI engine. Significant improvements have been observed in the performance and pollutant emissions. While the engine torque increased up to 8.3% at 2800 rpm in comparison to standard gasoline engine and TBL coated piston with 20% steam injection, specific fuel consumption, HC and NO_x emissions significantly decreased. It is clear that this study could be used by the real-engine designers by considering the effects of steam injection into the gasoline engine cylinder.

Keywords—Exhaust emissions, SI engine, Steam injection, Thermal barrier layer

I. INTRODUCTION

DUE to the emission legislations of internal combustion engines, engine designers has taken a precaution such as ceramic coated method to reduce flame-quenching areas. From that point of views, thermal barrier layer (TBL) coating have been successfully applied to gasoline engines to reduce particularly HC emissions. TBL coating have been used to increase component life and become a barrier against heat transfer and corrosion. Furthermore, engine warms up in a short time during the first start and heat transfer decrease in a

This work has been supported by The Scientific and Technological Research Council of Turkey and was performed within The Support Programme for Scientific and Technological Research Projects (1001) with the project number of 111M065 and Sakarya University Inter Discipline Scientific Projects Program with the project number of 2012-05-04-012.

Adnan Parlak is with Yildiz Technical University, Marine Engineering Dept., Istanbul, TURKEY (corresponding author to provide phone: 00902123832940; fax:00902123832941; e-mail: aparlak@yildiz.edu.tr).

Idris Cesur is with Sakarya University, Technology Faculty, Sakarya, TURKEY (e-mail: icesur@sakarya.edu.tr).

Vezir Ayhan is with Sakarya University, Technology Faculty, Sakarya, TURKEY (e-mail: vayhan@sakarya.edu.tr).

Barış Boru is with Sakarya University, Technology Faculty, Sakarya, TURKEY (e-mail: barisb@sakarya.edu.tr).

Görkem Kökkülünk is with Yildiz Technical University, Marine Engineering Dept., Istanbul, TURKEY (e-mail: gorkemk@yildiz.edu.tr).

combustion chamber, thus combustion efficiency increases [1,2]

From the open literature, there have been several studies of TBCs in gasoline engines about emissions and performance parameters [3-8]. Durat et al. investigated the temperature gradients in the standard and two different partially stabilized ceramic coated pistons and observed the sharp increase in the temperature of the coated area of the piston [9]. Chan studied that instead of using a single-property yttria-stabilized zirconia (YSZ) coating to achieve the thermal barrier for the piston crown to investigate the emissions and performance parameters [10]. Esfahanian et al. calculated the heat transfer to an engine piston crown with using three different methods for the combustion boundary condition and observed that using spatial and time averaged combustion side boundary condition is a suitable treatment method within engineering approximations [11]. Cerit et al. Investigated the influence of partially thermal barrier coating on piston temperature distribution and cold start HC emissions of a gasoline engine and results show that the surface temperature of the coated piston part was enhanced up to 100 °C [5]. Miller examined the thin thermal barrier coatings for protecting aircraft turbine section airfoils and the discussion focuses to TBC use for component life extension and more recently as an integral part of airfoil design [12]. Chan and Khor presented the work completed on a low heat rejection engine on a three-cylinder SI Daihatsu engine with piston crowns coated with a layer of ceramic, which consisted of yttria-stabilized zirconia (YSZ) to investigate engine performance [13].

In conclusion, ceramic coated applications are only used to reduce HC emissions however NO_x emissions increase with the high in-cylinder temperature, when piston has been coated with high thermal capacity component.

In this study; steam injected SI engine, TBL coated piston (MgOZrO₂ ceramic component) SI engine and TBL coated piston SI engine with steam injection have been compared in terms of performance and exhaust emissions with standard SI engine..

II. MATERIAL AND METHOD

A. Experimental Set-up [14]

The experiments were carried out with “Lombardini” SI engine. So as to measure brake torque, the engine is coupled with an electric dynamometer of 20 kW absorbing capacity using an “S” type load cell with the precision of 0.01kg. Table 1 shows the engine specification.

Table 1. Engine Specifications

Engine Type	Lombardini
Bore [mm]	72
Stroke [mm]	62
Cylinder Number	2
Stroke Volume [dm ³]	0.505
Effective Power, [kW]	15
Compression Ratio	10.7
Cooling Type	Water

MRU Spectra 1600 L type gas analyzer was used so as to measure exhaust emissions. The gas analyzer gives the amounts of CO, CO₂, NO, NO_x and HC emissions in (%) and ppm.

The piston is coated with ceramic material towards the top to center of the piston with 8 mm width and 0.5mm thickness. The TBL material of the piston is composed of MgO–ZrO₂ which has a low thermal conductivity, thermal diffusivity and a high heat capacitance causing the entrance temperature of the crevice to increase. Atmospheric plasma spray coating method was used to coat the combustion chamber components. The TBL composed of a 0.30 mm thick MgO–ZrO₂ layer over a NiCrAl bond coat of 0.20 mm thick [14].

In order to carry out the steam injection into the engine, electronically controlled steam injection system has been developed. Figure 1. shows steam rail and solenoid injectors fitted with suction manifold [14].



Figure 1. Injector slot placed in the suction manifold and steam injector fitted with injector slot

Experiments were done at variable engine speeds 1600, 2000, 2400, 2800, 3200 and 3600 rpm and full load condition [14].

III. RESULTS AND DISCUSSION

A. Performance Parameters

1) Engine Torque

Figure 2 illustrates the comparison of engine torque of

steam injected (S20), TBL coated piston (MgOZrO₂ ceramic component) (STD TBL), TBL coated piston with steam injection (TBL+S20) and Standard SI engine (STD). As can be seen from the Figure that the most increase in engine torque is 8.3% at 2800 rpm in comparison to standard gasoline engine and TBL coated piston with 20% steam injection. The maximum torque is found as 33.9 Nm at 3200 rpm with TBL+S20.

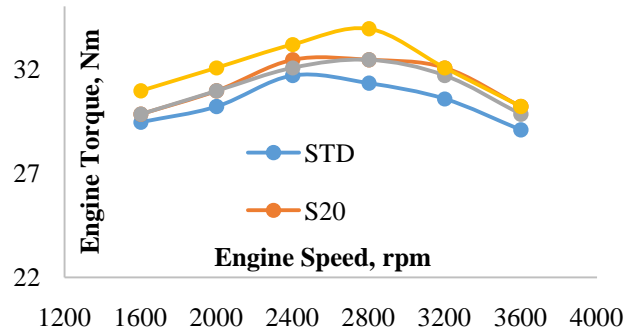


Figure 2. Comparison of Engine Torque

2) Effective Power

Figure 3 illustrates the comparison of effective power of steam injected (S20), TBL coated piston (MgOZrO₂ ceramic component) (STD TBL), TBL coated piston with steam injection (TBL+S20) and Standard SI engine (STD). As can be seen from the Figure that the most increase in effective power is 8.3% at 2800 rpm in comparison to standard gasoline engine and TBL coated piston with 20% steam injection. The maximum effective power is found as 11.4 kW at 3600 rpm with TBL+S20.

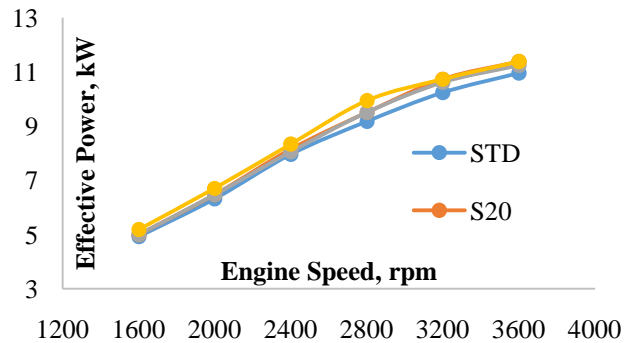


Figure 3. Comparison of Effective Power

3) Specific Fuel Consumption

Figure 4 illustrates the comparison of SFC of steam injected (S20), TBL coated piston (MgOZrO₂ ceramic component) (STD TBL), TBL coated piston with steam injection (TBL+S20) and Standard SI engine (STD). As can be seen from the Figure that the most decrease in SFC is 9.9% at 2800 rpm in comparison to standard gasoline engine and TBL coated piston with 20% steam injection. The minimum SFC is found as 255.6 g/kWh at 3200 rpm with TBL+S20.

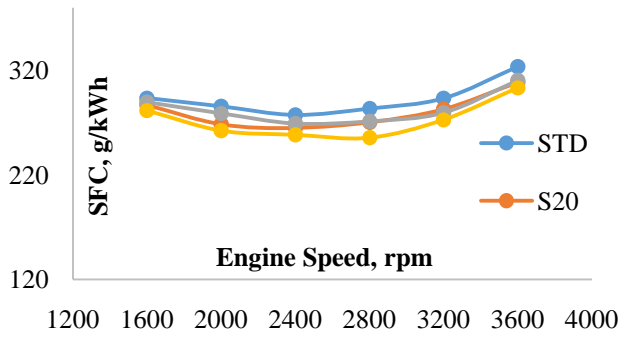


Figure 4. Comparison of Specific Fuel Consumption (SFC)

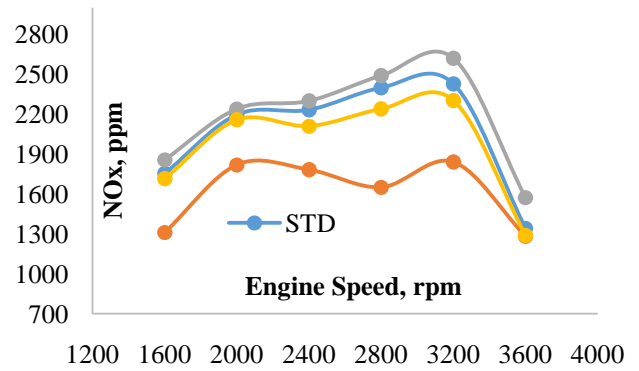


Figure 6. Comparison of NOx Emissions

B. Exhaust Emissions

1) HC Emissions

Figure 5 illustrates the comparison of HC Emissions of steam injected (S20), TBL coated piston (MgOZrO₂ ceramic component) (STD TBL), TBL coated piston with steam injection (TBL+S20) and Standard SI engine (STD). As can be seen from the Figure that the most decrease in HC Emissions is 38.1% at 3600 rpm in comparison to standard gasoline engine and TBL coated piston with 20% steam injection. The minimum HC emissions is found as 177 ppm at 3600 rpm with TBL+S20.

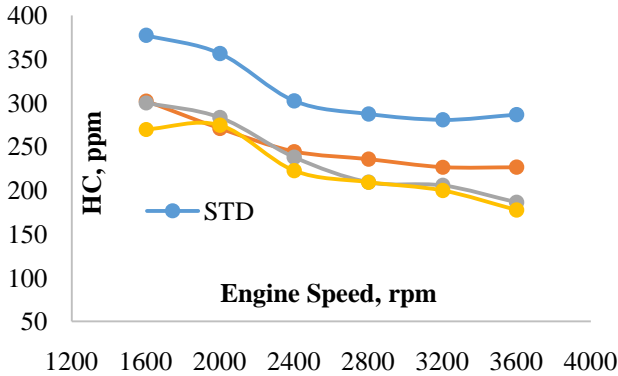


Figure 5. Comparison of HC Emissions

2) NOx Emissions

Figure 6 illustrates the comparison of NOx Emissions of steam injected (S20), TBL coated piston (MgOZrO₂ ceramic component) (STD TBL), TBL coated piston with steam injection (TBL+S20) and Standard SI engine (STD). As can be seen from the Figure that the most decrease in NOx Emissions is 50.7% at 2800 rpm in comparison to standard gasoline engine and 20% steam injection. The minimum NOx emissions is found as 1281 ppm at 3600 rpm with S20.

3) CO and CO₂ Emissions

Figure 7 and 8 illustrate the comparison of CO and CO₂ Emissions of steam injected (S20), TBL coated piston (MgOZrO₂ ceramic component) (STD TBL), TBL coated piston with steam injection (TBL+S20) and Standard SI engine (STD), respectively. As can be seen from the Figure that the most decrease in CO and CO₂ Emissions is 50.7% at 3600 rpm and 4.5% at 1600 rpm in comparison to standard gasoline engine and 20% steam injection, respectively. The minimum CO and CO₂ Emissions are found as 1.25% at 2000 rpm and 10.99% at 3600 rpm with Standard SI Engine, respectively.

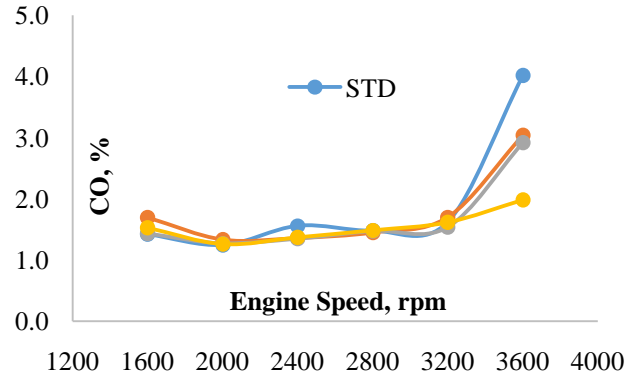


Figure 7. Comparison of CO Emissions

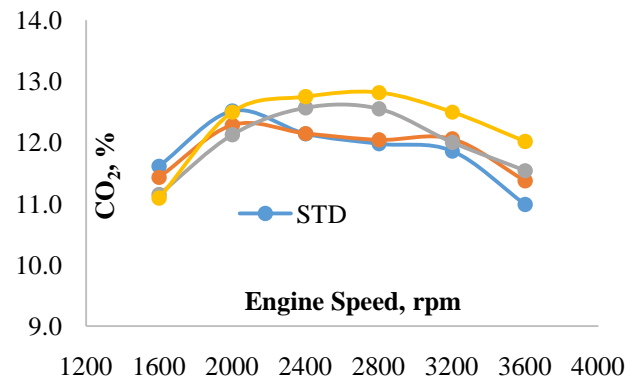


Figure 8. Comparison of CO₂ Emissions

IV. CONCLUSION

In the study, the effects of electronic controlled steam injection on standard SI engine and partially coated SI engine

are investigated experimentally. The study showed that when the steam injection is applied to both two SI engine modes, the performance and exhaust emissions have been improved significantly and corrosive side effects can be eliminated. The method can be adopted to SI engines in real applications.

ACKNOWLEDGMENT

This work has been supported by The Scientific and Technological Research Council of Turkey and was performed within The Support Programme for Scientific and Technological Research Projects (1001) with the project number of 111M065 and Sakarya University Inter Discipline Scientific Projects Program with the project number of 2012-05-04-012.

REFERENCES

- [1] A. Parlak, "The Investigation Experimental of Effect of Thermal Barrier Coating on a Turbo-Charged Diesel Engine Injection Timing and Compression Ratio", Sakarya University, Scientific Institute, PhD Thesis, 2000.
- [2] A. Parlak, "The effect of Heat Transfer on Performance of The Diesel Cycle and Exergy of The Exhaust Gas Stream in a LHR Diesel Engine at The Optimum Injection Timing", *Energy Conversion and Management* 46, pp. 167–179, 2005.
- [3] Muhammet Cerit, "Thermo mechanical analysis of a partially ceramic coated piston used in an SI engine", *Surface & Coatings Technology*, 205 (2011) 3499–3505.
- [4] A. Parlak, V. Ayhan, "Effect of using a piston with a thermal barrier layer in a spark ignition engine", *J. Energy Inst.* 80 (4) (2007).
- [5] M. Cerit, V. Ayhan, A. Parlak, H. Yasar, "Thermal analysis of a partially ceramic coated piston: Effect on cold start HC emission in a spark ignition engine", *Appl. Therm. Eng.* 31 (2–3) (2011) 336-341.
- [6] H.S. Soyhan, M. Yıldırım, M.I. Karamangil, A. Sürmen, Z. Gül, Third Mediterranean Combustion Symposium, Morocco, June 2003.
- [7] M.A. Marr, "An Investigation of Metal and Ceramic Thermal Barrier Coatings in a Spark-Ignition Engine", M.S thesis, Mechanical and Industrial Engineering, University of Toronto, 2009.
- [8] M. Weilenmann, P. Soltic, C. Saxer, A. Forss, N. Heeb, "Regulated and nonregulated diesel and gasoline cold start emissions at different temperatures", *Atmospheric Environment*, Volume 39, Issue 13, April 2005, Pages 2433–2441.
- [9] M. Durat, M. Kapsiz, E. Nart, F. Ficici, A. Parlak, "The effects of coating materials in spark ignition engine design", *Materials and Design* 36 (2012) 540–545.
- [10] S.H. Chan, "Performance and emissions characteristics of a partially insulated gasoline engine", *Int. J. Therm. Sci.* (2001) 40, 255–261.
- [11] V. Esfahanian, A. Javaheri, M. Ghaffarpour, "Thermal analysis of an SI engine piston using different combustion boundary condition treatments", *Applied Thermal Engineering* 26 (2006) 277–287.
- [12] R.A. Miller, "Thermal Barrier Coatings for Aircraft Engines: History and Directions", *Journal of Thermal Spray Technology*, Volume 6(1), (1997), 35-42.
- [13] S.H. Chan and K.A. Khor, "The Effect of Thermal Barrier Coated Piston Crown on Engine Characteristics", *Journal of Materials Engineering and Performance*, Volume 9(1), 2000, 103-109.
- [14] I. Cesur, A. Parlak, V. Ayhan, B. Boru, G. Gonca, "The effects of electronic controlled steam injection on spark ignition engine", *Applied Thermal Engineering*, Vol. 55 (2013) 61-68.

Authors Index

Abdellatif, N.	44, 123	Ibrahim, N. L. N.	173	Salleh, E.	173
Abdel-Meguid, M.	86	Kalogirou, K.	105	Sandhu, K. S.	149
Abdessamed, H.	123	Kalus, M.	74	Sandhu, K. S.	220, 232
Abdi, J.	216	Kiliánová, H.	227	Sandhu, N. S.	232
Abid, M.	211	Kökkülünk, G.	236	Sarbu, I.	30, 178
Aissaoui, A. G.	211	Kozłowski, A.	74	Sathans	166
Al-Duwaish, H.	160	Kumar, A.	111, 149	Sauhats, A.	38
Al-Hamouz, Z.	160	Kumar, M.	149	Sauhats, A.	50
Al-Isawi, S. J.	69	Lavrishchev, O. A.	197	Sebarchievici, C.	30
Almulla, L.	224	Lopes, J. B.	130	Sharma, N. K.	118
Anh, T. V.	63	Lopes, W. G. R.	130	Shrivastava, R.	118
Aoki, A. R.	130	Machar, I.	227	Siebert, L. C.	130
Ayhan, V.	236	Maraaba, L.	160	Silva Filho, J. F.	130
Bajaj, S.	220	Martins, L. B.	21	Singh, G. K.	204
Bekiaris, E.	105	Messerle, V. E.	197	Šiška, P.	98
Berjozkina, S.	50	Miedzinski, B.	74	Sivanagaraju, S.	57, 185
Bochkarjova, G.	38	Mudoun, A.	134	Sood, Y. R.	91, 118
Boru, B.	236	Murty, V. V. S. N.	111	Sopian, K.	173
Cesur, I.	236	Naresh Babu, A. V.	57	Srikumar, K.	57, 185
Chuong, T. T.	63	Neimane, V.	50	Suresh, C. V.	57, 185
Chuvychin, V.	38	Nollet, F.	211	Swarup, A.	80
Dahiya, R.	204	Nunes, M. L.	21	Tahour, A.	211
Dan, D.	30	Oliveira, R. F.	21	Teixeira, S. F.	21
Eddine, G. D.	44, 123	Pal, Y.	80	Tiwari, P. K.	91
El Berrichi, F. Z.	191	Parlak, A.	236	Ustimenko, A. B.	197
Elewa, M. T.	157	Pechanec, V.	227	Vadhera, S.	232
Essounbouli, N.	211	Petrichenko, L.	50	Valea, E. S.	178
FamilKhalili, A.	216	Petrichenko, R.	38	Vávra, A.	227
Ferreira, A. C.	21	Petsos, C.	105	Wahiba, K.	123
Ganesh, A.	204	Poláčik, S.	98	Wosik, J.	74
Ganesh, V.	185	Rohilla, J.	166	Yamakawa, E. K.	130
Guseva, S.	50	Sadin, M. F. M. A.	173	Zen, S.	191
Hatem, T. M.	86, 157	Saidi, H.	134		